

Femtosecond Multidimensional Electronic and Raman Spectroscopy towards the Study of Mn Complexes  
and the Oxygen Evolving Complex: Developing Understanding of Femtosecond Light Generation and  
Applying Femtosecond Multidimensional Electronic and Raman Spectroscopies to Model Systems

By

Paul C. Hebert

A dissertation submitted in partial fulfillment of  
the requirements for the degree of

Doctor of Philosophy  
(Chemistry)

at the

UNIVERSITY OF WISCONSIN-MADISON

2016

Date of final oral examination: 5/26/2016

The dissertation is approved by the following members of the Final Oral Committee:

John C. Wright, Professor, Chemistry

Timothy H. Bertram, Assistant Professor, Chemistry

Thomas Brunold, Professor, Chemistry

Randall H. Goldsmith, Assistant Professor, Chemistry

Deniz Yavuz, Professor, Physics

## Acknowledgements

Over the course of several years, one will undoubtedly interact with many people, especially within the confines of a graduate program. As such, before getting into the scientific content, I would like to acknowledge the contributions, assistance, and support many people and programs offered throughout my time here. In some semblance of an order, I would like to thank:

- the opportunity made available through funding by the National Science Foundation, both for the project encompassing the work described in this thesis as well as funding through the Graduate Research Fellowship Program;
- the various faculty members that have made time in their schedules to participate on the committees for my thesis background oral, original research proposal, and thesis defense, including: Tim Bertram (Thesis), Thomas Brunold (TBO, RP, and Thesis), Randy Goldsmith (Thesis), Frank Keutsch (TBO and RP), John Wright (TBO, RP, and Thesis), and Deniz Yavuz (Thesis);
- the faculty and staff that provided the opportunities to teach CHEM 524 and 621: Tim Bertram, Rob McClain, Lloyd Smith, and John Wright; these opportunities have been extremely valuable, providing not only the experience and opportunity to teach and interact with students more directly than I found was available through general chemistry assignments, but new outlooks and approaches towards thinking about chemical instrumentation and experimentation;
- Art Camire (Spectra-Physics), Joe Juenemann (Spectra-Physics), Gediminas Veitas (Light Conversion), Dave Virgillito (Spectra-Physics), and Dmitriy Vorobyev (Spectra-Physics), with whom my many interactions and communications have provided instructive and valuable insights into the fundamental processes at play in ultrafast lasers in addition to the experience and knowledge necessary for maintenance and alignment of these systems;
- the many current and former members of the academic, facilities, and support staff, without whom the challenges associated with research would not merely be challenging, but in many cases, impossible; I in no way, shape, or form attempt to pass this off as a complete list, but would mention specifically the contributions and assistance of: Phill Bloedow, Arrietta Clauss, Bill Goebel, Bruce Goldade, Brad Herring, Teresa Knudson, Sue Martin-Zernicke, Rob McClain, Steph Nagle, Jeff Nielsen, Dennis Reece, Kyle Roux, Matt Sanders, and Chad Skemp;
- the present and former graduate students and scientists of the Wright group, particularly: Stephen



Block, Lena (Yurs) Woodis, and Ross Lovely, who were among the first to welcome me into the group; Stephen, additionally for the valuable insights when first attempting to navigate the complex field of multidimensional spectroscopy and the initial instruction in picosecond OPA and system alignment; Andrei Pakoulev, for his insights, suggestions, and contributions throughout many discussions; Dan Kohler, for many intriguing and interesting conversations on numerous topics in nonlinear spectroscopy, as well as advice and insights into the capabilities and functionalities available in NumPy and SciPy; Skye Kain, for his extensive work on COLORS, without which the experiments described would not have been possible; Blaise Thompson, for his contributions maintaining and updating COLORS, and the advice and insights on the usage and functionalities of NumPy and SciPy; and Blaise, Dan, and Eric Hagee, with whom the experimental data in Ch. 4 was collected;

- John Wright, not only for the opportunity to pursue the research described herein, but the flexibility to pursue new directions as they presented themselves; additionally, for the many hours of instruction, both in class and the many interactions over the past several years, and without whose insights many of the connections and ideas described in this thesis would still be completely opaque;
- the many friends I have made during my time in Madison, and whose camaraderie and support provided a valuable network of advice, commiseration, surrogate family, and enjoyable times during our graduate careers and hopefully into the future; again, by no means claiming to invoke a complete list, including Shy Bhattacharya, Stephen Block, Jennifer Faust, Jaritza Gomez-Zayas, Elvin Morales-Perez, Leith Samad, and Kate Skog.
- my family, both immediate - my parents, Chris and Deb, and sister, Sarah; extended - especially my grandparents, Babci (Dorothy Cook), Dzia-Dzia (Robert Cook), Vó (Gloria), and Vô (Arthur); recently extended - Greg, Lisa, Andrew, and Amy Christison - and recently even more extended - Roy and Minerva Christison and Betty Slater. The support provided by family - both biological and by law - is irreplaceable, and without the foundation provided by the upbringing and opportunities from my parents, I would not be where I am today;
- and, finally, my friend and wife, Kelly, without whose advice, company, encouragement, levelheadedness, patience, stubbornness, and support I would not have gotten through graduate school; now, we get to pursue the next stage of our lives.

## Table of Contents

Acknowledgements . . . . .	i
Table of Contents . . . . .	iii
List of Figures . . . . .	vi
List of Tables . . . . .	vii
Abstract . . . . .	viii
<b>1 Introduction</b>	<b>1</b>
<b>2 Equipment</b>	<b>5</b>
2.1 Light Generation . . . . .	6
2.2 Chillers . . . . .	8
2.3 Light Manipulation and Detection . . . . .	9
<b>3 Theory</b>	<b>12</b>
3.1 Description of Electromagnetic Radiation . . . . .	13
3.1.1 Light as Electromagnetic Waves . . . . .	13
3.1.2 Polychromatic Electric Fields . . . . .	18
3.2 Polarizations . . . . .	24
3.2.1 Phase Matching of Nonlinear Experiments . . . . .	32
3.2.2 Susceptibilities . . . . .	36
3.3 Maxwell's Equations and the Wave Equation . . . . .	42
3.3.1 Wave Equation . . . . .	42
3.3.2 Maxwell's Equations . . . . .	43
3.3.3 Derivation of the Generalized Wave Equation . . . . .	45
3.4 Pulse Propagation in Dispersive Media . . . . .	47
3.4.1 General Treatment of Pulse Propagation in Dispersive Media . . . . .	47
3.4.2 Relaxing the Slowly Varying Amplitude Approximation . . . . .	57

3.4.3	The Propagation of Pulsed Gaussian Beams . . . . .	58
3.4.4	Integration of the Nonlinear Polarization Outside the Plane Wave Limit . . . . .	69
3.5	Group Velocity, Group Velocity Mismatch, and Group Velocity Dispersion . . . . .	74
3.5.1	Effects of Group Velocity and Group Velocity Dispersion . . . . .	75
3.5.2	Calculating Group Velocity and Group Velocity Dispersion . . . . .	79
3.6	Numerical Integration of Ordinary Differential Equations . . . . .	81
<b>4</b>	<b>Simulation of Sum-Frequency Idler Generation</b>	<b>86</b>
4.1	Background . . . . .	87
4.2	Methodology . . . . .	93
4.3	Results and Discussion . . . . .	100
<b>5</b>	<b>Manganese Tetraphenylporphine</b>	<b>124</b>
5.1	Background . . . . .	125
5.2	White Light Generation . . . . .	127
5.3	Experimental Deviations . . . . .	129
5.4	Results and Discussion . . . . .	130
<b>6</b>	<b>Broadband Coherent Raman Spectroscopy</b>	<b>136</b>
6.1	Background . . . . .	137
6.2	Experimental Deviations . . . . .	147
6.3	Results and Discussion . . . . .	150
<b>A</b>	<b>Appendix A</b>	<b>165</b>
<b>B</b>	<b>Appendix B</b>	<b>213</b>
B.1	Dispersion of Benzene . . . . .	214
B.2	Dispersion of BK7 Glass . . . . .	214
B.3	Dispersion of Air . . . . .	215
B.4	Dispersion of $\beta$ -Barium Borate . . . . .	215
<b>C</b>	<b>Appendix C</b>	<b>219</b>
C.1	<code>user_settings.py</code> . . . . .	221
C.2	<code>parameters.py</code> . . . . .	228
C.3	<code>material_params.py</code> . . . . .	233

C.4	nl_crystal.py . . . . .	244
C.5	phasematching.py . . . . .	258
C.6	efield.py . . . . .	266
C.7	controls.py . . . . .	270
C.8	algorithm.py . . . . .	290
C.9	gain_formulae.py . . . . .	295
C.10	plotting_routines.py . . . . .	305
<b>D</b>	<b>Appendix D</b>	<b>322</b>
D.1	parameters.py . . . . .	323
D.2	operations.py . . . . .	338
D.3	main.py . . . . .	356
	<b>References</b>	<b>362</b>

## List of Figures

3.1	Mode-locking of electric fields. . . . .	25
3.2	Simulation of the effects of group velocity. . . . .	77
3.3	Simulation of the effects of group velocity mismatch. . . . .	78
3.4	Simulation of the effects of group velocity dispersion. . . . .	80
4.1	Observed sum-frequency idler tuning in TOPAS-C. . . . .	94
4.2	Observed signal tuning in TOPAS-C. . . . .	95
4.3	Comparison of BBO group velocity mismatch as calculated from different dispersion formulae. . . . .	98
4.4	Results of second-harmonic test calculations. . . . .	104
4.5	First moment analysis of simulated signal tuning. . . . .	107
4.6	Zeroth moment analysis of simulated signal tuning. . . . .	108
4.7	Theoretical phase matching for Type I and Type II process in BBO. . . . .	109
4.8	Simulated tuning curves for sum-frequency idler simulations. . . . .	110
4.9	Simulated signal and idler spectra. . . . .	112
4.10	Simulated sum-frequency idler spectra. . . . .	113
4.11	Comparison of the sum-frequency idler simulation to the pump-idler and pump-signal group velocity mismatch. . . . .	116
4.12	Comparison of the sum-frequency idler simulation to phase matching bandwidth estimate. . . . .	118
4.13	Analysis of sum-frequency idler simulation in the context of published theory. . . . .	122
5.1	Manganese(III) Tetraphenylporphine Data Summary. . . . .	132
6.1	Narrowband Raman probe temporal profile. . . . .	149
6.2	Comparison of narrow- and broadband probing of broadband CARS. . . . .	152
6.3	Near infrared broadband CARS of carbon tetrachloride. . . . .	153
6.4	Near infrared broadband CARS of benzene. . . . .	155
6.5	Near infrared broadband CARS of benzene and pyridine. . . . .	156

6.6	Visible broadband CARS of benzonitrile. . . . .	159
6.7	Visible broadband CARS of benzene. . . . .	160
6.8	Spectrally broader near infrared broadband CARS of benzene. . . . .	161
6.9	Monochromator slices exploring modulations in broadband CARS. . . . .	162

## List of Tables

4.1	Parameters used for sum-frequency idler simulations. . . . .	101
4.2	Parameters used for second-harmonic test simulations. . . . .	103

**Abstract**

The oxygen evolving complex of photosystem II is a tetramanganese complex that catalyzes the oxidation of water to dioxygen. Many experimental methods have been employed to study this complex, including a variety of spectroscopic methods. The complexity of the surrounding protein environment challenges reliable interpretation of the spectral features and discrimination between changes in the complex and the many cofactors of photosystem II. We have proposed coherent multidimensional spectroscopy in the mixed time-/frequency-domain as a strategy for exploring the spectroscopy of this important system. Coherent multidimensional spectroscopy is performed by the temporal synchronization and spatial overlap of a sequence of fields to induce a polarization in the material. The fields induced by polarizations meeting certain energy- and momentum-criteria are sampled; the intensity of the fields as functions of frequency and time elucidate the spectral and temporal characteristics of the sample's quantum states. Here, we describe efforts to extend the spectroscopy of model transition metal complexes to the femtosecond regime. We present the implementation of white-light transient absorption and demonstrate our ability to reproduce the spectroscopic behavior of manganese (III) tetraphenylporphine with improved time resolution over previously published results; we discuss the limitations encountered when extending this spectroscopy to homodyne-detected transient grating methods. We have implemented a strategy for broadband coherent anti-Stokes Raman spectroscopy, showing the results of these efforts. A theoretical background into the pulse propagation effects in the ultrafast regime of femtosecond spectroscopy has been compiled. We have found these propagation effects to have profound importance in the tuning and amplification of femtosecond pulses, and we present the results of simulations exploring how these effects manifest and influence the behavior of a particular process employed in light generation in a commercial traveling-wave optical parametric amplifier.

CHAPTER 1

**Introduction**



Photosynthesis in algae, cyanobacteria, and plants is a cooperative effort involving an array of proteins.[1, 2] As an assembly, these proteins accumulate energy from the sun, using this energy to drive a sequence of redox reactions with the ultimate goal of sequestering carbon in the form of sugars.[2] The conversion of carbon dioxide to sugar is also accompanied by the four-electron oxidation of water to form dioxygen.[1, 2] This ensemble of reactions is facilitated by a wide variety of cofactors, including: carotenoids and chlorophylls that facilitate the transfer of energy; redox active species such as quinones and pheophytins that chaperone the exchange of charge; and, inorganic cofactors such as chloride and calcium.[2] The amino acids of the proteins are also understood to contribute in these reactions,[1, 2] and the larger protein environment aids in stabilizing the charge separation required throughout these processes.[1]

The specificity of photosystem II towards the oxidation of water has attracted significant attention in the hopes of reproducing its capabilities in synthetic catalysts. Photosystem II's catalytic center is the oxygen evolving complex (OEC), an inorganic complex constituting four manganese and one calcium, bridged by oxygen, and coordinated by various residues.[1, 2] The role of the OEC in photosynthesis is the accumulation of charge and potential to facilitate the four-electron oxidation of water.[2] The necessary charge and potential is accumulated during the Kok cycle, a five-state model for the catalytic process of the OEC.[1, 2] Each step of the Kok cycle is initiated by the absorption of a photon by various light-harvesting proteins; this energy is transferred to P680 by various chlorophyll and carotenoid cofactors.[2] This energy electronically excites P680, permitting a series of redox reactions involving cofactors such as pheophytins and quinones and facilitating charge separation: the electron is chaperoned to photosystem I, while the OEC is the final donor in a chain of exchanges that replace P680's lost electron.[2] Donation of this electron oxidizes the OEC, advancing the catalyst to the next stage of the Kok cycle, which is denoted as a transition from the state  $S_n$  to the state  $S_{n+1}$ . [1, 2] Four sequential oxidations provide the requisite charge and potential for catalysis of water oxidation.[2]

The OEC is tailored specifically towards the oxidation of water to dioxygen: its potential is such that oxidation only occurs upon the accumulation of four oxidizing equivalents.[2] This specificity has attracted significant attention, with many different experimental methods employed towards studying the structure and function of photosystem II and the OEC. These methods include x-ray absorption,[3–10] fluorescence,[11] diffraction,[12] and scattering;[13, 14] electron paramagnetic resonance;[6, 15–33] electronic spectroscopy;[34–56] vibrational spectroscopy;[57–62] and theoretical calculations.[22, 63–75]

However, each of the aforementioned experimental methods has challenges associated with it. X-ray-based spectroscopies have been shown capable of inducing redox damage to the OEC,[8, 10] raising questions whether x-ray characterization is truly characterizing the OEC in one of the states of the Kok cycle.[65,

66] While electron paramagnetic resonance (EPR) provides direct sampling of the manganese cluster, this method has traditionally been considered to be sensitive only to the  $S_2$  state. More recently, EPR spectra associated with the  $S_0$ ,<sup>[19, 28, 29]</sup>  $S_1$ ,<sup>[21, 26]</sup> and  $S_3$ <sup>[20, 21, 32, 76]</sup> states have been reported, though some of these signals require chemical additives in order to be detected.<sup>[19, 28–30]</sup> Chemical additives and the removal of certain cofactors can also modify the EPR signature of the different states of the OEC.<sup>[15, 21–23]</sup> Care must be taken to account for the changes induced by optical excitation, as near infrared and visible excitation have been reported to modify various EPR signatures of the OEC;<sup>[15–18, 20, 21, 25, 27, 32]</sup> these optically-induced changes are impacted by both temperature and photosystem II source.<sup>[18]</sup> Finally, spectroscopic methods - both electronic and vibrational - seek to characterize a complex mixture with many contributing species. In addition to the protein environment, many of the cofactors of photosystem II have been shown to exhibit significant spectroscopic contributions, either from changes in redox state or from changes in the surrounding dielectric environment.<sup>[35–38, 40, 46, 48–50, 52, 54–56, 77–84]</sup> These changes in the spectroscopy of the cofactors will also manifest in the difference spectra obtained from advancement through the Kok cycle,<sup>[36, 38, 40, 44, 50, 55, 56, 77, 83]</sup> challenging the specific identification of spectral changes definitively associated with the OEC.<sup>[41–43]</sup> In order to obtain insights from less complex systems, a variety of mimics have been synthesized and characterized. Some of these samples are structural mimics,<sup>[60, 85–88]</sup> while others are intended as functional mimics exhibiting catalytic activity.<sup>[89–97]</sup> It is not always obvious that similar electronic states and behaviors are expected from these mimics as are observed from the OEC, however.

We have proposed the application of coherent multidimensional spectroscopy (CMDS) to the OEC as a means to improve spectral resolution and specificity. As a multidimensional method, CMDS distributes the spectral information across multiple dimensions, improving our ability to resolve these features. Signals derived from coupled quantum states increase the specificity of the method, permitting more reliable assignment of the observed spectral features. In the mixed time- and frequency-domain, CMDS is performed through the temporal synchronization and spatial overlap of multiple ultrafast (picosecond or femtosecond) pulses. The sample serves as a nonlinear medium, coupling the fields through induced polarizations. The magnitude of these polarizations scales with the effective nonlinear susceptibility of the material; the susceptibility may be related to the properties of the quantum states of the sample, exhibiting enhancement through resonance. The resulting polarizations can either induce changes in one of the excitation fields through self-heterodyning or may be spatially resolved from the input fields through homodyne-detection. Spectral and spatial discrimination permit the isolation of contributions from distinct polarizations. Variation in the relative temporal ordering and the frequencies of the excitation fields permits the characterization

of the dynamics and lineshapes of the contributing quantum states.[98–100]

Here we describe efforts aimed towards the goal of characterizing the OEC by CMDS, reporting the implementation of femtosecond electronic spectroscopy of a representative transition metal complex and broadband coherent anti-Stokes Raman spectroscopy. We have found implementation of CMDS in the femtosecond domain to be complicated by various pulse propagation effects; we describe a theoretical framework for understanding these effects and their manifestation in light generation. These topics are organized as follows. In Ch. 2, we provide an overview of the Wright group’s femtosecond laser system and standard operating procedure; a collection of notes on the maintenance and alignment of the lasers constituting this system are compiled as a supplement in Appendix A. In Ch. 3, we outline a theoretical framework in which various pulse propagation effects may be understood, building up from the fundamental behavior of electric fields and polarizations to detailing the derivation of formulae that explicitly account for the effects of dispersion and polarizations on the propagation of ultrafast pulses. We apply this theory in Ch. 4, in which we attempt to unravel unexpected behavior in the generation of ultrafast pulses within our traveling-wave optical parametric amplifiers. Finally, Ch. 5 and Ch. 6 present experimental results on the topics mentioned previously. In Ch. 5, we describe the setup and implementation of white light transient absorption, present our ability to reproduce the transient absorption of manganese (III) tetraphenylporphine with better temporal resolution than previously reported, and discuss the extension of spectroscopy on this complex to homodyne-detected transient grating. Finally, Ch. 6 details our efforts implementing broadband coherent anti-Stokes Raman spectroscopy. Appropriate and specific background information on the topics relevant to Ch. 4, Ch. 5, and Ch. 6 is provided in the introduction to each chapter.

**CHAPTER 2**

**Equipment**

## 2.1 Light Generation

Here we will provide a brief description of the design, layout, and operating procedures of the Wright group's femtosecond laser system at this time. Throughout this discussion, we will use a tilde ( $\sim$ ) to indicate that the reported value is approximate: this will alternately be used to indicate that the reported value is an optimum from which some deviation should be anticipated, or to indicate the actual value is unimportant and we wish to merely provide an estimate of the average observed under standard operation. The information is derived from the manuals, interactions with the technicians, or experience maintaining and aligning the equipment. Detailed descriptions of alignment and maintenance procedures for the lasers will not be provided here; rather, the notes collected during interactions with the service technician have been digitized and appended in Appendix A. The reader is advised to consult these notes for details as needed.

The system begins with the Millennia V (Spectra-Physics, Santa Clara). This is a cw laser with a Nd:YVO<sub>4</sub> gain medium; the rod is excited by two diode lasers with emission  $\sim 809$  nm. The 1064 nm lasing of the Nd:YVO<sub>4</sub> undergoes intracavity frequency doubling in a temperature phase matched lithium triborate crystal. The Millennia V is capable of supplying up to 5.5 W of the resulting 532 nm radiation. Typically, the Millennia V is set to yield  $\sim 4$  W to pump the Ti:Al<sub>2</sub>O<sub>3</sub> femtosecond oscillator, the Tsunami (Spectra-Physics, Santa Clara). The Tsunami oscillates with a repetition rate of  $\sim 80$  MHz and yields pulses with  $\sim 60$  nm FWHM and  $\sim 30$ -35 fs duration. Mode locking can be initiated through an acousto-optic modulator via the Model 3955 electronics module control; it is believed that mode locking is intended to be sustained through Kerr lensing, though the acousto-optic modulator can also be used. With  $\sim 4$  W from the Millennia V, the output energy of the Tsunami is expected to be  $\sim 6$  nJ per pulse ( $\sim 500$  mW); typically cw operation yields slightly higher ( $\sim 30$  mW) power than mode locked operation.

The pulse train from the Tsunami is split ( $\sim 35\%/65\%$ ) to seed both the femtosecond (Spitfire Pro XP, Spectra-Physics, Santa Clara) and the picosecond (Spitfire Ace, Spectra-Physics, Santa Clara) regenerative amplifiers. The regenerative amplifiers are pumped by Q-switched, Nd:YLF nanosecond lasers (Empower, Spectra-Physics, Santa Clara). The Empower is a multimode laser with  $\sim 5$  ns duration. The Nd:YLF rod is pumped by diodes and lases at 1053 nm. Temperature phase matched lithium triborate is again used for frequency doubling. The Spitfire is designed to be pumped with 20 W from the Empower; ideally, this should be attained with  $\sim 20$  A of current supplied to the diodes. At this time, the Empower pumping the femtosecond Spitfire Pro XP requires  $\sim 22$  A to achieve this power: it is believed that the shorting of a diode clip introduced smoke or debris that is reducing the efficiency of the cavity, and that proper cleaning may return operation closer to expected specifications. Amplification in the Spitfire is based upon chirped pulse

amplification: the pulses from the Tsunami are stretched from  $\sim 30\text{-}35$  fs duration to hundreds of picoseconds in the stretcher. A pair of Pockels cells isolates single pulses from the Tsunami's pulse train for amplification; the isolation of these pulses reduces the repetition rate from  $\sim 80$  MHz to the repetition rate of the Empower, which is generally operated at the maximum allowed repetition rate of 1 kHz. Optimum amplification can usually be achieved with only 10 passes through the rod, though the Spitfire is often operated at 11 passes for long-term stability; if longer build up times are required, it is advisable to check on the alignment of the amplifier, as additional passes through the cavity will result in the accumulation of nonlinear chirp. The Pockels cells also provide the Q-switch to release the amplifier pulse from the cavity. After release from the cavity, the mode of the amplified pulse is expanded by a telescope prior to recompression. The recompressed output exhibits a bandwidth of  $\sim 35$  nm, a duration of  $\sim 35\text{-}40$  fs, and pulse energies of  $\sim 4$  mJ ( $\sim 4$  W at the standard 1 kHz repetition rate).

Outside the Spitfire, a sequence of beamsplitters and mirrors split the output ( $\sim 50\%/45\%/5\%$ ); the mirrors route the  $\sim 50\%$  and  $\sim 45\%$  portions to pump two traveling-wave optical parametric amplifiers (TOPAS-C, Light Conversion, Vilnius, Lithuania). Within each OPA, this pump beam is split 97.5%/2.5%. The smaller portion is split further (distribution unknown) and used to generate a seed pulse: a temporally dispersed white light continuum is produced using one fraction, and this continuum is overlapped in a  $\beta$ -barium borate crystal (BBO, 2.5 mm,  $\theta = 28^\circ$ ,  $\phi = 0^\circ$ ) with the other fraction. With proper angle tuning and delay compensation, the seed is amplified, ideally to yield  $\sim 1.5$   $\mu\text{J}$ . The seed is imaged onto a second BBO (2 mm,  $\theta = 28^\circ$ ,  $\phi = 0^\circ$ ), along with the 97.5% fraction of the pump. Optimization of temporal overlap and phase matching angle result in significant amplification of the seed: the sum of the energies of the resulting signal and idler may be as high as 700  $\mu\text{J}$ , though 500-650  $\mu\text{J}$  appears to be common. The TOPAS-C incorporates multiple mixer options for upconversion of the signal and idler to frequencies throughout ultraviolet, visible, and near infrared. The second harmonic of the signal and idler provide spectral coverage from  $\sim 570\text{-}800$  nm and  $\sim 800\text{-}1140$  nm, respectively. The crystal used to phase match both second-harmonic generation processes is a 0.3 mm BBO ( $\theta = 23^\circ$ ,  $\phi = 90^\circ$ ). Upconversion of signal and idler by sum-frequency generation with the residual pump provides coverage between  $\sim 470\text{-}530$  nm and  $\sim 535\text{-}610$  nm, respectively. The sum-frequency idler process is generated in the same crystal as second-harmonic generation (0.3 mm BBO,  $\theta = 23^\circ$ ,  $\phi = 90^\circ$ ); signal is upconverted in a different 0.3 mm BBO ( $\theta = 23^\circ$ ,  $\phi = 90^\circ$ ). It is noted here that the sum-frequency process between pump and idler (SFI) has been observed to yield unusual spectral character; this is the topic of Ch. 4. It is suspected that similar effects cause the sum-frequency process for signal to also exhibit sub-optimal characteristics, though the features are more subtle and the necessary characterization has not been performed to date. Though the output is

weak, the fourth harmonics of signal and idler can also be generated; these processes are phase matched in a 0.15 mm BBO ( $\theta = 35^\circ$ ,  $\phi = 90^\circ$ ) and provide spectral coverage between  $\sim 285$ -400 nm and  $\sim 403$ -480 nm, respectively. Crystals for difference frequency generation have been purchased and tested; they are not installed on the system at this time.

The TOPAS-C provide two separate tunable colors; for some experiments, including some of those detailed in later chapters, it is necessary to have a third source available. The third fraction of the fundamental ( $\sim 5\%$  of the amplifier output) provides this third color. When used, the beam size is reduced by a Galilean telescope formed from a  $f = -50$  mm and  $f \approx 100$  mm lens pair to better match the beam size of the TOPAS-C processes and to ensure compatibility with the 1" optics on the table.

## 2.2 Chillers

While the Spitfire rod is thermoelectrically cooled, it still requires an external cooling system. The Millennia V, Tsunami, and Empower also require the support of chillers. At present, the Millennia V, Tsunami, and Spitfires (Pro XP and Ace) share a chiller (Neslab Merlin M33), while the Empowers are each connected to a unique chiller (Polyscience P/N 6360T11SP20C and P/N 6360T11A120C for the femtosecond and picosecond system Empowers, respectively). Operating temperatures are adjusted to optimize performance of each laser. The most recent records indicate operating temperatures of  $18^\circ$  C,  $24.5^\circ$  C, and  $21^\circ$  C for Neslab Merlin M33, the femtosecond Empower Polyscience chiller, and the picosecond Empower Polyscience chiller, respectively. Maintenance on these chillers should be performed on a six-month cycle, with the procedure adapted from documentation; parts of this are also available in the dissertation of Nathan Matthew. It has been noted that Spectra-Physics updates the recommended chiller maintenance procedures from time to time; it is advisable to consult with Spectra-Physics representatives to be apprised up any changes. The current procedure is reproduced below for convenience:

- drain the existing chilling fluid. For Polyscience P/N 6360T11SP20C, this is easily done through the valve installed to the drain outlet on the back of the unit. Neither of the other units have such a valve installed, and can be drained by various methods, including syphoning and using the chiller's pump to drain the fluid. Care should be made to drain the fluid from the hoses and the filter reservoir;
- remove the existing filters;
- reconnect the hoses such that the flow path excludes the lasers, then fill the chillers with Nalco cleaning solution 460-CCL2567. The change in flow path is necessary to protect the lasers from the cleaning

solution. As the current hardware for the Polyscience P/N 6360T11SP20C does not support the exclusion of the femtosecond Empower cavity from the flow path, the usage of cleaning solution has been skipped in this unit, simply cycling distilled water instead. The chillers should be run as indicated for at least thirty minutes;

- drain the chillers, flushing the cleaning solution using distilled water. Distilled water should be added and drained from the chillers until suds are no longer observed. This usually takes a few gallons of distilled water per chiller, though more may be required;
- with the flow paths still excluding the lasers, fill the chillers with distilled water and cycle for at least fifteen minutes, then drain. Repeat this step, cycling the fresh distilled water for at least five minutes;
- drain the chillers once more, then reconnect the lasers, ensuring the flow direction is correct. Install fresh filters and refill the chillers with chilling fluid. All units can be run with distilled water as the chilling fluid. However, as the chilling fluid flows through the optical path of the Empower, Spectra-Physics recommends the usage of Nalco inhibitor 460-PCCL104.

Distilled water can be obtained from any source, but cannot be replaced by deionized water: deionization results in water that is too pure, and the usage of deionized water may cause leeching from the pump. Cleaning usually requires 8-10 gallons of distilled water. The cleaning solution is Nalco 460-CCL2567. This can be acquired from Spectra-Physics (P/N 1607-0547), though at the time of the most recent purchase, it could be purchased directly from Nalco for a lower price. Nalco 460-PCCL104 is the inhibitor solution, and it is also available from either Spectra-Physics (P/N 1607-0546) or Nalco; usually 1 gallon per chiller is necessary. The filters depend upon the chiller: the Neslab Merlin M33 uses a single Pentek P5-478 spun polypropylene filter, while a Harmsco PP-S-1 PolyPleat cartridge has been used in the Polyscience chillers.

### 2.3 Light Manipulation and Detection

Many of the experiments described later were performed in ways that deviate from the standard methodology and configuration. Such differences will be described when appropriate. Here, a brief discussion will be presented on the standard operation at this time.

Following light generation, periscopes based upon reflection at the Brewster angle ensure all processes from the OPAs are vertically polarized; a 90° periscope rotates the polarization of the residual fundamental from horizontal to vertical. The two OPAs and the residual fundamental permit two- or three-color experiments: for two-color experiments, the output from one OPA is split, yielding a series of interactions labeled



$\omega_1$ ,  $\omega_2$ , and  $\omega_2'$ ; for three-color experiments, rather than splitting the OPA, the fundamental is introduced, yielding interactions  $\omega_1$ ,  $\omega_2$ , and  $\omega_{800}$ . One beam is blocked for transient absorption.

The beams needed for an experiment are routed by a series of mirrors. Three delay lines are available for temporal synchronization of the pulses: these delay lines are corner-cube retroreflectors mounted on motorized stages. Commonly, a chopper is introduced to one of the beam lines for background subtraction. From the delay lines, the beams are aligned to an appropriate mask to satisfy the phase matching for a given experiment. The table is designed around a standard BOXCARS geometry with angles of  $\sim 1^\circ$  into the sample. This mask is robust for most experiments with a phase matching condition of  $\mathbf{k}_4 = \mathbf{k}_1 - \mathbf{k}_2 + \mathbf{k}_2'$ ; a small phase mismatch occurs if the difference between  $\omega_1$  and  $\omega_2$  is large (for example, phase matching within the cw approximation predicts phase mismatch should attenuate the intensity less than  $\sim 1\%$  for  $\lambda_1 = 495$  nm and  $\lambda_2 = 615$  nm). The beams are focused into the sample with a  $f = 1$  m mirror. Signal is collected, collimated, and focused into a monochromator. A variety of detectors are available for different frequency regions and different purposes. A homebuilt InGaAs array detector allows increased throughput for expedited signal tuning. For experiments, an InSb detector and a silicon photodiode are commonly used for near infrared and visible frequencies, respectively; both detectors are compatible with the same preamplifier. Photomultiplier tubes are available, but the amplification provided by the current preamplifier's gain limits reliable application: the gain of the preamplifier is sufficiently large that preventing saturation of the signal processing hardware requires operating the PMT with biases significantly below specifications.

The signal from the preamplifier is sampled by a boxcar integrator; synchronization of the integrator and aforementioned chopper allows active background subtraction. The settings on the boxcar are adjusted according to the detector and the sensitivity of the experiment. The output from the boxcar is collected on a National Instrument DAQ card. A LabVIEW program (COLORS) is used to collect the data and interface with the various hardware components. COLORS includes features that allow: tuning, setting, and scanning the OPAs; synchronization of the pulses through the motorized delay lines; and, data collection and processing.

The standard protocol for performing an experiment begins with optimizing light generation. After aligning the output of the regenerative amplifier into the OPAs, recompression is optimized, generally with respect to the white light in the TOPAS-C. Further alignment adjustments to the TOPAS-C are made as needed. The table is aligned according to the appropriate mask for an experiment. Tuning of the signal process in the OPAs can be completed through an automated routine in COLORS. After confirming the signal tuning is acceptable, upconversion processes can be tuned as needed: the recommended tuning procedure is to set the signal to the appropriate color and identify the crystal angle that maximizes the power of

the upconverted process. Alignment through a pinhole is used to achieve spatial overlap of the modes; the pinhole is appropriate for the  $f = 1$  m mirror, but it has been found that for shorter focal lengths it can be more accurate to optimize overlap by eye. Temporal overlap is determined through nonlinear processes in appropriate media. A sequence that has proven convenient is: find and optimize nonlinear signal in KTP, which provides a high nonlinearity and less sensitivity to crystal angle but limits temporal resolution due to available crystal lengths; find and optimize signal in BBO, which enables high temporal resolution due to its shorter length; and, finally, optimize temporal overlap based upon the nonresonant response of an organic solvent. Generally, the solvent is matched to the sample that will be studied, but at times it can be convenient to first find signal in carbon tetrachloride or carbon disulfide due to their high nonlinearities. Zero delay is determined as a function of frequency to permit automatic delay compensation.

CHAPTER 3

Theory

### 3.1 Description of Electromagnetic Radiation

#### 3.1.1 Light as Electromagnetic Waves<sup>i</sup>

In order to apply Maxwell's equations towards understanding the effects of a medium on the propagation of ultrafast pulses and the resulting consequences within nonlinear spectroscopic experiments, we will require both a qualitative and mathematical understanding of light. As we will see in § 3.3, Maxwell's equations predict that the propagation of electric and magnetic fields in free space will assume a functional form consistent with the classical wave equation:

$$\frac{\partial^2}{\partial z^2} f(z, t) = \frac{1}{v^2} \frac{\partial^2}{\partial t^2} f(z, t) \quad (3.1.1)$$

The solutions to the classical wave equation are expected to be wave functions,  $f(z, t)$ , consistent with some functional form propagating at a constant phase velocity,  $v$ . Within this definition of a wave, it is trivial to show the functional dependence of  $f$  on  $z$  and  $t$ . For example, let us consider that we have some functional form corresponding to the wave function at  $t = 0$ ,  $f(z, t = 0)$ . If we want to know the functional form of  $f(z, t)$ , then we simply have to consider: at time  $t$ , how much have we displaced the wave function? For a velocity of  $v$ , this corresponds to  $z = vt$ . Therefore, we would anticipate that  $f(z, t) = f(z \pm vt, 0)$ , where  $\pm vt$  describes displacement of the wave function through propagation in either direction along the  $z$  axis. Since both cases ( $+vt$  or by  $-vt$ ) can be shown to be solutions to Eq. 3.1.1, we can generalize the solution  $f(z, t)$  as their linear combination:[101]

$$f(z, t) = g(z - vt) + h(z + vt) \quad (3.1.2)$$

While any function consistent with Eq. 3.1.2 could describe a wave, a common functional form - and one that will prove a convenient starting point as a description for light - is the sinusoid:<sup>ii</sup>

$$f(z, t) = A \cos [k(z - vt) + \phi] \quad (3.1.3)$$

Within the functional form of Eq. 3.1.3,<sup>iii</sup>  $k$  is the wavenumber of the sinusoid, describing the angular

---

<sup>i</sup>This section is strongly influenced by Griffiths' text on electrodynamics.[101]

<sup>ii</sup>While the functional dependence of the sinusoid is given by the cosine function in Eq. 3.1.3, this is functionally equivalent to the sine function, differing only in the initial phase,  $\phi$ . However, it is more straightforward to relate the complex wave function to the cosine function (see Eq. 3.1.13).

<sup>iii</sup>Note that in Eq. 3.1.3 we have taken the dependence of  $f(z, t)$  upon  $z$  and  $t$  to be  $z - vt$ ; we could have just as easily

frequency of the wave's spatial oscillations: over a distance of  $\Delta z = 2\pi/k$ , the sinusoid completes one cycle. We can recognize this distance as one period of the wave and assign it to be the wavelength,  $\lambda$ , yielding the following relationship between the wavelength and the wavenumber:

$$k\lambda = 2\pi \tag{3.1.4}$$

However, the functional form of Eq. 3.1.3 indicates that changes in time will also cause an evolution of the wave function, with a characteristic frequency of  $kv$ . We can assign this frequency as the angular frequency,  $\omega$ , yielding the following relationships between the wavelength ( $\lambda$ ), linear frequency ( $\nu$ ), and the velocity ( $v$ ) of the wave or between the spatial ( $k$ ) and angular ( $\omega$ ) frequencies and the velocity of the wave:

$$v = \frac{\omega}{k} = \nu\lambda \tag{3.1.5}$$

Finally,  $\phi$  in Eq. 3.1.3 describes the initial phase of the wave, defining the relative delay of the oscillations.

In addition to predicting wave-like behavior for both electric and magnetic fields, Maxwell's equations predict the co-propagation of electric and magnetic fields, yielding electromagnetic radiation: light. The propagation of each field is consistent with the form in Eq. 3.1.3. We will take the electric and magnetic fields as plane waves propagating along an arbitrary  $z$ -axis. For now, it is sufficient to assume both fields to be monochromatic - each consisting of a single frequency component - and to behave as plane waves - with minimal dependence upon the transverse coordinates, taken to be the  $x$ - and  $y$ -axes.<sup>i</sup> Within this model, Maxwell's equations can provide some insight regarding the manner in which the electric and magnetic fields will co-propagate. We will identify the key relationships from Maxwell's equations when appropriate; otherwise, the reader is directed to § 3.3.2, where the forms of Maxwell's equations are presented.

First, since Maxwell's equations describe the behavior of electric and magnetic fields through vector operations, we should assume it is most appropriate to consider the fields as vectors, with separate components oriented along the  $x$ ,  $y$ , and  $z$  axes. We will assume all three components of each field oscillate in phase and

---

taken as convention that the field propagates in the opposite direction,  $z + vt$ . However, the direction of propagation being  $z - vt$  appears to be a common convention.

<sup>i</sup>The plane wave limit is cited as a reasonable approximation as long as the radius of curvature is sufficiently larger than the wavelength of the fields.[101]

at the same frequency:<sup>i</sup>

$$\tilde{\mathbf{E}}(z, t) = \begin{bmatrix} E_{0x} \cos(k_E z - \omega_E t + \phi_E) \hat{\mathbf{x}} \\ E_{0y} \cos(k_E z - \omega_E t + \phi_E) \hat{\mathbf{y}} \\ E_{0z} \cos(k_E z - \omega_E t + \phi_E) \hat{\mathbf{z}} \end{bmatrix} \quad (3.1.6a)$$

$$\tilde{\mathbf{B}}(z, t) = \begin{bmatrix} B_{0x} \cos(k_B z - \omega_B t + \phi_B) \hat{\mathbf{x}} \\ B_{0y} \cos(k_B z - \omega_B t + \phi_B) \hat{\mathbf{y}} \\ B_{0z} \cos(k_B z - \omega_B t + \phi_B) \hat{\mathbf{z}} \end{bmatrix} \quad (3.1.6b)$$

In Eq. 3.1.6a and 3.1.6b,  $\hat{\mathbf{x}}$ ,  $\hat{\mathbf{y}}$ , and  $\hat{\mathbf{z}}$  represent the unit vectors aligned with the  $x$ -,  $y$ -, and  $z$ -axis, respectively, specifying the contribution of each available polarization state to the total field. The magnitude of the contribution of a given polarization state is described as a sinusoid with an amplitude represented by the scalar quantities  $E_{0x}$ ,  $E_{0y}$ ,  $E_{0z}$ ,  $B_{0x}$ ,  $B_{0y}$ , and  $B_{0z}$ . As mentioned previously, each polarization state of a given field is presumed to exhibit the same sinusoidal oscillations as functions of  $z$  and  $t$ . For now, we will maintain a distinction between the frequencies and phases of the two fields, reflected in the notation  $k_E$  versus  $k_B$ ,  $\omega_E$  versus  $\omega_B$ , and  $\phi_E$  versus  $\phi_B$ . We will find that this distinction is unnecessary, however, as Maxwell's equations predict co-propagation of the electric and magnetic fields with matched frequency and phase.

The first simplification of Eq. 3.1.6a and 3.1.6b can be made by invoking Gauss' law and Gauss' law of magnetism. In free space, these laws define the divergence of both fields to be zero, i.e.  $\nabla \cdot \tilde{\mathbf{E}}(\mathbf{r}, z, t) = \nabla \cdot \tilde{\mathbf{B}}(\mathbf{r}, z, t) = 0$ . Since the plane wave limit describes both fields propagating along an arbitrary axis (taken to be the  $z$ -axis) without dependence upon the transverse coordinates, the derivative of the  $\hat{\mathbf{x}}$ -polarized component of each field with respect to  $x$  must be zero; the same must also be true of the derivative of the  $\hat{\mathbf{y}}$ -polarized component with respect to  $y$ . Gauss' laws then leave  $E_{0z} \partial/\partial z \cos(k_E z - \omega_E t + \phi_E) = 0$  and  $B_{0z} \partial/\partial z \cos(k_B z - \omega_B t + \phi_B) = 0$ . As the derivative of a sinusoid is a sinusoid,<sup>ii</sup> these relationships can only

---

<sup>i</sup>Note that we are introducing a notation consistent with Boyd[102] in which quantities oscillating rapidly (i.e. at optical frequencies) in time are denoted by a tilde.

<sup>ii</sup>Recalling  $\partial/\partial x \cos(x) = -\sin(x)$  and  $\partial/\partial x \sin(x) = \cos(x)$ .

be satisfied if  $E_{0z} = 0$  and  $B_{0z} = 0$ . This conclusion allows us to simplify Eq. 3.1.6a and 3.1.6b, yielding:

$$\tilde{\mathbf{E}}(z, t) = \begin{bmatrix} E_{0x} \cos(k_E z - \omega_E t + \phi_E) \hat{\mathbf{x}} \\ E_{0y} \cos(k_E z - \omega_E t + \phi_E) \hat{\mathbf{y}} \\ 0 \hat{\mathbf{z}} \end{bmatrix} \quad (3.1.7a)$$

$$\tilde{\mathbf{B}}(z, t) = \begin{bmatrix} B_{0x} \cos(k_B z - \omega_B t + \phi_B) \hat{\mathbf{x}} \\ B_{0y} \cos(k_B z - \omega_B t + \phi_B) \hat{\mathbf{y}} \\ 0 \hat{\mathbf{z}} \end{bmatrix} \quad (3.1.7b)$$

From these results, we must conclude that both the electric and magnetic fields are transverse waves, and can only be polarized perpendicular to the direction of propagation.

The other simplification to  $\tilde{\mathbf{E}}(z, t)$  and  $\tilde{\mathbf{B}}(z, t)$  can be made through either Faraday's law or Ampere's law. In free space, these laws parallel each other:  $\nabla \times \tilde{\mathbf{E}}(\mathbf{r}, z, t) = -\partial/\partial t \tilde{\mathbf{B}}(\mathbf{r}, z, t)$  and  $\nabla \times \tilde{\mathbf{B}}(\mathbf{r}, z, t) \propto \partial/\partial t \tilde{\mathbf{E}}(\mathbf{r}, z, t)$ .<sup>i</sup> Following Faraday's law ( $\nabla \times \tilde{\mathbf{E}}(\mathbf{r}, z, t) = -\partial/\partial t \tilde{\mathbf{B}}(\mathbf{r}, z, t)$ ), we can evaluate the expressions on both sides of the equality ( $\nabla \times \tilde{\mathbf{E}}(\mathbf{r}, z, t)$  and  $-\partial/\partial t \tilde{\mathbf{B}}(\mathbf{r}, z, t)$ ):

$$\nabla \times \tilde{\mathbf{E}}(z, t) = \begin{bmatrix} E_{0y} k_E \sin(k_E z - \omega_E t + \phi_E) \hat{\mathbf{x}} \\ -E_{0x} k_E \sin(k_E z - \omega_E t + \phi_E) \hat{\mathbf{y}} \\ 0 \hat{\mathbf{z}} \end{bmatrix} \quad (3.1.8a)$$

$$-\frac{\partial}{\partial t} \tilde{\mathbf{B}}(z, t) = \begin{bmatrix} -B_{0x} \omega_B \sin(k_B z - \omega_B t + \phi_B) \hat{\mathbf{x}} \\ -B_{0y} \omega_B \sin(k_B z - \omega_B t + \phi_B) \hat{\mathbf{y}} \\ 0 \hat{\mathbf{z}} \end{bmatrix} \quad (3.1.8b)$$

Faraday's law requires the results of Eq. 3.1.8a and 3.1.8b to be equivalent; we therefore end up with the following pair of equalities:

$$\begin{aligned} E_{0y} k_E \sin(k_E z - \omega_E t + \phi_E) &= -B_{0x} \omega_B \sin(k_B z - \omega_B t + \phi_B) \\ -E_{0x} k_E \sin(k_E z - \omega_E t + \phi_E) &= -B_{0y} \omega_B \sin(k_B z - \omega_B t + \phi_B) \end{aligned} \quad (3.1.9)$$

The equalities of Eq. 3.1.9 informs on two key properties of the co-propagating electric and magnetic fields. First, comparison of the sinusoidal terms on the opposing sides of each equality necessitates coherence between the fields: the equalities can only be satisfied if the electric and magnetic fields exhibit the same

---

<sup>i</sup>For now, it is sufficient to leave the relationship of Ampere's law as a proportionality.

frequency and phase. With this conclusion, we can divide through both equalities in Eq. 3.1.9 by the sinusoidal terms, leaving  $E_{0y} \propto -B_{0x}$  and  $E_{0x} \propto B_{0y}$ . It is trivial to show that this pair of relationships is consistent with:

$$\tilde{\mathbf{B}}(z, t) \propto \hat{\mathbf{z}} \times \tilde{\mathbf{E}}(z, t) \quad (3.1.10)$$

The relationship of Eq. 3.1.10, defining  $\tilde{\mathbf{B}}(z, t)$  by the cross-product of  $\hat{\mathbf{z}}$  - the direction of propagation - and  $\tilde{\mathbf{E}}(z, t)$ , imposes a requirement on the relative polarization of  $\tilde{\mathbf{B}}(z, t)$  and  $\tilde{\mathbf{E}}(z, t)$ : not only must both fields be transverse, but the fields must be perpendicular to each other and satisfy the right-hand-rule with respect to the direction of propagation.

Despite light constituting both electric and magnetic fields, our current scope is exploring the interaction of light and matter within the context of optical spectroscopies. The frequencies relevant to such experiments will generally exclude regimes for which we need to consider interactions between the magnetic field and the material.[99] Consequently, while experiments for which the material response to the magnetic field needs to be considered do exist, we will proceed throughout the following sections considering only the electric field. We will also generally only sample the electric field, and therefore be limited to characterizing the polarizations of two electric fields relative to each other. Even then, while the relative polarizations of interacting fields can be important, we will often be able to make approximations permitting the treatment of the fields as scalar quantities (as we will show in § 3.2.2). Under such assumptions, we can simplify the system described by Eq. 3.1.7a and 3.1.7b to a single expression:

$$\tilde{E}(z, t) = E_0(\omega) \cos(kz - \omega t + \phi) \quad (3.1.11)$$

While Eq. 3.1.11 is consistent with the observed behavior of light and conveniently yields a real-valued function, the form of the wave equation illustrates that the theoretical treatment of field propagation and nonlinear interactions will involve differential equations. In such circumstances, trigonometric functions increase the difficulty in evaluating the relevant expressions. Fortunately, we can make the treatment more tractable through Euler's formula ( $\exp(i\theta) = \cos(\theta) + i \sin(\theta)$ ), which demonstrates that complex exponentials are also oscillatory and - as linear combinations of solutions to the wave equation - valid descriptions of waves.



Therefore, we can consider the complex function:<sup>i</sup>

$$\tilde{E}(z, t) = E_0(\omega)e^{-i(kz - \omega t + \phi)} \quad (3.1.12)$$

as a valid representation for the behavior of an electric field. However, though exponentials are more compatible with differential equations, we still need to ensure that the electric field evaluates to be a real valued function.[101, 102] Some authors[101] address this by defining the real-valued field as the real part of the complex exponential, i.e.  $\tilde{E}(z, t) = \Re\{E_0(\omega) \exp[-i(kz - \omega t + \phi)]\}$ ; many other authors instead recognize the relationship:

$$\begin{aligned} \tilde{E}(z, t) &\propto E_0(\omega)e^{-i(kz - \omega t + \phi)} + \text{c.c.} \\ &\propto E_0(\omega)e^{-i(kz - \omega t + \phi)} + E_0^*(\omega)e^{i(kz - \omega t + \phi)} \\ &\propto E_0(\omega) [\cos(kz - \omega t + \phi) - i \sin(kz - \omega t + \phi) + \cos(kz - \omega t + \phi) + i \sin(kz - \omega t + \phi)] \\ &\propto E_0(\omega) \cos(kz - \omega t + \phi) \end{aligned} \quad (3.1.13)$$

where c.c. represents the complex conjugate of the complex field,  $E_0^*(\omega) \exp[i(kz - \omega t + \phi)]$ . In the second step of the scheme in Eq. 3.1.13, we have assumed  $E_0(\omega) = E_0^*(\omega)$ : since we have assumed  $E_0(\omega) \cos(kz - \omega t + \phi)$  is real-valued,  $E_0(\omega)$  must be real-valued and therefore equal to its conjugate. In the scheme in Eq. 3.1.13, we emphasize the relationship as a proportionality to raise awareness that different authors will scale this relationship differently: while a coefficient of 1/2 will yield a result that matches Eq. 3.1.11,[103] other authors use a coefficient of 1 for each exponential.[102] In order to maintain consistency with Boyd,[102] we will employ the convention that the coefficient of each exponential is 1; when evaluating nonlinear polarizations (see § 3.2), this will result in degeneracy factors that differ from those of other authors by a factor of 2.[103, 110]

### 3.1.2 Polychromatic Electric Fields

Throughout § 3.1.1, we have limited our focus to monochromatic fields - electric fields consisting of a single frequency. While this is a convenient starting point, it is rarely relevant in laser spectroscopy: even in a HeNe laser, it is trivial to end up with multiple cavity modes contributing to the output.[105] However, if a monochromatic field of the form in Eq. 3.1.12 is a valid solution to the relevant wave equation, polychromatic

---

<sup>i</sup>Note that we are taking the component with phase  $\exp[-i(kz - \omega t + \phi)]$  to be our complex wave function; this selection is made to ensure compatibility with our adopted mathematical conventions. This is consistent with some authors,[103–105] but the opposite of others.[99, 101, 102, 106–109]

fields defined as linear combinations of such monochromatic fields must also be valid solutions to the wave equation.[101] Such polychromatic fields can be defined as sums in the manner of Eq. 3.1.14:[102, 105, 111]

$$\tilde{E}(\mathbf{r}, z, t) = \sum_n \tilde{E}_n(\mathbf{r}, z, t) + \text{c.c.} \quad \{n : \omega_n \geq 0\} \quad (3.1.14)$$

where  $\tilde{E}_n(\mathbf{r}, z, t)$  is the monochromatic electric field at frequency  $\omega_n$ . This is equivalent to Eq. 3.1.15, where we have substituted for  $\tilde{E}_n(\mathbf{r}, z, t)$  according to the form in Eq. 3.1.12:

$$\tilde{E}(\mathbf{r}, z, t) = \sum_n E_0(\mathbf{r}, z, \omega_n) e^{-i[k(\omega_n)z - \omega_n t + \phi(\omega_n)]} + E_0^*(\mathbf{r}, z, \omega_n) e^{i[k(\omega_n)z - \omega_n t + \phi(\omega_n)]} \quad \{n : \omega_n \geq 0\} \quad (3.1.15)$$

In Eq. 3.1.14 and 3.1.15, we have introduced the notation  $\mathbf{r}$  to generalize the transverse coordinates ( $x, y$ ); as noted before, we can still treat the fields as plane waves as long as the functional dependence on the transverse coordinates involves changes at scales significantly larger than the wavelength of the field.[101] It should also be noted that we have allowed for the possibility that the amplitude,  $E_0(\mathbf{r}, z, t)$ , exhibits a functional dependence upon the spatial coordinates. This will facilitate our treatment of propagation effects (see § 3.4); we still require the amplitude to be real at this time. We can simplify Eq. 3.1.15 by introducing a complex amplitude that incorporates the phase factor,  $\exp[-i\phi(\omega)]$ .[101] Defining this complex amplitude function,  $\hat{a}(\mathbf{r}, z, \omega)$ :<sup>i</sup>

$$\hat{a}(\mathbf{r}, z, \omega) = E_0(\mathbf{r}, z, \omega) e^{-i\phi(\omega)} \quad (3.1.16)$$

we can simplify Eq. 3.1.15 to yield:

$$\tilde{E}(\mathbf{r}, z, t) = \sum_n \hat{a}(\mathbf{r}, z, \omega_n) e^{-i[k(\omega_n)z - \omega_n t]} + \hat{a}^*(\mathbf{r}, z, \omega_n) e^{i[k(\omega_n)z - \omega_n t]} \quad \{n : \omega_n \geq 0\} \quad (3.1.17)$$

However, we will once again give consideration to mathematical convenience. At the limit in which the summation in Eq. 3.1.17 is sampled over a continuous range of frequencies,[101–103] this summation tends towards the equivalent integral over  $\omega$ . Introducing the appropriate integration factor,<sup>ii</sup>[112, 113] the

---

<sup>i</sup>The notation of the envelope function as  $\hat{a}$  will be clear when we consider the form of the electric field in the regime of continuously varying frequencies.

<sup>ii</sup>The factor of  $2\pi$  introduced with the integration factor  $d\omega$  accounts for the variable of integration being angular frequency.[112, 113] We will ultimately show that the integral in Eq. 3.1.18 represents an inverse Fourier transform (see Eq. 3.1.26), and the one-dimensional Fourier transform between time and angular frequency requires this factor of  $2\pi$  for normalization. While a factor of  $\sqrt{2\pi}$  in both the Fourier transform and the inverse Fourier transform would ensure a unitary Fourier transform,[114] for now we will follow the example of Boyd and account for the normalization constant on the inverse Fourier transform only.[102]

summation approaches the limit of an integral with the following form:

$$\tilde{E}(\mathbf{r}, z, t) = \int_0^\infty \hat{a}(\mathbf{r}, z, \omega) e^{-i[k(\omega)z - \omega t]} + \hat{a}^*(\mathbf{r}, z, \omega) e^{i[k(\omega)z - \omega t]} \frac{d\omega}{2\pi} \quad (3.1.18)$$

Eq. 3.1.18 is consistent with a Laplace transform from the angular frequency domain to a purely imaginary Fourier domain.[112] This restriction of Eq. 3.1.18 corresponding to a Laplace transform arises from the bounds of integration: as negative frequencies have no meaning, we can only allow the integral to span between the bounds of 0 and  $\infty$ .[102] One approach in the literature[102] is to invoke the relationship between  $k$ ,  $\omega$ , and  $v$  (see Eq. 3.1.5), recognizing that we can define the wavenumber:  $k = \omega/v$ . With this definition for the wavenumber, we can consider the conjugate of the complex electric field:

$$\begin{aligned} \left[ \hat{a}(\mathbf{r}, z, \omega) e^{-i[k(\omega)z - \omega t]} \right]^* &= \left[ \hat{a}(\mathbf{r}, z, \omega) e^{-i[(\omega/v)z - \omega t]} \right]^* \\ &= \hat{a}^*(\mathbf{r}, z, \omega) e^{i[(\omega/v)z - \omega t]} \\ &= \hat{a}^*(\mathbf{r}, z, \omega) e^{-i[(-\omega/v)z - (-\omega)t]} \end{aligned} \quad (3.1.19)$$

From this scheme, we see that if we assume  $\hat{a}(\mathbf{r}, z, \omega)$  is Hermitian, that is we assume the equality  $\hat{a}^*(\mathbf{r}, z, \omega) = \hat{a}(\mathbf{r}, z, -\omega)$ , we can simplify Eq. 3.1.18 by extending the integration to all frequencies - positive and negative:[102]

$$\tilde{E}(\mathbf{r}, z, t) = \int_{-\infty}^\infty \hat{a}(\mathbf{r}, z, \omega) e^{-i[k(\omega)z - \omega t]} \frac{d\omega}{2\pi} \quad (3.1.20)$$

Within the form of Eq. 3.1.20, we now ensure the resulting field,  $\tilde{E}(\mathbf{r}, z, t)$ , is real-valued by allowing the negative frequencies in the integral to correspond to the conjugate terms of the positive frequency components according to Eq. 3.1.19.[102]

Unfortunately, this strategy is not robust: previously (see Eq. 3.1.16), we defined the complex amplitude function,  $\hat{a}(\mathbf{r}, z, \omega)$ , in order to incorporate the phase factor,  $\exp[-i\phi(\omega)]$ . As this phase factor is the only imaginary contribution to  $\hat{a}(\mathbf{r}, z, \omega)$ ,<sup>i</sup> if we assume  $\hat{a}(\mathbf{r}, z, \omega)$  to be a Hermitian function, we are implicitly assuming  $\exp[-i\phi(-\omega)] = \exp[i\phi(\omega)]$ . This assumption restricts the functional forms of  $\phi(\omega)$  to only those functions that exhibit odd symmetry. As  $\phi(\omega)$  is not required to be a function with odd symmetry, we must find an alternative approach to manipulate Eq. 3.1.18.

In contrast to Boyd's approach of assuming  $\hat{a}(\mathbf{r}, z, \omega)$  exhibits Hermitian symmetry,[102] we will instead begin by considering the distribution defined by  $\hat{a}(\mathbf{r}, z, \omega)$ . If we consider that this distribution can be

---

<sup>i</sup>Recalling Eq. 3.1.16, the only other contribution to  $\hat{a}(\mathbf{r}, z, \omega)$  is  $E_0(\mathbf{r}, z, \omega)$ . We have taken  $E_0(\mathbf{r}, z, \omega)$  to represent a scalar amplitude, thereby requiring it to be real-valued.

characterized by a distribution around a central frequency,  $\omega_0$ , we can find this characteristic frequency through the first moment of the distribution in the manner of Brabec and Krausz:[115]

$$\omega_0 = \frac{\int_0^\infty \omega |\hat{a}(\omega)|^2 d\omega}{\int_0^\infty |\hat{a}(\omega)|^2 d\omega} \quad (3.1.21)$$

where  $|\hat{a}(\omega)|^2 = \hat{a}(\omega)\hat{a}^*(\omega) = E(\omega)E^*(\omega)$  and  $E(\omega)$  is defined as the Fourier transform of  $E(t)$ . While Fourier transformation of  $E(t)$  will remove the terms describing the temporal oscillations,  $E(\omega)$  will still include a complex exponential describing the spatial oscillations. However, the product of  $E(\omega)$  and its complex conjugate,  $E^*(\omega)$ , will remove the exponentials, leaving only the amplitude function  $\hat{a}(\omega)$ , as in Eq. 3.1.21.

Having defined the characteristic carrier frequency, let us now reconsider the form of the continuously defined electric field from Eq. 3.1.18. As the integral of the sum of two functions is equal to the sum of the integrals of the same two functions,[116] we can express the integral in Eq. 3.1.18 in the form:

$$\tilde{E}(\mathbf{r}, z, t) = \int_0^\infty \hat{a}(\mathbf{r}, z, \omega) e^{-i[k(\omega)z - \omega t]} \frac{d\omega}{2\pi} + \int_0^\infty \hat{a}^*(\mathbf{r}, z, \omega) e^{i[k(\omega)z - \omega t]} \frac{d\omega}{2\pi} \quad (3.1.22)$$

From Eq. 3.1.22, we will consider two separate substitutions, introducing a new variable of integration,  $\Delta\omega$ . For the first integral of Eq. 3.1.22, we will consider this variable to be defined  $\Delta\omega = \omega - \omega_0$ , where  $\omega_0$  is the carrier frequency determined according to Eq. 3.1.21. Substitution for  $\Delta\omega$  will shift the lower bound of integration from  $\omega = 0$  to  $\Delta\omega = -\omega_0$ , but the upper bound will remain  $\infty$ . As for the integration factor, since  $\partial\Delta\omega/\partial\omega = 1$ ,  $d\omega$  can be directly replaced by  $d\Delta\omega$ . For the second integral in Eq. 3.1.22, we will define  $\Delta\omega$  to be  $\Delta\omega = \omega_0 - \omega$ . With this substitution, we will observe the opposite changes in our bounds of integration: instead of spanning  $\omega = 0$  to  $\omega = \infty$ , substitution according to  $\Delta\omega = \omega_0 - \omega$  will shift the bounds to span  $\Delta\omega = \omega_0$  to  $\Delta\omega = -\infty$ . Additionally, since  $\partial\Delta\omega/\partial\omega = -1$  for this second substitution, the integration factor  $d\omega$  will need to be replaced by  $-d\Delta\omega$ . Recognizing that these substitutions permit the definition of  $\omega$  as  $\omega = \omega_0 + \Delta\omega$  for the first integral and  $\omega = \omega_0 - \Delta\omega$  for the second, we can proceed with these substitutions to yield:

$$\begin{aligned} \tilde{E}(\mathbf{r}, z, t) = & \int_{-\omega_0}^\infty \hat{a}(\mathbf{r}, z, \omega_0 + \Delta\omega) e^{-i[k(\omega_0 + \Delta\omega)z - (\omega_0 + \Delta\omega)t]} \frac{d\Delta\omega}{2\pi} \\ & + \int_{\omega_0}^{-\infty} \hat{a}^*(\mathbf{r}, z, \omega_0 - \Delta\omega) e^{i[k(\omega_0 - \Delta\omega)z - (\omega_0 - \Delta\omega)t]} \frac{(-d\Delta\omega)}{2\pi} \end{aligned} \quad (3.1.23)$$

As the integral from  $\omega_0$  to  $-\infty$  just yields the negative value of the integral from  $-\infty$  to  $\omega_0$ , we can recall

our earlier definition of the wavenumber,  $k = \omega/v$ , permitting the simplification of Eq. 3.1.23 slightly:

$$\begin{aligned} \tilde{E}(\mathbf{r}, z, t) = & e^{-ik_0 z} e^{i\omega_0 t} \int_{-\omega_0}^{\infty} \hat{a}(\mathbf{r}, z, \omega_0 + \Delta\omega) e^{-i(\Delta\omega/v)z} e^{i\Delta\omega t} \frac{d\Delta\omega}{2\pi} \\ & + e^{ik_0 z} e^{-i\omega_0 t} \int_{-\infty}^{\omega_0} \hat{a}^*(\mathbf{r}, z, \omega_0 - \Delta\omega) e^{i[(-\Delta\omega)/v]z} e^{i\Delta\omega t} \frac{d\Delta\omega}{2\pi} \end{aligned} \quad (3.1.24)$$

where  $k_0 = k(\omega_0) = \omega_0/v$ .

From Eq. 3.1.24 we can make two further simplifications. First, if we assume that the behavior of  $\hat{a}(\mathbf{r}, z, \omega)$  is such that it does not evaluate to non-zero values beyond the allowed bounds of integration, i.e. for negative values of  $\omega$ , there is no functional difference between the integrals in Eq. 3.1.24 spanning  $\mp\omega_0$  and  $\pm\infty$  and the same integrals spanning the bounds of  $-\infty$  to  $\infty$ . Second, let us consider a second function,  $\hat{A}(\mathbf{r}, z, \Delta\omega)$ , that we will define relative to  $\hat{a}(\mathbf{r}, z, \omega)$  simply by shifting the center of the distribution:  $\hat{A}(\mathbf{r}, z, \Delta\omega) = \hat{a}(\mathbf{r}, z, \omega_0 + \Delta\omega)$ . In other words,  $\hat{A}(\mathbf{r}, z, \Delta\omega)$  is a function that exhibits the same functional behavior as  $\hat{a}(\mathbf{r}, z, \omega)$ , but is centered such that the distribution's carrier frequency,  $\omega_0$ , serves as the origin ( $\Delta\omega = 0$ ). With these two changes, we can modify Eq. 3.1.24 to define the electric field:

$$\begin{aligned} \tilde{E}(\mathbf{r}, z, t) = & e^{-ik_0 z} e^{i\omega_0 t} \int_{-\infty}^{\infty} \hat{A}(\mathbf{r}, z, \Delta\omega) e^{-i(\Delta\omega/v)z} e^{i\Delta\omega t} \frac{d\Delta\omega}{2\pi} \\ & + e^{ik_0 z} e^{-i\omega_0 t} \int_{-\infty}^{\infty} \hat{A}^*(\mathbf{r}, z, -\Delta\omega) e^{i[(-\Delta\omega)/v]z} e^{i\Delta\omega t} \frac{d\Delta\omega}{2\pi} \end{aligned} \quad (3.1.25)$$

The forms of the integrals in Eq. 3.1.25 correspond to the inverse Fourier transforms with respect to the difference frequency,  $\Delta\omega$ .<sup>i</sup> We can therefore consider Eq. 3.1.25 to be equivalent to:

$$\begin{aligned} \tilde{E}(\mathbf{r}, z, t) = & e^{-ik_0 z} e^{i\omega_0 t} \mathcal{F}^{-1} \left\{ \hat{A}(\mathbf{r}, z, \Delta\omega) e^{-i(\Delta\omega/v)z} \right\} \\ & + e^{ik_0 z} e^{-i\omega_0 t} \mathcal{F}^{-1} \left\{ \left[ \hat{A}(\mathbf{r}, z, -\Delta\omega) e^{-i[(-\Delta\omega)/v]z} \right]^* \right\} \end{aligned} \quad (3.1.26)$$

where  $\mathcal{F}^{-1}\{\}$  represents the inverse Fourier transform of the term in brackets.

If we define an envelope function  $A(\mathbf{r}, z, t) = \mathcal{F}^{-1}\{\hat{A}(\mathbf{r}, z, \Delta\omega) \exp[-i(\Delta\omega/v)z]\}$ ,<sup>ii</sup> we can use the identity  $\mathcal{F}^{-1}\{\hat{f}^*(-\omega)\} = f^*(t)$  [112] to see that Eq. 3.1.26 predicts the behavior of a polychromatic field to be

<sup>i</sup>Note that the form of our inverse Fourier transforms in Eq. 3.1.25 do not agree with the notation employed by Boyd.[102] Boyd takes the convention that the inverse Fourier transform is achieved by multiplying the frequency domain function by  $\exp(-i\omega t)$  and integrating over  $\omega$ . While this convention is consistent with some authors,[113, 117] we will follow the convention in which the Fourier transform is performed by multiplying the time domain function by  $\exp(-i\omega t)$  and the inverse Fourier transform by multiplying by  $\exp(i\omega t)$ . [112, 114]

<sup>ii</sup>We can simplify the assignment of  $A(\mathbf{r}, z, t)$  by considering the contributions from  $\exp[-i(\Delta\omega/v)z]$  to be negligible. We will generally adopt this approximation going forward, i.e. we will generally consider  $\mathcal{F}\{A(\mathbf{r}, z, t)\} \approx \hat{A}(\mathbf{r}, z, \Delta\omega)$ . However, we will note when it is convenient to relax this approximation. It is also trivial to explicitly account for this additional phase component numerically in a manner similar to Wang and Wang.[118]

consistent with that of the time domain envelope,  $A(\mathbf{r}, z, t)$ , propagating with carrier frequency,  $\omega_0$ :

$$\tilde{E}(\mathbf{r}, z, t) = A(\mathbf{r}, z, t)e^{-i(k_0z - \omega_0t)} + \text{c.c.} \quad (3.1.27)$$

Ignoring the factor of  $1/2$  as previously discussed,[102, 103, 110] this result is identical to the solution reported by Akhmanov et al.[103] The form of Eq. 3.1.27 suggests that it is satisfactory to consider the propagation of the complex field,  $A(\mathbf{r}, z, t) \exp[-i(k_0z - \omega_0t)]$ , and determine the resulting real-valued field through the predicted result and its complex conjugate.

Akhmanov et al give some insight into the nature of this pulse envelope  $A(t)$ . They treat the function as the product of a real-valued envelope,  $\rho(t)$ , and a phase factor,  $\exp[i\phi(t)]$ . Within this notation, a transform-limited pulse can be considered to be characterized by a pulse envelope that is real-valued, and thereby characterized by a phase dependence of  $\phi(t) = 0$ . Other functionalities of  $\phi(t)$  yield different behaviors associated with the resulting phase-modulation. For example, phase-modulation of the time-domain envelope according to  $\phi(t) = -(\alpha/2)t^2$  corresponds to frequency modulation of the form  $\omega(t) - \omega_0 = d\phi(t)/dt = -\alpha t$ , yielding a linear chirp.[103]

As we see in the derivation of Eq. 3.1.27, the formation of ultrashort pulses is predicated on forming polychromatic electric fields. However, not only does pulse formation require many contributing frequencies, it also requires a fixed phase relation between the various frequency components in order to permit its characterization as a single pulse envelope. This is demonstrated in Fig. 3.1. This figure illustrates how the linear combination of various monochromatic fields can introduce a beat pattern in the total field observed, resulting in a pulse train. More meaningfully, when there is a characteristic distribution applied to the amplitudes of the monochromatic fields, mode locking by defining a fixed phase relationship between the different frequency components results in the transformation of this distribution into the time-domain, as predicted by Eq. 3.1.26. On the other hand, the loss of a phase relation between the different frequency components prevents a well-defined pulse from forming.

This regime in which the time-dependent behavior of a pulse is adequately described as the product of an envelope function and a term describing the rapid oscillations at a central or carrier frequency is referred to as the slowly varying amplitude or envelope approximation. Unfortunately, there is a limit to the conditions for which this approximation is considered valid: if the pulse envelope is too short relative to the oscillations at the carrier frequency, it is no longer appropriate to consider the time evolution of the envelope distinct from the rapid oscillations at the carrier frequency. The limit to this approximation is therefore related to the pulse width,  $\tau$ , and the carrier frequency,  $\omega_0$ . However, different authors cite different limits to this

regime. Akhmanov et al cite the limiting bounds as  $\tau\omega_0 \approx 20\pi$ .<sup>[103]</sup> On the other hand, Brabec and Krausz present calculations that suggest the limit may even be as low as  $\tau\omega_0 \approx 2\pi$ .<sup>[115]</sup> For fields in the regime we commonly work on the Wright group's femtosecond system (in the visible and near infrared),  $\omega_0$  is in the range of  $1 - 4 \times 10^{15}$  Hz.<sup>i</sup> According to Akhmanov et al, the shortest pulse lengths at these frequencies for which the slowly varying envelope approximation would be considered valid are 16-60 fs; by Brabec and Krausz's conditions, though, the slowly varying envelope approximation should be reasonable down to pulse lengths as short as 2-6 fs.<sup>[103, 115]</sup>

### 3.2 Polarizations

Throughout § 3.1, we have focused on electromagnetic radiation propagating through free space. In such a scenario, Maxwell's equations predict the propagation of electric and magnetic fields to behave perfectly as a wave: propagating without distortion to the wave function. This behavior is expected as the propagation predicted by Maxwell's equations exhibits a functional form consistent with Eq. 3.1.1:<sup>ii</sup>

$$\frac{\partial^2}{\partial z^2} \tilde{\mathbf{E}}(\mathbf{r}, z, t) = \frac{1}{v^2} \frac{\partial^2}{\partial t^2} \tilde{\mathbf{E}}(\mathbf{r}, z, t) \quad (3.2.1)$$

However, when light propagates through matter, the field can interact with the dipoles of the material, perturbing the potential energy of the system according to:<sup>[99, 109]</sup>

$$\tilde{V} = \mu \cdot \tilde{\mathbf{E}} \quad (3.2.2)$$

where  $\mu$  is the dipole operator,  $\epsilon r$ . As the potential energy defined by Eq. 3.2.2 is of the form of a dot product, the relative orientation of the dipole and the field polarization is important; we will represent appropriate quantities as vectors until we note the assumptions that allow us to represent the system with scalar quantities.

The additional potential energy introduced by the interactions between the dipole and the field can be

---

<sup>i</sup>Corresponding to wavelengths between approximately 500 nm and 1500 nm, which covers the bounds of the sum-frequency signal, sum-frequency idler, second-harmonic signal, second-harmonic idler, and signal processes.

<sup>ii</sup>A result identical to Eq. 3.2.1 can also be predicted for magnetic fields.

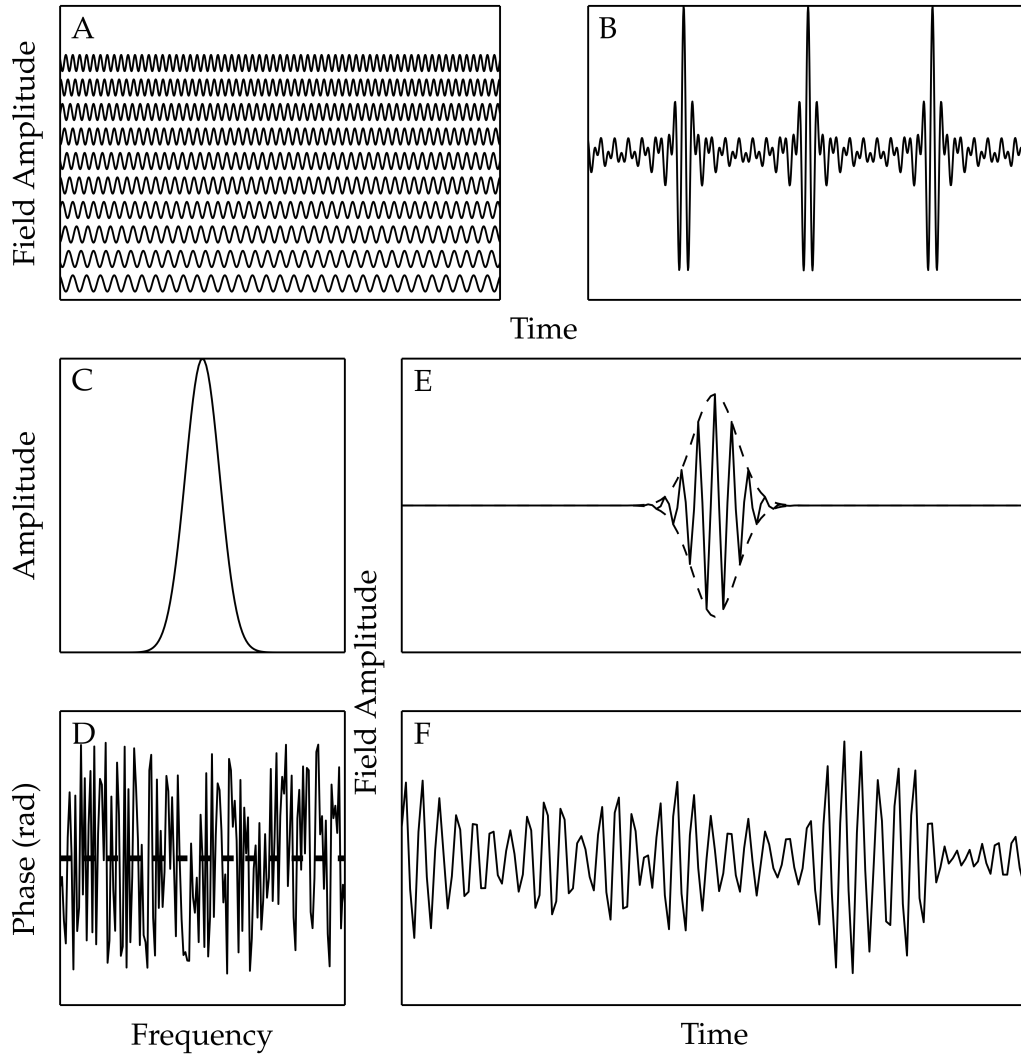


Figure 3.1: Formation of a polychromatic electric field through summation of monochromatic fields. (A) and (B) demonstrate the beating that arises in the polychromatic field (B) from the summation of a discrete set of monochromatic fields (A). The beats in (B) correspond to a pulse train with pulses occurring at points where all contributing fields are in phase. (C) shows a Gaussian amplitude envelope over a distribution of frequencies, while (D) shows two scenarios for the phase relation between the different frequency components: all frequencies have the same initial phase (dashed line), or the frequencies exhibit random phases (solid line). The polychromatic field resulting from the mode-locked frequencies exhibits the Gaussian temporal profile in (E): the solid line is the polychromatic field amplitude, and the dashed line outlines the Gaussian profile predicted by Fourier transformation of the frequency domain envelope in (C), scaled to match the peak of the solid trace. The randomly phased frequencies yield the polychromatic field in (F).



treated as a perturbation to the Hamiltonian,  $\mathcal{H}$ , describing the system:<sup>i</sup>

$$\begin{aligned}\mathcal{H} &= \mathcal{H}_0 + \tilde{V} \\ &= \mathcal{H}_0 + \mu \cdot \tilde{\mathbf{E}}\end{aligned}\tag{3.2.3}$$

where  $\mathcal{H}_0$  is the unperturbed Hamiltonian of the system. The effects of this perturbed Hamiltonian are described by the Liouville equation:

$$\frac{\partial}{\partial t} \rho = \frac{1}{i\hbar} [\mathcal{H}, \rho]\tag{3.2.4}$$

The resulting density matrix,  $\rho$ , permits prediction of the properties of the system, including the expectation value for the electric polarization induced by the field:

$$\langle \tilde{\mathbf{P}} \rangle = N \text{tr}(\rho \mu)\tag{3.2.5}$$

where  $N$  is the number density of the source of the dipole and  $\text{tr}$  is the trace.[99, 109] Going forward, we will simply express the polarization as  $\tilde{\mathbf{P}}$ .

As we have implied by the notation of  $\tilde{\mathbf{P}}$ , this resulting polarization will exhibit an oscillatory character, which we can consider to be of the form:[102, 109]

$$\tilde{\mathbf{P}}(t) = \mathbf{P}(\omega) e^{i\omega t} + \text{c.c.}\tag{3.2.6}$$

where  $\mathbf{P}(\omega)$  is the amplitude of the polarization at the frequency of oscillation,  $\omega$ . This polarization can couple to the electric field oscillating at the same frequency, modifying the manner in which the field propagates. The effect of this induced polarization upon the electric field manifests in the introduction of a new quantity: the displacement,  $\tilde{\mathbf{D}}(t)$ . The displacement describes the coupling of the electric field and induced polarization according to the relationship:

$$\tilde{\mathbf{D}}(t) = \epsilon_0 \tilde{\mathbf{E}}(t) + \tilde{\mathbf{P}}(t)\tag{3.2.7}$$

in the mks system of units, or:

$$\tilde{\mathbf{D}}(t) = \tilde{\mathbf{E}}(t) + 4\pi \tilde{\mathbf{P}}(t)\tag{3.2.8}$$

in the cgs or esu systems. In Eq. 3.2.7,  $\epsilon_0$  is the permittivity of free space.[101, 102, 109]

Thus far, we have only allowed for linear interactions between the field and the material. However, it is

---

<sup>i</sup>Note that an additional perturbation can be introduced corresponding to the interactions that provide relaxation pathways for the density matrix predicted by the Hamiltonian. Such a relaxation matrix is not explicitly noted in Eq. 3.2.3.

possible to expand the perturbation to higher terms in the electric field, resulting in a series of higher order perturbations to the density matrix. The  $n^{\text{th}}$ -order density matrix,  $\rho^{(n)}$ , will contribute a corresponding  $n^{\text{th}}$ -order polarization,  $\tilde{\mathbf{P}}^{(n)}(t)$ . The total polarization will be the sum of all such resulting polarizations:[109]

$$\begin{aligned}\tilde{\mathbf{P}}(t) &= \tilde{\mathbf{P}}^{(1)}(t) + \tilde{\mathbf{P}}^{(2)}(t) + \tilde{\mathbf{P}}^{(3)}(t) + \dots \\ &= \tilde{\mathbf{P}}^{\text{L}}(t) + \tilde{\mathbf{P}}^{\text{NL}}(t)\end{aligned}\tag{3.2.9}$$

In the second line of Eq. 3.2.9, we have introduced the notations  $\tilde{\mathbf{P}}^{\text{L}}(t)$  and  $\tilde{\mathbf{P}}^{\text{NL}}(t)$  to describe the linear and nonlinear polarizations, respectively: the linear polarization,  $\tilde{\mathbf{P}}^{\text{L}}(t)$ , corresponds to the first order term,  $\tilde{\mathbf{P}}^{(1)}(t)$ , and the nonlinear polarization,  $\tilde{\mathbf{P}}^{\text{NL}}(t)$ , generalizes the higher order terms. This reduction will prove useful going forward: we will show that the linear term describes absorptive and dispersive effects on the propagation of an ultrashort pulse, while we will generally only need to consider one term from the series represented by  $\tilde{\mathbf{P}}^{\text{NL}}(t)$ .

Since the  $n^{\text{th}}$ -order polarization requires an expansion of the Hamiltonian to provide an  $n^{\text{th}}$ -order perturbation, we can also express the series in Eq. 3.2.9 as an expansion in increasingly higher powers of the field. This expansion describes the increasingly higher order of interactions between the total field and the material:[99, 102, 109]

$$\tilde{\mathbf{P}}(t) = \epsilon_0 \chi^{(1)} \cdot \tilde{\mathbf{E}}(t) + \epsilon_0 \chi^{(2)} : \tilde{\mathbf{E}}^2(t) + \epsilon_0 \chi^{(3)} : \tilde{\mathbf{E}}^3(t) + \dots\tag{3.2.10}$$

in the mks system, or:

$$\tilde{\mathbf{P}}(t) = \chi^{(1)} \cdot \tilde{\mathbf{E}}(t) + \chi^{(2)} : \tilde{\mathbf{E}}^2(t) + \chi^{(3)} : \tilde{\mathbf{E}}^3(t) + \dots\tag{3.2.11}$$

when the quantities are in cgs or esu units. Note that the  $:$  operator in Eq. 3.2.10 and 3.2.11 provides an operation analogous to the dot product between the tensor,  $\chi^{(n)}$ , and the electric field product,  $\tilde{\mathbf{E}}^n(t)$ . [109] Within the expansions of Eq. 3.2.10 and 3.2.11, the coefficient  $\chi^{(n)}$  is the  $n^{\text{th}}$ -order susceptibility. These susceptibilities are appropriately considered to be  $(n + 1)^{\text{th}}$ -order tensors. However, we will generally be able to apply approximations or manipulations that allow us to consider the susceptibility as an effective scalar value representing a linear combination of the appropriate elements of the tensor as they are sampled according to the experimental conditions. [102, 106, 119] Under such approximations, it is sufficient to consider the following alternatives to Eq. 3.2.10 and 3.2.11, in which the relationship between the polarization and

the field is treated as a scalar relationship:

$$\tilde{P}(t) = \epsilon_0 \chi^{(1)} \tilde{E}(t) + \epsilon_0 \chi^{(2)} \tilde{E}^2(t) + \epsilon_0 \chi^{(3)} \tilde{E}^3(t) + \dots \quad (3.2.12a)$$

$$\tilde{P}(t) = \chi^{(1)} \tilde{E}(t) + \chi^{(2)} \tilde{E}^2(t) + \chi^{(3)} \tilde{E}^3(t) + \dots \quad (3.2.12b)$$

We will discuss how this can be approached in birefringent media, as well as provide a brief discussion of the contributions to the susceptibility, in § 3.2.2. However, in the context of later sections, it will be sufficient to consider the susceptibility at the phenomenological level of Eq. 3.2.10 and 3.2.11, or Eq. 3.2.12a and 3.2.12b.

Unfortunately, the expansion of the polarization into a series in the manner of Eq. 3.2.10 - 3.2.12b introduces another inconsistency in the treatment of different authors. The forms that have been presented are consistent with the convention of Boyd,[102] in which the polarization as an expansion of increasing powers in the electric field is considered to be a time-domain description of the interaction. In contrast, Shen expands the polarization as increasing powers of the field in the frequency domain.[109] The significance of this distinction relates to the behavior of multiplication between the time and frequency domains. For two functions  $f(t)$  and  $g(t)$  with Fourier transforms  $\mathcal{F}\{f(t)\} = \hat{f}(\omega)$  and  $\mathcal{F}\{g(t)\} = \hat{g}(\omega)$ , we can define the following relationships:[112]

$$\mathcal{F}\{f(t)g(t)\} = \frac{1}{2\pi}(\hat{f} * \hat{g})(\omega) \quad (3.2.13a)$$

$$\mathcal{F}\{(f * g)(t)\} = \hat{f}(\omega)\hat{g}(\omega) \quad (3.2.13b)$$

where  $*$  denotes the convolution of the functions.<sup>1</sup>

As can be seen from the relationships of Eq. 3.2.13a and 3.2.13b, Boyd and Shen are implying specific behaviors in their respective conventions. By taking the expansion of the polarization in powers of the field as the frequency domain description, Shen imposes behavior in the time-domain corresponding to the convolution of the fields and the material response, which allows the polarization to exhibit transient behavior corresponding to relaxation properties in the material.[99, 109] In contrast, Boyd's treatment describes an instantaneous response of the medium, with a response - the polarization - that requires the presence of the electric field to be sustained; such behavior is consistent with a nonresonant interaction, in which the field

---

<sup>1</sup>It should be noted that the factor of  $2\pi$  in Eq. 3.2.13a is necessary to compensate for the additional normalization constant that arises from the pair of Fourier transforms necessary to yield  $\hat{f}$  and  $\hat{g}$ . This normalization constant should be changed according to the normalization convention being taken. Upon a change in normalization convention, it is also necessary to consider whether a normalization coefficient needs to be introduced to Eq. 3.2.13b.[114]

is not resulting in the formation of long-lived polarizations. Within this treatment, the polarization must be able to be defined in the frequency domain as a convolution; this is consistent with Boyd's treatment of the polarization for a  $\chi^{(2)}$  experiment corresponding to the summation:[102]

$$P_i(\omega_n + \omega_m) = \sum_{jk} \sum_{(nm)} \chi_{ijk}^{(2)}(\omega_n + \omega_m, \omega_n, \omega_m) E_j(\omega_n) E_k(\omega_m) \quad (3.2.14)$$

where  $i$ ,  $j$ , and  $k$  correspond to the available polarization states and the summation over  $(nm)$  corresponds to summing over  $m$  and  $n$  in such a manner so as to maintain a constant sum,  $\omega_n + \omega_m$ . Ignoring the symmetry (the terms corresponding to summation of  $i$ ,  $j$ , and  $k$  in Eq. 3.2.14) and extending the summation to the form of a continuous integral, this is consistent with the convolution:

$$P(\omega) = \int \chi^{(2)} E(\omega') E(\omega - \omega') d\omega' \quad (3.2.15)$$

In contrast to Shen's approach, this treatment allows us to explicitly consider the permutations resulting from the frequency content of ultrafast pulses. Since the problems we will be seeking to address predominantly involve interactions reasonably considered nonresonant, we will adopt Boyd's convention moving forward. This convention has also been adopted by a variety of other authors concerned with systems involving both resonant and nonresonant response from the medium.[120–124]

If we wish adopt this treatment in order to consider fields with a broad frequency distribution, we will also need to consider the possibility of the polarization exhibiting a frequency distribution. Examining Eq. 3.2.6, it is clear that this mathematical description can be considered to describe a polarization exhibiting a single frequency, thereby coupling to a monochromatic field. To extend to the scenario in which multiple frequencies are present, we can treat the polarization defined by Eq. 3.2.6 in a manner similar to our extension of Eq. 3.1.13 to Eq. 3.1.14 in § 3.1.2, yielding the summation:[102]

$$\tilde{P}(\mathbf{r}, z, t) = \sum_n P(\mathbf{r}, z, \omega_n) e^{i\omega_n t} + \text{c.c.} \quad \{n : \omega_n \geq 0\} \quad (3.2.16)$$

Note that we have also introduced the spatial dependence  $(\mathbf{r}, z)$  we previously allowed the field to exhibit (see Eq. 3.1.15). Given our previous treatment of polychromatic fields, though, we expect that we might be able to extend this summation in a manner similar to the result of Eq. 3.1.27, allowing us to treat the polarization as the product of some envelope function,  $p(\mathbf{r}, z, t)$ , and rapid oscillations around the carrier

frequency:

$$\tilde{P}(\mathbf{r}, z, t) = p(\mathbf{r}, z, t)e^{i\omega_0 t} + \text{c.c.} \quad (3.2.17)$$

If such a treatment holds, we would predict that the envelope function would contain information on the frequency distribution in a manner analogous to the field envelope,  $A(\mathbf{r}, z, t)$ :

$$\hat{p}(\mathbf{r}, z, \Delta\omega) = P(\mathbf{r}, z, \omega_0 + \Delta\omega) \quad (3.2.18)$$

where  $P(\mathbf{r}, z, \omega_0 + \Delta\omega) = P(\mathbf{r}, z, \omega)$  is the coefficient in Eq. 3.2.16 and  $\hat{p}(\mathbf{r}, z, \Delta\omega)$  is defined as the Fourier transform of  $p(\mathbf{r}, z, t)$ ,  $\hat{p}(\mathbf{r}, z, \Delta\omega) = \mathcal{F}\{p(\mathbf{r}, z, t)\}$ .

If we consider a representative nonlinear process, we can show that the form of Eq. 3.2.17 is just a consequence of the pulse-like propagation of ultrafast electric fields, with  $p(\mathbf{r}, z, t)$  inheriting a form corresponding to the envelope functions of the driving fields,  $A(\mathbf{r}, z, t)$ . We will show how this might be evaluated for a representative example - second-harmonic generation - though extending this treatment to other nonlinear experiments simply requires an appropriate expansion of the total electric field.

In the case of second-harmonic generation, we are concerned with a total electric field consisting of contributions from two fields: the fundamental, characterized by a carrier frequency  $\omega_0 = \omega_1$ , and the second harmonic, which will exhibit a carrier frequency  $\omega_0 = \omega_2 = 2\omega_1$ . If we consider these fields to be defined in a manner consistent with Eq. 3.1.27, we expect the fields to propagate in the manner:

$$\tilde{E}_1(\mathbf{r}, z, t) = A_1(\mathbf{r}, z, t)e^{-ik_1 z}e^{i\omega_1 t} + A_1^*(\mathbf{r}, z, t)e^{ik_1 z}e^{-i\omega_1 t} \quad (3.2.19a)$$

$$\tilde{E}_2(\mathbf{r}, z, t) = A_2(\mathbf{r}, z, t)e^{-ik_2 z}e^{i\omega_2 t} + A_2^*(\mathbf{r}, z, t)e^{ik_2 z}e^{-i\omega_2 t} \quad (3.2.19b)$$

where Eq. 3.2.19a describes the fundamental field (noted  $\tilde{E}_1$ ) and Eq. 3.2.19b represents the second-harmonic field (noted  $\tilde{E}_2$ ). We can then define the total field,  $\tilde{E}$ :

$$\begin{aligned} \tilde{E}(\mathbf{r}, z, t) &= \tilde{E}_1(\mathbf{r}, z, t) + \tilde{E}_2(\mathbf{r}, z, t) \\ &= A_1(\mathbf{r}, z, t)e^{-ik_1 z}e^{i\omega_1 t} + A_1^*(\mathbf{r}, z, t)e^{ik_1 z}e^{-i\omega_1 t} \\ &\quad + A_2(\mathbf{r}, z, t)e^{-ik_2 z}e^{i\omega_2 t} + A_2^*(\mathbf{r}, z, t)e^{ik_2 z}e^{-i\omega_2 t} \end{aligned} \quad (3.2.20)$$

Substituting the total field of Eq. 3.2.20 into the appropriate term of the polarization expansion in Eq. 3.2.12a,  $\tilde{P}^{(2)}(\mathbf{r}, z, t) = \epsilon_0\chi^{(2)}(\tilde{E}(\mathbf{r}, z, t))^2$ ,<sup>i</sup> and expanding the quadratic dependence on the total field yields

---

<sup>i</sup>Note that the appropriate term from Eq. 3.2.12b,  $\tilde{P}^{(2)}(\mathbf{r}, z, t) = \chi^{(2)}(\tilde{E}(\mathbf{r}, z, t))^2$ , would be treated in an identical manner,

the result of Eq. 3.2.21:

$$\begin{aligned}
\tilde{P}^{(2)}(\mathbf{r}, z, t) = \epsilon_0 \chi^{(2)} & \left[ A_1(\mathbf{r}, z, t) A_1(\mathbf{r}, z, t) e^{-i2k_1 z} e^{i2\omega_1 t} + 2A_1(\mathbf{r}, z, t) A_2(\mathbf{r}, z, t) e^{-i(k_1+k_2)z} e^{i(\omega_1+\omega_2)t} \right. \\
& + 2A_1(\mathbf{r}, z, t) A_1^*(\mathbf{r}, z, t) + 2A_1(\mathbf{r}, z, t) A_2^*(\mathbf{r}, z, t) e^{i(k_2-k_1)z} e^{-i(\omega_2-\omega_1)t} \\
& + A_2(\mathbf{r}, z, t) A_2(\mathbf{r}, z, t) e^{-i2k_2 z} e^{i2\omega_2 t} + 2A_2(\mathbf{r}, z, t) A_1^*(\mathbf{r}, z, t) e^{-i(k_2-k_1)z} e^{i(\omega_2-\omega_1)t} \quad (3.2.21) \\
& + 2A_2(\mathbf{r}, z, t) A_2^*(\mathbf{r}, z, t) + A_1^*(\mathbf{r}, z, t) A_1^*(\mathbf{r}, z, t) e^{i2k_1 z} e^{-i2\omega_1 t} \\
& \left. + 2A_1^*(\mathbf{r}, z, t) A_2^*(\mathbf{r}, z, t) e^{i(k_1+k_2)z} e^{-i(\omega_1+\omega_2)t} + A_2^*(\mathbf{r}, z, t) A_2^*(\mathbf{r}, z, t) e^{i2k_2 z} e^{-i2\omega_2 t} \right]
\end{aligned}$$

Examining this expression, we observe five frequency contributions: two DC components describing optical rectification; the second harmonics of  $\omega_1$  and  $\omega_2$ ; the sum frequency,  $\omega_1 + \omega_2$ ; and, the difference frequency,  $\omega_2 - \omega_1$ . Considering the oscillatory terms, Eq. 3.2.21 consists of two terms at each frequency that simply differ in phase; we will consider these terms to reflect four complex polarizations - the terms oscillating according to  $\exp(i\omega t)$  - and their complex conjugates, the inclusion of which ensures the polarization is real valued. Thus, we can consider the four oscillating polarizations to be of a form analogous to Eq. 3.1.27:

$$\tilde{P}_{(2\omega_1)}^{(2)}(\mathbf{r}, z, t) = \epsilon_0 \chi^{(2)} [A_1(\mathbf{r}, z, t) A_1(\mathbf{r}, z, t) e^{-i2k_1 z} e^{i2\omega_1 t} + \text{c.c.}] \quad (3.2.22a)$$

$$\tilde{P}_{(2\omega_2)}^{(2)}(\mathbf{r}, z, t) = \epsilon_0 \chi^{(2)} [A_2(\mathbf{r}, z, t) A_2(\mathbf{r}, z, t) e^{-i2k_2 z} e^{i2\omega_2 t} + \text{c.c.}] \quad (3.2.22b)$$

$$\tilde{P}_{(\omega_2+\omega_1)}^{(2)}(\mathbf{r}, z, t) = 2\epsilon_0 \chi^{(2)} [A_1(\mathbf{r}, z, t) A_2(\mathbf{r}, z, t) e^{-i(k_1+k_2)z} e^{i(\omega_1+\omega_2)t} + \text{c.c.}] \quad (3.2.22c)$$

$$\tilde{P}_{(\omega_2-\omega_1)}^{(2)}(\mathbf{r}, z, t) = 2\epsilon_0 \chi^{(2)} [A_2(\mathbf{r}, z, t) A_1^*(\mathbf{r}, z, t) e^{-i(k_2-k_1)z} e^{i(\omega_2-\omega_1)t} + \text{c.c.}] \quad (3.2.22d)$$

Therefore, our assumption in treating the polarization in the manner of Eq. 3.2.17 appears justified. Within this treatment, we can consider the envelope function of the polarization,  $p(\mathbf{r}, z, t)$ , exhibiting contributions from:  $\epsilon_0$ , if appropriate;  $\chi^{(n)}$ , in the general case; an appropriate product of the temporal envelope functions of the driving fields,  $A(\mathbf{r}, z, t)$ ; and, a term describing the cooperation of the wave vectors,  $k$ , of the driving fields. We will see in § 3.4 that coupling between a field and polarization introduces a wave vector associated with the field, which together with this sum of wave vectors yields a term,  $\Delta k$ . The quantity  $\Delta k$  describes the quality of momentum conservation in the nonlinear process and, under conditions of non-zero  $\Delta k$ , can result in a decrease of the efficiency of the nonlinear process (see § 3.2.1)

---

yielding the same form as the result in Eq. 3.2.21, only omitting the factor of  $\epsilon_0$ .

### 3.2.1 Phase Matching of Nonlinear Experiments

As shown in Eq. 3.2.21 and 3.2.22a - 3.2.22d, the characteristic frequencies of polarizations induced by an electric field must satisfy energy conservation: namely, the frequency of the polarization - and the field to which it couples - must correspond to the appropriate sum of the carrier frequencies of the interacting pulses. For example, the generation of the second harmonic of  $\omega_1$  (Eq. 3.2.21 and 3.2.22a) must initiate a polarization at the energy-conserving frequency,  $\omega_2 = \omega_1 + \omega_1$ . Similarly, it can be shown that optical parametric generation/amplification and sum-frequency generation must satisfy the energy conservation corresponding to  $\omega_3 = \omega_2 + \omega_1$ : in optical parametric generation/amplification,  $\omega_3$ ,  $\omega_2$ , and  $\omega_1$  would correspond to the pump, signal, and idler (assuming  $\omega_2 > \omega_1$ ), while in sum-frequency generation,  $\omega_3$  would be the sum frequency generated from  $\omega_1$  and  $\omega_2$ .

However, Eq. 3.2.21 and 3.2.22a - 3.2.22d illustrate that the interaction of the frequencies in the nonlinear medium also imposes a momentum upon the induced polarization: for example, the polarization oscillating at  $2\omega_1$  also exhibits spatial oscillations at  $2k_1$ . We will see in § 3.4.1 that the field coupling to the polarization at  $2\omega_1 = \omega_2$  propagates with a dependence upon  $\exp(ik_2z)\tilde{P}_{(2\omega_1)}$ .<sup>i</sup> Together, the spatial oscillation of the field,  $\exp(ik_2z)$  and the oscillation of the polarization,  $\exp(-i2k_1z)$ , determine the efficiency of the nonlinear process: when perfect spatial resonance exists between the field and the corresponding polarization,[106] corresponding to the equality condition  $k_2 = 2k_1$ , enhancement of the field is optimized.[106, 125–129] This condition of momentum conservation can also be described by the quantity referenced previously,  $\Delta k$ , the phase mismatch; in our example of second-harmonic generation,  $\Delta k$  would be defined as the quantity:  $\Delta k = k_2 - 2k_1$ .<sup>ii</sup>[102, 125, 127]

The phase mismatch,  $\Delta k$ , can have a wide variety of consequences on nonlinear experiments. Within the limit of low depletion, it has been shown that the efficiency of the nonlinear process scales according to  $\sin(\Delta kL/2)/(\Delta kL/2)$  on the amplitude (field) level and  $\sin^2(\Delta kL/2)/(\Delta kL/2)^2$  on the intensity level, where  $L$  is the length of the nonlinear crystal; this dependence is also reported as the sinc function,  $\text{sinc}(\Delta kL/2)$  or  $\text{sinc}^2(\Delta kL/2)$ . [99, 102, 130] The fields generated by poorly phase matched processes have also been shown to exhibit phase modulation,[131, 132] the magnitude of which scales according to  $\Delta kL/2$ . [132] The final consequence of the phase mismatch we will mention is the limit imposed upon the phase matching bandwidth for a given process: the phase matching bandwidth is commonly taken to be the bandwidth over which  $\Delta k$  is

---

<sup>i</sup>In § 3.4.1 we will actually end up with a result in the frequency domain, such that the evolution of the field at  $\omega_2$  would depend upon  $\exp(ik_2z)P_{(2\omega_1)}$ , rather than  $\exp(ik_2z)\tilde{P}_{(2\omega_1)}$ . However, within the CW limit upon which this discussion is based, the distinction between the two is irrelevant.

<sup>ii</sup>Note that some authors define  $\Delta k$  as the negative value of the definition here; however, as the notation of Barnes and Corcoran shows,[125] it is generally the magnitude of  $\Delta k$  that matters.

less than  $\pi/L$ . [125, 127] This limit is imposed in both collinear [126, 127, 133] and noncollinear [120, 125, 127, 133–138] geometries. There are a variety of strategies that have been introduced to bypass phase-matching considerations; these include thin samples [139] and epi-directional detection, [140–142] pulse-shaping [143–145] to control phase in direct analogy to nuclear magnetic resonance, [144, 145] and high numerical aperture objectives to introduce a wide angular distribution to the excitation fields. [139, 140, 146–148] Otherwise, phase matching must be considered in both collinear and noncollinear experiments. [106]

In the collinear geometry, it is sufficient to consider a scalar representation of the phase matching condition. [106] We will show in § 3.4.1 that the wave vector can be defined  $k = n(\omega)\omega/c$  (Eq. 3.4.14), where  $n(\omega)$  is the refractive index of the material at frequency  $\omega$ . Generalizing our previous example, we could consider the frequency conversion process  $\omega_3 = \omega_2 + \omega_1$ ,  $\omega_3 \geq \omega_2 \geq \omega_1$ . For such a process, the phase matching condition would take the form  $k_3 = k_2 + k_1$ . By our definition of  $k$ , we can then frame the momentum conservation as  $n(\omega_3)\omega_3 = n(\omega_2)\omega_2 + n(\omega_1)\omega_1$ . In the manner of Boyd, [102] we can manipulate this relationship to show that this momentum conservation relation would require:  $n(\omega_3) - n(\omega_2) = [n(\omega_1) - n(\omega_2)](\omega_1/\omega_3)$ . Recognizing  $\omega_1/\omega_3$  must always be positive, the only way this equality can hold true is for  $n(\omega_3) > n(\omega_2)$  and  $n(\omega_1) > n(\omega_2)$  or for  $n(\omega_3) < n(\omega_2)$  and  $n(\omega_1) < n(\omega_2)$ ; under our assignment of  $\omega_3 \geq \omega_2 \geq \omega_1$ , this condition cannot be satisfied under normal dispersion, for which  $n(\omega)$  increases monotonically with  $\omega$ . [102, 106] While anomalous dispersion could permit momentum conservation, [102, 106] its application is not practical as it would require sufficiently reduced transparency that conversion is inefficient. [106] Instead, the birefringence of anisotropic materials is generally used as an alternative strategy for satisfying momentum conservation in collinear geometries. [102, 106]

Anisotropic crystals may be either biaxial or uniaxial. [106] In biaxial crystals, there are three unique refractive indices available, making consideration of effective index and phase matching more complicated. [106] However, there are a variety of biaxial crystals employed for different frequency conversion processes, such as bismuth triborate (BiBO), [149–151] lithium triborate (LBO), [152–157], and potassium titanyl phosphate (KTP). [158, 159] In contrast, uniaxial crystals exhibit only two refractive indices, the ordinary index ( $n_o$ ) and the extraordinary index ( $n_e$ ); the relative values of these refractive indices determine the nature of the uniaxial crystal: for negative uniaxial crystals,  $n_o > n_e$ , while  $n_e > n_o$  for positive uniaxial crystals. Many common uniaxial crystals - including potassium dihydrogen phosphate (KDP), [152, 160–163]  $\beta$ -barium borate (BBO), lithium niobate, [128, 133, 161, 162, 164, 165] silver gallium sulfide, [106, 166] and silver gallium selenide [106, 166] - are negative uniaxial crystals; BBO in particular has achieved wide-spread usage due to its high birefringence, low dependence of index upon temperature, [167] high damage threshold, [167, 168] low group velocity mismatch, and large nonlinearity. [126, 131, 168] In addition to the broad usage of BBO,



the behavior of uniaxial crystals is much more straightforward; we will consequently focus our discussion as related to birefringent media upon uniaxial crystals.

The indices of uniaxial crystals can be described according to the relation between the polarization state of the field, the wave vector ( $\mathbf{k}$ ) of the field, and the optic axis of the crystal ( $\mathbf{Z}$ ).<sup>[106]</sup> The orientation of the wave vector with respect to the crystalline axes is described by two angles: the phase matching angle,  $\theta$ , is the angle between the optic axis,  $\mathbf{Z}$ , and the wave vector, while the azimuthal angle,  $\phi$  is the angle between the  $\mathbf{X}$ -axis of the crystal and the projection of the wave vector in the crystal's  $\mathbf{XY}$  plane.<sup>[106]</sup> The field can be described as an ordinary or extraordinary beam, meanwhile, based upon the alignment of its polarization state with the principal plane formed by the optic axis and the wave vector. If the polarization of the field is perpendicular to this plane, the field is an ordinary beam and experiences the ordinary refractive index,  $n_o$ . On the other hand, if the polarization of the field is parallel to the principal plane, it is an extraordinary beam; in contrast to the ordinary polarization, extraordinary beams experience an index that exhibits a dependence upon  $\theta$ :

$$n(\theta) = n_o \sqrt{\frac{1 + \tan^2 \theta}{1 + (n_o/n_e)^2 \tan^2 \theta}} \quad (3.2.23)$$

It should be noted that for uniaxial crystals, the azimuthal angle,  $\phi$ , does not play a role in phase matching considerations.<sup>[106]</sup> This angle is important, however, in determining the symmetry of the crystal's nonlinear susceptibility; this is discussed in § 3.2.2.

The dependence of the effective refractive index of an extraordinary beam on  $\theta$  permits one method of phase matching, angle tuning. This strategy seeks to optimize  $\theta$  so as to minimize the phase mismatch associated with a particular process involving a certain set of frequencies. Due to the monotonic increase in index with increasing frequency, it is necessary to polarize the fields such that the highest frequency involved in the process is polarized such that it experiences the lower refractive index of the crystal:<sup>[102, 126, 169]</sup> in a negative uniaxial crystal, this requires extraordinary polarization for the highest frequency, while for a positive uniaxial crystal the highest frequency would be an ordinary beam. Phase matching requires the polarization of at least one of the two lower frequencies to be perpendicular to the polarization of the highest frequency; however, it is possible to have the two lower frequencies have either parallel (Type I) or perpendicular (Type II) polarization.<sup>[102, 106]</sup>

In BBO, these two options each present different advantages and disadvantages. Under parallel polarization, the signal and idler exhibit group velocities that cause both pulses to move away from the pump in the same direction.<sup>[126]</sup> As a consequence, Type I phase matching exhibits a finite pulse splitting length: when the crystal length is extended beyond the pulse splitting length, reduced gain is observed; gain ceases

when the length of the crystal is approximately twice the pulse splitting length.[170, 171] However, Type I phase matching also exhibits lower group velocity mismatches than Type II, which together with the higher effective nonlinearity, yields higher gain.[168, 172] This permits usage of lower pump energies.[173] Type I also exhibits one disadvantage associated with the lower group velocity mismatches: since the signal and idler exhibit a lower group velocity mismatch, Type I typically yields significantly greater amplification bandwidths, particularly when tuned close to degeneracy ( $\omega_2 \approx \omega_1$ ).[173, 174] Unfortunately, the increased bandwidth is not accompanied by a decrease in pulse duration, and the generated pulses are generally not near the transform limit.[175, 176]

In contrast, the perpendicular polarization of signal and idler in Type II phase matching causes the signal and idler to move in opposite directions with respect to the pump across much of the near infrared.[126, 171, 177] Within this regime, the gain represented by the pump pulse envelope synchronizes the propagation of the idler and signal pulses: this synchronization causes amplification similar to steady state behavior,[103] with exponential gain continuing even past the pulse splitting length.[126, 177] The steady state operation of this process yields consistent bandwidths across the tuning range.[173] While the bandwidths tend to be smaller than those obtained through Type I phase matching,[126] the pulses generated tend to be closer to the transform limit.[174, 175] While neither broadening nor gain saturation is expected within this regime,[170] pump depletion has been reported to have effects on the temporal characteristics of the generated pulses.[168, 171] As noted before, Type II phase matching is possible with either the signal or the idler polarized as an extraordinary beam; however, polarizing the idler (the lower frequency) parallel to the pump generally proves more feasible as it requires less birefringence for successful phase matching.[102]

One complication associated with angle tuning is spatial walk-off: due to the birefringence experienced by extraordinary beams when  $\theta \neq 0^\circ, 90^\circ$ , these beams exhibit a walk-off angle that is dependent upon the phase matching angle,  $\theta$ . [102, 106] This walk-off angle describes the relative angle between the wave vector and the Poynting vector,[106] the direction of flow for the energy density of the wave.[101, 106] This walk-off reduces the efficiency of the nonlinear process.[102] Temperature tuning is a strategy that has been employed to overcome this limitation.[102, 126] The strategy is based upon the dependence of refractive index upon temperature: while maintaining a constant phase matching angle,  $\theta = 90^\circ$ , temperature is adjusted to tune the refractive indices so as to achieve phase matching.[102] By operating at  $\theta = 90^\circ$ , walk off is avoided. This has been demonstrated in crystals such as LBO[153, 155, 170] and KDP.[127]

In contrast to collinear geometries, phase matching in a noncollinear geometry requires consideration of the directionality associated with the wave vector,  $\mathbf{k}$ . While this method is implemented in second-order frequency mixing processes,[125, 129, 152, 154, 171, 178–184] it is also of relevance in four-wave

mixing processes that access the third-order nonlinear susceptibility. In these third-order experiments, the BOXCAR geometry - in which the three excitation fields are aligned so as to occupy three of the four corners of a rectangle - is a common starting point for determining appropriate phase matching conditions.[120, 121, 135, 147, 185–189] Four-wave mixing experiments of this manner can be described according to the generalized process:

$$\omega_4 = c_1\omega_1 + c_2\omega_2 + c_3\omega_3 \quad (3.2.24)$$

where the set  $\{c_i\}$  describes the number and phase of interactions of each field in the experiment. For a given alignment, each field would have a characteristic wave vector  $\mathbf{k}_i$ ; according to the phase matching of the experiment, these wave vectors would cooperate to yield emission with a wave vector,  $\mathbf{k}'_4$ , satisfying the equation:

$$\mathbf{k}'_4 = c_1\mathbf{k}_1 + c_2\mathbf{k}_2 + c_3\mathbf{k}_3 \quad (3.2.25)$$

However, the magnitude of  $\mathbf{k}'_4$  may not necessarily be consistent with a field of frequency  $\omega_4$ . If the frequency  $\omega_4$  consistent with the energy conservation condition of Eq. 3.2.24 corresponds to a wave vector magnitude  $|\mathbf{k}_4| = n(\omega_4)\omega_4/c$ , the phase mismatch,  $\Delta k$ , for the process corresponds to the magnitude of the difference between  $\mathbf{k}'_4$  and the projection of  $\mathbf{k}_4$  on  $\mathbf{k}'_4$ :

$$\Delta k = \left| \mathbf{k}'_4 - \frac{|\mathbf{k}_4|}{|\mathbf{k}'_4|} \mathbf{k}'_4 \right| \quad (3.2.26)$$

Proper phase matching can be determined by identifying the angles that minimize the difference on the right hand side of Eq. 3.2.26. It should be noted that these angles correspond to the internal angles; in order to consider a mask for external alignment, it is necessary to consider the effects of refraction at the interface of the sample.

### 3.2.2 Susceptibilities

As we noted above, we will generally find it sufficient to consider the susceptibilities at the phenomenological level of Eq. 3.2.10 and 3.2.11. However, in this section we will introduce the various factors that contribute to the scale of the nonlinear susceptibility, as well as introduce the method of Midwinter and Warner for reducing the tensor character of uniaxial birefringent materials to an effective nonlinearity.

There are four key factors that contribute to the form of the susceptibility. The first two features we will discuss can be ascertained from Eq. 3.2.4 and 3.2.5. First, Eq. 3.2.5 illustrates that the nonlinear susceptibility scales with the number density of the oscillator; this property has a profound impact on the

contrasting behavior of (self-)heterodyned techniques - in which the signal is proportional to  $\chi^{(n)}$  - and homodyne-detected methods - in which the signal is proportional to  $|\chi^{(n)}|^2$ : in the former, the signal scales as  $N$ , while the latter scales as  $N^2$ . This difference will give differences in the detection level and sensitivity of heterodyne- and homodyne-detected techniques.[99, 190] Second, 3.2.4 and 3.2.5 illustrate that the nonlinear susceptibility provides insight into quantum mechanical properties of the oscillator; it is possible to show that Eq. 3.2.4 and 3.2.5 predict the nonlinear susceptibility to provide insight into the dipole strength, central frequency, and dephasing rate of the transitions.[99, 102, 109]

The third contribution to the susceptibilities is the local field enhancement factor. While we will generally know the macroscopic field,  $\tilde{\mathbf{E}}(t)$ , being applied, the interaction between the field and the material will be determined by the local field,  $\tilde{\mathbf{E}}_{\text{loc}}(t)$ , which will be influenced by induced polarizations. In this context, if we denote the molecular polarizability,  $\alpha$ , we can describe the linear polarization in terms of either the macroscopic field (Eq. 3.2.27a) or the local field (Eq. 3.2.27b):<sup>i</sup>

$$\tilde{\mathbf{P}}(t) = \epsilon_0 \chi^{(1)} \tilde{\mathbf{E}}(t) \quad (3.2.27a)$$

$$\tilde{\mathbf{P}}(t) = N\alpha \tilde{\mathbf{E}}_{\text{loc}}(t) \quad (3.2.27b)$$

In the mks system of units, the effect of the polarization on the local electric field in an isotropic medium is described by the Lorentz model:[107]

$$\tilde{\mathbf{E}}_{\text{loc}}(t) = \tilde{\mathbf{E}}(t) + \frac{1}{3\epsilon_0} \tilde{\mathbf{P}}(t) \quad (3.2.28)$$

Note that this contrasts with the Lorentz model for quantities in cgs or esu units:[102, 107, 109]

$$\tilde{\mathbf{E}}_{\text{loc}}(t) = \tilde{\mathbf{E}}(t) + \frac{4\pi}{3} \tilde{\mathbf{P}}(t) \quad (3.2.29)$$

By requiring the descriptions of the polarization in Eq. 3.2.27a and 3.2.27b to be equivalent, we can introduce the Lorentz model to yield:

$$\begin{aligned} \epsilon_0 \chi^{(1)} \tilde{\mathbf{E}}(t) &= N\alpha \tilde{\mathbf{E}}_{\text{loc}}(t) \\ &= N\alpha \left( \tilde{\mathbf{E}}(t) + \frac{1}{3\epsilon_0} \epsilon_0 \chi^{(1)} \tilde{\mathbf{E}}(t) \right) \end{aligned} \quad (3.2.30)$$

---

<sup>i</sup>Note that the form of Eq. 3.2.27a implies that the forms of these equations are appropriate for a system in which the quantities are reported in mks units. The following derivation of the local field effect can be reproduced with the appropriate modifications to describe quantities in cgs or esu units. However, as this derivation is presented by authors such as Boyd, Kittel, and Shen,[102, 107, 109] we will present the derivation of the appropriate correction for a system described in mks units.

Combining terms associated with  $\chi^{(1)}$  allows us to define the susceptibility:

$$\chi^{(1)} = \frac{N\alpha}{\epsilon_0 - N\alpha/3} \quad (3.2.31)$$

To proceed, we can invoke the definition of the dielectric constant,  $\epsilon = \epsilon_0(1 + \chi^{(1)})$ , [101] allowing substitution for  $\chi^{(1)}$ :

$$\epsilon_r - 1 = \frac{N\alpha}{\epsilon_0 - N\alpha/3} \quad (3.2.32)$$

where  $\epsilon_r$  is the relative permittivity,  $\epsilon_r = \epsilon/\epsilon_0$ . [101] If we manipulate Eq. 3.2.32 to isolate a quantity proportional to  $N\alpha$ , we arrive at the Clausius-Mossotti relation: [107]

$$\frac{\epsilon_r - 1}{\epsilon_r + 2} = \frac{N\alpha}{3\epsilon_0} \quad (3.2.33)$$

which has the analogous result for cgs/esu units: [102, 107]

$$\frac{\epsilon - 1}{\epsilon + 2} = \frac{4\pi N\alpha}{3} \quad (3.2.34)$$

with  $\epsilon$  defined in the cgs or esu unit systems as  $\epsilon = 1 + 4\pi\chi^{(1)}$ . From Eq. 3.2.33, we may multiply each side of the equation by  $-1$ , then add 1; the result of these operations can then be shown to yield the relationship:

$$\frac{\epsilon_r + 2}{3\epsilon_0} = \frac{1}{\epsilon_0 - \frac{N\alpha}{3}} \quad (3.2.35)$$

Recognizing that Eq. 3.2.31 relates the susceptibility to the product of the quantities  $N\alpha$  and  $1/(\epsilon_0 - N\alpha/3)$ , we can substitute according to Eq. 3.2.35 to define the susceptibility:

$$\chi^{(1)} = \frac{\epsilon_r + 2}{3\epsilon_0} N\alpha \quad (3.2.36)$$

where the term  $(\epsilon_r + 2)/3\epsilon_0$  is the local field correction factor. This contrasts with the correction factor appropriate for cgs or esu units:  $(\epsilon + 2)/3$ . [102, 109] However, in most materials, we will be able to relate  $\epsilon_r$  (mks units) or  $\epsilon$  (cgs/esu units) to the complex index of refraction,  $\bar{n}$ , according to the relationships:

$$\epsilon_r = \bar{n}^2 \quad (3.2.37a)$$

$$\epsilon = \bar{n}^2 \quad (3.2.37b)$$

The relationships of Eq. 3.2.37a and 3.2.37b allow us to substitute for the complex index of refraction in the local field correction factor, yielding factors of  $(\bar{n}^2+2)/3\epsilon_0$  and  $(\bar{n}^2+2)/3$  for mks and cgs/esu units, respectively.[102, 107]

This analysis can be extended to higher order susceptibilities.[102, 109] However, when this treatment is extended to consider the form of  $\chi^{(n)}$ , the result exhibits  $(n + 1)$  enhancement terms. In other words, the local field correction factor will assume the form  $((\bar{n}^2+2)/3\epsilon_0)^{n+1}$  (mks units) or  $((\bar{n}^2+2)/3)^{n+1}$  (cgs/esu units). This form arises due to the need to consider the enhancement arising at the frequency of the polarization (1 term) and the enhancement arising at each of the fields contributing to the polarization ( $n$  terms).[99, 102, 109]

Finally, the form of the nonlinear susceptibility can provide information regarding the symmetry of the medium. This behavior is particular pronounced in uniaxial birefringent media, for which it is possible to derive closed form solutions predicting the symmetry of the effective nonlinear susceptibility for experiments involving different combinations for the polarization states of the incident fields. The observed symmetry can have value in characterizing the structure of birefringent materials[191–193] and is an important consideration in determining the appropriate alignment[194] and efficiency of nonlinear crystals. The symmetry is defined according to the angles formed between the optical axes ( $\mathbf{X}$ ,  $\mathbf{Y}$ , and  $\mathbf{Z}$ ) and the wave vectors ( $\mathbf{k}$ ) of the electric fields.[106, 119, 195] We recall the definitions of the relevant angles ( $\theta$  and  $\phi$ ) from § 3.2.1:  $\theta$  reports the angle between  $\mathbf{k}$  and  $\mathbf{Z}$ , while  $\phi$  characterizes the angle between  $\mathbf{X}$  and the projection of  $\mathbf{k}$  on the  $\mathbf{XY}$  plane.[106] From these angles, the projections of the field onto each axis,  $E_{\mathbf{X}}$ ,  $E_{\mathbf{Y}}$ , and  $E_{\mathbf{Z}}$ , can be defined for ordinary beams:[119]

$$\begin{bmatrix} E_{\mathbf{X}}^o \\ E_{\mathbf{Y}}^o \\ E_{\mathbf{Z}}^o \end{bmatrix} = \begin{bmatrix} \sin(\phi) \\ -\cos(\phi) \\ 0 \end{bmatrix} E^o \quad (3.2.38)$$

where  $E^o$  is the amplitude of the electric field for the ordinary beam, and for extraordinary beams:[119]

$$\begin{bmatrix} E_{\mathbf{X}}^e \\ E_{\mathbf{Y}}^e \\ E_{\mathbf{Z}}^e \end{bmatrix} = \begin{bmatrix} -\cos(\theta)\cos(\phi) \\ -\cos(\theta)\sin(\phi) \\ \sin(\theta) \end{bmatrix} E^e \quad (3.2.39)$$

where  $E^e$  is the amplitude of the electric field for extraordinary beam.<sup>i</sup> While the symmetry of the tensor  $\chi^{(2)}$  is rigorously described by three polarization indices,  $\chi_{ijk}^{(2)}$ , [102, 106] under conditions in which Kleinman

---

<sup>i</sup>We note here that there appears to be an inconsistency in Dmitriev et al. For the effective electric field vectors, Dmitriev

symmetry is valid, the three dimensional representation of  $\chi_{ijk}^{(2)}$  or  $d_{ijk} = 1/2\chi_{ijk}^{(2)}$  can be reduced to a planar representation. This notation reduces  $d_{ijk}$  to  $d_{il}$ , where  $l = 1$  represents  $jk = 11$  (or  $jk = \mathbf{XX}$ ),  $l = 2$  corresponds to  $jk = 22$  (or  $jk = \mathbf{YY}$ ),  $l = 3$  arises from  $jk = 33$  (or  $jk = \mathbf{ZZ}$ ),  $l = 4$  replaces  $jk = 23$  and  $jk = 32$  (or  $jk = \mathbf{YZ}$  and  $jk = \mathbf{ZY}$ ),  $l = 5$  is a substitute for  $jk = 31$  or  $jk = 13$  (or  $jk = \mathbf{XZ}$  and  $jk = \mathbf{ZX}$ ), and  $l = 6$  derives from  $jk = 12$  or  $jk = 21$  (or  $jk = \mathbf{YX}$  and  $jk = \mathbf{XY}$ ).[102, 106] In addition to these substitutions, we also have to redefine  $P_i = 2d_{ijk}E_jE_k$ ; in the planar representation, the analogous form is  $P_i = 2d_{il}E_l^2$ . [102, 119] Alternatively, we can consider that we are sampling a particular polarization state, in which case the effective polarization is  $P = P_i \cdot (2d_{il}E_l^2)$ . Making substitutions in  $d_{il}$  appropriate to Kleinman symmetry, this yields:

$$P = 2 \begin{bmatrix} P_{\mathbf{X}} \\ P_{\mathbf{Y}} \\ P_{\mathbf{Z}} \end{bmatrix} \cdot \begin{bmatrix} d_{11} & d_{12} & d_{13} & d_{14} & d_{15} & d_{16} \\ d_{16} & d_{22} & d_{23} & d_{24} & d_{14} & d_{12} \\ d_{15} & d_{24} & d_{33} & d_{23} & d_{13} & d_{14} \end{bmatrix} \begin{bmatrix} E_{\mathbf{X}}^2 \\ E_{\mathbf{Y}}^2 \\ E_{\mathbf{Z}}^2 \\ E_{\mathbf{Y}}E_{\mathbf{Z}} + E_{\mathbf{Z}}E_{\mathbf{Y}} \\ E_{\mathbf{X}}E_{\mathbf{Z}} + E_{\mathbf{Z}}E_{\mathbf{X}} \\ E_{\mathbf{X}}E_{\mathbf{Y}} + E_{\mathbf{Y}}E_{\mathbf{X}} \end{bmatrix} \quad (3.2.40)$$

Population of  $d_{il}$  can be achieved according to the the crystal class of the material.

To demonstrate how this might be applied, we will consider the case of BBO. As BBO belongs to the 3m point group,[106] it exhibits nonzero tensor elements  $\mathbf{XZX} = \mathbf{YZY}$ ,  $\mathbf{XXZ} = \mathbf{YYZ}$ ,  $\mathbf{ZXX} = \mathbf{ZYY}$ ,  $\mathbf{ZZZ}$ ,  $\mathbf{YYY} = -\mathbf{YXX} = -\mathbf{XXY} = -\mathbf{XYX}$ . [102] In terms of  $d_{il}$ , this corresponds to  $15 = 24$  ( $\mathbf{XZX} = \mathbf{YZY}$  and  $\mathbf{XXZ} = \mathbf{YYZ}$ ),  $31 = 32$  ( $\mathbf{ZXX} = \mathbf{ZYY}$ ),  $33, 22 = -21 = -16$  ( $\mathbf{YYY} = -\mathbf{YXX} = -\mathbf{XXY} = -\mathbf{XYX}$ ). [106] Substituting according to these relationships and considering the two major processes for

et al use the phase:[106]

$$\begin{bmatrix} E_{\mathbf{X}}^o \\ E_{\mathbf{Y}}^o \\ E_{\mathbf{Z}}^o \end{bmatrix} = \begin{bmatrix} -\sin(\phi) \\ \cos(\phi) \\ 0 \end{bmatrix} E^o$$

for the ordinary beam, and for the extraordinary beam:[106]

$$\begin{bmatrix} E_{\mathbf{X}}^e \\ E_{\mathbf{Y}}^e \\ E_{\mathbf{Z}}^e \end{bmatrix} = \begin{bmatrix} \cos(\theta) \cos(\phi) \\ \cos(\theta) \sin(\phi) \\ -\sin(\theta) \end{bmatrix} E^e$$

Note that these phases are opposite those employed by Midwinter and Warner.[119] However, the formulae for the effective nonlinearities of BBO reported by Dmitriev et al are consistent with the notation of Midwinter and Warner, as well as Boyd.[102, 106, 119] At the intensity level, both results will be identical when only the nonlinearity of BBO is relevant - and it should be noted that Dmitriev et al acknowledge this by reporting only the relative signs of  $d_{22}$  and  $d_{31}$ [106] - but this inconsistency bears mentioning. As it appears to yield results consistent with all other authors,[102, 106, 119] we will adopt the phase reported by Midwinter and Warner.[119]

BBO (Type I:  $e \leftarrow oo$ ; Type II:  $e \leftarrow oe$ ), we can evaluate Eq. 3.2.40 for Type I phase matching:

$$\begin{aligned}
P &= 2 \begin{bmatrix} -\cos(\theta) \cos(\phi) \\ -\cos(\theta) \sin(\phi) \\ \sin(\theta) \end{bmatrix} \cdot \begin{bmatrix} 0 & 0 & 0 & 0 & d_{15} & -d_{22} \\ -d_{22} & d_{22} & 0 & d_{15} & 0 & 0 \\ d_{15} & d_{15} & d_{33} & 0 & 0 & 0 \end{bmatrix} \begin{bmatrix} \sin^2(\phi) \\ \cos^2(\phi) \\ 0 \\ 0 \\ 0 \\ -2 \cos(\phi) \sin(\phi) \end{bmatrix} E_{\text{sig}}^o E_{\text{id1}}^o \\
&= 2 \begin{bmatrix} -\cos(\theta) \cos(\phi) \\ -\cos(\theta) \sin(\phi) \\ \sin(\theta) \end{bmatrix} \cdot \begin{bmatrix} 2d_{22} \sin(\phi) \cos(\phi) \\ -d_{22} \sin^2(\phi) + d_{22} \cos^2(\phi) \\ d_{15} \end{bmatrix} E_{\text{sig}}^o E_{\text{id1}}^o \\
&= 2[-d_{22} \cos(\theta) \sin(3\phi) + d_{15} \sin(\theta)] E_{\text{sig}}^o E_{\text{id1}}^o
\end{aligned} \tag{3.2.41}$$

and for Type II phase matching:

$$\begin{aligned}
P &= 2 \begin{bmatrix} -\cos(\theta) \cos(\phi) \\ -\cos(\theta) \sin(\phi) \\ \sin(\theta) \end{bmatrix} \cdot \begin{bmatrix} 0 & 0 & 0 & 0 & d_{15} & -d_{22} \\ -d_{22} & d_{22} & 0 & d_{15} & 0 & 0 \\ d_{15} & d_{15} & d_{33} & 0 & 0 & 0 \end{bmatrix} \begin{bmatrix} -\cos(\theta) \cos(\phi) \sin(\phi) \\ \cos(\theta) \cos(\phi) \sin(\phi) \\ 0 \\ -\sin(\theta) \cos(\phi) \\ \sin(\theta) \sin(\phi) \\ \cos(\theta) \cos(2\phi) \end{bmatrix} E_{\text{sig}}^o E_{\text{id1}}^o \\
&= 2 \begin{bmatrix} -\cos(\theta) \cos(\phi) \\ -\cos(\theta) \sin(\phi) \\ \sin(\theta) \end{bmatrix} \cdot \begin{bmatrix} d_{15} \sin(\theta) \sin(\phi) - d_{22} \cos(\theta) \cos(2\phi) \\ 2d_{22} \cos(\theta) \cos(\phi) \sin(\phi) - d_{15} \sin(\theta) \cos(\phi) \\ 0 \end{bmatrix} E_{\text{sig}}^o E_{\text{id1}}^o \\
&= 2[d_{22} \cos^2(\theta) \cos(3\phi)] E_{\text{sig}}^o E_{\text{id1}}^o
\end{aligned} \tag{3.2.42}$$

Considering the effective polarization to be of the form  $P = 2d_{\text{eff}}E^2$ , we can use the results of the schemes in Eq. 3.2.41 and 3.2.42 to define  $d_{\text{eff}} = d_{15} \sin(\theta) - d_{22} \cos(\theta) \sin(3\phi)$  for Type I phase matching and  $d_{\text{eff}} = d_{22} \cos^2(\theta) \cos(3\phi)$  for Type II phase matching. This latter result is consistent with the published



formulae for  $d_{\text{eff}}$  for Type II phase matching;[102, 106, 119] for Type I phase matching, we note that Kleinman symmetry causes  $d_{15} = d_{31}$ ,[195] permitting substitution into our result in Eq. 3.2.41 to yield the more standard form,  $d_{\text{eff}} = d_{31} \sin(\theta) - d_{22} \cos(\theta) \sin(3\phi)$ . [102, 106, 119]

### 3.3 Maxwell's Equations and the Wave Equation

In § 3.1.1, we claimed that Maxwell's equations predict that the free space propagation of electric and magnetic fields are consistent with a wave equation of the form Eq. 3.1.1. We also introduced the form of Maxwell's equations as they apply to free space in order to explore the expected relationship between the electric and magnetic fields in light. In the following sections, we will outline the derivation of the wave equation from Maxwell's equations with the intention of arriving at a generalized result that can be applied to systems described in either cgs/esu or mks units. Throughout this section, we will continue to focus exclusively on the form of these equations as they relate to the electric field; a similar derivation can be performed to describe the magnetic field.[101] Throughout this section, we will end up alternating between noting quantities as vector and scalar values, but will explain at the appropriate point in § 3.3.3 why this is necessary. Various presentations of the wave equation, the final result of the derivation in § 3.3.3, are presented in § 3.3.1 for convenience.

#### 3.3.1 Wave Equation

As we will show in the succeeding sections, Maxwell's equations show that the propagation of an electric field,  $\tilde{E}(\mathbf{r}, z, t)$ , under the influence of an induced polarization,  $\tilde{P}(\mathbf{r}, z, t)$ , in a medium is predicted:

$$\nabla^2 \tilde{E}(\mathbf{r}, z, t) - \epsilon_0 \mu \frac{\partial^2}{\partial t^2} \tilde{E}(\mathbf{r}, z, t) = \mu \frac{\partial^2}{\partial t^2} \tilde{P}(\mathbf{r}, z, t) \quad (3.3.1)$$

when  $\tilde{E}(\mathbf{r}, z, t)$  and  $\tilde{P}(\mathbf{r}, z, t)$  are reported in mks units, with  $\epsilon_0 = 8.85 \times 10^{-12} \text{F/m}$  describing the permittivity of free space and  $\mu$  describing the permeability of the material. When  $\tilde{E}(\mathbf{r}, z, t)$  and  $\tilde{P}(\mathbf{r}, z, t)$  are represented by cgs units, the wave equation assumes the form:

$$\nabla^2 \tilde{E}(\mathbf{r}, z, t) - \frac{1}{c^2} \frac{\partial^2}{\partial t^2} \tilde{E}(\mathbf{r}, z, t) = \frac{4\pi}{c^2} \frac{\partial^2}{\partial t^2} \tilde{P}(\mathbf{r}, z, t) \quad (3.3.2)$$

where  $c$  is the speed of light. We will also adopt the generalization:

$$\nabla^2 \tilde{E}(\mathbf{r}, z, t) - b^2 d e \frac{\partial^2}{\partial t^2} \tilde{E}(\mathbf{r}, z, t) = a b^2 e \frac{\partial^2}{\partial t^2} \tilde{P}(\mathbf{r}, z, t) \quad (3.3.3)$$

where we use  $a$ ,  $b$ ,  $d$ , and  $e$  to stand in for the various constants. In the generalized form of Eq. 3.3.3, the values of  $a$  and  $b$  are  $a = b = 1$  for the mks unit system or  $a = 4\pi$  and  $b = c^{-1}$  for cgs and esu units. Meanwhile,  $d$  and  $e$  are used to represent the permittivity and permeability: in cgs or esu units,  $d = e = 1$ , while mks units require  $d = \epsilon_0$  and  $e = \mu$ .

In a similar manner to § 3.1, we will generally define a coordinate system such that the field is taken to propagate along the  $z$  direction. Within such a coordinate system, we can consider that  $\nabla^2$ , defined according to Eq. 3.3.4:

$$\nabla^2 = \frac{\partial^2}{\partial x^2} + \frac{\partial^2}{\partial y^2} + \frac{\partial^2}{\partial z^2} \quad (3.3.4)$$

has two key contributions: a term corresponding to the direction of propagation ( $\partial^2/\partial z^2$ ), and two terms corresponding to evolution of the field perpendicular to the direction of propagation (the transverse components,  $\partial^2/\partial x^2$  and  $\partial^2/\partial y^2$ ). As we introduced in § 3.1.2, we will generally not be concerned with differentiating  $x$  from  $y$ , and have accordingly been using the generalized transverse coordinate,  $\mathbf{r}$ . In a similar manner, we can introduce the operator  $\nabla_{\mathbf{T}}^2$  to generalize the transverse components of  $\nabla^2$ , defining this operator:

$$\nabla_{\mathbf{T}}^2 = \frac{\partial^2}{\partial x^2} + \frac{\partial^2}{\partial y^2} \quad (3.3.5)$$

With this operator, we can simplify Eq. 3.3.3 by splitting  $\nabla^2$  accordingly:

$$\nabla_{\mathbf{T}}^2 \tilde{E}(\mathbf{r}, z, t) + \frac{\partial^2}{\partial z^2} \tilde{E}(\mathbf{r}, z, t) - b^2 d e \frac{\partial^2}{\partial t^2} \tilde{E}(\mathbf{r}, z, t) = a b^2 e \frac{\partial^2}{\partial t^2} \tilde{P}(\mathbf{r}, z, t) \quad (3.3.6)$$

However, in the limit that the field can be considered to be a plane wave, we do not anticipate the field exhibiting any dependence upon the transverse coordinates; at this limit, we can assume  $\nabla_{\mathbf{T}}^2 \tilde{E}(z, t) = 0$ . This allows us to simplify Eq. 3.3.6 further, yielding:

$$\frac{\partial^2}{\partial z^2} \tilde{E}(z, t) - b^2 d e \frac{\partial^2}{\partial t^2} \tilde{E}(z, t) = a b^2 e \frac{\partial^2}{\partial t^2} \tilde{P}(z, t) \quad (3.3.7)$$

### 3.3.2 Maxwell's Equations

Here we will briefly list Maxwell's equations and discuss appropriate assumptions that might be made for common material systems. The dependence of the wave equation on the different unit systems indicated in § 3.3.1 stems from the forms of Maxwell's equations in each unit system. However, the variables  $a$  and  $b$

allow these equations to be generalized, yielding the forms in Eq. 3.3.8a - 3.3.8d:

$$\nabla \cdot \tilde{\mathbf{D}}(t) = a\rho \quad (3.3.8a)$$

$$\nabla \cdot \tilde{\mathbf{B}}(t) = 0 \quad (3.3.8b)$$

$$\nabla \times \tilde{\mathbf{E}}(t) = -b \frac{\partial}{\partial t} \tilde{\mathbf{B}}(t) \quad (3.3.8c)$$

$$\nabla \times \tilde{\mathbf{H}}(t) = ab\tilde{\mathbf{J}}(t) + b \frac{\partial}{\partial t} \tilde{\mathbf{D}}(t) \quad (3.3.8d)$$

As before, we will allow  $a = 4\pi$  and  $b = c^{-1}$  for cgs or esu unit systems, while we will require  $a = b = 1$  for the mks unit system.

Gauss' law (Eq. 3.3.8a) relates the changes in the displacement,  $\tilde{\mathbf{D}}(t)$ , to the free charges,  $\rho$ , in the medium. Generally, we will be able to assume that the medium contains no free charges ( $\rho = 0$ ), under which conditions Gauss' law reduces to  $\nabla \cdot \tilde{\mathbf{D}}(t) = 0$ . We have previously introduced the displacement (see § 3.2), through which we relate the dependence of the propagating field upon polarizations existing in the medium (see Eq. 3.2.7 and 3.2.8). However, the forms of Eq. 3.2.7 and 3.2.8 illustrate that we will also need to consider a generalized form for this quantity. This is achieved through our previous assignment of  $a$  and  $d$ ,  $a = 4\pi$  and  $d = 1$  for cgs and esu units, or  $a = 1$  and  $d = \epsilon_0$  for mks units. The introduction of these generalized constants yields:

$$\tilde{\mathbf{D}}(t) = d\tilde{\mathbf{E}}(t) + a\tilde{\mathbf{P}}(t) \quad (3.3.9)$$

While Gauss' law of magnetism (Eq. 3.3.8b) and Faraday's law (Eq. 3.3.8c) do not require further simplification, we will be able to make some modifications to Ampere's law (Eq. 3.3.8d). First, it will generally be reasonable to assume the absence of free currents ( $\tilde{\mathbf{J}}(t) = 0$ ), leaving:

$$\nabla \times \tilde{\mathbf{H}}(t) = b \frac{\partial}{\partial t} \tilde{\mathbf{D}}(t) \quad (3.3.10)$$

Second, we will often be able to assume that the medium is nonmagnetic or nearly so ( $\tilde{\mathbf{M}}(t) \approx 0$ ), in which case the magnetic field,  $\tilde{\mathbf{B}}(t)$ , is simply:  $\tilde{\mathbf{B}}(t) = e(\tilde{\mathbf{H}}(t) + \tilde{\mathbf{M}}(t)) \approx e\tilde{\mathbf{H}}(t)$ , where  $e = 1$  for cgs or esu units, but  $e = \mu$  for mks units. This then simplifies Ampere's law to yield:

$$\nabla \times \tilde{\mathbf{B}}(t) = be \frac{\partial}{\partial t} \tilde{\mathbf{D}}(t) \quad (3.3.11)$$

We will also note that at optical frequencies, we will generally be able to neglect the magnetic response of the material, permitting the assumption that  $\mu \approx \mu_0$  when we are concerned with mks units.

### 3.3.3 Derivation of the Generalized Wave Equation

An outline of the derivation of Eq. 3.3.3 is given by Boyd[102] for cgs/esu units. Powers [196] demonstrates how the wave equation would be derived for mks units, but restricts the derivation to the case of the linear optical response. These derivations are generalized and reproduced below.

We have previously outlined (§ 3.3.2) a handful of approximations and simplifications that we can make to Maxwell's equations, Eq. 3.3.8a - 3.3.8d. We start the derivation with Faraday's law:

$$\nabla \times \tilde{\mathbf{E}}(t) = -b \frac{\partial}{\partial t} \tilde{\mathbf{B}}(t) \quad (3.3.12)$$

and proceed to take the curl ( $\nabla \times$ ) of both sides. This results in:

$$\nabla \times \nabla \times \tilde{\mathbf{E}}(t) = -b \nabla \times \frac{\partial}{\partial t} \tilde{\mathbf{B}}(t) \quad (3.3.13)$$

However, since the curl only applies to the spatial variables, while the derivative in Eq. 3.3.13 is with respect to time, we can reverse the order in which these operations are applied:

$$\nabla \times \nabla \times \tilde{\mathbf{E}}(t) = -b \frac{\partial}{\partial t} \nabla \times \tilde{\mathbf{B}}(t) \quad (3.3.14)$$

However, from Eq. 3.3.11, we know  $\nabla \times \tilde{\mathbf{B}}(t) = be^{\partial/\partial t} \tilde{\mathbf{D}}(t)$ ; therefore, we can substitute for  $\nabla \times \tilde{\mathbf{B}}(t)$  in Eq. 3.3.14, yielding:

$$\begin{aligned} \nabla \times \nabla \times \tilde{\mathbf{E}}(t) &= -b \frac{\partial}{\partial t} \left( be \frac{\partial}{\partial t} \tilde{\mathbf{D}}(t) \right) \\ &= -b^2 e \frac{\partial^2}{\partial t^2} \tilde{\mathbf{D}}(t) \end{aligned} \quad (3.3.15)$$

At this point, it is common to use the identity:

$$\nabla \times \nabla \times \tilde{\mathbf{E}}(t) = \nabla[\nabla \cdot \tilde{\mathbf{E}}(t)] - \nabla^2 \tilde{\mathbf{E}}(t) \quad (3.3.16)$$

The advantage gained from this identity is that we have previously indicated that Gauss' law can generally be taken to be of the form:  $\nabla \cdot \tilde{\mathbf{D}}(t) = 0$ . Using the fact that  $\tilde{\mathbf{D}}(t)$  is of the form in Eq. 3.3.9, we can distribute the dot product to yield:[197]

$$\nabla \cdot \tilde{\mathbf{D}}(t) = d \nabla \cdot \tilde{\mathbf{E}}(t) + a \nabla \cdot \tilde{\mathbf{P}}(t) = 0 \quad (3.3.17)$$

Since the polarization is a function of the electric field, it is often assumed that the relationship in Eq. 3.3.17 implies that  $\nabla \cdot \tilde{\mathbf{E}}(t) = 0$ . [102] This then allows us to reduce  $\nabla \times \nabla \times \tilde{\mathbf{E}}(t)$  to the second term on the right hand side of Eq. 3.3.16,  $-\nabla^2 \tilde{\mathbf{E}}(t)$ , yielding:

$$\nabla^2 \tilde{\mathbf{E}}(t) = b^2 e \frac{\partial^2}{\partial t^2} \tilde{\mathbf{D}}(t) \quad (3.3.18)$$

Splitting the displacement according to Eq. 3.3.9 and combining the terms associated with the electric field then yields the wave equation:

$$\nabla^2 \tilde{\mathbf{E}}(t) - b^2 d e \frac{\partial^2}{\partial t^2} \tilde{\mathbf{E}}(t) = a b^2 e \frac{\partial^2}{\partial t^2} \tilde{\mathbf{P}}(t) \quad (3.3.19)$$

From Eq. 3.3.19, it is trivial to verify our claim that light behaves as a wave in free space: under such conditions,  $\tilde{\mathbf{P}}(t) = 0$ , leaving only the left hand side. Since the Laplacian operator contains the propagation and transverse evolution, we have a form of the wave equation in Eq. 3.3.19, with  $b^2 d e$  equal to  $1/v^2$ . Using our definitions for these generalized variables ( $b = 1$ ,  $d = \epsilon_0$ , and  $e = \mu \approx \mu_0$ , or  $b = c^{-1}$ ,  $d = 1$ , and  $e = 1$ ), we can then show that the speed of the wave predicted by Eq. 3.3.19 is  $c$ , the speed of light, in both systems of units.

Lax et al, [108] however, indicate that substitution according to the identity in Eq. 3.3.16 is not necessarily rigorous if we are later splitting the Laplacian operator in the manner of Eq. 3.3.6. Rather, they argue that it is more accurate to consider the separation of the longitudinal and transverse components in Eq. 3.3.15, taking the curl to be  $(\partial/\partial z + \nabla_T) \times$ . They justify this treatment by showing that the form of the wave equation resulting from applying the identity of Eq. 3.3.16 prior to separating the transverse and longitudinal components results in an inconsistency in the behavior of polarized fields. In their treatment - in which they apply the curl as  $(\partial/\partial z + \nabla_T) \times$  - it is relatively straightforward, but tedious, to show that Maxwell's equations predict a pair of coupled differential equations, one describing transverse propagation and the other describing longitudinal propagation, of the form:<sup>1</sup>

$$\nabla_T \left[ \nabla_T \cdot \tilde{\mathbf{E}}_T(t) + \frac{\partial}{\partial z} \tilde{E}_z(t) - i k_0 \tilde{E}_z(t) \right] - \left[ \nabla_T^2 + \frac{\partial^2}{\partial z^2} - i 2 k_0 \frac{\partial}{\partial z} - k_0^2 \right] \tilde{\mathbf{E}}_T(t) = -\frac{1}{c^2} \frac{\partial^2}{\partial t^2} \tilde{\mathbf{D}}_T^{(1)}(t) \quad (3.3.20a)$$

$$\frac{\partial}{\partial z} \left[ \nabla_T \cdot \tilde{\mathbf{E}}_T(t) \right] - i k_0 \nabla_T \cdot \tilde{\mathbf{E}}_T(t) - \nabla_T^2 \tilde{E}_z(t) = -\frac{1}{c^2} \frac{\partial^2}{\partial t^2} \tilde{D}_z^{(1)}(t) \quad (3.3.20b)$$

---

<sup>1</sup>It should be noted that Lax et al use the convention that the electric field accumulates phase according to  $\exp(ik_0 z)$ , rather than  $\exp(-ik_0 z)$ . The forms of Eq. 3.3.20a and 3.3.20b are derived in a manner appropriate to our convention; these only differ from the forms presented by Lax et al by the sign of the imaginary terms (substituting  $\pm ik_0$  by  $\mp ik_0$ ). [108]

Unfortunately, these coupled differential equations prove difficult to implement, with Lax et al needing approximations in order to describe the propagation of the  $\text{TEM}_{00}$  mode. Additionally, their result does not exhibit significant deviation from the model predicted by Eq. 3.3.6. Nevertheless, some authors[104] acknowledge the simplification introduced within the derivation shown above and consider the resulting wave equation to more accurately serve as a description for the scalar representation of the wave:

$$\nabla^2 \tilde{E}(t) - b^2 de \frac{\partial^2}{\partial t^2} \tilde{E}(t) = ab^2 e \frac{\partial^2}{\partial t^2} \tilde{P}(t) \quad (3.3.21)$$

We will adopt this convention proceeding forward.

### 3.4 Pulse Propagation in Dispersive Media

In this section, we will apply the wave equation (§ 3.3) to describe the effects of propagation on ultrafast pulses. This section will be divided into four subsections. In the first, we will derive the general treatment of ultrafast pulse propagation, concluding in the second section in which we consider the ramifications of the slowly varying amplitude approximation. The third and fourth sections will consider applications of the general treatment towards two specific scenarios: a description of  $\text{TEM}_{00}$  mode propagation, and the integration of an arbitrary polarization to predict the emitted field.

#### 3.4.1 General Treatment of Pulse Propagation in Dispersive Media

While Akhmanov et al[103] imply a strategy for deriving the results of the following treatment in the time domain, we will follow the lead of Boyd [102], who appears influenced by Brabec and Krausz,[115] with a derivation that proceeds mostly in the frequency domain. This approach relies upon (inverse) Fourier transformation between the time and frequency domains at multiple points during the derivation; this is done to make the application of different effects mathematically more tractable. While we will generally not explicitly show the introduction of the exponential and integration associated with these transforms, we will note when the introduction of the appropriate quantities has ramifications on the result. We will continue to follow the conventions we introduced previously: normalization required for transformation into and from the angular frequency domain will be incorporated during inverse Fourier transformation, and we will apply the exponentials  $\exp(-i\omega t)$  and  $\exp(i\omega t)$  for Fourier transformation and inverse Fourier transformation, respectively. The former convention is consistent with Boyd and others,[102, 112–114] while the latter is not consistent with Boyd,[102] but has precedence from other authors.[112, 114]. These conventions will result in a deviation from the derivation shown here and the derivation presented by Boyd;[102] we will note the point

at which the derivations begin deviating significantly. While we will work with general functions to note the electric field, polarization, and their respective envelope functions, we will assume these functions are compatible with Fourier transformation.[114] We will also assume the electric field and polarization exhibit forms compatible with Eq. 3.1.27 and 3.2.17 but will also assume it is sufficient to consider the propagation of only the complex field and the associated term of the polarization.

We will begin with the result of Eq. 3.3.7: while we will introduce the transverse propagation in later sections (see § 3.4.3 and § 3.4.4), it is sufficient to consider the following derivation within the plane wave limit. From Eq. 3.3.7, we will invoke the behavior of Eq. 3.2.9 and split the polarization on the right hand side into the linear and nonlinear contributions,  $\tilde{P}^L(z, t) = \tilde{P}^{(1)}(z, t)$  and  $\tilde{P}^{(NL)}(z, t)$ . Substituting the sum of these terms into Eq. 3.3.7 yields:

$$\frac{\partial^2}{\partial z^2} \tilde{E}(z, t) - b^2 d e \frac{\partial^2}{\partial t^2} \tilde{E}(z, t) - ab^2 e \frac{\partial^2}{\partial t^2} \tilde{P}^{(1)}(z, t) = ab^2 e \frac{\partial^2}{\partial t^2} \tilde{P}^{NL}(z, t) \quad (3.4.1)$$

In Eq. 3.4.1, we have also subtracted the term in  $\tilde{P}^{(1)}(z, t)$  from both sides; the advantage to doing so is that it allows us to introduce the linear displacement,  $\tilde{D}^{(1)}(z, t)$ . This quantity is defined in a manner analogous to Eq. 3.3.9, with the exception that the contributing polarization is restricted to the first-order term,  $\tilde{P}^{(1)}(z, t)$ , of the series. The generalized form of the linear displacement is then:

$$\tilde{D}^{(1)}(z, t) = d\tilde{E}(z, t) + a\tilde{P}^{(1)}(z, t) \quad (3.4.2)$$

The definition of  $\tilde{D}^{(1)}(z, t)$  in Eq. 3.4.2 allows us to combine the second and third terms on the left hand side of Eq. 3.4.1:

$$\frac{\partial^2}{\partial z^2} \tilde{E}(z, t) - b^2 e \frac{\partial^2}{\partial t^2} \tilde{D}^{(1)}(z, t) = ab^2 e \frac{\partial^2}{\partial t^2} \tilde{P}^{NL}(z, t) \quad (3.4.3)$$

In order to understand the convenience of substituting  $\tilde{D}^{(1)}(z, t)$  into Eq. 3.4.3, it is necessary to introduce the definition of this quantity. The linear displacement relates the permittivity of the medium,  $\epsilon$ , to the electric field:[101–103]

$$\tilde{D}^{(1)}(z, t) = \int \epsilon(t') \tilde{E}(t - t', z) dt' \quad (3.4.4a)$$

$$D^{(1)}(z, \omega) = \epsilon(\omega) E(\omega) \quad (3.4.4b)$$

where  $D^{(1)}(z, \omega) = \mathcal{F}\{\tilde{D}^{(1)}(z, t)\}$ . Eq. 3.4.4a provides the time-domain description of the linear displacement, and Eq. 3.4.4b is the frequency-domain description. In Eq. 3.4.4a and 3.4.4b, the dependence of

the displacement on  $\epsilon$  is independent of unit system. However, between unit systems, the permittivity or dielectric constant itself is defined differently, though it is always related to the linear susceptibility,  $\chi^{(1)}$ : [101, 107]

$$\epsilon = \epsilon_0(1 + \chi^{(1)}) \quad (3.4.5a)$$

$$\epsilon = 1 + 4\pi\chi^{(1)} \quad (3.4.5b)$$

In the mks unit system, an additional quantity - the relative permittivity,  $\epsilon_r$  - is also defined, and it is allowed to be the ratio of  $\epsilon$  and  $\epsilon_0$ ,  $\epsilon_r = \epsilon/\epsilon_0$ . The relative permittivity (in mks units) and the permittivity (in cgs/esu units) are significant, as both quantities are generally<sup>i</sup> equal to the square of the complex refractive index,  $\bar{n}^2$  (see Eq. 3.2.37a and 3.2.37b). [99, 101, 102, 107]

Based upon the forms of Eq. 3.4.4a and 3.4.4b, it will clearly be easier to apply the effects of linear displacement in the frequency domain. To achieve this, we can simply multiply both sides of Eq. 3.4.3 by the necessary exponential and integration factor, then integrate. We can determine the result of this transform by invoking the Fourier relations associated with the derivative: [112]

$$\mathcal{F}\{t^n f(t)\} = (-i)^n \frac{\partial^n}{\partial \omega^n} \hat{f}(\omega) \quad (3.4.6a)$$

$$\mathcal{F}\left\{\frac{\partial^n}{\partial t^n} f(t)\right\} = (i\omega)^n \hat{f}(\omega) \quad (3.4.6b)$$

where  $f(t)$  is an arbitrary function with  $\mathcal{F}\{f(t)\} = \hat{f}(\omega)$ . With these relationships, we can show the Fourier transform of Eq. 3.4.3 to be:

$$\frac{\partial^2}{\partial z^2} E(z, \omega) + b^2 e \omega^2 D^{(1)}(z, \omega) = -ab^2 e \omega^2 P^{\text{NL}}(z, \omega) \quad (3.4.7)$$

where  $D^{(1)}(z, \omega)$  is defined as before, and  $E(z, \omega) = \mathcal{F}\{\tilde{E}(z, t)\}$  and  $P^{\text{NL}}(z, \omega) = \mathcal{F}\{\tilde{P}^{\text{NL}}(z, t)\}$ . Substituting for  $D^{(1)}(z, \omega)$  in Eq. 3.4.7 according to the frequency-domain definition in Eq. 3.4.4b yields Eq. 3.4.8:

$$\frac{\partial^2}{\partial z^2} E(z, \omega) + b^2 e \omega^2 \epsilon(\omega) E(z, \omega) = -ab^2 e \omega^2 P^{\text{NL}}(z, \omega) \quad (3.4.8)$$

We can simplify Eq. 3.4.8 by spending some time considering the constants on both sides of the equation; in so doing, we can retain generalization, while reducing the number of terms to keep track of. Unfortunately,

---

<sup>i</sup>The caveat is explicitly included here, as the formal definition of the complex refractive index is  $\bar{n}^2 = (\epsilon\mu)/(\epsilon_0\mu_0)$ . However, as  $\mu \approx \mu_0$  in most materials, we can generally allow  $\bar{n}^2 \approx \epsilon_r$ . [101]



even though we arrive at the same result, we will need to consider the two unit systems (mks and cgs/esu) separately.

Starting with mks units, we recall that we have defined  $a = b = 1$ ,  $d = \epsilon_0$ , and  $e = \mu$ . Starting with the coefficient of the second term on the left hand side of Eq. 3.4.8, we can evaluate  $b^2 e \epsilon(\omega)$  as follows:

$$\begin{aligned}
 b^2 e \epsilon(\omega) &= \mu(\omega) \epsilon(\omega) \\
 &= \mu_r(\omega) \epsilon_r(\omega) \mu_0 \epsilon_0 \\
 &= \frac{\mu_r(\omega) \epsilon_r(\omega)}{c^2} \\
 &= \frac{[n(\omega) - i\kappa(\omega)]^2}{c^2}
 \end{aligned} \tag{3.4.9}$$

where we have used the relationship  $\epsilon_0 \mu_0 = c^{-2}$  between the second and third lines and have directly introduced  $n(\omega) - i\kappa(\omega)$ <sup>i</sup> in place of the complex index of refraction,  $\bar{n}$ . [99, 101, 102] Meanwhile, on the right hand side of Eq. 3.4.8, we have a coefficient of  $ab^2 e = \mu(\omega) \approx \mu_0$ . However, we can proceed further by recognizing that, when defined in mks units (see Eq. 3.2.10 or 3.2.12a),  $P^{\text{NL}}(z, \omega)$  will contain a factor of  $\epsilon_0$ . Therefore, if we define a new quantity,  $\bar{P}^{\text{NL}}(z, \omega) = [P^{\text{NL}}(z, \omega)]/\epsilon_0$ , we can redefine the right hand side of Eq. 3.4.8 as  $\mu_0 \epsilon_0 \omega^2 \bar{P}^{\text{NL}}(z, \omega)$ . With both  $\mu_0$  and  $\epsilon_0$ , we can use the identity above,  $\mu_0 \epsilon_0 = c^{-2}$ , to yield a right hand side of  $\omega^2/c^2 \bar{P}^{\text{NL}}(z, \omega)$ .

On the other hand, when we are in the cgs or esu unit systems, we have defined  $a = 4\pi$ ,  $b = c^{-1}$ , and  $d = e = 1$ . With these values, we can show that the coefficients  $b^2 e \epsilon(\omega)$  of the second term on the left hand side can be simplified:

$$\begin{aligned}
 b^2 e \epsilon(\omega) &= \frac{\epsilon(\omega)}{c^2} \\
 &\approx \frac{\epsilon(\omega) \mu(\omega)}{c^2} \\
 &\approx \frac{[n(\omega) - i\kappa(\omega)]^2}{c^2}
 \end{aligned} \tag{3.4.10}$$

where we have again directly introduced the quantity  $n - i\kappa$  to represent the complex index of refraction. We note that in the second line of Eq. 3.4.10, we have retained the approximate relation to emphasize that we assume  $\mu$  is negligible for most media. Meanwhile, for the right hand side of Eq. 3.4.8, we have  $ab^2 e \omega^2 = (4\pi \omega^2)/c^2$ . We have seen that we retain a factor of  $\omega^2 c^{-2}$  in mks units, but the factor of  $4\pi$  is unique

---

<sup>i</sup>Note that this definition for the complex index of refraction differs from most sources.[99, 101, 107] However, since we have taken as our convention that the field accumulates phase as  $\exp(-ikz)$ , it is necessary for the index of refraction and extinction coefficient to have opposite sign (see Eq. 3.4.13). Though they appear to work strictly with the linear susceptibility, Akhmanov et al. also treating the phase accumulation of the complex field as  $\exp(-ikz)$ , take the imaginary component of the susceptibility to be of opposite sign as the real component.[198] Given  $\bar{n}^2 = [n \pm i\kappa]^2 = 1 + a\chi^{(1)}$  ( $a = 4\pi$  for cgs/esu units, and  $a = 1$  for mks units),  $\Re\{a\chi^{(1)}\} = (n^2 - \kappa^2) - 1$  and  $\Im\{a\chi^{(1)}\} = \pm 2n\kappa$  (see Eq. 3.4.17). Since  $n$  and  $\kappa$  must both be real, the real and imaginary components of  $\chi^{(1)}$  will always have opposite signs only for  $\bar{n} = \pm n \mp i\kappa$ .

to cgs and esu units. However, we can use our new quantity,  $\bar{P}^{\text{NL}}(z, \omega)$ , to mask this term by defining  $\bar{P}^{\text{NL}}(z, \omega)$  in cgs or esu units:  $\bar{P}^{\text{NL}}(z, \omega) = 4\pi P^{\text{NL}}(z, \omega)$ . This then leaves  $\omega^2/c^2 \bar{P}^{\text{NL}}(z, \omega)$ .

We see then that we can generalize Eq. 3.4.8 to be:

$$\frac{\partial^2}{\partial z^2} E(z, \omega) + \frac{[n(\omega) - i\kappa(\omega)]^2 \omega^2}{c^2} E(z, \omega) = -\frac{\omega^2}{c^2} \bar{P}^{\text{NL}}(z, \omega) \quad (3.4.11)$$

with the behavior of  $\bar{P}^{\text{NL}}(z, \omega)$  defined to be  $\bar{P}^{\text{NL}}(z, \omega) = [P^{\text{NL}}(z, \omega)]/\epsilon_0$  in mks units or  $\bar{P}^{\text{NL}}(z, \omega) = 4\pi P^{\text{NL}}(z, \omega)$  in cgs or esu units.

Before continuing, let us consider the nature of the complex index of refraction in Eq. 3.4.9 and 3.4.10. The quantity consists of a real component,  $n(\omega)$ , and an imaginary component,  $\kappa(\omega)$ . While the index of refraction is routinely encountered, the imaginary component, the extinction coefficient, can be related to more recognizable quantities. To do so, let us consider the propagation of a plane wave in the absence of a nonlinear polarization. This is consistent with Eq. 3.4.11 when  $\bar{P}^{\text{NL}} = 0$ :

$$\frac{\partial^2}{\partial z^2} E(z, \omega) = -\left(\frac{[n(\omega) - i\kappa(\omega)]\omega}{c}\right)^2 E(z, \omega) \quad (3.4.12)$$

Recognizing Eq. 3.4.12 as a second-order ordinary differential equation, we might consider a trial solution for  $E$  of the form  $E(z, \omega) = E_0 \exp(-iaz)$ , where  $a$  is an arbitrary coefficient. Introducing this trial solution, we would find that  $a^2 = ([n(\omega) - i\kappa(\omega)]\omega/c)^2$ , which yields the solution:

$$E(z, \omega) = E_0 e^{-i[(n(\omega)\omega)/c]z} e^{-[(\kappa(\omega)\omega)/c]z} \quad (3.4.13)$$

We can see that the result in Eq. 3.4.13 exhibits two exponential terms: an oscillatory term with a wavenumber  $k = [n(\omega)\omega]/c$  and a term corresponding to exponential decay at a rate of  $[(\kappa(\omega)\omega)/c]$ .

Starting with the first term, we can recall our earlier definition of the wave number,  $k = \omega/v$  (see Eq. 3.1.5). Comparing these expressions, we see that the real part of the complex index of refraction behaves consistently with the index of refraction: the refraction of the medium reduces the velocity of light relative to the vacuum, yielding a speed,  $v(\omega) = c/n(\omega)$ . [101] This term also allows us to generalize our definition for the wavenumber of light:

$$k = \frac{n(\omega)\omega}{c} \quad (3.4.14)$$

Here we will note that the notation  $n(\omega)$  explicitly allows for a frequency dependence to the observed index of refraction. [99]

In order to describe  $\kappa(\omega)$ , it will be more convenient to consider the intensity of the solution in Eq. 3.4.13. Generally, the intensity of the electric field is proportional to the square magnitude of the field; the proportionality constant is either  $[cn(\omega)]/(8\pi)$  (in cgs or esu units) or  $[c\epsilon_0 n(\omega)]/2$  (in mks units).[99] However, it is sufficient to identify that the intensity of the field in Eq. 3.4.13 exhibits a spatial dependence:

$$I(z) \propto E_0^2 e^{-2[(\kappa(\omega)\omega)/c]z} \quad (3.4.15)$$

Comparing the intensity in Eq. 3.4.15 with the Beer-Lambert law,  $I(z) = I_0 \exp[-\alpha(\omega)z]$ , we can see that  $\kappa(\omega)$  is related to the absorption coefficient. If we set  $\alpha(\omega)$  equal to the coefficient in Eq. 3.4.15, we can see that  $\kappa(\omega)$  is defined:

$$\kappa(\omega) = \frac{c}{2\omega} \alpha(\omega) \quad (3.4.16)$$

where the notation  $\kappa(\omega)$  and  $\alpha(\omega)$  explicitly allow a potential frequency dependence for these quantities.[99]

Applying these insights, let us continue from Eq. 3.4.11. The first thing we will consider is expressing the coefficient to the second term on the left hand side,  $[n(\omega) - i\kappa(\omega)]^2 \omega^2 / c^2$ , in a more convenient manner. If we evaluate the term  $[n(\omega) - i\kappa(\omega)]^2$ :

$$[n(\omega) - i\kappa(\omega)]^2 = n^2(\omega) - i2n(\omega)\kappa(\omega) - \kappa^2(\omega) \quad (3.4.17)$$

we can see that the coefficient to this term can be evaluated:

$$\begin{aligned} \frac{[n(\omega) - i\kappa(\omega)]^2 \omega^2}{c^2} &= \frac{\omega^2}{c^2} [n^2(\omega) - i2n(\omega)\kappa(\omega) - \kappa^2(\omega)] \\ &= \left[ \frac{n(\omega)\omega}{c} \right]^2 - i2 \left[ \frac{n(\omega)\omega}{c} \right] \frac{\kappa(\omega)\omega}{c} - \frac{\kappa^2(\omega)\omega^2}{c^2} \end{aligned} \quad (3.4.18)$$

However, we have previously defined the wavenumber,  $k(\omega) = [n(\omega)\omega]/c$  (see Eq. 3.4.14), allowing us to substitute  $k(\omega)$  for both terms in brackets in Eq. 3.4.18. We can also consider our result for  $\kappa(\omega)$  in Eq. 3.4.16. From  $\kappa(\omega) = c/(2\omega)\alpha(\omega)$ , we can see that  $[2\kappa(\omega)\omega]/c$  in the second term of Eq. 3.4.18 is equivalent to  $\alpha(\omega)$ . Finally, if we assume  $\alpha(\omega)$  is sufficiently small, we can consider the third term, proportional to  $\alpha^2(\omega)$ , to be negligible relative to the first two terms due to their proportionality to  $k^2(\omega)$  and  $k(\omega)$ . This then leaves us:

$$\frac{\partial^2}{\partial z^2} E(z, \omega) + [k^2(\omega) - ik(\omega)\alpha(\omega)] E(z, \omega) = -\frac{\omega^2}{c^2} \bar{P}^{\text{NL}}(z, \omega) \quad (3.4.19)$$

From Eq. 3.4.19, we will make two substitutions: first, we will introduce the form of the electric field and

evaluate  $\partial^2/\partial z^2 E(z, \omega)$ ; second, we will consider  $k(\omega)$  as a Taylor expansion around the carrier frequency,  $\omega = \omega_0$ .

We indicated that we will consider the field to be of the form in Eq. 3.1.27, but consider it sufficient to track the propagation of the complex field, i.e.  $\tilde{E}(z, t) = A(r, t) \exp[-i(k_0 z - \omega_0 t)]$ . If we take the Fourier transform of this equation, we find  $E(z, \omega) = \hat{A}(z, \omega - \omega_0) \exp(-ik_0 z)$ , [112] consistent with our result in § 3.1.2 within the limit that the contribution of  $\exp[-i(\Delta\omega/v)z]$  is negligible; it will be trivial to relax this assumption later. If we then evaluate the first term of Eq. 3.4.19, we find the second derivative to yield:

$$\begin{aligned} \frac{\partial^2}{\partial z^2} E(z, \omega) &= \frac{\partial}{\partial z} \left[ \frac{\partial}{\partial z} \hat{A}(z, \Delta\omega) e^{-ik_0 z} \right] \\ &= \frac{\partial}{\partial z} \left[ -ik_0 \hat{A}(z, \Delta\omega) e^{-ik_0 z} + e^{-ik_0 z} \frac{\partial}{\partial z} \hat{A}(z, \Delta\omega) \right] \\ &= \left[ (-ik_0)^2 e^{-ik_0 z} - i2k_0 e^{-ik_0 z} \frac{\partial}{\partial z} + e^{-ik_0 z} \frac{\partial^2}{\partial z^2} \right] \hat{A}(z, \Delta\omega) \end{aligned} \quad (3.4.20)$$

where we have re-introduced our variable  $\Delta\omega = \omega - \omega_0$ . We can substitute the result of the scheme in Eq. 3.4.20 into Eq. 3.4.19. Since the evaluation in Eq. 3.4.20 removes the exponential term from the derivatives, we can also divide through the resulting expression by  $\exp(-ik_0 z)$ , leaving:

$$\left( \frac{\partial^2}{\partial z^2} - i2k_0 \frac{\partial}{\partial z} \right) \hat{A}(z, \Delta\omega) + [k^2(\omega) - k_0^2 - ik(\omega)\alpha(\omega)] \hat{A}(z, \Delta\omega) = -\frac{\omega^2}{c^2} e^{ik_0 z} \bar{P}^{\text{NL}}(z, \omega) \quad (3.4.21)$$

Meanwhile, we can define the Taylor series for the function  $f(x)$  around  $x = a$  by the general formula:[116]

$$f(x) = \sum_{n=0}^{\infty} \frac{1}{n!} \frac{\partial^n}{\partial x^n} f \Big|_{x=a} (x - a)^n \quad (3.4.22)$$

From the formula of Eq. 3.4.22, we can therefore evaluate  $k(\omega)$  around  $\omega = \omega_0$  as the sum:

$$k(\omega) = k_0 + \frac{\partial k(\omega)}{\partial \omega} \Big|_{\omega=\omega_0} (\omega - \omega_0) + \frac{1}{2} \frac{\partial^2 k(\omega)}{\partial \omega^2} \Big|_{\omega=\omega_0} (\omega - \omega_0)^2 + \dots \quad (3.4.23)$$

We will adopt the notation of Akhmanov et al and note the derivatives as  $k_1 = \partial k(\omega)/\partial \omega|_{\omega=\omega_0}$  and  $k_2 = \partial^2 k(\omega)/\partial \omega^2|_{\omega=\omega_0}$ ; [103] Boyd uses a similar notation for the first-order derivative, but generalizes the summation over all higher order terms into a single variable,  $D$ . [102] We can also relate these first two derivatives to meaningful quantities with respect to pulse propagation. The first-order derivative,  $k_1$ , is defined as the inverse of the group velocity,  $u_g$ , [101, 103] while the second-order derivative is the group velocity dispersion. [103] The form and behavior of these quantities will be discussed in a later section (see § 3.5).

The sum of Eq. 3.4.23 permits evaluation of the terms associated with  $k(\omega)$  in Eq. 3.4.21. We can apply some approximations to simplify the treatment, though. First, we will assume that the non-zeroth order terms are sufficiently small that their products with the absorption coefficient are negligible, leaving  $k(\omega)\alpha(\omega) \approx k_0\alpha(\omega)$ . Second, we will recognize that the Fourier relationships of derivatives (see Eq. 3.4.6a and Eq. 3.4.6b) cause terms in  $(\omega - \omega_0)^n$  to correspond to the derivatives  $\partial^n/\partial t^n$ ; therefore, we will only keep terms up to the second order in  $(\omega - \omega_0)$ . Under this second approximation, we can evaluate  $k^2(\omega)$  to be:

$$k^2(\omega) = k_0^2 + 2k_0k_1\Delta\omega + (k_0k_2 + k_1^2)\Delta\omega^2 \quad (3.4.24)$$

where we have again introduced  $\Delta\omega$  in place of  $(\omega - \omega_0)$ . Introducing these substitutions into Eq. 3.4.21 results in the form:

$$\begin{aligned} \left( \frac{\partial^2}{\partial z^2} - i2k_0 \frac{\partial}{\partial z} \right) \hat{A}(z, \Delta\omega) + [2k_0k_1\Delta\omega + (k_0k_2 + k_1^2)\Delta\omega^2 - ik_0\alpha(\omega)] \\ \times \hat{A}(z, \Delta\omega) = -\frac{\omega^2}{c^2} e^{ik_0z} \bar{P}^{\text{NL}}(z, \omega) \end{aligned} \quad (3.4.25)$$

At this point, it is common to invoke the slowly varying amplitude approximation, which assumes the effects of  $2k_0\partial/\partial z$  are significantly greater than the effects of  $\partial^2/\partial z^2$ , allowing us to neglect the second-order derivative.[102, 103] We will consider the case in which we do not apply this assumption at this point in § 3.4.2, but for now we will apply the slowly varying amplitude approximation, leaving:

$$-i2k_0 \frac{\partial}{\partial z} \hat{A}(z, \Delta\omega) + [2k_0k_1\Delta\omega + (k_0k_2 + k_1^2)\Delta\omega^2 - ik_0\alpha(\omega)] \hat{A}(z, \Delta\omega) = -\frac{\omega^2}{c^2} e^{ik_0z} \bar{P}^{\text{NL}}(z, \omega) \quad (3.4.26)$$

Unfortunately, within the context of simulating ultrafast propagation, group velocities tend to be sufficiently large that it is not feasible to define a sufficiently conservative grid that accommodates the delay introduced by the group velocity over practical distances. To overcome this limit, it is convenient to transfer to a moving coordinate system  $(\xi, \eta)$ , defined relative to the laboratory coordinates  $(z, t)$  as:

$$\xi = z \quad (3.4.27a)$$

$$\eta = t \pm k_{1r}z \quad (3.4.27b)$$

In Eq. 3.4.27b,  $k_{1r}$  is the reciprocal of the reference group velocity, usually taken as the group velocity of one of the pulses in the simulation; we will show that this form of  $\eta$  results in the reduction of the effective group velocity of the pulses. The  $\pm$  in Eq. 3.4.27b generalizes this expression, as the use of different conventions

may require the sign of the term  $k_{1r}z$  to be either positive or negative. We will ultimately end up needing the negative sign, i.e.  $\eta = t - k_{1r}z$ .

Recalling that terms in  $\omega^n$  correspond to the derivatives  $\partial^n/\partial t^n$  (see Eq. 3.4.6a and Eq. 3.4.6b), it is clear from examining Eq. 3.4.26 that migrating to the moving coordinate system  $(\xi, \eta)$  will require us to identify the operators equivalent to  $\partial/\partial z$  and  $\partial/\partial t$ . To do so, let us consider an arbitrary function,  $f$ , expressed as a function of  $\xi$  and  $\eta$ :  $f(\xi(z, t), \eta(z, t))$ . We can then use the chain rule to find the derivatives of  $f$  with respect to  $z$  and  $t$ , informing on the forms of the operators  $\partial/\partial z$  and  $\partial/\partial t$  in the moving frame:[116]

$$\frac{\partial}{\partial z} f(\xi(z, t), \eta(z, t)) = \left[ \frac{\partial}{\partial z} \xi(z, t) \frac{\partial}{\partial \xi} + \frac{\partial}{\partial z} \eta(z, t) \frac{\partial}{\partial \eta} \right] f(\xi(z, t), \eta(z, t)) \quad (3.4.28a)$$

$$\frac{\partial}{\partial t} f(\xi(z, t), \eta(z, t)) = \left[ \frac{\partial}{\partial t} \xi(z, t) \frac{\partial}{\partial \xi} + \frac{\partial}{\partial t} \eta(z, t) \frac{\partial}{\partial \eta} \right] f(\xi(z, t), \eta(z, t)) \quad (3.4.28b)$$

From the forms of Eq. 3.4.27a and 3.4.27b (recalling we will be using the case of  $-k_{1r}z$ ), it is trivial to evaluate  $\partial/\partial z \xi = 1$ ,  $\partial/\partial z \eta = -k_{1r}$ ,  $\partial/\partial t \xi = 0$ , and  $\partial/\partial t \eta = 1$ . With these derivatives, we can use Eq. 3.4.28a and 3.4.28b to find  $\partial/\partial z$  and  $\partial/\partial t$  in the moving frame:

$$\frac{\partial}{\partial z} = \frac{\partial}{\partial \xi} - k_{1r} \frac{\partial}{\partial \eta} \quad (3.4.29a)$$

$$\frac{\partial}{\partial t} = \frac{\partial}{\partial \eta} \quad (3.4.29b)$$

In order to bring Eq. 3.4.26 to the moving frame, we will need to return to the time domain. In contrast to Boyd,[102] however, we will consider the form of the polarization before applying the inverse Fourier transform. We assumed that the polarization is of the form in Eq. 3.2.17, i.e.  $\tilde{\tilde{P}}^{\text{NL}}(z, t) = \bar{p}^{\text{NL}}(z, t) \exp(i\omega_0 t)$ , where  $\bar{p}^{\text{NL}}(z, t)$  is an envelope function defined in the same manner as  $\tilde{\tilde{P}}^{\text{NL}}(z, t)$ .<sup>i</sup> In the same manner as the electric field, the Fourier transform of this yields  $\bar{P}^{\text{NL}}(z, \omega) = \hat{p}^{\text{NL}}(z, \omega - \omega_0)$ . [112] Substituting for  $\bar{P}^{\text{NL}}(z, \omega)$  then allows us to perform the Fourier transform of Eq. 3.4.26 with respect to  $\Delta\omega$  without having to consider residual exponentials or the expansion of  $\partial^2/\partial t^2 \tilde{\tilde{P}}^{\text{NL}}(z, t)$ : [102]

$$\begin{aligned} & \left[ -i2k_0 \left( \frac{\partial}{\partial z} + k_1 \frac{\partial}{\partial t} \right) - (k_0 k_2 + k_1^2) \frac{\partial^2}{\partial t^2} \right] A(z, t) - \mathcal{F}^{-1} \left\{ ik_0 \alpha(\omega) \hat{A}(z, \Delta\omega) \right\} \\ & = \frac{\omega^2}{c^2 \Delta\omega^2} e^{ik_0 z} \frac{\partial^2}{\partial t^2} \bar{p}^{\text{NL}}(z, t) \end{aligned} \quad (3.4.30)$$

where the notation of  $\mathcal{F}^{-1} \{ ik_0 \alpha(\omega) \hat{A}(z, \Delta\omega) \}$  denotes the inverse Fourier transform of the term in brackets.

---

<sup>i</sup>Recall we have defined  $\bar{P}^{\text{NL}}(z, \omega)$  to be  $[P^{\text{NL}}(z, \omega)]/\epsilon_0$  in mks units and  $4\pi P^{\text{NL}}(z, \omega)$  in cgs or esu units.  $\tilde{\tilde{P}}^{\text{NL}}(z, t)$  is the time domain form of  $\bar{P}^{\text{NL}}(z, \omega)$ , i.e.  $\tilde{\tilde{P}}^{\text{NL}}(z, t) = \mathcal{F}^{-1} \{ \bar{P}^{\text{NL}}(z, \omega) \}$ .

As  $\alpha(\omega)$  and  $\hat{A}(z, \Delta\omega)$  both exhibit frequency dependence, the inverse Fourier transform of this term is likely to correspond to a convolution in the time domain,[112] but the exact form of the result is of no consequence at this time; it is sufficient to leave this term in the form presented in Eq. 3.4.30.

From Eq. 3.4.30, we can transition to the moving frame. We will substitute for  $\partial/\partial z$  and  $\partial/\partial t$  according to Eq. 3.4.29a and 3.4.29b and can directly replace dependence upon  $z$  for dependence upon  $\xi$ . Since  $\eta$  is only shifted relative to  $t$ , we will also assume that  $A(z, t)$  and  $\hat{p}^{\text{NL}}$  can be mapped directly onto  $\eta$ . Making these substitutions and combining like terms yields:

$$\begin{aligned} \left[ -i2k_0 \left( \frac{\partial}{\partial \xi} + (k_1 - k_{1r}) \frac{\partial}{\partial \eta} \right) - (k_0 k_2 + k_1^2) \frac{\partial^2}{\partial \eta^2} \right] A(\xi, \eta) - \mathcal{F}^{-1} \left\{ ik_0 \alpha(\omega) \hat{A}(\xi, \Delta\omega) \right\} \\ = \frac{\omega^2}{c^2 \Delta\omega^2} e^{ik_0 \xi} \frac{\partial^2}{\partial \eta^2} \hat{p}^{\text{NL}}(\xi, \eta) \end{aligned} \quad (3.4.31)$$

The form of Eq. 3.4.31 is not of great utility: it is not feasible to apply the effects of group velocity dispersion in the time domain in simulations.[118, 199–201] Therefore, we will need to return to the frequency domain by performing the Fourier transform of Eq. 3.4.31 with respect to the reduced frequency,  $\Delta\omega$ , yielding:

$$\left[ -i2k_0 \left( \frac{\partial}{\partial \xi} + i\Delta\omega (k_1 - k_{1r}) \right) + (k_0 k_2 + k_1^2) \Delta\omega^2 - ik_0 \alpha(\omega) \right] \hat{A}(\xi, \Delta\omega) = -\frac{\omega^2}{c^2} e^{ik_0 \xi} \hat{p}^{\text{NL}}(\xi, \Delta\omega) \quad (3.4.32)$$

Rearranging the result in Eq. 3.4.32:

$$\begin{aligned} \frac{\partial}{\partial \xi} \hat{A}(\xi, \Delta\omega) = \left[ -i\Delta\omega (k_1 - k_{1r}) - i\frac{1}{2} \Delta\omega^2 \left( k_2 + \frac{k_1^2}{k_0} \right) - \frac{1}{2} \alpha(\omega) \right] \hat{A}(\xi, \Delta\omega) \\ - i\frac{\omega^2}{2c^2 k_0} e^{ik_0 \xi} \hat{p}^{\text{NL}}(\xi, \Delta\omega) \end{aligned} \quad (3.4.33)$$

Finally, from Eq. 3.4.33, it is possible to address a couple approximations:

$$\frac{\partial}{\partial \xi} \hat{A}(\xi, \Delta\omega) = \left[ -i\Delta\omega (k_1 - k_{1r}) - i\frac{1}{2} \Delta\omega^2 k_2 - \frac{1}{2} \alpha(\omega) \right] \hat{A}(\xi, \Delta\omega) - i\frac{\omega^2}{2c^2 k_0} e^{ik_0 \xi} \hat{p}^{\text{NL}}(\xi, \Delta\omega) \quad (3.4.34)$$

The first approximation we introduce in Eq. 3.4.34 is that  $k_1^2$  will be small relative to  $k_0$ , allowing us to neglect this term; while it is possible that close to the limit of the slowly varying amplitude approximation, the contribution from  $\Delta\omega^2$  may weaken this assumption, it should generally be reasonable.[103] The second change in Eq. 3.4.34 is that we have recognized that  $\mathcal{F}\{A(\xi, t)\} = \hat{A}(\xi, \Delta\omega) \exp[-i(\Delta\omega/v)\xi]$ . Throughout the derivation, it was sufficient to mask the contribution of the exponential within the envelope function,  $\hat{A}(z, \Delta\omega)$ ; in Eq. 3.4.34, however, we have reintroduced this contribution explicitly: if we assume  $\Delta\omega$  is

sufficiently small, the expansion of  $\partial/\partial\xi\hat{A}(\xi, \Delta\omega)\exp[-i(\Delta\omega/v)\xi]$  according to the product rule will be approximately  $\exp[-i(\Delta\omega/v)\xi]\partial/\partial\xi\hat{A}(\xi, \Delta\omega)$ . Dividing through the result by  $\exp[-i(\Delta\omega/v)\xi]$  yields  $\exp[i(\Delta\omega/v)\xi]$  on the right hand side; combining this term with  $\exp(ik_0\xi)$  yields the exponential  $\exp[ik(\omega)\xi]$  (see Eq. 3.1.24).

### 3.4.2 Relaxing the Slowly Varying Amplitude Approximation

In § 3.4.1, we traced through the derivation of treating pulse propagation effects, but introduced the slowly varying amplitude approximation prior to shifting to the moving frame. This neglects the term in  $\partial^2/\partial z^2$ ; as  $\partial/\partial z$  includes two contributions (see Eq. 3.4.29a), it should be expected that retaining this term into the moving frame will impact the resulting differential equation. We will apply this treatment here.

Starting from Eq. 3.4.25, we will directly shift this expression to the moving frame using Eq. 3.4.29a and 3.4.29b. As before, we will need to begin by performing an inverse Fourier transform to take Eq. 3.4.25 into the time domain. Substituting for  $\hat{p}(z, \Delta\omega)$  and performing this transformation yields a result similar to Eq. 3.4.30, only retaining the term associated with  $\partial^2/\partial z^2$ :

$$\begin{aligned} & \left[ \frac{\partial^2}{\partial z^2} - i2k_0 \left( \frac{\partial}{\partial z} + k_1 \frac{\partial}{\partial t} \right) - (k_0 k_2 + k_1^2) \frac{\partial^2}{\partial t^2} \right] A(z, t) - \mathcal{F}^{-1} \left\{ ik_0 \alpha(\omega) \hat{A}(z, \Delta\omega) \right\} \\ & = \frac{\omega^2}{c^2 \Delta\omega^2} e^{ik_0 z} \frac{\partial^2}{\partial t^2} \bar{p}^{\text{NL}}(z, t) \end{aligned} \quad (3.4.35)$$

Much like Eq. 3.4.30, we have left the term associated with absorption noted as simply the inverse Fourier transformation of the term in brackets,  $\mathcal{F}^{-1}\{\}$ , for simplicity.

We can now substitute according to Eq. 3.4.29a and 3.4.29b, yielding:

$$\begin{aligned} & \left[ \frac{\partial^2}{\partial \xi^2} - 2k_{1r} \frac{\partial}{\partial \xi} \frac{\partial}{\partial \eta} - i2k_0 \left( \frac{\partial}{\partial \xi} + (k_1 - k_{1r}) \frac{\partial}{\partial \eta} \right) - (k_0 k_2 + (k_1^2 - k_{1r}^2)) \frac{\partial^2}{\partial \eta^2} \right] A(\xi, \eta) \\ & - \mathcal{F}^{-1} \left\{ ik_0 \alpha(\omega) \hat{A}(\xi, \Delta\omega) \right\} = \frac{\omega^2}{c^2 \Delta\omega^2} e^{ik_0 \xi} \frac{\partial^2}{\partial \eta^2} \bar{p}^{\text{NL}}(\xi, \eta) \end{aligned} \quad (3.4.36)$$

Performing the Fourier transform on Eq. 3.4.36 to return to the frequency domain yields:

$$\begin{aligned} & \left[ \frac{\partial^2}{\partial \xi^2} - i2 \left[ (k_0 + k_{1r} \Delta\omega) \frac{\partial}{\partial \xi} + ik_0 \Delta\omega (k_1 - k_{1r}) \right] + (k_0 k_2 + (k_1^2 - k_{1r}^2)) \Delta\omega^2 \right] \hat{A}(\xi, \Delta\omega) - ik_0 \alpha(\omega) \\ & \times \hat{A}(\xi, \Delta\omega) = -\frac{\omega^2}{c^2} e^{ik_0 \xi} \hat{p}(\xi, \Delta\omega) \end{aligned} \quad (3.4.37)$$

From Eq. 3.4.37, we could take two approaches. The first would be to rearrange Eq. 3.4.37 in the manner of a second-order differential equation; though more difficult to evaluate numerically than a first-order differential



equation, it is still possible to arrive at a solution (see § 3.6).

Alternatively, it would also be possible to delay making the slowly varying amplitude approximation, only ignoring the second-order derivative after transferring to the moving frame. Eq. 3.4.38 shows the analogous expression to Eq. 3.4.34 within this treatment:

$$\begin{aligned} \frac{\partial}{\partial \xi} \hat{A}(\xi, \Delta\omega) = & \left[ -i \frac{k_0}{k_0 + k_{1r} \Delta\omega} \Delta\omega (k_1 - k_{1r}) - i \frac{1}{2} \frac{k_0}{k_0 + k_{1r} \Delta\omega} k_2 \Delta\omega^2 - \frac{1}{2} \frac{k_0}{k_0 + k_{1r} \Delta\omega} \alpha(\omega) \right] \\ & \times \hat{A}(\xi, \Delta\omega) - i \frac{\omega^2}{2(k_0 + k_{1r} \Delta\omega) c^2} e^{ik(\omega)\xi} \hat{p}(\xi, \Delta\omega) \end{aligned} \quad (3.4.38)$$

where we have assumed the term associated with  $(k_1^2 - k_{1r}^2)$  is negligible when divided by  $(k_0 + k_{1r} \Delta\omega)$  and have reintroduced the term  $\exp[-i(\Delta\omega/v)\xi]$ . Comparing Eq. 3.4.38 to the earlier equation, Eq. 3.4.34, we see that this treatment retains the first order term of the Taylor expansion of  $k(\omega)$  (see Eq. 3.4.23) when considering the derivative of the field. At the limit of narrow bandwidth pulses, the contributions of the first-order term  $(k_{1r} \Delta\omega)$  are negligible, and Eq. 3.4.38 approaches the same limiting behavior as Eq. 3.4.34. However, this first-order term in Eq. 3.4.38 allows for the deviation from the limiting behavior predicted by Eq. 3.4.34 as the pulse bandwidth broadens.

### 3.4.3 The Propagation of Pulsed Gaussian Beams

In § 3.4.1, we considered the effects of a medium upon the propagation of a pulsed electric field within the plane wave limit. The standard model for a TEM<sub>00</sub> mode arises from treating the field as a distortion to the plane wave limit,[104, 105] imposing the transverse coordinate dependence demonstrated by the TEM<sub>00</sub> mode. In this section, we will extend the treatments of Svelto[104] and Verdeyen[105] to account for the propagation effects of a medium upon a TEM<sub>00</sub> mode.

Starting from the plane wave limit, i.e.  $E(z) = E_0 e^{-ik_0 z}$ ,<sup>i</sup> Verdeyen and Svelto consider TEM<sub>00</sub> mode propagation to reflect a functional distortion describing the transverse dependence exhibited by the field: whereas Svelto considers the distortion to reflect a spatially-dependent amplitude,  $U(\mathbf{r}, z)$ , in place of the constant  $E_0$ , [104] Verdeyen treats the distortion as a function,  $\psi(r, z)$ , with the full field defined  $E(z) = E_0 \psi(\mathbf{r}, z) \exp(-ik_0 z)$ . [105] For clarity, we will adopt the style of Verdeyen; in this manner, we will assume we can consider the total field in a manner similar to Eq. 3.1.27, consisting of a frequency- or time-dependent envelope and oscillations at the carrier frequency, but with an additional function describing the distortion to the plane wave. However, as we will be incorporating dispersive effects into this distortion, we will not be

---

<sup>i</sup>Svelto and Verdeyen both treat the electric field amplitude as a scalar and consider propagation at the limit that the field is monochromatic.[104, 105] We will retain the previous approximation as noted in § 3.3.3, but will extend the treatment of TEM<sub>00</sub> mode propagation within the behavior of a pulsed electric field as described by Eq. 3.1.27.

able to consider the envelope function and the distortion separable in both the time and frequency domains: due to the Fourier relation between time and frequency, if these functions are separable in one domain, they must be convolved in the other. Considering the derivation in § 3.4.1, we will consider the envelope function and distortion to be separable in the frequency domain, which gives us the following descriptions for the field:

$$\tilde{E}(\mathbf{r}, z, t) = A(\mathbf{r}, z, t)e^{-ik_0z}e^{i\omega_0t} \quad (3.4.39a)$$

$$E(\mathbf{r}, z, t) = \hat{A}(\Delta\omega)e^{-i(\Delta\omega/v)z}\psi(\mathbf{r}, z, \Delta\omega)e^{-ik_0z} \quad (3.4.39b)$$

The time-domain model of the field in Eq. 3.4.39a is based upon the treatment of the field in Eq. 3.1.27, where we have allowed the envelope function,  $A(\mathbf{r}, z, t)$ , to exhibit the spatial dependence characteristic of the field. The frequency-domain model in Eq. 3.4.39b, meanwhile, is the Fourier transform with respect to  $\omega$  of Eq. 3.4.39a, with  $\mathcal{F}\{A(\mathbf{r}, z, t)\exp(i\omega_0t)\} = \hat{A}(\Delta\omega)\exp[-i(\Delta\omega/v)z]\psi(\mathbf{r}, z, \Delta\omega)$ . The first two terms ( $\hat{A}(\Delta\omega)$  and  $\exp[-i(\Delta\omega/v)z]$ ) arise in a similar manner as the treatment of Eq. 3.1.26 yields Eq. 3.1.27, though in the case of the Fourier transform, we recognize the relation  $\mathcal{F}\{f(t)\exp(\pm\omega_0t)\} = \hat{f}(\omega \mp \omega_0)$  [112]. Meanwhile, the function  $\psi(\mathbf{r}, z, \Delta\omega)$  reflects the distortion to the plane wave, isolating the spatial dependence of  $\hat{A}(\mathbf{r}, z, \Delta\omega)$  in Eq. 3.1.26 into a separate function.

In contrast to § 3.4.1, we will begin our treatment with Eq. 3.3.6. In a manner similar to § 3.4.1, though, we will consider  $\tilde{P}(\mathbf{r}, z, t)$  as the sum of the linear and nonlinear contributions,  $\tilde{P}^{(1)}(\mathbf{r}, z, t)$  and  $\tilde{P}^{\text{NL}}(\mathbf{r}, z, t)$ , respectively. We will assume that the field being considered has sufficiently low intensity that it does not experience any self-induced nonlinear effects, allowing us to let  $\tilde{P}^{\text{NL}}(\mathbf{r}, z, t)$  equal zero. Combining the derivatives of  $\tilde{E}(\mathbf{r}, z, t)$  and  $\tilde{P}^{(1)}(\mathbf{r}, z, t)$  with respect to time yields the derivative with respect to the linear displacement,  $\tilde{D}^{(1)}(\mathbf{r}, z, t)$ ; in the same manner as Eq. 3.4.3, we obtain:

$$\frac{\partial^2}{\partial z^2}\tilde{E}(\mathbf{r}, z, t) + \nabla_{\text{T}}^2\tilde{E}(\mathbf{r}, z, t) - b^2e\frac{\partial^2}{\partial t^2}\tilde{D}^{(1)}(\mathbf{r}, z, t) = 0 \quad (3.4.40)$$

From Eq. 3.4.40, we will next evaluate  $\partial^2/\partial z^2\tilde{E}(\mathbf{r}, z, t)$  in the manner of the scheme in Eq. 3.4.20; this yields:

$$e^{-ik_0z}\left[-k_0^2 - i2k_0\frac{\partial}{\partial z} + \frac{\partial^2}{\partial z^2}\right]A(\mathbf{r}, z, t)e^{i\omega_0t} + \nabla_{\text{T}}^2\tilde{E}(\mathbf{r}, z, t) - b^2e\frac{\partial^2}{\partial t^2}\tilde{D}^{(1)}(\mathbf{r}, z, t) = 0 \quad (3.4.41)$$

Next, let us consider the Fourier transformation of the result in Eq. 3.4.41. We will also make two simplifications: multiplying through the equation by  $\exp(ik_0z)$ , and substituting for the linear displacement according

to Eq. 3.4.4b. These changes yield:

$$\left[ -k_0^2 - i2k_0 \frac{\partial}{\partial z} + \frac{\partial^2}{\partial z^2} + e^{ik_0 z} \nabla_{\mathbf{T}}^2 e^{-ik_0 z} + b^2 e \omega^2 \epsilon(\omega) \right] \hat{A}(\Delta\omega) e^{-i(\Delta\omega/v)z} \psi(\mathbf{r}, z, \Delta\omega) = 0 \quad (3.4.42)$$

From Eq. 3.4.42, we can achieve a couple further simplifications. First, since the transverse Laplacian operator ( $\nabla_{\mathbf{T}}^2$ ) only involves the transverse coordinates, we can swap the order of  $\nabla_{\mathbf{T}}^2$  and  $\exp(-ik_0 z)$ ; we can then multiply  $\exp(ik_0 z)$  and  $\exp(-ik_0 z)$  to remove both exponentials. Second, we can substitute for  $b^2 e \omega^2 \epsilon(\omega)$  according to Eq. 3.4.9, 3.4.10, and 3.4.18; as before, these terms reduce to  $k^2(\omega) - ik(\omega)\alpha(\omega)$ , and can be combined with the leading term of  $k_0^2$ . Third, since  $\hat{A}(\Delta\omega)$  does not exhibit any dependence on the spatial coordinates, we can move it outside each derivative and divide Eq. 3.4.42 by this term. These changes yield:

$$\left[ \frac{\partial^2}{\partial z^2} - i2k_0 \frac{\partial}{\partial z} + \nabla_{\mathbf{T}}^2 + (k^2(\omega) - k_0^2 - ik(\omega)\alpha(\omega)) \right] e^{-i(\Delta\omega/v)z} \psi(\mathbf{r}, z, \Delta\omega) = 0 \quad (3.4.43)$$

From Eq. 3.4.43, we can achieve a few more simplifications. First, let us consider the remaining exponential. Once again recalling that the transverse Laplacian,  $\nabla_{\mathbf{T}}^2$ , has no longitudinal dependence, we can again switch the order of the Laplacian and the exponential, namely:  $\nabla_{\mathbf{T}}^2 \exp[-i(\Delta\omega/v)z] = \exp[-i(\Delta\omega/v)z] \nabla_{\mathbf{T}}^2$ . We can also consider the derivatives with respect to  $z$ . Considering these derivatives to be generalized in the form of the  $n^{\text{th}}$ -order derivative with respect to  $z$ ,  $\partial^n / \partial z^n \exp[-i(\Delta\omega/v)z] \psi(\mathbf{r}, z, \Delta\omega)$ , each operation of one of the  $n$  derivatives should yield two terms due to the product rule:[116] one corresponding to the derivative of the exponential ( $\partial / \partial z \exp[-i(\Delta\omega/v)z] = -i(\Delta\omega/v) \exp[-i(\Delta\omega/v)z]$ ), and one corresponding to the derivative of the function  $\psi(\mathbf{r}, z, \Delta\omega)$ . However, if we take  $\Delta\omega$  to be reasonably small, we can neglect the terms arising from the derivative of the exponential, thereby assuming:  $\frac{\partial^n}{\partial z^n} \exp[-i(\Delta\omega/v)z] \psi(\mathbf{r}, z, \Delta\omega) \approx \exp[-i(\Delta\omega/v)z] [\partial^n / \partial z^n \psi(\mathbf{r}, z, \Delta\omega)]$ . This allows us to divide through the equation by this remaining exponential. We can then also invoke the slowly varying amplitude approximation,  $2k_0 \partial / \partial z \gg \partial^2 / \partial z^2$ , and ignore the second-order derivative. Finally, we can also substitute for  $k^2(\omega)$  and  $k(\omega)$  according to Eq. 3.4.23 and 3.4.24. These changes and assumptions yield:

$$\left[ -i2k_0 \frac{\partial}{\partial z} + \nabla_{\mathbf{T}}^2 + 2k_0 k_1 \Delta\omega + (k_0 k_2 + k_1^2) \Delta\omega^2 - ik_0 \alpha(\omega) \right] \psi(\mathbf{r}, z, \Delta\omega) = 0 \quad (3.4.44)$$

The last consideration we will introduce before determining the nature of  $\psi(\mathbf{r}, z, \Delta\omega)$  is to bring Eq. 3.4.44 to the moving frame. Assuming an inverse Fourier transform of  $\psi(\mathbf{r}, z, \Delta\omega)$  exists, we can perform

the inverse Fourier transform of Eq. 3.4.44 to yield:

$$\left[ -i2k_0 \left( \frac{\partial}{\partial z} + k_1 \frac{\partial}{\partial t} \right) + \nabla_{\text{T}}^2 - (k_0 k_2 + k_1^2) \frac{\partial^2}{\partial t^2} \right] \mathcal{F}^{-1}\{\psi(\mathbf{r}, z, \Delta\omega)\} - \mathcal{F}^{-1}\{ik_0\alpha(\omega)\psi(\mathbf{r}, z, \Delta\omega)\} = 0 \quad (3.4.45)$$

In Eq. 3.4.45, it is sufficient to consider the inverse Fourier transforms of  $\psi(\mathbf{r}, z, t)$  and of  $ik_0\alpha(\omega)\psi(\mathbf{r}, z, \Delta\omega)$  to be noted as,  $\mathcal{F}^{-1}\{\psi(\mathbf{r}, z, \Delta\omega)\}$  and  $\mathcal{F}^{-1}\{ik_0\alpha(\omega)\psi(\mathbf{r}, z, \Delta\omega)\}$ , respectively. With Eq. 3.4.45, we can directly apply the substitutions (Eq. 3.4.29a and 3.4.29b) necessary to migrate to the moving frame:

$$\begin{aligned} & \left[ -i2k_0 \left( \frac{\partial}{\partial \xi} + (k_1 - k_{1r}) \frac{\partial}{\partial \eta} \right) + \nabla_{\text{T}}^2 - (k_0 k_2 + k_1^2) \frac{\partial^2}{\partial \eta^2} \right] \\ & \times \mathcal{F}^{-1}\{\psi(\mathbf{r}, \xi, \Delta\omega)\} - \mathcal{F}^{-1}\{ik_0\alpha(\omega)\psi(\mathbf{r}, \xi, \Delta\omega)\} = 0 \end{aligned} \quad (3.4.46)$$

With Eq. 3.4.46 now describing propagation within the moving frame, we can return to the frequency domain. We will also take the opportunity to divide through Eq. 3.4.46 by the term  $-i2k_0$  at the beginning; in addition to reducing the number of terms dependent upon  $k_0$ , it will also allow us to invoke the assumption that  $k_1^2/k_0$  is likely small and can be neglected. This leaves us with:

$$\left[ \frac{\partial}{\partial \xi} + i(k_1 - k_{1r})\Delta\omega + i\frac{1}{2k_0}\nabla_{\text{T}}^2 + i\frac{1}{2}k_2\Delta\omega^2 + \frac{1}{2}\alpha(\omega) \right] \psi(\mathbf{r}, \xi, \Delta\omega) = 0 \quad (3.4.47)$$

Moving forward, we will also introduce a new variable,  $\delta k(\Delta\omega)$ :<sup>i</sup>

$$\delta k(\Delta\omega) = i(k_1 - k_{1r})\Delta\omega + i\frac{1}{2}k_2\Delta\omega^2 + \frac{1}{2}\alpha(\omega) \quad (3.4.48)$$

Introducing  $\delta k(\Delta\omega)$  simplifies Eq. 3.4.47 further, leaving:

$$\left[ \frac{\partial}{\partial \xi} + i\frac{1}{2k_0}\nabla_{\text{T}}^2 + \delta k(\Delta\omega) \right] \psi(\mathbf{r}, \xi, \Delta\omega) = 0 \quad (3.4.49)$$

In Eq. 3.4.49, we now have a compact description of the effects of field propagation on the distortion function,  $\psi(\mathbf{r}, \xi, \Delta\omega)$ , within a moving coordinate system. Now, we will seek to develop a closed-form solution for this distortion function. We begin by considering the form of the transverse Laplacian,  $\nabla_{\text{T}}^2$ . We previously considered this operator in the form of Eq. 3.3.5, in which it is described in  $(x, y)$  coordinates. Since we expect the TEM<sub>00</sub> mode to exhibit Gaussian symmetry, though, it will prove more convenient to begin with

---

<sup>i</sup>Recall  $\Delta\omega$  has been introduced as a compact variable for  $\omega - \omega_0$ . Therefore, we could reasonably consider  $\delta k$  to be a function of either  $\omega$  or  $\Delta\omega$ , but it would be redundant to consider  $\delta k$  to be a function of both. As we have been describing the distortion as a function of  $\Delta\omega$ , we have opted to treat  $\delta k$  as a function of this variable rather than of  $\omega$ .

$\nabla_{\mathbf{T}}^2$  in cylindrical coordinates. In this coordinate system, the full Laplacian operator is defined:[101]

$$\nabla^2 = \frac{1}{r} \frac{\partial}{\partial r} r \frac{\partial}{\partial r} + \frac{1}{r^2} \frac{\partial^2}{\partial \phi^2} + \frac{\partial^2}{\partial \xi^2} \quad (3.4.50)$$

However, we have already defined the transverse Laplacian,  $\nabla_{\mathbf{T}}^2$ , as encompassing the terms of the Laplacian operator not associated with the longitudinal direction,  $\xi$ ; we can therefore neglect the last term in Eq. 3.4.50. We can also neglect the angular dependence in Eq. 3.4.50: since the distortion to the plane wave,  $\psi(r, \xi, \Delta\omega)$ ,<sup>i</sup> is expected to describe a two-dimensional Gaussian, we can invoke the cylindrical symmetry of this function to assume  $\partial^2/\partial\phi^2\psi(r, \xi, \Delta\omega) = 0$ . [104, 105] We are then left only with the first term, the dependence upon the radial coordinate,  $r$ . Through evaluation by the product rule, we can show that this remaining term leaves the following form of the transverse Laplacian operator:

$$\nabla_{\mathbf{T}}^2 = \frac{1}{r} \frac{\partial}{\partial r} r \frac{\partial}{\partial r} + \frac{\partial^2}{\partial r^2} \quad (3.4.51)$$

Substitution for the transverse Laplacian according to Eq. 3.4.51 then leaves:

$$\left[ \frac{\partial}{\partial \xi} + i \frac{1}{2k_0} \left( \frac{1}{r} \frac{\partial}{\partial r} r \frac{\partial}{\partial r} + \frac{\partial^2}{\partial r^2} \right) + \delta k(\Delta\omega) \right] \psi(r, \xi, \Delta\omega) = 0 \quad (3.4.52)$$

With Eq. 3.4.52, we can now determine the functional behavior of  $\psi(r, \xi, \Delta\omega)$ , beginning by defining a trial solution as well as appropriate boundary conditions. Starting with the latter, we will define the position  $\xi = 0$  as the focus of the mode. In the absence of dispersive effects, we will expect the radial dependence of  $\psi(r, \xi = 0, \Delta\omega)$  to be consistent with a two-dimensional Gaussian of width  $w_0$ ; in other words, we will expect a functional form of  $\exp(-r^2/w_0^2)$ . Meanwhile, when we introduce dispersive effects, we will assume that dispersion from the medium functionally depends upon the pathlength through the medium; in other words, we will require no dispersive effects at a point  $\xi = \xi'$  that corresponds to the beginning of the medium. Meanwhile, for a trial solution, we have two examples to consider. Verdeyen assumes a specific form for  $\psi(r, \xi)$ , taking the model  $\exp[-i(P(\xi) + (kr^2)/[2q(\xi)])]$ ; [105] while this trial solution is convenient when considering the final result for  $\psi(r, \xi)$  for free space propagation, it may not prove adequately general when dispersion is incorporated. Consequently, we will instead adopt a trial solution similar to that of Svelto, in which  $U(r, \xi)$ <sup>ii</sup> is taken as a functional form incorporating two functions  $\alpha(\xi)$

<sup>i</sup>It is noted here that since we are now considering the functional form of  $\psi(r, \xi, \Delta\omega)$  within the cylindrical coordinate system, we no longer have to consider the generalized vector  $\mathbf{r}$  for the transverse coordinates; it is sufficient to consider the functional dependence upon the scalar radial coordinate,  $r$ .

<sup>ii</sup>Recall, Svelto's model for distortion to the plane wave adopts the function  $U(r, \xi)$  in the same manner that Verdeyen

and  $\beta(\xi)$ ,  $U(r, \xi) = \exp[\alpha(\xi) - \beta(\xi)r^2]$ . [104] Using Svelto's treatment as a starting point, we also need to allow for frequency dependence due to our generalized dispersion variable  $\delta k(\Delta\omega)$ ; we will therefore tentatively allow  $\alpha$  and  $\beta$  to both exhibit a frequency dependence, yielding:

$$\psi(r, \xi, \Delta\omega) = e^{\alpha(\xi, \Delta\omega) - \beta(\xi, \Delta\omega)r^2} \quad (3.4.53)$$

Introducing this trial solution:

$$\left[ \frac{\partial}{\partial \xi} + i \frac{1}{2k_0} \left( \frac{1}{r} \frac{\partial}{\partial r} + \frac{\partial^2}{\partial r^2} \right) + \delta k(\Delta\omega) \right] \exp^{\alpha(\xi, \Delta\omega) - \beta(\xi, \Delta\omega)r^2} = 0 \quad (3.4.54)$$

From Eq. 3.4.54, we see that we will need to evaluate the derivatives of our trial solution with respect to  $\partial/\partial r$ ,  $\partial^2/\partial r^2$ , and  $\partial/\partial \xi$ . It can be shown that these derivatives evaluate to yield:

$$\frac{\partial}{\partial r} e^{\alpha(\xi, \Delta\omega) - \beta(\xi, \Delta\omega)r^2} = -2\beta(\xi, \Delta\omega)r e^{\alpha(\xi, \Delta\omega) - \beta(\xi, \Delta\omega)r^2} \quad (3.4.55a)$$

$$\frac{\partial^2}{\partial r^2} e^{\alpha(\xi, \Delta\omega) - \beta(\xi, \Delta\omega)r^2} = [-2\beta(\xi, \Delta\omega) + 4\beta^2(\xi, \Delta\omega)r^2] e^{\alpha(\xi, \Delta\omega) - \beta(\xi, \Delta\omega)r^2} \quad (3.4.55b)$$

$$\frac{\partial}{\partial \xi} e^{\alpha(\xi, \Delta\omega) - \beta(\xi, \Delta\omega)r^2} = \left[ \left( \frac{\partial}{\partial \xi} \alpha(\xi, \Delta\omega) \right) - r^2 \left( \frac{\partial}{\partial \xi} \beta(\xi, \Delta\omega) \right) \right] e^{\alpha(\xi, \Delta\omega) - \beta(\xi, \Delta\omega)r^2} \quad (3.4.55c)$$

If we consider the forms of Eq. 3.4.55a, 3.4.55b, and 3.4.55c, we see that evaluation of the derivatives leaves the exponential unchanged and no longer within derivative expressions. Upon substituting the results of Eq. 3.4.55a, 3.4.55b, and 3.4.55c into Eq. 3.4.54, we can then divide through the resulting expression by the exponential, leaving:

$$\left[ \left( \frac{\partial}{\partial \xi} \alpha(\xi, \Delta\omega) \right) - r^2 \left( \frac{\partial}{\partial \xi} \beta(\xi, \Delta\omega) \right) \right] + i \frac{1}{2k_0} [-4\beta(\xi, \Delta\omega) + 4\beta^2(\xi, \Delta\omega)r^2] + \delta k(\Delta\omega) = 0 \quad (3.4.56)$$

Examining Eq. 3.4.56, we see that the five terms can be divided into two groups: two terms with a dependence upon  $r^2$ , and three terms with no dependence upon  $r$ . Separating the terms accordingly yields:

$$r^2 \left[ - \left( \frac{\partial}{\partial \xi} \beta(\xi, \Delta\omega) \right) + i \frac{2}{k_0} \beta^2(\xi, \Delta\omega) \right] + \left[ \left( \frac{\partial}{\partial \xi} \alpha(\xi, \Delta\omega) \right) - i \frac{2}{k_0} \beta(\xi, \Delta\omega) + \delta k(\Delta\omega) \right] = 0 \quad (3.4.57)$$

However, we still require the left hand side of Eq. 3.4.57 to equal zero. In Eq. 3.4.57, though, we have terms dependent upon  $r^2$  as well as terms independent of  $r$ ; the only way to maintain the required equality is for

---

adopts  $E_0\psi(r, \xi)$ . [104, 105]

both terms in brackets to individually equal zero.[104, 105] Eq. 3.4.57 then is consistent with the following pair of differential equations:

$$\frac{\partial}{\partial \xi} \beta(\xi, \Delta\omega) = i \frac{2}{k_0} \beta^2(\xi, \Delta\omega) \quad (3.4.58a)$$

$$\frac{\partial}{\partial \xi} \alpha(\xi, \Delta\omega) = i \frac{2}{k_0} \beta(\xi, \Delta\omega) - \delta k(\Delta\omega) \quad (3.4.58b)$$

This system of differential equations can be evaluated to determine the functional forms of  $\alpha(\xi, \Delta\omega)$  and  $\beta(\xi, \Delta\omega)$ .

Of the differential equations in Eq. 3.4.58a and 3.4.58b, the former will be the more straightforward to solve, as it exhibits a dependence only upon the function  $\beta(\xi, \Delta\omega)$ . However, we note that the only dependence upon  $\Delta\omega$  in Eq. 3.4.58a is the dependence implied by our assumed function,  $\beta(\xi, \Delta\omega)$ . We can assume, therefore, that it is sufficient to consider  $\beta(\xi)$ , a function of  $\xi$  only. Framing Eq. 3.4.58a to be of the form  $\partial/\partial \xi \beta(\xi) = ia\beta^2(\xi)$ , with  $a = 2/k_0$ , it can be shown that the general solution is of the form:<sup>i</sup>

$$\beta(\xi) = (C - ia\xi)^{-1} \quad (3.4.59)$$

where  $C$  is a constant of integration. In order to determine the value of  $C$ , let us consider the evaluation of this general solution at  $\xi = 0$ . We previously indicated that we require the mode at the focus ( $\xi = 0$ ) to be consistent with a Gaussian function with size  $w_0$ ,  $\exp(-r^2/w_0^2)$ . Since our trial function is of the form  $\exp[\alpha(\xi, \Delta\omega) - \beta(\xi)r^2]$ , we therefore require  $\beta(\xi = 0) = w_0^{-2}$ . Given the general solution in Eq. 3.4.59,  $\beta(\xi = 0) = C^{-1}$ , allowing us to assign  $C = w_0^2$  and to define the solution for  $\beta(\xi)$ :

$$\beta(\xi) = \left( w_0^2 - i \frac{2}{k_0} \xi \right)^{-1} \quad (3.4.60)$$

However, we can follow the example of Verdeyen[105] and make the solution in Eq. 3.4.60 more meaningful by relating it to the quantities  $w(\xi)$  and  $R(\xi)$ , which describe the beam waist and radius of curvature, respectively, as a function of longitudinal position. The functional forms of these parameters are:

$$w(\xi) = w_0 \sqrt{1 + \left( \frac{\xi}{\xi_0} \right)^2} \quad (3.4.61)$$

---

<sup>i</sup>The general differential equation was evaluated with the calculator at wolframalpha.com.

$$R(\xi) = \begin{cases} \xi(1 + (\frac{\xi_0}{\xi})^2), & \text{for } z \neq 0, \pm\infty \\ 0, & \text{for } z = 0, \pm\infty \end{cases} \quad (3.4.62)$$

where the quantity  $\xi_0$  in Eq. 3.4.61 and 3.4.62 is the Rayleigh length of the mode;<sup>1</sup> this quantity is defined:

$$\xi_0 = \frac{\pi w_0^2}{\lambda} \quad (3.4.63)$$

Considering Eq. 3.4.61, we can see  $\xi_0$  corresponds to the distance over which the beam waist expands by a factor of  $\sqrt{2}$  from the focus. Returning to the beam waist and radius of curvature, the first step to relating  $\beta(\xi)$  to these quantities is to show that the solution for  $\beta(\xi)$  (Eq. 3.4.60) is equivalent to:

$$\beta(\xi) = i \frac{k_0}{2} (\xi + i\xi_0)^{-1} \quad (3.4.64)$$

We can simplify the form for  $\beta(\xi)$  in Eq. 3.4.64 by multiplying this result by  $(\xi - i\xi_0)/(\xi - i\xi_0)$ , from which  $\beta(\xi)$  is equivalent to the sum:

$$\beta(\xi) = \frac{k_0}{2} \frac{\xi_0}{\xi^2 + \xi_0^2} + i \frac{k_0}{2} \frac{\xi}{\xi^2 + \xi_0^2} \quad (3.4.65)$$

From Eq. 3.4.65, the next step is to multiply the first term by  $\xi_0^{-2}/\xi_0^{-2}$  and the second term by  $\xi^{-2}/\xi^{-2}$ . This yields:

$$\beta(\xi) = \frac{k_0}{2\xi_0} \frac{1}{(\xi/\xi_0)^2 + 1} + i \frac{k_0}{2} \frac{1}{\xi[1 + (\xi_0/\xi)^2]} \quad (3.4.66)$$

Considering the definitions of  $w(\xi)$ ,  $R(\xi)$ , and  $\xi_0$  (Eq. 3.4.61, 3.4.62, and 3.4.63), it is now straightforward to show Eq. 3.4.66 reduces to:

$$\beta(\xi) = \frac{1}{w^2(\xi)} + i \frac{k_0}{2R(\xi)} \quad (3.4.67)$$

With a solution for  $\beta(\xi)$ , it is now possible to consider Eq. 3.4.58b to determine the solution for  $\alpha(\xi, \Delta\omega)$ . It will turn out most convenient to use the form of Eq. 3.4.64 for substitution into Eq. 3.4.58b; introducing this solution yields:

$$\frac{\partial}{\partial \xi} \alpha(\xi, \Delta\omega) = i \frac{2}{k_0} \left[ i \frac{k_0}{2} (\xi + i\xi_0)^{-1} \right] - \delta k(\Delta\omega) \quad (3.4.68)$$

In a similar manner to our treatment of  $\beta(\xi)$ , we can consider Eq. 3.4.68 to be of the generalized form  $\partial/\partial \xi \alpha(\xi, \Delta\omega) = -(\xi + ia)^{-1} - b(\Delta\omega)$ , with  $a = \xi_0$  and  $b(\Delta\omega) = \delta k(\Delta\omega)$ . A differential equation of this form

---

<sup>1</sup>Note that it is more common to describe the Rayleigh length as  $z_0$ ; however, because we are using the coordinate of the moving frame,  $\xi$ , we are noting this length as  $\xi_0$  in an analogous manner. Note that because  $\xi = z$  (see Eq. 3.4.27a),  $\xi_0 = z_0$ .



will have a solution of the form:<sup>i</sup>

$$\alpha(\xi, \Delta\omega) = -\ln(a - i\xi) - ib(\Delta\omega)(a - i\xi) + C \quad (3.4.69)$$

Considering the form of the general solution in Eq. 3.4.69, we see that it involves two terms with dependence upon  $\xi$ : the first term,  $\ln(a - i\xi)$ , depends only upon  $\xi$ ; the second,  $-ib(\Delta\omega)(a - i\xi)$ , on the other hand exhibits a dependence upon  $\Delta\omega$  in addition to a dependence upon  $\xi$ . Therefore, let us consider  $\alpha(\xi, \Delta\omega)$  to represent the sum of two functions,  $\alpha_1(\xi)$  and  $\alpha_2(\xi, \Delta\omega)$ , corresponding to the first and second terms in Eq. 3.4.69, respectively:

$$\alpha_1(\xi) = -\ln(a - i\xi) + C_1 \quad (3.4.70a)$$

$$\alpha_2(\xi, \Delta\omega) = -ib(\Delta\omega)(a - i\xi) + C_2 \quad (3.4.70b)$$

where the sum of  $C_1$  (Eq. 3.4.70a) and  $C_2$  (Eq. 3.4.70b) is  $C$  (Eq. 3.4.69). The division of  $\alpha(\xi, \Delta\omega)$  into  $\alpha_1(\xi)$  and  $\alpha_2(\xi, \Delta\omega)$  isolates the frequency-dependence of  $\alpha(\xi, \Delta\omega)$  to  $\alpha_2(\xi, \Delta\omega)$ . The advantage of doing so is clear if we consider the scenario of free space propagation, for which  $\delta k(\Delta\omega) = 0$ : recalling  $b(\Delta\omega) = \delta k(\Delta\omega)$ ,  $\delta k(\Delta\omega) = 0$  causes  $\alpha_2(\xi, \Delta\omega)$  to be constant, allowing it to be incorporated into  $C_1$ . Therefore,  $\alpha_1(\xi)$  should be the solution for  $\alpha(\xi, \Delta\omega)$  when considering free-space propagation of the TEM<sub>00</sub> mode, with  $\alpha_2(\xi, \Delta\omega)$  providing the correction necessary to account for the dispersion introduced by a medium.

Within the treatment of  $\alpha(\xi, \Delta\omega)$  as the sum of  $\alpha_1(\xi)$  and  $\alpha_2(\xi, \Delta\omega)$ , we can address  $\alpha_1(\xi)$  and  $\alpha_2(\xi, \Delta\omega)$  separately. Starting with  $\alpha_1(\xi)$ , and recalling our assignment of the temporary variable  $a = \xi_0$ , we can show the formulation in Eq. 3.4.70a is identical to:

$$\alpha_1(\xi) = -\ln\left(1 - i\frac{\xi}{\xi_0}\right) - \ln(\xi_0) + C_1 \quad (3.4.71)$$

As  $\ln(\xi_0)$  will just have a constant value, we can incorporate it into the constant,  $C_1$ , leaving:

$$\alpha_1(\xi) = -\ln\left(1 - i\frac{\xi}{\xi_0}\right) + C_1 \quad (3.4.72)$$

We must then determine the appropriate value of  $C_1$ , first recalling that we have taken  $\alpha_1(\xi)$  to describe the behavior of  $\alpha(\xi, \Delta\omega)$  for free-space propagation of the TEM<sub>00</sub> mode. Previously, we indicated that in

---

<sup>i</sup>The general differential equation was evaluated with the calculator at wolframalpha.com; when evaluating, it is sufficient to consider  $b(\Delta\omega)$  as a constant as the differential equation is associated with the derivative with respect to  $\xi$ .

the absence of dispersion, or for free-space propagation, we expect a form consistent with  $\exp(-r^2/w_0^2)$  at  $\xi = 0$ . This necessitates  $\alpha_1(\xi = 0) = 0$ . Given the general solution of Eq. 3.4.72,  $\alpha_1(\xi = 0) = -\ln(1) + C_1$ . However,  $\ln(1) = 0$ , so  $\alpha_1(\xi = 0) = C_1$ , requiring  $C_1 = 0$  in order to satisfy our assignment of  $\alpha_1(\xi = 0) = 0$ . The solution for  $\alpha_1(\xi)$  must then be:

$$\alpha_1(\xi) = -\ln\left(1 - i\frac{\xi}{\xi_0}\right) \quad (3.4.73)$$

However, we can simplify the solution in Eq. 3.4.73 by considering  $(1 - i\xi/\xi_0)$  as a value in the complex plane: namely, as the product of its magnitude and a phase factor,  $\exp(i\phi)$ , where  $\phi = \arctan \Im\{1 - i\xi/\xi_0\}/\Re\{1 - i\xi/\xi_0\}$ . In this manner, we can find  $(1 - i\xi/\xi_0)$  to be equivalent to:<sup>i</sup>

$$\left(1 - i\frac{\xi}{\xi_0}\right) = \sqrt{1 + \left(\frac{\xi}{\xi_0}\right)^2} e^{-i\arctan(\xi/\xi_0)} \quad (3.4.74)$$

Substitution for  $(1 - i\xi/\xi_0)$  according to Eq. 3.4.74 into Eq. 3.4.73 then yields:

$$\alpha_1(\xi) = -\ln\sqrt{1 + \left(\frac{\xi}{\xi_0}\right)^2} + i\arctan\left(\frac{\xi}{\xi_0}\right) \quad (3.4.75)$$

Continuing with  $\alpha_2(\xi, \Delta\omega)$ , we can substitute according to our assignments of  $a = \xi_0$  and  $b(\Delta\omega) = \delta k(\Delta\omega)$  and distribute the term corresponding to  $-ib(\Delta\omega)$  to yield:

$$\alpha_2(\xi, \Delta\omega) = -i\xi_0\delta k(\Delta\omega) - \delta k(\Delta\omega)\xi + C_2 \quad (3.4.76)$$

In the same manner that we incorporated  $\ln(\xi_0)$  into  $C_1$  in Eq. 3.4.72, we can consider  $-i\xi_0\delta k(\Delta\omega)$  as a constant relative to mode propagation and combine it with  $C_2$  to yield the simplified result:

$$\alpha_2(\xi, \Delta\omega) = -\delta k(\Delta\omega)\xi + C_2 \quad (3.4.77)$$

From this simplified general solution for  $\alpha_2(\xi, \Delta\omega)$ , the last remaining step is to determine the exact solution by evaluating  $C_2$ . In contrast to  $\beta(\xi)$  and  $\alpha_1(\xi)$ , however, for  $\alpha_2(\xi, \Delta\omega)$ , it will not prove convenient to consider the behavior at  $\xi = 0$ ; we instead must consider what  $\delta k(\Delta\omega)$  represents. In Eq. 3.4.48, we defined  $\delta k(\Delta\omega)$  to represent the various contributions of the medium's dispersion upon the propagation of the field, and we expect these effects to scale with the propagation distance. Recalling that we have defined the point

---

<sup>i</sup>Note that  $\tan$  is an odd function ( $\tan(-\theta) = -\tan(\theta)$ ). [116] From this, it is possible to show  $\arctan(-\xi/\xi_0) = -\arctan(\xi/\xi_0)$ , i.e. that  $\arctan$  must also be odd.

$\xi = \xi'$  to represent the point at which the field enters the medium, we therefore consider that at  $\xi = \xi'$ , we have accumulated no effects of dispersion, and at all other points within the medium, we accumulate the effects of dispersion according to  $\xi - \xi'$ . Therefore, we will need to define  $C_2$  such that  $\alpha_2(\xi, \Delta\omega)$  assumes the form:

$$\alpha_2(\xi, \Delta\omega) = -\delta k(\Delta\omega)(\xi - \xi') \quad (3.4.78)$$

Having obtained solutions for  $\alpha_1(\xi)$ ,  $\alpha_2(\xi, \Delta\omega)$ , and  $\beta(\xi)$ , we can substitute these results into our trial solution (Eq. 3.4.53), yielding:

$$\psi(r, \xi, \Delta\omega) = \frac{1}{\sqrt{1 + (\xi/\xi_0)^2}} e^{i \arctan \xi/\xi_0} e^{-\delta k(\Delta\omega)(\xi - \xi')} e^{-r^2/w^2(\xi)} e^{-ik_0/[2R(\xi)]r^2} \quad (3.4.79)$$

Incorporating the definition of  $\delta k(\Delta\omega)$  (Eq. 3.4.48), then substituting this solution for  $\psi(r, \xi, \Delta\omega)$  into our original frequency-domain model for the field (Eq. 3.4.39b), we arrive at a result very consistent with the results of Svelto and Verdeyen:[104, 105]

$$E(r, \xi, \Delta\omega) = \hat{A}(\Delta\omega) \frac{1}{\sqrt{1 + (\xi/\xi_0)^2}} \exp \left[ -\frac{r^2}{w^2(\xi)} \right] \quad (3.4.80a)$$

$$\times \exp(-ik_0\xi) \exp \left( -i \frac{\Delta\omega}{v} \xi \right) \exp \left( i \arctan \frac{\xi}{\xi_0} \right) \quad (3.4.80b)$$

$$\times \exp \left( -i \frac{k_0}{2R(\xi)} r^2 \right) \quad (3.4.80c)$$

$$\times \exp \left[ -i(k_1 - k_{1r})\Delta\omega (\xi - \xi') - i \frac{1}{2} k_2 \Delta\omega^2 (\xi - \xi') \right] \quad (3.4.80d)$$

$$\times \exp \left[ -\frac{1}{2} \alpha(\omega) (\xi - \xi') \right] \quad (3.4.80e)$$

The presentation of the field across Eq. 3.4.80a - 3.4.80e allows us to separately consider the various contributions to the field in the manner of Verdeyen.[105] Eq. 3.4.80a contains the three terms that combine to describe the amplitude of the field independent of the medium (i.e. neglecting absorptive effects) and as a function of the spatial coordinates ( $r$  or  $\xi$ ) or of detuning ( $\Delta\omega$ ). Eq. 3.4.80b encompasses the contributions to the longitudinal phase of the field; these contributions may arise from either the spatial oscillations of the field,  $\exp(-ik_0\xi)$  and  $\exp[-i(\Delta\omega/v)\xi]$ , or from the Guoy phase,  $\exp[i \arctan(\xi/\xi_0)]$ . Eq. 3.4.80c describes the phase accumulated by the field due to the radius of curvature of the phase front. Finally, Eq. 3.4.80d and Eq. 3.4.80e provide the corrections necessary to account for the effects of a dispersive medium, introducing the changes arising from dispersion and absorption, respectively.

### 3.4.4 Integration of the Nonlinear Polarization Outside the Plane Wave Limit

In this section, we will discuss the adaptation of the method presented by Moosmüller et al.[202] for integration of the polarization induced by Gaussian beams, extending the approach to ultrashort pulses and crossed beam geometries. A variety of authors have addressed the integration of the nonlinear polarization induced by Gaussian beams in the literature.[139, 202–205] Some of these authors emphasize the importance of incorporating the effects of the Guoy phase,[139, 203] particularly in experiments that do not involve oppositely phase interactions of the same frequency. When two oppositely phase interactions have the same frequency, the Guoy phases of the interactions cancel; otherwise, the Guoy phase introduces additional interference effects in the same manner as phase mismatch. However, many of these authors focus on collinear experiments:[139, 202, 203] those that consider crossed beams appear to make approximations[204] or adopt similar methods that are less straightforward or less thoroughly documented than the method presented by Moosmüller et al.[205]

In a manner similar to § 3.4.3, we will allow the electric field to exhibit a transverse dependence. However, in contrast to the treatment in § 3.4.3, we cannot expect a closed-form solution for the transverse dependence; therefore, we will consider it sufficient to treat the field in the same manner as Eq. 3.1.27, with the envelope functions explicitly exhibiting dependence upon the spatial coordinates:

$$\tilde{E}(\mathbf{r}, z, t) = A(\mathbf{r}, z, t)e^{-ik_0z}e^{i\omega_0t} \quad (3.4.81a)$$

$$E(\mathbf{r}, z, \omega) = \hat{A}(\mathbf{r}, z, \Delta\omega)e^{-i(\Delta\omega/v)z}e^{-ik_0z} \quad (3.4.81b)$$

In Eq. 3.4.81a and 3.4.81b, we return to our notation of  $\mathbf{r}$  to generalize the transverse coordinates  $(x, y)$ . We make a similar assumption as in § 3.4.3, taking the relationship between the time- and frequency-domain models to be similar to Eq. 3.1.26, namely  $\mathcal{F}\{A(\mathbf{r}, z, t)\exp(i\omega_0t)\} = \hat{A}(\mathbf{r}, z, \Delta\omega)\exp[-i(\Delta\omega/v)z]$  when the Fourier transform is with respect to  $\omega$ . In contrast to § 3.4.3, however, we will consider the field described by Eq. 3.4.81a or 3.4.81b as it couples to a nonlinear polarization oscillating with central frequency  $\omega_0$ . In the same manner as Eq. 3.2.17 and 3.2.18, and in analogy with Eq. 3.4.81a and 3.4.81b, we will consider this nonlinear polarization to be described:

$$\tilde{P}^{\text{NL}}(\mathbf{r}, z, t) = p^{\text{NL}}(\mathbf{r}, z, t)e^{i\omega_0t} \quad (3.4.82a)$$

$$P^{\text{NL}}(\mathbf{r}, z, \omega) = \hat{p}^{\text{NL}}(\mathbf{r}, z, \Delta\omega) \quad (3.4.82b)$$

In the same manner as the field exhibits dependence upon both the transverse and longitudinal coordinates, the polarization is also allowed to do so through the envelope function,  $p^{\text{NL}}(\mathbf{r}, z, t)$  or  $\hat{p}^{\text{NL}}(\mathbf{r}, z, \Delta\omega)$ . Whereas the spatial dependence of the field will be assumed to arise from the spatial dependence of the polarization - which is to assume the field is created from the initiated nonlinear polarization - the polarization will be assumed to exhibit spatial dependence due to the manner of excitation.

We will begin our treatment in a very similar manner to § 3.4.3, starting from Eq. 3.3.6 and considering two contributions to the polarization: a linear polarization,  $\tilde{P}^{(1)}(\mathbf{r}, z, t)$ , and a nonlinear polarization,  $\tilde{P}^{\text{NL}}(\mathbf{r}, z, t)$ . However, whereas we were satisfied considering  $\tilde{P}^{\text{NL}}(\mathbf{r}, z, t) = 0$  in § 3.4.3, we will now consider there to be a previously induced nonlinear polarization existing within the medium, described according to Eq. 3.4.82a. From these assumptions, we can arrive at a result very similar to Eq. 3.4.40:

$$\frac{\partial}{\partial z^2} \tilde{E}(\mathbf{r}, z, t) + \nabla_{\text{T}}^2 \tilde{E}(\mathbf{r}, z, t) - b^2 e \frac{\partial^2}{\partial t^2} \tilde{D}^{(1)}(\mathbf{r}, z, t) = ab^2 e \frac{\partial^2}{\partial t^2} \tilde{P}^{\text{NL}}(\mathbf{r}, z, t) \quad (3.4.83)$$

where we have again combined the derivatives of the field and of the linear polarization with respect to time according to Eq. 3.4.3 to yield the linear displacement. Evaluating the derivative with respect to  $z$  yields:

$$\begin{aligned} e^{-ik_0 z} \left[ -k_0^2 - i2k_0 \frac{\partial}{\partial z} + \frac{\partial^2}{\partial z^2} \right] A(\mathbf{r}, z, t) e^{i\omega_0 t} + \nabla_{\text{T}}^2 \tilde{E}(\mathbf{r}, z, t) \\ - b^2 e \frac{\partial^2}{\partial t^2} \tilde{D}^{(1)}(\mathbf{r}, z, t) = ab^2 e \frac{\partial^2}{\partial t^2} \tilde{P}^{\text{NL}}(\mathbf{r}, z, t) \end{aligned} \quad (3.4.84)$$

Again following a similar strategy to § 3.4.3, we will Fourier transform Eq. 3.4.84 to yield the frequency-domain equivalent. We will proceed to substitute for the resulting frequency-domain terms  $E(\mathbf{r}, z, \omega)$  and  $P^{\text{NL}}(\mathbf{r}, z, \omega)$  according to Eq. 3.4.81b and 3.4.82b, though for convenience we will currently make the approximation that the term  $\exp[-i(\Delta\omega/v)z]$  in Eq. 3.4.81b is negligible as in § 3.4.1; as before, we will be able to relax this assumption later. Finally, we will multiply through the result by  $\exp(ik_0 z)$ . These changes yield:

$$\left[ \frac{\partial^2}{\partial z^2} - i2k_0 \frac{\partial}{\partial z} - k_0^2 + e^{ik_0 z} \nabla_{\text{T}}^2 e^{-ik_0 z} + b^2 e \omega^2 \epsilon(\omega) \right] \hat{A}(\mathbf{r}, z, \Delta\omega) = -ab^2 e \omega^2 e^{ik_0 z} \hat{p}^{\text{NL}}(\mathbf{r}, z, \Delta\omega) \quad (3.4.85)$$

From Eq. 3.4.85, we can apply a handful of simplifications that have previously been introduced. First, since the transverse Laplacian,  $\nabla_{\text{T}}^2$ , is only associated with the transverse coordinates,  $\nabla_{\text{T}}^2 \exp(-ik_0 z) = \exp(-ik_0 z) \nabla_{\text{T}}^2$ ; this identity allows us to remove the exponentials from this term in Eq. 3.4.85. Second, Eq. 3.4.9, 3.4.10, and 3.4.18 have shown we can introduce  $k^2(\omega) - ik(\omega)\alpha(\omega)$  as a substitute for  $b^2 e \omega^2 \epsilon(\omega)$ ; we can combine this result with the term  $k_0^2$  in Eq. 3.4.85, and use the expansion of Eq. 3.4.24 to yield

$2k_0k_1\Delta\omega + (k_0k_2 + k_1^2)\Delta\omega^2 - ik_0\alpha(\omega)$ . In § 3.4.1, we also showed that, by introducing  $\hat{p}^{\text{NL}}(\mathbf{r}, z, \Delta\omega)$ ,<sup>i</sup> we can substitute for  $ab^2e\omega^2$ , yielding  $\omega^2/c^2$  in both unit systems. Finally, we will also make the slowly varying amplitude approximation, assuming  $2k_0\partial/\partial z \gg \partial^2/\partial z^2$ . The result of applying these substitutions and approximations is:

$$\left[ -i2k_0\frac{\partial}{\partial z} + \nabla_{\text{T}}^2 + 2k_0k_1\Delta\omega + (k_0k_2 + k_1^2)\Delta\omega^2 - ik_0\alpha(\omega) \right] \hat{A}(\mathbf{r}, z, \Delta\omega) = -\frac{\omega^2}{c^2} e^{ik_0z} \hat{p}^{\text{NL}}(\mathbf{r}, z, \Delta\omega) \quad (3.4.86)$$

As in § 3.4.1 and § 3.4.3, we will want to transfer Eq. 3.4.86 to the moving frame as defined by Eq. 3.4.27a and 3.4.27b. Performing the inverse Fourier transform to bring Eq. 3.4.86 back to the time domain yields:

$$\begin{aligned} \left[ -i2k_0 \left( \frac{\partial}{\partial z} + k_1 \frac{\partial}{\partial t} \right) + \nabla_{\text{T}}^2 - (k_0k_2 + k_1^2) \frac{\partial^2}{\partial t^2} \right] A(\mathbf{r}, z, t) \\ - \mathcal{F}^{-1} \{ ik_0\alpha(\omega) \hat{A}(\mathbf{r}, z, \Delta\omega) \} = \frac{\omega^2}{c^2 \Delta\omega^2} e^{ik_0z} \frac{\partial^2}{\partial t^2} \bar{p}^{\text{NL}}(\mathbf{r}, z, t) \end{aligned} \quad (3.4.87)$$

With Eq. 3.4.87 in the time domain, we can substitute according to Eq. 3.4.29a and 3.4.29b to yield:

$$\begin{aligned} \left[ -i2k_0 \left( \frac{\partial}{\partial \xi} + (k_1 - k_{1r}) \frac{\partial}{\partial \eta} \right) + \nabla_{\text{T}}^2 - (k_0k_2 + k_1^2) \frac{\partial^2}{\partial \eta^2} \right] A(\mathbf{r}, \xi, \eta) \\ - \mathcal{F}^{-1} \{ ik_0\alpha(\omega) \hat{A}(\mathbf{r}, \xi, \Delta\omega) \} = \frac{\omega^2}{c^2 \Delta\omega^2} e^{ik_0\xi} \frac{\partial^2}{\partial \eta^2} \bar{p}^{\text{NL}}(\mathbf{r}, \xi, \eta) \end{aligned} \quad (3.4.88)$$

Once again, now that Eq. 3.4.88 represents propagation within the moving frame, we will return to the frequency domain; the Fourier transform of Eq. 3.4.88 yields:

$$\begin{aligned} \left[ -i2k_0 \left( \frac{\partial}{\partial \xi} + i(k_1 - k_{1r})\Delta\omega \right) + \nabla_{\text{T}}^2 + (k_0k_2 + k_1^2)\Delta\omega^2 - ik_0\alpha(\omega) \right] \\ \times \hat{A}(\mathbf{r}, \xi, \Delta\omega) = -\frac{\omega^2}{c^2} e^{ik_0\xi} \hat{p}^{\text{NL}}(\mathbf{r}, \xi, \Delta\omega) \end{aligned} \quad (3.4.89)$$

We can simplify the result of Eq. 3.4.89 slightly by dividing the equation by  $-i2k_0$ . As before, we will assume the resulting term  $k_1^2/k_0$  is sufficiently small so as to be negligible. This leaves:

$$\left[ \frac{\partial}{\partial \xi} + i(k_1 - k_{1r})\Delta\omega + i\frac{1}{2k_0}\nabla_{\text{T}}^2 + i\frac{1}{2}k_2\Delta\omega^2 + \frac{1}{2}\alpha(\omega) \right] \hat{A}(\mathbf{r}, \xi, \Delta\omega) = -i\frac{\omega^2}{2c^2k_0} e^{ik_0\xi} \hat{p}^{\text{NL}}(\mathbf{r}, \xi, \Delta\omega) \quad (3.4.90)$$

Note that at this point, we can adopt the approach of § 3.4.1 and relax the assumption that  $\exp[-i(\Delta\omega/v)\xi]$  is negligible; if we again allow  $\Delta\omega$  to be sufficiently small that the expansion of  $\partial/\partial \xi \hat{A}(\mathbf{r}, \xi, \Delta\omega) \exp[-i(\Delta\omega/v)\xi]$

---

<sup>i</sup>Recall that the quantity  $\bar{P}^{\text{NL}}(z, \omega)$  was defined  $\bar{P}^{\text{NL}} = [P^{\text{NL}}(z, \omega)]/\epsilon_0$  for mks units and  $\bar{P}^{\text{NL}} = 4\pi P^{\text{NL}}(z, \omega)$  for cgs or esu units. Here, we take  $\hat{p}^{\text{NL}}(\mathbf{r}, z, \Delta\omega)$  in the same manner, only including the transverse dependence neglected in the plane wave limit of § 3.4.1.

is approximately  $\exp[-i(\Delta\omega/v)\xi]^{\partial/\partial\xi}\hat{A}(\mathbf{r}, \xi, \Delta\omega)$ , we can divide through the result by the exponential. Re-combination of  $\exp[i(\Delta\omega/v)\xi]$  with  $\exp(ik_0\xi)$  yields  $\exp[ik(\omega)\xi]$  on the right hand side. We will apply this consideration going forward. We will also take the opportunity to introduce two variables to simplify the form of Eq. 3.4.90. Similar to § 3.4.3, we will introduce the variable  $\delta k(\Delta\omega)$ :

$$\delta k(\Delta\omega) = i(k_1 - k_{1r})\Delta\omega + i\frac{1}{2}k_2\Delta\omega^2 + \frac{1}{2}\alpha(\omega) \quad (3.4.91)$$

Second, in a manner similar to Moosmüller et al,[202] we will introduce a function representing the right hand side of Eq. 3.4.90:<sup>i</sup>

$$\rho(\mathbf{r}, \xi, \Delta\omega) = -i\frac{\omega^2}{2c^2k_0}e^{ik(\omega)\xi}\hat{p}^{\text{NL}}(\mathbf{r}, \xi, \Delta\omega) \quad (3.4.92)$$

With these variables, Eq. 3.4.90 becomes:

$$\left[ \frac{\partial}{\partial\xi} + i\frac{1}{2k_0}\nabla_{\text{T}}^2 + \delta k(\Delta\omega) \right] \hat{A}(\mathbf{r}, \xi, \Delta\omega) = \rho(\mathbf{r}, \xi, \Delta\omega) \quad (3.4.93)$$

From Eq. 3.4.93, we will begin applying the approach outlined by Moosmüller et al.[202] Their method is predicated upon performing a two-dimensional Fourier transform with respect to the transverse coordinate, masking the transverse propagation of the field by converting from the spatial domain to the spatial frequency domain. For example, if we consider the generalized transverse coordinate  $\mathbf{r}$  to correspond to a  $(x, y)$  coordinate system, this two-dimensional Fourier transform takes  $(x, y) \rightarrow (k_x, k_y)$ , where  $k_x$  and  $k_y$  are the spatial frequencies associated with  $x$  and  $y$ , respectively. We will generalize this transform as  $\mathbf{r} \rightarrow \mathbf{k}_{\text{T}}$ . However, given Eq. 3.4.93, we can see that we will need to understand how the transverse Laplacian,  $\nabla_{\text{T}}^2$ , transforms. By considering our definition for this operator (Eq. 3.3.5) and its application to an arbitrary function,  $f(\mathbf{r})$ , we can use the appropriate Fourier relation<sup>ii</sup> (see Eq. 3.4.6b) to determine the transform of

---

<sup>i</sup>Moosmüller et al notate this function as  $f$ ; as we have consistently used  $f$  throughout this chapter as an arbitrary, representative function, we have chosen to use a different notation in this capacity ( $\rho$ ). Additionally, in a manner similar to how we previously assumed it was sufficient to consider  $\delta k$  in § 3.4.3 as a function of just  $\Delta\omega$  while it contained both terms dependent upon  $\omega$  and upon  $\Delta\omega$ , we will consider it sufficient to treat  $\rho$  in Eq. 3.4.92 as a function of  $\Delta\omega$ .

<sup>ii</sup>It should be noted that the form of Eq. 3.4.6b is specific for Fourier transformation to the angular frequency domain.[112] When the Fourier transform is being taken to the linear frequency domain, the transform is instead  $\mathcal{F}\{\partial^n/\partial t^n f(t)\} = (i2\pi\nu)^n \hat{f}(\nu)$ , where  $\nu$  is the linear frequency.[114] We note here that we are using this relationship because we will be taking the generalized frequency  $\mathbf{k}_{\text{T}}$  to be a linear spatial frequency. Unfortunately, Moosmüller et al do not explicitly indicate whether they take their version of the generalized transverse spatial frequency to be angular or linear,[202] but by omitting the factor of  $(2\pi)^2$  that appears in Eq. 3.4.94, it appears to have been their intention to consider the frequency to be angular.

$\nabla_{\mathbf{T}}^2$ :

$$\begin{aligned}\mathcal{F}\{\nabla_{\mathbf{T}}^2 f(\mathbf{r})\} &= \mathcal{F}\left\{\left(\frac{\partial^2}{\partial x^2} + \frac{\partial^2}{\partial y^2}\right) f(\mathbf{r})\right\} \\ &= [(i2\pi)^2 k_x^2 + (i2\pi)^2 k_y^2] \hat{f}(\mathbf{k}_{\mathbf{T}}) \\ &= -4\pi^2 |\mathbf{k}_{\mathbf{T}}|^2 \hat{f}(\mathbf{k}_{\mathbf{T}})\end{aligned}\quad (3.4.94)$$

where we have used the relationship,  $|\mathbf{k}_{\mathbf{T}}|^2 = k_x^2 + k_y^2$ , appropriate for  $\mathbf{k}_{\mathbf{T}}$  providing generalization of the  $(k_x, k_y)$  coordinates.

Using the result of Eq. 3.4.94, the two-dimensional Fourier transform of Eq. 3.4.93 with respect to the transverse coordinates yields:

$$\left[\frac{\partial}{\partial \xi} - i\frac{2\pi^2}{k_0} |\mathbf{k}_{\mathbf{T}}|^2 + \delta k(\Delta\omega)\right] \hat{A}(\mathbf{k}_{\mathbf{T}}, \xi, \Delta\omega) = \rho(\mathbf{k}_{\mathbf{T}}, \xi, \Delta\omega) \quad (3.4.95)$$

The next step is to define a function,  $\hat{a}(\mathbf{k}_{\mathbf{T}}, \xi, \Delta\omega)$ :

$$\hat{a}(\mathbf{k}_{\mathbf{T}}, \xi, \Delta\omega) = \hat{A}(\mathbf{k}_{\mathbf{T}}, \xi, \Delta\omega) \exp\left[\left(-i\frac{2\pi^2}{k_0} |\mathbf{k}_{\mathbf{T}}|^2 + \delta k(\Delta\omega)\right) \xi\right] \quad (3.4.96)$$

The advantage of defining  $\hat{a}(\mathbf{k}_{\mathbf{T}}, \xi, \Delta\omega)$  is in recognizing that the derivative of  $\hat{a}(\mathbf{k}_{\mathbf{T}}, \xi, \Delta\omega)$  with respect to  $\xi$  yields:

$$\begin{aligned}\frac{\partial}{\partial \xi} \hat{a}(\mathbf{k}_{\mathbf{T}}, \xi, \Delta\omega) &= \frac{\partial}{\partial \xi} \left[ \hat{A}(\mathbf{k}_{\mathbf{T}}, \xi, \Delta\omega) \exp\left[\left(-i\frac{2\pi^2}{k_0} |\mathbf{k}_{\mathbf{T}}|^2 + \delta k(\Delta\omega)\right) \xi\right] \right] \\ &= \exp\left[\left(-i\frac{2\pi^2}{k_0} |\mathbf{k}_{\mathbf{T}}|^2 + \delta k(\Delta\omega)\right) \xi\right] \frac{\partial}{\partial \xi} \hat{A}(\mathbf{k}_{\mathbf{T}}, \xi, \Delta\omega) + \hat{A}(\mathbf{k}_{\mathbf{T}}, \xi, \Delta\omega) \\ &\quad \times \exp\left[\left(-i\frac{2\pi^2}{k_0} |\mathbf{k}_{\mathbf{T}}|^2 + \delta k(\Delta\omega)\right) \xi\right] \frac{\partial}{\partial \xi} \left[\left(-i\frac{2\pi^2}{k_0} |\mathbf{k}_{\mathbf{T}}|^2 + \delta k(\Delta\omega)\right) \xi\right] \\ &= \exp\left[\left(-i\frac{2\pi^2}{k_0} |\mathbf{k}_{\mathbf{T}}|^2 + \delta k(\Delta\omega)\right) \xi\right] \\ &\quad \times \left\{ \left[\frac{\partial}{\partial \xi} - i\frac{2\pi^2}{k_0} |\mathbf{k}_{\mathbf{T}}|^2 + \delta k(\Delta\omega)\right] \hat{A}(\mathbf{k}_{\mathbf{T}}, \xi, \Delta\omega) \right\}\end{aligned}\quad (3.4.97)$$

If we examine the term in curly brackets in the last line of the scheme in Eq. 3.4.97, we see that this quantity is identical to the left hand side of Eq. 3.4.95. Therefore, we can substitute according to Eq. 3.4.95 to relate  $\hat{a}(\mathbf{k}_{\mathbf{T}}, \xi, \Delta\omega)$  to the polarization function,  $\rho(\mathbf{k}_{\mathbf{T}}, \xi, \Delta\omega)$ :

$$\frac{\partial}{\partial \xi} \hat{a}(\mathbf{k}_{\mathbf{T}}, \xi, \Delta\omega) = \exp\left[\left(-i\frac{2\pi^2}{k_0} |\mathbf{k}_{\mathbf{T}}|^2 + \delta k(\Delta\omega)\right) \xi\right] \rho(\mathbf{k}_{\mathbf{T}}, \xi, \Delta\omega) \quad (3.4.98)$$

Integrating both sides of Eq. 3.4.98 from the beginning of the sample,  $\xi'$ , to the end of the sample,  $\xi_{\text{end}}$ ,



yields:

$$\hat{a}(\mathbf{k}_T, \xi_{\text{end}}, \Delta\omega) - \hat{a}(\mathbf{k}_T, \xi', \Delta\omega) = \int_{\xi'}^{\xi_{\text{end}}} \exp \left[ \left( -i \frac{2\pi^2}{k_0} |\mathbf{k}_T|^2 + \delta k(\Delta\omega) \right) \xi \right] \rho(\mathbf{k}_T, \xi, \Delta\omega) d\xi \quad (3.4.99)$$

Recalling we have defined  $\hat{a}(\mathbf{k}_T, \xi, \Delta\omega)$  as proportional to the field envelope  $\hat{A}(\mathbf{k}_T, \xi, \Delta\omega)$  (see Eq. 3.4.96), Eq. 3.4.99 describes the regime in which we are concerned with the changes induced in an existing field by the polarization. The opposite limit is the scenario in which the polarization creates the field, in which case  $\hat{a}(\mathbf{k}_T, \xi', \Delta\omega) = 0$ . This scenario is described:

$$\hat{a}(\mathbf{k}_T, \xi_{\text{end}}, \Delta\omega) = \int_{\xi'}^{\xi_{\text{end}}} \exp \left[ \left( -i \frac{2\pi^2}{k_0} |\mathbf{k}_T|^2 + \delta k(\Delta\omega) \right) \xi \right] \rho(\mathbf{k}_T, \xi, \Delta\omega) d\xi \quad (3.4.100)$$

We will continue forward considering the regime described by Eq. 3.4.100.

However, we will again recall that  $\hat{a}(\mathbf{k}_T, \xi, \Delta\omega)$  is only proportional to the field amplitude envelope,  $\hat{A}(\mathbf{k}_T, \xi, \Delta\omega)$ , which is the quantity with which we are actually concerned. Using Eq. 3.4.96, we can relate the integral over the polarization in Eq. 3.4.100 back to the field envelope at  $\xi = \xi_{\text{end}}$ :

$$\hat{A}(\mathbf{k}_T, \xi_{\text{end}}, \Delta\omega) = \int_{\xi'}^{\xi_{\text{end}}} \exp \left[ \left( i \frac{2\pi^2}{k_0} |\mathbf{k}_T|^2 - \delta k(\Delta\omega) \right) (\xi_{\text{end}} - \xi) \right] \rho(\mathbf{k}_T, \xi, \Delta\omega) d\xi \quad (3.4.101)$$

To obtain the form presented in Eq. 3.4.101, both sides have been divided by the exponential at  $\xi_{\text{end}}$  arising from the definition of  $\hat{a}(\mathbf{k}_T, \xi, \Delta\omega)$  (see Eq. 3.4.96); this term has been incorporated into the integral, yielding the difference between  $\xi_{\text{end}}$  and  $\xi$ . Eq. 3.4.101 can be considered to attribute the final field envelope as the summation of “slices” of  $\rho(\mathbf{k}_T, \xi, \Delta\omega)$  along  $\xi$ , incorporating the phase effects associated with the transverse frequency and material dispersion based upon the distance that “slice” has needed to propagate through the material.

### 3.5 Group Velocity, Group Velocity Mismatch, and Group Velocity Dispersion

In § 3.4.1, we presented the expansion of  $k(\omega)$  as a Taylor series in Eq. 3.4.23. From this series and the resulting expansion of  $k^2(\omega)$  (see Eq. 3.4.24), our retention of terms with  $\Delta\omega^n$ ,  $n \leq 2$  left the first and second derivatives of  $k(\omega)$  with respect to  $\omega$  remaining. While there are circumstances in which the third-order term can become important,[206, 207] it is generally sufficient to terminate the expansion after the second-order term.[103] These remaining terms correspond to the group velocity,  $u_g = 1/k_1$ , and the group velocity dispersion,  $k_2$ . In this section, we will consider the effects of these two quantities upon ultrafast pulse

propagation and present formulae that allow the calculation of these quantities under various circumstances.

### 3.5.1 Effects of Group Velocity and Group Velocity Dispersion

We will begin considering the effects of group velocity and group velocity dispersion through the lens of § 3.4.1. In § 3.4.1, we derived Eq. 3.4.34, which describes the changes in the envelope function of a plane wave as it is influenced by dispersion or absorption by the medium (the term in brackets) or by an induced nonlinear polarization within the medium. If we ignore absorption ( $\alpha(\omega) = 0$ ) and assume no polarizations have been induced ( $\hat{p}^{\text{NL}} = 0$ ), Eq. 3.4.34 reduces to:

$$\frac{\partial}{\partial \xi} \hat{A}(\xi, \Delta\omega) = \left[ -i(k_1 - k_{1r})\Delta\omega - i\frac{1}{2}k_2\Delta\omega^2 \right] \hat{A}(\xi, \Delta\omega) \quad (3.5.1)$$

As Eq. 3.5.1 is a differential equation, it would not be surprising to find an exponential to serve as a valid solution; taking the trial solution to be  $\hat{A}(\xi, \Delta\omega) = \exp(\alpha\xi)$ , it is trivial to show that Eq. 3.5.1 yields a solution of the form:

$$\hat{A}(\xi, \Delta\omega) = \hat{A}(\xi = \xi', \Delta\omega) \exp \left[ \left( -i(k_1 - k_{1r})\Delta\omega - i\frac{1}{2}k_2\Delta\omega^2 \right) \xi \right] \quad (3.5.2)$$

where  $\xi'$  corresponds to some initial position in space.

Considering the form of Eq. 3.5.2, it is straightforward to gain insight into the effects of group velocity. In the absence of group velocity dispersion ( $k_2 = 0$ ), the general solution in Eq. 3.5.2 reduces to:

$$\hat{A}(\xi, \Delta\omega) = \hat{A}(\xi = \xi', \Delta\omega) \exp[-i(k_1 - k_{1r})\Delta\omega\xi] \quad (3.5.3)$$

From the form of Eq. 3.5.3, it is clear that propagation through the medium results in a frequency-dependent accumulation of phase governed by  $(k_1 - k_{1r})$ . However, the effects become more obvious in the time domain. If we consider taking the inverse Fourier transform of the result in Eq. 3.5.3, we can identify the following transform relationship:[112]

$$\mathcal{F}\{f(t \pm t_0)\} = \hat{f}(\omega) \exp(\pm i\omega t_0) \quad (3.5.4)$$

where  $f(t)$  and  $\hat{f}(\omega)$  are defined such that  $\mathcal{F}\{f(t)\} = \hat{f}(\omega)$  and  $t_0$  represents some delay in the time domain. Applying this relationship shows that the phase introduced by the exponential in the frequency domain is

equivalent to the time-domain representation:

$$A(\xi, t) = A(\xi = \xi', t - (k_1 - k_{1r})\xi) \quad (3.5.5)$$

Therefore, the group velocity introduces a distance-dependent delay,  $(k_1 - k_{1r})\xi$ , relative to the pulse envelope at the initial position.

This behavior is exhibited in Fig. 3.2. In this figure, we show the effects of group velocity on the pulse envelope of a 35 fs pulse centered at 400 nm as a function of propagation distance, both on the intensity level - (A) and (D) - and on the real and imaginary components of the amplitude - (B), (C), (E), and (F). The consider how these effects manifest in both the time - (A), (B), and (C) - and frequency - (D), (E), and (F) - domains. (A) illustrates our conclusion from Eq. 3.5.5: we observe a linear change in the delay of the pulse envelope with increasing propagation distance. In Fig. (B) and (C), it is clear that this shift in delay does not influence the phase of the envelope: the envelope retains a purely real value at all distances. The frequency-domain profile, however, exhibits strong phase modulation, as shown in (E) and (F). This phase modulation does not create new frequencies: as shown in (D), the spectrum of the pulse is invariant.

Looking at the scale of the propagation distance in Fig. 3.2, though, it is clear that considering the group velocity referenced only to the laboratory frame is limiting: in these calculations, we observe the pulse envelope begin leaving the range of our time variable over only 50  $\mu\text{m}$ . This is the utility of considering the group velocity mismatch: the value of  $k_1$  for a given field relative to some other reference value. In the scenario of a single pulse, as in Fig. 3.2, it would be far more convenient to consider the pulse itself to be the reference, which would make the pulse appear to exhibit a constant center for all propagation distances. On the other hand, for the copropagation of multiple pulses, we might consider defining one to be the reference pulse, as is illustrated in Fig. 3.3.

In this figure, we consider the copropagation of two 35 fs pulses: one centered at 400 nm and the other at 800 nm. In (A), we display the total intensity of the two pulses: in this case, it is clear that we are observe the pulses beginning to split after approximately 100  $\mu\text{m}$  with essentially complete resolution between the pulses after approximately 200  $\mu\text{m}$ . This is in good agreement with the calculated pulse-splitting length of 107  $\mu\text{m}$  ( $L_w = \tau/|\Delta u^{-1}|$ , where  $\tau$  is the pulse length and  $|\Delta u^{-1}|$  is the group velocity mismatch) for 35 fs pulses at these colors. Once again, however, we see that the group velocity mismatch does not impact the spectral content of the pulses, shown in (B) and (C).

The functional form for the effects of group velocity dispersion is much less straightforward to evaluate, as there is not a tabulated result for the Fourier transformation of the exponential,  $\exp(-jk_2\Delta\omega^2/2)$ . However,

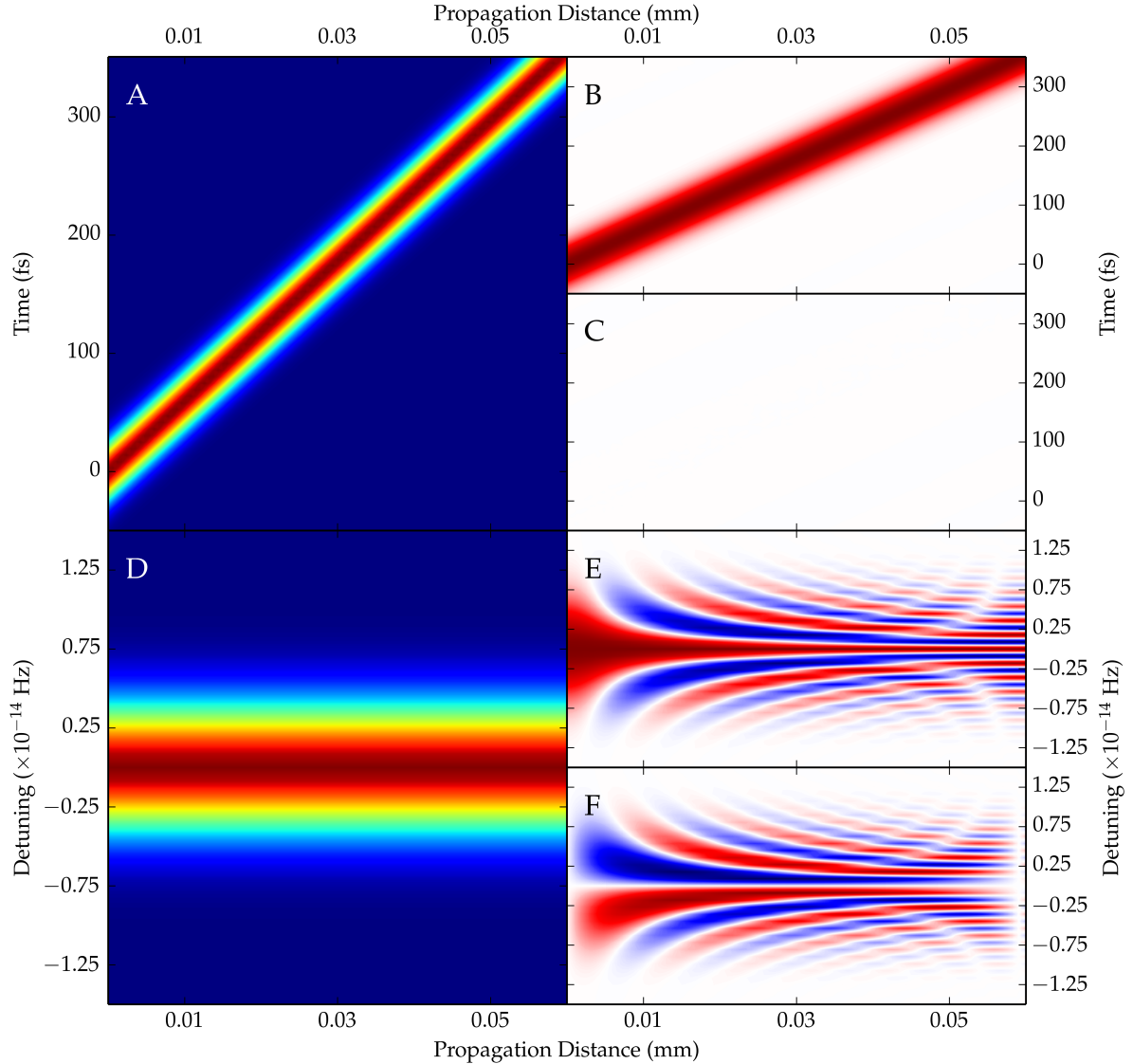


Figure 3.2: Simulations showing the effects of group velocity on the propagation of a 35 fs pulse centered at 400 nm when polarized along the ordinary axis of  $\beta$ -barium borate ( $k_1 = 5942 \text{ fs/mm}$ [208]). (A), (B), and (C) show the effects on the time-domain envelope,  $A(t)$ : (A) shows the intensity of the field,  $|A(t)|^2$ ; (B) shows the amplitude of the real component,  $\Re\{A(t)\}$ ; and (C) shows the amplitude of the imaginary component,  $\Im\{A(t)\}$ . (D), (E), and (F) show the effects on the frequency-domain envelope,  $\hat{A}(\Delta\omega)$ : (D) shows the intensity of the field,  $|\hat{A}(\Delta\omega)|^2$ , (E) shows the amplitude of the real component,  $\Re\{\hat{A}(\Delta\omega)\}$ ; and, (F) shows the amplitude of the imaginary component,  $\Im\{\hat{A}(\Delta\omega)\}$ . In the complex representation of (B), (C), (E), and (F), white corresponds to zero amplitude, while red and blue represent positive and negative amplitudes, respectively.

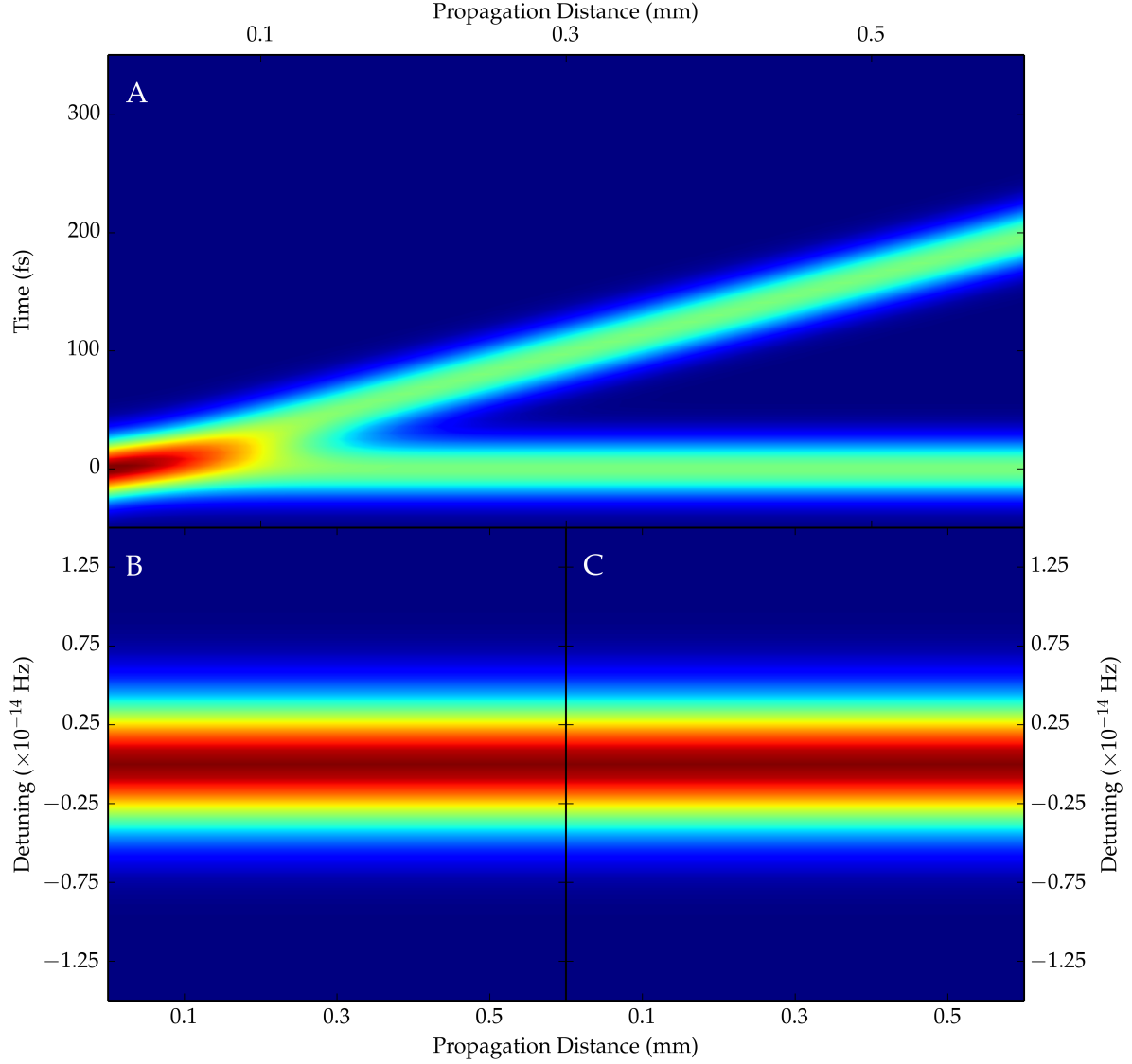


Figure 3.3: Simulation showing the effects of group velocity mismatch on the co-propagation of two 35 fs pulses, each polarized along the ordinary axis of  $\beta$ -barium borate: one centered at 400 nm ( $k_1 = 5942$  fs/mm[208]) and the other centered at 800 nm ( $k_1 = 5615$  fs/mm[208]), corresponding to a group velocity mismatch of 327 fs/mm. The 800 nm pulse is taken as the reference. (A), (B), and (C) all report the intensity of the field: (A) shows  $|A_{400}(t)|^2 + |A_{800}(t)|^2$  in the time domain, where  $A_{400}(t)$  and  $A_{800}(t)$  are the temporal pulse envelopes of the 400 nm and 800 nm pulses, respectively. (B) and (C) show  $|\hat{A}(\Delta\omega)|^2$  for the 400 nm (B) and 800 nm (C) pulses.

it is still trivial to simulate its effects, as shown in Fig. 3.4. Once again considering a 35 fs pulse at 400 nm, we see that the effects of group velocity dispersion are a little more complicated. (E) and (F) illustrate that the group velocity dispersion influences the phase of the envelope in the frequency domain; given the dependence of the effects of group velocity dispersion upon  $\Delta\omega^2$ , it is also not surprising that the effects are symmetric about  $\Delta\omega = 0$ . Unlike group velocity, however, the phase applied in the frequency domain does manifest in the time domain, as seen in (B) and (C). This phase applied to the time domain envelope worsens the time-bandwidth product of the pulse, and we consequently see broadening of the pulse in the time domain in (A). However, this broadening is only a consequence of the phase added to the envelope: the frequency content of the pulse, shown in (D), exhibits no changes as a function of propagation distance.

### 3.5.2 Calculating Group Velocity and Group Velocity Dispersion

In order to calculate the group velocity and group velocity dispersion in an arbitrary medium, we must first recall the Taylor expansion in Eq. 3.4.23. In this expansion, we assigned the coefficients  $k_1$  and  $k_2$  as:

$$k_1 = \left. \frac{\partial k(\omega)}{\partial \omega} \right|_{\omega=\omega_0} \quad (3.5.6a)$$

$$k_2 = \left. \frac{\partial^2 k(\omega)}{\partial \omega^2} \right|_{\omega=\omega_0} \quad (3.5.6b)$$

With the definition we obtained for  $k(\omega)$  (Eq. 3.4.14), it is trivial to find the result of the derivative defining  $k_1$ , and only slightly more difficult to evaluate the derivative for  $k_2$ . One form for these derivatives is:

$$k_1 = \frac{1}{c} \left[ n(\omega_0) + \omega_0 \left. \frac{\partial n(\omega)}{\partial \omega} \right|_{\omega=\omega_0} \right] \quad (3.5.7a)$$

$$k_2 = \frac{1}{c} \left[ 2 \left. \frac{\partial n(\omega)}{\partial \omega} \right|_{\omega=\omega_0} + \omega_0 \left. \frac{\partial^2 n(\omega)}{\partial \omega^2} \right|_{\omega=\omega_0} \right] \quad (3.5.7b)$$

However, we describe Eq. 3.5.7a and 3.5.7b as one form of the derivatives, as it will generally be more convenient to consider the dispersion of materials as  $\partial n(\lambda)/\partial \lambda$ . The reason for this is that the dispersion of many materials is reported either in the form Cauchy's formula[101] or in the manner of the Sellmeier formula;[209] in both models, the index is considered to be a function of wavelength,  $\lambda$ , rather than frequency. However, we can recognize that wavelength and frequency are related: recalling Eq. 3.1.5 and recognizing  $\omega = 2\pi\nu$ ,  $\lambda\omega = 2\pi c$ . Therefore, we can use the chain rule to expand the derivatives in Eq. 3.5.7a and 3.5.7b

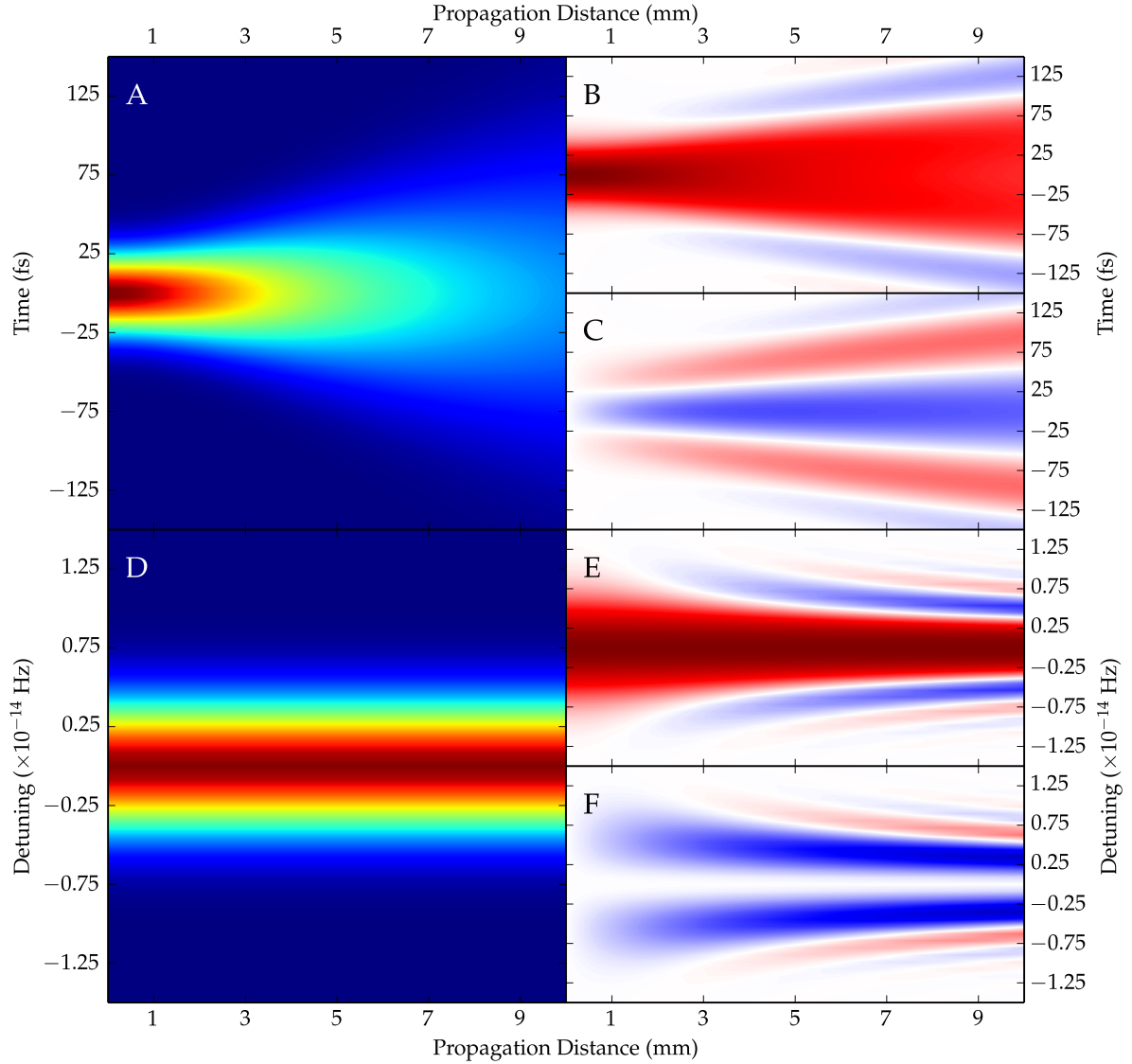


Figure 3.4: Simulations showing the effects of group velocity dispersion on the propagation of a 35 fs pulse centered at 400 nm when polarized along the ordinary axis of  $\beta$ -barium borate ( $k_2 = 215.17 \text{ fs}^2/\text{mm}$ [208]). (A), (B), and (C) show the effects on the time-domain envelope,  $A(t)$ : (A) shows the intensity of the field,  $|A(t)|^2$ ; (B) shows the amplitude of the real component,  $\Re\{A(t)\}$ ; and (C) shows the amplitude of the imaginary component,  $\Im\{A(t)\}$ . (D), (E), and (F) show the effects on the frequency-domain envelope,  $\hat{A}(\Delta\omega)$ : (D) shows the intensity of the field,  $|\hat{A}(\Delta\omega)|^2$ , (E) shows the amplitude of the real component,  $\Re\{\hat{A}(\Delta\omega)\}$ ; and, (F) shows the amplitude of the imaginary component,  $\Im\{\hat{A}(\Delta\omega)\}$ . In the complex representation of (B), (C), (E), and (F), white corresponds to zero amplitude, while red and blue represent positive and negative amplitudes, respectively.

to leave a wavelength-dependence:

$$k_1 = \frac{1}{c} \left[ n(\lambda_0) - \lambda_0 \left. \frac{\partial n(\lambda)}{\partial \lambda} \right|_{\lambda=\lambda_0} \right] \quad (3.5.8a)$$

$$k_2 = \frac{\lambda_0^3}{2\pi c^2} \left. \frac{\partial^2 n(\lambda)}{\partial \lambda^2} \right|_{\lambda=\lambda_0} \quad (3.5.8b)$$

With Eq. 3.5.8a and 3.5.8b, determining the group velocity or group velocity dispersion of a material requires only the derivatives of  $\partial n(\lambda)/\partial \lambda$  or  $\partial^2 n(\lambda)/\partial \lambda^2$ . These quantities can be determined from the appropriate dispersion curves, with several examples worked out in Appendix B.

### 3.6 Numerical Integration of Ordinary Differential Equations

The treatment of pulse propagation in § 3.4 focused upon the consideration of a single field, with that field coupling in some cases (§ 3.4.1 and § 3.4.4) to an induced nonlinear polarization. However, as we introduced in § 3.2, the induction of nonlinear polarizations can often involve the interaction of multiple pulses, thereby coupling the evolution and propagation of the field envelopes. In some circumstances, it is reasonable to approximate that the nonlinear interaction within the medium does not significantly deplete some of the fields, and that it is reasonable to consider the changes induced in a single field; under such circumstances, we are left with a single differential equation. However, there are also many conditions under which this approximation is not appropriate, such as simulation of the parametric processes within optical parametric amplifiers or oscillators.[102, 103, 118, 199–201, 208, 210–217] In such scenarios, it is necessary to consider the propagation of the fields as a system of coupled differential equations.

Fortunately, algorithms exist for numerical integration of systems of both first-order and second-order differential equations. While it is straightforward to consider a method as straightforward as the Euler method, there are fortunately more accurate methods, such as the Runge-Kutta algorithm. In the following sections, a background of such methods is provided with significant influence from the works of Press et al;[113, 218] for more information and information on computational implementation, the reader is directed to these sources.

Most methods of numerical integration are designed to evaluate a set of first order ordinary differential equations, described generically:

$$\frac{d}{dx} y_i(x) = f_i\{x, y_1, \dots, y_N\} \quad (3.6.1)$$

where  $i$  spans the range  $1, 2, \dots, N$  and  $f_i\{\}$  is of a known functional form and describes the coupling between



the set of functions  $\{y_1, y_2, \dots, y_N\}$ . However, while most methods are intended towards evaluation of first-order differential equations, systems of higher-order ordinary differential equations can generally be reduced to an equivalent set of first-order differential equations that can be evaluated by these methods.

Systems of first-order differential equations can be reduced to two generic categories based upon the known information: initial-value and two-point boundary problems. In the former, the entire set of functions is defined at an initial point, and the goal is to project the evolution of the set of functions according to the system of differential equations. Meanwhile, two-point boundary problems involve knowledge of the values of the functions at more than one point. Two-point boundary problems are consequently more complicated to solve, and require more advanced algorithms. Fortunately, the evolution of electric fields - where the fields are known for some initial condition and the goal is to calculate their propagation - is an example of an initial-value problem, for which the methods of evaluation are simpler.

The most simplistic approach to numerical integration of initial-value problems is the Euler method. In this method, the appropriate derivative,  $dy/dx$  is removed from the limit of infinitely small step sizes, yielding the case described by discrete steps,  $\Delta y/\Delta x$ . The change in the function  $y(x)$  can therefore be projected from its value at some position  $x$ ,  $y(x)$ , to its value at some position  $x + \Delta x$ ,  $y(x + \Delta x)$ , according to Eq. 3.6.2:

$$y(x_{n+1}) = y(x_n) + \Delta x f\{x_n, y(x_n)\} \quad (3.6.2)$$

Unfortunately, in this simple form, numerical integration of a system of differential equations can be unreliable. However, the reliability of the method can be improved by increasing the amount of information used to guide the evaluation of the differential equation.

This improvement is the basis of Runge-Kutta methods, in which a series of steps identical to the Euler method are evaluated; the results are then used to reconstruct a Taylor series expansion. These expansions can be evaluated to any arbitrary order, but the most common is the fourth-order Runge-Kutta method, which is outlined below. Runge-Kutta methods are not always the most efficient method for evaluating a system of differential equations, but the advantages associated with these methods are reliability, reasonable accuracy, and simple implementation. Two more efficient approaches to numerical integration - Richardson extrapolation, such as Bulirsch-Stoer methods, and predictor-corrector methods - are available, but both can be more difficult to implement and may not be robust to all problems. In methods based on Richardson extrapolation, the goal is to numerically evaluate the result that would be achieved at the limit of infinitely small step sizes. Predictor-corrector methods, on the other hand, base the value of the next point in the integration on the results of the prior point, using evaluation of the derivative to adjust the results

appropriately.

While these methods for numerical integration are oriented towards solving systems of first-order differential equations, it may be necessary to consider systems of second-order differential equations, generically described:

$$\frac{\partial^2}{\partial \xi^2} A_n(\xi) + C \frac{\partial}{\partial \xi} A_n(\xi) = F_n\{A_m(\xi)\} \quad (3.6.3)$$

where Eq. 3.6.3 describes the evolution of the envelope  $A_n(\xi)$  according to its functional dependence ( $F_n$ ) on a set of envelopes  $\{A_m(\xi)\}$ . However, if a new function,  $B_n(\xi)$ , is defined:

$$B_n(\xi) = \frac{\partial}{\partial \xi} A_n(\xi) \quad (3.6.4)$$

It is possible to define the second order differential equation in Eq. 3.6.3 as a pair of first-order differential equations:

$$\frac{\partial}{\partial \xi} A_n(\xi) = B_n(\xi) \quad (3.6.5a)$$

$$\frac{\partial}{\partial \xi} B_n(\xi) = -CB_n(\xi) + F_n\{A_m(\xi)\} \quad (3.6.5b)$$

While this treatment doubles the number of functions that need to be considered, we have now represented our previous system of second-order differential equations as a system of first-order differential equations. By reducing the system to first-order differential equations, it is now trivial to apply any desired method to evaluate the system.

The Euler method, which we introduced previously, serves as the starting point for the Runge-Kutta method. While using a single evaluation to project the evolution of the function can be unreliable, the Runge-Kutta method introduces additional evaluations to improve the projection of the function. At the lowest order, the Runge-Kutta method relies upon an additional evaluation of the derivative at the midpoint of the steps; for example, the derivative appropriate for the Euler method would be evaluated at  $x$ , then this information would be used to evaluate the derivative at  $x + \Delta x/2$ . These results would then be combined to project  $y(x + \Delta x)$ . As this improvement to the Euler method involves an evaluation at the midpoint, it is also called the midpoint method.

In order to combine the results of the evaluations at  $x$  and  $x + \Delta x/2$ , the model used mimics the Taylor series. However, just as the Taylor series can be extended to higher orders, so too can the Runge-Kutta methods. A common approach is to combine function evaluations to mimic the fourth-order Taylor series,

yielding the fourth-order Runge-Kutta method. This method is accomplished by evaluating the derivative of the function for four different points (Eq. 3.6.6a - 3.6.6d), then the results are used to project the propagation of the function according to Eq. 3.6.6e.

$$k_1 = \Delta x f\{x_n, y(x_n)\} \quad (3.6.6a)$$

$$k_2 = \Delta x f\left\{x_n + \frac{\Delta x}{2}, y(x_n) + \frac{k_1}{2}\right\} \quad (3.6.6b)$$

$$k_3 = \Delta x f\left\{x_n + \frac{\Delta x}{2}, y(x_n) + \frac{k_2}{2}\right\} \quad (3.6.6c)$$

$$k_4 = \Delta x f\{x_n + \Delta x, y(x_n) + k_3\} \quad (3.6.6d)$$

$$y(x_{n+1}) = y(x_n) + \frac{k_1}{6} + \frac{k_2}{3} + \frac{k_3}{3} + \frac{k_4}{6} \quad (3.6.6e)$$

One limitation of Runge-Kutta methods that should be noted is the importance of step-size. Though Runge-Kutta methods are generally reliable, care should be taken when implementing these methods to ensure that appropriate step sizes are used in the calculation. In order to do so, the integration should be repeated with at least two step sizes (such as  $\Delta x$  and  $\Delta x/2$ ) and the results compared to ensure consistent behavior. Alternatively, controlling the algorithm with a program that monitors the results and adapts the step size as appropriate can achieve the same result: guaranteeing that the numerical integration predicts the proper result, rather than a result influenced by the step size. Introducing a routine that facilitates adaptive stepping should allow the integration to be performed slightly more efficiently, as larger steps can be taken when the functional behavior is characterized by slow changes and smaller steps when faster changes occur.[218]

In § 3.4, we derived the wave equation describing the propagation of a field, leaving the result in the frequency domain. The reason is clear in the context of the Runge-Kutta method: while the algorithm can be directly implemented to solve the wave equation in the frequency domain to any desired order of dispersion,[118, 200, 201] the standard Runge-Kutta algorithm accommodates only derivatives with respect to one dimension, preventing direct consideration of dispersive effects in the time domain. However, Bakker et al[199] demonstrated a modified Runge-Kutta algorithm that directly incorporates first-order dispersive effects in the time domain. While we will consider the above discussion regarding the Runge-Kutta algorithm sufficient to discuss solution of the wave equation in the frequency-domain, we will outline the method presented by Bakker et al.

The modified Runge-Kutta algorithm described by Bakker et al treats the differential equation of each

field to be of the form:

$$\frac{\partial}{\partial z} f^n(z, \eta) = C_n \frac{\partial}{\partial \eta} f^n(z, \eta) + F^n \{f^m(z, \eta)\} \quad (3.6.7)$$

where  $\eta$  is a time coordinate in a moving frame of reference traveling at the group velocity of one of the fields;  $C_n$  corresponds to the GVM between the field described by  $f^n(z, \eta)$  and the field to which  $\eta$  is referenced; and  $F^n \{f^m(z, \eta)\}$  describes the functional dependence of the propagation of the field corresponding to  $f^n(z, \eta)$  on the set of fields  $\{f^m(z, \eta)\}$ . In this form, Bakker et al claim that the fourth-order Runge-Kutta method can be reproduced using the scheme described in Eq. 3.6.8:

$$\begin{aligned} K_1^n(z, \eta) &= F^n \{f^m(z, \eta)\} \\ K_2^n \left( z + \frac{\Delta z}{2}, \eta \right) &= F^n \left\{ f^m \left( z, \eta + \frac{C_m \Delta z}{2} \right) + \frac{\Delta z}{2} K_1^m \left( z, \eta + \frac{C_m \Delta z}{2} \right) \right\} \\ K_3^n \left( z + \frac{\Delta z}{2}, \eta \right) &= F^n \left\{ f^m \left( z, \eta + \frac{C_m \Delta z}{2} \right) + \frac{\Delta z}{2} K_2^m \left( z + \frac{\Delta z}{2}, \eta + \frac{C_m \Delta z}{2} \right) \right\} \\ K_4^n(z + \Delta z, \eta) &= F^n \left\{ f^m(z, \eta + C_m \Delta z) + \Delta z K_3^m \left( z + \frac{\Delta z}{2}, \eta + \frac{C_m \Delta z}{2} \right) \right\} \\ f^n(z + \Delta z, \eta) &= f^n(z, \eta + C_n \Delta z) + \frac{h}{6} K_1^n(z, \eta + C_n \Delta z) \\ &\quad + \frac{h}{3} K_2^n \left( z + \frac{\Delta z}{2}, \eta + \frac{C_n \Delta z}{2} \right) + \frac{h}{3} K_3^n \left( z + \frac{\Delta z}{2}, \eta + \frac{C_n \Delta z}{2} \right) \\ &\quad + \frac{h}{6} K_4^n(z + \Delta z, \eta) \end{aligned} \quad (3.6.8)$$

While it is valuable to recognize this algorithm for treating the effects of dispersion on the propagation of electric fields in the time-domain, it is also important to note the limitations that arise in the method. First, examination of the scheme in Eq. 3.6.8 demonstrates that evaluation of  $K_1^n$  is required for six different time scales:<sup>i</sup>  $\eta$ ;  $\eta + (\Delta z/2)(u_{g1}^{-1} - u_{g2}^{-1})$ ;  $\eta + (\Delta z/2)(u_{g1}^{-1} u_{g3}^{-1})$ ;  $\eta + \Delta z(u_{g1}^{-1} - u_{g2}^{-1})$ ;  $\eta + (\Delta z/2)(2u_{g1}^{-1} - u_{g2}^{-1} - u_{g3}^{-1})$ ; and,  $\eta + \Delta z(u_{g1}^{-1} - u_{g3}^{-1})$ . This necessitates nine different evaluations of the derivatives of each field, as opposed to the four required for frequency-domain evaluation. The second main limitation is that evaluating the functions at each of these positions requires the temporal grid to have sufficient resolution that  $\delta \Delta z/2$  can be evaluated for the different pairs of fields. This resolution can require several thousand points to adequately define the temporal grid. The burden of computing so many points limits the effects that can be considered in the calculations, such as the radial distribution of intensity in the TEM<sub>00</sub> beam and the explicit consideration of the amplification bandwidth limit imposed by the crystal, which would require Fourier transformation of all fields during each integration step.

---

<sup>i</sup>It should be noted that the particular points noted here are predicated on following the model of Bakker et al in which the field noted by the subscript 1 is the field to which  $\eta$  is referenced. In their example, this corresponds to either the signal or idler field in parametric amplification.

---

CHAPTER 4

**Simulation of Sum-Frequency Idler Generation**

## 4.1 Background

When doped in sapphire ( $\text{Al}_2\text{O}_3$ ), the electronic structure of  $\text{Ti}^{3+}$  is interpreted as a consequence of a cubic environment with distortions that result in splitting of the  ${}^2\text{T}_2$  and  ${}^2\text{E}$  degeneracies. The otherwise triply degenerate  ${}^2\text{T}_2$  ground state is split by a combination of a trigonal field and spin-orbit coupling, while the two  ${}^2\text{E}$  excited states are split by the Jahn-Teller effect.[219] The resulting system exhibits both absorption and emission characterized by broad absorption and emission bands: both are approximately 150 nm full width at half maximum, with the absorption centered near 500 nm and emission peaking near 750 nm. Under lasing conditions, the gain is slightly red-shifted to 800 nm, and the gain profile exhibits an approximately 200 nm full width at half maximum.[219]

The broad gain bandwidth of Ti:sapphire easily provides the breadth necessary to achieve ultrafast pulses, with sub-10 fs pulses having been reported.[220–224] These ultrashort pulses are described as “soliton-like”, exhibiting propagation very similar to solitons within optical fibers: the pulse is maintained by balancing the accumulation of linear phase and nonlinear phase from self-phase modulation with appropriate negative dispersion compensation.[222, 225–227] It is possible to optimize dispersion such that the pulse is limited by third- or fourth-order dispersion,[226, 228] but optimum performance is often observed with a slightly negative total group delay dispersion.[223, 226, 229] While other methods have been described,[224] the introduction of a prism pair is a common strategy for introducing negative dispersion.[159, 207, 220, 222, 226, 228, 230–232] However, as the integrated group delay dispersion is the quantity that matters,[222] some degree of flexibility exists in the functional dependence of the dispersion upon wavelength. However, pushing the limits of this tolerance is attributed as one source for the copropagation of multiple pulses within the cavity: this complication arises when different frequencies within the bandwidth experience dramatically different dispersion, incorrect applied dispersion,[226, 228] or a sufficiently low dispersion that third-order effects become dominant.[233] Copropagation of multiple pulses may also be observed in systems that sustain mode locking through Kerr lensing when over-pumping results in saturation of the Kerr effect.[229, 234]

Soliton-like propagation within an oscillator is both initiated and maintained through mode locking. Various methods of active and passive mode locking have been reported,[231, 232, 235] though regenerative methods[236] and external feedback[237] have also achieved the desired behavior. Active and passive mode locking introduce periodic modulations to the gains or losses of the cavity, inducing pulsed behavior.[238] Active mode locking yields temporal pulse envelopes that are Gaussian, but the use of active methods will generally limit the achievable pulse duration.[238] In contrast, passive mode locking schemes are capable of yielding shorter pulses[238] and exhibit very stable pulse trains with minimal timing jitter.[239] However,

the pulse envelope resulting from passive mode locking is a hyperbolic secant,[238, 240, 241] which exhibits broader wings than the Gaussian envelope of actively mode locked pulses.[242] Some authors have reasonably described passively mode locked systems within a Gaussian approximation, though.[243] While saturable absorbers can be used for passive mode locking, the broad bandwidth required for ultrashort pulses can make this a poor choice to achieve the shortest pulse durations.[221] The Kerr lens provides a much more convenient method for sustaining an ultrashort mode locked pulse:[220, 243] since it is based upon the intensity-dependent Kerr lens to reduce the losses or increase the gain of a pulse over cw operation during the pulse duration,[224, 238] it achieves the periodic gains and losses necessary for mode locking without the bandwidth limitations inherent to saturable absorbers.[221] Kerr lens mode locking can be achieved through either a hard or soft aperture.[224] Despite the advantages, one drawback to Kerr lens mode locking is initiation of mode locking: while the Kerr lens is an effective method for sustaining pulse propagation, it is less effective for self-starting.[221, 243] However, there are reports of self-starting oscillators based upon Kerr lens mode locking:[222, 231, 244] the key to such systems is that they must be designed such that the pulse experiences sufficiently greater gain than cw lasing.[244] As mentioned previously, systems based on Kerr lensing can also be subject to saturation of the Kerr effect, which allows copropagation of longer pulses or cw modes in addition to the desired ultrashort pulse.[229, 234]

The soliton-like propagation of Ti:sapphire oscillators provides a convenient avenue for the stable, reliable generation of ultrashort pulses. However, the oscillation of these lasers tend to be at high repetition rates, around 100 MHz.[221, 243] Such a high repetition rate results in a very low pulse energy, with values as low as 1-10  $\mu\text{J}$ .[245] Additionally, while the Ti:sapphire gain medium does exhibit a very broad gain bandwidth, allowing some tunability, the bandwidth still restricts oscillation and amplification to wavelengths around 800 nm. Fortunately, both of these limits can be addressed.

To overcome the pulse energy limits, regenerative amplification has been adapted to Ti:sapphire systems. Through a separate pump and cavity, regenerative amplification selects individual pulses from the oscillator's pulse train and amplifies these pulses by several orders of magnitude.[246] Such high pulse energies would result in catastrophic self-focusing in the cavity,[247] so these systems are generally based upon chirped pulse amplification.[245] This strategy is predicated upon introducing linear frequency modulation (chirp) to the pulses from the oscillator in order to generate longer pulses; the degree of stretching can vary based upon application: whereas it may be sufficient to stretch the pulses to a few picoseconds for low gain systems,[248] systems yielding higher energy may require significantly greater chirp.[249, 250] While a variety of strategies for pulse stretching and recompression exist,[248-251] care must be taken to minimize the introduction of effects such as pulse front tilt.[179] Regenerative amplification will often result in some degree of broad-

ening and residual chirp regardless of the stretching/recompression strategy.[245, 252, 253] Gain narrowing contributes part of the limit by introducing spectral narrowing and temporal broadening.[246, 248, 253] Additionally, the number of round trips required for optimum amplification allow the accumulation of both linear and nonlinear phase. Compressors generally cannot reduce any third-order dispersion accumulated.[245, 252] Meanwhile, the nonlinear phase accumulation described by the  $B$ -integral will exhibit a radial dependence due to the radial distribution of the mode's intensity, making compensation challenging.[247, 254]

Increasing the tuning range of Ti:sapphire based solid state systems is generally accomplished through a variety of parametric processes. If we consider the fundamental frequency of these Ti:sapphire systems to be  $\omega_P$ , harmonic generation makes the second,  $2\omega_P$ , and third,  $3\omega_P$ , harmonics accessible. However, the discretization of these available frequencies can be overcome through optical parametric generation (OPG) and optical parametric amplification (OPA).[126] In these nonlinear processes, a strong pump field at  $\omega_P$  interacts with a weak field at the signal frequency,  $\omega_S$ , or the idler frequency,  $\omega_I$ . The convention is for  $\omega_S > \omega_I$ . In a nonlinear medium, the pulse envelopes of these fields can be shown to evolve along the direction of propagation,  $z$ , according to a system of equations:[102, 103, 118, 126, 199–201, 210, 211, 215, 216] when incorporating effects of pulse propagation, the equations of this system adopt the form of Eq. 3.4.34:

$$\frac{\partial}{\partial z} \hat{A}_P = \left[ -i \frac{1}{2} \Delta\omega^2 k_{2,P} - \frac{1}{2} \alpha(\omega_P) \right] \hat{A}_P - i \frac{\omega_P^2}{2c^2 k_{0,P}} \chi_{\text{eff}}^{(2)} \mathcal{F}\{A_S A_I\} \quad (4.1.1a)$$

$$\frac{\partial}{\partial z} \hat{A}_S = \left[ -i \Delta\omega(k_{1,S} - k_{1,P}) - i \frac{1}{2} \Delta\omega^2 k_{2,S} - \frac{1}{2} \alpha(\omega_S) \right] \hat{A}_S - i \frac{\omega_S^2}{2c^2 k_{0,S}} \chi_{\text{eff}}^{(2)} \mathcal{F}\{A_P A_I^*\} \quad (4.1.1b)$$

$$\frac{\partial}{\partial z} \hat{A}_I = \left[ -i \Delta\omega(k_{1,I} - k_{1,P}) - i \frac{1}{2} \Delta\omega^2 k_{2,I} - \frac{1}{2} \alpha(\omega_I) \right] \hat{A}_I - i \frac{\omega_I^2}{2c^2 k_{0,I}} \chi_{\text{eff}}^{(2)} \mathcal{F}\{A_P A_S^*\} \quad (4.1.1c)$$

where we have taken the pump to be the reference pulse and retained the definitions of all quantities as in Ch. 3. We also mask the importance of symmetry in the nonlinear susceptibility through the use of the effective nonlinear susceptibility,  $\chi_{\text{eff}}^{(2)}$  (see § 3.2.2).[106, 119] For compactness, we have omitted the contributions of phase matching and do not explicitly note the frequency, space, or time dependence of the envelope functions.

The system of equations in Eq. 4.1.1a-4.1.1c illustrates a few key characteristics of OPA and OPG. First, in order for the polarizations corresponding to the product of pulse envelopes on the right hand side to feed the corresponding fields, the frequencies must satisfy the equality,  $\omega_P = \omega_S + \omega_I$ . Additionally, it illustrates the need for the initial weak field at either  $\omega_S$  or  $\omega_I$ : if both fields have no initial amplitude, the only changes predicted by the system of equations are the effects of dispersion on the pump. It is adequate to provide



a white light continuum as a broadband source for this initial interaction.[255] However, with a sufficiently strong pump, the vacuum field can be sufficient to initiate OPG; this superfluorescence requires much higher pump energies for stability[170] and may be limited by the presence of on- and off-axis components.[255] It is generally inadvisable to simultaneously seed the process with both signal and idler fields,[150, 170, 256] as group velocity differences can result in the formation of multiple pulses[170] and differences in phase can cause interference.[256] In the absence of pump depletion and dispersion, the system of equations predicts exponential growth of the amplitude of the signal and idler fields.[126] At high conversion rates, though, reconversion of the signal and idler according to Eq. 4.1.1a can become meaningful;[257–259] to avoid these effects, a conversion limit of  $\sim 20\%$  has been cited.[258] Group velocity mismatch also has important consequences on the behavior of different processes.[125, 126, 129, 138, 154, 163, 168, 170, 171, 173, 178, 179, 182, 260–269]

Frequency conversion by parametric generation can be achieved through many different strategies. A weaker pump can be used by enhancing the conversion through oscillation in a cavity. This strategy, optical parametric oscillation, can be achieved with different pump sources, including Ti:sapphire lasers;[126, 127, 164, 181, 211, 270, 271] however, while this achieves the goal of tuning the field, it still results in low pulse energy at high repetition rates,[126] and the oscillator may require some considerations for stability.[266] Alternatively, optical parametric amplification requires higher pump energy in order to achieve appreciable conversion; however, since the optical parametric amplifiers (OPAs) do not require a cavity, they can be more straightforward to operate. When OPAs are taken to the limit of high gain, amplification can be achieved in only a few passes through the nonlinear medium; such systems are described as traveling-wave optical parametric generators (TOPG).[170, 173, 174, 177, 272]

While reported conversion efficiencies of TOPGs suggest reconversion can be relevant, there are many potential advantages. At high gain, the TOPG operates in saturation: at this limit, the performance is relatively insensitive to fluctuations in the seed, improving operating stability.[170, 178, 273] While OPA ideally yields tunable pulses at approximately the duration of the pump pulse,[173, 174, 269] this should be more feasible by minimizing the number of passes: each pass through the nonlinear crystal reduces the amplification bandwidth,[178] limiting the achievable pulse duration.[271] However, there will be a limit as to how few passes are feasible. Decreasing the number of passes requires higher gain to achieve saturation,[178] but this increased gain also increases the chance of superfluorescence, which can negatively impact the performance of the amplifier.[269] Besides the effects of amplification bandwidth, the generated signal and idler are rarely at the transform limit,[133, 266] especially for femtosecond pulses.[176] The chirp accumulated by the signal and idler is attributed to group velocity dispersion and group velocity mismatch between the

pump and signal;[266] it is not uncommon for the signal and idler to exhibit similar bandwidths, but to exhibit opposite chirp.[172]

In contrast to lasers, in which the bandwidth is restricted by the resonances of the gain medium, OPA is usually achieved in a nonresonant medium.[154, 179] However, while resonances are generally not considered relevant in determining the bandwidth of the OPA, absorption associated with resonances can limit tuning ranges; for example, in BBO, the tuning range is limited in the infrared by absorption[131, 166, 170, 173, 177, 208, 263] by phonon modes[208] and in the UV by two-photon absorption.[138] Rather, the bandwidth of the OPA is generally a consequence of the need to satisfy momentum conservation by phase matching.[125, 127, 129, 138, 154] With broadband pulses, it may prove impossible to simultaneously satisfy phase matching for all relevant frequencies,[161, 162] introducing the limits described above upon the number of passes.[178, 271] The importance of the number of passes can be understood by considering the phase matching bandwidth. By expanding the phase mismatch in a Taylor series in a manner similar to Eq. 3.4.23, it is possible to show that the phase matching bandwidth will be restricted by both increasing crystal length[106, 126] and by increasing group velocity mismatch between the signal and the idler fields.[125, 126, 129, 138, 154, 170, 178, 179, 182, 267–269]

The effect of increasing group velocity mismatch proves a limit when trying to generate visible pulses:[168, 260, 265] in a collinear geometry, the group velocity mismatch becomes restrictive,[263, 272] especially with decreasing pulse duration.[168, 173, 260, 265] In addition to the limits imposed by the phase-matching bandwidth, collinear geometries also exhibit a lower range of acceptance angles into the crystal.[125] While the range of acceptance angles does not prove limiting if beam divergence is minimized,[181] noncollinear geometries have been found to exhibit broader ranges of acceptance angles,[125, 128, 167, 181] improving efficiency.[128, 167] Noncollinear geometries can also demonstrate improved phase matching bandwidth through group velocity compensation.[125, 152, 182] When the phase matching angle  $\theta \neq 0^\circ, 90^\circ$ , the birefringence causes a mismatch between the Poynting vector (the direction of energy) and the wave vector,  $\mathbf{k}$ :[106] in a noncollinear geometry, this walk-off angle yields an effective change in group velocity.[274] This walk-off can have consequences,[128, 181, 270, 275] particularly with respect to mode structure[275] and interaction length,[128] though some authors have reported strategies that achieve some compensation.[164, 276] However, walk-off is utilized in a noncollinear geometry as the change in effective group velocity it causes can help match group velocities in the crystal.[125, 129, 152, 154, 171, 178–184] Phase matching in such noncollinear geometries is facilitated by the formation of an angularly dispersed idler;[126, 154, 269] additionally, it has been demonstrated that there exists a noncollinear angle such that the proper phase matching angle of BBO is nearly independent of wavelength.[152, 277] However, with a noncollinear geometry, changing

the desired signal frequency can also change the output direction.[255] Some authors have achieved similar group velocity mismatch compensation with tilted pulse-fronts[255, 260, 261, 274] or chirped pulses.[278] An appropriate amount of negative chirp has also been reported to improve efficiency.[131] Meanwhile, while tilted pulse-fronts can compensate for changes in output direction,[255] it can result in other distortions that also manifest in a noncollinear geometry.[154, 171, 182, 183]

An alternative approach for achieving a broad tuning range is to couple OPA in the near infrared with appropriate upconversion processes,[265, 272] the strategy employed in the TOPAS-C. While absorption of the idler is attributed as the limit for this tuning range,[126, 131, 166, 170, 173, 177, 208, 263] near infrared conversion can be pumped by the fundamental of Ti:sapphire lasers directly. Avoiding harmonic generation makes higher pump energies available; when coupled with the lower group velocities in the near infrared, significantly higher energies can be achieved.[126, 263] Upconversion is accomplished by a variety of processes between the pump, signal, and idler from the initial near infrared OPA:[272] the combination of harmonics and sum-frequency generation with the pump provides tuning throughout the visible and near infrared. It has been reported that upconversion can restrict the available bandwidth;[184] group velocity mismatch can also prove limiting.[171, 262] However, a wide variety of reports have demonstrated that upconversion processes can have pronounced consequences on the spectral or temporal character,[133, 154, 156, 163, 170, 176, 258, 264, 265, 273, 274, 279, 280] particularly under conditions of significant conversion or depletion[154, 170] and pronounced effects of group velocity.[156, 163, 262, 264] The behavior can also change according to the initial delay between the involved fields.[264]

We believe that such behaviors are to account for unusual behavior observed when generating the sum-frequency between the idler and residual pump (SFI), as shown in Fig. 4.1.<sup>i</sup> Exploring the effects of changing the delay between the pump and the signal seed in the OPA showed that the spectral characteristics observed can be changed with this adjustment, and that optimized signal and idler conversion did not necessarily contribute to optimum sum-frequency generation. Despite the unusual spectral character observed in the SFI process, the signal process appeared consistent with normal operation (see Fig. 4.2); it is difficult to reliably characterize the idler, but the literature suggests the bandwidth of the signal and idler processes should be similar.[172] The unexpected behavior of SFI is consistent with the observations of Danielius et al.[272] When using a very similar system, but with longer pulses ( $\sim 100$  fs rather than  $\sim 30$  fs) and slightly longer (4 mm and 0.6 mm rather than 2 mm and 0.3 mm BBO for OPA and SFI, respectively), Danielius et al report very low conversion for the sum-frequency generation process between the idler and the pump

---

<sup>i</sup>Experimental data collected with Eric Hagee, Daniel Kohler, and Blaise Thompson.

except near 600 nm, where they observe  $\sim 50\%$  higher efficiency.[272] They do not observe similar behavior for sum-frequency generation between the pump and signal.[272] Their explanation for these observations is that the group velocity mismatch between signal and pump is nearly independent of signal wavelength and non-zero in the Type II phase matching of the OPA;[126, 172] when sum-frequency generation is performed, however, this reverses the group velocity mismatch, limiting the effects of the accumulated group delay between the pump and the signal on sum-frequency generation. In contrast, as Type II phase matching results in parallel polarizations for the pump and idler, the accumulated group delay between the pump and the idler is not reversed during sum-frequency generation; rather the group delay is increased by continued co-propagation through additional crystals. Unlike signal, though, the pump-idler group velocity mismatch exhibits significant dependence on idler wavelength, crossing zero near 2400 nm (signal wavelength, 1200 nm).[126, 172] The sum frequency of 2400 nm and the fundamental occurs at 600 nm, where Danielius et al observe the unusually high efficiency.[272] This is also near the wavelength at in which we observe the unusual spectral characteristics of Fig. 4.1. Unfortunately, Danielius et al do not provide spectral characterization of their system. The simulations reported here seek to confirm that the features in Fig. 4.1 are expected behavior for our system and improve our understanding of the underlying mechanisms.

## 4.2 Methodology

A wide variety of authors have attempted to explore the simulation of parametric processes.[118, 199–201, 212–217] Bakker et al appear to have described one of the earlier methods towards simulating ultrafast pulse propagation, introducing a modified Runge-Kutta algorithm that allowed solving a system exhibiting both spatial and time dependence (see § 3.6).[199] However, there are multiple drawbacks to their approach. First, the algorithm can only handle behaviors associated with the first derivative with respect to time.[199, 201] Second, while this algorithm can be coded and implemented, the number of evaluations and the density of data points necessary to incorporate the temporal dependence make the calculation prohibitively expensive. Gale et al have documented an alternative approach for evaluating the system of differential equations describing OPA, which permits evaluation to an arbitrary order of dispersion.[200, 201] This is possible through operating in both the time and frequency domains. At each step of the numerical integration, the polarization at each frequency is calculated, the results are Fourier transformed to the frequency domain, and the evolution of the fields projected. Evaluation of the field changes in the frequency domain permits direct application of the Runge-Kutta algorithm:[218] as shown in § 3.4.1, Fourier transformation of the relevant system of equations masks the differential behavior associated with dispersion. While Fourier transformation

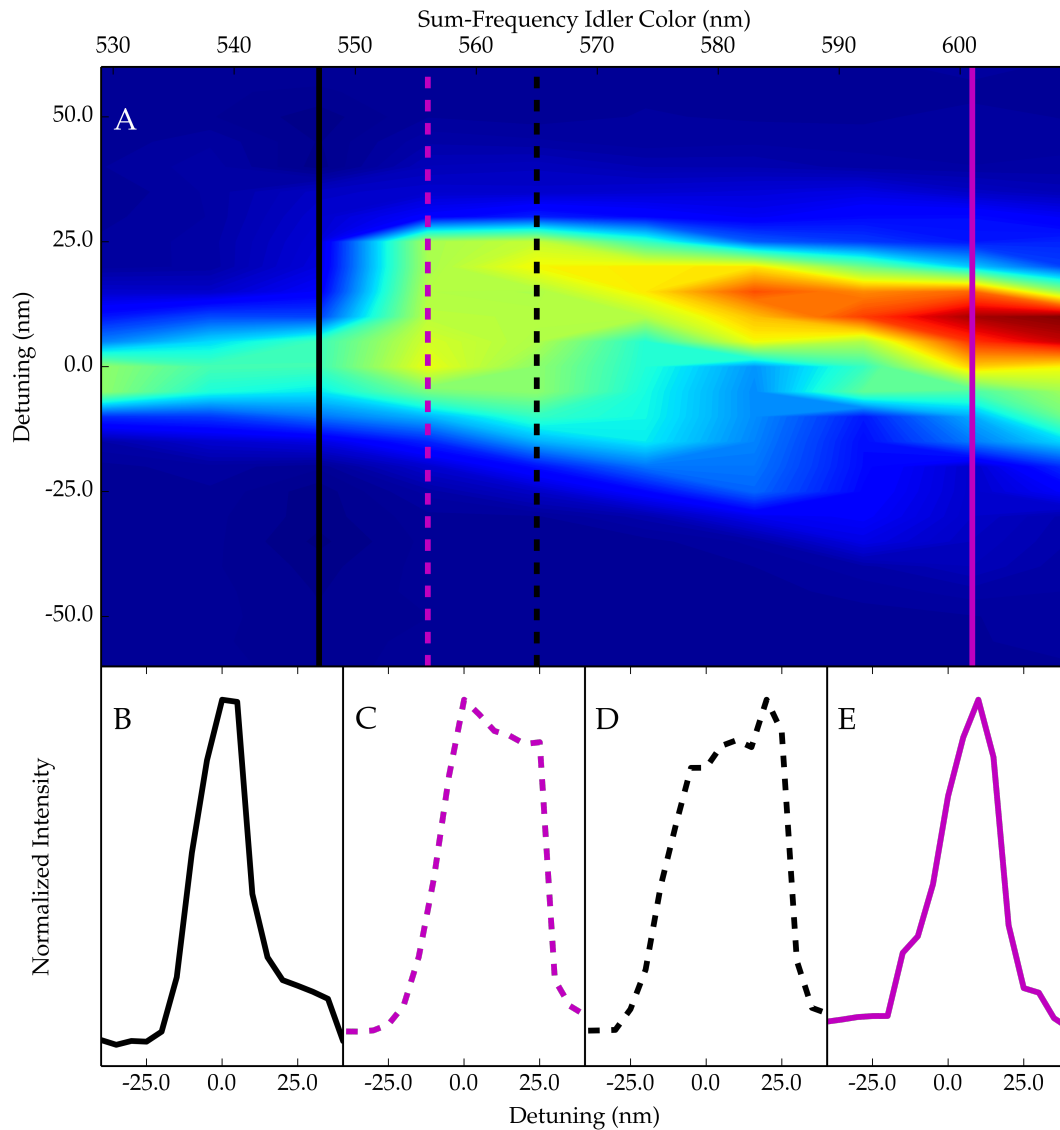


Figure 4.1: Results of sum-frequency idler process tuning. (A) shows the two dimensional representation of the tuning data, plotted as the detuning,  $\lambda_m - \lambda_0$ , versus assigned sum-frequency idler center color,  $\lambda_0$ , where  $\lambda_m$  is the wavelength of the monochromator at each point. (B), (C), (D), and (E) show the differences in spectral profile along different slices in the two-dimensional data set; the color and style of the line in each plot provide color- and style-coding to the slices in (A).

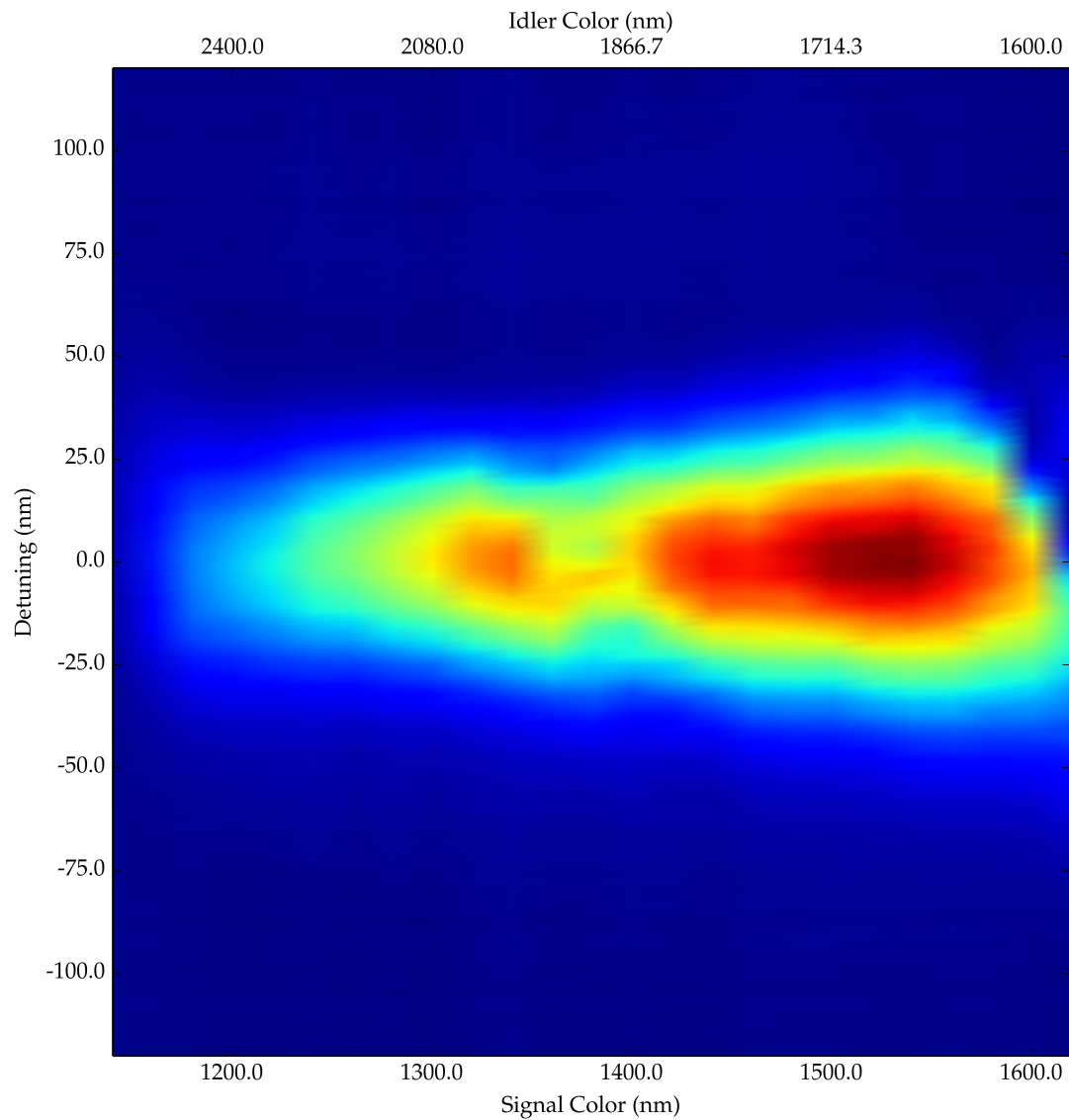


Figure 4.2: Results of signal process tuning prior to sum-frequency idler tuning of Fig. 4.1, plotted as the detuning,  $\lambda_m - \lambda_0$ , versus assigned signal center color,  $\lambda_0$ , where  $\lambda_m$  is the wavelength of the monochromator at each point.

permits consideration of dispersion to an arbitrary order, we follow the assumption in § 3.4.1 and only consider effects up to the second order in time/frequency. While this method follows the example of Gale et al[200, 201] and later authors employing the same approach,[118] we note that the system of equations we employ based upon the derivation in § 3.4.1 deviates slightly from the equations used by these authors.

The Python code developed for these calculations - with some modifications for presentation - is presented in Appendix C. It consists of a series of scripts containing discrete parts of the calculation. It should be noted that during development of the code, the architecture necessary for several features - such as support for isotropic media and adaptive stepping - were incorporated; however, as these features were not needed, they have not been developed. In earlier versions, the code necessary for evaluating second-order differential equations was maintained; however, testing has indicated it is reasonable to operate within the slowly varying amplitude approximation. Maintenance of this portion of the code has since been discontinued, and much of these portions of the code have been omitted in the appendix.

Before discussing the strategy we employed for simulating the SFI process, we will first outline the approximations implicit within the code. First, we adopt the plane wave limit for each field and neglect effects such as walk-off, phase effects of a  $TEM_{00}$  mode, refraction, and imaging. The effects of spatial walk-off are neglected for convenience: due to the short crystal lengths in the crystals in the TOPAS-C, the effects of walk-off that would be expected are comparable to the resolution we adopt in radial sampling. As it is common to put the crystal just after the focus of the pump,[126] the propagation of the  $TEM_{00}$  mode has the potential to be an important effect, especially when considering the imaging of the pump and the idler modes on the sum-frequency crystal. However, as we do not know the exact engineering of the TOPAS-C units, we neglect the phase terms associated with the  $TEM_{00}$  mode and simply consider the amplification and sum-frequency crystals to be in direct sequence. While we neglect the phase terms of the  $TEM_{00}$  mode, we do consider a radial intensity distribution consistent with a Gaussian profile; the handling of this is functionally equivalent to appropriately weighting the contributions of plane waves with different fluence. The beam sizes employed in the calculations are reported with the other characteristic parameters below; these have been adjusted within seemingly reasonable bounds so as yield conversion efficiencies comparable to those observed in the TOPAS-C.

In contrast with Gale et al and Wang and Wang,[118, 200, 201] we do not incorporate the effects of third-order nonlinear polarizations. While some authors suggest that the effects of third-order nonlinear polarizations during OPA may be important,[131, 281] others question the magnitude of their effects.[259] We also point out that some authors indicate TOPGs may be operated at lower gain levels in the later amplification stages;[170] the correspondingly lower pump intensities would be expected to reduce the sig-

nificance of any third-order effects. There also appear to be questions whether perceived third order effects are the result of third-order polarizations or cascaded effects;[118] see for instance that cascaded side bands can exhibit phase matching consistent with “self-diffraction” without clearly requiring a third-order polarization.[282–284] In addition to third-order polarizations, we also do not account for the possibility of parasitic processes,[172, 275, 285, 286] though it is clear that these can have consequences on the behavior of a system, either through spectral distortions or inefficiencies.[275]

While the Selmeier coefficients provided by Kato and Eimerl et al appear to be the standard description for the dispersion of BBO[106, 287, 288] and other authors have indicated they are reasonably accurate in the near infrared,[289] we have opted to employ the modified dispersion formulae reported by Zhang et al.[208] We note here that the group velocity mismatch curves projected by all three sources (Fig. 4.3) exhibit similarities, including a crossing point at which the pump-idler group velocity mismatch  $\Delta u_{pi}^{-1} = 0$  fs/mm; however, as Fig. 4.3 shows, this crossing point is projected at signal wavelengths as short as  $\lambda_s = 1108$  nm ( $\lambda_i = 2878$  nm)[288] or as long as  $\lambda_s = 1330$  nm ( $\lambda_i = 2008$  nm).[287] Consequently, while we hope to observe similar behavior as seen in Fig. 4.1 in our simulations, we do not anticipate an exact match for the wavelength at which the features might occur. Absorption data has been simulated to reproduce available information. Data describing the absorbance of BBO has been published by Eimerl et al,[287] but a clearer set of data are available online.<sup>i</sup> While no crystal length was reported for the online reference, comparison with the reported absorbance by Eimerl et al allowed approximate scaling. We estimated absorption coefficients at various colors and interpolated as necessary. The results of these interpolations yield a higher coefficient at 532 nm ( $\sim 0.05$  cm<sup>-1</sup> instead of 0.01 cm<sup>-1</sup>) and a lower coefficient near 2.55  $\mu$ m ( $\sim 0.3$  cm<sup>-1</sup> instead of 0.5 cm<sup>-1</sup>) than those reported by Dmitriev et al.[106] As the interpolated values are of the correct order of magnitude, our interpolated absorbance should provide a reasonable approximation, especially given the short crystal lengths employed in the TOPAS-C.

Because the generation of the seed in the TOPAS-C is accomplished in a noncollinear geometry, we could not accurately model this. Some testing was done approximating the noncollinear interaction using an effective group velocity as calculated according to the formula reported by Dubietis et al.[274] In this treatment, we used the model for white light described by Reisner and Gutmann.[217] The calculation of the white light field proved computationally expensive, but in these tests we found that the resulting seed was comparable to an envelope with a phase of  $\sim 40^\circ$ . We therefore have assumed the seed envelope to be described by a Gaussian profile of 35 fs duration with an initial phase of  $40^\circ$ . This neglects residual

---

<sup>i</sup>Located at u-oplaz.com.



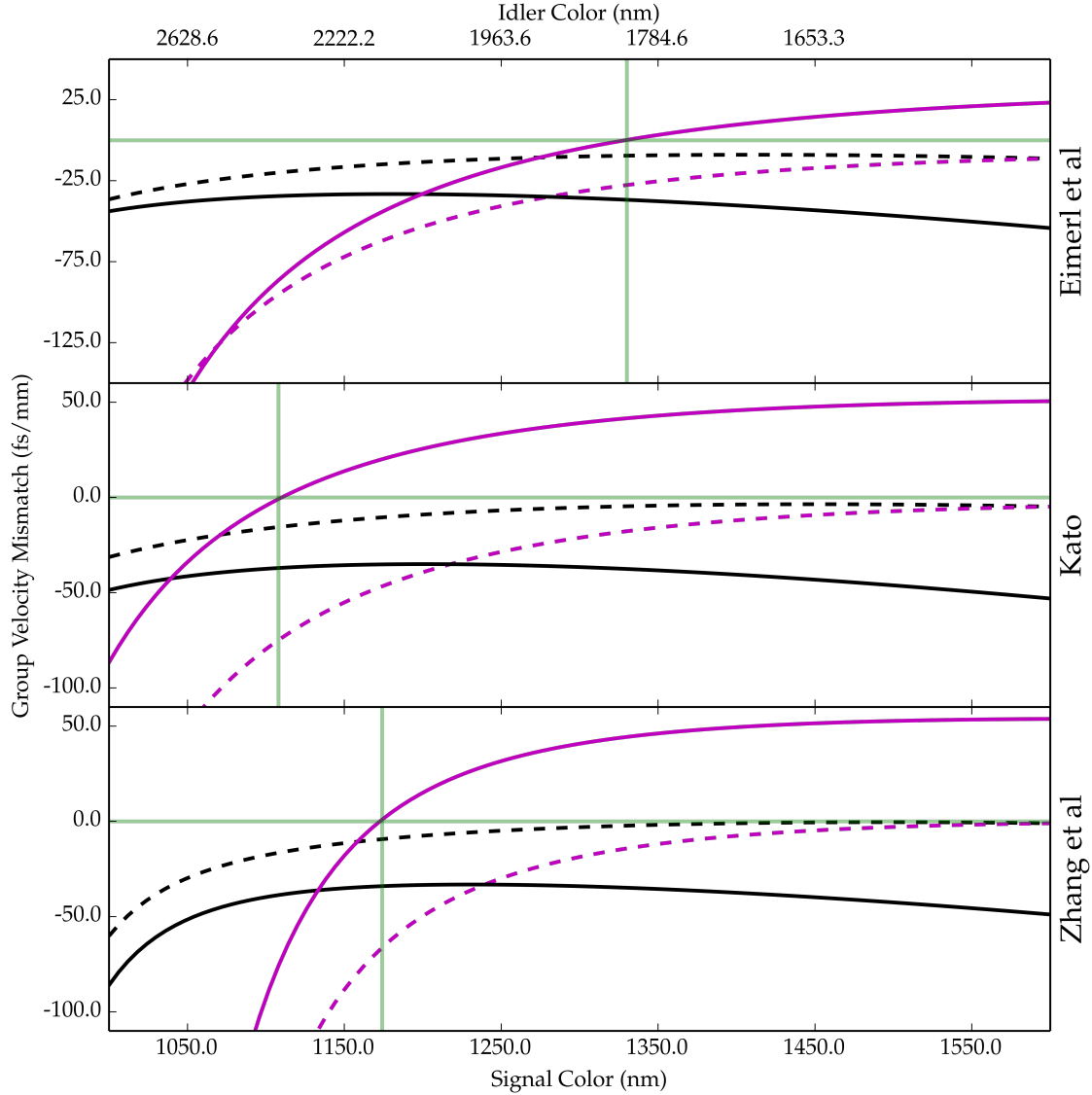


Figure 4.3: A comparison of the group velocity mismatch curves projected by the BBO dispersion curves from different authors, from top to bottom: Eimerl et al;[287] Kato;[288] and Zhang et al.[208] Magenta curves are pump-idler group velocity mismatch,  $\Delta u_{pi}^{-1} = 1/u_p - 1/u_i$ , and black curves are pump-signal group velocity mismatch,  $\Delta u_{ps}^{-1} = 1/u_p - 1/u_s$ . Dashed lines represent the group velocity mismatch curves for Type I ( $e \leftarrow oo$ ) phase matching, and solid lines are the curves resulting for Type II ( $e \leftarrow oe$ ) phase matching. The phase matching angle was determined within the CW limit. The green lines identify the point at which each source for BBO dispersion data predicts  $\Delta u_{pi}^{-1} = 0$  fs/mm.

chirp, which is also neglected in the pump. It has been reported that a slight negative chirp can compensate for dispersion in the crystal and improve performance accordingly;[131] as we optimize recompression in the regenerative amplifier to TOPAS-C performance, this is undoubtedly meaningful, but we have no good estimate for the effects.

In attempting to reproduce the behavior of Fig. 4.1, we have sought to emulate the tuning procedure employed on the femtosecond system as closely as possible. According to our approximation regarding the seed, we have assumed that the first amplification stage has already been well-tuned and that a signal seed at any desired frequency can be generated. We proceed to simulate the acquisition of multidimensional tuning data at a distribution of signal colors: two of these dimensions arise from changing the phase matching angle and the temporal delay between the seed and the pump, while the third represents the distribution of frequencies within the fields. This is directly analogous to the acquisitions of D2 versus C2 versus  $\lambda_m$  collected during tuning of the TOPAS-C. The resulting data set is reduced to two two-dimensional data sets that track the functional dependence upon phase matching angle and delay of the zeroth (integrated energy) and the first (mean, or central color) moments of the signal field. These metrics were selected as the data in Fig. 4.1 question the validity of the parameters of Gaussian fits as reliable characterization metrics. Tuning curves were generated by picking the optimum point in the two dimensional space of phase matching angle and delay; the corresponding tuning curve point was obtained by assigning these values to the central color as determined by the first moment. The first metric for determining the optimum point was to require the first moment to be within  $\sim 1.5$  nm of the central color of the seed; of points satisfying this first metric, the appropriate tuning position was then assigned on the basis of maximum integrated energy.

The resulting tuning curves (phase matching angle versus signal color and delay versus signal color) were interpolated using the `UnivariateSpline` function from `scipy.interpolate`. The knots/smoothing factor were set to 5/10000 for the phase matching angle and 3/1000 for the delay. These interpolation functions were used to tune the sum-frequency process. For a distribution of SFI colors, the appropriate signal color was calculated on the basis of energy conservation; the generation of this signal color and its corresponding idler were calculated using the phase matching angle and delay interpolated by the splined tuning curves. The pump and idler fields from this simulation were retained and assigned as the pump and idler fields for sum-frequency generation. The sum-frequency generation of these fields was simulated for a distribution of phase matching angles. For each SFI color, the optimum phase matching angle was chosen by maximizing the SFI energy, and the first moment of the corresponding sum-frequency spectrum was calculated. The functional dependence of phase matching angle and energy-conserving SFI color upon these first moments provided the SFI tuning curves: for a desired SFI color, the latter curve permitted identification of the

appropriate signal color for simulating pump and idler generation, while the former indicated the proper phase matching angle for sum-frequency generation. Both tuning curves were interpolated using the same `UnivariateSpline` function (5/10000 knots/smoothing factor).

With these tuning curves, both the base OPA and the SFI upconversion processes were simulated with an even distribution of assigned colors. These simulations are reported in the following section. The parameters used for these simulations are reported in Table 4.1. The field parameters for the SFI simulation were inherited from the appropriate OPA simulation.

### 4.3 Results and Discussion

In order to test the performance of the script, we simulated the second-harmonic generation of 2 ps, 800 nm pulses. Within the framework of § 3.4.1, this process would occur according to the system of equations relating the fundamental (F) and second harmonic (SH):

$$\frac{\partial}{\partial z} \hat{A}_F = \left[ -i \frac{1}{2} \Delta \omega^2 k_{2,F} - \frac{1}{2} \alpha(\omega_F) \right] \hat{A}_F - i \frac{\omega_F^2}{2c^2 k_{0,F}} \chi_{\text{eff}}^{(2)} \mathcal{F}\{A_F A_{\text{SH}}^*\} \quad (4.3.1a)$$

$$\frac{\partial}{\partial z} \hat{A}_{\text{SH}} = \left[ -i \Delta \omega (k_{1,\text{SH}} - k_{1,F}) - i \frac{1}{2} \Delta \omega^2 k_{2,\text{SH}} - \frac{1}{2} \alpha(\omega_{\text{SH}}) \right] \hat{A}_{\text{SH}} - i \frac{\omega_{\text{SH}}^2}{2c^2 k_{0,\text{SH}}} \chi_{\text{eff}}^{(2)} \mathcal{F}\{A_F A_F\} \quad (4.3.1b)$$

However, with such long pulse durations, dispersive effects should be negligible for reasonable crystal lengths.<sup>i</sup> Additionally, we can approximate the pulse envelope as the amplitude at the central frequencies,  $A_{0,F}$  and  $A_{0,\text{SH}}$ ; this allows us to also treat the frequencies of each field  $\omega_F$  and  $\omega_{\text{SH}}$  as the central frequencies,  $\omega_{0,F}$  and  $\omega_{0,\text{SH}}$ . Within this limit of narrowband pulses, we should also be able to assume phase matching is reasonably well satisfied across the spectrum. Finally, as we are dealing with visible frequencies, the absorbance of BBO should be minimal. This reduces the system of Eq. 4.3.1a and 4.3.1b to:

$$\frac{\partial}{\partial z} A_{0,F} = -i \frac{\omega_{0,F}^2}{2c^2 k_{0,F}} \chi_{\text{eff}}^{(2)} A_{0,F} A_{0,\text{SH}}^* \quad (4.3.2a)$$

$$\frac{\partial}{\partial z} A_{0,\text{SH}} = -i \frac{\omega_{0,\text{SH}}^2}{2c^2 k_{0,\text{SH}}} \chi_{\text{eff}}^{(2)} A_{0,F} A_{0,F} \quad (4.3.2b)$$

Note that as we are operating within the narrowband limit, we are no longer retaining a distinction between the frequency-domain amplitude ( $\hat{A}$ ) and the time-domain amplitude ( $A$ ). In the regime of low conversion, the effects of Eq. 4.3.2a will be perturbative to the fundamental field, allowing us to adopt the assumption

---

<sup>i</sup>For the dispersion curves given by Zhang et al.[208] the predicted group velocity mismatch for the second harmonic generation of 800 nm is 232 fs/mm. For 2 ps pulses, then, neglecting group velocity mismatch should be a reasonable approximation up to 8-9 mm.

<b>Parametric Amplification Parameters</b>	
Process	Parametric Amplification
Phase Matching	Type II
Crystal Length	0.2 cm
Azimuthal Angle	0°
Steps	250
<b>Sum-Frequency Generation Parameters</b>	
Process	Sum-Frequency Generation
Phase Matching	Type I
Crystal Length	0.03 cm
Azimuthal Angle	90°
Steps	150
<b>Shared Parameters</b>	
Dispersion Curve	Zhang et al[208]
Time Samples	128
Radial Samples	32

(a) Simulation Parameters

<b>Parameter</b>	<b>Pump</b>	<b>Signal</b>	<b>Idler</b>
Wavelength	800 nm	(variable)	(variable)
Center	0 fs	(variable)	0 fs
Gaussian Width	35 fs	35 fs	35 fs
Energy	1500 $\mu$ J	1 $\mu$ J	0 $\mu$ J
$1/e^2$ Size	1.0 cm	0.5 cm	0.5 cm
Envelope Phase	0°	40°	0°

(b) Field Parameters

Table 4.1: Parameters used for sum-frequency idler simulations.

that  $\partial/\partial z A_{0,F} = 0$ . This leaves only Eq. 4.3.2b with a constant source,  $A_{0,F}$ . The solution to this equation is straightforward to evaluate, yielding:

$$A_{0,SH} = -i \frac{\omega_{0,SH}^2}{2c^2 k_{0,SH}} \chi_{\text{eff}}^{(2)} A_{0,F}^2 z \quad (4.3.3)$$

under the assumption that no second harmonic is present at  $z = 0$ . In terms of energy, this result is equivalent to:

$$\frac{E_{SH}}{f(w_0)} = \frac{\omega_{0,SH}^4}{4c^4 k_{0,SH}^2} |\chi_{\text{eff}}^{(2)}|^2 \frac{E_F^2}{f(w_0)^2} z^2 \quad (4.3.4)$$

where  $E_{SH}$  and  $E_F$  are the energy of the second harmonic and fundamental pulses, respectively;  $f(w_0)$  is a beam size dependent distribution of that energy, and other variables are defined as before. From Eq. 4.3.4, we therefore anticipate that in the low conversion limit, the energy of the second harmonic should scale with a quadratic dependence upon length ( $z$ ) and fundamental energy ( $E_F$ ) and a reciprocal dependence upon the energy distribution function.<sup>1</sup> The parameters employed for these calculations are summarized in Table 4.2, and the results are summarized in Fig. 4.4.

In these simulations, we found the behavior of Eq. 4.3.4 to be observed until approximately 10% conversion; at this point, deviations from the expected dependence began to become significant. This is comparable to reported bounds at which reconversion begins to be expected in OPA ( $\sim 20\%$ ).<sup>[258]</sup> As indicated by the result of Eq. 4.3.4, the energy of the second harmonic is expected to exhibit quadratic dependence upon the fundamental energy and the crystal length, in very good agreement with the results in (A) and (C) of Fig. 4.4, where we observe high correlation with models that scale according to  $E_F^{1.9717}$  and  $L^{1.9183}$ . Meanwhile, the energy distribution we employ in the calculations is  $[(\pi/2)w_0^2]^{-1} \exp[-2(\tau/w_0)^2]$ , where  $w_0$  is half the provided  $1/e^2$  beam size. Within this model, we should expect the functional dependence upon beam size to scale as the non-exponential term,  $[(\pi/2)w_0^2]^{-1}$ . In (D), we see that the low conversion regime of second harmonic generation exhibits a very strong match to this model, scaling as  $w_0^{-1.9682}$ . The one limitation that is apparent in the script comes in (B): ideally, we should observe energy conservation in the process. It is clear that at low energies this is not the case. We attribute this limitation at small second-harmonic energies to the limited resolution of our sampling grid (32 spatial points, 128 temporal points). It is clear that the script converges to the correct behavior with respect to energy conservation at higher energies; from this, we take the sensitivity of the script to be at the level of  $10^{-2}$ - $10^{-1}$   $\mu\text{J}$ . As we will be simulating TOPG, we

---

<sup>1</sup>We note, too, that Eq. 4.3.4 exhibits a dependence upon central frequency, and that we have previously noted the omission of a phase matching dependence. Neither of these prove straightforward to incorporate cleanly, however. As the frequency influences  $\chi_{\text{eff}}^{(2)}$  through the phase matching angle  $\theta$  and  $k_0$  through both  $\omega_0$  and the phase velocity, the dependence upon  $\omega_0$  ends up more complicated than the quadratic dependence that first appears to be evident. Meanwhile, exploring the influence of  $\Delta k$  is computationally challenging as the phase modulation changes the characteristic step size between runs.

Dispersion Curve	Zhang et al.[208]
Process	Second-Harmonic Generation
Phase Matching	Type I
Crystal Length	0.5 cm
Azimuthal Angle	90°
Step Size	10 $\mu\text{m}$
Time Samples	128
Radial Samples	32

(a) Simulation Parameters

<b>Parameter</b>	<b>Fundamental</b>	<b>Second Harmonic</b>
Wavelength	800 nm	400 nm
Center	0 fs	0 fs
Gaussian Width	2 ps	2 ps
Energy	5 $\mu\text{J}$	0 $\mu\text{J}$
$1/e^2$ Size	1.0 cm	0.5 cm
Envelope Phase	0°	0°

(b) Field Parameters

Table 4.2: Parameters used for second-harmonic test simulations.

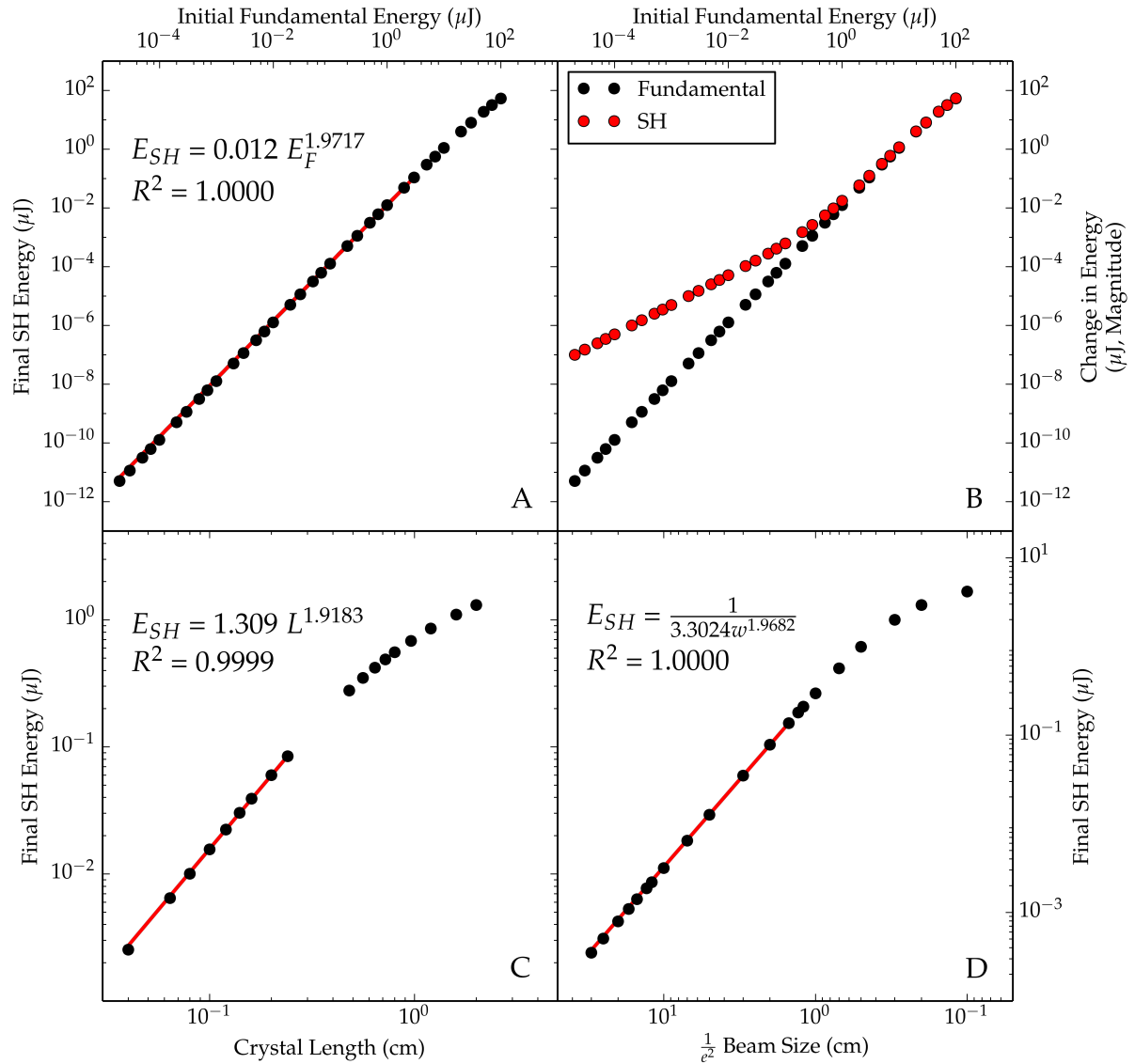


Figure 4.4: Results of simulations of second-harmonic generation as a function of fundamental energy (A), crystal length (C), and beam size (D). Simulations performed according to the parameters in Table 4.2. (B) shows the change in energy predicted for the fundamental and second harmonic at each initial fundamental energy tested in (A).

should generally be operating safely beyond this regime.

Having demonstrated that the behavior of the script is consistent with expectations and recognizing the sensitivity limits, we will present the results of the simulations of the sum-frequency idler process; after presenting the results, we will attempt to explain them in the context of published treatments of OPA and sum-frequency generation.

As noted in our outline of the methodology, the first step in these simulations was to emulate the tuning procedure employed on the femtosecond system. With the assumption that the preamplification stage has already been “well-tuned” and that nearly Gaussian seed profiles can be generated at any desired signal color, we explored the space corresponding to the pump-seed delay and the amplification crystal angle for a distribution of signal colors. As the resulting data forms a four-dimensional data set (amplitude/intensity versus frequency versus crystal angle versus delay), it is not convenient to analyze in its original state. However, in Fig. 4.5 and 4.6, we have reduced this four-dimensional data set to two three-dimensional data sets, characterizing the amplitude/intensity versus frequency dimensions according to their zeroth and first moments.

For seed colors with wavelengths longer than 1180 nm, we observe behavior in these results consistent with expectations. When examining the first moment (central color) as a function of angle versus delay in Fig. 4.5, we observe a dependence upon angle only. In the model example of these simulations, this is completely reasonable, as neither the seed nor pump have any time dependence; if we introduced chirp into the seed, which is likely more consistent with the character of the seed in the TOPAS-C, we would expect to observe some curvature or tilt to the contours appropriate to the functional form of the frequency modulation. The relationship between color and crystal angle is made clear by examining the phase matching angles predicted for BBO (as calculated from the dispersion curves described by Zhang et al[208]) within the cw approximation in Fig. 4.7: in the phase matching curve predicted for Type II phase matching, there is a monotonic trend of increasing phase matching angle with increasing signal color for all wavelengths longer than 1150 nm. This matches the behavior observed in Fig. 4.5, where a blue (red) shift is observed for decreasing (increasing) crystal angle. Meanwhile, at first glance, the results of the zeroth moment (integrated energy) in Fig. 4.6 for wavelengths longer than 1180 nm seem unusual. While it is not clear from Fig. 4.6 (the tuning curves shown in Fig. 4.8 illustrate this more clearly), there is a clear trend that the optimum delay is slightly negative; it seems reasonable that a slight delay would be optimum in order to compensate for the group velocity mismatch between the pump and the seed. However, the unusual trend is that optimum amplification appears to occur at smaller crystal angles than the angle assigned as the optimum tuning point. However, recall from § 3.2.2 that, in Type II phase matching,  $d_{\text{eff}}$  scales with respect



to  $d_{22}$  according to  $d_{22} \cos^2(\theta) \cos(3\phi)$ . Consequently, we would anticipate  $d_{\text{eff}}$  to actually increase as we decrease the phase matching angle; this would be expected to increase the gain at these smaller angles. We attribute the optimum amplification at smaller phase matching angles to this effect.

In contrast to wavelengths longer than 1180 nm, the results for 1140-1180 nm appear less straightforward; each of these wavelengths exhibits less straightforward behavior as a function of crystal angle and delay, both in terms of the trends observed and in the rate of these changes. However, recalling Fig. 4.3, we note that this region is where the dispersion curves of Zhang et al predict the pump-idler group velocity to reach zero.[208] As a consequence, this is where we anticipate deviations from ideal behavior to begin manifesting; under the high gain of the TOPG, reconversion between the pump and the signal and idler is expected, likely exacerbating any deviations already occurring.

The tuning curves projected by these optimum points are shown in Fig. 4.8 (A). As these tuning curves show, the optimum delay appears quite dynamic at lower wavelengths, likely due to the pump-idler group velocity mismatch crossing zero; otherwise, the behavior of the delay tuning curve appears to mostly be limited by the resolution of our sampling in the simulations. The combination of these two does appear to limit the accuracy of the tuning curve in predicting the optimum delay: this is apparent in Fig. 4.5 and 4.6, where the tuning point assigned by the tuning curve is predominantly shifted from the optimum point horizontally - along the delay axis. In contrast to delay, the tuning curve as a function of crystal angle is much more monotonic. At wavelengths longer than 1250 nm, the curve exhibits a trend very similar to the theoretical curves (Fig. 4.7) predicted using the dispersion curves of Zhang et al.[208] At shorter wavelengths, deviation from the theoretical curve is observed; in contrast to the behavior of delay, though, this deviation is relatively smooth and can be interpolated quite well.

The signal tuning curves permitted simulated tuning of the sum-frequency idler; the results of these simulations are much less insightful as they are interpreted solely on the basis of maximizing the zeroth moment (integrated energy). The resulting tuning curves from these simulations are shown in Fig. 4.8 (B). In the same manner as (A), there are two axes of relevance when trying to simulate a desired sum-frequency idler color: a phase matching angle and a color corresponding to the energy conservation condition of an appropriate signal point. The latter of these curves is quite monotonic and can be well described by an interpolated curve. On the other hand, the results for the phase matching angle are reasonably well interpolated as the sum-frequency idler wavelength increases until  $\sim 605$  nm, where a deviation from monotonic behavior is observed. This deviation occurs at frequencies corresponding to signal wavelengths of 1180 nm; from the group velocity mismatch curves in Fig. 4.3, it seems reasonable to attribute this lack of monotonicity to the pump-idler group velocity mismatch crossing from positive to negative values.

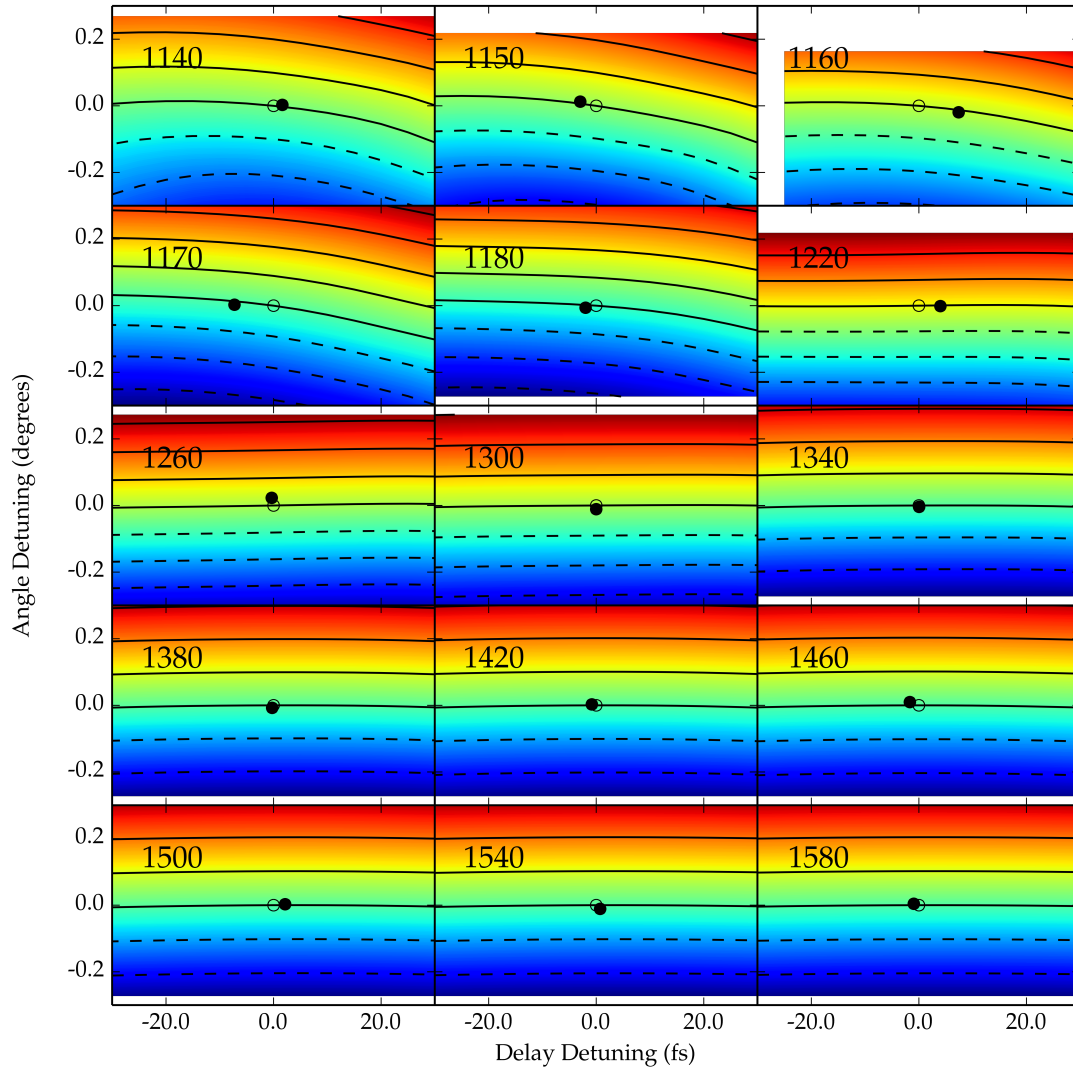


Figure 4.5: Results of simulations of signal tuning, presenting detuning of the first moment as a function of angle detuning and delay detuning. Angle (delay) detuning reflects the detuning of the phase matching angle (initial pump-signal delay) relative to the angle (delay) position assigned as optimum. Detuning of the first moment is measured relative to the first moment of the optimum point; contours reflect 5 nm increments to the blue (dashed) or the red (solid). The unfilled marker at (0,0) corresponds to the assigned optimum point; the filled marker indicates the delay and angle assigned by interpolation of the tuning curve. The label identifies the center wavelength of the seed used for the simulations.

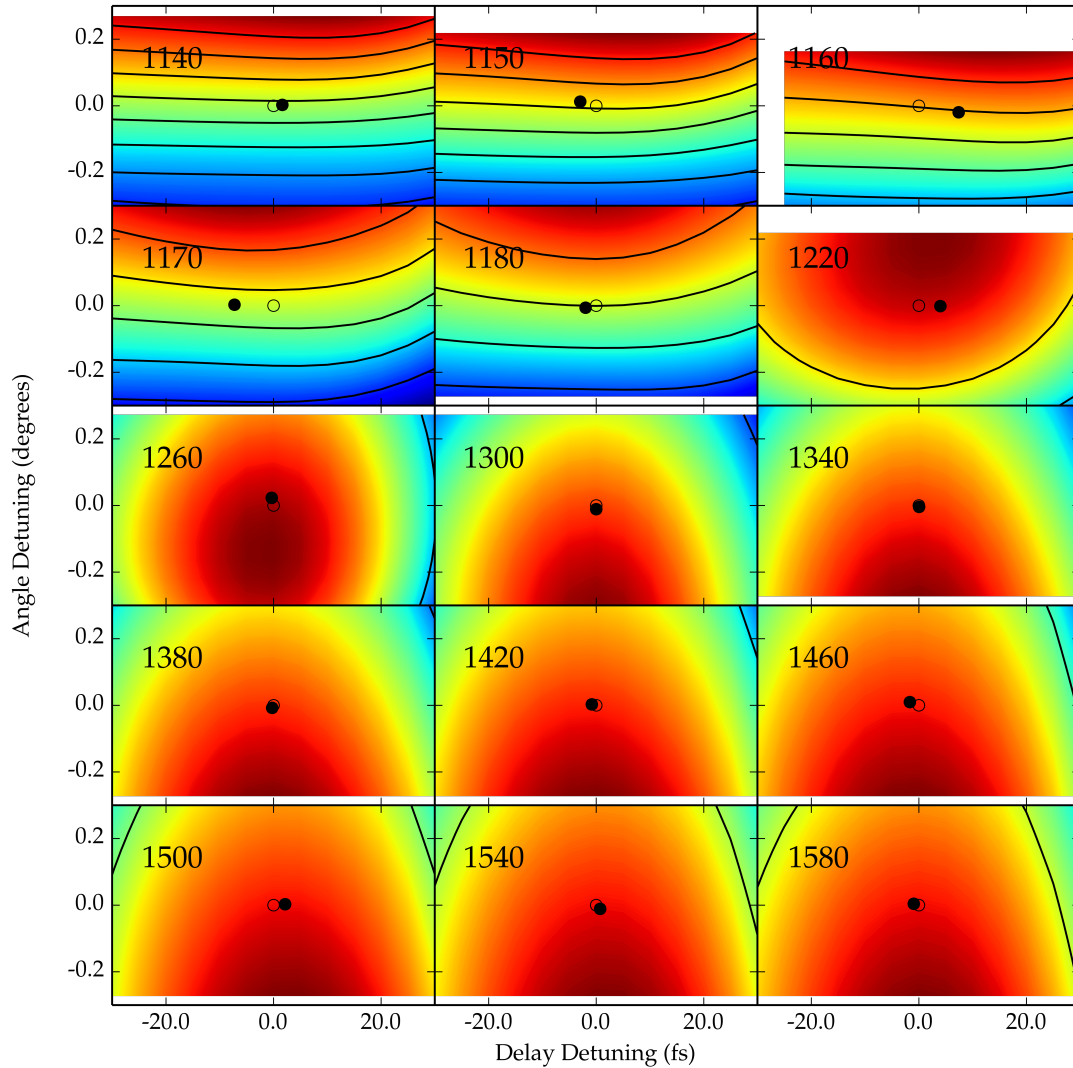


Figure 4.6: Results of simulations of signal tuning, presenting the zeroth moment (integrated signal pulse energy) as a function of angle detuning and delay detuning. Angle (delay) detuning reflects the detuning of the phase matching angle (initial pump-signal delay) relative to the value assigned as optimum. The contours represent steps corresponding to 10% of the maximum energy observed in the range of simulations for that seed wavelength. The unfilled marker at (0,0) corresponds to the assigned optimum point; the filled marker indicates the delay and angle assigned by interpolation of the tuning curve. The label identifies the center wavelength of the seed used for the simulations.

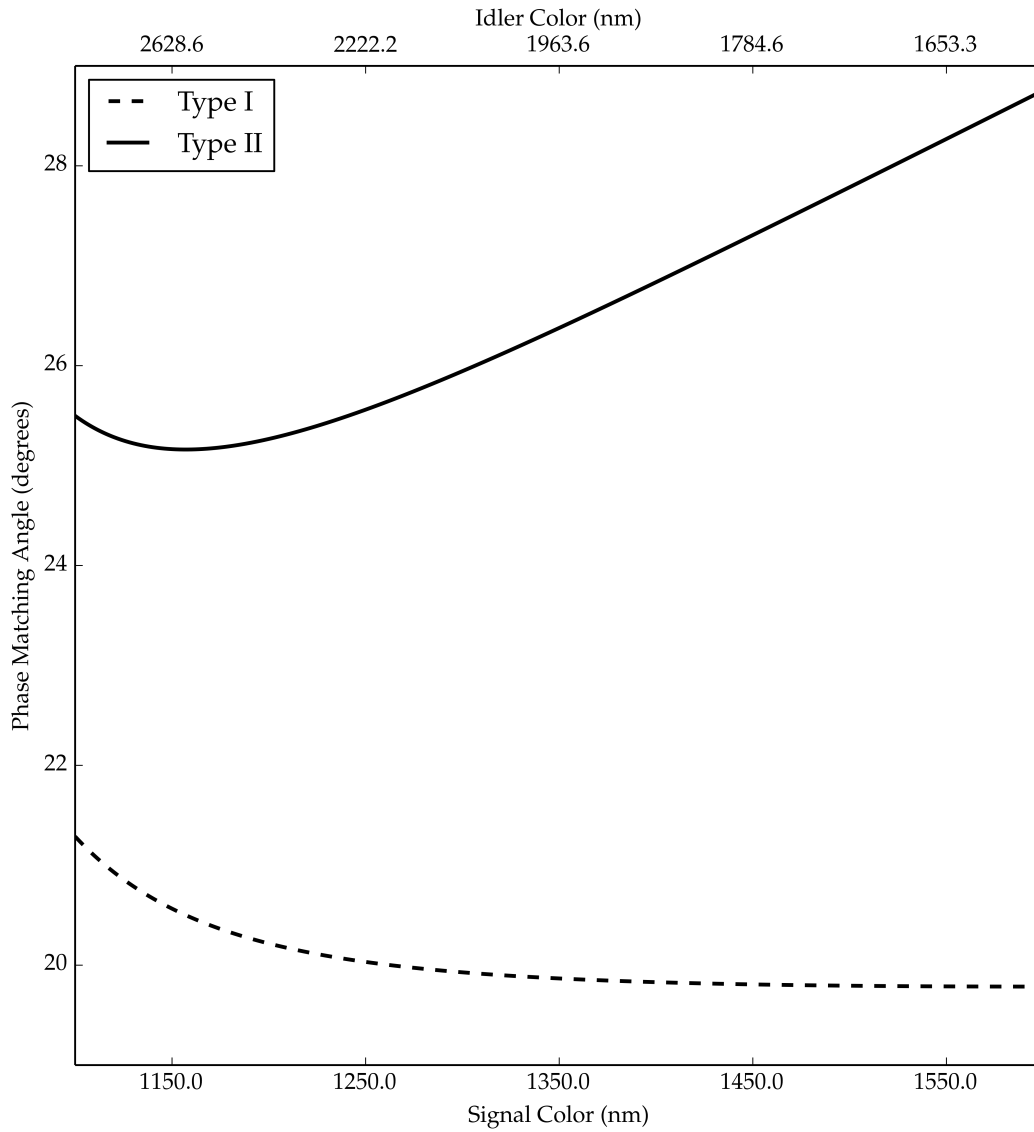


Figure 4.7: Theoretical tuning curves predicted for Type I and Type II phase matching in a BBO OPA according to the dispersion curves reported by Zhang et al[208] within the cw approximation.

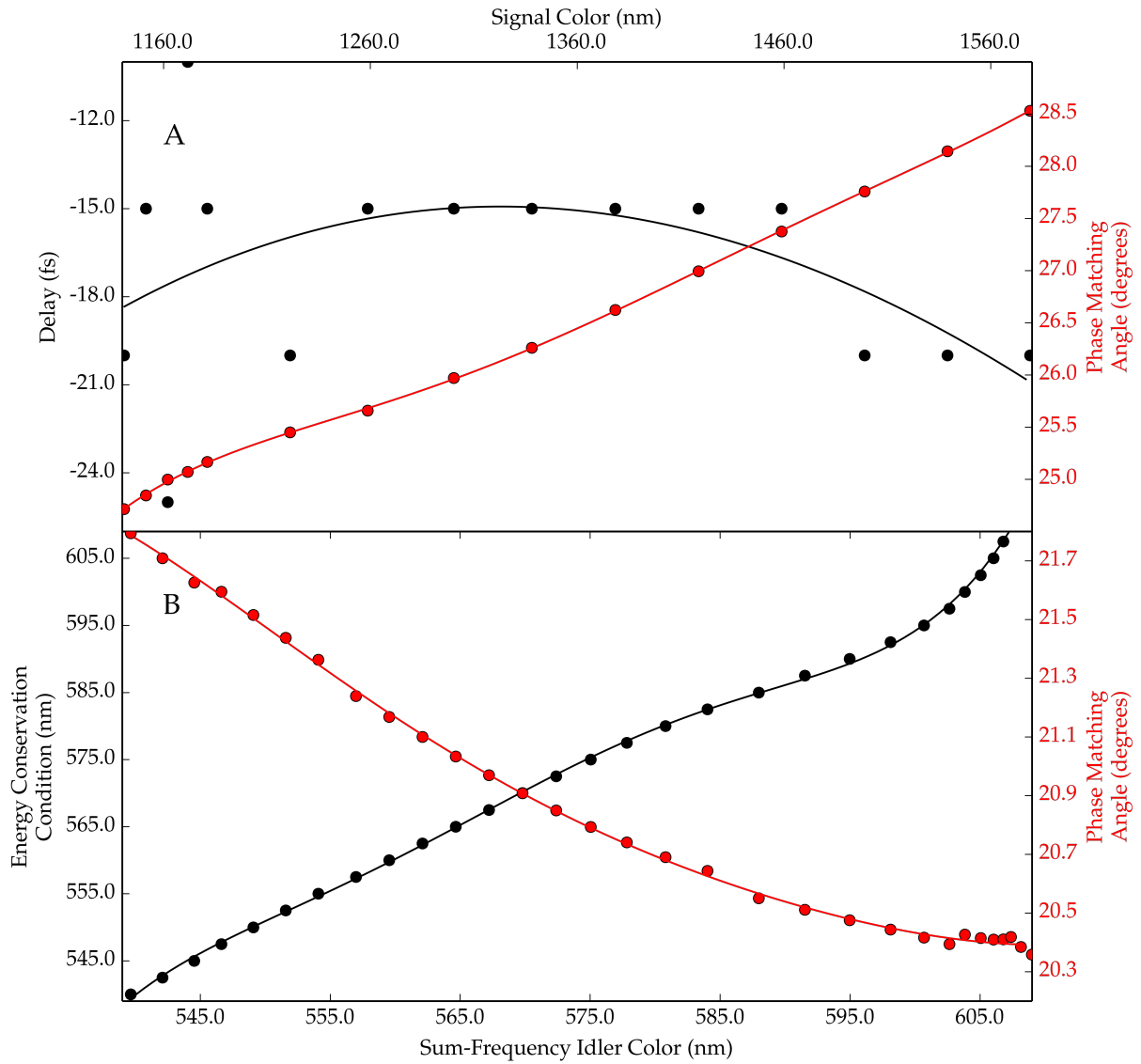


Figure 4.8: The tuning curves for the simulated optical parametric amplification (A) and sum-frequency idler (B) processes.

The results of simulating signal and idler amplification are shown in Fig. 4.9. (A) shows the spectrum predicted for the signal process; the results is reasonably symmetric and is consistent with some of the cleaner data sets collected of a well-tuned signal process. The idler, meanwhile, is also quite symmetric at shorter wavelengths. As the idler wavelength increases, though, the spectrum clearly becomes broader. However, due to the scaling of frequency and wavelength, it is difficult from visual examination to directly attribute the breadth to spectral broadening or to the scaling of a constant bandwidth at longer wavelengths. We will leave a more detailed analysis for later in this discussion of the simulation results. Unfortunately, we are not aware of a good data set exhibiting experimental analysis of the idler process: past efforts to do so have proven challenging due to a variety of software and hardware limitations.

The final set of results is the simulated sum-frequency idler spectrum. However, before discussing the results in detail, two details bear mentioning. First, we recall our conclusion from Fig. 4.3 that all models of BBO dispersion predict a different wavelength where pump-idler group velocity mismatch crosses from positive to negative; consequently, we will avoid making direct comparison of the wavelengths at which features are observed. We will instead focus on the qualitative observations and the relative ordering of these features. Second, we will note that we have assigned wavelengths according to the first moment, whereas COLORS frequently employs Gaussian fits for the assignment of center; this will cause different definitions of zero detuning for slices in the simulated data relative to slices in the experimental data.

Qualitatively, the two-dimensional data, given in (A) in both Fig. 4.1 and 4.10, exhibit many similarities. At short sum-frequency idler wavelengths, both appear to exhibit relatively symmetric line shapes, with a broadened feature extending to longer wavelengths (positive detunings) beginning to occur at longer wavelengths. After this broadening, the spectrum narrows again, and also reaches its most intense spectral features as the tuning curve reaches the longest wavelengths.

The progression of spectral distortion is shown more clearly by the slices in (B)-(E) of Fig. 4.1 and (B)-(G) in Fig. 4.10. Initially, the spectrum is relatively symmetric (Fig. 4.10, B), until a shoulder begins to develop at longer wavelengths (Fig. 4.1, B and Fig. 4.10, C). This shoulder grows in amplitude until it nearly matches the higher energy peak (Fig. 4.1, C and Fig. 4.10, D). As the sum-frequency idler color is tuned further to the red, though, what had been the higher wavelength shoulder becomes the main peak of the feature (Fig. 4.1, D and Fig. 4.10, E), and the shorter wavelength feature becomes a gradually weakening shoulder (Fig. 4.10, F). After this shoulder becomes sufficiently weak, all that remains is a skewed spectrum (Fig. 4.1, E and Fig. 4.10, G).

Before getting into the analysis, we will briefly discuss the metrics we will use throughout the following discussion. These metrics are based upon quantities analogous to the moments about the origin of a prob-

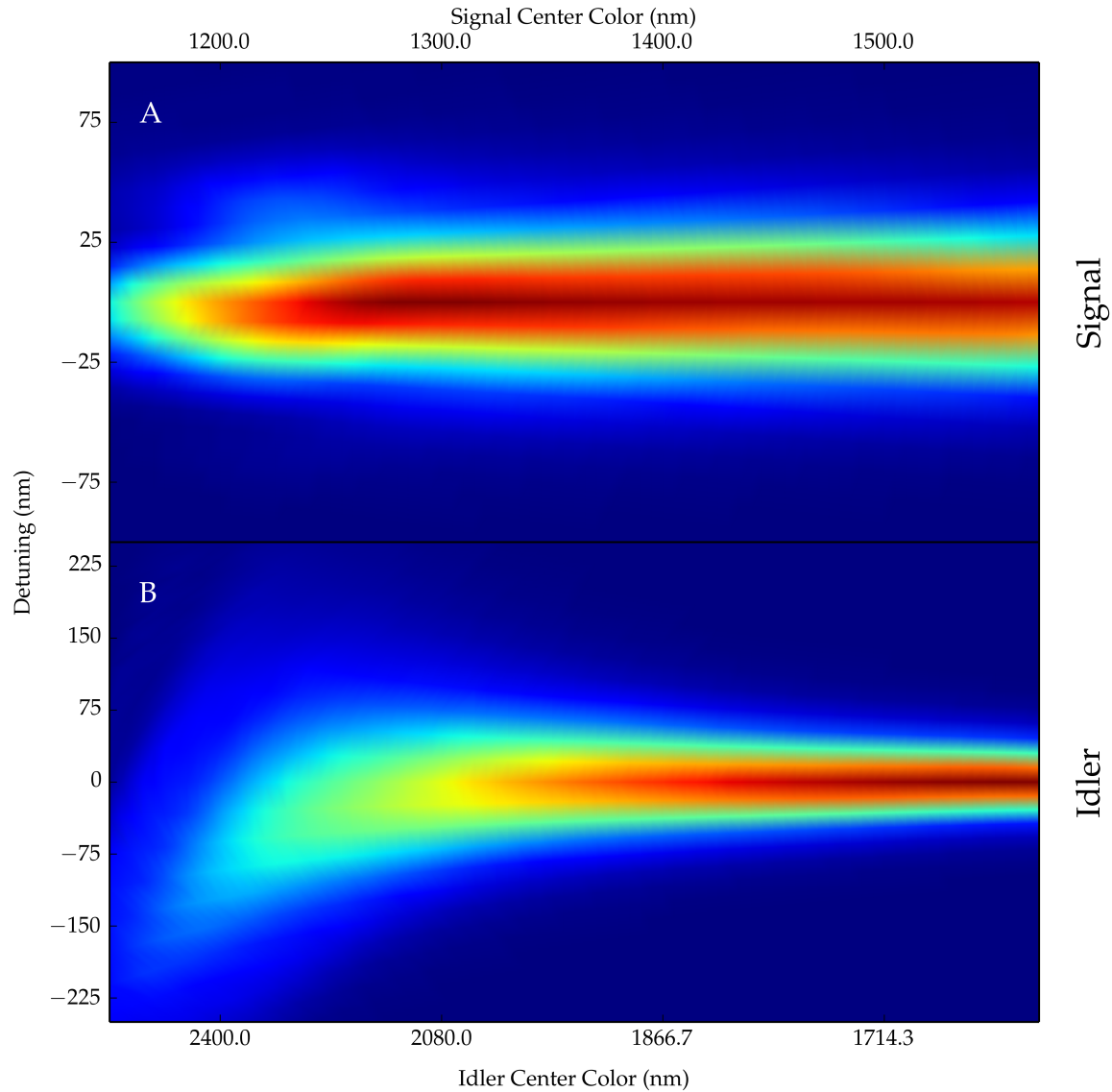


Figure 4.9: The results of simulations of optical parametric amplification of signal (A) and idler (B) processes under traveling-wave operation. Both provide the spectral content at each central frequency of the signal, presented as intensity versus detuning ( $\lambda_m - \lambda_0$ ) versus central wavelength,  $\lambda_0$ , of signal (based upon chosen wavelength) or idler (as calculated by energy conservation). The spectrum in (A) is provided in comparison to the signal tuning results in Fig. 4.2.

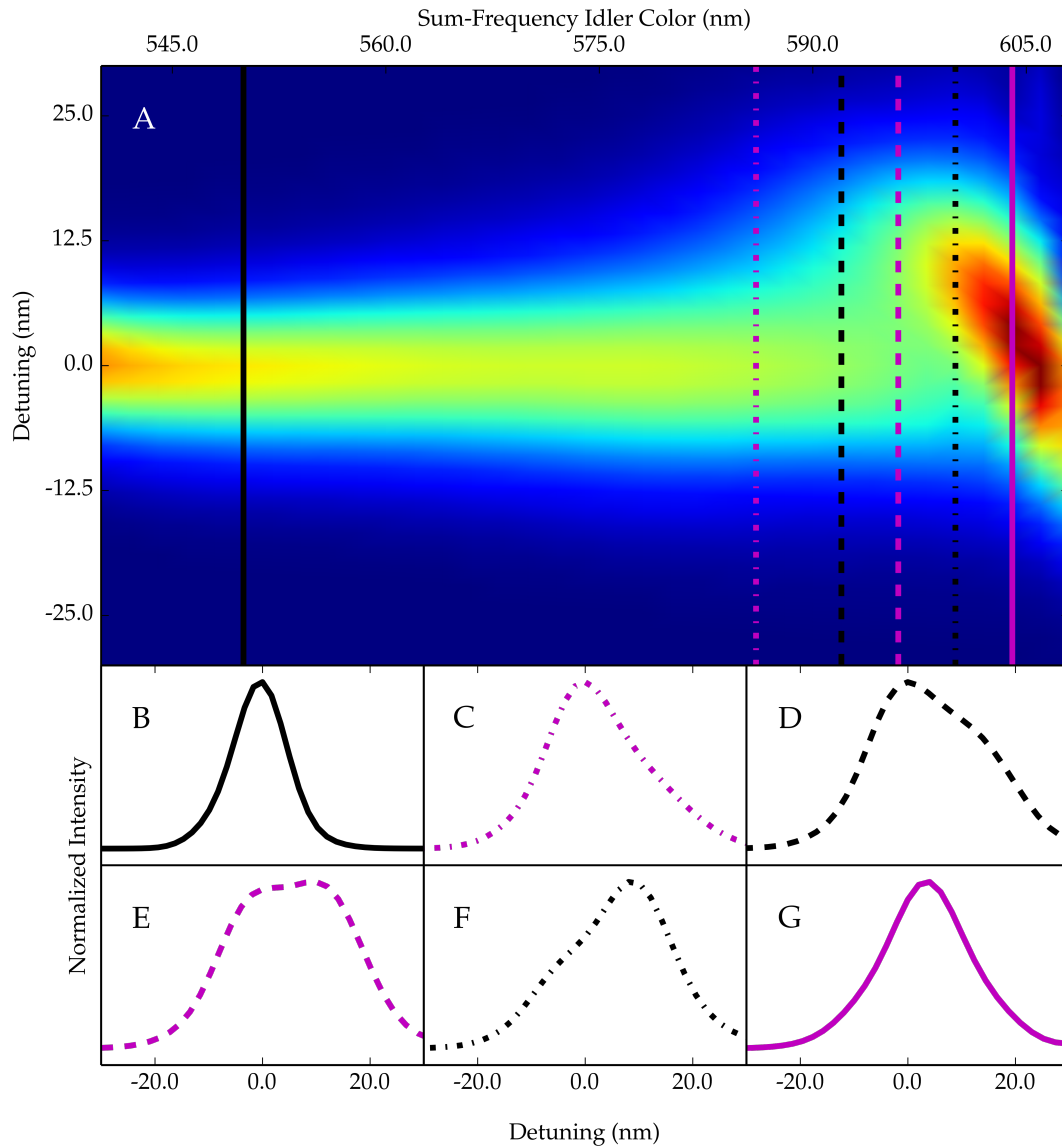


Figure 4.10: The results of simulations of sum-frequency idler produced by upconversion of the simulated idler in Fig. 4.9 (B) with the depleted pump. (A) presents a two-dimensional representation of the spectral content at each sum-frequency idler central wavelength. This is analogous to (A) in Fig. 4.1, presenting intensity as a function of detuning ( $\lambda_m - \lambda_0$ ) versus sum-frequency idler central wavelength ( $\lambda_0$ ). (B)-(G) present color- and style-coded slices from (A), presented as normalized intensity versus detuning ( $\lambda_m - \lambda_0$ ), in analogy to (B)-(E) of Fig. 4.1.



ability distribution; however, since the simulated spectra are not normalized, we will add a normalization factor in the manner of Eq. 3.1.21. This normalization results in a calculation of the  $n^{\text{th}}$  moment about the origin,  $\mu'_n$ : [290]

$$\mu'_n = \frac{\int_0^\infty \Delta\omega^n |\hat{A}(\Delta\omega)|^2 d\Delta\omega}{\int_0^\infty |\hat{A}(\Delta\omega)|^2 d\Delta\omega} \quad (4.3.5)$$

We will focus particularly upon the second and third moments,  $\mu'_2$  and  $\mu'_3$ . From the second moment, we will calculate the standard deviation describing the spectral width according to the first and second moments: [290, 291]

$$\sigma = \sqrt{\mu'_2 - \mu^2} \quad (4.3.6)$$

In Eq. 4.3.6,  $\mu$  is the mean and is calculated as  $\mu'_1$  according to Eq. 4.3.5. [290] For the purpose of this discussion, we will consider the standard deviation as calculated according to Eq. 4.3.6 to be an adequate representation of the spectral bandwidth. This bandwidth will be reported in units of energy ( $\text{cm}^{-1}$ ) to allow direct comparison within and across the different tuning regions. The third moment will be used to calculate the skew of the distribution, reported by  $\alpha_3$ . This quantity is calculated from the third moment about the mean,  $\mu_3$ : [290]

$$\alpha_3 = \frac{\mu_3}{\sigma^3} \quad (4.3.7)$$

where  $\sigma$  is the standard deviation calculated according to Eq. 4.3.6 and  $\mu_3$  is calculated from  $\mu'_3$ ,  $\mu'_2$ , and  $\mu$ : [290]

$$\mu_3 = \mu'_3 - 3\mu'_2\mu + 2\mu^3 \quad (4.3.8)$$

The value  $\alpha_3$  describes the skew of the distribution, the degree of asymmetry. [290] We generally will not be concerned with the actual value or sign of  $\alpha_3$ , but rather whether it is zero or nonzero (symmetric or asymmetric) and its relative magnitude.

Danielius et al [272] attribute the increased efficiency of idler upconversion in their OPG system near 600 nm to the minimization of the pump-idler group velocity mismatch. This is consistent with the understanding that the pump-idler and pump-signal group velocity mismatch can limit the gain of an OPA, [126] and that pre-existing group delay can impede sum-frequency generation. [103] This initially led us to suspect that the pump-idler group velocity mismatch may be responsible for the distortions observed in Fig. 4.1 and reproduced in Fig. 4.10.

In Fig. 4.11, we reproduce the two-dimensional representation of our SFI simulations from Fig. 4.10 in (A); we have also overlaid the simulated pulse energies. We have applied the statistical metrics in Eq. 4.3.6 and 4.3.7 to provide measurements of the bandwidth ( $\sigma$ , shown in (B) of Fig. 4.11) and skew ( $|\alpha_3|$ , shown in

(C) of Fig. 4.11). These metrics are compared to the pump-idler and pump-signal group velocity mismatch as calculated according to the dispersion curves of Zhang et al.[208]

A comparison of the pump-idler group velocity mismatch and the simulated pulse energy does show that the conversion is optimized when the group delay from the optical parametric amplification is minimized by the pump and idler exhibiting identical group velocities. This is consistent with the conclusions of Danielius et al.[272] In contrast, the group velocity mismatch is not minimized when we observe distortion to the spectral content: rather, as measured by the bandwidth ( $\sigma$ ) and skew ( $|\alpha_3|$ ), the distortion to the spectral character is maximized when mismatch still exists between the pump and idler group velocities.

The disagreement we observe in Fig. 4.11 between the frequencies at which we observe distortions to the sum-frequency idler spectral character and minimization of the pump-idler group velocity mismatch required us to consider other explanations for the behavior. We first considered the traditional approach in the literature for describing the bandwidth of phase matched processes. Within this approach, the phase matching bandwidth is defined according to the Taylor series expansion of the phase mismatch.[125, 129, 134, 170, 179, 265, 277, 292] Such an expansion is typically considered to predict that the phase matching bandwidth depends solely upon the signal-idler group velocity mismatch,[125, 129, 134, 170, 179, 265, 277, 292] though it has been noted that this approximation is only valid within the confines of a monochromatic or nearly monochromatic pump.[170, 172] Despite concerns that the accuracy of such approaches is limited in the regime of broad bandwidth pulses,[175] within our treatment, we find that the bandwidth predicted by a similar method yields reasonable results for some regions in the sum-frequency idler process (Fig. 4.12).

As noted above, the traditional view of the phase matching bandwidth is to perform the Taylor series expansion of the phase mismatch,  $\Delta k = k_P - k_I - k_S$ , with respect to the signal and idler frequencies:

$$\Delta k = \Delta k_0 + \left( \frac{\partial k_S}{\partial \omega} - \frac{\partial k_I}{\partial \omega} \right) \Delta \omega + \frac{1}{2} \left( \frac{\partial^2 k_S}{\partial \omega^2} - \frac{\partial^2 k_I}{\partial \omega^2} \right) \Delta \omega^2 + \dots \quad (4.3.9)$$

where the difference in the group velocities or group velocity dispersions arises because an increase (decrease) in the frequency of the signal must be accompanied by a decrease (increase) in the idler frequency. With the decrease in signal according to  $\text{sinc}^2(\Delta k L/2)$ , the phase matching bandwidth is typically defined as the bandwidth,  $\Delta \omega$ , for which  $|\Delta k| = \pi/L$ , where  $L$  is the crystal length.[125] Traditionally, this is only considered to the first order (only considering group velocities), with the group velocity dispersion taken into consideration when the group velocity mismatch is zero.[126, 170] As a first approximation, we extended this approach to consider all possible permutations of the fields in both processes (pump and signal, pump and idler, and signal and idler in optical parametric amplification and sum-frequency and pump, sum-frequency

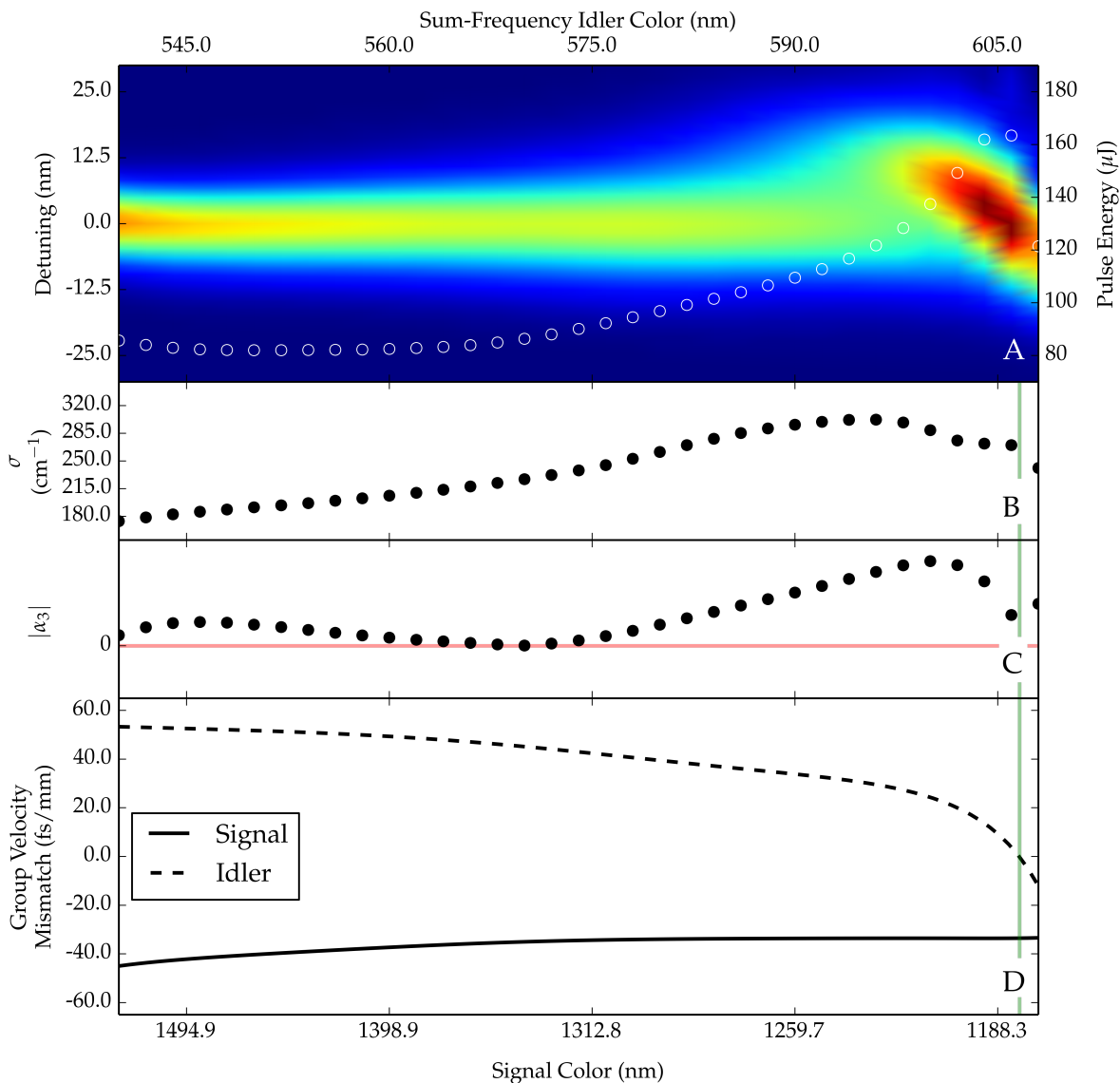


Figure 4.11: The results of simulations of sum-frequency idler generation and comparison to the group velocity mismatch curves calculated by the dispersion curves from Zhang et al.[208] (A) reproduces the two dimensional presentation of the simulated sum-frequency idler (see (A) in Fig. 4.10). (A) also contains an overlay (white markers) indicating the sum-frequency idler pulse energy predicted by the simulations. (B) and (C) show standard deviation ( $\sigma$ ) and skew ( $|\alpha_3|$ ) calculated from the simulation in (A); these values are calculated according to Eq. 4.3.6 and 4.3.7, respectively. (D) displays the calculated group velocity mismatch between the pump and either signal or idler based upon the dispersion formulae of Zhang et al.[208] The faded red line in (C) emphasizes zero, identifying the point at which symmetric spectra should be observed. The faded green lines in (B), (C), and (D) mark where the pump-idler group velocity mismatch is zero.

and idler, and pump and idler in sum-frequency generation), generalized in Eq. 4.3.10 to any  $i, j$  pair:

$$\Delta k = \Delta k_0 + \left( \frac{\partial k_i}{\partial \omega} - \frac{\partial k_j}{\partial \omega} \right) \Delta \omega + \frac{1}{2} \left( \frac{\partial^2 k_i}{\partial \omega^2} - \frac{\partial^2 k_j}{\partial \omega^2} \right) \Delta \omega^2 \quad (4.3.10)$$

Explicitly considering the expansion to the second order, we defined the phase matching bandwidth according to the maximum bandwidth allowed in any given process (optical parametric amplification or sum frequency generation) based upon the limit of  $|\Delta k| = \pi/L$ .

From an analysis of the predicted phase matching bandwidth, we found that the predicted bandwidth was limited by the optical parametric amplification process; based on similar situations described in the literature, we would therefore expect the bandwidth of the paired processes to be limited by the bandwidth predicted for optical parametric amplification.[170, 176, 285] In this first process, we found that the bandwidth permitted based upon the group velocity mismatch between the pump and either the signal or the idler was actually significantly greater than the limit imposed by the signal-idler group velocity mismatch. At shorter sum-frequency idler wavelengths, the maximum bandwidth was permitted by the pump-signal group velocity mismatch; this eventually gave way to the bandwidth allowed by the expansion of the phase mismatch with respect to the pump and idler. In Fig. 4.12 (B), we compare the maximum allowed bandwidth within this approximation to the bandwidth predicted by the second moment of the simulated spectra. We find that this approximation actually describes the bandwidth at shorter sum-frequency idler wavelengths quite well; however, while the maximum bandwidth predicted by this analysis is comparable to the maximum bandwidth observed in our simulations, we still observe that the distortion to the sum-frequency idler spectra occurs at different wavelengths than would be expected.

The theoretical treatment of Akhmanov et al for optical parametric amplification and sum-frequency generation appears to provide the best qualitative match to the behavior we observe in our simulations.[103] Unfortunately, we are restricted to a qualitative comparison. In their analysis of optical parametric amplification, Akhmanov et al assume equal pump-idler and pump-signal group velocity mismatch, while it is not clear whether their treatment is robust in the traveling-wave regime of high conversion.[103] On the other hand, their treatment of sum frequency generation is explicitly in the context of low conversion and does not incorporate the effects of pre-existing group delay.[103] Nevertheless, their models have been previously used as qualitative descriptions for the behavior of femtosecond parametric processes,[175, 176] as we shall do here.

Akhmanov et al describe optical parametric amplification within the typical regime of Type II phase

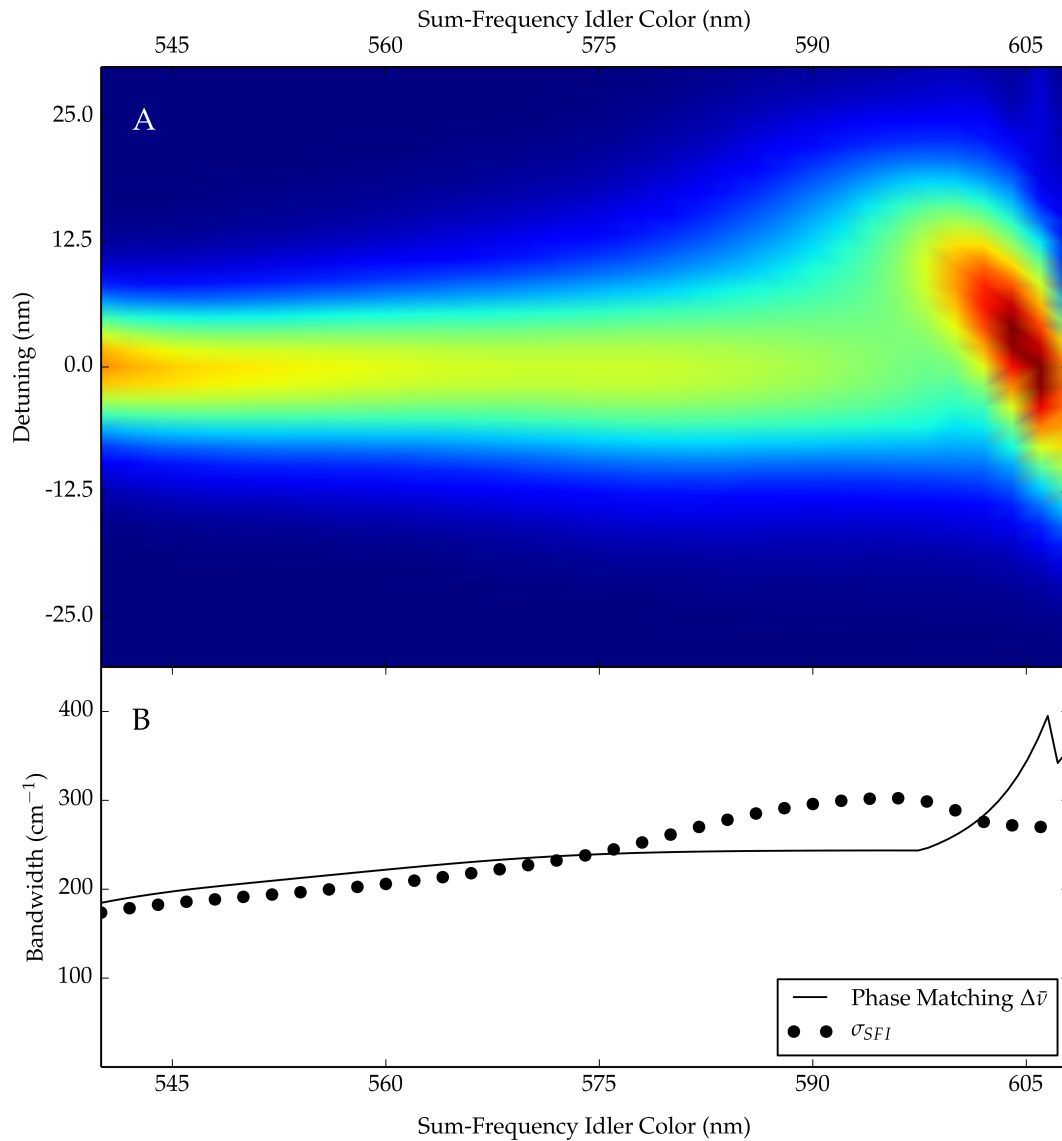


Figure 4.12: A comparison of the sum-frequency idler simulation to the estimated phase matching bandwidth. (A) reproduces the two-dimensional presentation of the simulation shown in Fig. 4.10 (A). (B) compares the bandwidth as calculated according to the second moment (see Eq. 4.3.6) to the maximum phase matching bandwidth as estimated by considering all permutations of Eq. 4.3.10.

matching - in which  $\Delta u_{i,p}^{-1} \Delta u_{s,p}^{-1} < 0$ , [126, 171] where  $\Delta u_{j,k}^{-1}$  is the group velocity mismatch between  $j$  and  $k$ ,  $u_j^{-1} - u_k^{-1}$  - compatible with permitting the “mode amplification” regime. [103] They consider amplification under such conditions to be a steady state mode of operation, though the behavior of the process changes based upon the characteristic lengths. The lengths of relevance are the pulse-splitting (or walk-off) length,  $L_w$ , and the amplification length,  $L_a$ . The pulse-splitting length can be defined in terms of the pulse duration of the pump:  $L_w = \tau_P / |\Delta u^{-1}|$ , where  $\tau_P$  is the pump pulse duration and  $\Delta u^{-1}$  is its group velocity mismatch with respect to another pulse. However, they indicate that it is more robust to consider the pulse-splitting length with respect to the bandwidth ( $\Delta\omega$ ) of the interacting pulses:

$$L_w = (|\Delta u^{-1}| \Delta\omega)^{-1} \quad (4.3.11)$$

Meanwhile, the amplification length is related to the exponential gain observed in the amplification process: for exponential gain of the signal on the amplitude level according to  $\exp(\Gamma z)$ , the amplification length is  $L_a = \Gamma^{-1}$ . [103]

From the ratio of  $L_w$  and  $L_a$ , Akhmanov et al define a quantity,  $m = L_w / L_a$ . When  $m < 1/2$ , exponential gain of the signal and idler is observed in the amplification process; they also predict that this steady state operation contributes to generating pulses with durations  $\tau = \tau_P / \sqrt{\Gamma L}$ , where  $\tau_P$  is the pump pulse duration and  $\Gamma$  is the gain. [103] Such behavior is consistent with the slight pulse shortening that has been reported for Type II phase matching. [168] On the other hand, when  $m > 1/2$  and the crystal is longer than the pulse-splitting width, exponential gain is still observed; however, the amplified pulses exhibit a decrease in duration,  $\tau = \tau_P / m$ . In both steady state regimes, the group delay accumulated is  $\tau_P / 2m$ . [103]

Meanwhile, for sum-frequency generation, Akhmanov et al provide two different regimes in which sum-frequency generation can occur, with different results for the spectrum of the upconverted field. The difference between the regimes stems from the pulse-splitting length of the fields being summed; Akhmanov et al label these fields 1 and 2, with  $u_1 > u_2$ . The pulse-splitting length is defined according to the bandwidth of field 1,  $L_w = (|\Delta u_{2,1}^{-1}| \Delta\omega_1)^{-1}$ . When the crystal length is less than the pulse splitting length, the separation of fields 1 and 2 is considered inconsequential, and the spectrum depends upon the group velocity of the sum frequency with respect to these fields,  $\Delta u_{s,0}^{-1}$ :

$$s(\Delta\omega) = \text{sinc}^2 \left( \frac{\Delta u_{s,0}^{-1} \Delta\omega L}{2} \right) s^{qss}(\Delta\omega) \quad (4.3.12)$$

where  $\Delta\omega$  is the detuning and  $s^{qss}(\Delta\omega)$  is the steady-state spectrum. We take that this spectrum should correspond to the ideal spectrum of the sum frequency, namely the convolution of the spectra of fields 1 and

2. Meanwhile, when the crystal length is longer than the pulse splitting length, a noticeably different result is predicted:

$$s(\Delta\omega) = \left[ 1 + \left( \frac{\Delta\omega \Delta u_{s,2}^{-1}}{\Delta\omega_1 \Delta u_{2,1}^{-1}} \right)^2 \right]^{-1} s^{qss}(\Delta\omega) \quad (4.3.13)$$

where all terms in Eq. 4.3.13 are defined as before.[103]

From Eq. 4.3.12 and 4.3.13, it is trivial to show that the sum frequency process narrows the steady-state spectrum according to a bandwidth<sup>i</sup> of  $\Delta\omega_{40\%} = \pi/L\Delta u_{s,0}^{-1}$  when  $z < L_w$  or  $\Delta\omega_{40\%} = 1.5\Delta\omega_1\Delta u_{2,1}^{-1}/\Delta u_{s,2}^{-1}$  when  $z > L_w$ . Alternatively, for  $z > L_w$ , this result is identical to  $\Delta\omega_{40\%} = 1.5/L_w\Delta u_{s,2}^{-1}$ .

In Fig. 4.13, we consider the sum-frequency idler simulations in the context of the theoretical treatment by Akhmanov et al. In (A), we see that the bandwidth of the sum-frequency idler process ( $\sigma_{SFI}$ ), is poorly described by the convolution of the idler and pump bandwidths:<sup>ii</sup> the convolution exhibits a broader width at short sum-frequency idler wavelengths ( $\lambda < \sim 575$  nm), a narrower bandwidth at intermediate wavelengths ( $\sim 575$  nm  $< \lambda < \sim 595$  nm), and reaches a peak at longer wavelengths than is observed for the sum-frequency idler. However, in (B), we see that the bandwidth that is expected to be imposed according to Eq. 4.3.12 (magenta markers) and Eq. 4.3.13 (cyan markers) exhibit very similar behavior to the sum-frequency idler bandwidth at shorter sum-frequency idler wavelengths. At longer wavelengths, though, their behaviors diverge: whereas the bandwidth predicted by Eq. 4.3.12 continues to increase with increasing sum-frequency idler wavelength, the bandwidth predicted by Eq. 4.3.13 exhibits a peak at approximately the same sum-frequency idler color as the peak observed in the bandwidth of the sum-frequency idler simulation in (A).

This change in the behavior predicted by Eq. 4.3.13 is readily apparent from the calculated pulse-splitting lengths in (E): at the same sum-frequency idler wavelength that we observe the peaks in the bandwidth of the simulated sum-frequency idler and the bandwidth predicted by Eq. 4.3.13, the pulse-splitting length is beginning to increase dramatically. This increase in the pulse-splitting length occurs despite the increased pump and idler bandwidths due to the rapid change in pump-idler group velocity mismatch near these frequencies (see (D) in Fig. 4.11). The increase in  $L_w$  also causes a sharp rise in  $m$ , as shown in (C); in calculating  $m$ , we have estimated  $L_a$  using a value of  $1.8 \text{ mm}^{-1}$  for  $\Gamma$ . A value of  $1.8 \text{ mm}^{-1}$  for  $\Gamma$  corresponds roughly to amplifying a  $1 \text{ }\mu\text{J}$  seed to  $400 \text{ }\mu\text{J}$ ; the value of  $\Gamma$  changes relatively slowly, though, for different

<sup>i</sup>Here, we are defining bandwidth as the detuning that results in a decrease in intensity to 40%, the losses induced by the sinc<sup>2</sup> function when the argument in brackets is equal to  $\pi/2$ . [125]

<sup>ii</sup>Here, we are restricted to considering the bandwidth of the convolved spectra within the limit that the spectra are Gaussian, namely that the variance of the convolution is the sum of the variances of the initial spectra. However, we note that both the pump and idler exhibit some degree of skew at longer sum-frequency idler wavelengths (not shown), so the bandwidth predicted in this manner is not expected to be exact.

final signal pulse energies.<sup>i</sup> Finally, we see in (D) that the lower values and gradual changes associated with  $m$  at shorter sum-frequency idler wavelengths result in the largest values and only slight changes in the group delay,  $\tau_g$ , between the pump and idler. When the pulse-splitting length increases dramatically at longer sum-frequency idler wavelengths, we see a correspondingly fast decrease in  $\tau_g$ .

Combining these results, we interpret the distortions observed in the sum-frequency idler spectra in the following manner. At short sum-frequency idler colors, we do not observe any unexpected behavior during parametric amplification, yielding reasonably symmetric signal and idler pulses (see Fig. 4.9). However, by operating at lower values for  $m$  at these wavelengths, the pump and idler accumulate the greatest initial group delay. This large initial group delay reduces the efficiency of the conversion, yielding lower output energy for the sum-frequency idler process. As we tune to longer sum-frequency idler colors, the decreasing group velocity mismatch between the sum frequency and the idler/pump (see the behavior for  $z < L_w$  in (B) of Fig. 4.13) increases the bandwidth of the sum-frequency idler according to Eq. 4.3.13. However, while we interpret the trends in Fig. 4.13 (B) as arising predominantly from the changes in the group velocity mismatch between the sum frequency and the pump/idler, there are also more gradual changes in the pump-idler group velocity mismatch. This gradually increases  $L_w$ : while not enough to overcome the changes in the sum frequency-pump/idler group velocity mismatch, it does result in a decrease in the group delay by increasing  $m$ , improving the conversion efficiency. Eventually, the pump-idler group velocity mismatch does change sufficiently quickly to overcome the decreasing sum frequency-pump/idler group velocity mismatch. At this point, we simultaneously observe: a sudden decrease in the initial group delay, improving the efficiency of the sum frequency process; and, a sudden decrease in the bandwidth predicted by Eq. 4.3.13, due to the increase in  $L_w$ . Eventually, the increase in  $L_w$  is sufficient to transition from the  $z > L_w$  regime to the  $z < L_w$  regime: this results in the sum-frequency idler bandwidth being limited by the convolution of the idler and pump bandwidths, which appears to be the trend at the longest sum-frequency idler wavelengths in Fig. 4.13 (A).

The proposal from Light Conversion to address the observed issues with sum-frequency idler generation is an upgrade that replaces the “depleted pump” upconversion strategy with one based upon a “fresh pump.” [194] Within the “fresh pump” strategy, the existing pump is split prior to parametric amplification: one fraction is used for amplification of the signal and the idler, while the other is routed through an external delay and recombined with the signal and idler for upconversion. Based upon the results of these simulations and previous reports in the literature, it seems reasonable to conclude that this would improve

---

<sup>i</sup>For example, a final pulse energy of only 180  $\mu\text{J}$  corresponds to  $\Gamma \approx 1.4 \text{ mm}^{-1}$ .



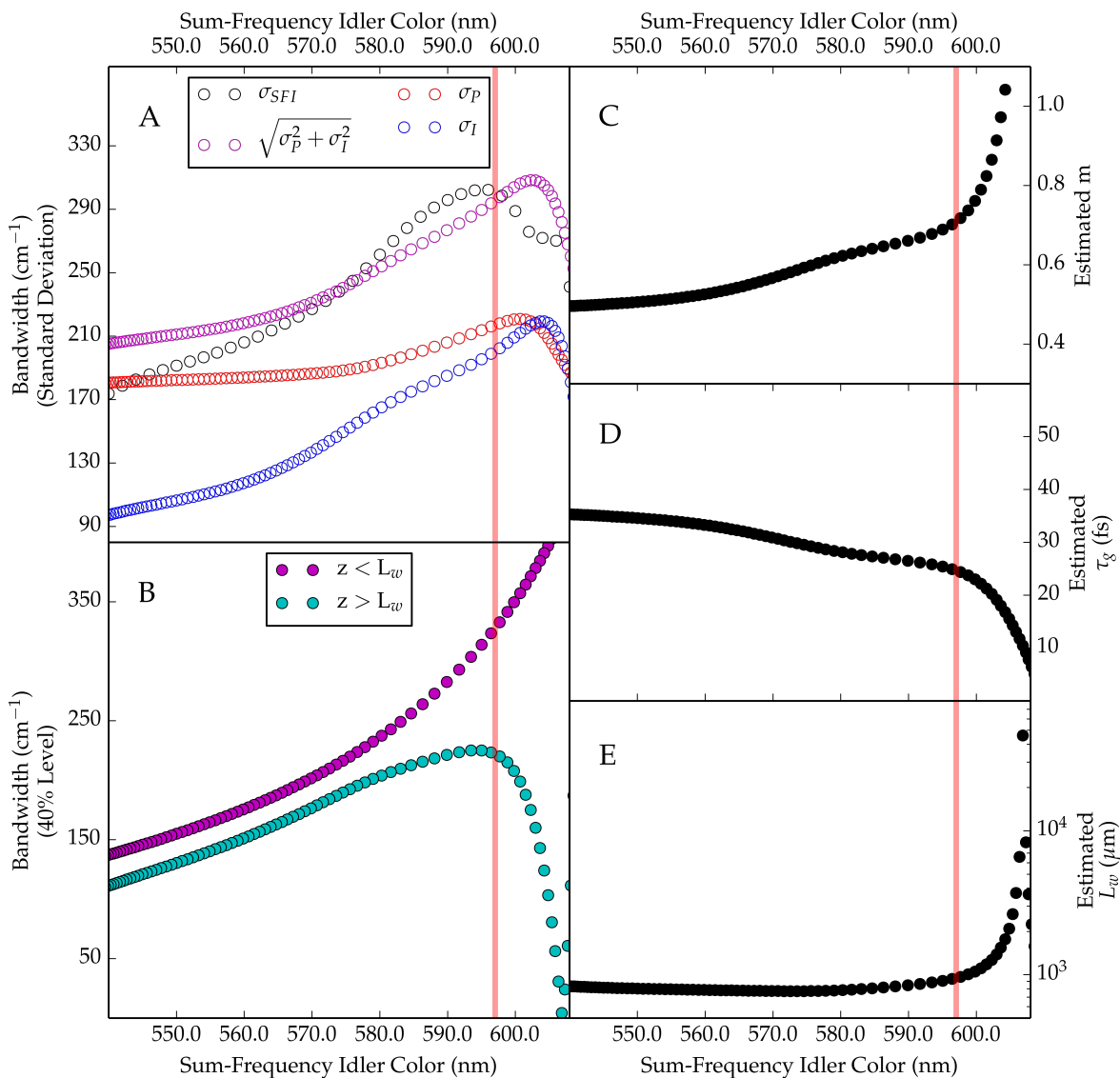


Figure 4.13: Interpretation of the sum-frequency idler simulation results in the context of the theory presented by Akhmanov et al.[103] (A) Comparison of the bandwidth observed for the simulated sum-frequency idler, the simulated pump, the simulated idler, and the square root of the sum of the variances of the simulated pump and idler. (B) Calculated bandwidth (at the 40% intensity level) of sum frequency idler generation for  $z < L_w$  (magenta markers) and for  $z > L_w$  (cyan markers) according to the theory of Akhmanov et al. See Eq. 4.3.12 and 4.3.13. (C) Estimation of  $m = L_w/L_a$  according to the bandwidths observed from the sum-frequency idler simulations.  $L_w$  is the pulse-splitting length and  $L_a$  is the amplification length for  $\Gamma = 1.8 \text{ mm}^{-1}$ . (D) Estimated group delay between the pump and idler accumulated during simulated parametric amplification, as calculated  $\tau_g = 35/2m$  fs. (E) Estimated pulse-splitting length in the sum frequency crystal according to the bandwidths calculated in sum-frequency idler simulations.

the performance of the sum-frequency idler process with respect to conversion efficiency.[103, 126] However, from the conclusions described above, it is not clear that compensating for the group delay would improve the spectral quality of the sum-frequency idler: while it seems reasonable to attribute the inconsistent conversion efficiency to the accumulated group delay, it appears more likely that the spectral character of the sum-frequency idler is controlled by the interplay of the group velocities of the sum-frequency, the pump, and the idler. It is not clear that the delay compensation incorporated in this “fresh pump” strategy would improve the spectral quality. While simulations could be performed to explore this behavior, it would also warrant communication with Light Conversion to determine what behavior they observe and anticipate from the proposed upgrade.

Additionally, while the sum-frequency signal process generally does not exhibit the asymmetric line shapes that are observed from the sum-frequency idler process, our experimental work with the sum-frequency signal process has led us to suspect that similar effects impact its time-bandwidth product. At this time, there has not been the opportunity to experimentally explore these suspicions, but it should be straightforward and more convenient to take the time to explore this possibility *in silico*.

CHAPTER 5

Manganese Tetraphenylporphine

## 5.1 Background

In various efforts to characterize photosystem II, a variety of authors have reported evidence of activity from the protein under near infrared (NIR) excitation.[15, 17–21, 34, 39, 44, 45, 61] Early detection of this signature was reported by Dismukes and Mathis,[39] but this signature has since been characterized further. Boussac et al published a sampling of reports in which they observe a change in the electron paramagnetic resonance (EPR) signal associated with the oxygen evolving center upon NIR exposure.[15, 17–21] By determining the yield of signal conversion, they have been able to trace out an activity spectrum exhibiting a peak near 820 nm. Baxter et al extended this to directly detect the absorbance of photosystem II, tracking the NIR transient absorbance upon the  $S_2 \rightarrow S_1$  dark-adaptation of a flash-excited sample.[34] The spectral profile they determine is very consistent with the activity spectrum reported by Boussac et al. Though their data set is limited, they find their data to be consistent with a Gaussian fit with center of  $12300 \text{ cm}^{-1}$  (813 nm) and half-width of approximately  $1000 \text{ cm}^{-1}$ . From estimating the chlorophyll content of their sample, Baxter et al estimate a transient absorptivity of  $50 \text{ cm}^{-1} \text{ M}^{-1}$ . Cua et al provide additional evidence for NIR activity through the observation of enhancement to low-frequency Raman modes with excitation near 820 nm; this enhancement is reduced when the excitation color is changed and is absent upon illumination or manganese depletion.[61] Most recently, Morton et al have published the results of NIR absorption and magnetic circular dichroism of photosystem II.[44] The combination of absorbance and MCD data allow Morton et al to make the strongest case for the origin of this feature, attributing the weak, with absorptivity  $< 30 \text{ cm}^{-1} \text{ M}^{-1}$ , absorbance found near 770 nm to d-to-d transitions localized on a manganese of the oxygen evolving center.[44]

The literature on the spectroscopy of manganese (III) provides support for this assignment. Many high-spin, monovalent coordination complexes of manganese (III) exhibit transitions in the NIR region, with different coordinating ligands resulting in NIR transitions at transition energies as low as  $5500 \text{ cm}^{-1}$  (1800 nm) and as high as  $14000 \text{ cm}^{-1}$  (714 nm).[293, 294] These transitions are characterized by very low absorptivities ( $\leq 100 \text{ cm}^{-1} \text{ M}^{-1}$ ), with the absorptivity generally decreasing with increasing transition energy.[294] The origin of these transitions is traced to the Jahn-Teller effect: due to its  $d^4$  electron configuration, six-coordinate manganese (III) centers are inclined to exhibit a distortion from octahedral symmetry in order to reduce the overall energy of the ground state.[293–299] The high resolution crystal structure of photosystem II has been interpreted to support the presence of Jahn-Teller distortions in the oxygen-evolving complex.[64]

As a representative system, manganese (III) trisacetylacetonate,  $\text{Mn}(\text{acac})_3$ , was selected as an initial test sample due to the convenient position of its NIR transition at the shorter wavelengths of the signal process

in the TOPAS-C optical parametric amplifiers and its availability from commercial sources. Unfortunately, experiments with this sample proved unsuccessful, with no signal clearly distinguishable in either transient absorption or transient grating experiments. Coming across the work of McCusker and co-workers, it became clear that a priori knowledge of the photophysics, or the ability to ascertain such information through methods such as white-light transient absorption, would be key in guiding future experiments.[300–302] These publications also traced the photophysics of a species,  $\text{Cr}(\text{acac})_3$ , with an absorptivity of very similar magnitude to the Jahn-Teller-allowed transition of manganese (III) coordination complexes. However, even in efforts to reproduce the reported results, we proved unable to replicate them: while very weak signal may have been present in transient absorption geometries, transient grating experiments yielded no signal.

At this point, it seemed probable that the low transition dipoles indicated by the low absorptivity of  $\text{Mn}(\text{acac})_3$  and  $\text{Cr}(\text{acac})_3$  may be proving limiting. Porphyrins and phthalocyanines seemed a convenient starting point for samples with stronger transitions. While manganese phthalocyanines seemed promising due to the presence of a NIR transition and evidence that the macrocycle and transition metal states exhibited significant interaction,[303–306] it became clear that manganese phthalocyanines also did not exhibit satisfactory stability in solution.[307] However, manganese (III) porphyrins also exhibit strong interaction between the transition metal and macrocycle states: the manganese d-orbitals are believed to be close in energy to the  $\pi$  and  $\pi^*$  states usually responsible for the Soret and Q-band in normal porphyrins.[306, 308, 309] The coupling between the metal and macrocycle states yields several transitions throughout the visible;[308] while it is not clear a definitive assignment of these transitions exist, it seems to be accepted that the states of the manganese (III) are involved in the spectroscopy.[308–311] While manganese (III) porphyrins generally exhibit little to no luminescence,[312] a variety of reports have explored the photophysics of manganese (III) tetraphenylporphine (MnTPP) following excitation with both pico- and femtosecond pulses.[313–316] The behavior observed in these experiments has been attributed to excitation of the  $^5\text{S}_0$  ground state to one of various  $^5\text{S}_n$  excited states, followed by an intersystem crossing to a “tripmultiplet” manifold including  $^3\text{T}_1$ ,  $^5\text{T}_1$ , and  $^7\text{T}_1$ . [313, 315, 316] The features observed in transient absorption upon excitation consistently include bleaching signals associated with the ground state features near 480 nm, 560 nm, and 600 nm, and excited state absorption near 500 nm.[314–316] While some reports suggest MnTPP can undergo photoreduction in tetrahydrofuran or be coordinated by solvents such as pyridine,[308, 317] there did not appear to be other concerns regarding stability; repeated measurements of solutions prepared from commercially-obtained MnTPP exhibited no spectral evidence of changes over time when dissolved in dichloromethane.

Given the exhibited stability and documented spectral signatures, we proceeded to adopt MnTPP as a

test sample. We hoped to be able to reproduce the transient absorbance results - with white light if feasible - and to extend the study of this molecule to transient grating geometries. We successfully reproduced the white light transient absorption for MnTPP. While we were able to observe transient grating signal, we found the nonresonant response to provide a competitively strong background. We also were unable to extend the use of white light to transient grating: though we could detect some signal in a nonresonant medium, signal levels were insufficient to detect with the existing system configuration. A sampling of results are presented in this chapter.

## 5.2 White Light Generation

White light generation provides a convenient method for obtaining broadband radiation from an ultrafast laser pulse; here we will provide a brief overview of the background on white light generation and describe the procedure used to generate white light for the reported experiments.

When generated from the fundamental of a Ti:Al<sub>2</sub>O<sub>3</sub> laser (near 800 nm), the white light will include new frequencies in both the near infrared and the visible, potentially spanning the entire visible region.[318, 319] The introduction of these new frequencies is attributed to self-phase-modulation and other nonlinear processes that arise due to the high intensities within filaments;[318, 320] these processes maintain coherence between the white light and the original field.[132, 321–326] Filamentation of the beam appears necessary to achieve the sustained intensity needed for white light generation. The formation of a stable filament is attributed to the interplay of focusing and defocusing mechanisms. The initial focusing of the laser arises through the Kerr effect, in which the intensity distribution of the laser modulates the refractive index, thereby causing the beam to be lensed: the significance of this contribution is clear by the threshold of white-light generation matching the threshold for Kerr lensing.[318, 320, 327–335] However, the effects of self-focusing eventually result in an intensity sufficiently high so as to induce defocusing; from this point, the filament is maintained by a sustained balance between the Kerr lensing and this defocusing. The traditional view for the mechanism appears to attribute defocusing to plasma generation; more recently, other authors have suggested that defocusing through plasma generation is specific to longer pulses, while the focusing of shorter pulses is arrested by higher order contributions to the Kerr effect.[234, 320, 326, 327, 330, 334–336] While condensed media provide a convenient route to reliably generate white light,[318–320, 325, 328, 337] some authors have reported filamentation and white light generation in air.[330–332, 338–341]

Broadening of the pulse during white light generation results in new frequencies at both low (Stokes broadening) and high (anti-Stokes broadening) frequencies; the breadth of the broadening can be described

by the derivative of the accumulated nonlinear phase due to self-phase-modulation with time (see § 3.1.2).[320] Due to the relationship between phase- and frequency-modulation, the Stokes and anti-Stokes components are attributed to the accumulated nonlinear phase at the leading and trailing edges of the pulse, respectively.[320, 342] The accumulation of nonlinear phase can be described by a quantity called the *B*-integral.[172, 247, 254, 320] Since they experience different contributions from the temporal envelope of the laser, the Stokes and anti-Stokes components are generally not symmetric. The anti-Stokes component is generally more enhanced and exhibits a characteristic plateau - an even energy distribution across the observed frequencies.[320, 328] Within the approximation that the driving field can be described by a sech field envelope, a closed form solution for the breadth of the anti-Stokes and Stokes components has been published.[320] While even energy distributions of the Stokes component have been reported, this behavior appears to be specific to particular media and is only observed at higher energies.[328] Such high energies can also induce modulations in the spectra.[328]

In addition to the differences between the Stokes and anti-Stokes components, the medium and experimental approach can also impact the breadth of the white light. In condensed media, correlation has been reported between the breadth of the anti-Stokes broadening and the band gap of the material: larger band gaps tend to support additional broadening. This behavior also translates to the wavelength of the initial beam, as higher frequency lasers exhibit enhanced broadening.[319] This band gap dependence results in halide crystals, such as LiF and CaF<sub>2</sub>, yielding far broader white light spectra than other condensed media.[319, 320] However, this advantage comes at a limitation, as these materials have been reported to be susceptible to damage when used for white light generation.[138, 178, 337] While the fluoride materials can be particularly susceptible to damage at the intensities in filaments, care should be taken regardless of the medium: at high numerical aperture (or short focal lengths), the threshold for optical breakdown can be lower than the threshold for filamentation.[333, 343]

In order to apply white light in experiments on the femtosecond system, the system described by Nikolaitchik et al was used as a model.[344] Like the Wright group's femtosecond system, the system described is seeded by a Millenia-pumped Tsunami, seeding a Spitfire that yields 100 fs (FWHM) pulses. They report using a fraction, approximately 0.2-0.3 mJ, of the fundamental to generate white light in a 3 mm sapphire plate or a 1 cm flow cell of ethylene glycol.[344] It is noted here that this number seems suspiciously high, as most sources cite threshold energies for white light generation in condensed media at hundreds of nJ to single  $\mu$ J.[322, 323, 328, 333, 343] More consistent with the literature, they report generating the white light by focusing the mode of the fundamental into the white light medium with a 100 mm focal length lens.[344] The documentation on the Spitfire Pro XP employed on the femtosecond system reports an expected  $1/e^2$  beam

diameter of 7-9 mm. If this is a reasonable estimate for the Spitfire employed by Nikolaitchik et al, their 100 mm focal length lens should result in a half-width waist within their white light medium of approximately  $3 \mu\text{m}$ ,<sup>[105]</sup> and a numerical aperture of approximately 0.03.<sup>[209]</sup> This value is consistent with the regime reported by Ashcom et al for which the threshold for continuum generation is lower than the threshold for damage to the medium.<sup>[343]</sup>

At the time of these experiments, the mirrors and beamsplitters dividing the fundamental from the Spitfire Pro XP also isolate a small fraction of the fundamental. The spot size of this beam was reduced by a Galilean telescope consisting of a  $f = -50 \text{ mm}$  and  $f \approx 100 \text{ mm}$  lens pair. The resulting beam was routed down the table by a series of mirrors; it could be configured to pass through one of the delay lines for use in three color experiments. After the telescope, the beam diameter is approximately 6 mm, and the telescope and other optics introduce losses that reduce the energy to approximately  $20 \mu\text{J}$ . Starting from the values reported by Nikolaitchik et al, we expected a 50-75 mm lens to yield the correct imaging properties, but we unfortunately found ourselves limited by the lenses available. While the 35 mm lens employed yields a numerical aperture of approximately 0.15, exceeding the numerical aperture for which the damage threshold is below the threshold for continuum generation in silica,<sup>[343]</sup> we found we could consistently generate and maintain a white light continuum in sapphire. In order to attain stable white light, we found we needed to attenuate the fundamental with an optical density of approximately 3.<sup>i</sup> We also attempted to generate the continuum in  $\text{CaF}_2$ : consistent with the literature,  $\text{CaF}_2$  yielded a much broader continuum than sapphire.<sup>[178, 319, 328]</sup> Unfortunately, the continuum could only be sustained for a short period, which we attribute to damage; at this point, we suspect that the stability of sapphire over the  $\text{CaF}_2$  may be consistent with the behavior of halide crystals as reported by Huber et al, Kohl-Landgraf et al, and Tzankov et al.<sup>[138, 178, 337]</sup> White light generation was performed just before the appropriate beam line; the sapphire plate was followed by a 25 mm lens, which was adjusted to yield the proper spot size at the sample.

### 5.3 Experimental Deviations

Experiments with MnTPP were performed by dissolving the sample in dichloromethane to achieve an appropriate absorbance,  $A \approx 1$ , in the spectral region of interest; this was often the frequency of the pump (in transient absorption) or  $\omega_2/\omega_{2'}$  (in transient grating). Samples were contained in a 1 mm glass cuvet

---

<sup>i</sup>It should be noted that this optical density is based upon the calibration reported by the manufacturer. Calibration has shown that the optical density of the filters exhibits some wavelength dependence, so the actual optical density is likely slightly different.



(Precision Cells).

For experiments not involving white light, standard operating procedures were employed for the experiments described in this section. Experiments were conducted using the second-harmonic and sum-frequency signal processes of the TOPAS-C. The supplied wavelength selector was used for the sum-frequency signal process. For second-harmonic signal, the wavelength selector was not used, but a heat filter was introduced to block the near infrared (wavelengths longer than  $\sim 700$ - $740$  nm).

For experiments involving white light, white light was generated as described before, and the table was aligned as described for two color experiments: the fundamental and white light served as  $\omega_1$ , and one of the OPAs was used to provide  $\omega_2$  and  $\omega_2'$ . For transient absorption experiments, signal could be detected when using the standard  $f = 1$  m mirror; however, the beamsplitter for the OPA had to be removed in order to provide sufficient pump energy. The silicon photodiode was used for detection, and the monochromator was scanned across the wavelength range of the white light (the probe). Zero delay compensation was implemented to reduce the effects of the chirp in the white light. Due to the exploratory nature of these scans, the chirp in the white light was not determined with sufficient resolution to characterize the nonlinearities in the chirp rate; however, the compensation was sufficient to ensure zero delay for all colors in the probe occurred within  $\sim 100$  fs of the assigned zero delay. For transient grating with the white light, no signal could be detected with the  $f = 1$  m mirror; however, by decreasing the focal length to  $f = 500$  mm, some signal was detected. This signal was strongest when  $\omega_1 \approx \omega_2$ ; the decrease in signal at longer wavelengths is believed to be a consequence of phase mismatch and changes in output direction. With the current detector (silicon photodiode), signal could only be detected in solvent. It is suspected that a more sensitive detector and modifications to the table layout to provide more a more intense white light and retain more energy from the OPA would be needed to make this method routine.

## 5.4 Results and Discussion

A summary of experimental data exploring the nonlinear electronic spectroscopy of MnTPP is provided in Fig. 5.1. (A)-(C) provide insights into the behavior of MnTPP in transient absorption along two different slices of the three-dimensional space: (A) and (B) present the change in optical density as the pump is tuned and the monochromator is scanned across the wavelengths of the white light probe; and, (C) explores the dynamics along delay at different probe wavelengths. (A) and (B) provide two alternative views of the same data set, while the data of (C) is shown only with the more dynamic color scale of (B). (D)-(H) explore the response of MnTPP in frequency-frequency and delay-delay space for transient grating/TriEE, the frequency-

domain analogue of 2D-ES,[345] corresponding to the phase-matched output  $\mathbf{k}_4 = \mathbf{k}_1 - \mathbf{k}_2 + \mathbf{k}_{2'}$ . In the frequency-frequency domain of (D), the detected intensity at  $\omega_m = \omega_1$  is presented as a function of  $\omega_2 = \omega_{2'}$  and  $\omega_1 = \omega_m$ . The time-time domain of (E)-(H) show the detected intensity at  $\omega_m = \omega_1$  as a function of the relative delays  $\tau_{21} = \tau_{2'1}$  and  $\tau_{2'2}$ ; in this domain, signal along  $\tau_{21} = \tau_{2'1} \leq 0$  tracks the population dynamics of the system, while signal along other directions track the dynamics of coherences under the conditions of these experiments ( $\omega_1 \neq \omega_2$  and  $\omega_2 = \omega_{2'}$ ).

The spectroscopy of MnTPP observed in Fig. 5.1 is consistent with previously described transient absorption of this compound.[314–316] In solution,<sup>i</sup> all authors<sup>ii</sup> report a strong excited state absorption (ESA) feature peaking near 490-500 nm and a weak ESA feature near 550 nm.[314–316] The broader probe of Kim et al allow them to also report an ESA feature between 400 and 450 nm;[315] they also show agreement with Yan et al in reporting a broad ESA feature starting near 650 nm and falling off into the near infrared.[315, 316] The ground state absorption of MnTPP is bleached, with a strong feature near 480 nm[314, 315] and weaker features near 580 nm and 620 nm.[315, 316]

Within the sensitivity of the white light transient absorption measurements, we observe each of these features. The bleach near 480 nm is the most pronounced feature of the transient absorption spectrum, consistent with Kim et al.[315] The contours in (A) hint at features corresponding to the ESA features reported between 400 and 470 nm and 495 and 530 nm and the bleaches of the ground state transitions near 580 nm and 620 nm. The alternative color bar in (B) accentuates these features. The scale also provides sufficient contrast to observe features consistent with the ESA near 550 nm and from 650 nm into the near infrared. The consistency of these features in (A), (B), and the cited works indicate that the transient absorption of MnTPP is relatively insensitive to excitation wavelength: Yan et al tune the pump to 355 nm or 532 nm to observe features between 500 and 650 nm or 650 and 900 nm, respectively;[316] Kim et al use a frequency-doubled Ti:sapphire amplifier at 390 nm;[315] Irvine et al appear to use a 597 nm dye laser;[314] and (A) and (B) illustrate the changes in transient absorption while scanning across the sum-frequency signal process (470-515 nm). This is consistent with previous assignments in the literature: excitation of the singlet states is followed by rapid relaxation to the lowest excited singlet state, which undergoes rapid intersystem crossing to yield states in the “tripmultiplet” manifold.[313, 315, 316] Consequently, despite the different

---

<sup>i</sup>It should be noted that Kim et al also study the transient absorption of MnTPP in molecular sieves; encapsulation in the molecular sieves results in changes to the ground state absorbance, attributed to interactions between the electronic states of MnTPP and the hydroxyl groups of the sieves.[315] When encapsulated, MnTPP also exhibits different spectral features in transient absorption.

<sup>ii</sup>It is noted that the wavelength scale for the data reported by Irvine et al is nearly illegible.[314] Their reported transient absorption spectra exhibit qualitative consistency with the results of Yan et al and Kim et al,[314–316] and from those numbers that can be made out, the features they observe appear to occur at the same wavelengths.

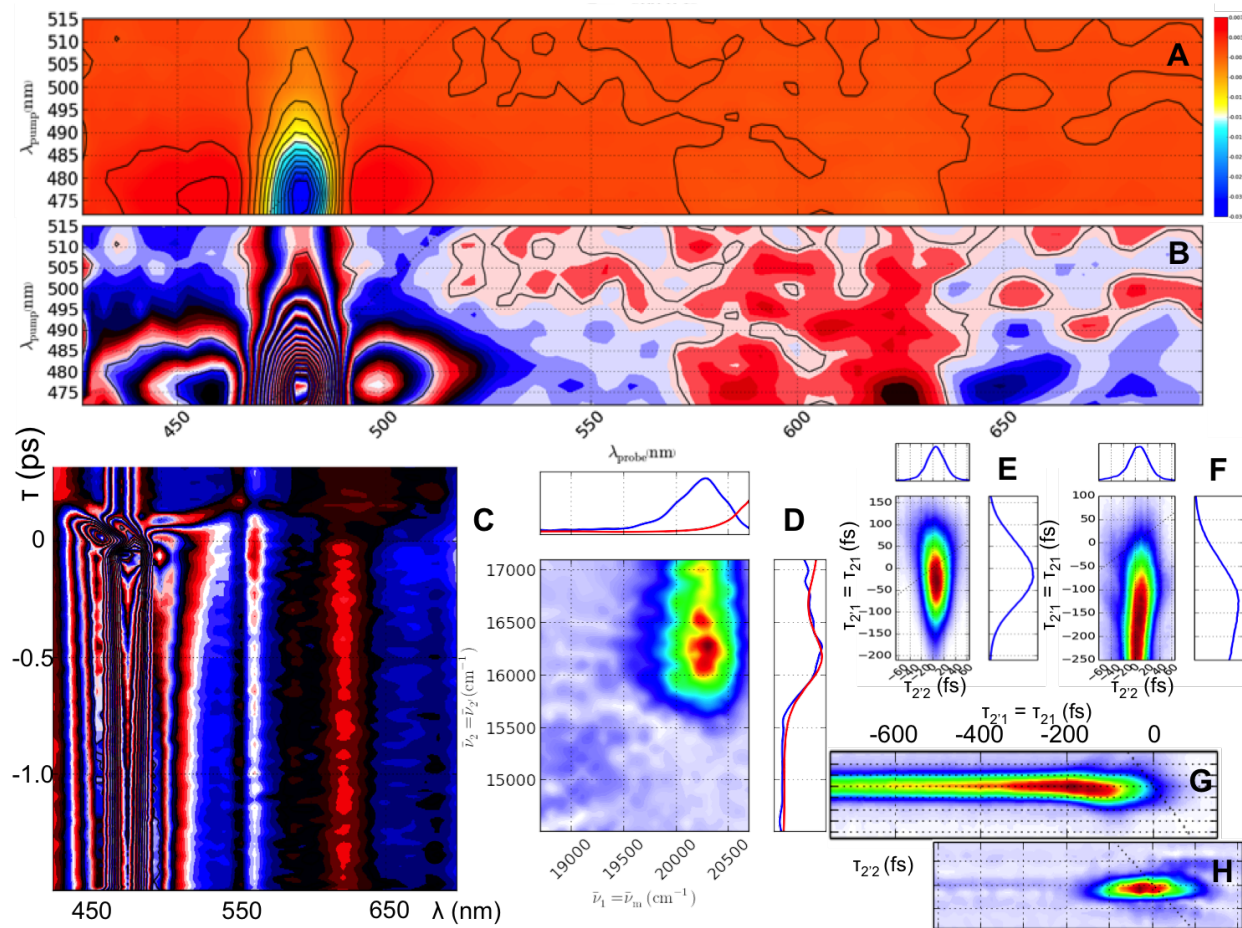


Figure 5.1: (A) and (B): White light transient absorption,  $\lambda_{\text{Pump}}$  versus  $\lambda_{\text{Probe}}$  at  $\tau \approx -500$  fs. B is the same data as A, but with a repeating color scheme to emphasize the weaker features. (C): White light transient absorption,  $\tau$  versus  $\lambda_{\text{Probe}}$  at  $\lambda_{\text{Pump}} = 475$  nm. This is the same repeating color scheme as (B). Optical density of the samples for (A), (B), and (C) are  $A \approx 1$  near 480 nm and  $A \approx 0.1 - 0.2$  near 610 nm. (D): Transient grating,  $\omega_2 = \omega_{2'}$  versus  $\omega_1 = \omega_m$ ,  $\tau_{21} = \tau_{2'1} = -500$  fs. Data in the side bars is absorbance (red) and integrated signal (blue). Optical density of the sample for (D) is  $A \approx 0.3$  near 16100  $\text{cm}^{-1}$  and  $A \approx 2.5$  near 20900  $\text{cm}^{-1}$ . (E), (F), (G), and (H): Transient grating,  $\tau_{21}$  versus  $\tau_{2'1}$ ,  $\lambda_2 = \lambda_{2'} \approx 605$  nm and  $\lambda_1 \approx 495$  nm. (E) and (F) provide a comparison of signal from dichloromethane (E) and MnTPP in dichloromethane (F),  $A \approx 0.7$  at both frequencies, near zero delay. (G) and (H) provide a comparison of signal from MnTPP in dichloromethane at two concentrations:  $A \approx 0.7$  (G) and  $A \approx 0.15$  (H). Signal in (E), (F), (G), and (H) are each normalized according to the maximum amplitude in each spectrum.

excitation frequencies, each of these reported experiments probe similar dynamics.

Panel (C) in Fig. 5.1 shows the reported configuration for white light transient absorption is also amenable to collecting the dynamics associated with the features in (A) and (B). Consistent with the literature,[314–316] the transients of MnTPP are very long lived, exhibiting very little change within the bounds of (C). Unfortunately, it is not possible to compare the dynamics at early times with the literature: the resolution of these experiments is much higher than the  $> 1$  ps time resolution of Irvine et al and Yan et al,[314, 316] and still appreciably higher than the 170 fs resolution reported by Kim et al.[315] The profile of the signal near zero delay illustrates that routine usage of white light transient absorption may be complicated by the challenge in correctly compensating for the chirp in the continuum. Based upon the behavior of MnTPP observed in transient grating, however, some of the complicated dynamics near zero delay in (C) may be attributable to the coherent artifact, which is observed in transient absorption for many different systems.[346–351]

The spectroscopy of MnTPP has been extended to transient grating, in which the signal consistent with the phase matching condition ( $\mathbf{k}_4 = \mathbf{k}_1 - \mathbf{k}_2 + \mathbf{k}_2'$ ) is homodyne detected. As shown in (D), the response observed in transient grating is consistent with the behavior in transient absorption and absorption. In the side-plot on the right of (D), the integrated signal as a function of pump frequency ( $\omega_2 = \omega_2'$ ) closely matches the absorbance of the sample: this can be seen by comparing the blue and red traces, corresponding to the integrated transient grating signal and the absorption spectrum, respectively. This behavior is to be expected.[185] Meanwhile, along the pump, we are observing signal corresponding to the ESA feature in (A) and (B); the peak of this signal is near 490 nm, consistent with the peak of the ESA in transient absorption. The sharp drop off in signal is likely the consequence of M-factors,[352] as achieving an appreciable absorbance at  $\omega_2$  required  $A \approx 2.5$  near 480 nm: the decrease in signal from the peak near  $20300 \text{ cm}^{-1}$  matches the increase in absorption from  $A \approx 0.3$  to  $A \approx 1-1.2$ .

Unfortunately, we were limited in the transient grating experiments of MnTPP to only longer delays; for example, the scan in (D) was collected at  $\tau_{21} = \tau_{2'1} = -500$  fs. This limit was imposed by the nonresonant background, as shown in (E)-(H). Between (E) and (F), we compare the dynamics observed at early times for a purely nonresonant system, dichloromethane (E), and a concentrated solution of MnTPP,  $A \approx 0.7$  at  $\omega_1$  and  $\omega_2$  (F). As this comparison shows, MnTPP exhibits a delay in the evolution of signal relative to the purely nonresonant response; we attribute this to the time required for singlet relaxation and intersystem crossing.[313, 315, 316] In contrast, when the concentration of MnTPP is reduced, the transient characteristic of MnTPP, (G), is nearly completely overwhelmed by the nonresonant background (H).

The nonresonant background manifests in transient grating due to the use of homodyne detection. Un-

der such conditions, the signal is proportional to  $|\chi^{(3)}|^2$ ,<sup>[190]</sup> rather than  $\chi^{(3)}$ . As a consequence, the signal depends upon the real and imaginary components of  $\chi^{(3)}$ , rather than just the imaginary component as in transient absorption;<sup>[190, 349]</sup> since the nonresonant response of the medium is predominantly real,<sup>[353]</sup> it is suppressed in transient absorption. Competition with resonant signals arise from scaling: since  $\chi^{(3)}$  is proportional to the number density,  $N$ ,<sup>[190]</sup> homodyne-detected signals scale with  $N^2$ ,<sup>[148]</sup> which can limit the detection limit for such methods.<sup>[122, 190, 354, 355]</sup> While it has been reported that nonresonant background may be enhanced under conditions of femtosecond excitation,<sup>[139, 140, 146, 356, 357]</sup> the magnitude of the problem was surprising: previous experiments on the Wright group’s femtosecond system with near infrared excitation have been robust at much lower sample absorbance.<sup>[358]</sup> However, it has also been reported that nonresonant signal can be influenced by excitation wavelength,<sup>[140, 148, 359]</sup> as well as pulse duration;<sup>[359]</sup> specifically, nonresonant background has been reported to be much worse under conditions of visible excitation,<sup>[140, 148]</sup> particularly when two-photon resonances are available.<sup>[139, 140]</sup>

In order to understand the limit imposed by the nonresonant background, we made measurements aimed at estimating and comparing the nonresonant response at near infrared and visible wavelengths. Beam energies were measured with a thermopile, and nonresonant signal was generated in a variety of transparent solvents. The response of the detector to the nonresonant signal and to one of the excitation beams were compared to provide an estimate of the energy emitted by the nonresonant process; we assumed the sampling efficiency was comparable for both color combinations. These measurements were consistent with a hundred-fold increase in  $\chi^{(3)}$  from near infrared excitation ( $\lambda_1 = \lambda_2 = \lambda_{2'} = 1300$  nm) to visible excitation ( $\lambda_1 = 495$  nm and  $\lambda_2 = \lambda_{2'} = 615$  nm). However, all solvents tested<sup>i</sup> exhibited nonlinear susceptibilities on the same order of magnitude. Very low correlation was observed between the measured susceptibilities ( $R^2 = 0.46$  to a linear trendline). Higher correlation ( $R^2 = 0.75$ ) was observed when the aromatic molecules (benzene and pyridine) were excluded: this may be consistent with the observation that the nonresonant nonlinear susceptibility is enhanced when two-photon resonances are available,<sup>[139, 140]</sup> as the aromatic compounds would be expected to exhibit the lowest transition energies.

Beyond this limit from higher nonresonant susceptibilities, the previous electronic experiments were able to achieve similar absorbance over the same pathlength at much lower concentrations than our MnTPP samples: these experiments would be performed at concentrations of tens of nM<sup>[358]</sup> rather than hundreds of  $\mu\text{M}$ . It can be shown that this  $10^4$  reduction in concentration would be expected to increase the nonlinear susceptibility by the same factor. If we generalize this factor as  $\phi$ , this relationship can be shown by

---

<sup>i</sup>The solvents tested were acetone, acetonitrile, benzene, carbon tetrachloride, dichloromethane, methanol, octane, and pyridine.

recognizing that the same absorbance over the same pathlength implies  $\alpha$  to be the same for both samples. However,  $\alpha$  can be related to both the optical cross-section,  $\sigma = \alpha/N$ , and to the optical properties of a hypothetical  $ba$  transition,  $\alpha \propto N\mu_{ba}^2/\Gamma_{ba}^2$ ,<sup>i</sup> where  $\mu_{ba}$  and  $\Gamma_{ba}$  are the transition dipole and dephasing rate of the transition, respectively.[99] From the former relationship, we can see that a reduction in  $N$  by a factor of  $\phi$  must be accompanied by an increase in  $\sigma$  by a factor of  $\phi$  to maintain constant  $\alpha$ . Second, by combining the two relationships,  $\sigma \propto \mu_{ba}^2/\Gamma_{ba}^2$ , and the factor of  $\phi$  increase in  $\sigma$  implies  $\mu_{ba}/\Gamma_{ba}$  must increase by a factor of  $\sqrt{\phi}$ . However,  $\chi^{(3)}$  is proportional to  $N\mu_{ba}^4/\Gamma_{ba}^4$ ,<sup>ii</sup>[99] the factor of  $\phi$  decrease in  $N$  and factor of  $\sqrt{\phi}$  increase in  $\mu_{ba}/\Gamma_{ba}$  then suggests  $\chi^{(3)}$  should be increased by a factor of  $\phi$ . Thus, since the homodyne-detected signal scales with  $|\chi^{(3)}|^2$ , [99, 190] these visible experiments with MnTPP not only require resolving against a background that is  $10^4$  times stronger, but seek to detect signals that are weaker by a factor of  $\phi^2$ , corresponding to a factor of  $10^8$  when comparing MnTPP to these prior systems.

In Fig. 5.1, we have demonstrated one of the strategies that is employed for suppression of nonresonant background: introducing a delay between the pulses to time resolve the resonant signal.[121, 165, 360] However, this limits access to the initial dynamics, such as those visible in panels (F) and (G). Another strategy for suppressing nonresonant background is to rotate the polarization of the excitation fields in order to interfere different symmetry components of the nonresonant response.[146, 361] Experiments performed with different polarization combinations (not shown) indicate that there could be promise to this strategy, though care would need to be taken to ensure that the consequences of the rotated polarizations are understood with respect to the analyte's symmetry. Heterodyne detection is another strategy that has been employed in electronic spectroscopy,[362–371] permitting discrimination between the nonresonant and resonant response on the basis of resolving the phase of  $\chi^{(3)}$ . [122, 123, 353–355] However, such a strategy is poorly suited to frequency-domain methods: it is more effective in collinear geometries,[355] and the change in pointing while scanning light sources can introduce further experimental complications.[372]

---

<sup>i</sup>We note that this is the case for resonance, i.e.  $\omega = \omega_{ba}$ ; otherwise, the detuning factor  $|\Delta_{ba}|^2 = |\omega_{ba} - \omega - i\Gamma_{ba}|^2$  should be used in lieu of  $\Gamma_{ba}^2$ . The other contributions to  $\alpha$  are  $(4\pi\omega F\Gamma_{ba})/(\hbar cn)$ . [99] Since the experiments being compared are electronic,  $\omega$  and  $\Gamma_{ba}$  should be of the same magnitude, and  $F/n$  should be similar for most organic solvents. Otherwise,  $4\pi/\hbar c$  are constants.

<sup>ii</sup>Once again, we assume resonance ( $|\Delta_{ba}|^2 \approx \Gamma_{ba}^2$ ) and the other contributing terms ( $F/(4D\hbar^3)$ ) should be similar or constant.

---

CHAPTER 6

**Broadband Coherent Raman Spectroscopy**

## 6.1 Background

Interaction between a medium and light can result in the scattering of photons by the constituent molecules. The majority of these photons will be scattered without any loss of energy through Rayleigh scattering. However, some of the photons will exchange energy with the medium through Raman scattering. The change in the energy of the photon represents the energy associated with a vibrational quantum of one of the molecule's Raman-active vibrational modes. For the energy of the vibrational mode,  $\Omega$ , the exchange of energy will yield a photons of frequencies,  $\omega_{\text{out}} = \omega_{\text{in}} \pm \Omega$ . The two cases reflect the two available directions for energy exchange: the frequency of the output photon corresponds to the sum in anti-Stokes Raman scattering, extracting energy from a vibrationally-excited molecule; the frequency will decrease in Stokes Raman scattering, in which the scattering results in vibrational excitation of the molecule. Identifying the frequency shifts can provide insight into the Raman-active vibrations of the molecules constituting the medium.[373]

Raman scattering can be considered to be a four-wave mixing process in which the interaction between the incident photons and the medium is described according to the third-order nonlinear susceptibility,  $\chi^{(3)}$ .[99] This third-order nonlinear susceptibility allows the molecules of the medium to mediate interactions between the incident photons and the vacuum field corresponding to the zero-point energy.[99, 374] The third-order susceptibility will exhibit a broad nonresonant background in addition to resonances associated with the vibrational modes; scattering will be enhanced when the energy difference between the incident photons and the vacuum field match these resonant frequencies.[120–122, 135, 139, 143, 147, 148, 186, 354, 360, 375, 376] The susceptibility is considered to be a complex quantity; according to the standard treatment, the nonresonant contributions are assumed to be only real, while the resonant parts will add to both the real and the imaginary components of  $\chi^{(3)}$ .[122, 123, 353, 355] Spontaneous Raman scattering is adequately described according to only the imaginary part of the susceptibility.[353] In addition to being linear with the scattering cross-section,[137, 190] the third order susceptibility is proportional to the number density of the molecules.[190]

Since spontaneous Raman scattering involves an interaction with the vacuum field, the scattered photons lack coherence,[139, 148, 186] yielding very low signal levels due to the low sampling efficiency.[186] The low efficiency limits the utility of spontaneous Raman scattering, preventing its application to media with high levels of background signal that may overwhelm the Raman scatter, or in which the acquisition times required may limit the ability to track the dynamics of short-lived species.[136, 377] Signal may be enhanced through electronic resonance, but electronic resonance may also enhance the background through fluorescence.[139,



378] It is also possible to increase the excitation power, but there are often limits to the extent that this is feasible.[148, 376]

Many of the disadvantages of spontaneous Raman scattering can be overcome through coherent Raman scattering, a broad category of different Raman-based nonlinear optical methods. These coherent methods yield significantly higher signal-to-noise ratios,[190, 377] allowing significantly faster acquisition.[136, 360] While coherent Raman scattering is generally less sensitive to fluorescence,[136, 375, 379] the higher signal-to-noise levels often allow the usage of weaker fields, reducing fluorescence and risk of damage to the sample.[148] Coherent Raman scattering methods still access the third-order nonlinear susceptibility, but are generally implemented with synchronized fields at different frequencies;[186, 190] the frequency difference between the fields determines the vibrational modes accessed during the experiment, as well as whether the process corresponds to anti-Stokes or Stokes Raman scattering.[186] While some authors suggest the improvement in signal arises from a higher cross-section,[375] most appear to attribute the improved signal-to-noise ratio in coherent Raman spectroscopies to the cooperative buildup and emission of signal:[139, 148, 186] the coherence of the scattered photons allows significant improvement in the sampling efficiency.[186]

Development of the various coherent Raman spectroscopies has been motivated by the potential benefits offered by Raman scattering. It is traditionally more straightforward to obtain broadband vibrational information by Raman scattering,[375, 378, 380] while still allowing the use of narrowband methods employing more sensitive detection.[380] Additionally, Raman-based methods also offer promise in microscopy applications:[381, 382] while the frequencies necessary for infrared absorbance measurements cannot be focused as effectively, Raman scattering can be achieved with visible or near infrared frequencies that can be focused more tightly.[139, 148] Finally, while femtosecond spectroscopy can be performed in the infrared,[383–387] there are additional challenges in effectively generating the required ultrashort infrared pulses.[137, 166] Coherent Raman spectroscopies have been realized in a number of ways, with methods having been applied to a variety of relevant systems, including transition-metal complexes,[388] chlorophyll a,[136] and proteins such as bacteriorhodopsin.[389]

A straightforward approach to coherent Raman spectroscopy is stimulated Raman spectroscopy. The general strategy for this method is to introduce two fields of different frequencies and overlap them in the sample.[190] The sample mediates the four-wave mixing process between these fields; when the frequency difference matches the frequency of a Raman-active vibration, the interaction will be enhanced. In stimulated Raman spectroscopies, the interaction is gauged by measuring the intensity of one of the fields: four-wave mixing will result in attenuation of the pump or gain of the probe.[136, 190, 378] Since the technique is self-heterodyned,[190, 390] it exhibits a linear dependence on the imaginary part of  $\chi^{(3)}$ . This has the advantage of

yielding information only associated with the vibrational resonances rather than the nonresonant background; it also makes the signal proportional to the number density of the Raman-active species.[190] However, the signal can be difficult to detect, as it requires resolving very small changes on a large background.[136, 137, 190, 391] It should be noted that in this context, we are only considering stimulated Raman spectroscopy to involve methods of the manner described above: this name has also been used for techniques in which a laser is focused into a sample, and Raman processes result in enhancement of new frequencies at the onset of self-focusing and filamentation or plasma generation. While these methods have been described to gain insight into condensed systems, the mechanism generally results in extreme or abnormal conditions.[392–396]

Of particular interest is femtosecond stimulated Raman spectroscopy (FSRS), a multiplexed version of stimulated Raman spectroscopy.[397] FSRS is generally accomplished by combining narrow- and broadband pulses in a single experiment.[137, 398] These experiments may employ either two or three beams.[137, 391, 399] The two beams incorporated in most FSRS implementations are the Stokes probe and Raman pump; typically the probe is a broadband, femtosecond pulse and the pump is a narrowband, picosecond pulse.[137, 391, 397, 400] Like the more general method of stimulated Raman spectroscopy, when the difference in frequency between the pump and probe match a vibrational resonance, gain is observed in the probe:[136, 190, 378] however, by implementing a broadband probe, FSRS allows the simultaneous measurement of many Raman shifts rather than requiring continuous tuning of the fields:[378, 400] this facilitates faster data acquisition, enabling more averaging and a correspondingly higher signal-to-noise ratio.[400] While the probe pulse is broadband, the spectral resolution of the method is limited by the convolution of the pump bandwidth and the line width of the vibrational mode.[136, 137, 378, 391, 399] Some authors also have incorporated a third beam into the FSRS experiment: the actinic pump which is an additional femtosecond pulse.[137, 391, 399, 400] The presence of this third beam allows the preparation of a particular excited state that is probed at some delay by the Raman pump and Stokes probe.[137, 391, 399] Despite the picosecond duration of the Raman pump in these experiments, the temporal resolution with respect to probing the excited state is determined solely by the cross-correlation of the actinic pump and Stokes probe,[137, 378, 391, 399, 401] allowing FSRS to simultaneously have spectral resolution on the scale of the vibrational modes and temporal resolution of tens of femtoseconds.[137, 390, 399] Due to the nature of the method, FSRS does not require any phase matching considerations,[136] permitting implementation in either a collinear or noncollinear geometry.[137, 398]

However, despite the advantages, there are also some drawbacks to FSRS. Just like the more general stimulated Raman spectroscopy, FSRS requires the ability to reliably measure small changes associated with the Raman gain on a large background.[136, 190, 391] Thus, while data can be acquired rapidly due to

the broadband nature of the technique,[400] achieving high signal-to-noise ratios does require averaging to overcome the otherwise inherent low signal-to-noise ratio.[137] There are also artifacts that can manifest in the data. While contamination from fluorescence is not considered to be a problem,[378, 390] transient absorption and stimulated emission can occur, manifesting as broad features in the Raman gain spectrum.[136, 137, 378] However, the application of shifted excitation Raman difference spectroscopy[402, 403] has been demonstrated to allow these artifacts to be corrected.[378] Trying to extend the method to resonant excitation or anti-Stokes configurations results in negative signals and complicated line shapes.[137, 398, 400] Finally, the use of a sufficiently strong pump has been shown to introduce cross-phase modulation in the probe;[136, 137] however, ensuring a smooth probe spectrum and shallower change in the pump's temporal envelope can minimize the consequences of phase modulation,[136] as can fibrillation of the pump[378] in a manner similar to correcting for scatter interference in other spectroscopies.[404, 405]

An alternative approach, Raman induced Kerr effect spectroscopy (RIKES), to broadband Raman has been proposed in the literature to overcome the large background inherent to FSRS.[397] This method is based on the optical Kerr effect: propagation of an intense, polarized pump results in an intensity-dependent change in the refractive index, inducing a temporary birefringence within the medium.[406] The birefringence is a result of the response of the medium, and the change may involve electronic, vibrational, rotational, or intermolecular contributions.[406–408] The induced birefringence will also affect other fields co-propagating through the medium by cross-phase-modulation. Specifically, if a linearly-polarized probe is introduced, the anisotropic change in refractive index will induce a change in the field's polarization state.[377, 406] Monitoring the change in the transmission of this probe through a crossed polarizer then informs on the resonant and non-resonant response of the medium through the third-order nonlinear susceptibility.[190, 377, 379, 397, 406–411] While this method has been applied to electronic resonances,[407, 410, 411] in RIKES, the goal is to specifically probe the resonance enhancement in the Kerr effect when the pump and probe frequencies differ by the frequency of one of the medium's Raman-active vibrational modes.[190, 377, 379, 397, 406]

Much like FSRS, RIKES does not require phase matching considerations,[377] allowing it to be performed in either a collinear or a noncollinear geometry.[190, 377, 379, 406] Broadband implementations of RIKES have also been reported.[379, 397] In contrast to FSRS, RIKES is dependent upon both the imaginary and real parts of the nonlinear susceptibility;[409, 410] thus nonresonant background is a concern,[190, 377, 397, 406] and the variety of mechanisms capable of contributing to the optical Kerr effect can yield background signals exhibiting dynamics.[407, 408, 410] However, circular polarization of the pump results in suppression of the nonresonant background when Kleinmann symmetry is valid.[190, 377, 397] An alterna-

tive approach to resolving challenges with nonresonant background is the introduction of a local oscillator for heterodyne-detection.[190, 379, 409, 410] This also has the added benefit of enhancing the sensitivity of the technique,[379] though it has been shown that RIKES can achieve similar signal-to-noise ratios to FSRS without optimization.[397] The sensitivity of RIKES can also be improved with enhancement through electronic resonance.[379]

While FSRS and RIKES have trivial phase matching, it is also possible to perform coherent Raman spectroscopy through a phase matched process: coherent (anti-)Stokes Raman spectroscopy. While the Stokes Raman based spectroscopy (CSRS) has been demonstrated,[186] the anti-Stokes process, CARS, is more common.[120–124, 139, 140, 143, 146–148, 353–357, 360, 375, 376, 380, 412, 413] While some authors have implemented pulse-shaping methods that allow CARS to be implemented with a single source,[122, 354] the general approach for CARS is based upon spatial and temporal overlap of two or three fields in a medium.[120, 121, 135, 139, 143, 147, 148, 186, 360, 375, 376] In the three pulse sequence, the pulses provide the Raman pump,  $\omega_P$ , the Stokes field,  $\omega_S$ , and the probe pulse,  $\omega_{P'}$ :[165, 354, 360] when reduced to two fields, the interaction with the probe field is replaced by a second interaction with the pump,  $\omega_{P'} = \omega_P$ .[120, 121, 135, 139, 143, 147, 148, 186, 360, 375, 376] The three interactions mediated by the medium will occur through the third-order susceptibility, yielding an output at the frequency  $\omega_{AS} = \omega_P - \omega_S + \omega_{P'}$ .[120–122, 135, 139, 143, 147, 148, 186, 354, 360, 375, 376] This illustrates the main advantage of CARS: since we require  $\omega_P > \omega_S$  for the anti-Stokes process,  $\omega_{AS}$  will always be a unique frequency and blue-shifted relative to the excitation fields. This makes CARS detection robust to scatter and fluorescence.[139, 190]

It is most common to implement CARS with homodyne detection.[120, 121, 123, 124, 139, 140, 143, 146, 148, 186, 356, 357, 360, 375, 376, 380, 412, 413] However, homodyne detection of  $\omega_{AS}$  will yield a signal proportional to  $|\chi^{(3)}|^2$ .[190] This introduces two main limitations to the method. First, because  $\chi^{(3)}$  is proportional to the number density ( $N$ ), homodyne detection results in signal scaling as  $N^2$ .[99, 122, 148, 190, 354] While this is valuable when the molecule of interest is a majority species in the sample,[122] it makes detection challenging for dilute species,[190, 354] imposes a limit on the sensitivity of the technique,[355] and makes quantification more difficult.[122, 353, 355] Additionally, the scaling of the homodyne-detected signal with  $|\chi^{(3)}|^2$  results in the signal containing contributions from both the imaginary and real parts of the nonlinear susceptibility. Contributions from the nonresonant response results in a background over which it is ideally possible to observe resonance enhancement when  $\omega_P - \omega_S$  matches the frequency of a Raman-active vibrational mode.[120–122, 135, 139, 143, 147, 148, 186, 354, 360, 375, 376] This can still introduce significant limitations.[121, 123, 139, 148, 165, 190, 355, 357, 360] The interference between the real components from the resonant and nonresonant responses of the medium distorts the vibrational line

shape.[136, 190, 353] Excitation at visible frequencies,[140, 148] especially when a two-photon resonance is available,[139, 140] can introduce significant levels of nonresonant background. While near infrared excitation can reduce this background,[140, 148] the scaling of the signal with  $N^2$  can still allow the nonresonant response to overwhelm the resonant signal through a larger number density in many applications.[121] Though femtosecond excitation allows more efficient delivery of higher peak powers without concern for damage or heating,[140, 376] it is also important to match the excitation bandwidth of at least one interaction to the line width of the vibrational modes: besides the spectral resolution made available by picosecond pulses,[139, 140] the increasing bandwidth of increasingly shorter pulses will eventually saturate the spectral width of the resonant process; beyond this point, the resonant process will be enhanced no further, while the nonresonant signal strength will continue to increase.[139, 140, 146, 356, 357] Many techniques have been shown to help suppress nonresonant background, though each has limitations and drawbacks. Phasing of the excitation fields by pulse shaping has been shown to help improve the resolution of the signal.[143] Polarization control can also be used by choosing polarizations for the excitation fields such that Kleinmann symmetry predicts the cancellation of nonresonant signal.[143, 146, 361] Time resolving the signal by delaying the final interaction (the probe field) also allows reduction of nonresonant background: by introducing an appropriate delay, the probe ideally only samples the free-induction decay of the induced vibrational coherence.[121, 165, 360] However, in highly scattering samples, efforts to control phase and polarization can be disrupted.[121] Meanwhile, changing the polarization of the excitation fields or delaying the arrival of the probe reduces the signal available.[355] Additionally, there are advantages to using high numerical aperture objectives in CARS; however, under such conditions, the paraxial approximation breaks down[139] and it is difficult to ensure polarization purity.[139, 414]

An alternative strategy to overcome the challenges of nonresonant background is the implementation of heterodyne detection[122, 353–355] due to its advantages. By interfering the CARS signal with a local oscillator, the heterodyned signal is proportional to the electric field of the CARS signal, rather than the intensity of the field;[122, 353–355] the signal is therefore proportional to  $\chi^{(3)}$ , rather than  $|\chi^{(3)}|^2$ . This leaves the signal proportional to the number density,[123] making quantification more straightforward[122, 353, 355] and simplifying the detection of weaker species.[190, 354, 355] The interference with the local oscillator can amplify the signal, improving sensitivity.[355] Heterodyne detection also allows the real and imaginary components of the nonlinear susceptibility to be resolved:[353–355] as the nonresonant background is predominantly associated with the real component of the nonlinear susceptibility, this allows the resonant response to be isolated.[122, 123, 353, 355] Despite these advantages, heterodyne detection is rarely implemented: while some authors have employed a pulse shaper to achieve heterodyne detection,[122, 354] it generally

requires an additional source to supply the local oscillator.[354] Additionally, due to the phase-matching of the process, it is really only practical to implement heterodyne detection in a collinear geometry.[355]

The phase matching requirements of CARS also provides the other challenge in implementing the technique. While RIKES and FSRS are satisfied by a trivial phase matching in the same manner as transient absorption,[136, 377] phase matching is important to consider in the CARS experiment. Like other nonlinear techniques, CARS must be performed such that we simultaneously satisfy the energy conservation condition,  $\omega_{AS} = \omega_P - \omega_S + \omega_{P'}$ , [120–122, 135, 139, 143, 147, 148, 186, 354, 360, 375, 376] and momentum conservation,  $k_{AS} = k_P - k_S + k_{P'}$ . [135, 361] Different approaches have been used to satisfy the phase-matching of CARS, but a common one is the BOXCARS geometry, in which the three input fields and the output occupy four corners of a rectangle.[120, 121, 135, 147, 186] However, this alignment can require relatively significant angles.[186] Additionally, it can be difficult to simultaneously phase match the CARS processes corresponding to different vibrational frequencies over a broad range of Raman shifts,[120, 136, 137] as changing the frequencies of the fields necessitates the use of different input angles.[135] The effects of phase matching can also complicate the interpretation of observed line shapes; [120, 147] care must be taken in alignment and focusing, as the presence of higher-order transverse modes[205] and the Guoy phase shift[139, 203] can both complicate the interpretation of phase matching. However, there are some situations where phase matching can be neglected. If the interaction region is short,[139] phase matching can be ignored: in the limit of minimal depletion of the excitation fields, signal intensity is proportional to  $\text{sinc}^2(L\Delta k/2)$ , where  $L$  is the interaction length and  $\Delta k$  is the phase mismatch; short pathlengths then make the experiment less sensitive to phase matching. Alternatively, if dispersion is sufficiently weak, such as in a gas, the phase matching condition reduces to the energy conservation condition.[135] Broadband phase matching has also been proposed by introducing a wide-angle probe to simultaneously satisfy the phase-matching of different processes; such an alignment necessitates moving the detector to measure the intensity of CARS signal associated with different Raman shifts, however.[135]

The concept of reducing the constraints of phase matching with sufficiently wide-angle excitation has lead to the implementation of CARS in microscopy.[139, 140, 146, 148, 165, 355–357, 375, 380, 412] In this application, CARS provides a sensitive, label-free method of imaging; [165, 357, 380, 412] additionally, the dependence of the signal upon the overlap of multiple beams improves the spatial resolution.[148] In microscopy, the limit of phase matching the CARS process can be overcome by the use of high numerical aperture objectives: this provides sufficiently wide-angle excitation so as to relax the phase matching condition,[139, 140, 146–148] as well as reducing the interaction length.[139] High numerical aperture objectives even allow collinear geometries,[146] facilitating the application of heterodyne detection.[355] The tighter fo-

cus also increases spatial selectivity[139, 375] and improves the image quality.[139] However, high numerical aperture objectives cannot be implemented for all systems, and the filtering schemes necessary to isolate the CARS signal can result in a loss of sensitivity.[147]

While a few reported implementations of CARS employ only picosecond[139, 148, 355] or femtosecond[120, 122, 143, 147, 354, 357, 413] excitation, many other implementations of CARS[121, 146, 186, 353, 356, 360, 375, 376, 412] - as well as various implementations of FSRs[136, 137, 378, 389–391, 398, 399, 401, 415] and RIKES[379, 397] - have sought to achieve multiplexing while retaining spectral resolution on the order of the line width of vibrational modes.[390, 401] While this could be achieved by synchronization of femtosecond and picosecond lasers,[390] it is difficult to reliably achieve synchronization without timing jitter.[376, 415] While continuum generation is possible with picosecond pulses,[318, 320, 332, 416] the higher peak intensity of femtosecond pulses generally yields higher efficiencies[417] since the nonlinear processes associated with light generation are generally nonresonant.[139, 140, 146, 356, 357] As a consequence, rather than start with picosecond pulses and achieve multiplexing through continuum generation, most reports describe starting with femtosecond pulses and the application of a variety of strategies to improve spectral resolution.[136, 137, 165, 186, 356, 357, 376, 378, 380, 389–391, 397, 399–401, 412, 417–419] In addition to reporting strategies for narrowing their excitation pulses, some authors also give consideration to increasing the breadth of their pulses in order to maximize the range of Raman shifts accessible.[122, 354]

Many of the efforts to extend the accessible range of Raman shifts are based upon white light generation.[136, 137, 356, 375, 378–380, 397, 398, 420] A brief overview on the generation of white light has been provided in Ch. 5. However, an alternative strategy that has been employed for generating broadband pulses is cascaded frequency mixing processes.[400] By crossing two beams with wave vectors  $k_1$  and  $k_2$ , various mixing processes are cascaded to form spatially resolved orders satisfying various phase matching conditions generalized  $(n + 1)k_1 - nk_2$ . [282–284, 421] These cascaded side bands are broad and tunable,[283, 306, 400] providing an alternative to white light generation. However, unlike white light generation, these side-bands are reasonably well-compressed pulses with durations on the order of the driving fields.[283, 400]

Strategies for developing narrowband pulses from broadband sources are diverse, but can be considered to fall into three categories: filtering, in which only a small bandwidth from the original broadband source is retained; methods based on appropriate chirp of the broadband source; and, narrowing through parametric processes in a nonlinear crystal. Some of these methods also introduce picosecond optical parametric amplifiers that are pumped by the narrowed source, providing the capability to tune the narrowed pulse.[391, 400, 415]

Three main strategies for filtering broadband sources have been reported in the literature. All three are

inherently inefficient, with reported efficiencies less than 0.3%, since they are predicated on passing only a small bandwidth from the original source.[399, 417, 419] The simplest filtering scheme that has been reported is the use of a pair of commercial filters that together reduced the bandwidth to  $17 \text{ cm}^{-1}$ . [136, 137] This corresponds to a pulse duration slightly shorter than one picosecond (800 fs), but this strategy restricts the tuning of the pump according to the availability of appropriate filters. A limited ability to tune the Raman pump was introduced through grating-based filters; the design is based upon a  $4f$  pulse shaper: two gratings separated by a distance of  $4f$  and by two lenses (focal lengths of  $f$ ), with the lenses positioned to have a shared image plane at which a slit is positioned. [121, 186, 378] Some authors have simplified the configuration by using a flat mirror at the image plane, allowing the use of a single grating. [380, 415] These grating-based filters allow significantly longer pulse durations, up to 8-9 picoseconds, and the ability to tune within the bandwidth of the broadband source. [378] However, in order to achieve such short pulses, it is necessary to use very small slits; this can introduce perturbations to the mode. [390] The symmetry of the resulting pulses have also been reported to introduce ringing, [390] though some authors have suggested it can be reduced for some temporal profiles. [400] Besides the inherent inefficiency due to the restricted bandwidth, grating-based filters suffer from further inefficiencies from diffraction off the grating. [390] The final filtering strategy that has been described is the use of Fabry-Pérot etalons. [390] The motivation for filtering using Fabry-Pérot etalons is their earlier application in other spectroscopies, such as sum-frequency generation. [422] Fabry-Pérot etalons offer high efficiency at the central color and are capable of very narrow bandwidths (as low as  $3 \text{ cm}^{-1}$  reported). [390] The narrowed pulses exhibit an exponential profile in the time domain: such a profile helps enhance the vibrationally resonant signal relative to the nonresonant background by matching the dephasing of the coherence. [390] While it can be difficult to simultaneously achieve a sufficient free spectral range and a narrow bandwidth affordably, etalons can be combined with other filters to compensate for the free spectral range. [423] The main additional limitation associated with Fabry-Pérot etalons is that the cost can be significant. [390]

The inefficiency associated with spectral filtering led a variety of attempts to improve efficiency through chirped pulses. The first of these methods has been termed “spectral focusing.” [412] This method was motivated by an earlier observation that the presence of chirp in the excitation fields can actually improve the resolution of the CARS process. [146] An early implementation of applying chirp followed this observation by overlapping a broadly chirped pulse and a compressed pulse: as the interaction necessary for the CARS process is only possible during temporal overlap, the resolution is controlled by the “temporal slit” resulting from the chirp rate and the femtosecond pulse duration. [376] However, by applying an equal degree of chirp to both the pump and Stokes pulses, other authors have shown the potential to apply the entire bandwidth of



broadband pulses to drive processes corresponding to a target Raman shift: with appropriate adjustment of chirp and delay, the instantaneous frequencies temporally overlapped correspond to excitation of a particular vibrational mode throughout the entire duration of the pulse.[356, 357, 401, 412] An alternative method for improving resolution through chirp involves spectral compression by the sum-frequency generation of counter-chirped pulses. In this scheme, a pulse is split to yield two pulses; each pulse is passed through a stretcher to apply chirp: however, one pulse has a positive chirp applied, while the other pulse is negatively chirped. These pulses are then mixed to yield a narrow band pulse.[391, 400, 424]

However, this method involving counter-chirped beams requires careful alignment of a pair of stretchers so as to add equal chirp to both beams;[419] a handful of authors have reported an alternative that bypasses this complication. Rather than apply chirp, these authors use the large group velocity mismatch between a fundamental and its second harmonic to impose a very narrow phase matching bandwidth on the second-harmonic generation process.[165, 399, 417–419] This allows tuning of the pulse-duration by changing crystal material - and therefore the group velocity mismatch - or by changing the crystal length.[399] However, the narrow phase-matching bandwidth does not significantly reduce the efficiency. Rather, the spectral compression can be considered to arise from a series of mixing processes between frequencies of  $\omega_0 + \Delta\omega$  and  $\omega_0 - \Delta\omega$ : for any value of  $\Delta\omega$ , the sum-frequency will be  $2\omega_0$ .[417] Even without the ability to simultaneously phase-match the sum-frequency generation for every value of  $\Delta\omega$ , the cooperation of the sum-frequency and second-harmonic generation processes towards spectral narrowing make this method very efficient,[399, 417] with efficiencies reportedly approaching 40%. [417] The main limitation to this method is in the resulting line shape: as the mixing process is most efficient at the beginning of the crystal - when the pulses are most intense - the pulses exhibit a temporal profile with a sharp edge and an approximately quadratic tail.[399, 417, 418] However, unlike Fabry-Pérot etalons, the tails of these spectrally-compressed pulses decay in the reverse direction relative to the vibrational dephasing: the edge of the pulse artificially attenuates the free-induction decay of the coherence, introducing ringing in the spectrum.[399] While a filtering scheme to improve the line shape and reduce this ringing has been proposed, it calls for a grating-based spectral filter.[399] Additionally, it has been reported that introducing some phase-mismatch to the second-harmonic generation can influence the line shape.[417] An alternative solution has been the introduction of periodically-poled crystals, such as periodically poled lithium niobate or stoichiometric lithium tantalate.[165, 417–419] These engineered materials exhibit attractive properties for spectral compression: high group velocity mismatch, high second-order susceptibility, and periodic poling to avoid spatial walk-off.[417] However, by tuning the periodicity of the materials, it has been demonstrated that it is possible to engineer desired temporal profiles for the spectrally compressed pulse.[165, 418, 419]

A variety of methods have been employed to study the vibrational structure of the photosystem II and various co-factors of the protein,[57] including infrared absorption[60, 62, 84] and (resonance) Raman.[58, 59, 61, 79] However, the number of transitions available in photosystem II results in very complicated absorption spectra;[62] the resonance-enhancement yields simpler spectra, but the use of spontaneous Raman results in relatively weak signals[58, 59, 61] and fluorescence can be a concern.[61] Coherent Raman spectroscopies offer the potential to improve the sensitivity of these latter experiments and provide intrinsic resistance to fluorescence. For testing the application of broadband coherent Raman spectroscopy, benzene was used as an initial test sample due to the strong Raman-active mode at  $992\text{ cm}^{-1}$ . [406] Manganese tetraphenylporphine was selected as a model system for exploring resonance enhancement: previous reports indicate that at least one of the electronic transitions (Band V, near 480 nm) is believed to exhibit strong contributions from the manganese, and that excitation of this band results in resonance-enhancement of the Raman mode associated with the low frequency vibration between the manganese and the axial ligand.[309]

## 6.2 Experimental Deviations

The broadband CARS experiments reported in this section were performed as four color experiments. The two femtosecond TOPAS-C provided two femtosecond pulses as the Raman pump ( $\bar{\nu}_1$ ) and Stokes ( $\bar{\nu}_2$ ) pulses and were tuned so the frequency difference between the TOPAS-C was close to the frequency of the target vibrational mode. The Raman probe pulse was derived from the residual fundamental from the Spitfire Pro XP regenerative amplifier. In contrast to the standard alignment of the fundamental, the beam was not turned directly into the appropriate delay line. Rather, a set of three mirrors was introduced to allow the introduction of a volume Bragg grating for spectral narrowing with an appropriate angle between the incident and diffracted beams.

While the enhancement of vibrational dephasing attributed to the temporal profile of pulses narrowed with Fabry-Pérot etalons[390] was attractive, calculations suggested that it would be difficult for a reasonably affordable etalon to simultaneously provide wide tuning capability, high throughput, narrow spectral profiles, and a wide free spectral range. However, it has been reported that etalons with a narrow free spectral range may be combined with volume Bragg gratings to simultaneously achieve narrow spectral profiles and broad free spectral ranges.[423] These gratings are prepared by imaging a sinusoidal refractive index grating in a material; based on the period of these modulations ( $\Lambda$ ), the index of the material ( $n$ ), and the incident angle

( $\theta$ ), a very narrow bandwidth centered around a wavelength,  $\lambda_0$ :

$$\lambda_0 = \cos \left( \arcsin \left( \frac{\sin(\theta)}{n} \right) \right) \frac{\Lambda}{2n} \quad (6.2.1)$$

is diffracted with high efficiency.[423]

The grating (Optigrate; Oviedo, FL) employed in these experiments was 2.1 mm x 5 mm x 5 mm and designed to operate around a central wavelength of 805.3 nm, yield a spectral width of  $\sim 0.25$  nm (FWHM), and achieve  $> 97\%$  diffraction efficiency. Testing indicated a  $\sim 35^\circ$  angle between the incident beam and the diffracted beam optimized the overlap of the diffracted color ( $\sim 785$  nm at  $30^\circ$  and  $\sim 795$  nm at  $40^\circ$ ) with the center of the regenerative amplifier output; it should be noted, though, that these measurements were collected with an OceanOptics USB-2000 that exhibits a sharp decrease in response near 800 nm and consequently reports distorted spectra for  $\sim 35$  fs pulses centered near 800 nm. The central color observed in these experiments was  $\sim 794$  nm; however, we are not confident that the Jobin Yvon MicroHR monochromator provided sufficient resolution to reliably characterize the spectrum. Consequently, Raman shifts reported in all CARS spectra have been determined by matching the observed vibrational features to the reported frequencies for the sample; sources for the frequencies are for benzene ( $993 \text{ cm}^{-1}$ ),[425] benzonitrile ( $1601 \text{ cm}^{-1}$ ),[426] and pyridine ( $992$  and  $1031 \text{ cm}^{-1}$ ).[186] The temporal profile of the diffracted pulse, shown in Fig. 6.1, was determined through a nonresonant CARS process in carbon tetrachloride with the TOPAS-C tuned to  $\bar{\nu}_1 = 8000 \text{ cm}^{-1}$  and  $\bar{\nu}_2 = 7000 \text{ cm}^{-1}$ . It should be noted that this spectrum does represent convolution of the temporal profile of the diffracted pulse with the TOPAS-C output; however, as the durations of the latter two pulses are  $\sim 40$  fs, the convolution should be a minor effect. With the conventions of delay on the table, the tail of the diffracted pulse should match the dephasing of the vibrational mode in a manner similar to an etalon.

Phase matching angles for these experiments were calculated within the cw approximation for the center of each pulse. These calculations indicated two key details. First, it proved necessary to use a faster focusing mirror for all experiments: the angles calculated for near infrared excitation required a  $f = 50$  cm mirror, while for the experiments with visible excitation this had to be reduced further to  $f = 20$  cm. The other key detail indicated by these calculations was the narrow phase matching bandwidths: within this cw approximation, it was anticipated that the phase matching bandwidth would be significantly narrowed in the visible.

The CARS experiments were performed as one- or two-dimensional acquisitions involving only the monochromator frequency and the relative delays. The TOPAS-C were set to generate particular colors

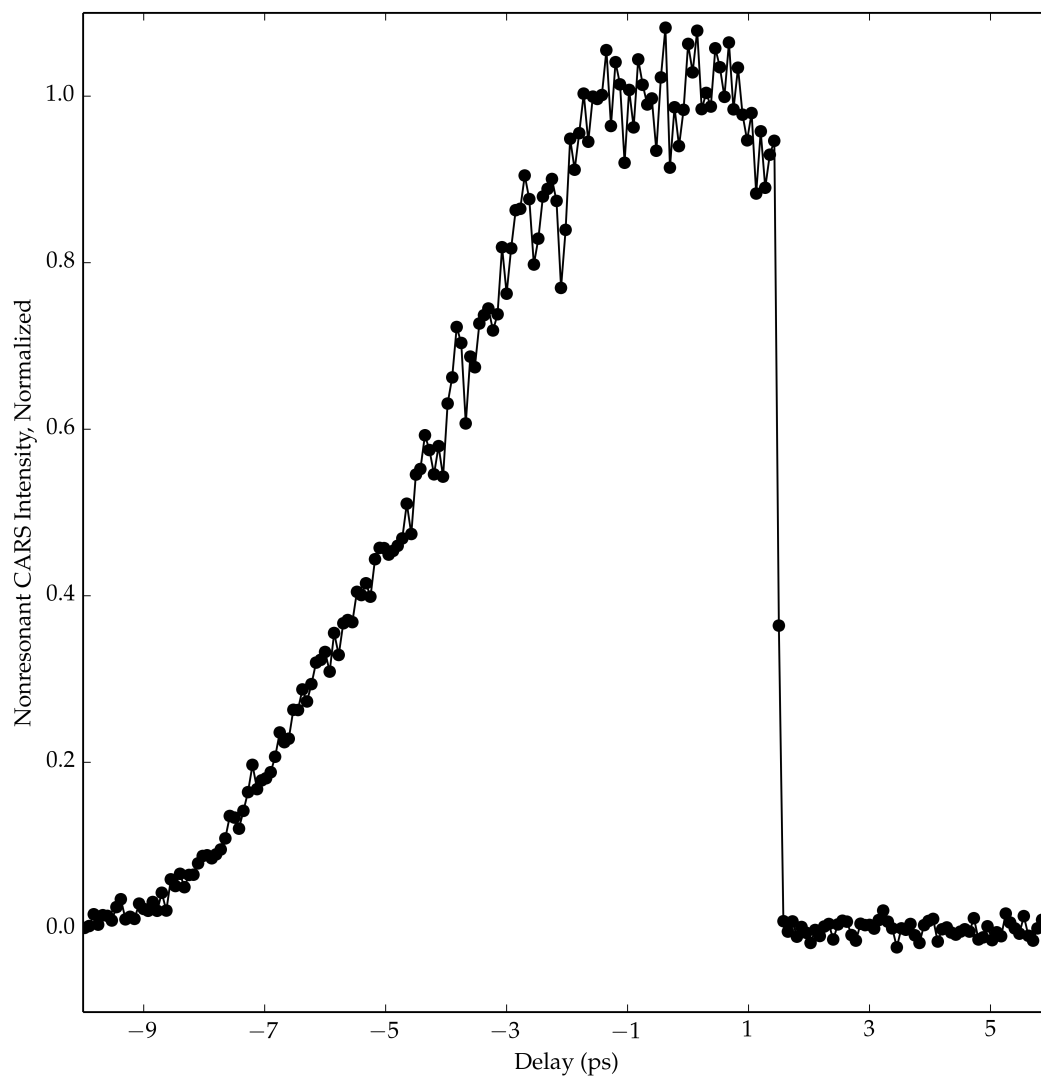


Figure 6.1: Temporal profile of the narrowed  $\sim 794$  nm probe as determined by nonresonant CARS ( $\bar{\nu}_1 = 8000 \text{ cm}^{-1}$  and  $\bar{\nu}_2 = 7000 \text{ cm}^{-1}$ ) in carbon tetrachloride.

for  $\bar{\nu}_1$  and  $\bar{\nu}_2$ . The convolution of the spectral content of these pulses determined the accessible vibrational frequencies; [120–124] by scanning the monochromator, we determined the frequencies of the vibrational coherences created by this convolution based upon the intensity of the upconverted Raman probe at each frequency. As before, the preamplifier limited reliable application of available photomultiplier tubes; a silicon photodiode was used for detection instead. Reported usage of “spectral focusing” [356, 357, 401, 412] indicated the importance of considering any chirp or other frequency modulation present in the pump and Stokes pulses. Due to suspicions of the upconversion processes in the TOPAS-C, this was expected to be a particular concern in experiments using sum-frequency signal. Two-dimensional acquisitions monitoring the CARS spectrum as a function of relative delay between the pump and Stokes pulses suggested this was not a large concern in the near infrared (data not shown); similar scans collected with the pump and Stokes pulses derived from the sum-frequency signal process will be shown in the Results and Discussion.

### 6.3 Results and Discussion

Consistent with previous reports, [399, 417, 419] the use of filtering to achieve spectrally narrow pulses resulted in a dramatic reduction in beam energy. Prior to introducing the Bragg grating, we measured a per pulse energy of 40  $\mu\text{J}$  in the residual fundamental; with the grating in place, this energy was reduced to 370 nJ per pulse. Even with the reported  $> 97\%$  diffraction efficiency, these losses correspond to 0.9% efficiency; based upon the reported efficiencies of other filtering strategies, [399, 417, 419] this observed efficiency is consistent with the reduction in bandwidth. However, besides the limits to spectral resolution arising from a femtosecond probe, Fig. 6.2 shows that the picosecond probe also provides a high degree of discrimination against the nonresonant background. A theoretical foundation for this has been previously reported: [140] as the pulse duration decreases, both nonresonant and resonant signal increase; however, while nonresonant signal continues to increase, the resonant response only scales so long as the excitation bandwidth is less than or comparable to the vibrational line width. Consequently, under purely femtosecond excitation, the ratio of resonant to nonresonant signal is predicted to be quite small. [139, 140, 146, 356, 357] In Fig. 6.2, we show that even a single picosecond interaction is sufficient to improve this ratio.

All scans in Fig. 6.2 were collected under conditions of near infrared excitation:  $\bar{\nu}_1 = 8000 \text{ cm}^{-1}$  and  $\bar{\nu}_2 = 7000 \text{ cm}^{-1}$ . Under the conditions of the initial table alignment (femtosecond probe pulse), we measured the dynamics associated with both carbon tetrachloride ( $\text{CCl}_4$ ) and benzene ( $\text{C}_6\text{H}_6$ ). Most of the signal for both samples was consistent with the nonresonant response arising from cross-correlation of the three excitation pulses. However, in benzene, we do observe weak signal above the baseline at long delays,

consistent with the longer dynamics expected for a vibrational coherence. Nevertheless, the ratio of this signal to the nonresonant response at zero delay is very low: as the scale in (A) shows, it is approximately one to one hundred, which is reasonable in the context of previous calculations.[140] This contrasts with the behavior observed when the narrowed, picosecond probe is used, (B). The signal from carbon tetrachloride suggests that the weaker excitation from the picosecond probe yields a lower sensitivity, as the nonresonant signal is only two orders of magnitude over the baseline, rather than the three orders of magnitude in (A); this is consistent with the higher contrast expected due to the peak intensity available from femtosecond excitation.[140] In exchange for the lower sensitivity, though, (B) shows that we can achieve much greater specificity for the vibrational dynamics: where the femtosecond probe yielded a resonant to nonresonant ratio of about one to one hundred, the picosecond probe achieves ratios of about seven to ten, a seventy-fold improvement.

With the spectrally-narrowed probe, we explored the reliability, sensitivity, and resolution of broadband CARS with near infrared excitation ( $\bar{\nu}_1 = 8000 \text{ cm}^{-1}$  and  $\bar{\nu}_2 = 7000 \text{ cm}^{-1}$ ). A sampling of these results is reported in Fig. 6.3, 6.4, and 6.5. All three figures present a two-dimensional acquisition (A) reporting signal on a logarithmic (base-10) scale as a function of delay versus Raman shift; the delay corresponds to the relative delay of the probe relative to the temporally overlapped pump and Stokes pulses. Zero delay is defined according to the sharp falling edge in the nonresonant signal due to the rising edge of the probe pulse. (B) and (C) present one-dimensional views of the data: (B) presenting vertical (delay) slices, and (C) showing horizontal (frequency) slices. All slices shown in (B) and (C) are color- and style-coded to correspond to the vertical and horizontal, respectively, slices shown in (A).

Consistent with the Raman properties of carbon tetrachloride,<sup>i</sup> Fig. 6.3 shows no evidence of vibrational resonances for Raman shifts between  $850$  and  $1200 \text{ cm}^{-1}$ . This is evidenced by the sharp edge at a delay of  $0 \text{ ps}$ , and the broad, featureless spectral character across the frequency range. The dip near a Raman shift of  $850 \text{ cm}^{-1}$  is attributed to noise. The slices in (B) and (C) show that the nonresonant response in carbon tetrachloride gives us sensitivity of approximately one and a half orders of magnitude (signal levels above baseline) in these experiments.

In contrast to Fig. 6.3, the presence of a vibrational resonance yields a very clear signature in the two-dimensional spectrum, as shown for neat benzene in Fig. 6.4. In the two-dimensional spectrum, the vibrational resonance at  $993 \text{ cm}^{-1}$  is seen clearly above the baseline. Contrasting the vertical slices at  $975 \text{ cm}^{-1}$  and  $993 \text{ cm}^{-1}$ , the dashed and solid vertical slices respectively, we see in (B) that an exponential

---

<sup>i</sup>Available at [webbook.nist.gov](http://webbook.nist.gov).

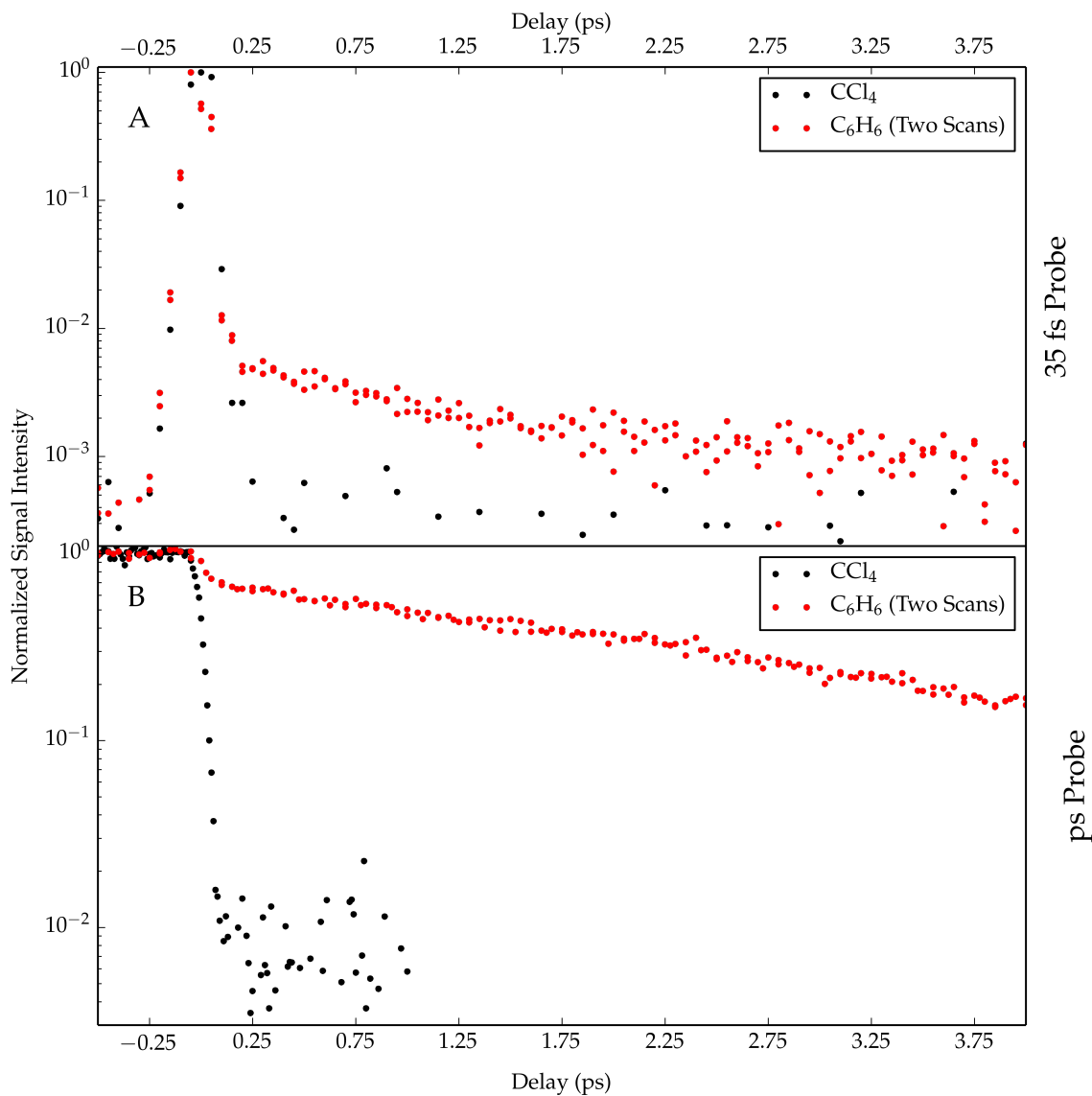


Figure 6.2: Comparison of CARS signal with ps and fs probe pulses. All scans report normalized signal versus the delay between the probe pulse and the overlapped Raman pump ( $\bar{\nu} = 8000 \text{ cm}^{-1}$ ) and Stokes ( $\bar{\nu} = 7000 \text{ cm}^{-1}$ ) pulses; the monochromator was set to the wavelength at which the CARS signal associated with benzene's  $993 \text{ cm}^{-1}$  vibrational mode was expected. (A) and (B) are the results for carbon tetrachloride and benzene with a femtosecond, 800 nm probe and the spectrally narrowed picosecond probe, respectively. The data presented for benzene represent all data accumulated over two scans.

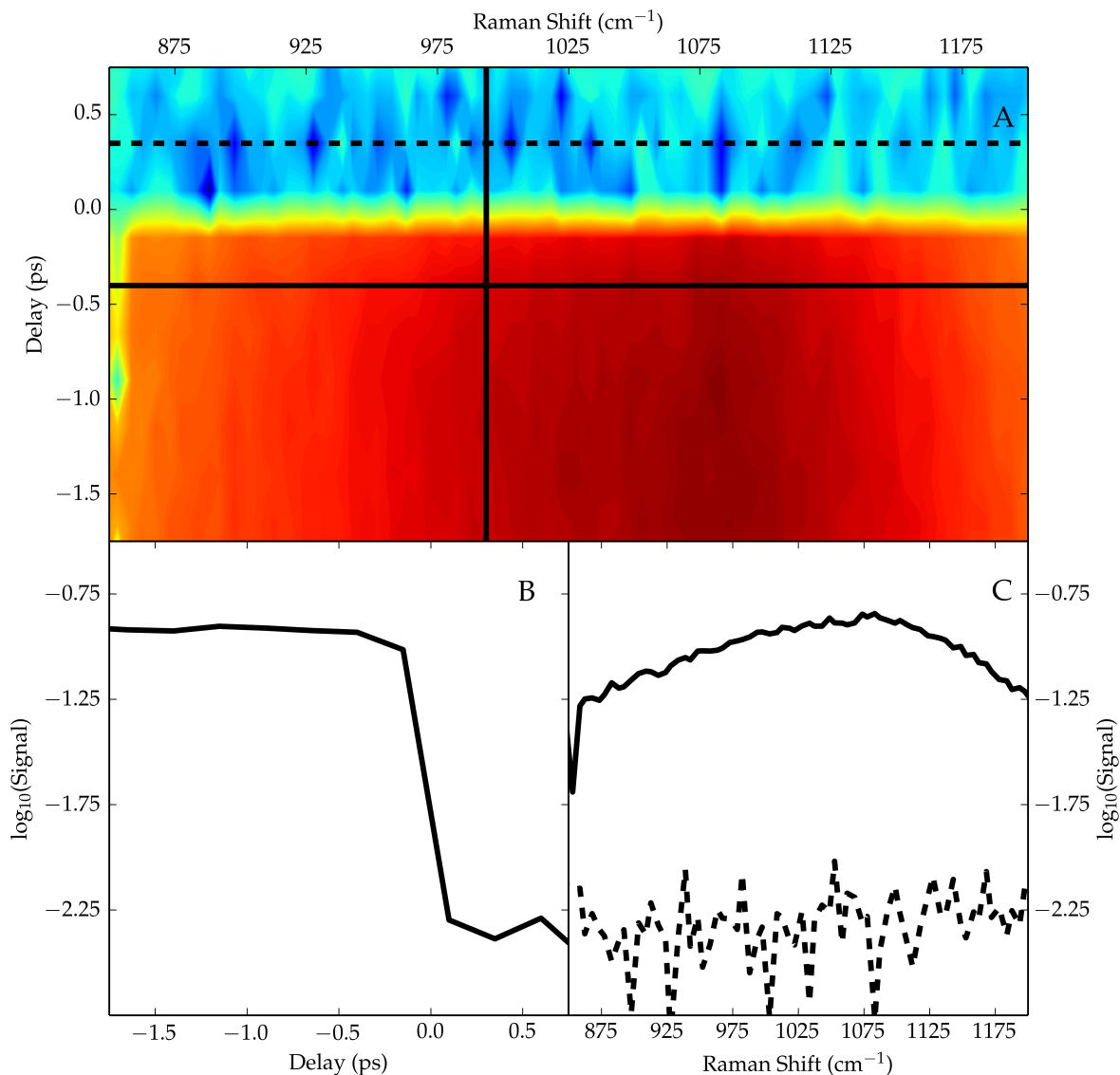


Figure 6.3: Broadband CARS of carbon tetrachloride ( $\text{CCl}_4$ ) with Raman pump pulse  $\bar{\nu}_1 = 8000 \text{ cm}^{-1}$ , Stokes pulse  $\bar{\nu}_2 = 7000 \text{ cm}^{-1}$ , and narrowband probe ( $\sim 794 \text{ nm}$ ). (A) Signal (base-10 logarithmic scale) as a function of delay and Raman shift. Delay is relative delay between the probe pulse and the overlapped Raman pump and Stokes pulses. Raman shifts are assigned on the basis of matching time-resolved vibrational resonances in benzene and pyridine to known values.[186, 425] The solid vertical line identifies the slice plotted in (B), and the solid and dashed horizontal lines represent the points from which the slices in (C) are derived. (B) and (C) are signal (base-10 logarithmic scale) versus relative probe delay (B) or Raman shift (C).



decay is clearly visible when the monochromator is set to detect resonant signal (Raman shift of  $993\text{ cm}^{-1}$ ), whereas signal is only present during pulse overlap when off resonance. In (C), the solid trace shows a horizontal slice of the signal during pulse overlap. In this slice, we see clear evidence of interference between the nonresonant background and the vibrational resonance in the dip in signal near  $1025\text{ cm}^{-1}$  - this is quite close to the Raman shift at which Levenson and Bloembergen observe a minimum resulting from this interference ( $1020\text{ cm}^{-1}$ ).<sup>[110]</sup> However, we observe nearly an order of magnitude of contrast between the resonant and nonresonant response; the improvement over the signal in Fig. 6.2 is attributed to more accurate setting of the monochromator: in the data acquired for Fig. 6.2, the monochromator was set based upon the expected wavelength for the CARS signal rather than the wavelength of maximum signal. Recall, the dispersion of the MicroHR monochromator limits our ability to know the frequency of the probe with high precision. In contrast to pulse overlap, time resolution of the signal - given by the dashed line in (C) - allows isolation of the vibrational resonance; consistent with concerns over the use of time resolution for nonresonant background suppression,<sup>[355]</sup> we do observe some loss of signal ( $\sim 12\%$  on the logarithmic scale). While the strong response of benzene does leave us with high sensitivity after these losses - signal approximately one and a half orders of magnitude over baseline - this loss of signal could prove a limitation with dilute species or those with weaker response.<sup>[355]</sup>

As expected, the narrowed probe pulse provides significant improvements in resolution. Not only is the vibrational lineshape in Fig. 6.4 distinguishable, but we see in Fig. 6.5 that we can clearly resolve two close vibrational modes. In Fig. 6.5, we show the CARS spectrum of a mixture of benzene and pyridine under near infrared excitation. These compounds exhibit vibrational frequencies very close to each other: benzene exhibits a Raman-active vibration at  $993\text{ cm}^{-1}$ ,<sup>[425]</sup> while pyridine exhibits a pair of resonances, one at  $992\text{ cm}^{-1}$  and the other at  $1031\text{ cm}^{-1}$ .<sup>[186]</sup> Signals consistent with the vibrational frequencies are present in the two-dimensional acquisition of (A). The time-resolved slice in (C), given by the spectrum in the dashed line, show that we achieve baseline resolution between the vibrations at  $992/993\text{ cm}^{-1}$  and the vibration at  $1031\text{ cm}^{-1}$ ; this is comparable with the resolution in the time-resolved CSRS results reported by Pestov et al, and both data sets appear to exhibit better resolution than the spontaneous Raman spectrum reported by the same authors.<sup>[186]</sup> We will also point out the dip in nonresonant signal near a Raman shift of  $1150\text{ cm}^{-1}$ ; we will address this feature later in this chapter.

In order to increase the applicability of these broadband Raman processes towards resonance enhancement, we sought to extend the methods towards visible excitation. The same methods were employed as were used to acquire the previously described near infrared excited CARS spectra, only substituting visible Raman pump and Stokes pulses generated through the TOPAS-C second-harmonic signal (SHS) or sum-

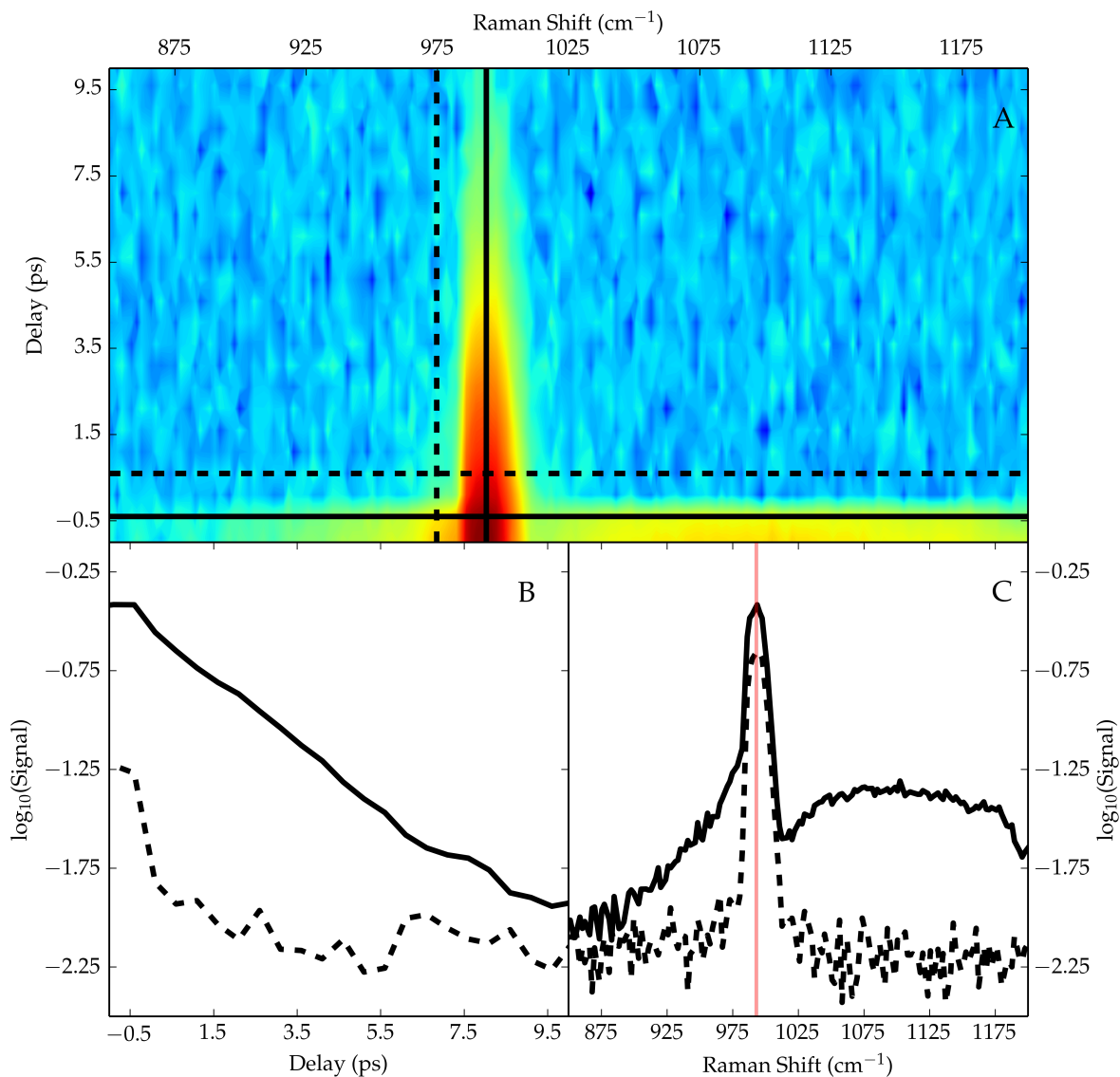


Figure 6.4: Broadband CARS of benzene ( $\text{C}_6\text{H}_6$ ) with Raman pump pulse  $\bar{\nu}_1 = 8000 \text{ cm}^{-1}$ , Stokes pulse  $\bar{\nu}_2 = 7000 \text{ cm}^{-1}$ , and narrowband probe ( $\sim 794 \text{ nm}$ ). (A) Signal (base-10 logarithmic scale) as a function of delay and Raman shift. Delay is relative delay between the probe pulse and the overlapped Raman pump and Stokes pulses. Raman shifts are assigned on the basis of matching the time-resolved vibrational resonance of benzene to its known value.[425] The solid and dashed vertical lines identify the slices plotted in (B), and the solid and dashed horizontal lines represent the points from which the slices in (C) are derived. (B) and (C) are signal (base-10 logarithmic scale) versus relative probe delay (B) or Raman shift (C). The faded red line in (C) marks the vibrational frequency of benzene,  $993 \text{ cm}^{-1}$ .

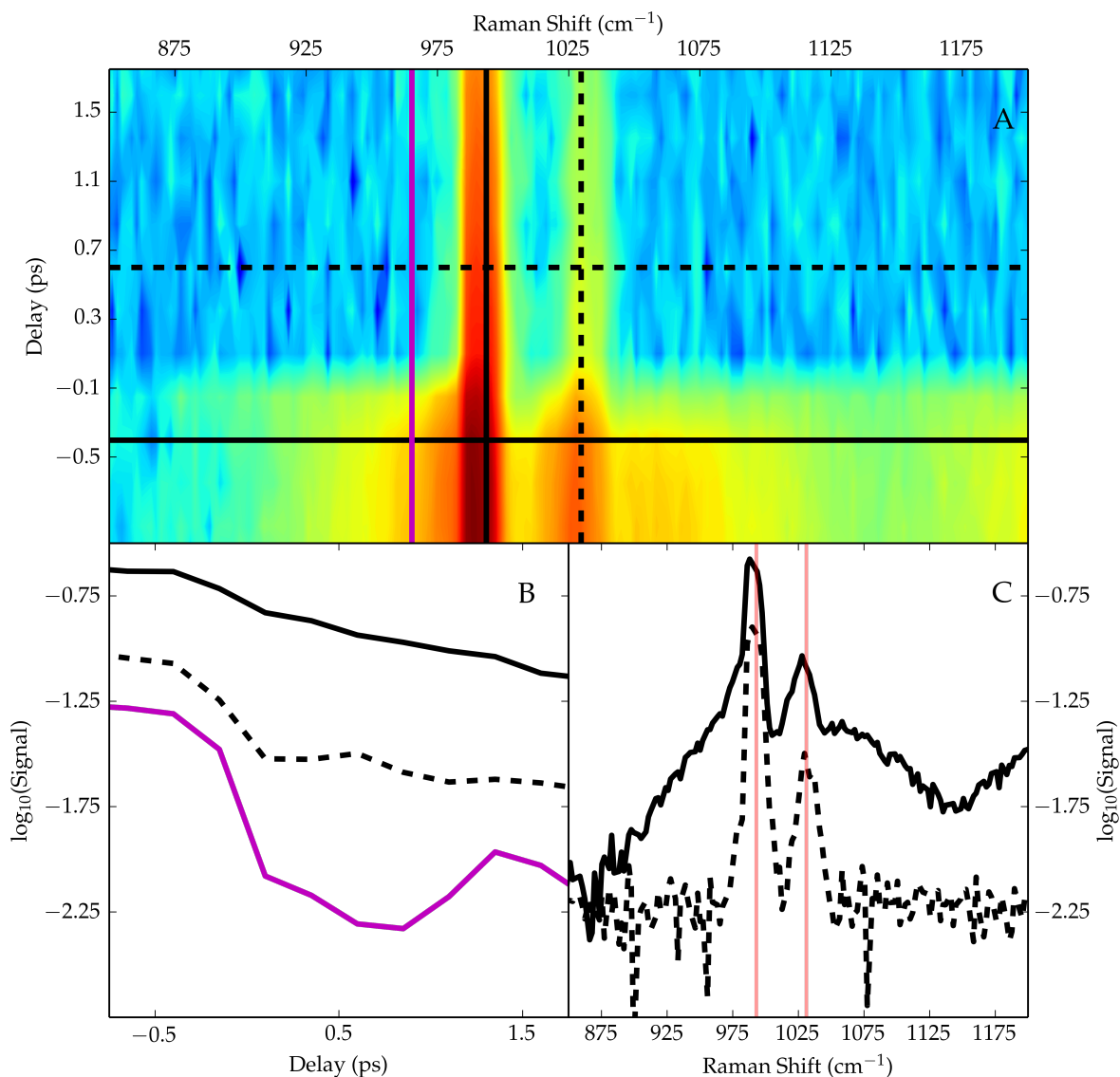


Figure 6.5: Broadband CARS of a mixture of benzene and pyridine ( $C_5H_5N$ ) with Raman pump pulse  $\bar{\nu}_1 = 8000 \text{ cm}^{-1}$ , Stokes pulse  $\bar{\nu}_2 = 7000 \text{ cm}^{-1}$ , and narrowband probe ( $\sim 794 \text{ nm}$ ). (A) Signal (base-10 logarithmic scale) as a function of delay and Raman shift. Delay is relative delay between the probe pulse and the overlapped Raman pump and Stokes pulses. Raman shifts are assigned on the basis of matching the time-resolved vibrational resonances of benzene and pyridine to known values.[186, 425] The vertical lines are color- and style-coded to match the slices plotted in (B), and the solid and dashed horizontal lines represent the points from which the slices in (C) are derived. (B) and (C) are signal (base-10 logarithmic scale) versus relative probe delay (B) or Raman shift (C). The faded red lines in (C) mark the vibrational frequencies of benzene and pyridine,  $993 \text{ cm}^{-1}$  and  $1031 \text{ cm}^{-1}$ .

frequency signal (SFS) processes. Fig. 6.6 shows the broadband CARS spectrum acquired for benzonitrile using SHS-derived pump and Stokes pulses. In this spectrum, we observe a feature consistent with the  $1601\text{ cm}^{-1}$  vibrational mode of benzonitrile. The dynamics exhibited are short but can be clearly resolved. The sensitivity of this signal is also weaker, which is consistent with the excitation pulses being derived from a second harmonic process. More energy is available from the SFS process, which was used to acquire the CARS data in Fig. 6.7.

We have previously discussed the problems that manifest upon upconversion of the idler in the TOPAS-C (see Ch. 4), and we have consequently speculated that the accumulated group delay and pump-signal group velocity mismatch may also manifest in the SFS process. For example, in experimental applications of the SFS process, it is not uncommon to see temporal profiles significantly broader than would be anticipated (see for instance the vertical line width in (E) of Fig. 5.1). Consequently, rather than collect CARS spectra studying the dynamics of the vibrational coherence, the two-dimensional acquisition of Fig. 6.7 seemed for more important. The results of this two-dimensional acquisition are signal (presented on a logarithmic scale) as a function of relative delay between the pump and Stokes pulses and the Raman shift (A). After background subtraction, the first moment of the signal was calculated, with the result overlaid in (A) as the black line; it should be noted that the noise at Raman shifts less than  $950\text{ cm}^{-1}$  yielded a handful of meaningless data points - such points have been ignored. As the remaining points show, there does appear to be some degree of frequency-modulation, with the first moment exhibiting a change of  $\sim 50\text{ fs}$  between Raman shifts of  $950$  and  $1220\text{ cm}^{-1}$ . The interpretation of the broadband CARS signal as the convolution of the pump and Stokes pulses[120–124] complicates the assignment of this result to a particular frequency-modulation profile, but it warrants consideration in other experiments involving light generation through this nonlinear process.

The other pane (B) in Fig. 6.7 is the signal (on a base-10 logarithmic scale) of (A) integrated along vertical slices. Within this treatment, a feature that may be attributed to the  $993\text{ cm}^{-1}$  vibrational mode of benzene is still apparent. However, the contrast in this scan is significantly lower than in Fig. 6.4: whereas we observed approximately one order of magnitude contrast between the resonant and nonresonant signal under near infrared excitation, with the pump and Stokes pulses generated by the SFS process, our contrast is only approximately half of one order of magnitude. This is consistent with previous reports that nonresonant background becomes increasingly important at higher frequencies,[140, 148] as well as our measurements of nonresonant susceptibilities in Ch. 5. We also note that the width of the nonresonant background appears reduced. Under near infrared excitation, the nonresonant background is above baseline across much of the  $\sim 350\text{ cm}^{-1}$  window of Raman shifts in Fig. 6.3, 6.4, and 6.5 and is visible over a much broader range than

is shown in these figures. On the other hand, the nonresonant background appears to be above baseline over a range of only  $\sim 200\text{-}300\text{ cm}^{-1}$ ; this is consistent with the steeper phase matching conditions observed for visible excitation under the cw approximation and in agreement with concerns over operational bandwidth in these phase matched experiments.[120, 136, 137]

With pump and Stokes pulses derived from SFS, we also tried to find signal associated with resonance-enhanced CARS in MnTPP consistent with the reported resonance Raman of the complex.[309] However, while realignment to a different mask allowed detection of signal at the appropriate Raman shifts ( $\sim 400\text{ cm}^{-1}$ ), we could not detect any signal consistent with MnTPP. Referring back to our concerns in Ch. 5 regarding the sensitivity of experiments involving these metal species, it is not too surprising that we had difficulty finding signal as we have replaced two electronic resonances with a nonresonant interaction (the Raman probe). It may be worth returning to these efforts if the capability to tune the Raman probe over a broader frequency range is developed or acquired. Under such a situation, these CARS processes could be performed with four resonant interactions: just as we managed to detect signal under some conditions with MnTPP, the four resonant interactions may be sufficient to enable electronically enhanced CARS experiments.

Recall we mentioned when discussing Fig. 6.5 the decrease in nonresonant signal near  $1150\text{ cm}^{-1}$ . The behavior yielding this feature is shown more fully in Fig. 6.8, in which it is clear that we observe a sequence of modulations as a function of Raman shift. However, these features are only observed during pulse overlap. Characterization of these modulations along different available axes is shown in Fig. 6.9. (C) makes it very clear that these modulations are not an interference effect associated with the monochromator slits: for increasing slit size, the only change in the signal is broadening and an increase in amplitude, each consistent with increasing slit width. Meanwhile, changing the sample from carbon tetrachloride to pyridine or benzene has a pronounced effect (D), but there is no obvious trend associated with changing the sample composition with respect to benzene and pyridine. From panes (A) and (B), it is clear that changing the TOPAS-C set points has pronounced effects. When these effects were first observed, modulations were observed when the spectral output of the OPAs was checked; however, retuning removed the modulations in the OPA spectral output, but not in the CARS spectra. Realignment of the table following retuning also changed the position and spacing of the fringes with respect to the benzene resonance.

We were unable to find any descriptions or reports of similar modulations in the nonresonant background of CARS spectra in the literature. The only other mention of modulations of any sort is from Pontecorvo et al.[399] who report the observation of ringing in FSRS spectra when employing a narrowband pump with a sharp cutoff rather than a sharp rise as we observe. The authors attribute this ringing to the sudden cutoff

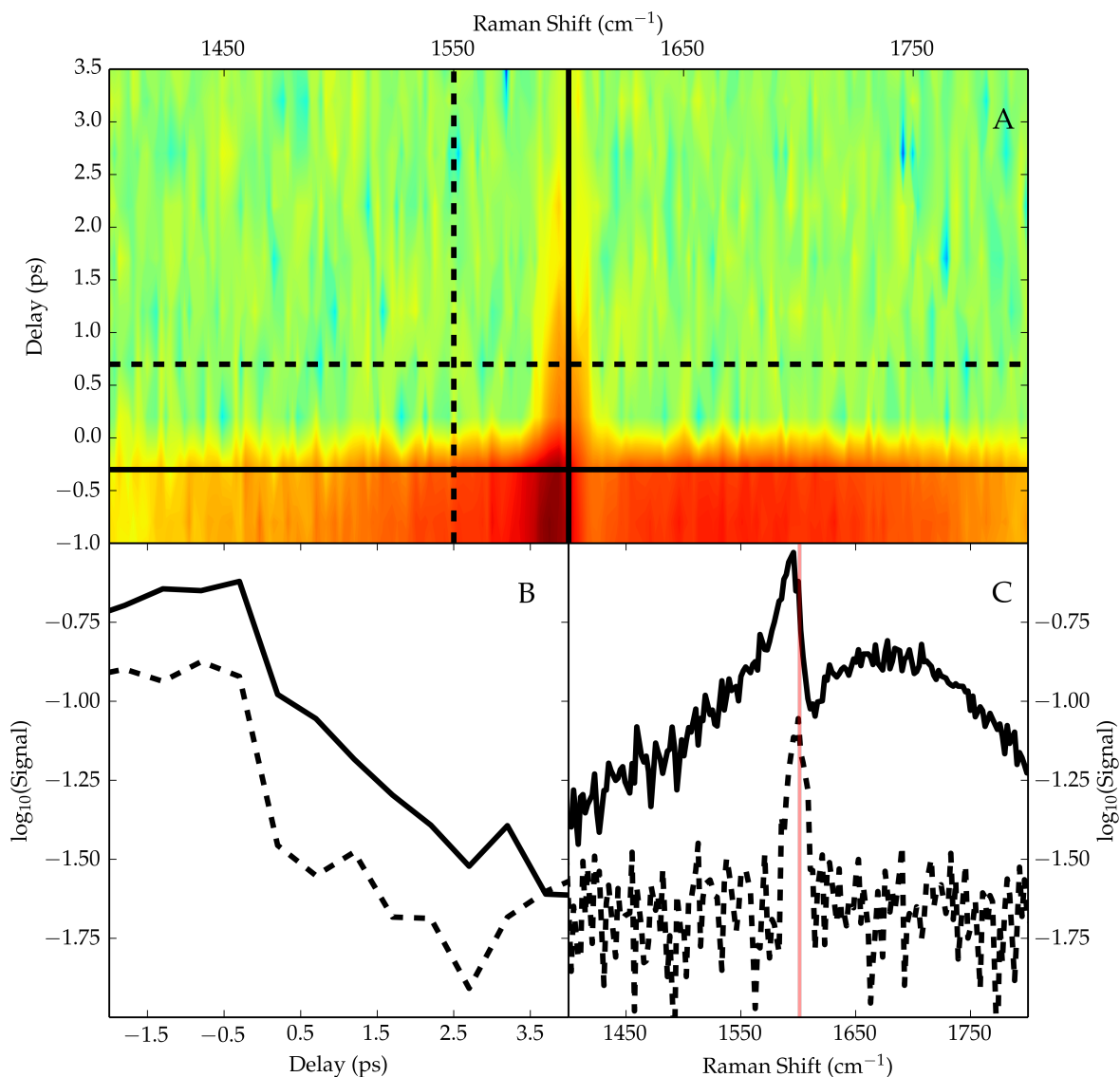


Figure 6.6: Broadband CARS of benzonitrile ( $C_7H_5N$ ) with Raman pump pulse  $\bar{\nu}_1 = 16400 \text{ cm}^{-1}$ , Stokes pulse  $\bar{\nu}_2 = 15100 \text{ cm}^{-1}$ , and narrowband probe ( $\sim 794 \text{ nm}$ ). (A) Signal (base-10 logarithmic scale) as a function of delay and Raman shift. Delay is relative delay between the probe pulse and the overlapped Raman pump and Stokes pulses. Raman shifts are assigned on the basis of matching the time-resolved vibrational resonance of benzonitrile to its known value.[426] The dashed and solid vertical lines match the dashed and solid slices plotted in (B), and the solid and dashed horizontal lines represent the points from which the slices in (C) are derived. (B) and (C) are signal (base-10 logarithmic scale) versus relative probe delay (B) or Raman shift (C). The faded red line in (C) marks the vibrational frequency of benzonitrile,  $1601 \text{ cm}^{-1}$ .

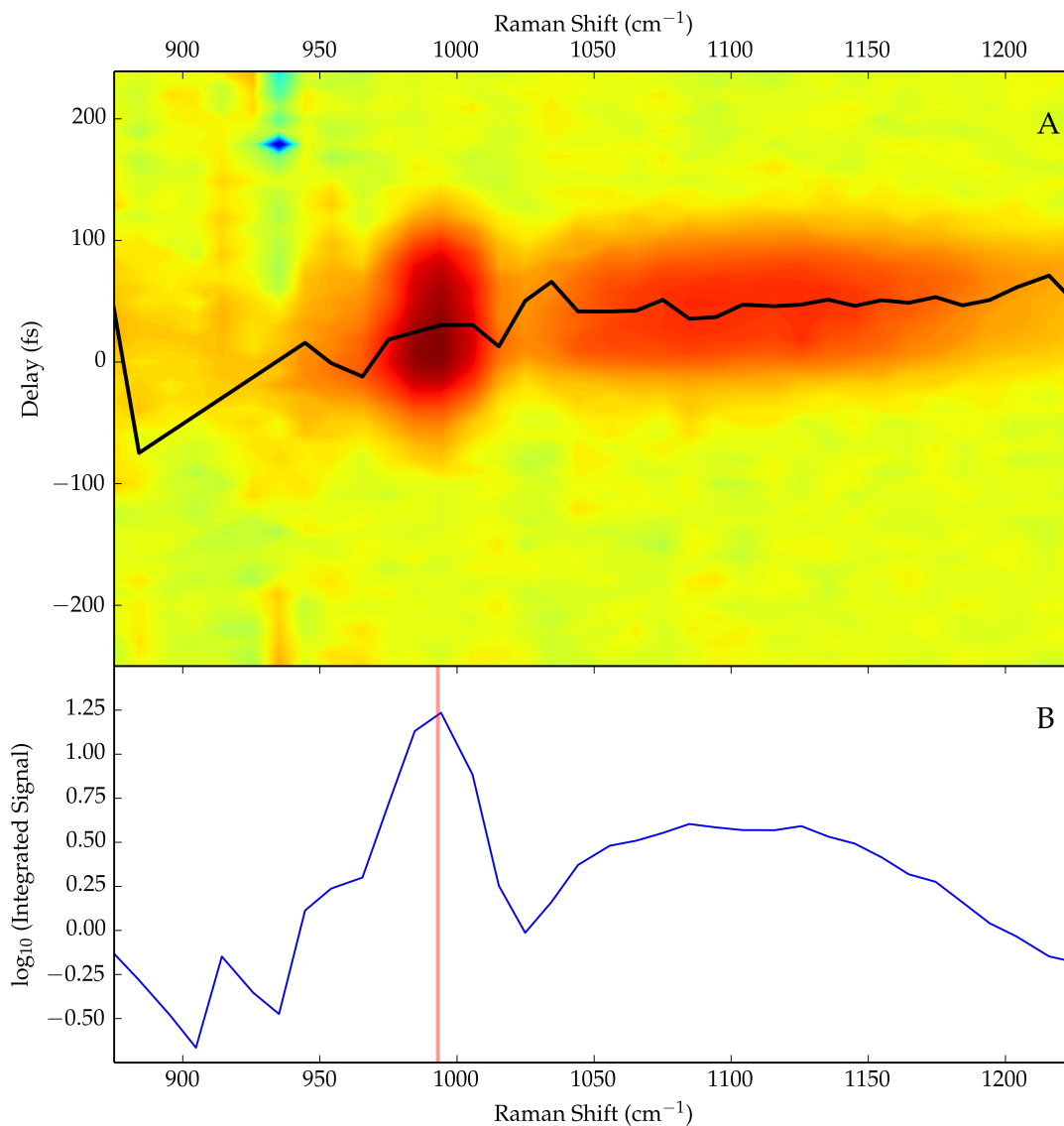


Figure 6.7: Broadband CARS of benzene ( $\text{C}_6\text{H}_6$ ) with Raman pump pulse  $\bar{\nu}_1 = 20800 \text{ cm}^{-1}$ , Stokes pulse  $\bar{\nu}_2 = 19800 \text{ cm}^{-1}$ , and narrowband probe ( $\sim 794 \text{ nm}$ ). (A) Signal (base-10 logarithmic scale) as a function of delay and Raman shift. Delay is the relative delay between the pump and Stokes pulses; overlap of both pulses with the probe is expected for all relative delays. Raman shifts are assigned on the basis of matching the vibrational resonance of benzene to its known value.[425] The black trace is the first moment of the signal, excluding the values calculated for several Raman shifts  $< 950 \text{ cm}^{-1}$ . (B) Is the base-10 logarithm of the results of (A) integrated over all delay values at each Raman shift. The faded red line marks the vibrational frequency of benzene,  $993 \text{ cm}^{-1}$ .

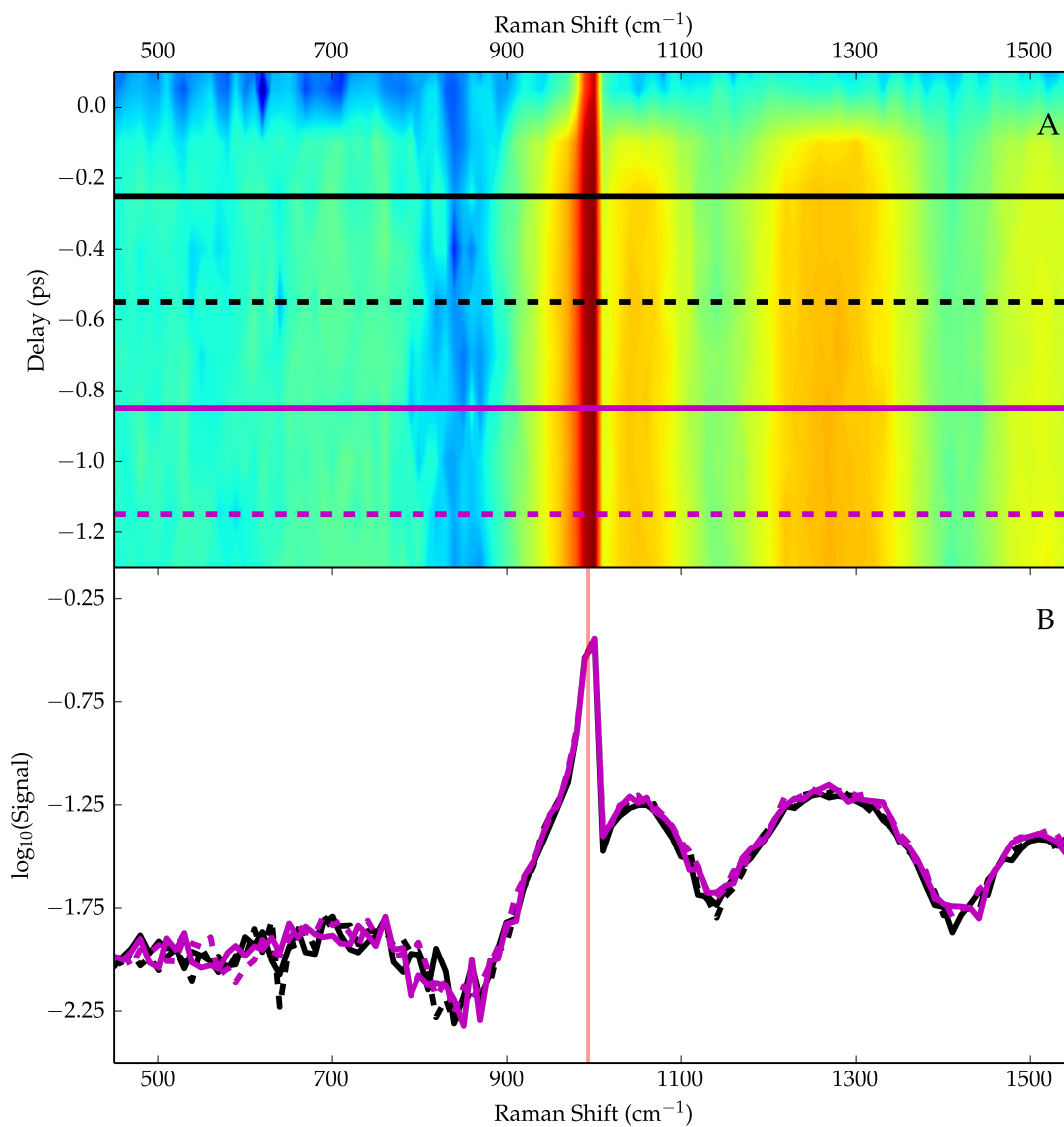


Figure 6.8: A spectrally broader broadband CARS of benzene ( $C_6H_6$ ) with Raman pump pulse  $\bar{\nu}_1 = 8000$   $cm^{-1}$ , Stokes pulse  $\bar{\nu}_2 = 7000$   $cm^{-1}$ , and narrowband probe ( $\sim 794$  nm). (A) Signal (base-10 logarithmic scale) as a function of delay and Raman shift. Delay is relative delay between the probe pulse and the overlapped Raman pump and Stokes pulses. Raman shifts are assigned on the basis of matching the time-resolved vibrational resonance of benzene to known value.[425] The horizontal lines are color- and style-coded to the slices in (B). (B) shows signal (base-10 logarithmic scale) versus Raman shift for different horizontal slices of (A). The faded red line in (B) marks the vibrational frequency of benzene,  $993$   $cm^{-1}$ .



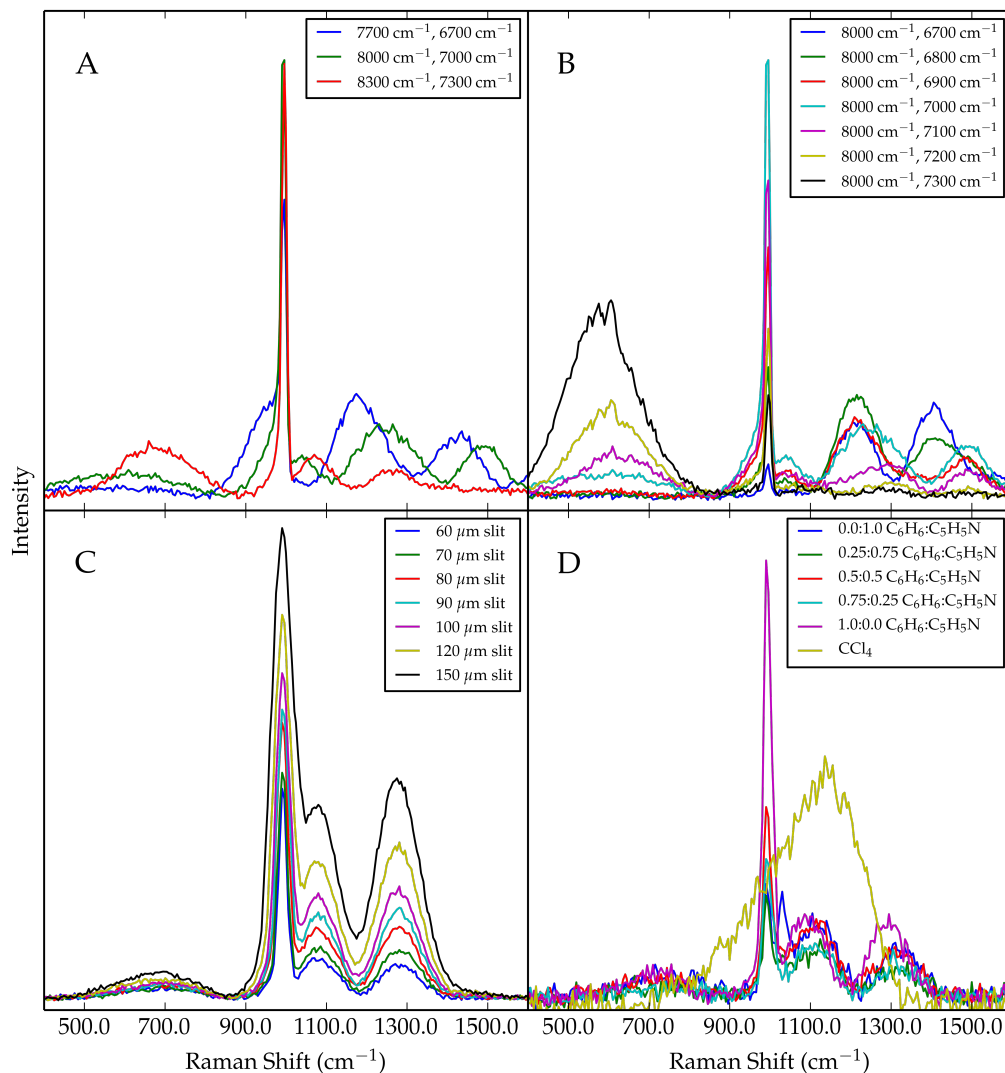


Figure 6.9: Broadband CARS with near infrared Raman pump and Stokes pulses. (A) Monochromator slices of CARS signal from benzene versus Raman shift for different pairs of Raman pump/Stokes pulse frequencies with a constant detuning ( $1000\text{ cm}^{-1}$ ). (B) Monochromator slices of CARS signal from benzene versus Raman shift for constant Raman pump pulse frequency and variable Stokes pulse frequency. (C) Monochromator slices of CARS signal from benzene versus Raman shift for different monochromator slit widths for Raman pump  $\bar{\nu}_1 = 8000\text{ cm}^{-1}$  and Stokes pulse  $\bar{\nu}_2 = 7000\text{ cm}^{-1}$ . (D) Monochromator slices of CARS signal from different solvent systems versus Raman shift for Raman pump  $\bar{\nu}_1 = 8000\text{ cm}^{-1}$  and Stokes pulse  $\bar{\nu}_2 = 7000\text{ cm}^{-1}$ . Ratios of benzene:pyridine are volumetric. Data in (A) and (B) collected before OPA retuning; data in (C) and (D) collected after OPA retuning.

of the pump during the vibrational dephasing; the artificial attenuation of the natural free induction decay manifests as ringing with a modulation frequency and amplitude related to how early the cutoff occurs during the free induction decay.[399] A similar cause would be consistent with the observation of modulations in pyridine and benzene, but their absence in carbon tetrachloride (see (D) in Fig. 6.9): as the latter is purely nonresonant, there are no free induction decays to artificially attenuate. It would also be expected to occur regardless of the state of the system.

However, there are many reasons to dismiss the application of this theory to explain these modulations. First, the exponential tail of the temporal profile of the Raman probe used here is believed to follow the decay of the vibrational free induction decay. The sharp leading edge of the pulse gives the sharp edge observed in the CARS spectra when the probe is delayed relative to the pump and Stokes pulses. This temporal profile is the reverse of the envelope described by Pontecorvo et al.[399] Additionally, the mechanism for the ringing observed by Pontecorvo et al is inconsistent with our observation of the modulations only during pulse overlap, as well as the lack of change in the modulations throughout the pulse overlap region (see (B) in Fig. 6.8). Thirdly, while ringing would be consistent with the recurrence of the modulations after retuning and realignment, the ringing should be a function of the vibrational mode's dephasing and the attenuation of this decay: this should have little dependence upon the frequencies used to prepare the coherence, raising questions as to why we would observe such significant changes in the modulations as we changed the excitation frequencies.

In order to understand these modulations, we attempted to simulate nonresonant processes capturing as many of the relevant factors, including the phase of the Gaussian field and dispersion across the spectral profiles of the pump and Stokes pulses; the resulting script is included in Appendix D. However, in capturing these different effects, the script yielded a parameter space far broader than could be reasonably explored. Surveys were conducted exploring a few of these parameter spaces, illustrating the complexity of the system; however, a few key insights were gained.

First, the effects of dispersion on these experiments is very pronounced. When the propagation of the fields is described only by the central color, the nonresonant contribution to the signal is a very smooth envelope. This is consistent with the description of the signal inheriting character according to the convolution of the pump and Stokes pulse envelopes.[120–124] The resulting signal will match this envelope if the sample exhibits low dispersion,[135] such as a gas,[120] or arises from a thin sample,[139] as when scattering from a powder.[121] However, the simulations illustrate that when dealing with a bulk sample as in the present experiments, the dispersion across the spectrum adds a further degree of complexity to interpreting the anticipated spectral character of the signal. Rather than attempt to explore the several parameters that

control the phase matching angles in the simulations, it may be more straightforward to perform future experiments within the previously described limit of thin samples.

The other effect that proved pronounced was the effect of mismatch between the focal planes of the excitation beams. Various authors have previously discussed the importance of the Guoy phase term in nonlinear experiments,[139, 203, 427] and this manifested in the simulations: depending upon the relative focal point of the pump and Stokes pulses, the spectrum of the output could exhibit both pronounced oscillations and significant changes in amplitude. Unfortunately, this is a very difficult axis to gauge proper values with any degree of accuracy due to the imaging conditions on the table at the time of these experiments. When performing these experiments, we performed knife edge measurements to gauge the beam sizes: the results were consistent with beam waists of 20  $\mu\text{m}$  for the Stokes and probe pulses, but 40  $\mu\text{m}$  for the pump. This suggests that the pump pulse was smaller than the other beams at the focusing mirror, which is consistent with estimates of the beam sizes at the mirror based upon the measurement of aperture diameters that passed half the beam energy. According to the optics of Gaussian beams, this smaller beam waist for the pump will not only cause the focal spot size to be larger, but will also shift the focus;[105] with our measurements, this could correspond to shifts in focus of hundreds of micrometers - well within the range the simulations suggest modulations could be introduced. It is clear that when progressing to three- and four-color experiments, it is crucial to not only consider our usual quality metrics - spectral content, energies, alignment, sample - but also consider whether the alignment achieves the correct imaging in order to minimize artifacts and unexpected behavior induced by phase effects such as the Guoy phase.

**CHAPTER A**  
**Appendix A**

Damage in Regen:

- high pump power? NO
- Bandwidth? 45 nm  
 ↓  
 not stretched optimally?  
 too much peak power?

1000 H - 1 A increase instead of at 0.1 A

100% current  $\Rightarrow$  No power  
 Should be 5.5 W      22-23 A  
 (100% current - what is current? 39.5 A }  
 how much SHG?      No power out - not even visible.

SHG out. { current - 10

IR Viewer more sensitive than 407 A

~36 nm out of cavity }  
 ~3% out of compressor } ~ 2 nm difference between cavity and post compressor

~10 nm lost between stretcher and cavity.

Dave: Let him know when/what we plan to do RE: fs system (extra crystals, mixer install)

Set to 4.0 W, set to that current, adjust SHG Temp + Back Mirror  $\Rightarrow$  maximize power

Skype - Tsunami

use previous mirror to center pump on each mirror in turn } beam dump  
 P2 is important!!

M4 - 0

- 1) make sure pump is centered on all optics
- 2) cavity fluorescence and mode centered on all optics }
- 3) beam straight thru prisms + AOM  $\rightarrow$  MS??

- 1) Clipping  $\rightarrow$  no photodiode signal  
 MS  $\rightarrow$  move MS to maximize photodiode signal and compensate w/ oc
- 2) next week Dave's open!!!

Dave Visit

TFP - ~~Monday~~ Tues or Wed

Here on Mon after noon



Skype

Dave visit - 2/4/2013 -

diodes: 809 nm  $\rightarrow$   $\sim$  808.5 nm  
each fiber:  $\sim$  13 W  $\times$  2 : 26 W pump  
w/ inefficiency and conversion rates get the  $\sim$  5 W green

①

little fiber  
 $\rightarrow$  light bulb  
for Millenia  
 $\rightarrow$  CM6839

laser driver LBO  $\rightarrow$  LBO can get damaged if air is moist  
Nd:YVO4 gain

Tsunami: can change angle of M2, M3

do NOT change the translation  $\rightarrow$  do not change the ~~front~~ distances

Millenia: gray box: cavity for IR?  $\rightarrow$  has adjustment for HR on end close to output  
contains HR and OC  
piping "briggs" IR to LBO cavity  
external HR tweaks adjust HR for green cavity

when case is off - yellow tab at the front is a HR

when Dave arrived 23.5 A  $\rightarrow$  13 W D2 808.5 nm } Diode temp shifts wavelength  
22.4 A  $\rightarrow$  13 W D1 809.1 nm }

current is  $\sim$  38k } Check info info screen and scroll down  $\rightarrow$  max 30 A  $\rightarrow$  end of life } Should be 13 W  
 $\sim$  5000 hrs lifetime } 20 A  $\rightarrow$  beginning } 809 nm w/  $\sim$  3 nm bandwidth  
20000 is the nominal }  
35k is average }

Need to be in SP mode on the board inside the laser head, switch pin 4 on the DIP switch

@ 100% current - should be 5.5 W  $\rightarrow$  Dave needs to make adjustment so that is the case

Diode: 15k a piece  
do not scratch fiber! will need diode replaced

diode temp - changes power because you are tuning to spectrum to the VO4 spectrum  
 $\rightarrow$  do not adjust after Dave has set.

ideally, only adjust:  
- end mirror  
- LBO temp

monitor current at pump power  
 $\rightarrow$  when there is a significant change in running current, take a look at those logs!

may need several adjust to LBO temp

Millenia mode - check  
Soc distance (20 ft?)  
away - don't bother  
looking at low power -  
check @  $\sim$  4.5 W.

Monitor Tsunami - when bandwidth or power change, check Millenia

w/ Millennia:

(2)

@ 13 W from each diode - should hit 6 W

Dave then sets the current value, from which the Millennia derives power curve

↳ this is why the diodes will run at different currents → that's how Dave got 6 W

trimpot on the board - offset for internal photodiode

"SP Current" service level control

Dave has set the power curve - 100% current should now result in 5.5 W

↳ 22.2 A  
23.4 A

"Pass back current" → when Millennia needs to drive the diodes @ 2 A over max set point error

diodes - look ok  
"should" replace @  
20k hrs; can last  
on average ~35k hrs  
and max is ~50k

Tsunami: // don't pump w/ more than 5 W → could damage things

Brewster windows: were dirty

could have been the source of the problem

these can be removed and cleaned - usually only outside needs cleaning, but

the inside of the Brewster windows were also dirty

dirty window - would disrupt the mode sufficiently

Alignment

look at external card - overlap back reflection from HR  
use OC to overlap back reflection between M4 + M5

during slit  
up = redides tone  
down = blue ←  
to a visible  $\lambda$  → look at M4  
center laser on M4 w/ M3

recover laser  
look @ M5 → use M4 to center laser on M5  
recover laser

use M5 to get output centered on OC  
↳ this is when you try to maximize photodiode signal

to get locking } external:  
M5 center the "laser"  
from M3 in the alignment  
square.

dirty optics  
can screw you up  
↳ use dry MeOH or  
acetone

pump: on P1: pump should be between the "claws" of the holder

ADM: RF frequencies sent into quartz crystals → the RF frequencies help mode lock  
↳ accounts optical

new alignment: 3.8 W pump; 420 mW CW; 375 mW  
01 nm  $\Delta\lambda$

(3)

## Rees Spectrometer

Slit width - controlled by a set screw between the  $\lambda$  and  $\Delta\lambda$  knobs

sets the width between the razors  $\rightarrow$  lets more light through for a given

GVD compensation

when trying to adjust pump power to get appropriate bandwidth

$\rightarrow$  make adjustments of  $\sim 100-200$  mW at a time

Should not  
be done  
on a  
regular  
basis

AOM: when knocking, affects the power of the CW mode

want to optimize coarse adjustment to ① gain mode-locking - will see movement <sup>in the spectrum</sup> when getting close

② retain peak power

~~"phase"~~ changes frequency of the AOM

phase - adjust phase of the AOM signal to the cavity frequency

40.03-40.58 ?

$\rightarrow$

range of frequencies necessary  
as you add or remove glass,

frequency of the cavity changes

$\rightarrow$  need to change frequency of  
the AOM needs to change  
to match

Tsunami alignment:

- $\sim 440-450$  mW
- 300 nm, ~~centered~~ w/  $\sim 60$  nm bandwidth available
- mode locked "not working" need to turn on AOM, reduce bandwidth to  $\sim 50$  nm  
then will bandwidth back up after mode locked

pumped w/ 4.2 W

$\rightarrow$  Mirrors: D1 = 21.2 A  
D2 = 22.4 A

The ocean optics devices we have do not agree w/ Dove's

$\rightarrow$  they show  $\sim 10$  nm difference in Tsunami center  
our device calibrated for Vis (as per Pam), while Dove's is calibrated for NIR (and was just recalibrated)

a master spectrum has been collected ("2013 02 05 Dove Align Final")

$\rightarrow$  this should be the guide to which future alignments are made.

See



Spitfire

4

Stretchers:

- use external mirrors to align through Faraday isolator
- use first two stretch mirrors after isolator to align to alignment tool prior to stretchers
- set Tsunami to a CW wavelength in the middle of the bandwidth
  - ↳ if the four dots of the grating are not overlapped, adjust stretcher angle to get them overlapped
- use mirror after stretchers and the first seed mirror outside of the "cabin" to get the beam aligned to the alignment tool before the periscope
- use periscope and seed mirror before extra-cavity Pockels cell to align the seed to the alignment tool:

while aligning, Dave recentered the extra-cavity Pockels cell vis-a-vis the seed alignment through the alignment tool

- ① between the periscope and final seed mirror (before extra-cavity Pockels cell)
- ② center on Pockels cell
- ③ center on alignment tool between the cavity and mirror (the one w/out the photodiode) and the intra-cavity Pockels cell → need find R

- Pump alignment:
  - o get pump laser working (at 9.7 A or of mid Jan 2013)
  - o align to alignment tool:
    - use first pump mirror to align pump to the alignment tool before the rod
    - use second pump mirror to align pump to the alignment tool after the rod
    - align back reflection w/ pump mirror on the other side of the rod

- At this point, Dave rotated wave plate to try to get CW lasing
  - ↳ looked at card before compressor to try and see lasing
  - moved wave plate between extra cavity Pockels cell and TFP → try to get more seed into cavity for better alignment.
  - ↳ can visibly see seed - rotate wave plate to maximize light

Dave did this after seed alignment into cavity but before pump alignment

Dave iterated these 2 steps  
 # need find R to see seed during this alignment

to realign TFP: placed alignment tool between micro cavity mirror (near extra-cavity Pockels cell) and the rod - rotated TFP until beam was aligned to alignment tool → vertical alignment: press on mount → bends slightly  
 ↳ Dave then placed alignment tool in front of the cavity mirror that immediately follows the rod (the first mirror that the pump transmits through) and used to other pump-transmitting cavity mirror to align to the tool

Checked that the beam was centered on the mirror just before the end mirror w/ the photodiode behind it; used this mirror to align the seed to the alignment tool in front of the end mirror w/ photodiode

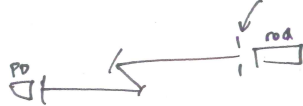
↳ checked that back reflection off the end mirror returned → placed alignment tool in front of the small cavity mirror before the end mirror w/ the photodiode and adjusted the end mirror to get the back reflection aligned

cannot really see back reflection @ the other end mirror

w/ wave plate <sup>red dot @ the top of the wave plate.</sup> between extracavity Pockels cell and TFP: → wherever you can get the wave plate to fit (5)  
 - placed the alignment tool between end mirror (w/out photodiode) and intracavity Pockels cell:  
 iterate ↗ used last seed mirror to align seed to tool  
 - placed the alignment tool before extra-cavity Pockels cell - used periscope to align seed

- redid cavity alignment:
  - o end mirror (w/out photodiode) to aperture before TFP
  - o mount pump-transmitting cavity mirror after TFP through rod to alignment tool in front of the other pump-transmitting mirror
  - o made sure beam centered on cavity mirror before end mirror w/ photodiode
  - o aligned back reflection of end mirror

↳ looked @ back reflection between in front of rod



next looked @ back of aperture to try to see back reflection  
 ↳ manually pressed on end mirror (w/ photodiode) to try to distinguish back reflection from incoming seed

w/ back-reflection "hopefully close enough", returned wave plate  
 ↳ could kill lasing because of the change in the pump → shift from bright red rod to orangish rod

'walking' the cavity mode - can see the cavity mode well enough on the end mirrors  
 ↳ make a small adjustment to one end mirror, compensate with an opposite change on the other end mirror

beam  
 cavity mode not aligned to the first telescope mirror → Dave rotated the extra cavity polarizer to bring it back to alignment to the mirror  
 ↳ knew seed aligned in the cavity → did not have much effect

Dave felt both Pockels cells were a little misaligned - translated both Pockels cells

2/5/2013  
 TFP replaced - could not really be aligned w/o mode hitting one of the damaged spots → old TFP in optics cabinet

w/ CW lasing:

touching up the power:  
 start w/ green: use the second and third pump mirrors - do not make adjustments w/ the first pump mirror  
 ↳ iterate between the two, one axis at a time → went to get the forward pass and the back-reflection overlapped in the red rod  
 next tweak cavity end mirrors → do not do internal mirrors - these were already been aligned for the seed  
 goal: ~~1.5 W~~ 1.5-4 W pre-compressor → Dave got 3.2 W

Dave was not able to make significant changes to the output pointing of the cavity → moved the first telescope mirror

Compressor alignment:

- use the first telescope mirror to align to the alignment tool before the first square mirror preceding the compressor
- use the second telescope mirror to align to the alignment tool when placed between the square mirrors preceding the compressor

enabling Q-switch:

Dave set Ch 3 to high value (~25 round trips), then enabled 3,2,1

↳ important only when seed is entering cavity

Q-switched w/o seed: 5.2 W  
w/ seed: ~5.1 W

Ch.1 and Ch.2. separated by only ~10 ns → should be more like 20 ns?

↳ Dave made adjustments to the two channels → trying to get the greatest signal for the main pulse and suppress the post pulses

No difference between pulse train when Ch.1 enabled and disabled → Pockels cell not working correctly? board not working correctly?

Dave has requested another board? ↳ overnight? here on the 6th?

↳ Dave removed plastic cover

ORA 6805E → should be 75 Ω across each → one measured 75 Ω the other measured 0 Ω

Buildup reduction time should be at least 30 ns - could be as high as 60 ns

only for extra cavity Pockels cell { usually the resistors are the first things to go - check these first if a Pockels cell doesn't appear to be working correctly

Compressor:

- grating damage - rotate grating 180° so the bar hits it instead of the intense recompressed output?

↳ also noticed: what looked like a thumb's point damage where the uncompressed pulse hits the grating

↳ Dave did this 2/5/2013

Some scratches

rotated grating and measured to avoid the scratches - pay attention for shadow lines in the mode structure!

↳ pay attention to bar alignment - could damage Wg if they are present in the mode

Autocorrelation:

Delta Autocorrelator

Minioptric Technology, Inc.

~\$5k

Tsunami alignment guide:

① M2+M3 focus - when laser is achieved, should small adjustments be made to maximize power, or should we just leave them as you have them? → No to focus

② Mirrors to 5 W? or only for install? → shouldn't be necessary

Tsunami rep rate is now 76.11 MHz

↳ to get more bandwidth, Dave had to give the beam more glass  
more glass increases the effective length of the cavity → lower rep rate

~~Dave measured~~

(7)

Dave measured Spitfire pulse width w/ autocorrelator - ~97 fs

Spitfire, continued

~~two polarizers~~

Pockels cell alignment (extra cavity):

two pieced polarizer

set up one polarizer in front of the Pockels cell and the other after

↳ the two polarizers should be crossed - order matters

w/ wrong order: just see bright spot

w/ correct order and aligned Pockels cell:



shaded area should be dark.

New pulse picker board received - replaced 2/6/2012

↳ Build-up time reduced by an extra ~20 ns

the when one of Dave's business cards is placed at the exit port, it now looks purple rather than red.

↳ it "looks like an ultraviolet pulse"

when Ch.1 not working properly, the cavity was not being properly seeded, limiting its ability to actually yield the proper pulse length

stretchers and compressor: there are key screws that provide external control for the grating angles  
both can be set externally

stretchers: align to get the  $\frac{\pi}{2}$  } external control: only ~1/8 turns

compressor: optimal angle given by where the shortest pulse is achieved

↳ ~1/2 turns

then compensate w/ motor delay } keep iterating

from the shape of the w. gen in the auto correlation, you can see if there is clipping in the compressor

w/ adjustments to compressor grating angle:  
↳ should be symmetric

got 49.5 fs pulses

spectrum: centered @ 798 nm  
~35 nm FWHM

grating angle: 65° 20'

Yesterday, Dave had returned the grating to its original mounting arrangement (wiring on top);

however, he had shifted the grating one to avoid the "walk mark" → this caused the laser spatially clipped bars in the compressor to clip on the v-mirror assembly not on the motorized delay

↳ Dave moved the grating back one to ensure the bars did not clip on these mirrors

inside compressor:

⑧

the bars of light do not have to overlap on the mirrors on the motorized delay

on the compressor grating, should see 

on the mirrors on the motorized delay, ~~okay to see~~ 

Compressor grating: a f5k

~~delay~~

Compressor retroreflector

↳ would probably need to go back to factory to replace mirror

Spitfire:

pump optics:

~~the lenses in the block holders actually have two optical elements~~

the block holder after the second pump mirror actually contains both a polarizer and a lens  
↳ in order to clean this lens, need to remove the polarizer + get at the second surface

↳ the lens has the soft AR coating

w/ further adjustments: 5.4 W ⇒ CW

Ch1 103 }  
Ch2 123 } timing  
Ch3 232 } settings

5.35 W ⇒ Q-switch

5.2 W ⇒ seeded

4 W post compressor

~41.3 fs pulse initially

w/ further adjustments to compressor: ~40 fs

15 ps for build up }  
11-12 ps for build up } 30-40 ns build up reduction time

output: usually shifted from seed center by a few nm  
bandwidth ~35 nm?

have factory specs for Spitfire - see email from Dave w/ service reports  
Spitfire 35fs on 243 Test Report.pdf

single end pumping should increase build up time by 1-2 round trips

when operating Spitfire in free running mode ~~measure~~  
Q-switch mode (but w/o seed) } measure spectrum - will get better performance if we  
match the Tsunami output to the spectral properties of the non seeded cavity.

pulse picker board  
PN 90022027

TOPAS

w/ new optics setup:  
 Harry: 1.85 W  
 Sally: 1.8 W

Harry initial touchup: ~~~670 mW S+I (no WS)~~ ~~~680 mW S+I (no WS)~~  
 Sally initial touchup: (9)

align to external aperture and the white light aperture | will end up aligned to the aperture in front of the pre-amp BBO?

white light - do not want the concentric circles  
~~do not~~ want it to be circular and stable

white light delay - the second mirror of the retroreflector has adjustments for alignment thru the aperture in front of the pre-amp BBO

use the two mirrors after the pre-amp BBO to align the signal through the amp BBO and the post BBO aperture

if focus into the crystal (C2) is too tight, can get white light generation - "OPG" =>

to align crystal in mixer stage: rotate the knob on the bottom of the mixer stage

Harry: ~670 mW S+I (no WS)  
 Sally: ~670-680 mW S+I (no WS) | @ 1300 nm

to touch up overlap of the output, Dave adjusted the pump mirror just before C2

to get a baseline for the mixer behavior:  
 @ 590 nm

w/ adjustments for collinearity

Harry: S+I w/o WS: ~670 mW

Harry: 340-350 mW

Sally: 220 mW => however, looks more yellow than orange

when Mixer moved to a post disassembled from the OPG,

power @ 590 for Harry: ~280 mW | actual frequency: ~586 nm

↳ Dave didn't feel that things were right - misaligning yielded more power

Software: Dave ~~re-installed~~ Existing (current) OPA and Mixer tune files for both OPAs saved and stored in a new folder on the Desktop (2013 02 06 Dave next initial tuning...)

Dave then installed the new WinTOPAS software (v 3.2.236)

and copied the configuration file folder Configuration (1074x on the drive received from light conversion to Program Files(x86) / WinTOPAS 3

to get:

Devices: load new configuration for the TOPAS

need to reload tuning curves

boards get installed on the main board that is where the USB and power connectors are - cables then run from the back of the boards to the mixer connectors at the rear of the OPA.

in WinTOPAS: service => install license

↳ need to open bottom of OPA, and work the cable across the bottom of the bread board

→ have to reload all curves

WinTOPAS service access "SVIESA"

since yesterday, DI has shifted - should it on a day to day basis? NO

"send motor home" = "reset" | sends motor to a home position to set a "zero" position allows the stepper motors to recover positions

Have WinTOPAS installed on my laptop



installed new mixers on both OPAs

Sally: ~560 mW S+I → 650 mW w/ further adjustment (@ 1300 nm)

w/ Mixer 1 installed at the head of Sally:

⑩  
beam block after preamp BBO: try to block all other processes except seed

reloaded manufacturers tuning curves | Harry:

for 1300 nm → needed to send DI to ~6800  
OPA 2 → CZ has been replaced, as per Andrei  
↳ installed wrong?

configuration files - the aliases in Harry's conf. files have been changed. in order to use our tuning files, need the correct aliases

700 mW S+I ←

finally got OPA 2 working w/ an old configuration file - why does OPA 2 require a different conf file?

↳ created hybrid conf. files that allow Mixer 2+3 to be used, but which work w/ our tuning curves

Harry: ~700 mW S+I  
~100 mW @ 590 nm | when mixer expected  
↳ even less than mixer attached to Harry  
Dave wasn't too pleased w/ stability  
↳ tuning motor: ~280 mW  
@ 1100 nm: ~90 mW

Dave: next week - end of next week?

compute alignment of TOPAS

damage in Spitfire?:

- gratings
- comp. delay retro

HR damage: do not pinch apertures before the OPAs

before Dave visit:

- skye - crystals?
- filters?

Sally: ~620-640 mW S+I  
~230 w/ large motor movement { ~175-180 @ 590 nm → still more yellowish  
↳ still looks more yellow than orange

Dave's visit - approx May 8-9 2013

(1)

~~Tsunami stability - temperature more important~~

$\approx 1^\circ$  adequate for Tsunami stability - no need for the extreme of  $0.01^\circ$  or  $0.1^\circ$

with some adjustments to the Tsunami, Dave got to a little over 500 mW when CW (centered a little over 800 nm), and  $\approx 490$  mW when mode-locked

↳ still a little unstable, but Dave didn't want to spend

Sphere: Dave made small adjustments to tweak up seed pointing  
checked the bandwidth detector - made angles adjustment, and looked at the

Empower: Dave measuring over 20 W at 20.1 A - I measured 20. W at the current yesterday | double checked the measurement - Dave's 407A and ours do not match up  $\rightarrow$  our 407A is a little mis-calibrated. @ 20 W, difference is  $\approx 1$  W, but what is the difference @ lower powers?

LBO temp adjust:

there are three pots on the left side of the Empower. The far left pot when facing the Empower is the pot for LBO over temp.  
Can measure the voltage of the thermocouple in the LBO over with the D-sub connector in the back and where the umbilical attaches  
↳ measure Voltage @ pins 4 and 14.  
↳ Dave does not know what the other two pots are for - has never needed to adjust them

there is an opening into side of the sealed metal pump chamber where these three pots are

the LBO over temp is protected } two things Dave checked re: concerns over Empower: - chiller temp  
- LBO over temp

when the pressure case of the Empower is removed, there is not an interlock - the interlock is only inside the metal case inside

Sphere: in free-running mode, Dave initially saw 4.6 W pre compressor; tweaking pump mirror and one cavity end mirror only increased the power to  $\approx 4.8$  W

↳ Dave removed the polarization rotator from the lens assembly (the black holder after the second pump mirror). Clean Cleaning

the polarization rotator and lens increased power to  $\approx 5$  W

↳ when returning the polarization rotator back into the holder, need to tweak up proper orientation. Does not have a huge neg. effect on the power, but every little bit helps

Dave continued going through, cleaning the pump optics one at a time.

Dave got the free-running power up to 5.2 W through cleaning optics and tweaking up cavity and pump.

when D-switching into seed, Dave got  $\approx 5.2$  W with about 16 round trips; initially profile of the pulse train

Dave made small adjustments to Channel 3 to ~~adjust~~  
clean up the pulse train - to remove the last peak



②

Before tuning up seed pointing, Dave had 5 W w/ 13 round trips

for seed adjustment, Dave used the first seed mirror after the stretcher (outside the "cabin") and the periscope adjustment in tandem to walk the beam seed down to the cavity mode and optimize power.

~~in the beam~~ Timing now, Dave tweaked the zero delay adjustment

↳ tweaks the delay between the pump firing and the seed selection - allows optimum build-up of saturation in the rod

with his adjustments, Dave got up to 4 W post compressor

↳ requires 13 round trips

Dave was reasonably satisfied with the pump alignment between the Spitfire and the OPAs

### Sally (10943)

~1300 nm: seed overlap w/  $Cl = -3.867^\circ$  } these positions used from Dan's tuning curve - should be ~1305 nm  
 $Dl = 2.222$  mm

Dave measured ~1.8 W out of Spitfire to 10943

@ 1300 nm: seed "looks pretty red" → want the seed looking red

@ 1300 nm, Dave optimized compression,  $Cl$ , and  $Dl$  to maximize the power of the seed as measured by →

↳ ~~target~~ his goal was to reach ~1.5 mW

only managed ~1.1 mW w/ these degrees of freedom; Dave began optimizing internal degrees of freedom

↳ mostly just pre-amp pump optics

Dave also adjusted the focus of the pumps pre-amp pump - wanted to minimize the "superfluorescence" in the  $Cl$  on the optic just before  $Cl$ ; Dave used a card to make sure the pump and white light were overlapping

↳ to optimize collinearity - pump and white light collinear

after the adjustments to the pumps and pump, could only get ~250  $\mu$ W

↳ additionally, Dave was no longer seeing the red seed post pre-amp

with an adjustment to pump focus (returning the focus to original position?) Dave managed to get the red back

w/ tweaking external degrees (compression,  $Dl$ ,  $Cl$ ) managed to break 1 mW; Dave used tweezers mirrors - eventually managed to get the power to ~1.1 mW. increasing the white light aperture opening increased the power significantly

Dave decided to stick ~1.1 mW however

in when service technician access: see  $Cl$

Curves → new timing curves

③

using the WinTOPAS routine, created a tuning curve for Sally's preamp  
power amp alignment and tuning:

@ 1300 nm: Dave used the last two pump mirrors to enter the pump on C2, then adjusted the manual control for P2 to find parametric output

while adjusting for collinearity, Dave noticed that the seed pairing was off, so he adjusted it - only used the two corner mirrors after C1

for collinearity, Dave adjusted the delay so the seed and pump were not temporally overlapped  
↳ could see the doubled pump (blue) and the seed (red) after the HR  
Dave used the last two pump optics to overlap these in the near field (just outside the OPG) and the far field (down the table)  
↳ once overlapped, Dave fixed the temporal overlap and touched up the collinearity in the far field

1140 nm	100 mW
1160 nm	240 mW
1180 nm	300 mW
1200 nm	370 mW
1220 nm	400 mW
1240 nm	420 mW
1260 nm	440 mW
1280 nm	460 mW
1300 nm	460 mW → 480 mW
1320 nm	480 mW
1340 nm	490 mW
1360 nm	460 mW
1380 nm	430 mW
1400 nm	440 mW
1420 nm	430 mW
1440 nm	450 mW
1460 nm	450 mW
1480 nm	440 mW
1500 nm	440 mW
1520 nm	420 mW
1540 nm	420 mW
1560 nm	400 mW
1580 nm	300 mW
1600 nm	300 mW
1620 nm	300 mW

At this point, Dave tried adjusting the switchout times on the Spitfire

after completing the tuning curve, Dave noticed that there was OPG in the pre amp - likely the source of the inconsistency we were seeing in the second half of the curve  
↳ from when Dave changed the switchout times?

to fix the presence of the OPG:

Dave adjusted the focus of the pre amp pump - changed the lens to try to:  
- minimize OPG  
- keep the pump going through the aperture.

this adjustment dropped the power at 1300 nm to only ~400 mW  
↳ changed the focus again slightly  
power increased to nearly 480 mW @ 1300 nm

10742  
Harry Tuning

(4)

when getting on initial alignment in Harry, Dave noticed scatter on the mirror just before CI - cleaned it to remove the dirt

① 1300 nm: motor controls increased seed power to ~0.95 mW; internal pointing adjustment increased the power past 1 mW  
Dave adjusted the set screw on an optic before the white light delay (DI) - adjustment of neutral density (variable filter) for the pump going to the white light plate

↳ if aperture is open all the way, should get white light - it will be saturated, but should be there

Dave was seeing no white light when he opened the white light aperture all the way. He adjusted the neutral density because of this. Adjustment of the variable filter is a change he can make, though he generally shouldn't need to.

used the "create new trig curve" protocol in WINTOFS to create a curve for the pre amp positions.

Dave optimized collinearity ~~in the pump stage~~ in the power amp stage

re optimized compression to Sally (10743) - got a 500 mW @ 1300 out of Harry (10742)

↳ when simply optimized compression to Harry (10742) power amp, got maybe 530 mW

1140 nm	150 mW	1520 nm	550 mW
1160 nm	340 mW	1540 nm	510 mW
1190 nm	420 mW	1660 nm	500 mW
1200 nm	490 mW	1580 nm	450 mW
1230 nm	500 mW	1600 nm	490 mW
1240 nm	520 mW		
1260 nm	550 mW		
1280 nm	560 mW		
1300 nm	580 mW		
1320 nm	580 mW		
1340 nm	590 mW		
1360 nm	580 mW		
1380 nm	590 mW		
1400 nm	580 mW		
1420 nm	590 mW		
1440 nm	580 mW		
1460 nm	580 mW		
1480 nm	560 mW		
1500 nm	560 mW		

⑤

Mixer Stage Calibration

10743

SH1

800 nm	45 mW
810 nm	50 mW
820 nm	60 mW
830 nm	62 mW
840 nm	61 mW
850 nm	60 mW
860 nm	60 mW
870 nm	58 mW
880 nm	55 mW
890 nm	53 mW
900 nm	50 mW
910 nm	45 mW
920 nm	46 mW
930 nm	45 mW
940 nm	44 mW
950 nm	41 mW
960 nm	41 mW
970 nm	38 mW
980 nm	36 mW
990 nm	35 mW
1000 nm	34 mW
1010 nm	32 mW
1020 nm	32 mW
1030 nm	32 mW
1040 nm	32 mW
1050 nm	31 mW
1060 nm	30 mW
1070 nm	30 mW
1080 nm	29 mW
1090 nm	30 mW
1100 nm	30 mW
1110 nm	30 mW
1120 nm	30 mW
1130 nm	32 mW
1140 nm	32 mW

SH5

590 nm	24 mW
590 nm	54 mW
590 nm	77 mW
600 nm	88 mW
610 nm	91 mW
620 nm	84 mW
630 nm	105 mW → unstable - needed to finish up calibration
640 nm	105 mW
650 nm	100 mW
660 nm	100 mW
670 nm	90 mW
680 nm	85 mW
690 nm	78 mW
700 nm	68 mW
710 nm	64 mW
720 nm	68 mW
730 nm	62 mW
740 nm	60 mW
750 nm	54 mW
760 nm	49 mW
770 nm	46 mW
780 nm	41 mW
790 nm	28 mW
800 nm	22 mW

TOPS 35041  
1150 nm 38 mW  
1160 nm



The second morning, the Spirefire output power was lower (3.5 W). Dave measured the Tsunami, and it had not lost power  $\rightarrow$  500 mW (6)

$\rightarrow$  adjusted the width and wavelength to match master - power  $\approx$  490 mW

pointing adjustments only increased the power slightly; Dave increased the current from 20.0 A to 20.2 A  $\rightarrow$  power  $\approx$  4 W.

~~Out of 10743, we only got  $\approx$  400 mW, w/ pointing changes got 500 mW~~

$\rightarrow$  did not get improvement w/ next round trip in the Spirefire (14 round trips instead of 13)

$\rightarrow$  when switching from 13  $\rightarrow$  14 round trips, needed to move compression delay forward

### 10743 Mixer continued

<u>SFI</u>		<u>SFS</u>		<u>DFG</u>	
535 nm	150 mW	470 nm	130 mW	2500 nm	<del>2 mW</del> 1.7 mW
540 nm	150 mW	475 nm	235 mW	2750 nm	1.8 mW
545 nm	150 mW	480 nm	250 mW	3000 nm	1.4 mW ?
550 nm	150 mW	485 nm	255 mW	3250 nm	4.3 mW
555 nm	150 mW	490 nm	245 mW	3500 nm	4.5 mW
560 nm	155 mW	495 nm	245 mW	3750 nm	4.2 mW
565 nm	160 mW	500 nm	230 mW	4000 nm	3.1 mW
570 nm	170 mW	505 nm	220 mW	4250 nm	2.6 mW
575 nm	170 mW	510 nm	210 mW	4500 nm	2.4 mW
580 nm	180 mW	515 nm	210 mW	4750 nm	1.7 mW
585 nm	175 mW	520 nm	210 mW	5000 nm	1.5 mW
590 nm	160 mW	525 nm	210 mW	4600 nm	1.1 mW
595 nm	170 mW	530 nm	190 mW	6600 nm	0.7 mW
600 nm	170 mW			7000 nm	0.7 mW
605 nm	140 mW			7500 nm	0.7 mW
610 nm	110 mW			8000 nm	0.6 mW
				8500 nm	0.6 mW
				9000 nm	0.6 mW
				9500 nm	0.6 mW
				10000 nm	0.5 mW
				11000 nm	0.4 mW

7

10742

1300 nm 580 nm

pumping w/ 1.9-2W

10742 Mixer Calibration

SPI

SMS

SFI

900 nm	70 mW	1160 nm	36 mW	590 nm	50 mW	535 nm	148 mW 153 mW
910 nm	74 mW	1120 nm	39 mW	590 nm	97 mW	540 nm	150 mW
920 nm	80 mW	1130 nm	42 mW	590 nm	115 mW	545 nm	150 mW
930 nm	78 mW	1140 nm	45 mW	600 nm	120 mW	550 nm	155 mW
940 nm	78 mW	1150 nm	50 mW	610 nm	125 mW	555 nm	150 mW
950 nm	76 mW	1160 nm	57 mW	620 nm	130 mW	560 nm	160 mW
960 nm	74 mW			630 nm	130 mW	565 nm	150 mW
970 nm	74 mW			640 nm	130 mW	570 nm	170 mW
980 nm	71 mW			650 nm	125 mW	575 nm	175 mW
990 nm	69 mW			660 nm	120 mW	580 nm	180 mW
900 nm	64 mW			670 nm	110 mW	585 nm	190 mW
910 nm	60 mW			680 nm	90 mW	590 nm	200 mW
920 nm	58 mW			690 nm	66 mW	595 nm	190 mW
930 nm	54 mW			700 nm	76 mW	600 nm	180 mW
940 nm	51 mW			710 nm	18 mW	605 nm	170 mW
950 nm	49 mW			720 nm	6 mW	610 nm	135 mW
960 nm	47 mW			730 nm	26 mW		
970 nm	44 mW			840 nm	52 mW		
980 nm	42 mW			750 nm	61 mW		
990 nm	41 mW			760 nm	62 mW		
1000 nm	40 mW			770 nm	57 mW		
1010 nm	38 mW			780 nm	54 mW		
1020 nm	38 mW			790 nm	44 mW		
1030 nm	36 mW			800 nm	42 mW		
1040 nm	35 mW						
1050 nm	34 mW						
1060 nm	34 mW						
1070 nm	34 mW						
1080 nm	34 mW						
1090 nm	35 mW						
1100 nm	35 mW						

## 10742 Mixer Calibration

SFS		SHSH I		SHSH S*		DFC		
470 nm	250 mW	395 nm	NA	295 nm	10 mW	2500 nm	3.7 mW	
475 nm	290 mW	398 nm	NA	297 nm	13 mW	2850 nm	7.6 mW	
480 nm	265 mW	403 nm	20 mW	292 nm	18 mW	3000 nm	9.9 mW	
485 nm	290 mW	408 nm	24 mW	297 nm	20 mW	3250 nm	10.1 mW	
490 nm	260 mW	413 nm	24 mW	302 nm	21 mW	3500 nm	9.2 mW	
495 nm	270 mW	418 nm	24 mW	307 nm	21 mW	3750 nm	8.6 mW	
500 nm	255 mW	423 nm	22 mW	312 nm	22 mW	4000 nm	7.7 mW	118.518°
505 nm	235 mW	428 nm	21 mW	317 nm	23 mW	4250 nm	7.2 mW	119.28°
510 nm	230 mW	433 nm	18 mW	322 nm	23 mW	4500 nm	6.4 mW	121.455°
515 nm	230 mW	438 nm	18 mW	327 nm	24 mW	5000 nm	5.3 mW	123.622°
520 nm	220 mW	443 nm	16 mW	332 nm	24 mW	5500 nm	4.3 mW	125.747°
525 nm	220 mW	448 nm	14 mW	337 nm	26 mW	6000 nm	3.5 mW	127.993°
530 nm	220 mW	453 nm	12 mW	342 nm	25 mW	6500 nm	3.3 mW	128.909°
		458 nm	11 mW	347 nm	24 mW	7000 nm	3.0 mW	130.409°
		463 nm	10 mW	352 nm	23 mW	7500 nm	2.9 mW	
		468 nm	9 mW	357 nm	23 mW	8000 nm	2.7 mW	
		473 nm	7 mW	362 nm	20 mW	8500 nm	2.5 mW	
		478 nm	7 mW	367 nm	19 mW	9000 nm	2.3 mW	
		483 nm	8 mW	372 nm	17 mW	9500 nm	2.0 mW	
				377 nm	15 mW	10000 nm	1.7 mW	
				382 nm	13 mW	11000 nm	1.4 mW	
				387 nm	11 mW			
				392 nm	8 mW			
				397 nm	7 mW			
				402 nm	NA			
				407 nm	NA			

\* NOTE: Dave's autocards double the 800 nm

Ti:sapph output because of a dye fluorescent dye incorporated into the card stock. The dye also fluoresces blue when exposed to UV. You can use this to confirm the existence of UV when turning/calibrating the SHSHS process.

After Mixer Calibration, Dave took a second look at Tsunami. This time, he opened it up to check the slatwork.

↳ tightened the mount holders and mounted to the counter. Still observed sensitivity.

checked to Millenia - tapping on the table near the Millenia and on the Millenia case - no effect. Dave does not suspect the Millenia is the problem.

a lot of scatter off MZ - Dave cleaned the optic, and the scatter was gone

Dave managed to make the Spalt Tsunami a little <sup>less</sup> sensitive, but still not perfect. He advised that we keep the mode locked on for now.

TOPS form 35041

MODE M.Z.A

↳ after his adjustments ~500 mW out of Tsunami; 7 bars lit on the photodiode

After Dave left, collected power curve w/ our 402A

9

Sprtfire status: 3.9 W

13 round trips (99.50, 124.50, and 253.50)

Touched up compression to 10743 @ 130 nm → maximized power

10743

10742

<u>Wavelength</u>	<u>S+I</u>	<u>S (pre-unifier)</u>	<u>S+I</u>	<u>S (pre-unifier)</u>
1140 nm	100 mW	55 mW	100 mW	60 mW
1160 nm	220 mW	130 mW	280 mW	200 mW
1180 nm	315 mW	180 mW	400 mW	290 mW
1200 nm	380 mW	230 mW	440 mW	300 mW
1220 nm	400 mW	245 mW	500 mW	340 mW
1240 nm	370 mW	225 mW	540 mW	360 mW
1240 nm	390 mW (a little unstable)			
1260 nm	440 mW (a little unstable)	270 mW	580 mW	360 mW
1280 nm	480 mW	285 mW	580 mW	370 mW
1300 nm	500 mW	290 mW	600 mW	380 mW
1320 nm	490 mW	275 mW	600 mW	370 mW
1340 nm	490 mW	260 mW	600 mW	360 mW
1360 nm	460 mW	240 mW	580 mW	340 mW
1380 nm	420 mW	210 mW	600 mW	350 mW
1400 nm	440 mW	220 mW	600 mW	340 mW
1420 nm	370 mW	185 mW	610 mW	340 mW
1440 nm	420 mW	210 mW	600 mW	340 mW
1460 nm	430 mW	215 mW	600 mW	330 mW
1480 nm	440 mW	220 mW	580 mW	300 mW
1500 nm	400 mW	190 mW	560 mW	300 mW
1520 nm	380 mW	180 mW	570 mW	280 mW
1540 nm	400 mW	180 mW	510 mW	260 mW
1560 nm	350 mW	170 mW	500 mW	240 mW
1580 nm	260 mW	100 mW	410 mW	190 mW
1600 nm	300 mW	90 mW	470 mW	150 mW
1620 nm	260 mW	45 mW		



June 10, 25-28, 2013

check #3

F3 fuse → front of power supply; quarter turn - 220 N 10 A? - look in manual

if blown, replace

open: two red wires → to heaters } on red leads. }  
100 Ω

turn off power supply and unplugging

MOC3040  
1560 150COM  
IS27W

is there a way to tell whether one is blown?

fan in power supply?

if you pull F3 fuse, diodes should start cooling?

black heads: thermal cut outs

red wires go to each heater  
↳ follow to same heater

Millenia - manual is the only customer manual

boot sequence

microprocessor

EEPROM - Err B1

start compressor

interlock - 95

\* turn heater on

< 3 min

turn compressor on

safety kill = second click

write 8 pin chip  
↳ opto isolator  
3/8" x 3/8"

follow the wires?

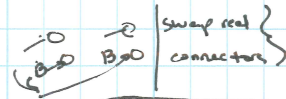
check heater temp before and after  
first click  
turn compressor on → check cooling error  
second click

Joe - ask for fire rod - T40 power supply for Millenia V

set screw holds the fire rod in place  
↳ no distinction between the wires

just crimped on connector?

4 screws remove inside front



- 0 Ω across = single thermal cut out

swap the heaters?  
v off the front panel board?

if OK, board not doing its job

remove front panel board  
↳ check connector to heaters

↳ shunt red JL:  
across the connector...

double check the wiring...

~7 min  
2 clicks P  
stalling

reset button  
↳ square  
locking valve  
red or blue  
↳ in back on top

let D2 drop completely → both diodes should cool to ~20° ~10°  
↳ 5 min?

big fan - white → middle of the power supply  
↳ compressor hot? → should feel hot

↳ bearings seize up → replace motor if that the case  
\$5k? for compressor  
can motor \$50

Cooling test → heating test

↳ just tries to heat and sees if it heats

Dave visit - May 12 - 14 2014

Empower filter: should be vacuumed out ~ quarterly  
filter is in the back of the power supply - see photo.

blow out in Millennia T40 every once in a while

Millennia: touch up work | Checked HR+ SHG temp - both pretty close  
updated power curve (did not look @ diode output - just looked at  
switch Pin 4 } doesn't matter whether or not laser is on

main screen: can set

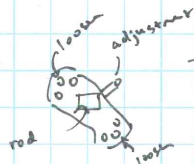
in SP Current mode:

- can set operating current on <sup>info</sup> screen - direct control of D1 and D2 current
- provides both a coarse and fine adjustment on the SHG temp
  - ↳ accessed in the same fashion as in standard modes
  - just provides coarse adjustment as well as fine.
  - measurements are made as a number of bits of resolution - no direct physical way w/o knowing the range of the temperature control
  - ↳ more positive increases LBO temp
  - more negative decreases LBO temp

- main: can enter temps for diodes, currents that give 13 W out of diodes

- when new values are entered in the new menu in SP Current mode, switch to normal power and let it sit → the new power curve will be written
- ↳ switch pin 4 to leave ~~SP current~~ technician access after power curve written

Tsunami: rod translation:



There are six screws that hold the rod mount in place.

The center one loosens the mount, and the one out on its own allows translation

rod cleaning: MeOH, acetone, toluene, etc. - any are fine

tuning slit was open too wide - only need ~3 mm or so (maybe a little more)

Dave entered on optics w/ the tuning slit in place ⇒ really doesn't matter whether the tuning slit is there or not

- ↳ other than getting the initial loss, he left the tuning slit in place

(2)

(Tsunami, continued)

w/ 4.0 W on the Millennia, Dave was targeting ~400 mW out of Tsunami?

M2 translation - not taboo, but once Dave has set them to ~~efficiently~~ get good performance, we should not need to touch it

However, NEVER translate M3

P2 is actually a focusing mirror - there is a small screw that allow to ~~any~~ adjustment of the focus of the beam; should not need adjustment unless the focus out of the Millennia changes

Dave was being tricky getting sufficient bandwidth (to his ~~tricky~~ liking) - he translated M3  
 ↳ ~~M3 just slides along the crossbar~~ M3 has a small set screw that allow translation

M3 has a line on it and on its mount hardware to gauge translation

↳ M2 and M3 often need to be moved in tandem - if one is moved forward/back, the other likely needs to be moved forward/back

**A NEVER DO THIS!!!**

After the adjustments, Dave was able to get up to ~70 nm bandwidth (FWHM)

reducing to ~60 nm, Dave could push the ~~present~~ pump power to ~4.3 W w/o CW breakthrough

However, after closing and reopening the shutter, Dave could not recover mode-locking - something on M3?

w/ 4.0 W pump: 480 mW out, w/ 60 nm bandwidth

could tap pretty aggressively w/o loss of mode-locking

3

Watching pico Spire install:

To get the Empower output entering correctly, Dave put the alignment tool right inside the shutter

Bandwidth detector: old photodiodes: pick up any color light  
in picosecond Spire, seem the new photodiodes are only sensitive to 800nm

Dave does not use free-running mode for alignment anymore. in the SW systems, he ~~see~~ finds that he often burns through the Thin Film Polarizer

Charcoal packs: 6 no cycle?

Grady - MeOH?  
drizzle

To align intracavity Pockels cell:

piece of diffuser after TFP

↔ polarizer before intracavity Pockels cell  
↑ polarizer after  
↓ look before wave plate

w/ all Pockels cells off, but wave plate between extra cavity Pockels cell and TFP  
↳ allows all seed pulses into the cavity

optimize Pockels cell by optimizing cross pattern

New TFP - does not suppress loss  
no pulse train looks weird  
still needed for ns (asy) - needed to trap a fluorescence photon?

Ch. 1: allow seed in ; Ch. 2: rotate 90°, trapping ; Ch. 3: rotate 90°, ~~to~~  
a single pulse dumps all light

V gets trapped in cavity  
quarter wave plate - light gets rotated 180° w/ 2 passes } time the pulse comes back from the end mirror  
turns off after → off by the  
↳ the selected pulse get rotated 270°

TDCs: Delay 750: relative delay between Empower and Tsunami triggers | optimize by watching pulse train  
↳ try to get pulse train as early as possible?

Ch. 2:

Ch. 1: optimize by trying to bring pulse train as far to the left as possible on most systems; then one is behaving weirdly.



(4)

on: 3,2,1 } for manual turn on  
 off: 1,2,3 }

to overcome bwd: disable check of Ch. 1,2,3 out of TDG?  
 → have to be in service mode

Timing → use BWD → check boxes 1,2,3

ASE - since the TFP does not hold back long when the Pockets cells are off, there is likely some ASE component to the output - gets lost in the compressor (compressor appears less efficient because of this)

amplified spontaneous emission

w/ new units: need to switch out Ch.3 earlier in order to optimize seed pointing  
 cannot disover Ch.3 to optimize pulse train - risk of damage

chiller fluid: ~~cools~~ helps pull heat away from the rod } if rod temp is too high consistently, may need an additional chiller for the Spithues  
 Cool high-speed driver

turn off High Voltage in TDG before checking pulse pickup board

HV: if no voltage, the HV jumper in the TDG is probably dead. there are 2 - one for each Pockets cell

if no current / Pockets cells not firing, there is a problem w/ either the HV jumper or the High speed driver

can see the ~~voltage~~ voltage and current in the TDG / timing menu while in service mode

Regens: can run w/ under 20 w. HOWEVER: if you run w/ under 20 w:

- but build up will be slower - more passes will be required to reach peak power
- this will introduce more nonlinear chirp that cannot be compensated for in the compressor
- more nonlinear chirp  $\equiv$  broader pulses

(5)

Empower LBO: heated to  $\sim 320^\circ\text{F}$

held in place by a pair of springs: on one side and on top

hold the LBO in place and allow room for expansion

can be cleaned - MeOH is fine?

need to let it cool first

LBO temp adjust - for left trimpot (of the 3)

Intercavity Pockets cell: enable only Ch. 2

to align the compressor, Dave switches out Ch. 3 early so that the power is reduced.

↳ easier to align?

Less likely to damage things?

to check alignment of compressor graty: can turn the power down and turn the graty to put the back reflection through the alignment tool - if it isn't able to go through, use vertical adjustment.

the output of the compressor and the input to the compressor should be over each other: if they are not, can ~~move~~ change the V-mirror assembly (the one not on the delay line)

to clean the compressor graty: drizzle with MeOH (from a squirt bottle) and blow off w/ Nitrogen  
to put back, just push to back of mount

when the new compressor is placed in:

- check vertical by back reflection through the alignment tool
- check horizontal by checking checking the overlap of in and out of compressor

to touch up vertical: use vertical adjustment on graty mount

↳ touch up horizontal: use the V-mirror assembly (tune until the horizontal is correct)

expected efficiency:  $\sim 80\%$

10/21/2014

Questions

- Diff in the Tsunami ... ~ 1-2% ... Is this expected?
- AOM cleaning: appropriate solvents?

- TOPAS WL optimization
- running Spire ...

MZ values?

High power systems: how to switch out Ch. 3 earlier when turbine and mirrors / pump arrives

Optimize comp alignment: to optimize pump, it is best to block the back reflection to optimize the forward pass, then optimize the back reflection otherwise, the two are coupled and you may end up at a local rather than global optimum

2014 10 21

Questions

- pump lease for Tsunami? → Millenia vj; Melior; 150k or 20k
- speak to Jonathan re: issues in visible CPA - lots of damage
- focus in TOPAS?
- AOM cleaning - appropriate solvents? - MeOH, acetone - just watch out for the wires

- Millenia: diodes still available
- used parts questionable
- Melior: all external knobs / adjustments software controlled

Millenia: set to 3.96 W  
 P1 21.7 A 22.4°C  
 P2 22.9 A 29.4°C

Dave started - 1 Tsunami

↳ focused in pump ... HR + DC  
 tried to auto lock ... got part ~ 50 mm bar → suggest something is dirty / misaligned  
 cleaned AOM + input Brewster window, P1, P2  
 after cleaning AOM, M4 → cont increase bar to 56.57 mm  
 after cleaning Brewster window + pump → slow rise

aligned M3 opt - Dave RH for fluorescence in signal misaligned out | the fluorescence is the main of the fluorescence through the AOM

cleaned P1 and P2  
 cleaned M3

transferred the rod, changed focus of M2 | Did not adjust M3 - M3 is not a sensitive since it doesn't have a microscope  
 ↳ there is only the 1st, and being off by 1/4 of the thickness of the lens can matter

TOPS → 3504: (transition)

59 nm line query for fs system  
 when Dave changed the pump focus → 1/8? 1/16? : f a ten - small adjustment  
 he recovered and reoptimized everything  
 - using P2 to align the fluorescence out of the cavity (laser outside)  
 - using M1 + M2 to optimize the power

P2 translation adjustment allowed Dave to get ~540 mW

Dave reduced pump to 3.0 W, then returned to 3.8 W

Dave finally decided to treat M3 beam

w/ alignment to our spectrum: Dave's spectrometer read 199 nm (central @)  
 55-57 nm (FWHM)  
 → 56-58 nm?  
 power: ~500-510 mW  
 pump @ 4 W

The bandwidth could be extended under at well

Spurious

Ch1 and Ch2 timing adjustments just trying to push power down as early in time as possible  
 → water pulse train and power

Losses in TFP can vary

Pulse train can look like



where at saturation, there is a dip - Dave went over the case... He did indicate that this is sometimes occurs when the waveplate is not rotated correctly.

However it could also be mitigated by adjusting Ch1 and Ch2 timing

Checking external Poekels cell

put lens paper before Poekels cell and wave plate between Poekels cell and TFP } with the seed.  
 ↳ set to maximize light strength } (block the pump)  
 optimize Poekels cell for con pattern

(Suzuki) Dave picked up red mirror (M4) - 530 mW



Dave visit: 11/21/2014

Questions: - AR coating on Pockels cells? if so, how easily damaged? + Yes, has AR coating.  
- Q: tip things for cleaning? - TERWIFE

Compressor breadboard: improve stability

separated from the main breadboard by a series of pads  
less thermal/vibrational effects on the compressor

New Spindles: TDA has HV generators

The gold boxes are high speed drivers - switch the HV to the Pockels cells on and off quickly.

Pulse pickup board - delays the HV signal to extracavity Pockels cell.

~~Compressor~~ Pockels cell:

Before installing Pockels cell, Dave checked alignment - sent the seed into seed train into the cavity, and placed crossed polarizers before and after the intracavity Pockels cell.

Empower pump chamber:

- open plastic cover
- turn off chiller
- open grey pump chamber cover
- the pump chamber is in an enclosure whose lid is held down by 4 screws. Remove these.
- remove the connector + the pump chamber (held by 2 screws)
- there are four screws mounting the pump chamber. Remove these.

There are 3 gold colored blocks that are the diode banks  
 electrical connection are made by 6 gold clips: two spring to each of the anodes of  
 electrodes of each diode bank

a metal block through which the screen pan mounts the gold clips and introduces electrical  
 contact through the screen

When we removed the top diode there was a black spot on the electrode on the  
 clip and on the diode block.

↳ Dave said it would be possible to sand off the damage to the clip, but the  
 replacement had arrived so we used one of those  
 as for the diode block, sand off the corrosion, place a little solder on the end,  
 then sand down

↳ be careful of the diodes! do not touch

for both cases, fine sand paper should be used

LBO -3.147

need ~21.9 A to get 20 w  
 LBO adjustment did not help

} when clip corroded, smoke → dirtied optics?  
 it is possible to clean diodes in MeOH, not acetone.

Dave visit - 11/6/15

when Pockets call gets damaged, likely an issue w/ the seed  
 ↳ is the seed getting stretched sufficiently?  
 need ~ 200 ps to avoid damage.

Tsunami: vertical drift normal - this is usually the change that occurs

no good answer on why we need to reduce pump power to reduce CW breakthrough → associated w/ deterioration of cavity quality?

Miles: Dave usually turns up SWR first, then adjusts HR pointing

factory: ~ 12 passes to build up to peak power  
 nearly the same as current Ace operation

Dave started by checking seed band width

~ 60 nm FWHM in

poststretch: ~ 2.5 nm FWHM w/ 800 nm center | this is comparable to BW @ install

w/ high power systems, when introducing seed: disable all Pockets calls, unblock seed, then reenable all channels

↳ just to be as cautious as possible

TSP: most likely to get damaged when part problem w/ cavity

Pockets call: most likely to get damaged when problem w/ seed

↳ damage to Pockets call is why you need to watch out for CW / CW breakthrough on the Tsunami

Zero delay: used to be optimized to the pulse train

now Dave just optimizes to power

To check seed: - Dave set K power lower (15-16 A)

- disabled all Pockets calls channels

- switched out Ch. 3 much earlier

- unblocked seed

- enabled Pockets calls

- peaked up seed pointing

↳ even for final tweaks to seed pointing

Dave switches out Ch. 3 earlier

Ch. 2 adjustment - trying to get pulse train as early as possible  $\rightarrow$  as much to the left as possible  
 $\hookrightarrow$  same w/ Ch 1

if Rodels cell gets dinged before translating should clean the surface - when the cell gets dinged it can generate a piece of stuff that coats the surface  $\rightarrow$  this can facilitate further damage.

The next morning, the spectrum looked a pulse train was a little weaker. Dave poked the end mirror to recover the pulse train  
 $\hookrightarrow$  before doing so switch out earlier.

Empire: if internal leak, humidity would cause loss of power, and if too much, just won't lose  
 see box - to clean YCF rod

Low chiller fluid - likely an external leak, probably the filter case or the fittings  
 will not see a puddle - will see casing stuff on the filter housing or the fittings  
 if there is a leak, the tank can also get sucked in - that is why the lid looks weird.

Dave visit - 4/9/2015

Damage specifically to the Pockels cell and only the Pockels cell is unusual - Dave has not previously seen this occur?

- usually TFP can get drilled, but if the Pockels cell gets drilled it is a significant enough problem that other optics in the cavity (rod, TFP, etc.) get drilled as well

- Dmitry is concerned about effects of the seed, but Jonathan has indicated that the Pockels cell has drilled on him w/o the seed, so Dave is concerned about contributions from the Emponer

↳ esp. given the change in current necessary to get consistent performance from the Spitfire since install.

Dave is wondering whether the beam out of the Emponer could have changed.

- apparently the exit of the Emponer has a lens as a dust shield if a lens gets dirty, the surface grime can get heated and act as a lens - thermal lensing; this can change the focal lengths of the lens

↳ Dave has even seen situations where the coating on a flat optic gets damaged, and heating causes thermal lensing from that optic

Grain pattern in Spitfire beam

- Dave sometimes sees this
- ↳ Jonathan gave a back reflection off of one of the other optics - nothing to worry about in this case can determine if it is real or not with a fine diode outside the Spitfire.
- If Ch. 3 doesn't suppress it, probably the wave plate slightly ~~may~~ ~~could~~ be necessary to remove it

Pockels cell damage:

- is the beam waist of the cavity made in the Pockels cell? if so, then could be why the Pockels cell is getting drilled.

↳ Dave does not know where the factory tries to make the waister waist, but does not suspect the Emponer has much role in determining the position of the beam waist

- the cavity end mirrors are both curved

- Dmitry suggested trying up Emponer focus to try + compensate

↳ Dave tried tracking the internal focus for power, but it had no effect. Little impact

"Other" waists (such as the old pos Spitfire): you'd want to adjust the focus of the pump to get peak

power, then back it off - having the focus of the pump on the face of the rod could result in damage

↳ Dave's not sure why focus in the rod vs. at the face of the rod makes a difference

2

Dave was adjusting the focus for the focusing mirror of the pump beam reflector - the positioning of the screw hole on the mounting block didn't allow him to get the position he wanted, so he moved the mounting block back one inch.

While Dave was taking a lunch break, I spoke to John to pass on what Dave had said Re: the factory's thoughts on what is causing the damage to the Poché's cell. According to John:

- it is common for the beam waist to not be in the rod.
- the reason for this is that you want the cavity mode to fill the excitation volume inside the rod.
- however, John also felt that the cavity mode should be determined by the imaging of the end mirrors, and could not see an easy answer as to why the focus of the Ermpow beam into the rod should change the location of the beam waist of the cavity mode.

Beam waist according to Darity, should be in the center of the rod.

Darity suggested that a cavity optic might be damaged - damage to a cavity could be creating a new beam or a hot spot - Darity suggested that the most definitive way to determine this is to remove and examine each optic.

from talking  
w/ Darity

Dave started by trying to adjust the position of the tuning mirror that the Ermpow beam first hits. Dave looked at the optics when he breeched/breached on the two end mirrors, there was some clear spots on the surfaces.

After exposing a new Polaron part of the Poché's cell surface, Dave was still getting the red spot. Dave rotated the two end mirrors in their cradle in order to expose fresh surfaces.

↳ 90° rotation

Next, Dave moved to the cavity mirror that comes after the TFP.

↳ for this one, he wanted to rotate 180°

he pulled this mirror out to examine it.

Dave spoke to Darity again. From what it sounds like, the factory is thinking:

- PM1 and PM2 from a reflective telescope to expand the pump beam.
- a lens then focuses the pump into the rod.
- given that we are not end-on pumping, the divergence is different, so the pump is getting focused more tightly in the rod.
- the tighter focus is probably a smaller cavity mode with sufficient intensity to damage the Poché's cell.

↳ given by eye, the cavity mode looks about the same size on each optic, so the end mirrors must have among a very shallow focus.

3

First thing to try: switch from the default <sup>500</sup> 600mm lens to a <sup>600</sup> 650mm lens

- Dave measured the current distance to the rod, and moved the base mount back an appropriate amount
- the lens is the 2<sup>nd</sup> optic in the mount on the side with the notch for the locking screw on the mount base

After swapping the lens and taking up cavity and mirrors/pump pointing, Dave was getting  $\sim 5.8 \text{ W}$  w/ 17W pump

↳ no significant difference in the

Dave's 402A vs. ours: when he measured  $\sim 16.5 \text{ W}$ , we measured  $\sim 16 \text{ W}$

gain.

mode structure: cooling of the rod can affect it, alignment

after swapping out the lens, Dave was still seeing the "halo" around the rods - a sign that the pump is overburdened

Dave spoke with Darity: they agree they don't want to leave us with just the replaced lens - this likely will not be a viable solution

- Dave is going to move the beam expanded outside the Spitfire; hopefully, this will give a more "normal" beam diameter into the rod.
- returned the 500mm lens
- set up the optics as follows:

External:

Internal



- after the change, Dave was able to get some lasing from the cavity - not wasn't very good, but we gave a little more, enough to touch up cavity and pump pointing
- however, Dave felt that the beam was too small on the lens, and when he raised the power he still felt that the beam size was an issue - however, he also felt that the beam was too large at the lens

↳ Dave tried moving the second to mirrors of the beam expanded forward and backward, but it had little effect - he still felt the mode looked too large in the rod

Dave decided he would leave things running w/  $\sim 6 \text{ W}$  out of the regas

↳ this required  $\sim 20 \text{ A}$  and  $\sim 250 \text{ ns}$  build up time

(21 A is apparently  $\sim 20 \text{ W}$ )

output mode a lot smaller - Dave was concerned re: leaving it running - like this

Dave's visit - 4/27/2015

Millenia's down to 3.9 W - why?

↳ Blake doesn't know; ask Kyle

The telescope Newport sent: these are the mirrors that should be in a Spitfire Ace

↳ Davey wanted to try these in case a different set of mirrors had been installed when the Ace was set up

when the optics were swapped, Dave said the radius of curvature looked similar, and the size of the beam on the lens didn't change appreciably

He test up on additional mirror and traced the beam down to the wall (by the dry erase board)

↳ starting from the 9.5" the factory indicated, Dave moved the telescope separation forward and back (down to ~8" and out to ~17") and gauged the collimation

The beam was mostly still diverging at the full distance for all mirror separations;

however, at the distance across the table, the beam appeared roughly collimated ~13", give or take. Dave left the mirrors with a separation of 13.5" 13.25"

After touching up the cavity of cw, Dave switched to ns Q-switch

↳ while operating in ns Q-switch, there was a large envelope under the normal ns pulse train profile

Dave used adjusting the Pockels cell voltage (in service mode) to see if that could suppress it

↳ was concerned RE: whether Pockels cell is fully rotatory polarizer and consequently not holding back the cavity

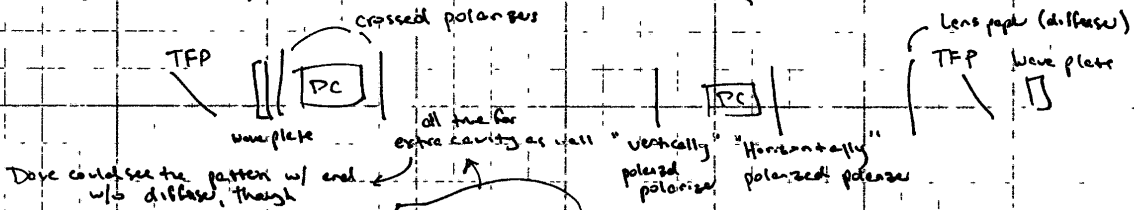
next, he tried switching to a clean surface on the existing Pockels cell

in new regens: HV generated in the TDG and sent down in the umbilical, along with a DAC that carries the timing information

the green gold boxes in the new regens use the timing signal and the HV to generate the short pulses of HV to trigger the Pockels cells

checking extra cavity Pockels cell:

intracavity Pockels cell



when you do it this way, you should have a pattern like?

Dave's not sure the absolute polarization he had to move the diffuser close to the Pockels cell in order to get enough light though



when looking at the extra cavity Pickett cell:

the pattern looked more like



w/ ripples - Dave didn't think think the  
lens correct

Dave concerned by the size on the rod - w/ 20 W, only getting ~5.5 W } thinks the spot size is too large  
↳ build up time is also ~100 ns longer } on the rod

Dave spoke w/ Deering: his suggestion was that collimation was off

↳ Dave decided he would try adjusting the telescope spacing while watching the size of the mode on the rod - he would keep adjusting until they looked about right to him  
↳ Dave ultimately ended up at the same spot we arrived at on the basis of collimation every other position he tried (greater and less separation) yielded a large spot on the rod.

next. Dave started trying to tweak the position of the lens to peak power.

↳ eventually, Dave first made smaller adjustments to the positioning of the first telescope mirror - adjustment on the scale of  $\sim 1/8$ "

with this adjustment (on the basis of power) he began to see improvements

↳ Dave kept making adjustments to the telescope separation (decreasing the separation) and seeing improvement in power and e. reduction - build up time

He decided since he never saw the beam size on the rod be "too small"

that he would just keep decreasing the separation until the power stopped increasing. Power appeared to peak after moving the front mirror forward  $\sim 1.5$ "

20 W @ 20.5 A

↳ at this Dave was getting a beam under 6.8 W  $\rightarrow$  didn't like

that so he switched to 20 A  $\rightarrow$  6.4 W out

After the adjustment, Dave was getting ~6.2-6.4 W w/ 20 A

↳ build up was ~70 ns longer. He tried adjusting zero delay, with no significant gains

$\rightarrow$  ~6.1 W when needed

build up is ~60 ns longer than before

at the factory, they had essentially the same thing as Dave had had as install

↳ using a ~100 fs oscillator - Dave felt that the entire power in the rod could explain some of the difference

Pockels cells are cut on an angle. when mounted, the wedge introduces a vertical change in the cavity - need to tune to cavity to account for this  
 ↳ after installation of the new Pockels cell, Dave allowed the seed into the cavity and tweaked the seed mirror to compensate for the change introduced by the Pockels cell

when operating region is switched, mode lock pretty good  
 ↳ when seed is introduced, mode shows a "halo", and seems narrower

after replacing Pockels cell - cavity peaked  $\sim 6.1$  W  
 $\sim 4.4$  W out of compressor

Dave tweaked up stretch alignment, including trying to get to B2B a little more stable

When Dave got in Tues morning, he noticed that the lid did not appear to be fully opening the shutter  
 ↳ because the beam is legal going into the Spitfire now, it is clipping when the lid is a bit tightened down  
 ↳ even when the screws are tightened, pressing on the lid still opens the shutter a little more

Dave wanted to adjust this slightly so that the lid does open the shutter fully

Dave also spoke with Daming wants to check the seed bandwidth - if it is too narrow, it might not be getting stretched enough, hence the smaller beam size input when seeded  
 ↳ looked at the output bandwidth -  $\sim 2.2$  -  $2.3$  nm FWHM; Dave felt this should be fine  
 ↳ outside the Spitfire ↳ factory had 1.5 nm for a 1.2 ps pulse

To fix the issue with the entrance shutter, Dave created a shim out of a wad of duck tape and fixed it on the lid

↳ otherwise Dave would have had to shift the mode down, and realign the Spitfire to match the new pump pointing

the shim of duck tape seemed to do the trick

even though the beam size is smaller when seeded, Dave isn't too concerned about damage to the compressor  
 ↳ the focal size of the mode is about right

Dave visit - 09/08/2015

Per Dave:

we're the only group he's aware of using a 30fs oscillator  
 absent other group is one that uses a 30fs oscillator to seed a 30fs and 100fs regens  
 so they built the entire system in one go, so the factory developed a telescope to get to  
 seed size current

new T box: switch is on a board in the power supply

R18: trimpot for the diode

in new Millennia, there are 3 trimpots, but it is still R18

in SP Current mode, the Millennia "remembers the old set points"

w/ 23A to D1 } ~5.7W  
 24.1A to D2 }

want 13W @ 809nm  
 should get 6W out

on the mesh screen in SP Current mode: reports current power

allows you to directly set the current on each diode

2.8 W diodes

↳ cannot let the current ramp too high

wouldn't hurt to update power curves every 5000 hrs or so

Est A @ 13W

↳ D1 set; D2 set

process:

↳ both current and temp need to be set in the Setup screen

in SP Current mode: set current and temp to get 16W and proper diode performance

switch to Power mode: will reset the current to get ~5.5W

↳ will only allow you to go ~2 A over

need to wait ~5 min to re-calibrate

after, go to 100% in current mode - 100% should yield ~5.5W

Recalibration

D1	24.8°C		2.8-2.9 nm
	23 A		
D2:	29.2°C	13 W @ 809 nm	3.1-3.2 nm
	24.1 A	on 9/8/2015	bandwidth

Diode: 809 nm

w/ < 3.5 nm FWHM  
 as long as it's symmetrical

Millenia is microcavity doubled

if you remove the fiber, hope to come in at an angle so you don't scratch the end

↳ let the edge of the fiber find the housing, rather than the tip of the fiber

keep the fiber also at least ~1" away from the power meter - the back reflection can cause

damage due to the heat

with SP Current mode:  $\sim 6.2$  W

↳ after Diode adjustment

touched up HR: no meaningful gains maybe to 6.4 W

after assigning the set points, switch over to Power mode (NOT SP Power mode) and wait  $\sim 5$  min

22 → 21.5 } Last week: 22 A after calibration 21.5 A  
23.2 → 22.7 } 23.2 A 22.7 A

4 W @ 96% Current

5.2 W @ 100% Current

could be worth peaking up SHG - make  $\sim 5$  unit steps and give time to equilibrate  
better to err on the side of cooler rather than warmer  
↳ more negative

Millenia output does shift vertically over time - Dave is not sure why

modulation of the Tsunami spectrum occurs when the ARM is on but is not at the correct frequency

Dave didn't do much w/ the Tsunami - HE, QC, bandwidth, wavelength

set to 60 nm FWHM, 800 nm center

Dave was getting  $\sim 490$  nm when mode locked → 4.0 W pump

mode locks w/ the ARM

saved an image of the 60 nm bandwidth 800 nm center as 2015.09.08.dv.dot

Factory sent 3 mirrors: +200 FL

-100 FL → gave too large a beam

-75 FL

apparently the beam was also clipping on the aperture of the Faraday isolator

to do this adjustment, want  
the CW color close to the operating  
Cold

There was a stripe across the mode after the stretchers. Dave was concerned about alignment, so he sent the  
Tsunami CW; the spots did not line up.

Dave said misalignment could introduce shoulder, but otherwise probably nothing too significant

in order to get things better aligned, Dave had to change the angle of the grating as well as  
rotate the V-mirror assembly

Dave observed the line down the mode even after the adjustment

↳ he usually doesn't see this until the 1500 groove gratings

the picosecond system has a 2200 groove grating

↳ need the extra dispersion in order to get down to picosecond bandwidths

~~and to~~

after adjusting the stretchers, Dave took a small iris and walked it across the mode vertically and horizontally:

he watched the spectrum as he moved the iris:

changes in the spectrum as he moved the iris vertically inform on misalignment of the roof assembly

changes in the spectrum as he moved the iris horizontally inform on an error in the focus of the mirror behind the stretchers

↳ need to adjust translation

he wasn't sure what caused these effects, though, other than that it checks that the seed is correctly chirped

CAW: 803 nm, 2.5-2.6 nm bandwidth

no major changes - nothing significant (maybe 0.1 nm if you believe the fluctuations)

↳ Dave usually sees a few nm of change, though this is usually in femtosecond units

The carrier on the bandwidth detector can be loosened to adjust the phase of each decade

↳ Dave spread the diodes out a little wider

Dave then replaced the Pockels cell

↳ he started using a wave plate to introduce the seed and use the seed to align the cavity

to align Pockels cell:

first polarizer set to pass, second to block

The Tsunami is going CW - Dave is concerned that a back reflection from the lenses might be making it back to the oscillator and causing disruption to the mode

Additionally, when looking at the seed, Dave felt it looked

↳ by narrowing the beam to get it through "squished" by the two + reaches the cavity?

Dave brought the lenses closer together - appeared

↳ vertical only  
"squished" is the cavity  
the Faraday isolator, is the mode ending up

↳ make the problem worse

Looking at the mode of the Tsunami over an extended path length ( $\sim 30$  ft) the mode out of the Tsunami looks OK

Concern regarding the focusing with the stretchers?

Generally the mode of the Tsunami is not perfect

$\hookrightarrow$  the mode of the regen is controlled more strongly by the quality of the cavity, the aperture etc. i.e. the regen, not the seed

Dave wanted to check for proper alignment of the grating: adjusted the vertical of the first focusing mirror (the one where the mask is) to check that the grating retroreflected (for this test, Dave set the Tsunami CW)

The factory designed the laser for usage with a 10 nm seed?  $\rightarrow$  11.3 nm bandwidth

$\hookrightarrow$  intended a bandpass filter to be used to cut the bandwidth to 10 nm, but Dave found that it cut out too much of the seed energy.

Looking into the at the mode, we noticed it looked "squished" before the extracting Pockels cell, but not before the polarizer

$\hookrightarrow$  it looks like Dave hadn't realigned the passage after being chiro, because the beds were high on the alignment tool  
consequently, it was clipping on the polarizer perhaps, which was causing the shape

For Pockels cell alignment:

Dave had a stack of 3 polarizers (major  $\uparrow \leftrightarrow \downarrow$ ); putting this stack before the Pockels cell achieved the same result as the two polarizers (one before and one after)

Dave swapped back to the old Pockels cell

$\hookrightarrow$  tried to get long

had to align the cavity to the seed - used end mirror only.

when he rotated the wave plate, got a little loss - a higher TEM - apparently the different TEM have different sensitivity to cavity alignment

got some power; switched over to Q-switch

$\hookrightarrow$  internal photodiode requires 50  $\Omega$  input impedance, full bandwidth

with the old Pockels cell, Dave was getting  $\sim 5.6$  W when on a bad spot,  $\sim 6.0$  W on a good spot

$\hookrightarrow$  at this position, the mode appeared to be clipping on the edge of the Pockels cell

Dave moved to a new point on the Pockels cell

getting  $\sim 5.8$  W w/ Q-switched and seeded

when seeded, getting a **buff BURT** of 40 ns instead of 20 ns

$\hookrightarrow$  due to the mode of the seed being smaller?

factory: 40 ns build up reduction time

mode looks smaller; ring is visible around the mode

↳ seed usually doesn't impact the size of the mode

but we're seeing that with the seed introduced, the output mode is maybe 80% of the size of the ns mode

the hole we are seeing is due to overshoot of the pump

↳ Dmitri went Dave to change the timing of the Q-switch in the Empower

Dave connected the Empower to the laptop by RS232 cable and started the Empower software

Did not receive communication from the Empower

↳ tried Dave's computer, and it still could not communicate

Dave had to change the channel from COM2 to COM1 in order to get communication

returned to the computer used to drive the Ace - still no communication - the computer is already recognizing the Empower as COM1

after restarting the computer, we got communication

↳ Dave set the Empower pulse width to 2000 ns (from 5000 ns)

the gist is that you want to deliver the energy to the rod as efficiently

as possible - if the pulse is either too long or too short it will not pump the rod as efficiently

no change in the performance - in fact, power may be a little lower, but not a significant change

↳ the hole is still there

Dmitri said that the mode when seeded is expected to be smaller than the mode when Q-switched

Dave wanted to see whether the mode looked a little brighter on the cavity mirror after the TFP

↳ he translated the mirror, then peaked up the cavity again

reached 6.4 W up to the seed and 46.3 W up to the seed (was ~5.6-5.8 W before translating the mirror)

Dave replaced the Pockels cell and touched up the cavity alignment again

Pattern when Pockels cell is aligned: isogyr (isogyre)

As long as you make sure not to try to run it like that, you can send the Tsunami CW to align the cavity,  
 ↳ in the AC, this could be useful given how dim the seed is

↳ new Pockets cell took some effort to keep it centered

ended w/ Q-switch yielding ~6.3 W w/ Ch. 3: 311 ns (about same as before)

seeded w/ Ch. 3: 231 ns yielded only 4.5 W

went back to Q-switch now down to ~5 W

spot on the Pockets cell much brighter

↳ looking at the Pockets cell, there appear to be 3 burns - this would suggest that it was even getting damaged  
 during Q-switch operation

the marks are much larger than usual - Jonathan says he's seen such large spots before; when he cleans  
 the surface, they go away, and only a small spot remains

Dave tried a new spot, and, once again the Pockets cell appear to have gotten drilled or worn as the seed was introduced



Dave visit - September 23, 29 2015

Air flow in the Spitzfire XP:

in the rod chamber, Dave noticed white lines on the box plots that were signs of water.

- goes from the TCU into the rod chamber
- after the rod chamber, the tubing arrives at the a board - this is the humidity sensor
- from the humidity sensor the air returns to the TCU

to check for air flow, Dave disconnected the input into the rod chamber and connected a short stretch of hose to the end - he dipped that end into a beaker of water to watch for air flow  
 ↳ air flow is slow - about 1 bubble per second; Dave said this is about right

inside the TCU:

- the pump is the apparatus right before the desiccant tubing
- Dave checked the airflow before the desiccant tube and after - airflow was much faster than observed in the regen
- Dave replaced the stretch of tubing right after the desiccant tube

After the desiccant tube, the small metal mount is a needle gauge; Dave backed that off to increase air flow.

↳ initially humidity dropped, but soon increased again

↳ afterwards Dave checked the air flow in the regen, and saw it was too fast

we connected ~~probe~~ the purge gas generator output and let  $N_2$  to the humidity sensor - humidity still did not go down

↳ Dave tightened the connector on the humidity sensor input and the screw holding the PCB

after that, we saw humidity reading  $< 5\%$

Dave checked the flow through the humidity sensor and it was OK

Dave blew into the tubing - humidity shot up to  $\sim 90\%$

it took a couple minutes for humidity to start dropping, but once it did it dropped fast.

Next checked the air flow before and after the rod - slow air flow before (but about right)

no air flow after

Dave bypassed the rod and fibred the air from the TCU directly to the humidity sensor

↳ with the bypass, measured humidity did seem to go down slowly

Dave swapped out the desiccant cartridge - with the used one, humidity gets much lower

↳ humidity quickly dropped to  $\sim 15\%$ , then slowly continued decreasing

Dave tried putting fresh helium tape onto the other end of the "new" cartridge  
 ↳ the new cartridge still doesn't pump down enough

Dave wasn't concerned about the lack of airflow out of the rod chamber

with the old cartridge, humidity drops to ~15% within ~5 min  
 ↳ fast bubbling on the source, and much slower after the rod

after ~30 min, humidity  
 < 10%

ACE:

Dave checked the bandwidth after the stretchers for the Tsunami CW and mode locked

↳ almost no difference - mode locked yielded a 2.6 nm bandwidth, CW yielded a 2.4 nm bandwidth

The current thought is that it may be necessary to move the stretcher grating forward  
 ↳ this thought came from the fact that Dave had needed to move the compressor  
 delay all the way up at inco!

Dave removed the masks and went to Tsunami CW, used the focusing mirror near the compressor to  
 align the passes on the other focusing mirror (closest to the Empower).

Dave then moved the stretcher forward ~2", and optimized the angle based on the image on the focusing mirror  
 closest to the Empower

↳ wanted the beam centered on the stretcher and focusing mirror simultaneously

with the beam from the stretcher grating centered on the first focusing mirror, Dave could not get the  
 four passes vertically arranged correctly

↳ Dave used the adjustments on the first focusing mirror to center the beam on the  
 second focusing mirror (closest to the compressor)

Dave was asking about other masks - it turns out there was a whole stack of extra  
~~to mm slit~~ 2 ↳ we should have one 16 mm slit and one 20 mm slit  
 we have a 13 and 15 mm slits  
 ↳ installed was ~ 10 mm

Mask assembly wasn't moving - pin cannot be tight

Dave wants to switch out the cavity mirrors on either side of the rod - one showed some damage, the other he just  
 wants to be safe

Dave left us with ~5 W out of the cavity - we will see if it burns before now and next week

Still measuring  $\sim 2.3-2.5$  nm FWHM

↳ getting  $\sim 1.8-1.9$  nm FWHM for CO

3

first pass in the stretcher decreases bandwidth to  $\sim 1$  nm

Leahy indicated Dave could just leave the stretcher graty where he had moved it last week

↳ in order to avoid clipping on the graty. Dave had needed to set the beam very high on the

vertical mirror - Dave chose to move the graty back in order to not clip and be able to have the beam better centered

after moving the graty, Dave placed the alignment tool in front of the mirror with the

mask

↳ wanted to check that the vertical adjustment of the graty was correct

could also look at the back reflection when the alignment tool is near the retro - more

light when you put the tool in front of the focusing mirror though

at one point when aligning the stretcher, Dave the Thomson's CW mode was jumping around on Dave

↳ to avoid this, Dave increased the gain on the Millennia

Dave replaced the new Cavity mirror after the IEP - the one close to the back mirror that directs the

second pass

↳ P/W G0588-002

ring around the output mode - overfocusing of the pump or the seed

**CHAPTER B**  
**Appendix B**

In this section, we will present the evaluation of the derivatives  $\partial n(\lambda)/\partial \lambda$  and  $\partial^2 n(\lambda)/\partial \lambda^2$  for a variety of systems employed in the calculations presented in different chapters. These systems include benzene, a representative glass (BK7), air, and  $\beta$ -barium borate, BBO (at  $\theta = 0^\circ, 90^\circ$  and  $\theta \neq 0^\circ, 90^\circ$ ).

### B.1 Dispersion of Benzene

The dispersion curve for benzene follows the model reported by Moutzouris et al:[428]

$$n(\lambda) = \sqrt{2.170184597 + 0.00059399\lambda^2 + \frac{0.02303464}{\lambda^2} - \frac{0.000499485}{\lambda^4} + \frac{0.000178796}{\lambda^6}} \quad (\text{B.1.1})$$

The wavelengths from which this dispersion has been determined range from 450 nm to 1550nm. From Eq. B.1.1, the first derivative with respect to  $\lambda$  necessary to calculate the group velocity can be found:

$$\frac{\partial}{\partial \lambda} n(\lambda) = \frac{1}{2} \frac{1}{n(\lambda)} \left( 0.00118798\lambda - \frac{0.04606928}{\lambda^3} + \frac{0.00199794}{\lambda^5} - \frac{0.001072776}{\lambda^7} \right) \quad (\text{B.1.2})$$

where  $n(\lambda)$  is as calculated from Eq. B.1.1. The derivative of Eq. B.1.2 yields the second-order derivative necessary for calculating the group velocity dispersion:

$$\frac{\partial^2}{\partial \lambda^2} n(\lambda) = \frac{1}{2} \frac{1}{n(\lambda)} \left( 0.00118798 + \frac{0.13820784}{\lambda^4} - \frac{0.0099897}{\lambda^6} + \frac{0.007509432}{\lambda^8} \right) - \frac{1}{n(\lambda)} \left( \frac{\partial}{\partial \lambda} n(\lambda) \right)^2 \quad (\text{B.1.3})$$

where  $n(\lambda)$  is again calculated according to Eq. B.1.1, and  $\partial/\partial \lambda n(\lambda)$  is calculated using Eq. B.1.2.

### B.2 Dispersion of BK7 Glass

When the dispersion information of glass is required, BK7 is used as a representative glass. The dispersion is determined according to the dispersion reported by Schott.<sup>i</sup> The index of refraction can be calculated:

$$n(\lambda) = \sqrt{1 + \frac{1.03961212\lambda^2}{\lambda^2 - 0.00600069867} + \frac{0.231792344\lambda^2}{\lambda^2 - 0.0200179144} + \frac{1.01046945\lambda^2}{\lambda^2 - 103.560653}} \quad (\text{B.2.1})$$

The first derivative of  $n(\lambda)$  is then:

$$\frac{\partial}{\partial \lambda} n(\lambda) = \frac{1}{2} \frac{1}{n(\lambda)} \left( \frac{2.07922424\lambda}{\lambda^2 - 0.00600069867} - \frac{2.07922424\lambda^3}{(\lambda^2 - 0.00600069867)^2} + \frac{0.463584688\lambda}{\lambda^2 - 0.0200179144} - \frac{0.463584688\lambda^3}{(\lambda^2 - 0.0200179144)^2} + \frac{2.0209389\lambda}{\lambda^2 - 103.560653} - \frac{2.0209389\lambda^3}{(\lambda^2 - 103.560653)^2} \right) \quad (\text{B.2.2})$$

<sup>i</sup>The documentation and formula are available at [refractiveindex.info](http://refractiveindex.info).

where  $n(\lambda)$  is calculated according to Eq. B.2.1. The second derivative can be evaluated from Eq. B.2.2:

$$\begin{aligned} \frac{\partial^2}{\partial \lambda^2} n(\lambda) = \frac{1}{n(\lambda)} & \left[ \frac{1}{2} \left( \frac{2.07922424}{\lambda^2 - 0.00600069867} - \frac{10.3961212\lambda^2}{(\lambda^2 - 0.00600069867)^2} + \frac{8.31689696\lambda^4}{(\lambda^2 - 0.00600069867)^3} \right. \right. \\ & + \frac{0.463584688}{\lambda^2 - 0.0200179144} - \frac{2.31792344\lambda^2}{(\lambda^2 - 0.0200179144)^2} + \frac{1.854338752\lambda^4}{(\lambda^2 - 0.0200179144)^3} \\ & \left. \left. + \frac{2.0209389}{\lambda^2 - 103.560653} - \frac{10.1046945\lambda^2}{(\lambda^2 - 103.560653)^2} + \frac{8.0837556\lambda^4}{(\lambda^2 - 103.560653)^3} \right) - \left( \frac{\partial}{\partial \lambda} n(\lambda) \right)^2 \right] \end{aligned} \quad (\text{B.2.3})$$

where  $n(\lambda)$  is again determined by Eq. B.2.1, and  $\partial/\partial \lambda n(\lambda)$  is calculated with Eq. B.2.2.

### B.3 Dispersion of Air

The dispersion for air is derived from Ciddor.[429] The index of refraction is calculated:

$$n(\lambda) = 1 + \frac{0.05792105}{238.0185 - \lambda^{-2}} + \frac{0.00167917}{57.362 - \lambda^{-2}} \quad (\text{B.3.1})$$

While in calculations we will generally neglect the dispersion from air, the group velocity and group velocity dispersion are usually still made available, using the first and second derivatives of the index:

$$\frac{\partial}{\partial \lambda} n(\lambda) = -\frac{0.1158421}{\lambda^3(238.0185 - \lambda^{-2})^2} - \frac{0.00335834}{\lambda^3(57.362 - \lambda^{-2})^2} \quad (\text{B.3.2})$$

$$\frac{\partial^2}{\partial \lambda^2} n(\lambda) = \frac{0.3475263}{\lambda^4(238.0185 - \lambda^{-2})^2} + \frac{0.4633684}{\lambda^6(238.0185 - \lambda^{-2})^3} + \frac{0.01007502}{\lambda^4(57.362 - \lambda^{-2})^2} + \frac{0.01343336}{\lambda^6(57.362 - \lambda^{-2})^3} \quad (\text{B.3.3})$$

### B.4 Dispersion of $\beta$ -Barium Borate

The final material system that will be discussed is BBO. This is also the most difficult, as it is necessary to consider the dispersion of the ordinary index of refraction, the extraordinary index of refraction, and the effective index of refraction when the phase-matching angle is neither  $0^\circ$  nor  $90^\circ$ . Further, there are multiple sources for dispersion formulae with subtle differences. The first two sources - Eimerl et al[287] and Kato[288] - appear to be the most established; both use the same general formula for the dispersion of BBO:

$$n(\lambda) = \sqrt{A + \frac{B}{\lambda^2 + C} + D\lambda^2} \quad (\text{B.4.1})$$

The coefficients for an ordinary beam are  $A = 2.7405$ ,  $B = 0.0184 \mu\text{m}^2$ ,  $C = -0.0179 \mu\text{m}^2$ , and  $D = -0.0155 \mu\text{m}^{-2}$  according to Eimerl et al and  $A = 2.7359$ ,  $B = 0.01878 \mu\text{m}^2$ ,  $C = -0.01822 \mu\text{m}^2$ ,  $D = -0.01354 \mu\text{m}^{-2}$

according to Kato, while those for an extraordinary beam are  $A = 2.3730$ ,  $B = 0.0128 \mu\text{m}^2$ ,  $C = -0.0156 \mu\text{m}^2$ , and  $D = -0.0044 \mu\text{m}^{-2}$  according to Eimerl et al and  $A = 2.3753$ ,  $B = 0.01224 \mu\text{m}^2$ ,  $C = -0.01667 \mu\text{m}^2$ , and  $D = -0.01516 \mu\text{m}^{-2}$  according to Kato.[287, 288] Unfortunately, these coefficients were only determined based upon characterization of BBO out to  $1\mu\text{m}$ . However, Eimerl et al are among those that report absorption by BBO beginning around  $2 \mu\text{m}$ :[106, 208, 287] Zhang et al[208] indicate that this absorption arises from phonon modes and causes corresponding changes to the index of refraction at these longer wavelengths. While Lu and Liu indicate the formulae of Eimerl et al and Kato are reasonably consistent with sum-frequency generation involving wavelengths in this region,[289] Zhang et al modeled the behavior of NIR optical parametric processes in order to expand the model for the refractive index to incorporate higher-order terms accounting for the phonon modes.[208] The result is a model of the form:

$$n = \sqrt{A + \frac{B}{\lambda^2 + C} + D\lambda^2 + E\lambda^4 + F\lambda^6} \quad (\text{B.4.2})$$

In modeling the parametric performance of an optical parametric generator/optical parametric amplifier system, Zhang et al found the following coefficients to be appropriate: for the ordinary refractive index,  $A = 2.7359$ ,  $B = 0.01878 \mu\text{m}^2$ ,  $C = -0.01822 \mu\text{m}^2$ ,  $D = -0.01471 \mu\text{m}^{-2}$ ,  $E = 0.0006081 \mu\text{m}^{-4}$ , and  $F = -0.00006740 \mu\text{m}^{-6}$ ; and, for the extraordinary refractive index,  $A = 2.3753$ ,  $B = 0.01224 \mu\text{m}^2$ ,  $C = -0.01667 \mu\text{m}^2$ ,  $D = -0.01627 \mu\text{m}^{-2}$ ,  $E = 0.0005716 \mu\text{m}^{-4}$ , and  $F = -0.00006305 \mu\text{m}^{-6}$ .[208]

The derivation of the form in Eq. B.4.2 from the original dispersion formula, Eq. B.4.1, fortunately causes the derivatives of Eq. B.4.1 and Eq. B.4.2 to be very similar. The first derivative of Eq. B.4.1 is:

$$\frac{\partial}{\partial \lambda} n(\lambda) = \frac{\lambda}{n(\lambda)} \left[ D - \frac{B}{(\lambda^2 + C)^2} \right] \quad (\text{B.4.3})$$

while the first derivative of Eq. B.4.2 is:

$$\frac{\partial}{\partial \lambda} n(\lambda) = \frac{\lambda}{n(\lambda)} \left[ -\frac{B}{(\lambda^2 + C)^2} + D + 2E\lambda^2 + 3F\lambda^4 \right] \quad (\text{B.4.4})$$

Extending these to the second derivatives yields:

$$\frac{\partial^2}{\partial \lambda^2} n(\lambda) = \frac{1}{n(\lambda)} \left[ \frac{4B\lambda^2}{(\lambda^2 + C)^3} - \left( \frac{\partial}{\partial \lambda} n(\lambda) \right)^2 \right] + \frac{1}{\lambda} \frac{\partial}{\partial \lambda} n(\lambda) \quad (\text{B.4.5})$$

for the model employed by Kato and Eimerl et al (Eq. B.4.1), or:

$$\frac{\partial^2}{\partial \lambda^2} n(\lambda) = \frac{1}{n(\lambda)} \left[ 4\lambda^2 \left( \frac{B}{(\lambda^2 + C)^3} + E + 3F\lambda^2 \right) - \left( \frac{\partial}{\partial \lambda} n(\lambda) \right)^2 \right] + \frac{1}{\lambda} \frac{\partial}{\partial \lambda} n(\lambda) \quad (\text{B.4.6})$$

for the extended model of Zhang et al (Eq. B.4.2).

However, the derivatives  $\partial/\partial \lambda n(\lambda)$  and  $\partial^2/\partial \lambda^2 n(\lambda)$  in Eq. B.4.3 and Eq. B.4.5 or Eq. B.4.4 and Eq. B.4.6 only hold for ordinary or extraordinary polarizations within the crystal, namely when the phase-matching angle,  $\theta$ , is either  $0^\circ$  or  $90^\circ$ . When the phase-matching angle is at neither  $0^\circ$  nor  $90^\circ$ , the effective index of refraction,  $n_\theta(\lambda)$ , is determined based upon the phase-matching angle and the ordinary and extraordinary dispersion curves,  $n_o(\lambda)$  and  $n_e(\lambda)$ , respectively. The functional dependence of  $n_\theta(\lambda)$  upon these quantities is:[106]

$$n_\theta(\lambda) = n_o(\lambda) \sqrt{\frac{1 + \tan^2(\theta)}{1 + [n_o^2(\lambda)/n_e^2(\lambda)] \tan^2(\theta)}} \quad (\text{B.4.7})$$

Therefore, when we evaluate the derivative, we end up with a much more complicated expression. While the proper value of  $\theta$  will be dependent upon the wavelengths, it will be constant for a given experimental condition; therefore, we can treat it as a constant and only consider the evaluation of the derivatives based upon the dispersion curves of  $n_o(\lambda)$  and  $n_e(\lambda)$ . Evaluating the first derivative yields:

$$\frac{\partial}{\partial \lambda} n_\theta(\lambda) = \frac{n_\theta(\lambda)}{n_o(\lambda)} \frac{\partial}{\partial \lambda} n_o(\lambda) + \frac{n_\theta^3(\lambda) \tan^2(\theta)}{n_o(\lambda) n_e^2(\lambda) [1 + \tan^2(\theta)]} \left[ \frac{n_o(\lambda)}{n_e(\lambda)} \frac{\partial}{\partial \lambda} n_e(\lambda) - \frac{\partial}{\partial \lambda} n_o(\lambda) \right] \quad (\text{B.4.8})$$

where  $\partial/\partial \lambda n_o(\lambda)$  and  $\partial/\partial \lambda n_e(\lambda)$  are derivatives evaluated according to Eq. B.4.3 or Eq. B.4.4 with the appropriate coefficients for the ordinary index ( $\partial/\partial \lambda n_o(\lambda)$ ) or for the extraordinary index ( $\partial/\partial \lambda n_e(\lambda)$ ). We can continue with the result of Eq. B.4.8 to also determine the second derivative of  $n_\theta(\lambda)$  with respect to  $\lambda$ :

$$\begin{aligned} \frac{\partial^2}{\partial \lambda^2} n_\theta(\lambda) = & \left[ \frac{1}{n_o(\lambda)} - \frac{\tan^2(\theta)}{1 + \tan^2(\theta)} \frac{3n_\theta^2(\lambda)}{n_o(\lambda)n_e^2(\lambda)} \right] \left( \frac{\partial}{\partial \lambda} n_o(\lambda) \right) \left( \frac{\partial}{\partial \lambda} n_\theta(\lambda) \right) \\ & + \left[ \frac{\tan^2(\theta)}{1 + \tan^2(\theta)} \frac{n_\theta^3(\lambda)}{n_o^2(\lambda)n_e^2(\lambda)} - \frac{n_\theta(\lambda)}{n_o^2(\lambda)} \right] \left( \frac{\partial}{\partial \lambda} n_o(\lambda) \right)^2 \\ & + \left[ \frac{n_\theta(\lambda)}{n_o(\lambda)} - \frac{\tan^2(\theta)}{1 + \tan^2(\theta)} \frac{n_\theta^3(\lambda)}{n_o(\lambda)n_e^2(\lambda)} \right] \left( \frac{\partial^2}{\partial \lambda^2} n_o(\lambda) \right) \\ & + \frac{\tan^2(\theta)}{1 + \tan^2(\theta)} \left[ \frac{2n_\theta^3(\lambda)}{n_o(\lambda)n_e^3(\lambda)} \left( \frac{\partial}{\partial \lambda} n_o(\lambda) \right) \left( \frac{\partial}{\partial \lambda} n_e(\lambda) \right) \right. \\ & \quad \left. + \frac{3n_\theta^2(\lambda)}{n_e^3(\lambda)} \left( \frac{\partial}{\partial \lambda} n_e(\lambda) \right) \left( \frac{\partial}{\partial \lambda} n_\theta(\lambda) \right) \right. \\ & \quad \left. - \frac{3n_\theta^3(\lambda)}{n_e^4(\lambda)} \left( \frac{\partial}{\partial \lambda} n_e(\lambda) \right)^2 + \frac{n_\theta^3(\lambda)}{n_e^3(\lambda)} \left( \frac{\partial^2}{\partial \lambda^2} n_e(\lambda) \right) \right] \end{aligned} \quad (\text{B.4.9})$$



In Eq. B.4.9, the partial derivatives  $\partial/\partial\lambda n_o(\lambda)$  and  $\partial/\partial\lambda n_e(\lambda)$  are calculated as in Eq. B.4.8. The partial derivative of  $n_\theta(\lambda)$ ,  $\partial/\partial\lambda n_\theta(\lambda)$ , can be calculated using the result of Eq. B.4.8. Finally,  $\partial^2/\partial\lambda^2 n_o(\lambda)$  and  $\partial^2/\partial\lambda^2 n_e(\lambda)$  are the second derivatives of the ordinary and extraordinary indices, respectively, with respect to  $\lambda$ ; these may be calculated by Eq. B.4.5 or B.4.6.

We will note that the results of Eq. B.4.8 and B.4.9 are general for any material for which the index at the phase-matching angle,  $\theta$ , is determined as in Eq. B.4.7. As this relationship holds for any uniaxial crystal, the results of Eq. B.4.8 and Eq. B.4.9 can be applied to any such material. However, the appropriate forms of the necessary derivatives -  $\partial^n/\partial\lambda^n n_\alpha(\lambda)$ ,  $n \in \{1, 2\}$  and  $\alpha \in \{o, e\}$  - would need to be determined. While there are other crystals - such as lithium niobate[106] - for which dispersion relations of the same form as Eq. B.4.1 or B.4.2 are used, many other common crystals adopt other models for calculating the refractive index.

CHAPTER C  
Appendix C

In this appendix, we present the code developed for the calculations in Ch. 4. This code has been developed in Python for operation on MacOS and other UNIX-based systems. There are some aspects of operation, such as the implementation of multiprocessing, that would likely make this code unsuitable for operation directly on Windows-based systems. The code consists of ten individual scripts, each containing a subset of the functions and classes. These scripts have been reproduced in the sections that follow, with some modifications for presentation.

Basic operation of this script requires several packages to be loaded, then a sequence of functions from the other scripts to be executed. This sequence is outlined in the function `basic_operation()` below, which would generate a list `fields` that may be manipulated further. The list of “developed packages” in the preamble are the ten scripts mentioned above. These are presented in the subsequent sections of this appendix.

```
# Native python packages
import numpy as np
import matplotlib.pyplot as plt
import scipy.interpolate as inter
import multiprocessing, threading, os, itertools

# Developed python packages
import parameters, efield, algorithm, controls
import user_settings as user
import material_params as mat
import gain_formulae as gain
import plotting_routines as pltr
import phasematching as pm
import nl_crystal as nl

def basic_operation():

    # Initialize user specifications and parameters
    u = user.user_specs()
    p = parameters.parameters(u)
```

```

# Modify the parameters appropriately
controls.modify_params(p)

# Initialize the fields
fields = controls.initialize(p)

# Save and plot the fields as appropriate
if p.u.save:
    controls.save_output(p, fields, 'initial')
elif p.u.show:
    pltr.plot2d(fields, p, 'initial_fields')

# Perform the numerical integration
fields = controls.drive_algorithm(p, fields)

# Save and plot the resulting fields as appropriate
if p.u.save:
    controls.save_output(p, fields, 'final')
elif p.u.show:
    pltr.plot2d(fields, p, 'final_fields')

```

### C.1 user\_settings.py

The script `user_settings.py` contains the definitions of two classes that provide parameters for the operation of different parts of the script. The class `gain_selections` defines the options available to the user for enabling and disabling the different contributions to the gain functions. The class `user_specs` outlines the various settings that define the details of the simulation to be performed.

```

# Native python packages
import numpy as np
import socket
import os

# Developed python packages
# (none)

```

```
class gain_selections:

    def __init__(self):

        # Options for calculations within the
        # slowly varying amplitude approximation:

        self.sva_group_velocity = True
        self.sva_GVD = True
        self.sva_absorption = True
        self.sva_amplification = True

        self.sva_in_lab_frame = True

        # Options for second order calculations
        # (no longer maintained)

        self.so_space_time_coupling = True
        self.so_gvm = True
        self.so_gvd = True
        self.so_gvm_sq = True
        self.so_absorption = True
        self.so_amplification = True

class user_specs:

    def __init__(self):

        # The following adjust the material properties:
        self.L = 0.2          # material length, in cm
        self.material = 'BBO (Zhang)'

        # Currently supported materials:
```



```

self.energy_conservation = 20.

    # tolerance in testing energy conservation
    # 10 tolerates ~0.05nm in error from MIR idler
    # 80 tolerates ~0.05nm in error from a 800nm pump
    # 10 tolerates ~0.05nm for SHG

# Initial field conditions:
self.energy = {
    '1' : 0.,
    '2' : 0.,
    '3' : 0.}

    # field energies (in uJ)
self.e2_size = {
    '1' : 0.,
    '2' : 0.,
    '3' : 0.}

    # 1/e2 beam size (cm)
self.field_envelopes = {
    '1' : 'Gaussian',
    '2' : 'Gaussian',
    '3' : 'Gaussian'}

# Identifies field source
# Options are:
    # 'zero':          Defines a field that evaluates to
    #                  0 V/m at all points in time
    # 'Gaussian':     Defines a field described
    #                  by a Gaussian intensity
    #                  envelope
    # 'file':         Uses the contents of a file to
    #                  define the field. load_params
    #                  must be populated.

self.Gauss_widths = {
    '1' : 0.,
    '2' : 0.,
    '3' : 0.}

    # width of Gaussians (fs)

```

```

self.Gauss_centers = {      '1' : 0.,
                            '2' : 0.,
                            '3' : 0.}

    # centers of Gaussians (fs)
self.load_params = {
    '1' : ['file', ['re_column', 'im_column']],
    '2' : ['file', ['re_column', 'im_column']],
    '3' : ['file', ['re_column', 'im_column']]
    # identifies file (including subdirectories) to be
    # used as the source for the field. (Untested)
self.field_phase = {      '1' : 0.,
                            '2' : 0.,
                            '3' : 0.}

    # pulse envelope phase (deg)
self.loaded_time_scale = 35.

    # When loading fields from file, use this to
    # estimate the characteristic time of the field.

# The following provide optional modifications or settings to the
# calculations and/or operation of the script.

# The standard "main" function will only save if .save is set to True.
# .save_dir identifies the desired directory.

    self.save = True
    self.save_dir = ' '

# The standard "main" function will only show the results if
# .show is set to True.

    self.show = False

# .silent limits the output to terminal during operation.

    self.silent = False

```



```
# .timer controls whether time stamps are printed.
    self.timer = True

# .threading controls whether multiprocessing is used. .cores allows
# user-defined number of processes. If .cores is 'Default', N-1
# processes will be initiated, where N is the cores available.
# If .limit_override = False and .cores is greater than N, 'Default'
# behavior will be used.
    self.threading = True
    self.cores = 0
    self.limit_override = True
    self.radial_samples = 0

# .adaptive_steps controls whether the simulation is iterated over a
# fixed number of spatial steps or whether an adaptive algorithm is
# employed to use the fewest steps while ensuring accuracy.
    self.adaptive_steps = False # NOT YET IMPLEMENTED
    self.steps = 1000

    self.modify_T_window = False
    self.alt_T_window = 800. #fs

# The following allow optional modification of derived parameters:
    self.slowly_varying_amp = True

# apply_contrast allows suppression of the wings of the field
# any points with magnitude less than .contrast will be set to 0.
    self.apply_contrast = False
    self.contrast = 1.e-13

# Modify the phase matching angle
```

```
self.modify_theta = False
self.alt_theta = 22.2

# Modify the effective nonlinearity

self.modify_chi2eff = False
self.modify_chi3eff = False
self.alt_chi2eff = 0.
self.alt_chi3eff = 0.

# Modify the group velocities

self.modify_ug = False
self.alt_ug = {'1' : 0., '2' : 0., '3' : 0.}
    # These are group velocities and cannot be set to 0.

# Modify the time sampling. Default is 512 samples.
# More than ~5k-7.5k is not advised; numpy broadcasting is
# used throughout the calculations, and this becomes less
# efficient around grids of ~10k points.

self.modify_sampling = True
self.alt_time_samples = 128

# Simulate noncollinearity by changes in the effective
# group velocity according to .gamma.

self.noncollinear = False
self.gamma = 0.5
```

## C.2 parameters.py

The code in `parameters.py` defines a class `parameters`. This class takes the settings defined by the user in an instance of `user_settings.user_specs` (see § C.1) and manipulates them: these values are used to define other necessary parameters and modify existing settings.

```
# Native python packages
import numpy as np
import matplotlib.pyplot as plt
import sys

# Non-native python packages
import user_settings as user
import material_params as mat

class parameters:
    def __init__(self, user_settings):

        # Locally define the user settings, and convert to MKS units
        self.u = user_settings
        if self.u.silent:
            pass
        else:
            print('Initializing parameters')
        self.user_settings_conversions()

        # Initialize parameters describing the material environment
        # and phase-matching process

        if self.u.parametric_process == 'second-harmonic generation' \
            or self.u.parametric_process == 'parametric amplification' \
            or self.u.parametric_process == 'sum-frequency generation':
```

```

        self.m = mat.birefringent_params(self.u)
        self.mat_type_marker = 'birefringent'

elif self.u.parametric_process == 'self-phase modulation':
    self.m = mat.isotropic_params(self.u)
    self.mat_type_marker = 'isotropic'

else:
    print('Unsupported process. Ending process.')
    exit()

self.material_conversions()

# Identify the time-scales involved in the interacting pulses

if 'file' in self.u.field_envelopes:
    self.time_scale = min(self.u.loaded_time_scale, np.min(\
        np.asarray(self.u.Gauss_widths.values())[np.nonzero(\
            self.u.Gauss_widths.values())]))
else:
    self.time_scale = np.min(np.asarray(\
        self.u.Gauss_widths.values())[np.nonzero(\
            self.u.Gauss_widths.values())])

# Initialize time and frequency windows. Determining the ranges
# follows the method described by Gale et al (JOSAB 1998 15(2) 702)

if self.u.modify_sampling:
    self.time_samples = self.u.alt_time_samples
else:
    self.time_samples = 512.

```

```

if self.u.modify_T_window:
    self.T_window = self.u.alt_T_window*1e-15
else:
    self.T_window = ((self.time_scale)\
                     *np.sqrt(self.time_samples/0.44))
self.time = np.linspace(-self.T_window/2, self.T_window/2, \
                        self.time_samples)

self.freq_samples = self.time_samples

self.freq = np.linspace(-np.pi/abs(self.time[1]-self.time[0]), \
                        np.pi/abs(self.time[1]-self.time[0]),\
                        self.freq_samples + 1)[::-1]
self.freq_window = abs(self.freq[-1] - self.freq[0])

# Describe the TEM mode of each field

self.r_max = np.max(np.asarray(self.u.e2_size.values()))
if self.u.radial_samples == 'Default':
    self.r_samples = 15
else:
    self.r_samples = self.u.radial_samples
self.r = np.linspace(0., 1.25*self.r_max, self.r_samples)
self.fluence = {}
for j in self.u.e2_size:
    if self.u.e2_size[j] == 0:
        self.fluence[j] = np.zeros(len(self.r))
    else:
        self.fluence[j] = (self.u.energy[j]/((np.pi/2)\
        *((0.5*self.u.e2_size[j])**2))\
        *np.exp(-2*((self.r/(0.5\
        *self.u.e2_size[j]))**2))

```

```
# Define initial position of the fields

self.z = 0.

def n(self, wavelength, field):
    if self.mat_type_marker == 'birefringent':

        if self.m.polarization[field] == 'extraordinary':

            return self.m.cry.eff(wavelength, self.m.theta)

        elif self.m.polarization[field] == 'ordinary':

            return self.m.cry.ord(wavelength)

    elif self.mat_type_marker == 'isotropic':
        exit()

    else:
        exit()

def user_settings_conversions(self):

    self.c = 3.E8
        # speed of light, m/s
    self.hbar = 1.054571E-34
        # Planck's constant, J*s
    self.u.L *= 0.01
        # convert material length from cm to m
```

```

for i in self.u.Gauss_widths:
    self.u.Gauss_widths[i]*=1.E-15
        # convert from fs to s
    self.u.Gauss_centers[i]*=1.E-15
        # convert from fs to s
    self.u.e2_size[i]*=0.01
        # convert from cm to m
    self.u.energy[i]*=1.E-6
        # convert from uJ to J

self.u.loaded_time_scale*=1.E-15
        # convert from fs to s

self.cutoff = 0.
if self.u.material == 'BBO (Eimerl)':
    self.cutoff = (2*np.pi*self.c*1.e9)/13290.
elif self.u.material == 'BBO (Kato)':
    self.cutoff = (2*np.pi*self.c*1.e9)/12500.
elif self.u.material == 'BBO (Zhang)':
    self.cutoff = (2*np.pi*self.c*1.e9)/5830.
elif self.u.material == 'LiNbO3':
    self.cutoff = (2*np.pi*self.c*1.e9)/13400.

def material_conversions(self):

    for i in self.m.ug:
        self.m.ug[i]*=1.e12
            # convert mm/fs to m/s
        self.m.gvd[i]*=1.e-27
            # convert fs2/mm to s2/m
    self.m.chi2eff*=1.e-12

```

```

        # convert pm/V to m/V
self.m.dk*=100.

        # convert from 1/cm to 1/m

def plot_tem(self):
    plt.clf()
    for j in self.fluence:
        plt.plot(self.r, self.fluence[j])
    plt.show()

```

### C.3 material\_params.py

We previously referenced `material_params` in § C.2. The classes in this script, `birefringent_params` and `isotropic_params`, are called according to the process being simulated. At this time, it has not been necessary to develop `isotropic_params`, but `birefringent_params` performs the calculations and manipulations necessary to identify the phase matching angle and effective nonlinearity for the process.

```

# Native python packages
import math
import numpy as np
import sys

# Non-native python packages
import nl_crystal as nl
import phasematching as pm

class birefringent_params:

    def __init__(self, user_sett):

        self.cry = nl.NLcrystals()
        self.cry.selection = user_sett.material

```



```

# populate the local wavelength and field property dictionaries
self.def_mask(user_sett)

# redefine the keys to match internal notation

for i in [user_sett.wavelengths, user_sett.energy, user_sett.e2_size,\
         user_sett.field_envelopes, user_sett.Gauss_widths,\
         user_sett.Gauss_centers, user_sett.load_params, \
         user_sett.field_phase]:
    for j in self.mask:
        i[j] = i.pop(self.mask[j])

    ini_keys = i.keys()

    for j in ini_keys:
        if j in self.mask:
            pass
        else:
            i.pop(j, None)

self.chi3eff = 0.

if user_sett.parametric_process == 'second-harmonic generation':
    self.shg_pm(user_sett)
elif user_sett.parametric_process == 'parametric amplification' \
     or user_sett.parametric_process == 'sum-frequency generation':
    if user_sett.process == 'Type I':
        self.type_one_pm(user_sett)
    elif user_sett.process == 'Type II':
        self.type_two_pm(user_sett)

```

```

elif user_sett.process == 'Type III':
    self.type_three_pm(user_sett)
else:
    print('Unsupported process requested. Ending script.')
    exit()

return

def shg_pm(self, u):
    if math.isnan(pm.type_one(self.cry, u.wavelengths['SHG'], \
        u.wavelengths['Fundamental'])):
        print('No phase matching angle is available.\
            Setting theta to 90deg.')
        self.theta = 90.
    else:
        self.theta = pm.type_one(self.cry, u.wavelengths['SHG'], \
            u.wavelengths['Fundamental'])
    self.ug = {
        'Fundamental' : self.cry.ord_vg(u.wavelengths['Fundamental']),
        'SHG' : self.cry.ex_vg(u.wavelengths['SHG'], self.theta)}
    self.gvd = {
        'Fundamental' : self.cry.ord_gvd(u.wavelengths['Fundamental']),
        'SHG' : self.cry.ex_gvd(u.wavelengths['SHG'], self.theta)}
    self.rho = {
        'Fundamental' : 0,
        'SHG' : (180/np.pi)*np.arctan((((self.cry.ord(\
            u.wavelengths['SHG'])))**2)\
            /((self.cry.ex(u.wavelengths['SHG'])))**2))\
            *np.tan((np.pi/180)*self.theta)) - self.theta}
    self.dk = pm.type_one_mismatch(self.cry, u.wavelengths['SHG'], \
        u.wavelengths['Fundamental'], self.theta)
    self.chi2eff = 2*self.cry.deff(self.theta, u.phi, 'Type I')

```

```

return

def type_one_pm(self, u):
    if math.isnan(pm.type_one(self.cry, u.wavelengths['Pump'],\
        u.wavelengths['Signal'])):
        print('No phase matching angle is available.\
            Setting theta to 90deg.')
        self.theta = 90.
    else:
        self.theta = pm.type_one(self.cry, u.wavelengths['Pump'],\
            u.wavelengths['Signal'])
    self.ug = {
        'Pump' : self.cry.ex_vg(u.wavelengths['Pump'], self.theta),
        'Signal' : self.cry.ord_vg(u.wavelengths['Signal']),
        'Idler' : self.cry.ord_vg(u.wavelengths['Idler'])}
    self.gvd = {
        'Pump' : self.cry.ex_gvd(u.wavelengths['Pump'], self.theta),
        'Signal' : self.cry.ord_gvd(u.wavelengths['Signal']),
        'Idler' : self.cry.ord_gvd(u.wavelengths['Idler'])}
    if u.noncollinear:
        self.rho = {
            'Pump' : (180/np.pi)*np.arctan((((self.cry.ord(\
                u.wavelengths['Pump'])))**2)\
                /((self.cry.ex(u.wavelengths['Pump'])))**2))\
                *np.tan((np.pi/180)*self.theta) - self.theta,
            'Signal' : 0.,
            'Idler' : 0.}
    self.dk = pm.type_one_mismatch(self.cry, u.wavelengths['Pump'],\
        u.wavelengths['Signal'], self.theta)
    self.chi2eff = 2*self.cry.deff(self.theta, u.phi, 'Type I')

```

```

return

def type_two_pm(self, u):
    if math.isnan(pm.type_two(self.cry, u.wavelengths['Pump'],\
        u.wavelengths['Signal'])):
        print('No phase matching angle is available.\
            Setting theta to 90deg.')
        self.theta = 90.
    else:
        self.theta = pm.type_two(self.cry, u.wavelengths['Pump'],\
            u.wavelengths['Signal'])

    self.ug = {
        'Pump' : self.cry.ex_vg(u.wavelengths['Pump'], self.theta),
        'Signal' : self.cry.ord_vg(u.wavelengths['Signal']),
        'Idler' : self.cry.ex_vg(u.wavelengths['Idler'], self.theta)}

    self.gvd = {
        'Pump' : self.cry.ex_gvd(u.wavelengths['Pump'], self.theta),
        'Signal' : self.cry.ord_gvd(u.wavelengths['Signal']),
        'Idler' : self.cry.ex_gvd(u.wavelengths['Idler'], self.theta)}

    if u.noncollinear:
        self.rho = {
            'Pump' : (180/np.pi)*np.arctan((((self.cry.ord(\
                u.wavelengths['Pump'])))**2)/((self.cry.ex(\
                u.wavelengths['Pump'])))**2))*np.tan((np.pi\
                /180)*self.theta)) - self.theta,
            'Signal' : 0.,
            'Idler' : (180/np.pi)*np.arctan((((self.cry.ord(\
                u.wavelengths['Idler'])))**2)/((self.cry.ex(\
                u.wavelengths['Idler'])))**2))*np.tan((np.pi\
                /180)*self.theta)) - self.theta}

    self.dk = pm.type_two_mismatch(self.cry, u.wavelengths['Pump'],\
        u.wavelengths['Signal'], self.theta)

```

```

self.chi2eff = 2*self.cry.deff(self.theta, u.phi, 'Type II')

return

def type_three_pm(self, u):
    if math.isnan(pm.type_three(self.cry, u.wavelengths['Pump'],\
        u.wavelengths['Signal'])):
        print('No phase matching angle is available.\
            Setting theta to 90deg.')
        self.theta = 90.
    else:
        self.theta = pm.type_three(self.cry, u.wavelengths['Pump'],\
            u.wavelengths['Signal'])

    self.ug = {
        'Pump' : self.cry.ex_vg(u.wavelengths['Pump'], self.theta),
        'Signal' : self.cry.ex_vg(u.wavelengths['Signal'], self.theta),
        'Idler' : self.cry.ord(u.wavelengths['Idler'])}

    self.gvd = {
        'Pump' : self.cry.ex_gvd(u.wavelengths['Pump'], self.theta),
        'Signal' : self.cry.ex_gvd(u.wavelengths['Signal'], self.theta),
        'Idler' : self.cry.ord_gvd(u.wavelengths['Idler'])}

    if u.noncollinear:
        self.rho = {
            'Pump' : (180/np.pi)*np.arctan((((self.cry.ord(\
                u.wavelengths['Pump'])))**2)/((self.cry.ex(\
                u.wavelengths['Pump'])))**2))*np.tan((np.pi\
                /180)*self.theta)) - self.theta,
            'Signal' : (180/np.pi)*np.arctan((((self.cry.ord(\
                u.wavelengths['Signal'])))**2)/((self.cry.ex(\
                u.wavelengths['Signal'])))**2))*np.tan((np.pi\
                /180)*self.theta)) - self.theta,
            'Idler' : 0.}

```

```

self.dk = pm.type_three_mismatch(self.cry, u.wavelengths['Pump'],\
                                u.wavelengths['Signal'], self.theta)
self.chi2eff = 2*self.cry.deff(self.theta, u.phi, 'Type III')

def def_mask(self, u):

    if u.parametric_process == 'second-harmonic generation':
        if abs(u.wavelengths['1'] - 2*u.wavelengths['2'])\
            *180. < u.energy_conservation \
            or abs(u.wavelengths['2'] - 2*u.wavelengths['1'])\
            *180. < u.energy_conservation:

            pass

        else:

            print('The chosen colors exceed the specified tolerance \
                    for energy conservation.')

            exit()

    if u.wavelengths['1'] < u.wavelengths['2']:

        # Field 2 is the fundamental and Field 1 is the SHG

        self.mask = {

            'Fundamental' : '2',

            'SHG' : '1'}

    elif u.wavelengths['2'] < u.wavelengths['1']:

        # Field 1 is the fundamental and Field 2 is the SHG

        self.mask = {

            'Fundamental' : '1',

            'SHG' : '2'}

    if u.material == 'BBO (Kato)' or u.material == 'BBO (Eimerl)' \
        or u.material == 'LiNbO3' or u.material == 'BBO (Zhang)':

```

```

        self.polarization = {
            'Fundamental' : 'ordinary',
            'SHG' : 'extraordinary'}
    else:
        print('Will not be able to calculate phase matching for\
            the selected material. Ending script.')
        sys.exit()

elif u.parametric_process == 'parametric amplification' \
    or u.parametric_process == 'sum-frequency generation':

    if u.wavelengths['1'] == 0 or u.wavelengths['2'] == 0 \
        or u.wavelengths['3'] == 0:

        print('Cannot run parametric amplification with a field\
            with zero wavelength. Ending script.')
        exit()

    if u.wavelengths['1'] < u.wavelengths['2'] and\
        u.wavelengths['1'] < u.wavelengths['3']:

        # Field 1 is the pump

        if abs((1E9/u.wavelengths['1'])-(1E9/u.wavelengths['2'])\
            -(1E9/u.wavelengths['3']))<u.energy_conservation:

            pass

        else:

            print('The chosen colors exceed the specified\
                tolerance for energy conservation.')

```

```

exit()

if u.wavelengths['2'] < u.wavelengths['3'] or\
    u.wavelengths['2'] == u.wavelengths['3']:

    # Field 2 is the signal and Field 3 is the idler
    self.mask = {
        'Pump' : '1',
        'Signal' : '2',
        'Idler' : '3'}

elif u.wavelengths['3'] < u.wavelengths['2']:

    # Field 3 is the signal and Field 2 is the idler
    self.mask = {
        'Pump' : '1',
        'Signal' : '3',
        'Idler' : '2'}

elif u.wavelengths['2'] < u.wavelengths['1'] and\
    u.wavelengths['2'] < u.wavelengths['3']:

    # Field 2 is the pump

if abs((1E9/u.wavelengths['2'])-(1E9/u.wavelengths['1'])\
    -(1E9/u.wavelengths['3']))<u.energy_conservation:
    pass
else:
    print('The chosen colors exceed the specified\
        tolerance for energy conservation.')
    exit()

if u.wavelengths['1'] < u.wavelengths['3'] or \
    u.wavelengths['1'] == u.wavelengths['3']:

```



```

# Field 1 is the signal and Field 3 is the idler

self.mask = {
    'Pump' : '2',
    'Signal' : '1',
    'Idler' : '3'}

elif u.wavelengths['3'] < u.wavelengths['1']:
    # Field 3 is the signal and Field 1 is the idler
    self.mask = {
        'Pump' : '2',
        'Signal' : '3',
        'Idler' : '1'}

elif u.wavelengths['3'] < u.wavelengths['1'] and\
     u.wavelengths['3'] < u.wavelengths['2']:

# Field 3 is the pump

if abs((1E9/u.wavelengths['3'])-(1E9/u.wavelengths['2'])\
      -(1E9/u.wavelengths['1']))<u.energy_conservation:

    pass

else:

    print('The chosen colors exceed the specified\
          tolerance for energy conservation.')
    exit()

if u.wavelengths['1'] < u.wavelengths['2'] or \
   u.wavelengths['1'] == u.wavelengths['2']:

# Field 1 is the signal and Field 2 is the idler

```

```

        self.mask = {
            'Pump' : '3',
            'Signal' : '1',
            'Idler' : '2'}
elif u.wavelengths['2'] < u.wavelengths['1']:

    # Field 2 is the signal and Field 1 is the idler

    self.mask = {
        'Pump' : '3',
        'Signal' : '2',
        'Idler' : '1'}

if u.process == 'Type I':

    self.polarization = {
        'Pump' : 'extraordinary',
        'Signal' : 'ordinary',
        'Idler' : 'ordinary'}

elif u.process == 'Type II':

    self.polarization = {
        'Pump' : 'extraordinary',
        'Signal' : 'ordinary',
        'Idler' : 'extraordinary'}

elif u.process == 'Type III':

    self.polarization = {
        'Pump' : 'extraordinary',

```

```
'Signal' : 'extraordinary',
'Idler' : 'ordinary'}
```

```
return
```

```
class isotropic_params:
```

```
    def __init__(self, user_sett):
```

```
        print('Sorry, this hasn\'t been developed yet. Exiting...')
        exit()
```

#### C.4 nl\_crystal.py

In § C.3, the code references two non-native Python scripts: `phasematching.py` and `nl_crystal.py`. Here, we present the latter (`nl_crystal.py`), as the class this script contains (`NLcrystals`) is also referenced by `phasematching.py` (§ C.5). The class of `nl_crystal.py` (`NL_crystals`) contains the optical properties of a variety of nonlinear crystals and performs the calculations necessary to determine the index, group velocity, and group velocity dispersion for both ordinary and extraordinary polarizations and the effective nonlinearity.

```
# Native python packages
```

```
import numpy as np
```

```
# Non-native python packages
```

```
# (none)
```

```
class NLcrystals:
```

```

selection = 'LiNbO3'
process = 'Type I'

def available_crystals(self):
    print('\LiNbO3\ ', \BBO (Kato)\ ', \BBO (Eimerl)\ ', \
          \BBO (Zhang)\ ', \AgGaS2\ ', \AgGaSe2\ ')

def available_processes(self):
    print('\Type I\ ', \Type II\ ', \Type III\ ')

def Selmeier(self, ex_or_ord):

# LiNbO3 Selmeier coefficients from Lambda Photometrics data
# coefficients from refractiveindex.info did not give correct performance
# format of Selmeier equation for these coefficients consistent with BBO

    if self.selection == 'LiNbO3':
        if ex_or_ord == 'extraordinary':
            return [4.582, 0.099169, -0.044432, -0.02195]
        if ex_or_ord == 'ordinary':
            return [4.9048, 0.11768, -0.0475, -0.027169]

    if self.selection == 'BBO (Kato)':
        if ex_or_ord == 'extraordinary':
            return [2.3753, 0.01224, -0.01667, -0.01516]
        elif ex_or_ord == 'ordinary':
            return [2.7359, 0.01878, -0.01822, -0.01354]

    if self.selection == 'BBO (Eimerl)':
        if ex_or_ord == 'extraordinary':
            return [2.3730, 0.0128, -0.0156, -0.0044]
        elif ex_or_ord == 'ordinary':

```

```

        return [2.7405, 0.0184, -0.0179, -0.0155]

if self.selection == 'BBO (Zhang)':
    if ex_or_ord == 'extraordinary':
        return [2.3753, 0.01224, -0.01667, -0.01627,\
                0.0005716, -0.00006305]
    elif ex_or_ord == 'ordinary':
        return [2.7359, 0.01878, -0.01822, -0.01471,\
                0.0006081, -0.00006740]

if self.selection == 'AgGaS2':
    if ex_or_ord == 'extraordinary':
        return [3.5873, 1.9533, -0.11066, 2.3391, -1030.7]
    elif ex_or_ord == 'ordinary':
        return [3.3970, 2.3982, -0.09311, 2.1640, -950]

if self.selection == 'AgGaSe2':
    if ex_or_ord == 'extraordinary':
        return [3.3132, 3.3616, -(0.38201*0.38201),\
                1.7677, -1600]
    elif ex_or_ord == 'ordinary':
        return [3.9362, 2.9113, -(0.38821*0.38821),\
                1.7954, -1600]

def ord(self, wavelength):

    Sel = self.Selmeier('ordinary')
    l = wavelength/1000.

    if self.selection == 'LiNbO3' or self.selection == 'BBO (Kato)'\
        or self.selection == 'BBO (Eimerl)':

```

```

        return np.sqrt(Sel[0]+(Sel[1]/(1*1+Sel[2]))+(Sel[3]*1*1))
    if self.selection == 'AgGaS2' or self.selection == 'AgGaSe2':
        return np.sqrt(Sel[0] + ((Sel[1]*1*1)/(1*1+Sel[2])) \
            + ((Sel[3]*1*1)/(1*1+Sel[4])))
    if self.selection == 'BBO (Zhang)':
        return np.sqrt(Sel[0] + (Sel[1]/(1*1 + Sel[2]))) + (Sel[3]*1*1) \
            + (Sel[4]*1*1*1*1) + (Sel[5]*1*1*1*1*1*1))

def ex(self, wavelength):

    Sel = self.Selmeier('extraordinary')
    l = wavelength/1000.

    if self.selection == 'LiNbO3' or self.selection == 'BBO (Kato)' \
        or self.selection == 'BBO (Eimerl)':
        return np.sqrt(Sel[0]+(Sel[1]/(1*1+Sel[2]))+(Sel[3]*1*1))
    if self.selection == 'AgGaS2' or self.selection == 'AgGaSe2':
        return np.sqrt(Sel[0] + ((Sel[1]*1*1)/(1*1+Sel[2])) \
            + ((Sel[3]*1*1)/(1*1+Sel[4])))
    if self.selection == 'BBO (Zhang)':
        return np.sqrt(Sel[0] + (Sel[1]/(1*1 + Sel[2]))) + (Sel[3]*1*1) \
            + (Sel[4]*1*1*1*1) + (Sel[5]*1*1*1*1*1*1))

def eff(self, wavelength, theta):

    no = self.ord(wavelength)
    ne = self.ex(wavelength)

    q = (np.pi/180)*theta

    return no*np.sqrt((1+np.tan(q)*np.tan(q))/(1 \
        + ((no*no)/(ne*ne))*np.tan(q)*np.tan(q)))

```

```

def ord_vg(self, wavelength):

    if self.selection == 'LiNbO3' or self.selection == 'BBO (Kato)' \
        or self.selection == 'BBO (Eimerl)' \
        or self.selection == 'BBO (Zhang)':

        c = 3E10 #cm/s
        n = self.ord(wavelength)
        l = wavelength/1000.
        Sel = self.Selmeier('ordinary')

        if self.selection == 'LiNbO3' or self.selection == 'BBO (Kato)' \
            or self.selection == 'BBO (Eimerl)':

            B = Sel[1]
            C = Sel[2]
            D = Sel[3]

            dnd1 = (1/n)*(D-(B/((1*1+C)*(1*1+C))))

        elif self.selection == 'BBO (Zhang)':

            B = Sel[1]
            C = Sel[2]
            D = Sel[3]
            E = Sel[4]
            F = Sel[5]

            dnd1 = (1/n)*(D+2*E*1*1+3*F*1*1*1*1\
                -(B/((1*1+C)*(1*1+C))))

    return c*(1E-14)*(1/(n-1*dnd1))        # in mm/fs

```

```

def ex_vg(self, wavelength, theta):

    if theta == 90 or theta == 0:

        if theta == 90:

            if self.selection == 'LiNbO3' \
                or self.selection == 'BBO (Kato)' \
                or self.selection == 'BBO (Eimerl)' \
                or self.selection == 'BBO (Zhang)':

                c = 3E10 #cm/s
                n = self.ex(wavelength)
                l = wavelength/1000.
                Sel = self.Selmeier('extraordinary')

                if self.selection == 'LiNbO3' \
                    or self.selection == 'BBO (Kato)' \
                    or self.selection == 'BBO (Eimerl)':

                    B = Sel[1]
                    C = Sel[2]
                    D = Sel[3]

                    dnd1 = (1/n)*(D-(B/((1*1+C)*(1*1+C))))

            elif self.selection == 'BBO (Zhang)':

                B = Sel[1]
                C = Sel[2]
                D = Sel[3]
                E = Sel[4]

```



```

F = Sel[5]

dndl = (1/n)*(D + 2*E*l*l + 3*F*l*l*l*l \
        - (B/((l*l + C)*(l*l + C))))

return c*(1E-14)*(1/(n-l*dndl))
        # in mm/fs

elif theta == 0:

    return self.ord_vg(wavelength)

else:

if self.selection == 'LiNbO3' or self.selection == 'BBO (Kato)' \
    or self.selection == 'BBO (Eimerl)' \
    or self.selection == 'BBO (Zhang)':

q = (np.pi/180)*theta
c = 3E10 #cm/s
no = self.ord(wavelength)
ne = self.ex(wavelength)
n = no*np.sqrt(((1+np.power(np.tan(q),2))/(1\
                    +np.power(((no/ne)*np.tan(q)),2))))

l = wavelength/1000
Sel_ord = self.Selmeier('ordinary')
Sel_ex = self.Selmeier('extraordinary')

if self.selection == 'LiNbO3' \
    or self.selection == 'BBO (Kato)'\
    or self.selection == 'BBO (Eimerl)':

Bo = Sel_ord[1]
Co = Sel_ord[2]
Do = Sel_ord[3]

```

```

Be = Sel_ex[1]
Ce = Sel_ex[2]
De = Sel_ex[3]

dnedl = (1/ne)*(De-(Be/((1*1+Ce)*(1*1+Ce))))
dnodl = (1/no)*(Do-(Bo/((1*1+Co)*(1*1+Co))))

elif self.selection == 'BBO (Zhang)':

Bo = Sel_ord[1]
Co = Sel_ord[2]
Do = Sel_ord[3]
Eo = Sel_ord[4]
Fo = Sel_ord[5]
Be = Sel_ex[1]
Ce = Sel_ex[2]
De = Sel_ex[3]
Ee = Sel_ex[4]
Fe = Sel_ex[5]

dnodl = (1/no)*(Do + 2*Eo*1*1 + 3*Fo*1*1*1*1 \
            - (Bo/((1*1 + Co)*(1*1 + Co))))
dnedl = (1/ne)*(De + 2*Ee*1*1 + 3*Fe*1*1*1*1 \
            - (Be/((1*1 + Ce)*(1*1 + Ce))))

dndl = (n/no)*dnodl \
        + ((n**3)/(no*ne*ne))*((np.tan(q))**2)/(1\
        +((np.tan(q))**2))*((dnodl) - ((no*dnedl)/(ne)))

return c*(1E-14)*(1/(n-1*dndl))          # in mm/fs

def ord_gvd(self, wavelength):

```

```

if self.selection == 'LiNbO3' or self.selection == 'BBO (Kato)' \
    or self.selection == 'BBO (Eimerl)' \
    or self.selection == 'BBO (Zhang)':
    c = 3E10 #cm/s
    n = self.ord(wavelength)
    l = wavelength/1000.
    Sel = self.Selmeier('ordinary')

if self.selection == 'LiNbO3' or self.selection == 'BBO (Kato)'\
    or self.selection == 'BBO (Eimerl)':

    B = Sel[1]
    C = Sel[2]
    D = Sel[3]

    dnd1 = (1/n)*(D-(B/((1+l+C)*(1+l+C))))
    d2nd12 = (dnd1/l) - (((dnd1)**2)/n) \
        + ((4.*l*l*B)/(n*((1+l+C)**3)))

elif self.selection == 'BBO (Zhang)':

    B = Sel[1]
    C = Sel[2]
    D = Sel[3]
    E = Sel[4]
    F = Sel[5]

    dnd1 = (1/n)*(D + 2*E*l*l + 3*F*l*l*l \
        - (B/((1+l + C)*(1*l + C))))
    d2nd12 = (dnd1/l) - ((dnd1**2)/n) + ((4.*l*l)/n)\
        *(E + 3.*F*l*l + (B/((1+l+C)**3)))

```



```

elif self.selection == 'BBO (Zhang)':

    B = Sel[1]
    C = Sel[2]
    D = Sel[3]
    E = Sel[4]
    F = Sel[5]

    dnd1 = (1/n)*(D + 2*E*1*1 + 3*F*1*1*1*1 \
              - (B/((1*1 + C)*(1*1 + C))))
    d2nd12 = (dnd1/1) - ((dnd1**2)/n) \
              + ((4.*1*1)/n)*(E + 3.*F*1*1 \
              + (B/((1*1+C)**3)))

    return ((1**3)/(2*np.pi*c*c))*d2nd12*(1.E25)
        # in fs2/mm

else:

    if self.selection == 'LiNbO3' or self.selection == 'BBO (Kato)'\
        or self.selection == 'BBO (Eimerl)'\
        or self.selection == 'BBO (Zhang)':

        q = (np.pi/180)*theta
        c = 3E10 #cm/s
        no = self.ord(wavelength)
        ne = self.ex(wavelength)
        n = no*np.sqrt(((1+np.power(np.tan(q),2))/(1\
            +np.power(((no/ne)*np.tan(q)),2))))

        l = wavelength/1000

        Sel_ord = self.Selmeier('ordinary')
        Sel_ex = self.Selmeier('extraordinary')

```

```

if self.selection == 'LiNbO3' \
    or self.selection == 'BBO (Kato)'\
    or self.selection == 'BBO (Eimerl)':

    Bo = Sel_ord[1]
    Co = Sel_ord[2]
    Do = Sel_ord[3]
    Be = Sel_ex[1]
    Ce = Sel_ex[2]
    De = Sel_ex[3]

    dned1 = (1/ne)*(De-(Be/((1*1+Ce)*(1*1+Ce))))
    d2ned12 = (dned1/1) - (((dned1)**2)/ne) \
        + ((4.*1*1*Be)/(ne*((1*1+Ce)**3)))
    dnod1 = (1/no)*(Do-(Bo/((1*1+Co)*(1*1+Co))))
    d2nod12 = (dnod1/1) - (((dnod1)**2)/no) \
        + ((4.*1*1*Bo)/(no*((1*1+Co)**3)))

elif self.selection == 'BBO (Zhang)':

    Bo = Sel_ord[1]
    Co = Sel_ord[2]
    Do = Sel_ord[3]
    Eo = Sel_ord[4]
    Fo = Sel_ord[5]
    Be = Sel_ex[1]
    Ce = Sel_ex[2]
    De = Sel_ex[3]
    Ee = Sel_ex[4]
    Fe = Sel_ex[5]

    dned1 = (1/ne)*(De + 2*Ee*1*1 + 3*Fe*1*1*1*\

```

```

- (Be/((1*1 + Ce)*(1*1 + Ce)))
d2nedl2 = (dnedl/1) - ((dnedl**2)/ne) \
+ ((4.*1*1)/ne)*(Ee + 3.*Fe*1*1\
+ (Be/((1*1+Ce)**3)))
dnodl = (1/no)*(Do + 2*Eo*1*1 + 3*Fo*1*1*1*\
- (Bo/((1*1 + Co)*(1*1 + Co)))
d2nodl2 = (dnodl/1) - ((dnodl**2)/no) \
+ ((4.*1*1)/no)*(Eo + 3.*Fo*1*1\
+ (Bo/((1*1+Co)**3)))

dndl = (n/no)*dnodl + ((n**3)/(no*ne*ne))\
*(((np.tan(q))**2)/(1.+(np.tan(q))**2))\
*((dnodl) - ((no*dnedl)/ne))

# Because of the length of the expression, the
# calculation of d2ndl2 is broken into pieces
A = ((1/no) - (((np.tan(q))**2)/(1.+(np.tan(q))**2)))\
*((3.*n*n)/(no*ne*ne))*dnodl*dndl)
B = ((n/no) - (((np.tan(q))**2)/(1.+(np.tan(q))**2)))\
*((n*n*n)/(no*ne*ne))*d2nodl2)
C = -(n/(no*no)) - (((np.tan(q))**2)/(1\
+((np.tan(q))**2)))*((n*n*n)/(no*no*ne*ne)))\
*(dnodl)*dnodl)

# D, E, F, and G need to be multiplied
# by the factor tan2/1+tan2
D = ((2.*n*n*n)/(no*ne*ne*ne))*dnodl*dnedl)
E = ((3.*n*n)/(ne*ne*ne))*dnedl*dndl)
F = - ((3.*n*n*n)/(ne**4))*((dnedl)**2)
G = ((n*n*n)/(ne*ne*ne))*d2nedl2)
d2ndl2 = A + B + C \
+ (((np.tan(q))**2)/(1+(np.tan(q))**2))\
*(D + E + F + G)

```

```

return ((l**3)/(2*np.pi*c*c))*d2ndl2*(1.E25)
        # in fs2/mm

def deff(self, theta, phi, process):

    if self.selection == 'LiNbO3' or self.selection == 'BBO (Kato)'\
        or self.selection == 'BBO (Eimerl)' \
        or self.selection == 'BBO (Zhang)':

        if self.selection == 'LiNbO3':
            d22 = 2.4
            d31 = -4.52

        elif self.selection == 'BBO (Kato)' \
            or self.selection == 'BBO (Eimerl)'\
            or self.selection == 'BBO (Zhang)':
            d22 = 2.3
            d31 = -0.16

        if process == 'Type I':

            return abs(d31*np.sin((np.pi/180)*theta)\
                -d22*np.cos((np.pi/180)*theta)\
                *np.sin(3*(np.pi/180)*phi))

        elif process == 'Type II' or process == 'Type III':

            return abs(d22*np.cos((np.pi/180)*theta)\
                *np.cos((np.pi/180)*theta)\
                *np.cos(3*(np.pi/180)*phi))

    else:

```



```
return
```

### C.5 phasematching.py

The other non-native script called by `material_params.py` is presented here. Note that while it is not listed as a dependency, `phasematching.py` does require `nl_crystal.py`, as the functions `phasematching.py` contains require an object of class `NLcrystals`.

```
# Native python packages
import numpy as np

# Non-native python packages
# (none)

# phase matching calculation for e --> oo
# requires:
#     - an object of Class nl_crystal.NLcrystals (crystal)
#     - two floats (pump and signal)
def type_one(crystal, pump, signal):

    idler = 1/((1/pump) - (1/signal))

    wp = 2*np.pi*3E17*(1/pump)
    ws = 2*np.pi*3E17*(1/signal)
    wi = 2*np.pi*3E17*(1/idler)

    nop = crystal.ord(pump)
    nep = crystal.ex(pump)
    ns = crystal.ord(signal)
    ni = crystal.ord(idler)

    return (180/np.pi)\
```

```

*np.arccos(np.sqrt((1/(nep*nep-nop*nop))\
*(np.power(((wp*nop*nep)/(ni*wi+ns*ws)),2)-nop*nop)))

# phase matching calculation for e --> oe
# requires:
#     - an object of Class nl_crystal.NLcrystals (crystal)
#     - two floats (pump and signal)
def type_two(crystal, pump, signal):

    idler = 1/((1/pump)-(1/signal))

    wp = 2*np.pi*3E17*(1/pump)
    ws = 2*np.pi*3E17*(1/signal)
    wi = 2*np.pi*3E17*(1/idler)

    nop = crystal.ord(pump)
    nep = crystal.ex(pump)
    ns = crystal.ord(signal)
    noi = crystal.ord(idler)
    nei = crystal.ex(idler)

    A = np.power(ns*ns*ws*ws*(nei*nei-noi*noi)*(nep*nep-nop*nop),2)

    B = 2*((np.power(ns*ns*ws*ws*nop,2)\
-np.power(wp*ns*ws*nop*nep,2))*(nep*nep-nop*nop)\
*(nei*nei-noi*noi)*(nei*nei-noi*noi)+(np.power(ns*ns*ws*ws*noi,2)\
-np.power(ns*ws*wi*noi*nei,2))*(nei*nei-noi*noi)\
*(nep*nep-nop*nop)*(nep*nep-nop*nop))

    C = ((np.power(wp*nop*nep,4)+np.power(ns*ws*nop,4)\
-2*np.power(wp*ns*ws*nop*nep,2))*(nei*nei-noi*noi)\
*(nei*nei-noi*noi))+((np.power(wi*nei*noi,4)+np.power(ns*ws*noi,4)\

```

```

-2*np.power(ns*ws*wi*noi*noi*nei,2))*(nep*nep-nop*nop)\
*(nep*nep-nop*nop))+((4*np.power(ns*ns*ws*ws*noi*nop,2)\
-2*np.power(wi*wp*nop*nep*noi*nei,2)\
-4*np.power(wp*ns*ws*nop*nep*noi,2)\
-4*np.power(ns*ws*wi*noi*nei*nop,2))\
*(nep*nep-nop*nop)*(nei*nei-noi*noi))

D = ((2*np.power(wp*nop*nep,4)*noi*noi\
+2*np.power(ns*ws*nop,4)*noi*noi\
-2*np.power(wi*wp*nop*nep*noi*nei*nop,2)\
-4*np.power(wp*ns*ws*nop*nep*noi*nop,2)\
-2*np.power(ns*ws*wi*noi*nei*nop*nop,2))*(nei*nei-noi*noi))\
+((2*np.power(wi*nei*noi,4)*nop*nop\
+2*np.power(ns*ws*noi,4)*nop*nop\
-2*np.power(wi*wp*nop*nep*noi*nei*noi,2)\
-2*np.power(wp*ns*ws*nop*nep*noi*noi,2)\
-4*np.power(ns*ws*wi*noi*nei*nop*noi,2))*(nep*nep-nop*nop))

E = np.power(noi*wp*nop*nep,4)+np.power(wi*nei*noi*nop,4)\
+np.power(ns*ws*noi*nop,4)\
-2*np.power(wi*wp*nop*nep*noi*nei*nop*noi,2)\
-2*np.power(wp*ns*ws*nop*nep*nop*noi*noi,2)\
-2*np.power(ns*ws*wi*noi*nei*noi*nop*nop,2)

roots = np.roots([A,B,C,D,E])

for i in roots:
    if i.imag == 0:
        if 0<= i.real <= 1:
            return (180/np.pi)*np.arccos(np.sqrt(i.real))

# phase matching calculation for e --> eo

```

```

# requires:
#     - an object of Class nl_crystal.NLcrystals (crystal)
#     - two floats (pump and signal)
def type_three(crystal, pump, signal):

    idler = 1/((1/pump)-(1/signal))
    return type_two(crystal, pump, idler)

# the following return the phase mismatch (in cm-1) for
# the given process at a given crystal angle
# all require:
#     - an object of Class nl_crystal.NLcrystals (crystal)
#     - three floats (pump, signal, and theta)

# Type I: e --> oo
def type_one_mismatch(crystal, pump, signal, theta):

    idler = 1/((1/pump)-(1/signal))

    wp = 2*np.pi*3E17*(1/pump)
    ws = 2*np.pi*3E17*(1/signal)
    wi = 2*np.pi*3E17*(1/idler)

    nop = crystal.ord(pump)
    nep = crystal.ex(pump)
    ns = crystal.ord(signal)
    ni = crystal.ord(idler)

    npu = np.sqrt(1/((np.power(((np.sin((np.pi/180)*theta))/nep),2))\
        +(np.power(((np.cos((np.pi/180)*theta))/nop),2))))

    return np.abs((npu*wp-ns*ws-ni*wi)*(1/(3E10)))

```

```

# Type II: e --> oe
def type_two_mismatch(crystal, pump, signal, theta):

    idler = 1/((1/pump)-(1/signal))

    wp = 2*np.pi*3E17*(1/pump)
    ws = 2*np.pi*3E17*(1/signal)
    wi = 2*np.pi*3E17*(1/idler)

    nop = crystal.ord(pump)
    nep = crystal.ex(pump)
    ns = crystal.ord(signal)
    noi = crystal.ord(idler)
    nei = crystal.ex(idler)

    npu = np.sqrt(1/((np.power(((np.sin((np.pi/180)*theta))/nep),2))\
        +(np.power(((np.cos((np.pi/180)*theta))/nop),2))))
    ni = np.sqrt(1/((np.power(((np.sin((np.pi/180)*theta))/nei),2))\
        +(np.power(((np.cos((np.pi/180)*theta))/noi),2))))

    return np.abs((npu*wp-ns*ws-ni*wi)*(1/(3E10)))

# Type III: e --> eo
def type_three_mismatch(crystal, pump, signal, theta):

    idler = 1/((1/pump)-(1/signal))

    wp = 2*np.pi*3E17*(1/pump)
    ws = 2*np.pi*3E17*(1/signal)
    wi = 2*np.pi*3E17*(1/idler)

```

```

nop = crystal.ord(pump)
nep = crystal.ex(pump)
ni = crystal.ord(idler)
nos = crystal.ord(signal)
nes = crystal.ex(signal)

npu = np.sqrt(1/((np.power(((np.sin((np.pi/180)*theta))/nep),2))\
                +(np.power(((np.cos((np.pi/180)*theta))/nop),2))))
ns = np.sqrt(1/((np.power(((np.sin((np.pi/180)*theta))/nes),2))\
                +(np.power(((np.cos((np.pi/180)*theta))/nos),2))))

return np.abs((npu*wp-ns*ws-ni*wi)*(1/(3E10)))

# Type IV: e --> ee
def type_four_mismatch(crystal, pump, signal, theta):

    idler = 1/((1/pump)-(1/signal))

    wp = 2*np.pi*3E17*(1/pump)
    ws = 2*np.pi*3E17*(1/signal)
    wi = 2*np.pi*3E17*(1/idler)

    nop = crystal.ord(pump)
    nep = crystal.ex(pump)
    noi = crystal.ord(idler)
    nei = crystal.ex(idler)
    nos = crystal.ord(signal)
    nes = crystal.ex(signal)

    npu = np.sqrt(1/((np.power(((np.sin((np.pi/180)*theta))/nep),2))\
                    +(np.power(((np.cos((np.pi/180)*theta))/nop),2))))
    ns = np.sqrt(1/((np.power(((np.sin((np.pi/180)*theta))/nes),2))\
                    +(np.power(((np.cos((np.pi/180)*theta))/nos),2))))

```

```

        +(np.power(((np.cos((np.pi/180)*theta))/nos),2)))
ni = np.sqrt(1/((np.power(((np.sin((np.pi/180)*theta))/nei),2))\
        +(np.power(((np.cos((np.pi/180)*theta))/noi),2))))

return np.abs((npu*wp-ns*ws-ni*wi)*(1/(3E10)))

# Type V:  o --> oo
def type_five_mismatch(crystal, pump, signal, theta):

    idler = 1/((1/pump)-(1/signal))

    wp = 2*np.pi*3E17*(1/pump)
    ws = 2*np.pi*3E17*(1/signal)
    wi = 2*np.pi*3E17*(1/idler)

    npu = crystal.ord(pump)
    ni = crystal.ord(idler)
    ns = crystal.ord(signal)

    return np.abs((npu*wp-ns*ws-ni*wi)*(1/(3E10)))

# Type VI:  o --> oe
def type_six_mismatch(crystal, pump, signal, theta):

    idler = 1/((1/pump)-(1/signal))

    wp = 2*np.pi*3E17*(1/pump)
    ws = 2*np.pi*3E17*(1/signal)
    wi = 2*np.pi*3E17*(1/idler)

    npu = crystal.ord(pump)
    noi = crystal.ord(idler)

```

```

nei = crystal.ex(idler)
ns = crystal.ord(signal)

ni = np.sqrt(1/((np.power(((np.sin((np.pi/180)*theta))/nei),2))\
                +(np.power(((np.cos((np.pi/180)*theta))/noi),2))))

return np.abs((npu*wp-ns*ws-ni*wi)*(1/(3E10)))

# Type VII: o --> eo
def type_seven_mismatch(crystal, pump, signal, theta):

    idler = 1/((1/pump)-(1/signal))

    wp = 2*np.pi*3E17*(1/pump)
    ws = 2*np.pi*3E17*(1/signal)
    wi = 2*np.pi*3E17*(1/idler)

    npu = crystal.ord(pump)
    ni = crystal.ord(idler)
    nos = crystal.ord(signal)
    nes = crystal.ex(signal)

    ns = np.sqrt(1/((np.power(((np.sin((np.pi/180)*theta))/nes),2))\
                    +(np.power(((np.cos((np.pi/180)*theta))/nos),2))))

    return np.abs((npu*wp-ns*ws-ni*wi)*(1/(3E10)))

# Type VIII: o --> ee
def type_eight_mismatch(crystal, pump, signal, theta):

    idler = 1/((1/pump)-(1/signal))

```



```

wp = 2*np.pi*3E17*(1/pump)
ws = 2*np.pi*3E17*(1/signal)
wi = 2*np.pi*3E17*(1/idler)

npu = crystal.ord(pump)
noi = crystal.ord(idler)
nei = crystal.ex(idler)
nos = crystal.ord(signal)
nes = crystal.ex(signal)

ns = np.sqrt(1/((np.power(((np.sin((np.pi/180)*theta))/nes),2))\
                +(np.power(((np.cos((np.pi/180)*theta))/nos),2))))
ni = np.sqrt(1/((np.power(((np.sin((np.pi/180)*theta))/nei),2))\
                +(np.power(((np.cos((np.pi/180)*theta))/noi),2))))

return np.abs((npu*wp-ns*ws-ni*wi)*(1/(3E10)))

```

## C.6 efield.py

The script `efield.py` contains the `electric_field` class; this class has been defined in order to not only contain the electric fields, but also to provide functionalities and properties necessary throughout the script.

```

# Native python packages
import numpy as np
import matplotlib.pyplot as plt
import math
import sys
import os
import datetime
from scipy import interpolate
import glob

# Non-native python packages

```

```
import phasematching as pm
import parameters as p

class electric_field:

    def __init__(self, field, params):

        self.E = (np.empty(len(params.freq)))
        self.id = str(field)
        self.l = params.u.wavelengths[str(field)]
        self.n0 = params.n(self.l, str(field))
        self.w0 = 2*np.pi*params.c*(1E9/self.l)

    def fill(self, params, fluence):

        if params.u.field_envelopes[self.id] == 'Gaussian':
            self.gaussian(params, fluence)

        elif params.u.field_envelopes[self.id] == 'zero':

            self.zero()

        elif params.u.field_envelopes[self.id] == 'file':

            # Not implemented
            exit()

        elif params.u.field_envelopes[self.id] == 'rectangular':

            self.rectangular(params, fluence)
```

```

        return

def int(self):

    return (1.33E-3)*(self.n0)*(np.real(self.E)**2 + np.imag(self.E)**2)

def gaussian(self, params, fluence):

    reEt = np.empty(len(params.time))
    imEt = np.empty(len(params.time))

    sum = ((np.exp((-4.*np.log(2))*((params.time \
        - params.u.Gauss_centers[self.id])\
        /params.u.Gauss_widths[self.id])**2)))\
        *(params.time[1]-params.time[0])).sum()
    reA = ((np.cos((np.pi/180)*params.u.field_phase[self.id]))**2)\
        *(fluence/sum)
    imA = ((np.sin((np.pi/180)*params.u.field_phase[self.id]))**2)\
        *(fluence/sum)
    reEt = np.sqrt((reA/((1.33E-3)*self.n0))*np.exp((-4.*np.log(2))\
        *(((params.time - params.u.Gauss_centers[self.id])\
        /params.u.Gauss_widths[self.id])**2)))
    imEt = np.sqrt((imA/((1.33E-3)*self.n0))*np.exp((-4.*np.log(2))\
        *(((params.time - params.u.Gauss_centers[self.id])\
        /params.u.Gauss_widths[self.id])**2)))

    self.ft(reEt, imEt, params)

    if params.u.apply_contrast:

        retemp = np.real(self.E)

```

```

        imtemp = np.imag(self.E)

        gmax = max(max(np.abs(retemp)), max(np.abs(imtemp)))
        retemp[np.where(np.abs(retemp)<gmax*params.u.contrast)] = 0.
        imtemp[np.where(np.abs(imtemp)<gmax*params.u.contrast)] = 0.

        self.E = retemp + 1j*imtemp

    return

def zero(self):

    self.E = np.zeros(len(self.E)) + 1j*np.zeros(len(self.E))

def rectangular(self, params, fluence):

    self.E = (np.empty(len(params.freq),dtype=complex))

    for i in range(len(params.freq)):
        if i < 5 or i > len(params.freq) - 5:
            self.E[i] = complex(0.)
        else:
            self.E[i] = 1.+1j*0.

    self.E *= np.sqrt(fluence/(self.int()).sum())*self.E

    return

def ft(self, reEt, imEt, params):

```

```

reE = np.empty(len(params.freq))
imE = np.empty(len(params.freq))

self.E = (1/np.sqrt(len(params.time)))*np.sum( (reEt+1j*imEt)[None,:]\
        *np.exp(-1j*params.freq[:,None]*params.time[None,:]), axis = 1)

return

def ift(self, params):

    return (1/np.sqrt(len(params.time)))*np.sum( self.E[None,:]\
        *np.exp(1j*params.freq[None,:]*params.time[:,None]), axis = 1)

def pulse_energy(self, params):

    Et = self.ift(params)

    return ((1.33e-3)*self.n0*(np.real(Et)*np.real(Et) \
        + np.imag(Et)*np.imag(Et))\
        *(params.time[1]-params.time[0])).sum()

```

## C.7 controls.py

The script `controls.py` contains many of the central functions of the script: once the parameters are defined through `parameters.py`, many of the manipulations and executions are executed through functions in `controls.py`.

```

# Native python packages
import numpy as np
import matplotlib.pyplot as plt
import scipy.interpolate as interp

```

```

import multiprocessing, threading, datetime, os, functools, math
# Non-native python packages
import parameters, efield, algorithm
import user_settings as user
import material_params as mat
import gain_formulae as gain
import plotting_routines as pltr
import phasematching as pm
import nl_crystal as nl

# modify_params modifies constants and values in the parameters object
# appropriate to user specifications

def modify_params(p):

    if p.u.modify_theta:
        p.m.theta = p.u.alt_theta
        if p.u.parametric_process == 'second-harmonic generation':
            p.m.dk = pm.type_one_mismatch(p.m.cry, p.u.wavelengths['SHG'],\
                p.u.wavelengths['Fundamental'], p.m.theta)
        elif p.u.parametric_process == 'parametric amplification':
            if p.u.process == 'Type I':
                p.m.dk = pm.type_one_mismatch(p.m.cry,\
                    p.u.wavelengths['Pump'],\
                    p.u.wavelengths['Signal'], p.m.theta)
            elif p.u.process == 'Type II':
                p.m.dk = pm.type_two_mismatch(p.m.cry,\
                    p.u.wavelengths['Pump'],\
                    p.u.wavelengths['Signal'], p.m.theta)
            elif p.u.process == 'Type III':
                p.m.dk = pm.type_three_mismatch(p.m.cry,\
                    p.u.wavelengths['Pump'],\

```

```

                                p.u.wavelengths['Signal'], p.m.theta)
    p.m.dk*=100.

    if p.u.modify_chi2eff:
        p.m.chi2eff = p.u.alt_chi2eff
    if p.u.modify_chi3eff:
        p.m.chi3eff = p.u.alt_chi3eff
    if p.u.modify_ug:
        for i in [p.u.alt_ug]:
            for j in p.m.mask:
                i[j] = i.pop(p.m.mask[j])

            ini_keys = i.keys()

            for j in ini_keys:
                if j in p.m.mask:
                    pass
                else:
                    i.pop(j, None)
        for i in p.u.alt_ug:
            p.m.ug[i] = p.u.alt_ug[i]*1.e12

def initialize(p):

    if p.u.silent:
        pass
    else:
        print('Initializing fields')

    fields = []

```

```

for i in range(len(p.r)):
    fields.append({})
    for j in p.u.wavelengths:
        fields[i][j] = efield.electric_field(j,p)
        fields[i][j].fill(p, p.fluence[j][i])
        fields[i][j].E[np.where((fields[i][j].w0+p.freq)<=
                                p.cutoff)] = complex(0.)

return fields

def drive_algorithm(p, fields):

    if p.u.silent:
        pass
    else:
        print('Starting algorithm')

    if p.u.slowly_varying_amp:

        if p.u.adaptive_steps:
# Adaptive stepping has not yet been developed; when this capability is developed,
# this is how it may be implemented
#
            fields = adaptive_stepping(p,fields)
            pass
        else:
            fields = fixed_stepping(p, fields)

    else:

        if p.u.adaptive_steps:
# Adaptive stepping has not yet been developed; when this capability is developed,
# this is how it may be implemented

```



```

#             fields = second_order_adaptive_stepping(p, fields)
pass
else:
    fields = second_order_fixed_stepping(p, fields)

return fields

def fixed_stepping(p, fields):

    step_size = p.u.L/p.u.steps

    parameter_dict = {

        'curr_position' : p.z,
        'step_size' : step_size,
        'c' : p.c,
        'dw' : p.freq,
        'w' : {},
        'k' : {},
        'n0' : {},
        'w0' : {},
        'chi2eff' : p.m.chi2eff,
        'chi3eff' : p.m.chi3eff,
        'ug' : {},
        'gvd' : {},
        'parametric_process' : p.u.parametric_process,
        'dk' : p.m.dk,
        'cutoff' : p.cutoff,
        'time' : p.time,
        'NaN_flag' : False}

    field_iter = []

```

```

for i in fields[0]:
    parameter_dict['n0'][fields[0][i].id] = fields[0][i].n0
    parameter_dict['w0'][fields[0][i].id] = fields[0][i].w0
    parameter_dict['w'][fields[0][i].id] = p.freq.copy() + fields[0][i].w0
    parameter_dict['ug'][fields[0][i].id] = p.m.ug[fields[0][i].id]
    parameter_dict['gvd'][fields[0][i].id] = p.m.gvd[fields[0][i].id]
    parameter_dict['k'][fields[0][i].id] = \
        np.empty(len(parameter_dict['w'][fields[0][i].id]))

    for j in range(len(parameter_dict['w'][fields[0][i].id])):

        if parameter_dict['w'][fields[0][i].id][j] >= p.cutoff:
            wavelength = ((2*np.pi*p.c)\
                /(parameter_dict['w'][fields[0][i].id][j]))*1.e9
            parameter_dict['k'][fields[0][i].id][j] = \
                (p.n(wavelength, fields[0][i].id)\
                    *parameter_dict['w'][fields[0][i].id][j])/p.c

        else:

            parameter_dict['w'][fields[0][i].id][j] = 0.
            parameter_dict['k'][fields[0][i].id][j] = 0.

for i in range(len(p.r)):
    field_iter.append({})

    for j in fields[0]:
        field_iter[i][j] = fields[i][j].E.copy()

counter = 0

```

```
if p.u.timer:
    start_time = str(datetime.datetime.now()).split(' ')[-1]

while counter < p.u.steps:

    counter += 1

    if p.u.silent:
        pass
    else:
        print('Starting iteration '+str(counter)+' of '+str(p.u.steps)\
              +' at '+str(datetime.datetime.now()))

    if p.u.threading:

        if p.u.cores != 'Default' \
           and p.u.cores <= multiprocessing.cpu_count() \
           and p.u.cores > 0:

            pool = multiprocessing.Pool(processes = p.u.cores)
            chunk_size = int(math.ceil(len(field_iter)/p.u.cores))

        elif p.u.cores != 'Default' and p.u.limit_override == True:

            pool = multiprocessing.Pool(processes = p.u.cores)
            chunk_size = int(math.ceil(len(field_iter)/p.u.cores))

        else:

            if p.u.cores == 'Default':
                pass
```

```

elif p.u.cores > multiprocessing.cpu_count() \
    or p.u.cores<1:
    print('An invalid number of cores was requested.\
        Defaulting to '\
        +str(multiprocessing.cpu_count()-1)\
        +' cores.')
```

```

pool = multiprocessing.Pool(processes = \
    (multiprocessing.cpu_count()-1))
chunk_size = int(math.ceil(len(field_iter)\
    /(multiprocessing.cpu_count()-1)))

results = pool.map(functools.partial(algorithm.Runge_Kutta, \
    parameter_dict), field_iter, \
    chunksize = chunk_size)

pool.close()
for i in range(len(results)):
    for j in results[i]:
        field_iter[i][j] = results[i][j].copy()

del results

else:
    for i in range(len(p.r)):

        results = algorithm.Runge_Kutta(parameter_dict, \
            field_iter[i])

        for j in results:
            field_iter[i][j] = results[j].copy()

parameter_dict['curr_position'] += step_size
```

```

        if parameter_dict['NaN_flag']:
            break

    for i in range(len(p.r)):
        for j in fields[0]:
            fields[i][j].E = field_iter[i][j].copy()

    p.z = parameter_dict['curr_position']

    if p.u.timer:
        end_time = str(datetime.datetime.now()).split(' ')[-1]
        print 'Run time: '+str((int(str(end_time).split(':')[0]) \
            - int(str(start_time).split(':')[0]))*60.*60.\
            +(int(str(end_time).split(':')[1]) \
            - int(str(start_time).split(':')[1]))*60.\
            +(float(str(end_time).split(':')[2]) \
            - float(str(start_time).split(':')[2])))+' seconds'

    return fields

def second_order_fixed_stepping(p, fields):

    step_size = p.u.L/p.u.steps

    parameter_dict = {
        'curr_position' : p.z,

```

```

        'step_size' : step_size,
        'c' : p.c,
        'dw' : p.freq,
        'w' : {},
        'k' : {},
        'n0' : {},
        'w0' : {},
        'chi2eff' : p.m.chi2eff,
        'chi3eff' : p.m.chi3eff,
        'ug' : {},
        'gvd' : {},
        'parametric_process' : p.u.parametric_process,
        'dk' : p.m.dk,
        'cutoff' : p.cutoff,
        'NaN_flag' : False}

field_iter = []

for i in fields[0]:
    parameter_dict['n0'][fields[0][i].id] = fields[0][i].n0
    parameter_dict['w0'][fields[0][i].id] = fields[0][i].w0
    parameter_dict['w'][fields[0][i].id] = p.freq.copy() + fields[0][i].w0
    parameter_dict['ug'][fields[0][i].id] = p.m.ug[fields[0][i].id]
    parameter_dict['gvd'][fields[0][i].id] = p.m.gvd[fields[0][i].id]
    parameter_dict['k'][fields[0][i].id] = \
        np.empty(len(parameter_dict['w'][fields[0][i].id]))

    for j in range(len(parameter_dict['w'][fields[0][i].id])):

        if parameter_dict['w'][fields[0][i].id][j] >= p.cutoff:

            wavelength = ((2*np.pi*p.c)\
                /(parameter_dict['w'][fields[0][i].id][j]))*1.e9

```

```

        parameter_dict['k'][fields[0][i].id][j] = \
            (p.n(wavelength, fields[0][i].id)\
             *parameter_dict['w'][fields[0][i].id][j])/p.c

    else:

        parameter_dict['w'][fields[0][i].id][j] = 0.
        parameter_dict['k'][fields[0][i].id][j] = 0.

for i in range(len(p.r)):
    field_iter.append({})

    for j in fields[0]:
        field_iter[i][j] = {}
        field_iter[i][j]['field'] = fields[i][j].E.copy()
        field_iter[i][j]['first derivative'] = \
            np.zeros(len(fields[i][j].E)) \
            + 1j*np.zeros(len(fields[i][j].E))

counter = 0

if p.u.timer:
    start_time = str(datetime.datetime.now()).split(' ')[-1]

while counter < p.u.steps:

    counter += 1

    if p.u.silent:
        pass
    else:
        print('Starting iteration '+str(counter)+' of '\

```

```

+str(p.u.steps)+' at '+str(datetime.datetime.now())

if p.u.threading:

    if p.u.cores != 'Default' \
        and p.u.cores <= multiprocessing.cpu_count() \
        and p.u.cores > 0:

        pool = multiprocessing.Pool(processes = p.u.cores)
        chunk_size = int(math.ceil(len(field_iter)/p.u.cores))

    elif p.u.cores != 'Default' and p.u.limit_override == True:

        pool = multiprocessing.Pool(processes = p.u.cores)
        chunk_size = int(math.ceil(len(field_iter)/p.u.cores))

    else:

        if p.u.cores == 'Default':
            pass

        elif p.u.cores > multiprocessing.cpu_count() \
            or p.u.cores<1:
            print('An invalid number of cores was requested.\
                Defaulting to '\
                +str(multiprocessing.cpu_count()-1)\
                +' cores.')

        pool = multiprocessing.Pool(processes \
            = (multiprocessing.cpu_count()-1))
        chunk_size = int(math.ceil(len(field_iter)\
            /(multiprocessing.cpu_count()-1)))

```



```

results = pool.map(functools.partial(\
                    algorithm.second_order_Runge_Kutta, \
                    parameter_dict), field_iter, \
                    chunksize = chunk_size)

pool.close()
for i in range(len(results)):
    for j in results[i]:
        field_iter[i][j]['field'] = \
            results[i][j]['field'].copy()
        field_iter[i][j]['first derivative'] = \
            results[i][j]['first derivative'].copy()

del results

else:
    for i in range(len(p.r)):

        results = algorithm.second_order_Runge_Kutta(\
                    parameter_dict, field_iter[i])

        for j in results:
            field_iter[i][j]['field'] = \
                results[j]['field'].copy()
            field_iter[i][j]['first derivative'] = \
                results[j]['first derivative'].copy()

parameter_dict['curr_position'] += step_size

if parameter_dict['NaN_flag']:
    break

```

```

for i in range(len(p.r)):
    for j in fields[0]:
        fields[i][j].E = field_iter[i][j]['field'].copy()

p.z = parameter_dict['curr_position']

if p.u.timer:
    end_time = str(datetime.datetime.now()).split(' ')[-1]
    print 'Run time: '+str((int(str(end_time).split(':')[0]) \
        - int(str(start_time).split(':')[0]))*60.*60.\
        +(int(str(end_time).split(':')[1]) \
        - int(str(start_time).split(':')[1]))*60.\
        +(float(str(end_time).split(':')[2]) \
        - float(str(start_time).split(':')[2])))+' seconds'

return fields

def save_output(p, fields, state):

    curr = os.getcwd()

    if state == 'initial':

        folder_name = ''

        for i in ((str(datetime.datetime.now()).split('.')[0]).split(':')):

```

```

        folder_name += i+'_'
    for i in p.u.wavelengths:
        folder_name += str(p.u.wavelengths[i])+ '_'
    folder_name+=p.u.parametric_process+'_'+p.u.material+'_'+p.u.process

    if p.u.save_dir[-1]=='/':
        p.u.save_dir += folder_name
    else:
        p.u.save_dir += '/' + folder_name

    if os.path.exists(p.u.save_dir):
        pass
    else:
        os.makedirs(p.u.save_dir)

os.chdir(p.u.save_dir)

if state == 'initial':

    write_parameters(p)

    write_fields(p, fields, 'initial')

    pltr.plot2d(fields, p, 'initial_fields_freq')
    pltr.plot2dtime(fields, p, 'initial_fields_time')
    pltr.plot2dweighted(fields, p, 'initial_fields_freq_weighted')

elif state == 'final':

    write_fields(p, fields, 'final')

    pltr.plot2d(fields, p, 'final_fields_freq')
```

```

        pltr.plot2dtime(fields, p, 'final_fields_time')
        pltr.plot2dweighted(fields, p, 'final_fields_freq_weighted')

    os.chdir(curr)

    return

def write_parameters(p):

    f = open('simulation_parameters.txt', 'w+')

    f.write('Simulation Parameters\n\n')

    f.write('Wavelengths\n')

    for i in p.u.wavelengths:
        f.write(str(i)+':\t'+str(p.u.wavelengths[i])+' nm\n')
    f.write('\n')
    f.write('Material Parameters\n')

    if p.mat_type_marker == 'birefringent':
        f.write(p.u.material+' : '+str(p.u.L*100)+' cm, theta: '\
                +str(p.m.theta)+' deg, phi: '+str(p.u.phi)+' deg\n')
    elif p.mat_type_marker == 'isotropic':
        f.write(p.u.material+' : '+str(p.u.L*100)+' cm\n')
    f.write('Number of steps: {0}\n'.format(p.u.steps))

    if p.u.parametric_process == 'parametric amplification':
        f.write('Process: '+p.u.parametric_process+', '+p.u.process+'\n')
    else:
        f.write('Process: '+p.u.parametric_process+'\n')

```

```

f.write('\n')

f.write('Beam Parameters\n')

for i, j in [('Initial Delay', p.u.Gauss_centers), ('Beam Size', p.u.e2_size), \
            ('Pulse Width', p.u.Gauss_widths), ('Initial Phase', p.u.field_phase)]:

    curr_string = i+':'

    if i == 'Initial Delay' or i == 'Pulse Width':
        modifier = 1.e15
        unit = 'fs'
    if i == 'Beam Size':
        modifier = 100.
        unit = 'cm'
    if i == 'Initial Phase':
        modifier = 1.
        unit = 'deg.'

    for k in j:
        curr_string += '\t'+k+': '+str(j[k]*modifier)+' '+unit+';'
    curr_string+= '\n'

    f.write(curr_string)
    del curr_string

f.write('\n')

if p.u.noncollinear or p.u.modify_ug or p.u.modify_chi2eff or p.u.modify_chi3eff:
    f.write('Modifications\n')

    if p.u.noncollinear:

```

```

        f.write('Noncollinear angle: '+str(p.u.gamma)+' deg\n')
    if p.u.modify_chi2eff:
        f.write('Alternate chi2: '+str(p.m.chi2eff*1E12)+' pm/V\n')
    if p.u.modify_chi3eff:
        f.write('Alternate chi3: '+str(p.m.chi3eff)+'\n')
    if p.u.modify_ug:
        f.write('Group velocities:\n')
        for i in p.m.ug:
            f.write(str(i)+':\t'+str(p.m.ug[i]*1e-12)+' mm/fs\n')

f.close()
return

def write_fields(p, fields, state):

    if state == 'initial':
        f = open('initial_fields.txt', 'w+')
    elif state == 'final':
        f = open('final_fields.txt', 'w+')

    for i in range(len(p.r)):
        f.write('Fields at r = '+str(p.r[i]*1000)+' mm\n\n')

        f.write('Detuning (PHz)')

        for j in fields[i]:
            f.write('\tRe('+str(j)+')\tIm('+str(j)+')')

        f.write('\n')

    for j in range(len(p.freq)):

```

```

f.write(str(p.freq[j]*1e-15))

for k in fields[i]:

    f.write('\t'+str(np.real(fields[i][k].E[j]))+'\t'\
            +str(np.imag(fields[i][k].E[j])))

f.write('\n')

f.write('\n\n')

f.close()

del f

if state == 'initial':
    f = open('initial_integrated_spectrum.txt', 'w+')
elif state == 'final':
    f = open('final_integrated_spectrum.txt', 'w+')

int_Int = {}

for j in fields[0]:
    Int = []

    for i in range(len(p.r)):
        Int.append(fields[i][j].int())

    int_Int[j] = []

    for i in range(len(p.freq)):
        sum = 0

```

```

        for k in range(len(p.r)):
            sum+=2*np.pi*Int[k][i]*p.r[k]*(p.r[1]-p.r[0])
        int_Int[j].append(sum)

    del Int

energy = {}

for j in fields[0]:

    sum = 0

    for i in range(len(p.r)):
        sum += 2*np.pi*(fields[i][j].pulse_energy(p))\
            *p.r[i]*(p.r[1]-p.r[0])

    energy[j] = sum

f.write('Final Pulse Energies\n')

for j in energy:
    f.write(j+':\t'+str(energy[j]*1.e6)+' uJ\n')

f.write('\n\n')

f.write('Integrated Spectra\n\n')

f.write('Detuning (PHz)')

for j in int_Int:
    f.write('\t'+str(j))

```



```

f.write('\n')

for j in range(len(p.freq)):

    f.write(str(p.freq[j]*1e-15))

    for k in int_Int:

        f.write('\t'+str(int_Int[k][j]))

    f.write('\n')

f.close()

```

## C.8 algorithm.py

The two functions in `algorithm.py` execute one step of the Runge-Kutta algorithm when called.

```

# Native python packages
import numpy as np
import matplotlib.pyplot as plt

# Non-native python packages
import gain_formulae as gain
import efield

def Runge_Kutta(pd, fields):

    fm = {}
    fm['z'] = pd['curr_position']

    for i in fields:

```

```
fm[i] = fields[i].copy()

KI = {}

for i in fields:
    KI[i] = gain.gain(pd, i, fm)
    KI[i] *= pd['step_size']

del fm
fm = {}
fm['z'] = pd['curr_position'] + 0.5*pd['step_size']

for i in fields:
    fm[i] = (fields[i] + 0.5*KI[i]).copy()

KII = {}

for i in fields:
    KII[i] = gain.gain(pd, i, fm)
    KII[i] *= pd['step_size']

del fm
fm = {}
fm['z'] = pd['curr_position'] + 0.5*pd['step_size']

for i in fields:
    fm[i] = (fields[i] + 0.5*KII[i]).copy()
```

```

KIII = {}

for i in fields:
    KIII[i] = gain.gain(pd, i, fm)
    KIII[i] *= pd['step_size']

del fm
fm = {}
fm['z'] = pd['curr_position'] + pd['step_size']

for i in fields:
    fm[i] = (fields[i] + KIII[i]).copy()

KIV = {}

for i in fields:
    KIV[i] = gain.gain(pd, i, fm)
    KIV[i] *= pd['step_size']

output = {}

for i in fields:
    output[i] = (fields[i]+(1./6.)*KI[i]+(1./3.)*KII[i]+(1./3.)*KIII[i]\
                + (1./6.)*KIV[i]).copy()
    if np.isnan(output[i].sum()):
        print('nan present in '+i)

del fm, KI, KII, KIII, KIV

return output

def second_order_Runge_Kutta(pd, fields):

```

```

fm = {}
fm['z'] = pd['curr_position']

for i in fields:
    fm[i] = {}
    fm[i]['field'] = fields[i]['field'].copy()
    fm[i]['first derivative'] = fields[i]['first derivative'].copy()

KI = {}

for i in fields:
    KI[i] = gain.second_order_gain(pd, i, fm)
    KI[i]['field'] *= pd['step_size']
    KI[i]['first derivative'] *= pd['step_size']

del fm
fm = {}
fm['z'] = pd['curr_position'] + 0.5*pd['step_size']

for i in fields:
    fm[i] = {}
    fm[i]['field'] = (fields[i]['field'] + 0.5*KI[i]['field']).copy()
    fm[i]['first derivative'] = (fields[i]['first derivative'] \
                                + 0.5*KI[i]['first derivative']).copy()

KII = {}

for i in fields:
    KII[i] = gain.second_order_gain(pd, i, fm)
    KII[i]['field'] *= pd['step_size']

```

```

KII[i]['first derivative'] *= pd['step_size']

del fm
fm = {}
fm['z'] = pd['curr_position'] + 0.5*pd['step_size']

for i in fields:
    fm[i] = {}
    fm[i]['field'] = (fields[i]['field'] + 0.5*KII[i]['field']).copy()
    fm[i]['first derivative'] = (fields[i]['first derivative'] \
        + 0.5*KII[i]['first derivative']).copy()

KIII = {}

for i in fields:
    KIII[i] = gain.second_order_gain(pd, i, fm)
    KIII[i]['field'] *= pd['step_size']
    KIII[i]['first derivative'] *= pd['step_size']

del fm
fm = {}
fm['z'] = pd['curr_position'] + pd['step_size']

for i in fields:
    fm[i] = {}
    fm[i]['field'] = (fields[i]['field'] + KIII[i]['field']).copy()
    fm[i]['first derivative'] = (fields[i]['first derivative'] \
        + KIII[i]['first derivative']).copy()

KIV = {}

for i in fields:

```

```

KIV[i] = gain.second_order_gain(pd, i, fm)
KIV[i]['field'] *= pd['step_size']
KIV[i]['first derivative'] *= pd['step_size']

output = {}

for i in fields:
    output[i] = {}
    output[i]['field'] = (fields[i]['field'] + (1./6.)*KI[i]['field'] \
                        + (1./3.)*KII[i]['field'] \
                        + (1./3.)*KIII[i]['field'] \
                        + (1./6.)*KIV[i]['field']).copy()
    output[i]['first derivative'] = (fields[i]['first derivative'] \
                                     + (1./6.)*KI[i]['first derivative'] \
                                     + (1./3.)*KII[i]['first derivative'] \
                                     + (1./3.)*KIII[i]['first derivative'] \
                                     + (1./6.)*KIV[i]['first derivative']).copy()
    if np.isnan(output[i]['field'].sum()) \
       or np.isnan(output[i]['first derivative'].sum()):
        print('nan present in ' + i)
        pd['NaN_flag'] = True

del fm, KI, KII, KIII, KIV

return output

```

### C.9 gain\_formulae.py

While the code in § C.8 performs the sequence of calculations necessary for one iteration of the Runge-Kutta algorithm, it is programmed such that it invokes an external function to provide the gain formulae representing the system of differential equations. For the parametric processes being simulated, these formulae are

provided in `gain_formulae.py`. It should be noted that - as written - the functions defining the gain formulae look to `user_settings.py` (the `gain_selections` class) to determine which terms from the differential equation should be incorporated.

```
# Native python packages
import numpy as np
import scipy.interpolate as interp
import matplotlib.pyplot as plt

# Non-native python packages
import user_settings as user

def gain(pd, id, fm):

    u = user.gain_selections()

    if u.sva_absorption:

        # Enables accounting of absorption by BBO

        wl_array = [150, 170, 190, 195, 220, 235, 255, 280, 300.78125, 335, 375,\
                    421.875, 500, 578.125, 644.53125, 700, 1000, 1500, 1600, 1660,\
                    2000, 2085.9375, 2310, 2355, 2400, 2460, 2500, 2610, 2655,\
                    2725, 2775, 2785.15625, 2899.15966, 2921.875, 3000, 3020,\
                    3050, 3060, 3100, 3120, 3150, 3170, 3200, 3300, 40000]

        alpha_array = [0.2808, 0.195909, 0.14617, 0.129779, 0.089947, \
                      0.07212557, 0.05990443, 0.04796, 0.125, 0.102, 0.0788, 0.06827,\
                      0.05797, 0.04194, 0.03528, 0.02354, 0.02518, 0.02518, 0.02518,\
                      0.01305, 0.01305, 0.025177, 0.3999, 0.3629, 0.3999, 0.1547,\
                      0.2043, 0.4533, 0.6349, 0.4533, 0.6297, 0.7851, 0.7851, 0.8935,\
                      1.0038, 1.3202, 1.2058, 1.5426, 1.5426, 1.2808, 1.2808, 1.5931,\
                      1.7605, 1.7605, 1.7605]
```

```

freq_array = (2*np.pi*3.e8*1.e9*(1/np.asarray(wl_array))).copy()
alpha_array = np.asarray(alpha_array)*100.

# It should be noted that interp.interp1d may require
# 'np.asarray(freq_array)[::-1]' and
# 'np.asarray(alpha_array)[::-1]'. The behavior of this seemed
# inconsistent between Mint (Linux distribution) and Mac OS.
alpha_func = interp.interp1d(freq_array, alpha_array, kind = 'slinear',\
                             bounds_error = False, fill_value = 1.)

if pd['parametric_process'] == 'second-harmonic generation' \
    or pd['parametric_process'] == 'parametric amplification' \
    or pd['parametric_process'] == 'sum-frequency generation':

    if pd['parametric_process'] == 'second-harmonic generation':
        ref = 'Fundamental'
    elif pd['parametric_process'] == 'parametric amplification':
        ref = 'Pump'
    elif pd['parametric_process'] == 'sum-frequency generation':
        ref = 'Signal'

gain = np.zeros(len(pd['w'][id])) + 1j*np.zeros(len(pd['w'][id]))

k0 = (pd['n0'][id]*pd['w0'][id])/pd['c']

if u.sva_group_velocity:

    if id == ref:
        pass
    else:
        if u.sva_in_lab_frame:

```



```

gain += - (1j)*((1/(pd['ug'][id]))\
            -(1/(pd['ug'][ref])))*(pd['w'][id] \
            - pd['w0'][id])*fm[id]

else:

gain += - (1j)*((k0)/(k0 + (1/pd['ug'][ref]))\
                *(pd['w'][id] - pd['w0'][id]))\
            *((1/(pd['ug'][id]))\
            -(1/(pd['ug'][ref])))\
            *(pd['w'][id] - pd['w0'][id])*fm[id]

if u.sva_GVD:

    if u.sva_in_lab_frame:

        gain += -(1j)*((pd['w'][id] - pd['w0'][id])**2)\
                *0.5*pd['gvd'][id]*fm[id]

    else:

        gain += - 1j*((k0)/(2.*(k0 + (1/pd['ug'][ref]))\
                *(pd['w'][id] - pd['w0'][id])))\
                *pd['gvd'][id]\
                *((pd['w'][id] - pd['w0'][id])**2)*fm[id]

if u.sva_absorption:

    if u.sva_in_lab_frame:

        gain += - (alpha_func(pd['w'][id])/2.)*fm[id]

```

```

else:

    gain += - ((k0)/(2.*(k0 + (1/pd['ug'][ref])*(pd['w'][id]\
        - pd['w0'][id]))))*alpha_func(pd['w'][id])\
        *fm[id]

if u.sva_amplification:

    if u.sva_in_lab_frame:

        coeff = (1./(2.*k0))

    else:

        coeff = (1./(2.*(k0 + (1/pd['ug'][ref])*(pd['w'][id] \
            - pd['w0'][id]))))

if pd['parametric_process'] == 'second-harmonic generation':

    if id == 'Fundamental':

        temp_fund = fm['Fundamental'].copy()
        temp_SHG = fm['SHG'].copy()
        temp_fund[np.where(pd['w']['Fundamental'] \
            <= pd['cutoff'])] = complex(0.)
        temp_SHG[np.where(pd['w']['SHG'] \
            <= pd['cutoff'])] = complex(0.)

        fund_time = (1/np.sqrt(len(pd['dw'])))\
            *np.sum(np.exp(-1j\
                *pd['k']['Fundamental'][None,:]\
                *fm['z'])*temp_fund[None,:]*np.exp(1j\

```

```

        *pd['dw'][None,:]\
        *pd['time'][:,None]),axis=1)
shg_time = (1/np.sqrt(len(pd['dw'])))\
        *np.sum(np.exp(-1j\
        *pd['k']['SHG'][None,:]\
        *fm['z'])*temp_SHG[None,:]*np.exp(1j\
        *pd['dw'][None,:]\
        *pd['time'][:,None]),axis=1)

polzn = ((2*pd['chi2eff'])\
        /np.sqrt(len(pd['dw'])))\
        *np.sum(np.conj(fund_time)[None,:]\
        *shg_time[None,:]\
        *np.exp(-1j*pd['dw'][:,None]\
        *pd['time'][None,:]), axis=1)
polzn[np.where(pd['w']['Fundamental'] \
        <= pd['cutoff'])] = complex(0.)

del temp_fund, temp_SHG, fund_time, shg_time

elif id == 'SHG':

temp_fund = fm['Fundamental'].copy()
temp_fund[np.where(pd['w']['Fundamental'] \
        <= pd['cutoff'])] = complex(0.)

fund_time = (1/np.sqrt(len(pd['dw'])))\
        *np.sum(np.exp(-1j\
        *pd['k']['Fundamental'][None,:]\
        *fm['z'])*temp_fund[None,:]*np.exp(1j\
        *pd['dw'][None,:]\
        *pd['time'][:,None]),axis=1)

```

```

polzn = (pd['chi2eff']/np.sqrt(len(pd['dw'])))\
        *np.sum(fund_time[None,:]\
        *fund_time[None,]*np.exp(-1j\
        *pd['dw'][:,None]\
        *pd['time'][None,:]), axis=1)
polzn[np.where(pd['w']['SHG'] \
              <= pd['cutoff'])] = complex(0.)

del temp_fund, fund_time

elif pd['parametric_process'] == 'parametric amplification' \
     or pd['parametric_process'] == 'sum-frequency generation':

    if id == 'Pump':

        temp_signal = fm['Signal'].copy()
        temp_idler = fm['Idler'].copy()
        temp_signal[np.where(pd['w']['Signal'] \
                          <= pd['cutoff'])] = complex(0.)
        temp_idler[np.where(pd['w']['Idler'] \
                          <= pd['cutoff'])] = complex(0.)

        signal_time = (1/np.sqrt(len(pd['dw'])))\
                      *np.sum(np.exp(-1j\
                      *pd['k']['Signal'][None,:]\
                      *fm['z'])*temp_signal[None,]*np.exp(1j\
                      *pd['dw'][None,:]\
                      *pd['time'][:,None]),axis=1)
        idler_time = (1/np.sqrt(len(pd['dw'])))\
                    *np.sum(np.exp(-1j\

```

```

        *pd['k']['Idler'][None,:]\
        *fm['z'])*temp_idler[None,:]*np.exp(1j\
        *pd['dw'][None,:]\
        *pd['time'][:,None]),axis=1)

    polzn=((2*pd['chi2eff']/np.sqrt(len(pd['dw'])))\
        *np.sum(signal_time[None,:]\
        *idler_time[None,:]*np.exp(-1j\
        *pd['dw'][:,None]\
        *pd['time'][None,:]), axis=1)
    polzn[np.where(pd['w']['Pump'] \
        <= pd['cutoff'])] = complex(0.)

    del temp_signal, temp_idler,\
        signal_time, idler_time

elif id == 'Signal':

    temp_pump = fm['Pump'].copy()
    temp_idler = fm['Idler'].copy()
    temp_pump[np.where(pd['w']['Pump'] \
        <= pd['cutoff'])] = complex(0.)
    temp_idler[np.where(pd['w']['Idler'] \
        <= pd['cutoff'])] = complex(0.)

    pump_time = (1/np.sqrt(len(pd['dw'])))\
        *np.sum(np.exp(-1j\
        *pd['k']['Pump'][None,:]\
        *fm['z'])*temp_pump[None,:]\
        *np.exp(1j*pd['dw'][None,:]\
        *pd['time'][:,None]),axis=1)
    idler_time = (1/np.sqrt(len(pd['dw'])))\

```

```

* np.sum(np.exp(-1j\
* pd['k']['Idler'][None,:]*fm['z'])\
* temp_idler[None,:]*np.exp(1j\
* pd['dw'][None,:]\
* pd['time'][:,None]),axis=1)

polzn = ((2*pd['chi2eff'])\
/np.sqrt(len(pd['dw'])))\
* np.sum(pump_time[None,:]\
* np.conj(idler_time)[None,:]\
* np.exp(-1j*pd['dw'][:,None]\
* pd['time'][None,:]), axis=1)
polzn[np.where(pd['w']['Signal'] \
<= pd['cutoff'])] = complex(0.)

del temp_pump, temp_idler, pump_time, idler_time

elif id == 'Idler':

temp_pump = fm['Pump'].copy()
temp_signal = fm['Signal'].copy()
temp_signal[np.where(pd['w']['Signal'] \
<= pd['cutoff'])] = complex(0.)
temp_pump[np.where(pd['w']['Pump'] \
<= pd['cutoff'])] = complex(0.)

pump_time = (1/np.sqrt(len(pd['dw'])))\
* np.sum(np.exp(-1j\
* pd['k']['Pump'][None,:]*fm['z'])\
* temp_pump[None,:]*np.exp(1j\
* pd['dw'][None,:]\
* pd['time'][:,None]),axis=1)

```

```

signal_time = (1/np.sqrt(len(pd['dw'])))\
    *np.sum(np.exp(-1j\
    *pd['k']['Signal'][None,:]\
    *fm['z'])*temp_signal[None,:]\
    *np.exp(1j*pd['dw'][None,:]\
    *pd['time'][:,None]),axis=1)

polzn = ((2*pd['chi2eff'])\
    /np.sqrt(len(pd['dw'])))\
    *np.sum(pump_time[None,:]\
    *np.conj(signal_time)[None,:]\
    *np.exp(-1j*pd['dw'][:,None]\
    *pd['time'][None,:]), axis=1)
polzn[np.where(pd['w']['Idler'] \
    <= pd['cutoff'])] = complex(0.)

del temp_pump, temp_signal, \
    pump_time, signal_time

gain += -1j*((coeff)/(pd['c']*pd['c']))*np.exp(1j\
    *pd['k'][id]*fm['z'])*(pd['w'][id]*pd['w'][id])*polzn

del polzn

return gain

else:
    exit()

def second_order_gain(pd, id, fm):

```

```
# This has not been maintained...
```

### C.10 plotting\_routines.py

The final script, `plotting_routines.py`, defines the functions previously called for plotting the results of the simulations.

```
# Native python packages
```

```
import matplotlib.pyplot as plt
```

```
import numpy as np
```

```
# Non-native python packages
```

```
# (none)
```

```
def plot2d(fields, p, filename):
```

```
    Refields = {}
```

```
    Imfields = {}
```

```
    Int = {}
```

```
    int_Int = {}
```

```
    for j in fields[0]:
```

```
        Refields[j] = []
```

```
        Imfields[j] = []
```

```
        Int[j] = []
```

```
        for i in range(len(p.r)):
```

```
            Refields[j].append(np.real(fields[i][j].E))
```

```
            Imfields[j].append(np.imag(fields[i][j].E))
```

```
            Int[j].append(fields[i][j].int())
```



```

int_Int[j] = []

for i in range(len(p.freq)):
    sum = 0
    for k in range(len(p.r)):
        sum+=2*np.pi*int_Int[j][k][i]*p.r[k]*(p.r[1]-p.r[0])
    int_Int[j].append(sum)

plt.clf()
plt.figure(1, figsize=(12,8))

subplots = 1
show_title = True
units_y = False
label_x = False
counter = 1
for j in fields[0]:

    globalmax = max(np.amax(np.asarray(Refields[j])), \
                    np.amax(np.asarray(Imfields[j])), \
                    abs(np.amin(np.asarray(Refields[j]))), \
                    abs(np.amin(np.asarray(Imfields[j]))))

    freqs = (fields[0][j].w0 + p.freq)*(1/(2.*np.pi*3.e10))
    for i in range(len(freqs)):
        if freqs[i] < 1.4227e14*(1/(2*np.pi*3.e10)):
            freqs[i] = 0.

    if globalmax == 0:
        pass

```

```

else:
    cmin = min(np.amin(np.asarray(Refields[j]).T/globalmax), \
               np.amin(np.asarray(Imfields[j]).T/globalmax))
    cmax = max(np.amax(np.asarray(Refields[j]).T/globalmax), \
               np.amax(np.asarray(Imfields[j]).T/globalmax))

globalmin = min(np.amin(np.asarray(Refields[j])), \
                 np.amin(np.asarray(Imfields[j])), \
                 abs(np.amax(np.asarray(Refields[j]))), \
                 abs(np.amax(np.asarray(Imfields[j]))))

plt.subplot(len(fields[0]), 4, subplots)

if globalmax == 0:
    plt.contourf(p.r*1000., freqs, np.asarray(Refields[j]).T,200, \
                 cmap='seismic', levels=np.linspace(-1,1,200))
else:
    plt.contourf(p.r*1000., freqs, np.asarray(Refields[j]).T\
                 /globalmax,200, cmap='seismic', \
                 levels=np.linspace(-1,1,200))

if label_x:
    plt.xlabel('cross section (mm)')
else:
    plt.tick_params(axis='x', which='both', labeltop='off', \
                    labelbottom='off')

if units_y:
    plt.ylabel(j+'\nangular frequency (x10-15)')
else:
    plt.ylabel(j+'\n')

if show_title:

```

```

        plt.title('Re(E)')
plt.clim(-1,1)
plt.ylim(freqs[0], freqs[-1])
subplots+=1

plt.subplot(len(fields[0]), 4, subplots)

if globalmax == 0:
    plt.contourf(p.r*1000., freqs, np.asarray(Imfields[j]).T,200, \
                cmap='seismic', levels=np.linspace(-1,1,200))
else:
    plt.contourf(p.r*1000., freqs, np.asarray(Imfields[j]).T\
                /globalmax,200, cmap='seismic', \
                levels=np.linspace(-1,1,200))
if label_x:
    plt.xlabel('cross section (mm)')
else:
    plt.tick_params(axis='x', which='both', labeltop='off', \
                    labelbottom='off')
plt.tick_params(axis='y', which='both', labelright='off', \
                labelleft='off')
if show_title:
    plt.title('Im(E)')

plt.clim(-1,1)
plt.ylim(freqs[0], freqs[-1])
subplots+=1

plt.subplot(len(fields[0]), 4, subplots)
plt.contourf(p.r*1000., freqs, np.asarray(Int[j]).T, 200, cmap='seismic')

```

```

if label_x:
    plt.xlabel('cross section (mm)')
else:
    plt.tick_params(axis='x', which='both', labeltop='off', \
                    labelbottom='off')
plt.tick_params(axis='y', which='both', labelright='off', \
                labelleft='off')
if show_title:
    plt.title('Intensity')
if np.max(Int[j]) == 0:
    plt.clim(-1,1)
else:
    plt.clim(-np.max(Int[j]), np.max(Int[j]))
plt.ylim(freqs[0], freqs[-1])
subplots+=1

binned_scaling = 3
plt.subplot(len(fields[0]), 4*binned_scaling, \
            binned_scaling*subplots-(binned_scaling-1))
plt.plot(np.asarray(int_Int[j]), freqs)

plt.xticks([])
plt.tick_params(axis='y', which='both', labelright='off', \
                labelleft='off')

if max(int_Int[j])==0:
    plt.xlim(-0.2,1)
else:
    plt.xlim(-0.1*max(int_Int[j]), max(int_Int[j])\
            +0.1*max(int_Int[j]))
plt.ylim(freqs[0], freqs[-1])

```

```
subplots+=1

counter += 1

if counter != 1:
    show_title = False
if counter == int(len(fields[0])/2):
    units_y = True
else:
    units_y = False
if counter == len(fields[0]):
    label_x = True

if p.u.save:

    plt.savefig(filename+'.png', format='png', transparent=True)

if p.u.show:

    plt.show()

plt.close()
return

def plot2dtime(fields, p, filename):

    Refields = {}
```

```

Imfields = {}
Int = {}
int_Int = {}

for j in fields[0]:
    Refields[j] = []
    Imfields[j] = []
    Int[j] = []

    for i in range(len(p.r)):
        Refields[j].append(np.real(fields[i][j].ift(p)))
        Imfields[j].append(np.imag(fields[i][j].ift(p)))
        Int[j].append((1.33E-3)*(fields[i][j].n0)\
            *(Refields[j][i]**2 + Imfields[j][i]**2))

    int_Int[j] = []

    for i in range(len(p.freq)):
        sum = 0
        for k in range(len(p.r)):
            sum+=2*np.pi*Int[j][k][i]*p.r[k]*(p.r[1]-p.r[0])
        int_Int[j].append(sum)

plt.clf()
plt.figure(1, figsize=(12,8))

subplots = 1
show_title = True
units_y = False
label_x = False
counter = 1

```

```

for j in fields[0]:

    globalmax = max(np.amax(np.asarray(Refields[j])), \
                    np.amax(np.asarray(Imfields[j])), \
                    abs(np.amin(np.asarray(Refields[j]))), \
                    abs(np.amin(np.asarray(Imfields[j]))))

    if globalmax == 0:
        pass
    else:
        cmin = min(np.amin(np.asarray(Refields[j]).T/globalmax), \
                  np.amin(np.asarray(Imfields[j]).T/globalmax))
        cmax = max(np.amax(np.asarray(Refields[j]).T/globalmax), \
                  np.amax(np.asarray(Imfields[j]).T/globalmax))

    globalmin = min(np.amin(np.asarray(Refields[j])), \
                    np.amin(np.asarray(Imfields[j])), \
                    abs(np.amax(np.asarray(Refields[j]))), \
                    abs(np.amax(np.asarray(Imfields[j]))))

    plt.subplot(len(fields[0]), 4, subplots)

    if globalmax == 0:
        plt.contourf(p.r*1000., p.time*1e15, np.asarray(Refields[j]).T,\
                    200, cmap='seismic', levels=np.linspace(-1,1,200))
    else:
        plt.contourf(p.r*1000., p.time*1e15, np.asarray(Refields[j]).T\
                    /globalmax,200, cmap='seismic', \
                    levels=np.linspace(-1,1,200))

    if label_x:

```

```

        plt.xlabel('cross section (mm)')
else:
    plt.tick_params(axis='x', which='both', labeltop='off', \
                    labelbottom='off')
if units_y:
    plt.ylabel(j+'\ntime (fs)')
else:
    plt.ylabel(j+'\n')
if show_title:
    plt.title('Re(E)')

plt.clim(-1,1)
plt.ylim(p.time[0]*1e15, p.time[-1]*1e15)

subplots+=1

plt.subplot(len(fields[0]), 4, subplots)

if globalmax == 0:
    plt.contourf(p.r*1000., p.time*1e15, np.asarray(Imfields[j]).T,\
                200, cmap='seismic', levels=np.linspace(-1,1,200))
else:
    plt.contourf(p.r*1000., p.time*1e15, np.asarray(Imfields[j]).T\
                /globalmax,200, cmap='seismic',\
                levels=np.linspace(-1,1,200))
if label_x:
    plt.xlabel('cross section (mm)')
else:
    plt.tick_params(axis='x', which='both', labeltop='off', \
                    labelbottom='off')
plt.tick_params(axis='y', which='both', labelright='off', \

```



```

        labelleft='off')
if show_title:
    plt.title('Im(E)')
plt.clim(-1,1)
plt.ylim(p.time[0]*1e15, p.time[-1]*1e15)
subplots+=1

plt.subplot(len(fields[0]), 4, subplots)
plt.contourf(p.r*1000., p.time*1e15, np.asarray(Int[j]).T, 200, \
            cmap='seismic')

if label_x:
    plt.xlabel('cross section (mm)')
else:
    plt.tick_params(axis='x', which='both', labeltop='off', \
                    labelbottom='off')
plt.tick_params(axis='y', which='both', labelright='off', \
                labelleft='off')
if show_title:
    plt.title('Intensity')
if np.max(Int[j]) == 0:
    plt.clim(-1,1)
else:
    plt.clim(-np.max(Int[j]), np.max(Int[j]))
plt.ylim(p.time[0]*1e15, p.time[-1]*1e15)
subplots+=1

binned_scaling = 3
plt.subplot(len(fields[0]), 4*binned_scaling, \
            binned_scaling*subplots-(binned_scaling-1))
plt.plot(np.asarray(int_Int[j]), p.time*1e15)

```

```
plt.xticks([])
plt.tick_params(axis='y', which='both', labelright='off', \
                labelleft='off')
if max(int_Int[j])==0:
    plt.xlim(-0.2,1)
else:
    plt.xlim(-0.1*max(int_Int[j]), max(int_Int[j])\
            +0.1*max(int_Int[j]))
plt.ylim(p.time[0]*1e15, p.time[-1]*1e15)

subplots+=1

counter += 1

if counter != 1:
    show_title = False
if counter == int(len(fields[0])/2):
    units_y = True
else:
    units_y = False
if counter == len(fields[0]):
    label_x = True

if p.u.save:

    plt.savefig(filename+'.png', format='png', transparent=True)

if p.u.show:

    plt.show()
```

```

plt.close()

return

def plot2dweighted(fields, p, filename):

    Refields = {}
    Imfields = {}
    Int = {}
    int_Int = {}
    Int_for_int = {}

    for j in fields[0]:
        Refields[j] = []
        Imfields[j] = []
        Int[j] = []
        Int_for_int[j] = []

        for i in range(len(p.r)):
            Refields[j].append(np.real(fields[i][j].E)*2*np.pi*p.r[i])
            Imfields[j].append(np.imag(fields[i][j].E)*2*np.pi*p.r[i])
            Int[j].append(fields[i][j].int()*2*np.pi*p.r[i])
            Int_for_int[j].append(fields[i][j].int())

        int_Int[j] = []

        for i in range(len(p.freq)):
            sum = 0
            for k in range(len(p.r)):

```

```

        sum+=2*np.pi*Int_for_int[j][k][i]*p.r[k]*(p.r[1]-p.r[0])
    int_Int[j].append(sum)

del Int_for_int

plt.clf()
plt.figure(1, figsize=(12,8))

subplots = 1
show_title = True
units_y = False
label_x = False
counter = 1
for j in fields[0]:

    globalmax = max(np.amax(np.asarray(Refields[j])), \
                    np.amax(np.asarray(Imfields[j])), \
                    abs(np.amin(np.asarray(Refields[j]))), \
                    abs(np.amin(np.asarray(Imfields[j]))))

    freqs = (fields[0][j].w0 + p.freq)*(1/(2.*np.pi*3.e10))
    for i in range(len(freqs)):
        if freqs[i] < 1.4227e14*(1/(2*np.pi*3.e10)):
            freqs[i] = 0.

    if globalmax == 0:
        pass
    else:
        cmin = min(np.amin(np.asarray(Refields[j]).T/globalmax), \
                  np.amin(np.asarray(Imfields[j]).T/globalmax))
        cmax = max(np.amax(np.asarray(Refields[j]).T/globalmax), \

```

```

        np.amax(np.asarray(Imfields[j]).T/globalmax))

globalmin = min(np.amin(np.asarray(Refields[j])), \
                np.amin(np.asarray(Imfields[j])), \
                abs(np.amax(np.asarray(Refields[j]))), \
                abs(np.amax(np.asarray(Imfields[j]))))

plt.subplot(len(fields[0]), 4, subplots)

if globalmax == 0:
    plt.contourf(p.r*1000., freqs, np.asarray(Refields[j]).T,200,\
                cmap='seismic', levels=np.linspace(-1,1,200))
else:
    plt.contourf(p.r*1000., freqs, np.asarray(Refields[j]).T\
                /globalmax,200, cmap='seismic', \
                levels=np.linspace(-1,1,200))

if label_x:
    plt.xlabel('cross section (mm)')
else:
    plt.tick_params(axis='x', which='both', labeltop='off', \
                    labelbottom='off')

if units_y:
    plt.ylabel(j+'\nangular frequency (x10-15)')
else:
    plt.ylabel(j+'\n')

if show_title:
    plt.title('Re(E)')

plt.clim(-1,1)
plt.ylim(freqs[0], freqs[-1])

```

```

subplots+=1

plt.subplot(len(fields[0]), 4, subplots)

if globalmax == 0:
    plt.contourf(p.r*1000., freqs, np.asarray(Imfields[j]).T,200, \
                cmap='seismic', levels=np.linspace(-1,1,200))
else:
    plt.contourf(p.r*1000., freqs, np.asarray(Imfields[j]).T\
                /globalmax,200, cmap='seismic', \
                levels=np.linspace(-1,1,200))

if label_x:
    plt.xlabel('cross section (mm)')
else:
    plt.tick_params(axis='x', which='both', labeltop='off', \
                    labelbottom='off')

plt.tick_params(axis='y', which='both', labelright='off', \
                labelleft='off')

if show_title:
    plt.title('Im(E)')

plt.clim(-1,1)
plt.ylim(freqs[0], freqs[-1])
subplots+=1

plt.subplot(len(fields[0]), 4, subplots)
plt.contourf(p.r*1000., freqs, np.asarray(Int[j]).T, 200, cmap='seismic')

if label_x:

```

```

        plt.xlabel('cross section (mm)')
else:
    plt.tick_params(axis='x', which='both', labeltop='off', \
                    labelbottom='off')
plt.tick_params(axis='y', which='both', labelright='off', \
                labeleft='off')
if show_title:
    plt.title('Intensity')
if np.max(Int[j]) == 0:
    plt.clim(-1,1)
else:
    plt.clim(-np.max(Int[j]), np.max(Int[j]))
plt.ylim(freqs[0], freqs[-1])

subplots+=1

binned_scaling = 3
plt.subplot(len(fields[0]), 4*binned_scaling, \
            binned_scaling*subplots-(binned_scaling-1))
plt.plot(np.asarray(int_Int[j]), freqs)

plt.xticks([])
plt.tick_params(axis='y', which='both', labelright='off', \
                labeleft='off')
if max(int_Int[j])==0:
    plt.xlim(-0.2,1)
else:
    plt.xlim(-0.1*max(int_Int[j]), max(int_Int[j])\
            +0.1*max(int_Int[j]))
plt.ylim(freqs[0], freqs[-1])

```

```
subplots+=1

counter += 1

if counter != 1:
    show_title = False
if counter == int(len(fields[0])/2):
    units_y = True
else:
    units_y = False
if counter == len(fields[0]):
    label_x = True

if p.u.save:

    plt.savefig(filename+'.png', format='png', transparent=True)

if p.u.show:

    plt.show()

plt.close()
return
```



**CHAPTER D**  
**Appendix D**

In this appendix, we present code developed to simulate the evolution of signal arising from an arbitrary polarization. This code has been implemented for operation on MacOS and other UNIX-based systems. We have sought to incorporate as many considerations in simulating signal generation as could be considered, including the phase of the driving fields and pulse propagation effects. This code consists of three scripts: `parameters.py`, `operations.py`, and `main.py`.

Once again, the code has been formatted for this presentation.

### D.1 `parameters.py`

The code in `parameters.py` defines a class that outlines the parameters for the system to be simulated and the functions used to calculate and determine the optical properties of the material. It should be noted that in these functions, it would be trivial to add additional materials and solvents as desired.

```
import numpy as np
from numpy import power as pow
import os
import matplotlib.pyplot as plt
from scipy.interpolate import interp1d
from functools import partial

class parameters:

    def __init__(self):

        ###          Options

        # parameters.diagnostic is a Boolean that controls whether diagnostic plots are
        # displayed during operation
            self.diagnostic = False

        # parameters.smoothing is a Boolean the controls whether the loaded signal files
```

```
# are baseline subtracted and smoothed (True) or are just modified by having the
# baseline subtracted (False). parameters.baseline_percentage is a scalar value,
# N, that defines all points within N% of the maximum difference from the initial
# point in the loaded arrays as "baseline". parameters.boxcar is a scalar value
# that defines the half-width of the smoothing boxcar, and only has an impact
# when smoothing is enabled. parameters.cutoffs defines the threshold of
# smoothing: all points in the arrays for which  $y(kx)y^*(kx)$  is below the cutoff
# will be smoothed. parameters.smooth_mode has been added to control whether the
# smoothing is performed in the loaded domain or in the Fourier domain; it seems
# that smoothing in the Fourier domain is more effective for suppressing baseline
# noise, whereas smoothing in the loaded domain appears to be better when the
# feature is noisy.
```

```
self.smoothing = True
self.smooth_mode = {'w1' : 'fourier', 'w2' : 'fourier', 'w3' : 'loaded'}
self.baseline_percentage = 2.
self.boxcar = 8
self.cutoffs = {'w1' : 2.e-4, 'w2' : 4.e-4, 'w3' : 9.e-5}
```

```
# parameters.characteristic_length is an estimate for the temporal width of the
# pulses. This value needs to be a reasonable estimate for the shortest pulses
# involved in the experiment, but does not have to be exact; it is just used to
# define time/frequency grids with approximately equal sampling of the
# polarization in both domains. parameters.time_points defines the number of
# points should be used in constructing the grids.
```

```
self.characteristic_length = 75.
self.time_points = 128
```

```
# parameters.z_points defines the number of transverse slices that should be
# taken for the integration
```

```
self.z_points = 701
```

```
# parameters.x_points and parameters.y_points defines the desired number of
# points along the x and y axes of each transverse slice. The program has some
```

```
# flexibility to override this if it is necessary to ensure sufficient bounds of
# the transverse slices.
    self.x_points = 128
    self.y_points = 128

# parameters.absorption, parameters.gvm_in, parameters.gvm_out, parameters.gvd_in
# and parameters.gvd_out control what absorptive and dispersive properties of the
# system should be considered. The dispersion of the air is neglected, but
# the dispersion of windows and material are both considered. The GVM and GVD
# can be enabled/disabled on the input and output fields separately.
    self.absorption = True
    self.gvm_in = True
    self.gvm_out = True
    self.gvd_in = True
    self.gvd_out = True
    self.mono_convolution = False

# parameters.dispersive_k controls whether the wave vector of the fields
# should be treated according to the propagation at the carrier frequency (False)
# of that each frequency should exhibit a unique wave vector (True)
    self.dispersive_k = False

# parameters.save controls whether the polarization slices are saved during
# operation. parameters.save_final controls whether the final field is saved.
# parameters.folder directs the program to the desired save location.
# Note that even ~128x128x128 slices will yield ~180MB files, and double the time
# required for the polarization_slice function to execute.
    self.save = False
    self.save_final = True
    self.save_folder=''
    self.save_file = 'final_field'

    # Omit format; output will be saved to .txt
```

```
self.multiprocessing = True
self.processes = 8
self.chunksize = 1

# Modification to the nonresonant electronic nonlinear susceptibility reported by
# Levenson and Bloembergen.
self.elec_modifier = 150000.

### Experimental Configuration

# Beam placement and distance of the focusing optics from the sample
self.mask = {'w1' : [-0.5, 2.0], 'w2' : [0., -2.], 'w3' : [1, 1.75]}
self.d = 24.*2.54

# Phase-matching coefficients and experimental degeneracy
self.phase_matching = {'w1' : 1, 'w2' : -1, 'w3' : 1}
self.degeneracy = 6.

# Monochromator characteristics
self.N = 300.          # grooves/mm
self.f_len = 140.     # mm
# Slit width
self.slits = 100.    # microns

### Sample and window characteristics

# Sample path length in mm
self.L = 1.

# Window path length in mm
self.win_len = (12.5-1.)/2.

# Materials
self.sample = {'benzene' : 1.0}
self.windows = 'glass'

### Imaging Parameters
```

```

self.focus_shift = {'w1' : 0., 'w2' : 0., 'w3' : 0.}
self.focus_offset = {'w1' : [0., 0.], 'w2' : [0., 0.], 'w3' : [0., 0.]}
self.waist = {'w1' : 40.5, 'w2' : 23., 'w3' : 23.}

```

### ### Field Properties and Parameters

```

self.colors = {'w1' : '8000', 'w2' : '7000', 'w3' : 'delay'}
self.w0 = {'w3' : ((3.e8)/(794.038e-9))*2*np.pi}
        # Define w0 for w3
self.phase = {'w1' : 0., 'w2' : 0., 'w3' : 0.}
self.delay = {'t31' : 0., 't32' : 0.}
self.rel_lengths = {'w1' : 'short', 'w2' : 'short', 'w3' : 'long'}
self.energy = {
                'w1' : {'8300' : 0.000000719,
                        '8000' : 0.000001103,
                        '7700' : 0.000001198},
                'w2' : {'7300' : 0.000001074,
                        '7000' : 0.000001007,
                        '6700' : 0.000000671},
                'w3' : {'delay' : 0.0000003739}}      # in J

```

### ### Parameters for file loading and processing

```

self.folder = ''
self.files = {
                'w1' : {'8300' : '',
                        '8000' : '',
                        '7700' : ''},
                'w2' : {'7300' : '',
                        '7000' : '',
                        '6700' : ''},

```

```

        'w3' : {
            'delay' : ''}}
self.columns = {'w1' : [8, 21], 'w2' : [8, 21], 'w3' : [12, 16]}

### Other:

self.c = 3.e8
self.L *= 1000. # Convert from mm to microns
self.win_len *= 1000. # Convert from mm to microns

# Calculate external angles
self.theta_ext = {}
for i in self.mask:
    self.theta_ext[i] = [ (np.arctan(self.mask[i][j]/self.d)) \
                          for j in [0,1] ]

# time_freq_grids()
# Uses the provided characteristic_length and time_points parameters to determine
# time and frequency grids that should provide even sampling of the electric
# fields and polarization in both domains.
def time_freq_grids(self):
    # Calculate the point spacing required in the time domain
    delta = self.characteristic_length*np.sqrt(np.pi/self.time_points)
    # Calculate the bounds of the time array (half the full spread of the grid)
    half_width = (delta*self.time_points)/2.
    # Calculate the grids.
    self.t = np.linspace(-1*half_width, half_width, self.time_points)
    self.w = np.linspace(-np.pi/(delta*1e-15),np.pi/(delta*1.e-15),\
                          len(self.t)+1)[: -1]
    return

def spatial_grids(self):

```

```

# Calculate the half-width bounds for the x and y axes.
xy_hw = [(0.5 * i * min(self.waist.itervalues()) * np.sqrt(np.pi/i)) \
          for i in [self.x_points, self.y_points]]

# Define the x,y grids
self.x = np.linspace(-xy_hw[0], xy_hw[0], self.x_points)
self.y = np.linspace(-xy_hw[1], xy_hw[1], self.y_points)
self.kx = np.linspace(-1/(2*abs(self.x[1] - self.x[0])), \
                      1/(2*abs(self.x[1] - self.x[0])), self.x_points+1)[: -1]
self.ky = np.linspace(-1/(2*abs(self.y[1] - self.y[0])), \
                      1/(2*abs(self.y[1] - self.y[0])), self.y_points+1)[: -1]
ds = [self.L*np.tan(self.theta['w4'][0]), \
      self.L*np.tan(self.theta['w4'][1]), \
      self.L]
ds = np.sqrt(np.dot(np.asarray(ds), np.asarray(ds)))
deltaz = max(np.amax(abs(self.x))*np.tan(self.theta['w4'][0]), \
            np.amax(abs(self.y))*np.tan(self.theta['w4'][1]))
self.z = np.linspace(-(0.5* + deltaz), (0.5*ds + deltaz), self.z_points)
return

```

```

# This method calculates the optical properties at the relevant frequencies
# It adds a property to the class for each optical property, with each property
# being a dictionary containing the values of those properties for each field.

```

```

def calculate_optical_properties(self, w = 'default'):

```

```

    if w == 'default':
        del w
        w = self.w

    self.n0, self.nw, self.nwin, self.nair = {}, {}, {}, {}
        # indices of refraction
    self.ug = {}

```



```

        # group velocity
self.gvd, self.gvdw = {}, {}

        # group velocity dispersions
self.a0, self.aw = {}, {}

        # absorption coefficients

for i in self.w0:

    self.nair[i] = self.calc_index(((2*np.pi*3.e17)/self.w0[i]),\
        'air')
    self.nwin[i] = self.calc_index(((2*np.pi*3.e17)/self.w0[i]), \
        self.windows)

# The index of refraction of the sample will be calculated as the sum of the
# products of each component's refractive index and volume fraction (the
# Arago-Biot model. While it seems that this model is not as accurate as the
# Lorentz-Lorentz model, it is reasonably accurate and much simpler.

self.n0[i] = sum( ((self.calc_index( ((2 * np.pi * 3.e17)\
    /self.w0[i]), j)* self.sample[j]) for j in self.sample) )
nw_temp = []
nw_temp.extend( (sum( ((self.calc_index(((2 * np.pi * 3.e17)\
    /self.w0[i] + self.w[j])), k) * self.sample[k]) \
    for k in self.sample))) for j in range(len(w))
self.nw[i] = np.asarray(nw_temp)

# The Arago-Biot model, i.e.  $n = \sum n_i f_i$  where  $n_i$  and  $f_i$  are the index and
# volume fraction of the  $i$ 'th sample component, can be extended to calculate
# the group velocity of a mixture. From the definition of the group velocity
#  $u_g = (dk/dw)^{-1}$ : given  $k = nw/c$ ,  $dk/dw = d/dw (nw/c)$ . If we treat  $n$  as the
# index of a mixture:  $dk/dw = d/dw ((\sum n_i f_i) w/c) = \sum d/dw ((n_i f_i) w/c)$ 
# But  $f_i$  is independent of frequency, so:  $dk/dw = \sum f_i * d/dw (n_i w/c)$ 
# We can recognize  $d/dw (n_i w/c)$  as  $dk/dw$  of the  $i$ 'th component, so  $dk/dw$  of

```

```

# the mixture is the sum of  $f_i \cdot (dk/dw)_i$ , or  $ug^{-1} = \sum (f_i/ug_i)$ .
self.ug[i] = (1.e18)/(sum((((1/self.calc_gv(((2 * np.pi * 3.e17)\
    /self.w0[i]), j))*self.sample[j]) for j in self.sample)))

# Given GVD is  $d^2k/dw^2$ , it is trivial to show  $(d^2k/dw^2) = \sum f_i \cdot (d^2k/dw^2)_i$ .
self.gvd[i] = 1.E-33 * sum( ((self.calc_gvd(((2 * np.pi * 3.e17)\
    /self.w0[i]), j) * self.sample[j]) for j in self.sample))
self.gvdw[i] = self.calc_gvd(((2*np.pi*3.e17)/self.w0[i]),\
    self.windows)*1.E-33

self.a0[i] = self.alpha(((2*np.pi*3.e17)/self.w0[i])) * 1.e-4
aw_temp = []
aw_temp.extend( ((self.alpha(((2*np.pi*3.e17)/(self.w0[i]+j))) \
    * 1.e-4) for j in w) )
self.aw[i] = np.asarray(aw_temp)
del aw_temp, nw_temp

# If a key for w4 exists, calculate the nonlinear susceptibility
if 'w4' in self.w0:
    chi_temp = []
    chi_temp.extend((sum(((self.calc_chi(self.w0['w4'] + j, i) \
        * 1.e12 * self.sample[i]) for i in self.sample)) \
        for j in w))
    self.chi = np.asarray(chi_temp)
    del chi_temp

return

# This method calculates the internal angles of each field

def calculate_internal_angles(self):

    self.theta = {}

```

```

# For each key in the property describing external angles (i.e. 'w1', 'w2', 'w3')
# calculate the internal angles for each of these fields using Snell's law.
    for i in self.theta_ext:
        self.theta[i] = [(np.arcsin((self.nair[i]*\
            np.sin(self.theta_ext[i][j])) \
            /self.n0[i])) for j in [0,1] ]
    del i

# If a key exists in theta for 'w1', 'w2', and 'w3', calculate the internal
# angles for the output field according to the phase-matching conditions.
    if 'w1' in self.theta and 'w2' in self.theta and 'w3' in self.theta:
# Calculate the magnitude of the k-vector for each field in 1/micron
        kmag = {}
        for i in self.w0:
            kmag[i] = (self.w0[i]*self.n0[i]/(3.e8))*1.e-6
                # in 1/micron
        del i

# Find thetax and thetay for the output field that satisfy the relationships:
#  $k_{4x} = c_1*k_{1x} + c_2*k_{2x} + c_3*k_{3x}$ 
#  $k_{4y} = c_1*k_{1y} + c_2*k_{2y} + c_3*k_{3y}$ 
# This may not necessarily be the exact solution since it neglects  $k_z$  but
# hopefully should be close for most cases.
        sums = [sum( ((self.phase_matching[i]*kmag[i]\
            *np.sin(self.theta[i][j])) \
            for i in self.theta)) for j in [0,1]]
        self.theta['w4'] = [ (np.arcsin(sums[i]/kmag['w4'])) \
            for i in [0,1]]

# Use the calculated angles to calculate the actual k-vectors
        k = {}
        for i in self.theta:
            k[i] = kmag[i]*np.asarray([np.sin(self.theta[i][0]),
                np.sin(self.theta[i][1]), np.sqrt(1 \

```



```

elif material == 'glass':
    # Precision Cells does not appear to give the type of glass
    # BK7 is used as a representative blend
    a1, b1 = 1.03961212, -0.00600069867
    a2, b2 = 0.231792344, -0.0200179144
    a3, b3 = 1.01046945, -103.560653
    return np.sqrt(1 + sum( ((i * pow(wl, 2) * pow((pow(wl, 2) + j), \
        -1)) for i,j in [(a1,b1), (a2,b2), (a3,b3)])) ))

elif material == 'air':
    a1, b1 = 0.05792105, 238.0185
    a2, b2 = 0.00167917, 57.362
    return 1 + sum( ((i * pow((j - pow(wl, -2)), -1)) \
        for i,j in [(a1,b1), (a2,b2)])) )

# material_properties.gv(WAVELENGTH, MATERIAL)
# Takes WAVELENGTH (in nm) and the name of a material (as a string)
# Returns the group velocity of MATERIAL at WAVELENGTH in units mm/fs
# Group velocity is dw/dk, or (dk/dw)^-1

def calc_gv(self, wavelength, material):

    # Defined as (dw/dk) (or (dk/dw)^(-1))

    wl = wavelength/1000.

    if material == 'benzene':
        a, b, c, d, e = 2.170184597, 0.00059399, 0.02303464, \
            -0.000499485, 0.000178796
        dndl = 0.5*pow(self.calc_index(wavelength, material), -1) \
            * (2*b*wl - 2*c*pow(wl, -3) - 4*d*pow(wl, -5) \
            - 6*e*pow(wl, -7))

```

```

elif material == 'glass':
    a1, b1 = 1.03961212, -0.00600069867
    a2, b2 = 0.231792344, -0.0200179144
    a3, b3 = 1.01046945, -103.560653
    dndl = 0.5*pow(self.calc_index(wavelength, material), -1) \
            * sum(((2 * i * wl * pow((pow(wl,2) + j), -1) \
                    - 2 * i * pow(wl,3) * pow((pow(wl,2) + j), -2)) \
                    for i,j in [(a1,b1), (a2,b2), (a3,b3)]))

elif material == 'air':
    a1, b1 = 0.05792105, 238.0185
    a2, b2 = 0.00167917, 57.362
    dndl = sum( ((-2 * i * pow(wl,-3) * pow((j - pow(wl,-2)), -2)) \
                for i,j in [(a1,b1), (a2,b2)]))

return self.c * pow((self.calc_index(wavelength, material) - wl*dndl), \
                    -1)*1.e-12
    # in mm/fs

# parameters.gvd(WAVELENGTH, MATERIAL)
# Takes WAVELENGTH (in nm) and the name of a material (as a string)
# Returns the group velocity dispersion of MATERIAL at WAVELENGTH
# in units fs2/mm
# Group velocity dispersion is d2k/dw2

def calc_gvd(self, wavelength, material):

    wl = wavelength/1000.

    if material == 'benzene':
        a, b, c, d, e = 2.170184597, 0.00059399, 0.02303464,\
                        -0.000499485, 0.000178796
        dndl = 0.5*pow(self.calc_index(wavelength, material), -1) \

```

```

        * (2*b*w1 - 2*c*pow(w1, -3) - 4*d*pow(w1, -5) \
        - 6*e*pow(w1, -7))
d2nd12 = 0.5*pow(self.calc_index(wavelength, material), -1) \
        * (2*b + 6*c*pow(w1, -4) + 20*d*pow(w1, -6) \
        + 42*e*pow(w1, -8)) + -0.5\
        *pow(self.calc_index(wavelength, material), -2) \
        * dnd1 * (2*b*w1 - 2*c*pow(w1, -3) \
        - 4*d*pow(w1, -5) - 6*e*pow(w1, -7))
elif material == 'glass':
    a1, b1 = 1.03961212, -0.00600069867
    a2, b2 = 0.231792344, -0.0200179144
    a3, b3 = 1.01046945, -103.560653
    dnd1 = 0.5*pow(self.calc_index(wavelength, material), -1) \
            * sum(((2 * i * w1 * pow((pow(w1,2) + j), -1) \
            - 2 * i * pow(w1,3) * pow((pow(w1,2) + j),-2)) \
            for i,j in [(a1,b1), (a2,b2), (a3,b3)]))
d2nd12 = 0.5 * pow(self.calc_index(wavelength, material), -1) \
        * sum(((2 * i * pow((pow(w1,2) + j),-1) \
        - 10 * i * pow(w1,2) * pow((pow(w1,2) + j),-2) \
        + 8 * i * pow(w1,4) * pow((pow(w1,2) + j),-3)) \
        for i,j in [(a1,b1), (a2,b2), (a3,b3)])) \
        - 0.5*pow(self.calc_index(wavelength, material), \
        -2) * dnd1 * sum( ((2 * i * w1 * pow((pow(w1,2) \
        + j),-1) - 2 * i * pow(w1,3) \
        * pow((pow(w1,2) + j),-2)) \
        for i,j in [(a1,b1), (a2,b2), (a3,b3)]))
elif material == 'air':
    a1, b1 = 0.05792105, 238.0185
    a2, b2 = 0.00167917, 57.362
    d2nd12 = sum(((6 * i * pow(w1,-4) * pow((j - pow(w1,-2)),-2)\
            + 8 * i * pow(w1,-6) * pow((j - pow(w1,-2)),-3))\
            for i,j in [(a1,b1), (a2,b2)]))

```

```

        return (((w1)**3)/(2*np.pi*(self.c**2))*d2ndl2)*(1e21) #fs2/mm

# parameters.alpha(WAVELENGTH)
# Takes WAVELENGTH (in nm)
# Returns the absorbance coefficient of the sample at WAVELENGTH in units 1/cm

def alpha(self, wavelength):
    return 0.

# parameters.chi(p, FREQUENCY, INDICES)
# Takes angular frequency (in 1/s)
# Currently set to return the non-resonant electronic and Raman
# response of benzene's 992cm-1 mode in a CARS experiment
# in which (w1-w2) prepare the vibrational coherence
# Returns the chi3 value in units of m2/V2

def calc_chi(self, freq, material):
    if material == 'benzene':

        # Convert to the frequency shift in wavenumbers from frequency of w3
        wn = ((freq - self.w0['w3'])/(2*np.pi))*(1/3.e10)

        # Terms from Levenson and Bloembergen, J Chem Phys 60 1323 with a
        # modifier to increase the electronic response under fs excitation. Note
        # that we neglect the imaginary contribution described by Levenson and
        # Bloembergen. (They do not give a fixed value, and it is >200 times
        # weaker than the real, and within the bounds of their reported error.)
        chi_elec = 0.64e-36*self.elec_modifier
        chi_vib = 1.74e-35 * (992./((992.**2) - (wn**2) + 1j*2.*wn*1.15))

        # Local field enhancement factor
        F = reduce(lambda x,y: x*y, (((((self.n0[i]**2) + 2.)/3.)) \
            for i in self.n0))

```



```

# Chi3 in cgs units; factor of 0.5 accounts for difference in degeneracy
    chi_cgs = 6.75e21*(chi_elec+chi_vib)*F*0.5
# Convert chi3 from cgs units to SI units
    return chi_cgs*4*np.pi*(1.e-4)*((299.79)**(-2))

```

## D.2 operations.py

The second script associated with these calculations, `operations.py`, contains many of the functions necessary for proper execution.

```

import numpy as np
from numpy import power as pow
import os, itertools, datetime
import matplotlib.pyplot as plt
from scipy.interpolate import interp1d
from functools import partial
from itertools import product

# operations.load_field (FOLDER, FILE, COLUMNS)
# Takes two strings (FOLDER and FILE) and a 2-element list (COLUMNS). FOLDER and FILE
# identify the location and name of the file containing the raw tuning data for one
# field. COLUMNS is a two-element list that specifies the indices (with indexing starting
# at 0) of the columns containing the data for the x (COLUMNS[0]) and y (COLUMNS[1]) data.
def load_field(folder, file, columns):
# Initialize the arrays.
    x_axis, y_axis = [], []
# Open the target file.
    f = open(folder + '/' + file)
# Load each line and append the values in the appropriate columns to x and y arrays.
    for line in f:
        x_axis.append(float(line.split('\t')[columns[0]]))
        y_axis.append(float(line.split('\t')[columns[1]]))

```

```

    f.close()

    del f, line

# Return the loaded files as a tuple of arrays (x,y)
    return np.asarray(x_axis), np.asarray(y_axis)

# Initialize the matplotlib figure and axes objects necessary to ensure proper operation
# for diagnostics enabled or disabled.
def initialize_diagnostics(modes, diagnostic, smoothing):
# Initialize a matplotlib figure object and a dictionary for storing the axes
    fig1, fig2 = plt.figure(), plt.figure()
    axes1, axes2 = {}, {}

# If diagnostics are not enabled, just populate axes1 and axes2 as dummy variables.
    if not diagnostic:
        for i in ['w1', 'w2', 'w3']:
            axes1[i] = [None, None]
            axes2[i] = [None, None]

# Otherwise, populate axes according to whether smoothing is enabled or not.
    else:
        if smoothing:
            # Populate axes1 according to the manner of smoothing.
            for i,j,k in [('w1',1,1), ('w2',3,2), ('w3',5,3)]:
                if modes[i] == 'fourier':
                    axes1[i] = [fig1.add_subplot(3,2,j), \
                                fig1.add_subplot(3,2,j+1)]
                elif modes[i] == 'loaded':
                    axes1[i] = [fig1.add_subplot(3,1,k), None]

            del i, j, k
        elif not smoothing:
            for i,j in [('w1', 1), ('w2', 2), ('w3',3)]:
                axes1[i] = [fig1.add_subplot(3,1,j), None]
            for i,j in [('w1', 1), ('w2', 3), ('w3', 5)]:
                axes2[i] = [fig2.add_subplot(3,2,j), fig2.add_subplot(3,2,j+1)]

```

```

return fig1, axes1, fig2, axes2

# operations.smooth(X,Y,CUTOFF, BOXCAR, BASE_PER, DIAG, AX, MODE)
# Takes two numpy arrays (X,Y), three scalar values (CUTOFF, BOXCAR, and BASE_PER), a
# boolean (DIAG), and an axis object from matplotlib.pyplot (only necessary if
# DIAG is True). Performs baseline subtraction and smoothing on the Y array. CUTOFF
# specifies the threshold under which smoothing is performed, and BOXCAR specifies the
# limit for the half-width of the smoothing boxcar. BASE_PER specifies the percentage
# used to define which points in the Y array constitute "baseline". DIAG indicates
# the routine making the function call is performing diagnostic plotting; if True, smooth
# requires an axis object on which it can plot the results of processing.
def smooth(x, y, cutoff, boxcar= 6, base_per= 2., diag= False, ax=None, mode='fourier'):
# Baseline subtraction.
    y = baseline_subtract(y = y, perc = base_per)
# If the smoothing mode is to operate in the Fourier domain:
    if mode == 'fourier':
# If necessary, define an array corresponding to the Fourier domain of the x array
        kx = np.linspace(-1/(2*abs(x[1]-x[0])), 1/(2*abs(x[1]-x[0])),\
            len(x)+1)[: -1]
# Perform the 1DFT
        y_ft = (1/np.sqrt(len(x))) * (y[:,None] \
            * np.exp(1j*2*np.pi*x[:,None]*kx[None,:])).sum(axis=0)
# If diagnostics are enabled, plot y(kx)
        if diag:
            ax.plot(kx, y_ft*np.conj(y_ft), 'k-')
            ax.set_yscale('log')
# Initialize the smoothed array as a copy of the original array.
        y_ft_sm = y_ft.copy()
# Only perform smoothing for points where y(kx)y*(kx) are below the cutoff. It
# should be noted that this algorithm assumes a feature in the middle of the data
# with continuous background that needs to be smoothed.
        for i in np.where(y_ft*np.conj(y_ft) < cutoff)[0]:

```

```

# Define initial averaging window as the span of i +/- boxcar.
    upper = i + boxcar + 1
    lower = i - boxcar

# If lower < 0, the boxcar reaches the beginning of the array; in this case, only
# average over the points up to the upper bound.
    if lower < 0:
        y_ft_sm[i] = np.mean(y_ft[:upper])

# If upper extends the range of the boxcar beyond the end of the array, the
# average is taken from the lower bound to the end of the array, incorporating
# the first point, due to the symmetry of the FT.
        elif upper > (len(y_ft) - 1):
            y_ft_sm[i] = np.mean(np.concatenate((y_ft[lower:],\
                                                y_ft[:1])))

# Otherwise, perform the average between upper and lower. However, so we are
# only averaging out noise, we check to make sure that the bounds of the boxcar do
# not significantly extend into the main features of the array; if the bounds do
# extend into the main features of the array (i.e. those above the cutoff level),
# the bounds are gradually decreased as the index approaches the main feature(s).
    else:
        upper += -2
        lower += 2
        check1, check2 = 0,0
        while upper not in np.where(y_ft*np.conj(y_ft) \
            < cutoff)[0]:
            upper += -1
            check1 += 1
            if check1 > boxcar:
                break
        while lower not in np.where(y_ft*np.conj(y_ft) \
            < cutoff)[0]:
            lower += 1
            check2 += 1

```

```

        if check2 > boxcar:
            break

        upper += 2
        lower += -2

        y_ft_sm[i] = np.mean(y_ft[lower:upper])
# If diagnostics are enabled, plot the smoothed y(kx) data.
    if diag:
        ax.plot(kx, y_ft_sm*np.conj(y_ft_sm), 'r-')
# Perform the 1DFT to convert the smoothed y(kx) to a smoothed y(x)
    y_sm = (1/np.sqrt(len(kx))) * (y_ft_sm[:,None] \
        * np.exp(-1j*2*np.pi*kx[:,None]*x[None,:])).sum(axis=0)
    del y_ft, y_ft_sm
# Ensure the smoothed array is real-valued.
    y_sm = np.real(np.sqrt(y_sm*np.conj(y_sm)))
# Otherwise, just perform smoothing on the background subtracted raw data.
    elif mode == 'loaded':
        y_sm = np.empty(np.shape(y))
        for i in range(len(y)):
            if i < boxcar:
                y_sm[i] = np.mean(y[:i+boxcar+1])
            elif i > (len(y) - boxcar - 1):
                y_sm[i] = np.mean(y[i-boxcar:])
            else:
                y_sm[i] = np.mean(y[i-boxcar:i+boxcar+1])
# Since the Fourier smoothing algorithm will yield all values greater than or equal to
# zero, we will perform one more baseline subtraction, then return the result.
    return baseline_subtract(y = y_sm, perc = base_perc)

# operations.baseline_subtract(Y, PERC)
# Takes a numpy array Y and a scalar value PERC (corresponding to the desired cutoff
# percentage). Averages all points within PERC% of the maximum deviation from the

```

```

# initial point in Y, subtracts this value from the array, and returns the result.
def baseline_subtract(y, perc, **kwargs):
    baseline = np.mean(y[np.where(abs(y-y[0]) < (perc/100.)\
        *np.amax(abs(y - y[0])))[0]])
    return y - baseline

# operations.center_freq(GUESS, W, WL, SIG)
# Takes a scalar value (GUESS) and three arrays(W, WL, SIG). WL and SIG define the
# spectrum of the field in question. Starting from the GUESS of the central frequency,
# center_freq interpolates SIG onto a regular frequency grid, W (centered at 0), and
# calculates the true central frequency and returns the result.
def center_freq(guess, w, wl, sig):
    # Calculate an angular frequency grid centered at guess from the wavelength grid
    f = 2*np.pi*(3.e17/wl) - guess
    # Generate a model for interpolating the signal onto an arbitrary frequency grid.
    if f[1] > f[0]:
        model = interp1d(f, sig, bounds_error = False, fill_value = 0.)
    else:
        model = interp1d(f[::-1], sig[::-1], bounds_error = False, \
            fill_value = 0.)
    # Calculate the central frequency sum(I*w)/sum(I)
    w0 = (((model(w))*(w + guess)).sum())/((model(w)).sum())
    # Ensure the value is real-valued, and return it
    return float(np.real(np.sqrt(w0*np.conj(w0))))

# operations.grid_spectrum(W0, W, WL, SIG)
# Takes a scalar value (W0) and three arrays (W, WL, SIG). WL and SIG define the
# spectrum of a field that may not necessarily be gridded regularly. grid_spectrum
# takes the WL grid and converts it to a frequency grid centered at 0 (where the
# frequency is W0). A 1D interpolation is then performed to map the SIG array
# onto the provided frequency grid, W.
def grid_spectrum(w0, w, wl, sig):

```

```

# Calculate an angular frequency grid from the loaded wavelength grid
    f = (2*np.pi*(3.e17/wl)) - w0
# Generate a model for interpolating the signal onto an arbitrary frequency grid.
    if f[1] > f[0]:
        model = interp1d(f, sig, bounds_error = False, fill_value = 0.)
    else:
        model = interp1d(f[::-1], sig[::-1], bounds_error = False, \
            fill_value = 0.)
# Return the interpolation of the raw data onto the provided frequency grid.
    return model(w)

# operations.calculate_field(X_AX, SIG, NO, WAIST, ENERGY, T_OR_W, diagnostic, returnt)
# Takes two arrays (X_AX and SIG), three scalars (NO, WAIST, and ENERGY), a
# string (T_OR_W), and a boolean (diagnostic). SIG is the intensity-level spectrum on
# the X_AX grid, which should either be an angular frequency grid in 1/s or a time grid
# in femtoseconds. T_OR_W informs whether X_AX is a frequency grid (T_OR_W='frequency')
# or a time grid (T_OR_W = 'time'). NO, WAIST, and ENERGY are used to determine the
# proper scaling factor for converting SIG to an electric field gridded onto X_AX. If
# diagnostic is True, the function will also print out a line comparing the energy
# calculated with the resulting scaling factor to the provided energy. returnt allows the
# user to request calculate_field to return the internal t grid.
# The electric field is returned in units of V/micron*s (the per second is essentially
# per unit frequency/per unit time).
def calculate_field(x_ax,sig,n0,waist,energy,t_or_w,perc,diagnostic=False,returnt=False):
    if t_or_w == 'frequency':
# If x_ax is frequency, define a time grid and perform the 1DFT to get I(t)
        t = np.linspace(-np.pi/(abs(x_ax[1]-x_ax[0])), np.pi/(abs(x_ax[1]\
            -x_ax[0])), len(x_ax)+1)[: -1]
        intensity = (1/np.sqrt(len(x_ax))) * (sig[:,None] \
            * np.exp(1j*x_ax[:,None]*t[None,:])).sum(axis=0)
# Ensure I(t) is real-valued with a mean baseline of 0.

```

```

intensity = np.real(np.sqrt(intensity*np.conj(intensity)))
intensity = baseline_subtract(y = intensity, perc = perc)
t *= 1.e15      # convert the resulting time axis to fs

elif t_or_w == 'time':
# If x_ax is in time, only need to copy the x_ax and sig variables.
    t = x_ax
    intensity = sig.copy()
# Define temporary x,y grids
    xy_hw = 64.*waist*np.sqrt(np.pi/128.)
    x,y = np.linspace(-xy_hw, xy_hw, 128), np.linspace(-xy_hw, xy_hw, 128)
# Calculate the amplitude spectrum.
    amp = np.where(intensity < 0, -np.sqrt(-intensity), np.sqrt(intensity))
# Define the electric field at the waist E(t,x,y)
    E = amp[:,None,None] \
        * np.exp(-(((x[None,:,None])**2) + ((y[None,None,:])**2))/(waist**2))
# Calculate the integral of EE* over t,x,y, i.e. total energy for current amp
    integral = (1.33e-3) * n0 * (((np.real(E*np.conj(E)) * abs(t[1] - t[0]) \
        * 1.e-15 * abs(x[1] - x[0]) * 1.e-6 * abs(y[1] - y[0]) \
        * 1.e-6).sum(axis = 2)).sum(axis = 1)).sum(axis = 0))

    del E
# If diagnostic is true, the provided energy and integrated energy will be printed.
    if diagnostic:
        E = (amp*np.sqrt(integral))[:,None,None] \
            * np.exp(-(((x[None,:,None])**2) \
            + ((y[None,None,:])**2))/(waist**2))
        integral2 = (1.33e-3) * n0 * (((np.real(E*np.conj(E)) \
            * abs(t[1] - t[0]) * 1.e-15 * abs(x[1] - x[0]) \
            * 1.e-6 * abs(y[1] - y[0]) \
            * 1.e-6).sum(axis = 2)).sum(axis = 1)).sum(axis = 0))
        print 'Calculated energy: {0}; Reported energy: {1}'\
            .format(integral2, energy)
# Return the normalized amplitude-level signal and - if requested - the time grid

```



```

if returnt:
    return amp*np.sqrt(energy/integral)*1.e-6, t
else:
    return amp*np.sqrt(energy/integral)*1.e-6
# The factor of 1.e-6 returns the field in unis of V/micron instead of V/m.

# operations.field_slice is a function called by polarization_slice
# **kwargs is expected to provide values associated with specific keywords, so it is not
# advised to use this function directly without reviewing the behavior.
def field_slice(**kwargs):
# Generate rotation matrices to rotate by thetax around the y axis (A) and by -thetay
# around the x-axis (B) (the negative is required due to sign conventions).
    A = np.asarray([[np.cos(kwargs['theta'][0]), 0, np.sin(kwargs['theta'][0])],\
                    [0,1,0],\
                    [-np.sin(kwargs['theta'][0]), 0, np.cos(kwargs['theta'][0])]])
    B = np.asarray([[1,0,0],\
                    [0, np.cos(-kwargs['theta'][1]), -np.sin(-kwargs['theta'][1])],\
                    [0, np.sin(-kwargs['theta'][1]), np.cos(-kwargs['theta'][1])]])
# Calculate the field's local coordinates [x',y',z'] as A (dot) B (dot) [x,y,z]
    xp = np.empty(np.shape(kwargs['x']))
    yp = np.empty(np.shape(kwargs['x']))
    zp = np.empty(np.shape(kwargs['x']))
# For whatever reason, it proved necessary to calculate the product elementwise.
    for i,j in product(range(np.size(kwargs['x'],axis=0)),\
                       range(np.size(kwargs['x'],axis=1))):
        [xp[i,j], yp[i,j], zp[i,j]] = np.dot(A, np.dot(B, \
                np.asarray([kwargs['x'][i,j], kwargs['y'][i,j], \
                kwargs['z'][i,j]])))
# For linear effects, we need the pathlength from the start of the sample.
    [x0,y0,z0] = np.dot(A,np.dot(B,np.asarray([kwargs['x'],kwargs['y'],\
        -kwargs['L']/2])))

```

```

dzp = zp - z0
del x0, y0, z0
# Apply the offsets and shift to the sample coordinates.
xp += kwargs['focus_offset'][0]
yp += kwargs['focus_offset'][1]
zp += kwargs['focus_shift']
# Calculate derived properties: sample wavelength, Rayleigh length, w(z), 1/R(z)
wl = (2*np.pi*(3.e14)/kwargs['w0'])/kwargs['n0']
    # sample wavelength, in microns
z0 = (np.pi*(kwargs['waist']**2))/(wl)
    # Rayleigh length
wzp = kwargs['waist']*np.sqrt(1 + ((zp/z0)**2))
Rzpinv = np.where(zp != 0., pow((zp*(1 + ((z0/zp)**2))), -1), 0.)

# For 'long' pulses, we can calculate the field in time, since dispersion is minor.
# We also do not need to be concerned about the separability of A and psi, as
# neglecting dispersion and treating absorption only according to w0 removes the
# frequency dependence of psi.
    if kwargs['rel_length'] == 'long':
# The spatial effects of TEM00 mode propagation are calculated.
    E = kwargs['Et'][:,None,None] * (1/np.sqrt(1 + ((zp[None, :, :]/z0)**2))) \
        * np.exp(-(((xp[None, :, :])**2) + ((yp[None, :, :])**2))/\
            ((wzp[None, :, :])**2)) * np.exp(1j\
            *np.arctan(zp[None, :, :]/z0)) \
        * np.exp(-1j*(((xp[None, :, :])**2) + ((yp[None, :, :])**2))\
            *(np.pi/wl) * Rzpinv[None, :, :]) \
        * np.exp(-1j * ((kwargs['n0']*kwargs['w0'])/(3.e14)) \
            * zp[None, :, :])
# Absorptive effects are applied according to the absorption at w0.
    if kwargs['absorption']:
        E *= np.exp(-0.5*kwargs['a0']*dzp[None, :, :])

```

```

# For 'short' pulses, dispersive effects need to be applied in the frequency domain.
    elif kwargs['rel_length'] == 'short':
# 1DFT of E(t) to E(w)
        E = (1/np.sqrt(len(kwargs['t']))) * (kwargs['Et'][:,None] \
            * np.exp(-1j*kwargs['t'][:,None]*1.e-15\
            *kwargs['w'][None,:])).sum(axis=0)
# Calculation of the spatial effects of TEM00 mode propagation
        Ew = E[:,None,None] * (1/np.sqrt(1 + ((zp[None,,:,]/z0)**2))) \
            * np.exp(-(((xp[None,,:,]**2) + ((yp[None,,:,]**2))\
            /((wzp[None,,:,]**2)) * np.exp(1j\
            *np.arctan(zp[None,,:,]/z0)) \
            * np.exp(-1j*(((xp[None,,:,]**2) + ((yp[None,,:,]**2))\
            *(np.pi/wl) * Rzpinv[None,,:,:])))
# Apply the effects of longitudinal phase
        if kwargs['disp']:
            Ew *= np.exp(-1j * ((kwargs['nw'][:,None,None] * (kwargs['w0']\
                + kwargs['w'][:,None,None]))/(3.e14)) * zp[None,,:,:])
        else:
            Ew *= np.exp(-1j * ((kwargs['n0']*kwargs['w0'])/(3.e14)) \
                * zp[None,,:,:])

        del E
# Absorptive effects are applied, accounting for the wavelength-dependence.
        if kwargs['absorption']:
            Ew *= np.exp(-0.5 * kwargs['aw'][:,None,None] * dzp[None,,:,:])
# GVM effects are applied.
        if kwargs['gvm_in']:
            Ew *= np.exp(-1j * ((1/kwargs['ug']) - (1/kwargs['ugr']))) \
                * kwargs['w'][:,None,None] * dzp[None,,:,:])
# GVD effects are applied, accounting effects of both the sample and the window.
        if kwargs['gvd_in']:
            if kwargs['win_len'] > 0:

```

```

thetaw = []
for i in [0,1]:
    thetaw.append(np.arcsin((kwargs['n0'] * \
        np.sin(kwargs['theta'][i]))\
        /kwargs['nwin'])))
del i
d = [kwargs['win_len'] * np.tan(thetaw[0]), \
    kwargs['win_len'] * np.tan(thetaw[1]), \
    kwargs['win_len']]
d = np.sqrt(np.dot(np.asarray(d), np.asarray(d)))
else:
    d = 0.
Ew *= np.exp(-1j * 0.5 * kwargs['gvd'] \
    * ((kwargs['w'][:,None,None])**2) \
    * dzp[None,[:,None,None]]) * np.exp(-1j * 0.5 * kwargs['gvdw'] \
    * ((kwargs['w'][:,None,None])**2) * d)
# Perform the 1DFT to get E(t,x,y,z) from E(w,x,y,z).
E = np.empty(np.shape(Ew), dtype=complex)
for i in range(np.size(Ew, 2)):
    E[:, :, i] = (1/np.sqrt(len(kwargs['w']))) * (Ew[:, None, :, i] \
        * np.exp(1j * kwargs['w'][:, None, None] \
        * kwargs['t'][None, :, None] * 1.e-15)).sum(axis=0)
return E      # Return the 3D E(t,x,y,z)

```

```
def polarization_slice(z, **kwargs):
```

```

# Rotation matrices calculate x',y',z' (z' _|_ the sample) from x,y,z (z||k4); since
# w4's internal angles are measured relative to sample normal, need their negatives.
# A is the rotation matrix around the y-axis by an angle of -thetax, while B is the
# rotation matrix around the x-axis by an angle of -thetay (actually need --thetay).

```

```

A = np.asarray([[np.cos(-kwargs['theta']['w4'][0]), 0, \
                 np.sin(-kwargs['theta']['w4'][0])],\
               [0, 1, 0],\
               [-np.sin(-kwargs['theta']['w4'][0]), 0, \
                np.cos(-kwargs['theta']['w4'][0])]])
B = np.asarray([[1,0,0],\
               [0, np.cos(kwargs['theta']['w4'][1]), \
                 -np.sin(kwargs['theta']['w4'][1])],\
               [0, np.sin(kwargs['theta']['w4'][1]), \
                np.cos(kwargs['theta']['w4'][1])]])

# Apply the rotation matrices to calculate the sample coordinates x',y',z'. These are
# 2D arrays with dimensions inherited from the transverse slice's x and y coordinates.
[xp, yp, zp] = np.dot(A, \
                      np.dot(B, np.asarray([kwargs['x'][:,None],\
                                             kwargs['y'][None,:], z])))

# Calculate the TEM00 mode for each field. This employs a temporary function that
# reduces the function call to a single field identifier 'fld'.
lam = lambda fld: field_slice(x = xp, y = yp, z = zp, t = kwargs['t'], \
                              w = kwargs['w'], theta = kwargs['theta'][fld], \
                              focus_offset = kwargs['focus_offset'][fld], \
                              focus_shift = kwargs['focus_shift'][fld], L = kwargs['L'], \
                              w0 = kwargs['w0'][fld], waist = kwargs['waist'][fld], \
                              n0 = kwargs['n0'][fld], nw = kwargs['nw'][fld], \
                              rel_length = kwargs['rel_length'][fld], \
                              Et = kwargs['Et'][fld], a0 = kwargs['a0'][fld], \
                              aw = kwargs['aw'][fld], ug = kwargs['ug'][fld], \
                              ugr = kwargs['ug']['w3'], gvd = kwargs['gvd'][fld], \
                              win_len = kwargs['win_len'], nwin = kwargs['nwin'][fld], \
                              gvdw = kwargs['gvdw'][fld], absorption = kwargs['absorption'], \
                              gvm_in = kwargs['gvm_in'], gvd_in = kwargs['gvd_in'], \
                              disp = kwargs['disp'])

E1 = lam('w1')

```

```

E2 = lam('w2')
E3 = lam('w3')
del lam

# Multiply the time-domain electric fields according to the phase-matching scheme.
prod = 1.
for i,j in [('w1', E1), ('w2', E2), ('w3',E3)]:
    if kwargs['phase_matching'][i] > 0:
        prod *= (j**kwargs['phase_matching'][i])
    elif kwargs['phase_matching'][i] < 0:
        prod *= (np.conj(j)**abs(kwargs['phase_matching'][i]))
del i, j#, E1, E2, E3

# Perform the 1DFT to take the product from the time domain to the frequency domain.
P = np.empty(np.shape(prod), dtype=complex)
for i in range(np.size(prod, axis=2)):
    P[:, :, i] = (1/np.sqrt(len(kwargs['t']))) * (prod[:, None, :, i] \
        * np.exp(1j * kwargs['t'][:, None, None] * 1.e-15 \
        * kwargs['w'] [None, :, None])).sum(axis=0)

del prod, i

Pk = np.empty(np.shape(P), dtype=complex)

for i in range(len(kwargs['w'])):
# Multiply the field product by the nonlinear susceptibility and degeneracy.
    P[i, :, :] = kwargs['degeneracy'] * np.where(zp <= kwargs['L']/2., \
        np.where(zp >= -kwargs['L']/2., kwargs['chi'][i], \
        complex(0.)), complex(0.)) * P[i, :, :]

# Perform the 1DFT from x --> kx, generating the 2D array temp(y,kx)
    temp = (1/np.sqrt(len(kwargs['x']))) * (P[i, :, :, None] \
        * np.exp(-1j * 2 * np.pi * kwargs['x'][:, None, None] \
        * kwargs['kx'] [None, None, :])).sum(axis=0)

# Populate the ith 2D slice of Pk with the result of the 1DFT of the array temp,
# yielding the final slice in (kx,ky)

```

```

Pk[i,:,:] = (1/np.sqrt(len(kwarg['y']))) * (temp[:,:,:None] \
      * np.exp(-1j * 2 * np.pi * kwarg['y'][:,:,:None] \
      * kwarg['ky'][None,None,:])).sum(axis=0)

del temp

del i

# If the polarization slices are to be saved, this is accomplished here.
if kwarg['save']:
# Save the current directory so that the program can return to it.
curr_dir = os.getcwd()

# If the subdirectories don't exist, create them.
if not os.path.exists((kwarg['folder']+'/slices/'))\
      .split(os.path.commonprefix(\
      [os.getcwd(), kwarg['folder']]))+''')[-1]):
os.makedirs((kwarg['folder']+'/slices/'))\
      .split(os.path.commonprefix(\
      [os.getcwd(), kwarg['folder']]))+''')[-1])

# Change to the save directory
os.chdir(kwarg['folder']+'/slices')

# Create the file and write the array
f = open('slice_at_z_{0}_2.txt'.format(z), 'w')
f.write('Frequency (Hz) \t x-pos (microns) \
      \t y-pos (microns) \t Polarization \n')
f.writelines('{0}\t{1}\t{2}\t{3}\n'.format(kwarg['w'][i[0]]\
      +kwarg['w0']['w4'], kwarg['x'][i[1]],\
      kwarg['y'][i[2]], P[i[0], i[1], i[2]]) \
      for i in itertools.product(range(len(kwarg['w'])), \
      range(len(kwarg['x'])), range(len(kwarg['y']))))

# Close the file and return to the original directory.
f.close()

del f

os.chdir(curr_dir)

```

```

# To calculate the contribution of this polarization slice to the output field, it
# will be more convenient to have the wave vector magnitude available.
    k0 = ((kwargs['n0']['w4']*kwargs['w0']['w4'])/(3.e14))
# Now, multiply the polarization by the various relevant contributions:
# Multiply the polarization by the longitudinal phase term, exp(ikz)
    if kwargs['disp']:
        Pk *= np.exp(1j * ((kwargs['nw']['w4'][:,None,None] \
            * (kwargs['w0']['w4'] + kwargs['w'][:,None,None]))/(3.e14)) * z)
    else:
        Pk *= np.exp(1j * ((kwargs['n0']['w4']*kwargs['w0']['w4'])/(3.e14)) * z)

# Multiply the polarization by the frequency, speed of light, and wavenumber
    Pk *= -1j * ((kwargs['w0']['w4'] + kwargs['w'][:,None,None])**2) \
        * (1/(2 * ((3.e14)**2) * k0))

# Multiply the polarization by the exponential accounting for transverse evolution of
# the plane wave.
    Pk *= np.exp(1j * ((2 * (np.pi**2))/k0) * (((kwargs['kx'][None,:,None])**2) \
        + ((kwargs['ky'][None,None,:])**2)) * (kwargs['z_end'] - z))

# Now, we will multiply the polarization by the various terms describing the
# dispersive character of the medium, if enabled:
    if kwargs['gvm_out']:
        Pk *= np.exp(-1j * ((1/kwargs['ug']['w4']) - (1/kwargs['ug']['w3']))) \
            * kwargs['w'][:,None,None] * (kwargs['z_end'] - z)
    if kwargs['gvd_out']:
        Pk *= np.exp(-1j * 0.5 * kwargs['gvd']['w4'] \
            * ((kwargs['w'][:,None,None])**2) * (kwargs['z_end'] - z))
    if kwargs['absorption']:
        Pk *= np.exp(-0.5 * (kwargs['aw']['w4'][:,None,None]) \
            * (kwargs['z_end'] - z))

return Pk # Return the modified slice

```



```

def intensity(E, mono_conv, w, t, N, f, slits, n0, w0):
# Intensity of an electric field when the field is in mks units
    I = 1.33e-3 * n0 * E * np.conj(E)
    if mono_conv:
        rec_lin_disp = (1./N)*(1./f)*1.e-3
            # reciprocal linear dispersion, nm/microns
# Determine the wavelength grid corresponding to the frequency grid.
        dwl = ((2*np.pi*3.e17)/((w0)**2))*w
# Define the instrument function of the monochromator as a triangle function.
        mono = np.where(((1. - (1/(rec_lin_disp*slits))*abs(dwl)) > 0., (1. - \
            (1/(rec_lin_disp*slits))*abs(dwl)), 0.)
# Since convolving functions in a domain is equivalent to multiplication of their
# Fourier transforms, 1DFT both the intensity and instrument functions
        It = (1/np.sqrt(len(w))) * (I[:,None] * np.exp(1j * w[:,None] \
            * t[None,:] * 1.e-15)).sum(axis=0)
        monot = (1/np.sqrt(len(w))) * (mono[:,None] * np.exp(1j * w[:,None] \
            * t[None,:] * 1.e-15)).sum(axis=0)
# Convert the Fourier transforms to real-valued functions.
        It,monot = np.real(np.sqrt(It*np.conj(It))),\
            np.real(np.sqrt(monot*np.conj(monot)))
# Multiply the intensity by the instrument function.
        It *= np.sqrt(len(w))*monot
# FT the result back to the frequency domain.
        I = (1/np.sqrt(len(t))) * (It[:,None] * np.exp(-1j * t[:,None] \
            * w[None,:] * 1.e-15)).sum(axis=0)
        del It, monot, mono, dwl, rec_lin_disp
# Return the real-valued result.
        return np.real(np.sqrt(I*np.conj(I)))

def save_output(E, E_slice, I, folder, file, w, x, y):
# Save the 3D array E(w, x, y) and integrated 1D slice E(w) to a file.

```

```

curr_dir = os.getcwd()
# If the target save directory doesn't exist, create it and any higher directories
if not os.path.exists(folder.split(os.path.commonprefix( \
    [os.getcwd(), folder]))+'/'[-1]):
    os.makedirs(folder.split(os.path.commonprefix( \
    [os.getcwd(), folder]))+'/'[-1])
# Navigate to the target directory
os.chdir(folder)
now = datetime.datetime.now()
# Format file names
file1d, file3d = file + '_1d', file + '_3d'
for i in str(now).replace('-', ' ').replace(':', ' ').split('.')[0].split(' '):
    file1d, file3d = file1d + '_' + i, file3d + '_' + i
file1d, file3d = file1d+'.txt', file3d+'.txt'
# Write data to files
for i,j in [(file1d, '1d'), (file3d, '3d')]:
    f = open(i, 'w')
    if j == '3d':
        f.write('Frequency (Hz)\tx-pos (microns)\ty-pos (microns)\n'
            '\tField (V/m)\n')
        f.writelines('{0}\t{1}\t{2}\t{3}\n'.format(w[i[0]], x[i[1]],\
            y[i[2]], E[i[0], i[1], i[2]]*1.e6) for i in \
            itertools.product(range(len(w)), \
            range(len(x)), range(len(y))))
    if j == '1d':
        f.write('Frequency (Hz) \t Field (V/m) \t Power \n')
        f.writelines('{0}\t{1}\t{2}\n'.format(w[i], E_slice[i], I[i]) \
            for i in range(len(w)))
    f.close()
    del f
# Return to the original directory, and return to the function call
os.chdir(curr_dir)

```

```
return
```

### D.3 main.py

The final script - `main.py` - initializes an instance of the class from `parameters.py`, then calls the various functions from `operations.py` as necessary. For different applications, this script may need to be heavily modified according to the desired fields.

```
import numpy as np
from numpy import power as pow
import os, datetime, itertools
import matplotlib.pyplot as plt
from scipy.interpolate import interp1d
from functools import partial
from multiprocessing import Pool
import parameters, operations
reload(parameters), reload(operations)

def main(p = 'default', ret_I = False):
# Clear and close existing files; ensure interactive mode is on
    plt.clf(), plt.close(), plt.ion()
# Initialize an object of the parameters class.
    if p == 'default':
        p = parameters.parameters()

# Define a temporary function for loading files, which calls operations.load_field,
# but reduces the call to a single variable, a string that serves as field identifier.
    lam = lambda w: operations.load_field(folder = p.folder, \
        file = p.files[w][p.colors[w]], columns = p.columns[w])
    w1_col, w1_sig = lam('w1')
    w2_col, w2_sig = lam('w2')
```

```

w3_del, w3_sig = lam('w3')

del lam

# I know that my w3_sig data is a negative signal, so I multiply by a factor of -1.
w3_sig *= -1

# Initialize matplotlib figure and axes objects for diagnostic plots.
fig1, ax1, fig2, ax2 = operations.initialize_diagnostics(modes = p.smooth_mode,\
               diagnostic = p.diagnostic, smoothing = p.smoothing)

# Generate a temporary function for data processing, whether this is just baseline
# subtraction or baseline subtraction and smoothing. The function generalizes the
# calls of operations.smooth and operations.baseline_subtract, filling an unused kwarg
# with extraneous variables in operations.baseline_subtract.
if p.smoothing:
    lam = lambda x,y,w,ax: operations.smooth(x = x, y = y, \
            cutoff = p.cutoffs[w], boxcar = p.boxcar, \
            base_per = p.baseline_percentage, \
            diag = p.diagnostic, ax = ax, mode = p.smooth_mode[w])
elif not p.smoothing:
    lam = lambda x,y,w,ax: operations.baseline_subtract(y = y, \
            perc = p.baseline_percentage, x = x, w = w, ax = ax)

# Processed data is generated by calling the temporary function for each field.
w1_sig_sm = lam(w1_col, w1_sig, 'w1', ax1['w1'] [1])
w2_sig_sm = lam(w2_col, w2_sig, 'w2', ax1['w2'] [1])
w3_sig_sm = lam(w3_del, w3_sig, 'w3', ax1['w3'] [1])

# Plot the processed and unprocessed data if diagnostics are enabled.
if p.diagnostic:
    for i,j,k,l in [('w1',w1_col, w1_sig, w1_sig_sm), \
            ('w2',w2_col, w2_sig, w2_sig_sm),\
            ('w3', w3_del, w3_sig, w3_sig_sm)]:
        ax1[i] [0].plot(j, k, 'k-', j, l, 'r-')
    else: plt.close(fig1), plt.close(fig2)

# Overwrite the signal variables with the smoothed arrays.
w1_sig, w2_sig, w3_sig = w1_sig_sm.copy(), w2_sig_sm.copy(), w3_sig_sm.copy()

```

```

del w1_sig_sm, w2_sig_sm, w3_sig_sm, lam

if p.diagnostic: del i, j, k, l

# Create time and frequency grids that should yield even sampling of the polarization
# on each grid. These grids are saved in the existing parameters.parameters object.
p.time_freq_grids()

# Calculate the central frequencies for w1 and w2 fields based on the loaded tuning
# files and save the results in p.w0, then calculate the central frequency for w4.
for i, j, k in [('w1', w1_col, w1_sig), ('w2', w2_col, w2_sig)]:
    p.w0[i] = operations.center_freq(guess = (float(p.colors[i])*(3.e10)\
        *2*np.pi), w1 = j, sig = k, w = p.w)

del i, j, k
p.w0['w4'] = 0.
for i in ['w1', 'w2', 'w3']:
    p.w0['w4'] += p.phase_matching[i]*p.w0[i]
del i

# Create dictionaries that will contain the optical properties at each w0.
p.calculate_optical_properties()

# Calculate the internal angles for each field
p.calculate_internal_angles()

# Interpolate w1_sig and w2_sig onto the previously calculated w grid.
w1_sig = operations.grid_spectrum(w0 = p.w0['w1'], w = p.w, \
    w1 = w1_col, sig = w1_sig)
w2_sig = operations.grid_spectrum(w0 = p.w0['w2'], w = p.w, \
    w1 = w2_col, sig = w2_sig)

del w1_col, w2_col

# Convert the loaded spectra to electric field amplitudes, with units V/micron.
lam = lambda x, y, w, tw, returnt: operations.calculate_field(x_ax = x, sig = y, \
    n0 = p.n0[w], waist = p.waist[w], energy = p.energy[w][p.colors[w]], \
    t_or_w = tw, perc = p.baseline_percentage, \
    diagnostic = p.diagnostic, returnt = returnt)

```

```

E1t, t1 = lam(p.w, w1_sig, 'w1', 'frequency', True)
E2t, t2 = lam(p.w, w2_sig, 'w2', 'frequency', True)
E3t = lam(w3_del, w3_sig, 'w3', 'time', False)
del lam, w1_sig, w2_sig, w3_sig

# Grid the resulting electric fields, incorporating assumed initial delays and phase.
Et = {}
for i, j, k, l in [('w1', t1, E1t, p.delay['t31']), \
                  ('w2', t2, E2t, p.delay['t32']), \
                  ('w3', w3_del, E3t, 0.)]:
    if j[1] > j[0]:
        model = interp1d(j - 1, k*np.exp(1j*p.phase[i]*np.pi/180), \
                        bounds_error = False, fill_value = complex(0.))
    else:
        model = interp1d(j[::-1] - 1, k[::-1]\
                        *np.exp(1j*p.phase[i]*np.pi/180), \
                        bounds_error = False, fill_value = complex(0.))
    Et[i] = model(p.t)
    del model
    if p.diagnostic:
        ax2[i][0].plot(p.t, np.real(Et[i]), 'k-', p.t, \
                      np.real(Et[i]), 'ko')
        ax2[i][1].plot(p.t, np.imag(Et[i]), 'k--', p.t, \
                      np.imag(Et[i]), 'ko')
    del i, j, k, l, E1t, E2t, E3t, t1, t2, w3_del

# Determine the bounds and spacing of the z grid and the x, y, kx, and ky grids
p.spatial_grids()

polzn_call = partial(operations.polarization_slice, x = p.x, y = p.y, kx = p.kx, \
                    ky = p.ky, t = p.t, w = p.w, Et = Et, \
                    focus_offset = p.focus_offset, \
                    focus_shift = p.focus_shift, \
                    rel_length = p.rel_lengths, waist = p.waist, \

```

```

        phase_matching = p.phase_matching, theta = p.theta, \
        w0 = p.w0, n0 = p.n0, nw = p.nw, a0 = p.a0, aw = p.aw,
        ug = p.ug, gvd = p.gvd, nwin = p.nwin, gvdw = p.gvdw, \
        chi = p.chi, L = p.L, win_len = p.win_len, \
        deltak = p.deltak, degeneracy = p.degeneracy, \
        gvm_in = p.gvm_in, gvm_out = p.gvm_out, \
        gvd_in = p.gvd_in, gvd_out = p.gvd_out, \
        absorption = p.absorption, save = p.save, \
        folder = p.save_folder, z_end = p.z[-1], \
        disp = p.dispersive_k)

# Initialize an array to perform the summation.
    sum = np.zeros((len(p.w), len(p.kx), len(p.ky)), dtype=complex)

    if not p.multiprocessing:
# For each point in the z grid:
        for i in p.z:
# Add the result of calculating the polarization slice to the running sum,
# modified by the integration constant dz
            sum += polzn_call(z = i) * abs(p.z[1] - p.z[0])
    elif p.multiprocessing:
# initialize the multiprocessing pool
        pool = Pool(processes = p.processes)
# Perform the calculations asynchronously, adding each result to the running sum
# (modified by the integration factor dz) as that slice is available.
        for i in pool.imap_unordered(polzn_call, p.z, chunksize=p.chunksize):
            sum+=i * abs(p.z[1] - p.z[0])
        pool.close()
        pool.join()
        del i

# Perform the 2DFT necessary to convert the sum from the (kx,ky) domain to the (x,y)

```

```

# domain.
    E = np.empty(np.shape(sum), dtype=complex)
    for i in range(len(p.w)):
# Introduce a temporary array temp(ky,x) that is the result of performing the
# 1DFT of kx --> x on the resulting sum.
        temp = (1/np.sqrt(len(p.kx))) * (sum[i,:,:,:None] * np.exp(1j * 2 * np.pi \
            * p.kx[:,None,None] * p.x[None,None,:])).sum(axis=0)
# Perform the second 1DFT (ky --> y) on the temporary array temp and save the
# result to the initialized E array.
        E[i,:,:] = (1/np.sqrt(len(p.ky))) * (temp[:,:,:None] * np.exp(1j * 2 \
            * np.pi * p.ky[:,None,None] * p.y[None,None,:])).sum(axis=0)
        del temp
    del sum

# The field as a function of frequency is then the integral of E(w,x,y) over the x,y
# dimensions.
    E_slice = ((E * 1.e6 * abs(p.x[1] - p.x[0]) * abs(p.y[1] - p.y[0]) \
        * 1.e-6 * 1.e-6).sum(axis=2)).sum(axis=1)
# Calculate the intensity, convolving with the monochromator if relevant.
    I = operations.intensity(E = E_slice, mono_conv = p.mono_convolution, w = p.w, \
        t = p.t, N = p.N, f = p.f_len, slits = p.slits, \
        n0 = p.n0['w4'], w0 = p.w0['w4'])

    if p.save_final:
        operations.save_output(E = E, E_slice = E_slice, I = I, \
            folder = p.save_folder, file = p.save_file, \
            w = p.w+p.w0['w4'], x = p.x, y = p.y)

    if ret_I:
        return p.w+p.w0['w4'], I
    else:
        return p.w+p.w0['w4'], E_slice

```



## References

- (1) Dau, H.; Haumann, M. The manganese complex of photosystem II in its reaction cycle - Basic framework and possible realization at the atomic level. *Coordination Chemistry Reviews* **2008**, *252*, 273.
- (2) McEvoy, J. P.; Brudvig, G. W. Water-Splitting Chemistry of Photosystem II. *Chemical Reviews* **2006**, *106*, 4455.
- (3) Dau, H.; Liebisch, P.; Haumann, M. The structure of the manganese complex of Photosystem II in its dark-stable S<sub>1</sub>-state - EXAFS results in relation to recent crystallographic data. *Physical Chemistry Chemical Physics* **2004**, *6*, 4781.
- (4) Glöckner, C.; Kern, J.; Broser, M.; Zouni, A.; Yachandra, V.; Yano, J. Structural Changes of the Oxygen-evolving Complex in Photosystem II during the Catalytic Cycle. *The Journal of Biological Chemistry* **2013**, *288*, 22607.
- (5) Penner-Hahn, J. E.; Fronko, R. M.; Pecoraro, V. L.; Yocum, C. F.; Betts, S. D.; Bowlby, N. R. Structural Characterization of the Manganese Sites in the Photosynthetic Oxygen-Evolving Complex Using X-ray Absorption Spectroscopy. *Journal of the American Chemical Society* **1990**, *112*, 2549.
- (6) Pushkar, Y.; Yano, J.; Sauer, K.; Boussac, A.; Yachandra, V. K. Structural changes in the Mn<sub>4</sub>Ca cluster and the mechanism of photosynthetic water splitting. *Proceedings of the National Academy of Sciences of the United States of America* **2008**, *105*, 1879.
- (7) Weng, T.-C.; Hsieh, W.-Y.; Uffelman, E. S.; Gordon-Wylie, S. W.; Collins, T. J.; Pecoraro, V. L.; Penner-Hahn, J. E. XANES Evidence Against a Manganyl Species in the S<sub>3</sub> State of the Oxygen-Evolving Complex. *Journal of the American Chemical Society* **2004**, *126*, 8070.
- (8) Yano, J.; Kern, J.; Irrgang, K.-D.; Latimer, M. J.; Bergmann, U.; Glatzel, P.; Pushkar, Y.; Biesiadka, J.; Loll, B.; Sauer, K.; Messinger, J.; Zouni, A.; Yachandra, V. K. X-ray damage to the Mn<sub>4</sub>Ca complex in single crystals of photosystem II: A case study for metalloprotein crystallography. *Proceedings of the National Academy of Sciences of the United States of America* **2005**, *102*, 12047.
- (9) Yano, J.; Kern, J.; Sauer, K.; Latimer, M. J.; Pushkar, Y.; Biesiadka, J.; Loll, B.; Saenger, W.; Messinger, J.; Zouni, A.; Yachandra, V. K. Where Water Is Oxidized to Dioxygen: Structure of the Photosynthetic Mn<sub>4</sub>Ca Cluster. *Science* **2006**, *314*, 821.
- (10) Yano, J.; Yachandra, V. K. Where Water Is Oxidized to Dioxygen: Structure of the Photosynthetic Mn<sub>4</sub>Ca Cluster from X-ray Spectroscopy. *Inorganic Chemistry* **2008**, *47*, 1711.

- (11) Bergmann, U.; Grush, M. M.; Horne, C. R.; DeMarois, P.; Penner-Hahn, J. E.; Yocum, C. F.; Wright, D. W.; Dubé, C. E.; Armstrong, W. H.; Christou, G.; Eppley, H. J.; Cramer, S. P. Characterization of the Mn Oxidation States in Photosystem II by K $\beta$ X-ray Fluorescence Spectroscopy. *The Journal of Physical Chemistry B* **1998**, *102*, 8350.
- (12) Umena, Y.; Kawakami, K.; Shen, J.-R.; Kamiya, N. Crystal structure of oxygen-evolving photosystem II at a resolution of 1.9 Å. *Nature* **2011**, *473*, 55.
- (13) Glatzel, P.; Bergmann, U.; Yano, J.; Visser, H.; Robblee, J. H.; Gu, W.; de Groot, F. M.; Christou, G.; Pecoraro, V. L.; Cramer, S. P.; Yachandra, V. K. The Electronic Structure of Mn in Oxides, Coordination Complexes, and the Oxygen-Evolving Complex of Photosystem II Studied by Resonant Inelastic X-ray Scattering. *Journal of the American Chemical Society* **2004**, *126*, 9946.
- (14) Glatzel, P.; Schroeder, H.; Pushkar, Y.; Boron III, T.; Mukherjee, S.; Christou, G.; Pecoraro, V. L.; Messinger, J.; Yachandra, V. K.; Bergmann, U.; Yano, J. Electronic Structural Changes of Mn in the Oxygen-Evolving Complex of Photosystem II during the Catalytic Cycle. *Inorganic Chemistry* **2013**, *52*, 5642.
- (15) Boussac, A.; Girerd, J.-J.; Rutherford, A. W. Conversion of the Spin State of the Manganese Complex in Photosystem II Induced by Near-Infrared Light. *Biochemistry* **1996**, *35*, 6984.
- (16) Boussac, A. Inhomogeneity of the EPR multiline signal from the S<sub>2</sub>-state of the photosystem II oxygen-evolving enzyme. *Journal of Biological Inorganic Chemistry* **1997**, *2*, 580.
- (17) Boussac, A.; Un, S.; Horner, O.; Rutherford, A. W. High-Spin States ( $S \geq 5/2$ ) of the Photosystem II Manganese Complex. *Biochemistry* **1998**, *37*, 4001.
- (18) Boussac, A.; Kuhl, H.; Un, S.; Rögner, M.; Rutherford, A. W. Effect of Near-Infrared Light on the S<sub>2</sub>-State of the Manganese Complex of Photosystem II from *Synechococcus elongatus*. *Biochemistry* **1998**, *37*, 8995.
- (19) Boussac, A.; Kuhl, H.; Ghibaudi, E.; Rögner, M.; Rutherford, A. W. Detection of an Electron Paramagnetic Resonance Signal in the S<sub>0</sub> State of the Manganese Complex of Photosystem II from *Synechococcus elongatus*. *Biochemistry* **1999**, *38*, 11942.
- (20) Boussac, A.; Sugiura, M.; Kirilovsky, D.; Rutherford, A. W. Near-infrared-induced Transitions in the Manganese Cluster of Photosystem II: Action Spectra for the S<sub>2</sub> and S<sub>3</sub> Redox States. *Plant & Cell Physiology* **2005**, *46*, 837.

- (21) Boussac, A.; Sugiura, M.; Lai, T.-L.; Rutherford, A. W. Low-temperature photochemistry in photosystem II from *Thermosynechococcus elongatus* induced by visible and near-infrared light. *Philosophical Transactions of the Royal Society B* **2008**, *363*, 1203.
- (22) Charlot, M.-F.; Boussac, A.; Blondin, G. Towards a spin coupling model for the Mn<sub>4</sub> cluster in Photosystem II. *Biochimica et Biophysica Acta* **2005**, *1708*, 120.
- (23) Chrysina, M.; Zahariou, G.; Ioannidis, N.; Petrouleas, V. Conversion of the  $g = 4.1$  EPR signal to the multiline conformation during the S<sub>2</sub> to S<sub>3</sub> transition of the oxygen evolving complex of Photosystem II. *Biochimica et Biophysica Acta* **2010**, *1797*, 487.
- (24) Cox, N.; Rapatskiy, L.; Su, J.-H.; Pantazis, D. A.; Sugiura, M.; Kulik, L.; Dorlet, P.; Rutherford, W. A.; Neese, F.; Boussac, A.; Lubitz, W.; Messinger, J. Effect of Ca<sup>2+</sup>/Sr<sup>2+</sup> Substitution on the Electronic Structure of the Oxygen-Evolving Complex of Photosystem II: A Combined Multifrequency EPR, <sup>55</sup>Mn-ENDOR, and DFT Study of the S<sub>2</sub> State. *Journal of the American Chemical Society* **2011**, *133*, 3635.
- (25) Horner, O.; Rivière, E.; Blondin, G.; Un, S.; Rutherford, A. W.; Girerd, J.-J.; Boussac, A. SQUID Magnetization Study of the Infrared-Induced Spin Transition in the S<sub>2</sub> State of Photosystem II: Spin Value Associated with the  $g = 4.1$  EPR Signal. *Journal of the American Chemical Society* **1998**, *120*, 7924.
- (26) Hsieh, W.-Y.; Campbell, K. A.; Gregor, W.; Britt, R. D.; Yoder, D. W.; Penner-Hahn, J. E.; Pecoraro, V. L. The first spectroscopic model for the S<sub>1</sub> state multiline signal of the OEC. *Biochimica et Biophysica Acta* **2004**, *1655*, 149.
- (27) Ioannidis, N.; Petrouleas, V. Electron Paramagnetic Resonance Signals from the S<sub>3</sub> State of the Oxygen-Evolving Complex. A Broadened Radical Signal Induced by Low-Temperature Near-Infrared Light Illumination. *Biochemistry* **2000**, *39*, 5246.
- (28) Kulik, L. V.; Epel, B.; Lubitz, W.; Messinger, J. <sup>55</sup>Mn Pulse ENDOR at 34 GHz of the S<sub>0</sub> and S<sub>2</sub> States of the Oxygen-Evolving Complex in Photosystem II. *Journal of the American Chemical Society* **2005**, *127*, 2392.
- (29) Kulik, L. V.; Epel, B.; Lubitz, W.; Messinger, J. Electronic Structure of the Mn<sub>4</sub>O<sub>x</sub>Ca Cluster in the S<sub>0</sub> and S<sub>2</sub> States of the Oxygen-Evolving Complex of Photosystem II Based on Pulse <sup>55</sup>Mn-ENDOR and EPR Spectroscopy. *Journal of the American Chemical Society* **2007**, *129*, 13421.

- (30) Peloquin, J. M.; Campbell, K. A.; Randall, D. W.; Evanchik, M. A.; Pecoraro, V. L.; Armstrong, W. H.; Britt, R. D.  $^{55}\text{Mn}$  ENDOR of the  $\text{S}_2$ -State Multiline EPR Signal of Photosystem II: Implications on the Structure of the Tetranuclear Mn Cluster. *Journal of the American Chemical Society* **2000**, *122*, 10926.
- (31) Rapatskiy, L.; Cox, N.; Savitsky, A.; Ames, W. M.; Sander, J.; Nowaczyk, M. M.; Rögner, M.; Boussac, A.; Neese, F.; Messinger, J.; Lubitz, W. Detection of the Water-Binding Sites of the Oxygen-Evolving Complex of Photosystem II Using W-Band  $^{17}\text{O}$  Electron-Electron Double Resonance-Detected NMR Spectroscopy. *Journal of the American Chemical Society* **2012**, *134*, 16619.
- (32) Sanakis, Y.; Ioannidis, N.; Sioros, G.; Petrouleas, V. A Novel  $S = 7/2$  Configuration of the Mn Cluster of Photosystem II. *Journal of the American Chemical Society* **2001**, *123*, 10766.
- (33) Su, J.-H.; Cox, N.; Ames, W.; Pantazis, D. A.; Rapatskiy, L.; Lohmiller, T.; Kulik, L. V.; Dorlet, P.; Rutherford, W. A.; Neese, F.; Boussac, A.; Lubitz, W.; Messinger, J. The electronic structures of the  $\text{S}_2$  states of the oxygen-evolving complexes of photosystem II in plants and cyanobacteria in the presence and absence of methanol. *Biochimica et Biophysica Acta* **2011**, *1807*, 829.
- (34) Baxter, R.; Krausz, E.; Wydrzynski, T.; Pace, R. J. Identification of the Near-Infrared Absorption Band from the Mn Cluster of Photosystem II. *Journal of the American Chemical Society* **1999**, *121*, 9451.
- (35) Boussac, A.; Zimmermann, J.-L.; Rutherford, A. W.; Lavergne, J. Histidine oxidation in the oxygen-evolving photosystem-II enzyme. *Nature* **1990**, *347*, 303.
- (36) Dekker, J. P.; van Gorkom, H. J.; Brok, M.; Ouwehand, L. Optical Characterization of Photosystem II Electron Donors. *Biochimica et Biophysica Acta* **1984**, *764*, 301.
- (37) Dekker, J. P.; van Gorkom, H. J.; Wensink, J.; Ouwehand, L. Absorbance Difference Spectra of the Successive Redox States of the Oxygen-Evolving Apparatus of Photosynthesis. *Biochimica et Biophysica Acta* **1984**, *767*, 1.
- (38) Dekker, J. P.; Plijter, J. J.; Ouwehand, L.; van Gorkom, H. J. Kinetics of Manganese Redox Transitions in the Oxygen-Evolving Apparatus of Photosynthesis. *Biochimica et Biophysica Acta* **1984**, *767*, 176.
- (39) Dismukes, G. C.; Mathis, P. A near infrared electronic transition associated with conversion between S-states of the photosynthetic  $\text{O}_2$ -evolving complex. *FEBS Letters* **1984**, *178*, 51.

- (40) Hillmann, B.; Schlodder, E. Electron transfer reactions in Photosystem II core complexes from *Synechococcus* at low temperature - difference spectrum of  $P680^+Q_A^-/P680 Q_A$  at 77 K. *Biochimica et Biophysica Acta* **1995**, *1231*, 76.
- (41) Kretschmann, H.; Dekker, J. P.; Saygin, Ö.; Witt, H. T. An agreement on the quaternary oscillation of ultraviolet absorption changes accompanying the water splitting in isolated Photosystem II complex from the cyanobacterium *Synechococcus* sp. *Biochimica et Biophysica Acta* **1988**, *932*, 358.
- (42) Lavergne, J. Optical-difference spectra of the S-state transitions in the photosynthetic oxygen-evolving complex. *Biochimica et Biophysica Acta* **1987**, *894*, 91.
- (43) Lavergne, J. Difference Spectra of the Oxidized Intermediates in the Photosynthetic Oxygen-Evolving System: Evidence for a Small  $S_0 \rightarrow S_1$  Absorption Change. *Photochemistry and Photobiology* **1989**, *50*, 235.
- (44) Morton, J.; Akita, F.; Nakajima, Y.; Shen, J.-R.; Krausz, E. Optical Identification of the long-wavelength (700-1700 nm) electronic excitations of the native reaction centre,  $Mn_4CaO_5$  cluster and cytochromes of photosystem II in plants and cyanobacteria. *Biochimica et Biophysica Acta* **2015**, *1847*, 153.
- (45) Pace, R. J.; Stranger, R. What spectroscopy reveals concerning the Mn oxidation levels in the oxygen evolving complex of photosystem II: X-ray to near infra-red. *Dalton Transactions* **2012**, *41*, 11145.
- (46) Saygin, Ö.; Witt, H. T. Evidence for the electrochromic identification of the change of charges in the four oxidation steps of the photoinduced water cleavage in photosynthesis. *FEBS Letters* **1985**, *187*, 224.
- (47) Saygin, Ö.; Witt, H. T. Optical characterization of intermediates in the water-splitting enzyme system of photosynthesis - possible states and configurations of manganese and water. *Biochimica et Biophysica Acta* **1987**, *893*, 452.
- (48) Schatz, G. H.; van Gorkom, H. J. Absorbance difference spectra upon charge transfer to secondary donors and acceptors in Photosystem II. *Biochimica et Biophysica Acta* **1985**, *810*, 283.
- (49) Stewart, D. H.; Nixon, P. J.; Diner, B. A.; Brudvig, G. W. Assignment of the  $Q_Y$  Absorbance Bands of Photosystem II Chromophores by Low-Temperature Optical Spectroscopy of Wild-Type and Mutant Reaction Centers. *Biochemistry* **2000**, *39*, 14583.
- (50) Van Gorkom, H. J. Identification of the Reduced Primary Electron Acceptor of Photosystem II as a Bound Semiquinone Anion. *Biochimica et Biophysica Acta* **1974**, *347*, 439.

- (51) Van Leeuwen, P. J.; Vos, M. H.; van Gorkom, H. J. Photosynthetic oxygen evolution. **1990**, *1018*, 173.
- (52) Van Leeuwen, P. J.; van Gorkom, H. J.; Dekker, J. P. Analysis of UV absorption changes with periodicity four in oxygen-evolving photosystem II membranes. *Journal of Photochemistry and Photobiology B: Biology* **1992**, *15*, 33.
- (53) Van Leeuwen, P. J.; Heimann, C.; Gast, P.; Dekker, J. P.; van Gorkom, H. J. Flash-induced redox changes in oxygen-evolving spinach Photosystem II core particles. *Photosynthesis Research* **1993**, *38*, 169.
- (54) Van Leeuwen, P. J.; Heimann, C.; van Gorkom, H. J. Absorbance difference spectra of the S-state transitions in Photosystem II core particles. *Photosynthesis Research* **1993**, *38*, 323.
- (55) Velthuys, B. R. Spectroscopy characterization of the acceptor state  $Q_A^-$  and the donor state S2 of Photosystem II of spinach in the blue, red and near-infrared. *Biochimica et Biophysica Acta* **1988**, *933*, 249.
- (56) Witt, K. Further Evidence of X-320 as a Primary Acceptor of Photosystem II in Photosynthesis. *FEBS Letters* **1973**, *38*, 116.
- (57) Barry, B. A.; Cooper, I. B.; De Riso, A.; Brewer, S. H.; Vu, D. M.; Dyer, R. B. Time-resolved vibrational spectroscopy detects protein-based intermediates in the photosynthetic oxygen-evolving cycle. *Proceedings of the National Academy of Sciences of the United States of America* **2006**, *103*, 7288.
- (58) Chen, J.; Barry, B. A. Ultraviolet Resonance Raman Microprobe Spectroscopy of Photosystem II. *Photochemistry and Photobiology* **2008**, *84*, 815.
- (59) Chen, J.; Yao, M.; Pagba, C. V.; Zheng, Y.; Fei, L.; Fend, Z.; Barry, B. A. Directly probing redox-linked quinones in photosystem II membrane fragments via UV resonant Raman scattering. *Biochimica et Biophysica Acta* **2015**, *1847*, 558.
- (60) Chu, H.-A.; Hillier, W.; Law, N. A.; Babcock, G. T. Vibrational spectroscopy of the oxygen-evolving complex and of manganese model compounds. *Biochimica et Biophysica Acta* **2001**, *1503*, 69.
- (61) Cua, A.; Stewart, D. H.; Reifler, M. J.; Brudvig, G. W.; Bocian, D. F. Low-Frequency Resonance Raman Characterization of the Oxygen-Evolving Complex of Photosystem II. *Journal of the American Chemical Society* **2000**, *122*, 2069.
- (62) Noguchi, T. *Coordination Chemistry Reviews* **2008**, *252*, 336.

- (63) Ames, W.; Pantazis, D. A.; Krewald, V.; Cox, N.; Messinger, J.; Lubitz, W.; Neese, F. Theoretical Evaluation of Structural Models of the S<sub>2</sub> State in the Oxygen Evolving Complex of Photosystem II. *Journal of the American Chemical Society* **2011**, *133*, 19743.
- (64) Gatt, P.; Petrie, S.; Stranger, R.; Pace, R. J. Rationalizing the 1.9 Å Crystal Structure of Photosystem II - A Remarkable Jahn-Teller Balancing Act Induced by a Single Proton Transfer. *Angewandte Chemie International Edition* **2012**, *51*, 12025.
- (65) Kurashige, Y.; Chang, G. K.-L.; Yanai, T. Entangled quantum electronic wavefunctions of the Mn<sub>4</sub>CaO<sub>5</sub> cluster in photosystem II. *Nature Chemistry* **2013**, *5*, 660.
- (66) Lubner, S.; Rivalta, I.; Umena, Y.; Kawakami, K.; Shen, J.-R.; Kamiya, N.; Brudvig, G. W.; Batista, V. S. S<sub>1</sub>-State Model of the O<sub>2</sub>-Evolving Complex of Photosystem II. *Biochemistry* **2011**, *50*, 6308.
- (67) Petrie, S.; Stranger, R.; Pace, R. J. Structural, Magnetic Coupling and Oxidation State Trends in Models of the CaMn<sub>4</sub> Cluster in Photosystem II. *Chemistry: A European Journal* **2008**, *14*, 5482.
- (68) Siegbahn, P. E. M. Structures and Energetics for O<sub>2</sub> Formation in Photosystem II. *Accounts of Chemical Research* **2009**, *42*, 1871.
- (69) Siegbahn, P. E. M. An Energetic Comparison of Different Models for the Oxygen Evolving Complex of Photosystem II. *Journal of the American Chemical Society* **2009**, *131*, 18238.
- (70) Siegbahn, P. E. M. The Effect of Backbone Constraints: The Case of Water Oxidation by the Oxygen-Evolving Complex in PSII. *ChemPhysChem* **2011**, *12*, 3274.
- (71) Sproviero, E. M.; Gascon, J. A.; McEvoy, J. P.; Brudvig, G. W.; Batista, V. S. Characterization of synthetic oxomanganese complexes and the inorganic core of the O<sub>2</sub>-evolving complex in photosystem II: Evaluation of the DFT/B3LYP level of theory. *Journal of Inorganic Biochemistry* **2006**, *100*, 786.
- (72) Sproviero, E. M.; Gascón, J. A.; McEvoy, J. P.; Brudvig, G. W.; Batista, V. S. QM/MM Models of the O<sub>2</sub>-Evolving Complex of Photosystem II. *Journal of Chemical Theory and Computation* **2006**, *2*, 1119.
- (73) Sproviero, E. M.; Gascón, J. A.; McEvoy, J. P.; Brudvig, G. W.; Batista, V. S. Quantum Mechanics/Molecular Mechanics Study of the Catalytic Cycle of Water Splitting in Photosystem II. *Journal of the American Chemical Society* **2008**, *130*, 3428.
- (74) Sproviero, E. M.; Gascón, J. A.; McEvoy, J. P.; Brudvig, G. W.; Batista, V. S. Computational studies of the O<sub>2</sub>-evolving complex of photosystem II and biomimetic oxomanganese complexes. *Coordination Chemistry Reviews* **2008**, *252*, 395.



- (75) Yamanaka, S.; T., S.; Kanda, K.; Isobe, H.; Umena, Y.; Kawakami, K.; Shen, J.-R.; Kamiya, N.; Okumura, M.; Nakamura, H.; Yamaguchi, K. Structure and Reactivity of the Mixed-Valence  $\text{CaMn}_4\text{O}_5(\text{H}_2\text{O})_4$  and  $\text{CaMn}_4\text{O}_4(\text{OH})(\text{H}_2\text{O})_4$  Clusters at Oxygen Evolution Catalyst of Photosystem II. Hybrid DFT (UB3LYP and UBHandHLYP) Calculations. *International Journal of Quantum Chemistry* **2012**, *112*, 321.
- (76) Boussac, A.; Sugiura, M.; Rutherford, A. W.; Dorlet, P. Complete EPR Spectrum of the  $\text{S}_3$ -State of the Oxygen-Evolving Photosystem II. *Journal of the American Chemical Society* **2009**, *131*, 5050.
- (77) Bensasson, R.; Land, E. J. Optical and Kinetic Properties of Semireduced Plastoquinone and Ubiquinone: Electron Acceptors in Photosynthesis. *Biochimica et Biophysica Acta* **1973**, *325*, 175.
- (78) Candeias, L. P.; Turconi, S.; Nugent, J. H. A. Tyrosine  $\text{Y}_Z$  and  $\text{Y}_D$  of photosystem II Comparison of optical spectra to those of tyrosine oxidised by pulsed radiolysis. *Biochimica et Biophysica Acta* **1998**, *1363*, 1.
- (79) Cua, A.; Stewart, D. H.; Brudvig, G. W.; Bocian, D. F. Selective Resonance Raman Scattering from Chlorophyll Z in Photosystem II via Excitation into Near-Infrared Absorption Band of the Cation. *Journal of the American Chemical Society* **1998**, *120*, 4532.
- (80) Dashdorj, N.; Xu, W.; Martinsson, P.; Chitnis, P. R.; Savikhin, S. Electrochromic Shift of Chlorophyll Absorption in Photosystem I from *Synechocystis* sp. PCC 6803: A Probe of Optical and Dielectric Properties around the Secondary Electron Acceptor. *Biophysical Journal* **2004**, *86*, 3121.
- (81) Dau, H.; Sauer, K. Electric field effect on chlorophyll fluorescence and its relation to Photosystem II charge separation reactions studied by a salt-jump technique. *Biochimica et Biophysica Acta* **1991**, *1098*, 49.
- (82) Guo, Z.; Lin, S.; Woodbury, N. W. Utilizing the Dynamic Stark Shift as a Probe for Dielectric Relaxation in Photosynthetic Reaction Centers During Charge Separation. *The Journal of Physical Chemistry B* **2013**, *117*, 11383.
- (83) Melis, A.; Brown, J. S. Stoichiometry of system I and system II reaction centers and of plastoquinone in different photosynthetic membranes. *Proceedings of the National Academy of Sciences of the United States of America* **1980**, *77*, 4712.
- (84) Razeghifard, M. R.; Kim, S.; Patzlaff, J. S.; Hutchison, R. S.; Krick, T.; Ayala, I.; Steenhuis, J. J.; Boesch, S. E.; Wheeler, R. A.; Barry, B. A. *The Journal of Physical Chemistry B*. **1999**, *103*, 9790.

- (85) Albela, B.; Chottard, G.; Girerd, J.-J. Biomimetic approach to the oxygen evolving center: resonance Raman investigation of a manganese  $\mu$ -oxo dimer in three oxidation states. *Journal of Biological Inorganic Chemistry* **2001**, *6*, 430.
- (86) Blondin, G.; Davydov, R.; Philouze, C.; Charlot, M.-F.; Styring, S.; Åkermark, B.; Girerd, J.-J.; Boussac, A. Electron paramagnetic resonance study of the  $S = \frac{1}{2}$  ground state of a radiolysis-generated manganese(III)-trimanganese(IV) form of  $[\text{Mn}^{\text{IV}}_4\text{O}_6(\text{bipy})_6]^{4+}$  (bipy = 2,2'-bipyridine). Comparison with the photosynthetic Oxygen Evolving Complex. *Journal of the Chemical Society, Dalton Transactions* **1997**, *6*, 4069.
- (87) Collomb, M.-N.; Deronzier, A.; Richardot, A.; Peécaut, J. Synthesis and characterization of a new kind of  $\text{Mn}_2^{\text{III,IV}}$   $\mu$ -oxo complex:  $[\text{Mn}_2\text{O}_2(\text{terpy})_2(\text{H}_2\text{O})_2](\text{NO}_3)_3 \cdot 6 \text{H}_2\text{O}$ , terpy = 2,2':6'2"-terpyridine. *New Journal of Chemistry* **1999**, *23*, 351.
- (88) Vincent, J. B.; Christou, G. Model complexes suggest certain S-state changes of the photosynthetic water-oxidation enzyme may involve an Mn(II)-Mn(III) transition. *FEBS Letters* **1986**, *207*, 250.
- (89) Chen, H.; Tagore, R.; Olack, G.; Vrettos, J. S.; Weng, T.-C.; Penner-Hahn, J.; Crabtree, R. H.; Brudvig, G. W. Speciation of the Catalytic Oxygen Evolution System:  $[\text{Mn}^{\text{III/IV}}_2(\mu\text{-O})_2(\text{terpy})_2(\text{H}_2\text{O})_2](\text{NO}_3)_3 + \text{HSO}_5^-$ . *Inorganic Chemistry* **2007**, *46*, 34.
- (90) Limburg, J.; Brudvig, G. W.; Crabtree, R. H.  $\text{O}_2$  Evolution and Permanganate Formation from High-Valent Manganese Complex. *Journal of the American Chemical Society* **1997**, *119*, 2761.
- (91) Limburg, J.; Vrettos, J. S.; Liable-Sands, L. M.; Rheingold, A. L.; Crabtree, R. H.; Brudvig, G. W. A Functional Model for O-O Bond Formation by the  $\text{O}_2$ -Evolving Complex in Photosystem II. *Science* **1999**, *283*, 1524.
- (92) Limburg, J.; Vrettos, J. S.; Chen, H.; de Paula, J. C.; Crabtree, R. H.; Brudvig, G. W. Characterization of the  $\text{O}_2$ -Evolving Reaction Catalyzed by  $[(\text{terpy})(\text{H}_2\text{O})\text{Mn}^{\text{III}}(\text{O})_2\text{Mn}^{\text{IV}}(\text{OH}_2)(\text{terpy})](\text{NO}_3)_3$  (terpy = 2,2':6,2"-Terpyridine). *Journal of the American Chemical Society* **2001**, *123*, 423.
- (93) Lundberg, M.; Blomberg, M. R. A.; Siegbahn, P. E. M. Oxyl Radical Required for O-O Bond Formation in Synthetic Mn-Catalyst. *Inorganic Chemistry* **2004**, *43*, 264.
- (94) Tagore, R.; Crabtree, R. H.; Brudvig, G. W. Oxygen Evolution Catalysis by a Dimanganese Complex and Its Relation to Photosynthetic Water Oxidation. *Inorganic Chemistry* **2008**, *47*, 1815.

- (95) Yagi, M.; Narita, K. Catalytic O<sub>2</sub> Evolution from Water Induced by Adsorption of [(OH<sub>2</sub>) (Terpy) Mn (μ-O)<sub>2</sub> Mn (Terpy) (OH<sub>2</sub>)]<sup>3+</sup> Complex onto Clay Compounds. *Journal of the American Chemical Society* **2004**, *126*, 8084.
- (96) Yamazaki, H.; Igarashi, S.; Nagata, T.; Yagi, M. Substituent Effects on Core Structures and Heterogeneous Catalytic Activities of Mn<sup>III</sup>(μ-O)<sub>2</sub>Mn<sup>IV</sup> Dimers with 2,2':6',2''-Terpyridine Derivative Ligands for Water Oxidation. *Inorganic Chemistry* **2012**, *51*, 1530.
- (97) Young, K. J.; Brennan, B. J.; Tagore, R.; Brudvig, G. W. Photosynthetic Water Oxidation: Insights from Manganese Model Chemistry. *Accounts of Chemical Research* **2015**, *48*, 567.
- (98) Pakoulev, A. V.; Rickard, M. A.; Kornau, K. M.; Mathew, N. A.; Yurs, L. A.; Block, S. B.; Wright, J. C. Mixed Frequency-/Time-Domain Coherent Multidimensional Spectroscopy: Research Tool or Potential Analytical Method? *Accounts of Chemical Research* **2009**, *42*, 1310.
- (99) Wright, J. Lecture Notes: Experimental Spectroscopy, Chemistry 623.; 2012.
- (100) Wright, J. C. Multiresonant Coherent Multidimensional Spectroscopy. *Annual Review of Physical Chemistry* **2011**, *62*, 209.
- (101) Griffiths, D. J., *Introduction to Electrodynamics*, Third; Prentice-Hall: Upper Saddle River, NJ, 1999.
- (102) Boyd, R. W., *Nonlinear Optics*, Second; Academic Press: San Diego, 2003.
- (103) Akhmanov, S. A.; Vysloukh, V. A.; Chirkin, A. S., *Optics of Femtosecond Laser Pulses*; American Institute of Physics: New York, 1992.
- (104) Svelto, O., *Principles of Lasers*, Second; Plenum Press: New York, 1982.
- (105) Verdeyen, J. T., *Laser Electronics*; Prentice-Hall: Englewood Cliffs, NJ, 1981.
- (106) Dmitriev, V. G.; Gurzadyan, G. G.; Nikogosyan, D. N., *Handbook of Nonlinear Optical Crystals*, Second; Springer Series in Optical Sciences; Springer: Berlin, 1997.
- (107) Kittel, C., *Introduction to Solid State Physics*, Eighth; John Wiley & Sons: Hoboken, NJ, 2005.
- (108) Lax, M.; Louisell, W. H.; McKnight, W. B. From Maxwell to paraxial wave optics. *Physical Review A* **1975**, *11*, 1365.
- (109) Shen, Y. R., *The Principles of Nonlinear Optics*; John Wiley & Sons: New York, 1984.
- (110) Levenson, M. D.; Bloembergen, N. Dispersion of the nonlinear optical susceptibilities of organic liquids and solutions. *The Journal of Chemical Physics* **1974**, *60*, 1323.

- (111) Iga, K., *Fundamentals of Laser Optics*; Lasers, Photonics, and Electro-Optics; Plenum Press: New York, 1994.
- (112) Poularikas, A. D., *The Handbook of Formulas and Tables for Signal Processing*; The Electrical Engineering Handbook Series; CRC Press: Boca Raton, FL, 1999.
- (113) Press, W. H.; Teukolsky, S. A.; Vetterling, W. T.; Flannery, B. P., *Numerical Recipes in C: The Art of Scientific Computing*, Third; Cambridge University Press: New York, 2007.
- (114) Bracewell, R. N., *The Fourier Transform and Its Applications*, Third; McGraw Hill: Boston, 2000.
- (115) Brabec, T.; Krausz, F. Nonlinear Optical Pulses in the Single-Cycle Regime. *Physical Review Letters* **1997**, *78*, 3282.
- (116) Stewart, J., *Calculus: Early Transcendentals*, Fifth; Thomson Brooks/Cole: Mason, OH, 2007.
- (117) Arfken, G. B.; Weber, H. J., *Mathematical Methods for Physicists*, Sixth; Elsevier: Burlington, MA, 2005.
- (118) Wang, J.-C.; Wang, J.-K. Experimental and theoretical analysis of white-light seeded, collinear phase-matching, femtosecond optical parametric amplifiers. *Journal of the Optical Society of America B* **2004**, *21*, 45.
- (119) Midwinter, J. E.; Warner, J. The effects of phase matching method and of uniaxial crystal symmetry on the polar distribution of second-order non-linear optical polarization. *British Journal of Applied Physics* **1965**, *16*, 1135.
- (120) Compton, R.; Filin, A.; Romanov, D. A.; Levis, R. J. Elucidating the spectral and temporal contributions from the resonant and nonresonant response to femtosecond coherent anti-Stokes Raman scattering. *The Journal of Chemical Physics* **2008**, *128*, 154517.
- (121) Pestov, D.; Murawski, R. K.; Ariunbold, G. O.; Wang, X.; Zhi, M.; Sokolov, A. V.; Sautenkov, V. A.; Rostovtsev, Y. V.; Dagariu, A.; Huang, Y.; Scully, M. O. Optimizing the Laser-Pulse Configuration for Coherent Raman Spectroscopy. *Science* **2007**, *316*, 265.
- (122) Von Vacano, B.; Backup, T.; Motzkus, M. Highly sensitive single-beam heterodyne coherent anti-Stokes Raman scattering. *Optics Letters* **2006**, *31*, 2495.
- (123) Wang, X.; Zhang, A.; Zhi, M.; Sokolov, A. V.; Welch, G. R.; Scully, M. O. Heterodyne coherent anti-Stokes Raman scattering for spectral phase retrieval and signal amplification. *Optics Letters* **2010**, *35*, 721.

- (124) Zeytunyan, A.; Crampton, K. T.; Zadoyan, R.; Apkarian, V. A. Supercontinuum-based three-color three-pulse time-resolved coherent anti-Stokes Raman scattering. *Optics Express* **2015**, *23*, 24019.
- (125) Barnes, N. P.; Corcoran, V. J. Parametric generation processes: spectral bandwidth and acceptance angles. *Applied Optics* **1976**, *15*, 696.
- (126) Cerullo, G.; De Silvestri, S. Ultrafast optical parametric amplifiers. *Review of Scientific Instruments* **2003**, *74*, 1.
- (127) Gloster, L. A. W.; Jiang, Z. X.; King, T. A. Characterization of an Nd:YAG-Pumped  $\beta$ -BaB<sub>2</sub>O<sub>4</sub> Optical Parametric Oscillator in Collinear and Noncollinear Phase-Matched Configurations. *IEEE Journal of Quantum Electronics* **1994**, *30*, 2961.
- (128) Milton, M. J. T.; McIlveen, T. J.; Hanna, D. C.; Woods, P. T. High-efficiency infrared generation by difference-frequency mixing using tangential phase matching. *Optics Communications* **1992**, *87*, 273.
- (129) Nautiyal, A.; Bisht, P. B.; Bindra, K. S.; Oak, S. M. Effects of thickness of  $\beta$ -barium borate and angle of non-collinearity of the fs pulse generation by optical parametric amplification. *Optics & Laser Technology* **2009**, *41*, 539.
- (130) Maker, P. D.; Terhune, R. W.; Nisenoff, M.; Savage, C. M. Effects of Dispersion and Focusing on the Production of Optical Harmonics. *Physical Review Letters* **1962**, *8*, 21.
- (131) Joosen, W.; Bakker, H. J.; Noordam, L. D.; Muller, H. G.; van Linden van den Heuvell, H. B. Parametric generation in  $\beta$ -barium borate of intense femtosecond pulses near 800 nm. *Journal of the Optical Society of America B* **1991**, *8*, 2537.
- (132) Song, L.; Leng, Y.; Zhang, C.; Wang, J.; Li, C.; Li, R. Carrier-envelope phase offset for pulses from a tunable optical parametric amplifier. *Optics Communications* **2011**, *284*, 3047.
- (133) Seilmeier, A.; Spanner, K.; Laubereau, A.; Kaiser, W. Narrow-band tunable infrared pulses with sub-picosecond time resolution. *Optics Communications* **1978**, *24*, 237.
- (134) Guo, X.; Wang, C.; Leng, Y.; Li, R. Bandwidth analysis of type-I optical parametric chirped pulse amplification systems. *Journal of the Optical Society of America B* **2014**, *31*, 2615.
- (135) Laufer, G.; Miles, R. B. Angularly Resolved Coherent Raman Spectroscopy. *Optics Communications* **1979**, *28*, 250.
- (136) McCamant, D. W.; Kukura, P.; Mathies, R. A. Femtosecond Broadband Stimulated Raman: A New Approach for High-Performance Vibrational Spectroscopy. *Applied Spectroscopy* **2003**, *57*, 1317.

- (137) McCamant, D. W.; Kukura, P.; Mathies, R. A. Femtosecond Time-Resolved Stimulated Raman Spectroscopy: Application to the Ultrafast Internal Conversion in  $\beta$ -Carotene. *The Journal of Physical Chemistry A* **2003**, *107*, 8208.
- (138) Tzankov, P.; Buchvarov, I.; Fiebig, T. Broadband optical parametric amplification in the near UV-VIS. *Optics Communications* **2002**, *203*, 107.
- (139) Cheng, J.-X.; Volkmer, A.; Sunney Xie, X. Theoretical and experimental characterization of coherent anti-Stokes Raman scattering microscopy. *Journal of the Optical Society of America B* **2002**, *19*, 1363.
- (140) Cheng, J.-X.; Volkmer, A.; Book, L. D.; Sunney Xie, X. An Epi-Detected Coherent Anti-Stokes Raman Scattering (E-CARS) Microscopy with High Spectral Resolution and High Sensitivity. *The Journal of Physical Chemistry B* **2001**, *105*, 1277.
- (141) Garbacik, E. T.; Korterik, J. P.; Otto, C.; Herek, J. L.; Offerhaus, H. L. Epi-detection of vibrational phase contrast coherent anti-Stokes Raman scattering. *Optics Letters* **2014**, *39*, 5814.
- (142) Wang, P.; Slipchenko, M. N.; Zhou, B.; Pinal, R.; Cheng, J.-X. Mechanisms of Epi-Detected Stimulated Raman Scattering Microscope. *IEEE Journal of Selected Topics in Quantum Electronics* **2012**, *18*, 384.
- (143) Oron, D.; Dudovich, N.; Yelin, D.; Silberberg, Y. Narrow-Band Coherent Anti-Stokes Raman Signals from Broad-Band Pulses. *Physical Review Letters* **2002**, *88*, 063004.
- (144) Shim, S.-H.; Strasfeld, D. B.; Ling, Y. L.; Zanni, M. T. Automated 2D IR spectroscopy using a mid-IR pulse shaper and application of this technology to the human islet amyloid polypeptide. *Proceedings of the National Academy of Sciences of the United States of America* **2007**, *104*, 14197.
- (145) Tian, P.; Keusters, D.; Suzuki, Y.; Warren, W. S. Femtosecond Phase-Coherent Two-Dimensional Spectroscopy. *Science* **2003**, *300*, 1553.
- (146) Cheng, J.-X.; Volkmer, A.; Book, L. D.; Sunney Xie, X. Multiplex Coherent Anti-Stokes Raman Scattering Microspectroscopy and Study of Lipid Vesicles. *The Journal of Physical Chemistry B* **2002**, *107*, 8493.
- (147) Romanov, D.; Filin, A.; Compton, R.; Levis, R. Phase matching in femtosecond BOXCARs. *Optics Letters* **2007**, *32*, 3161.
- (148) Zumbusch, A.; Holtom, G. R.; Sunney Xie, X. Three-Dimensional Vibrational Imaging by Coherent Anti-Stokes Raman Scattering. *Physical Review Letters* **1999**, *82*, 4142.

- (149) Gaydardzhiev, A.; Nikolov, I.; Buchvarov, I.; Petrov, V.; Noack, F. Ultrabroadband operation of a femtosecond optical parametric generator based on BiB<sub>36</sub> in the near-IR. *Optics Express* **2008**, *16*, 2363.
- (150) Ghotbi, M.; Beutler, M.; Petrov, V.; Gaydardzhiev, A.; Noack, F. High-energy, sub-30 fs near-IR pulses from a broadband optical parametric amplifier based on collinear interaction in BiB<sub>36</sub>O<sub>6</sub>. *Optics Letters* **2009**, *34*, 689.
- (151) Nikolov, I.; Gaydardzhiev, A.; Buchvarov, I.; Tzankov, P.; Noack, F.; Petrov, V. Ultrabroadband continuum amplification in the near infrared using BiB<sub>36</sub> nonlinear crystals pumped at 800 nm. *Optics Letters* **2007**, *32*, 3342.
- (152) Cerullo, G.; Nisoli, M.; De Silvestri, S. Generation of 11 fs pulses tunable across the visible by optical parametric amplification. *Applied Physics Letters* **1997**, *71*, 3616.
- (153) Hao, Q.; Huang, Y.-C. Two-octave polarized supercontinuum generated from a Q-switched laser pumped doubly resonant parametric oscillator. *Optics Letters* **2013**, *38*, 1863.
- (154) Kobayashi, T.; Baltuska, A. Sub-5 fs pulse generation from a noncollinear optical parametric amplifier. *Measurement Science & Technology* **2002**, *13*, 1671.
- (155) Virgillito, D., Personal Communication.
- (156) Wang, H.; Weiner, A. M. A Femtosecond Waveform Transfer Technique Using Type II Second Harmonic Generation. *IEEE Journal of Quantum Electronics* **2004**, *40*, 937.
- (157) Yu, L. et al. Optimization for high-energy and high-efficiency broadband optical parametric chirped-pulse amplification in LBO near 800 nm. *Optics Letters* **2015**, *40*, 3412.
- (158) Baer, T. Large-amplitude fluctuations due to longitudinal mode coupling in diode-pumped intracavity doubled Nd:YAG lasers. *Journal of the Optical Society of America B* **1986**, *3*, 1175.
- (159) Kafka, J. D.; Baer, T. Prism-pair dispersive delay lines in optical pulse compression. *Optics Letters* **1987**, *12*, 401.
- (160) Akhmanov, S. A.; Chirkin, A. S.; Drabovich, K. N.; Kovrigin, A. I.; Khokhlov, R. V.; Sukhorukov, A. P. Nonstationary Nonlinear Optical Effects and Ultrashort Light Pulse Formation. *IEEE Journal of Quantum Electronics* **1968**, *4*, 598.
- (161) Comly, J.; Garmire, E. Second Harmonic Generation from Short Pulses. *Applied Physics Letters* **1968**, *12*, 7.

- (162) Glenn, W. H. Second-Harmonic Generation by Picosecond Optical Pulses. *IEEE Journal of Quantum Electronics* **1969**, *5*, 284.
- (163) Stabinis, A.; Valiulis, G.; Ibragimov, E. A. Effective sum frequency pulse compression in nonlinear crystals. *Optics Communications* **1991**, *86*, 301.
- (164) Falk, J.; Murray, J. E. Single-Cavity Noncollinear Optical Parametric Oscillation. *Applied Physics Letters* **1969**, *14*, 245.
- (165) Selm, R.; Winterhalder, M.; Zumbusch, A.; Krauss, G.; Hanke, T.; Sell, A.; Leitenstorfer, A. Ultra-broadband background-free coherent anti-Stokes Raman scattering microscopy based on a compact Er: fiber laser system. *Optics Letters* **2010**, *35*, 3282.
- (166) Fecko, C. J.; Loparo, J. J.; Tokmakoff, A. Generation of 45 femtosecond pulses at 3  $\mu\text{m}$  with a  $\text{KNbO}_3$  optical parametric amplifier. *Optics Communications* **2004**, *241*, 521.
- (167) Bhar, G. C.; Datta, P. K.; Rudra, A. M.; Chatterjee, U. Tangentially phase-matched efficient difference frequency generation in beta barium borate crystal. *Optics Communications* **1994**, *105*, 95.
- (168) Nisoli, M.; Stagira, S.; De Silvestri, S.; Svelto, O.; Valiulis, G.; Varanavicius, A. Parametric generation of high-energy 14.5-fs light pulses at 1.5  $\mu\text{m}$ . *Optics Letters* **1998**, *23*, 630.
- (169) Harris, S. E.; Oshman, M. K.; Byer, R. L. Observation of Tunable Optical Parametric Fluorescence. *Physical Review Letters* **1967**, *18*, 732.
- (170) Danielius, R.; Piskarskas, A.; Stabinis, A.; Banfi, G. P.; Di Trapani, P.; Righini, R. Traveling-wave parametric generation of widely tunable, highly coherent femtosecond light pulses. *Journal of the Optical Society of America B* **1993**, *10*, 2222.
- (171) Di Trapani, P.; Andreoni, A.; Solcia, C.; Foggi, P.; Danielius, R.; Dubietis, A.; Piskarskas, A. Matching of group velocities in three-wave parametric interaction with femtosecond pulses and application to traveling-wave generators. *Journal of the Optical Society of America B* **1995**, *12*, 2237.
- (172) Reed, M. K.; Steiner-Shepard, M. K.; Armas, M. S.; Negus, D. K. Microjoule-energy ultrafast optical parametric amplifiers. *Journal of the Optical Society of America B* **1995**, *12*, 2229.
- (173) Banfi, G. P.; Di Trapani, P.; Danielius, R.; Piskarskas, A.; Righini, R.; Sa'nta, I. Tunable femtosecond pulses close to the transform limit from traveling-wave parametric conversion. *Optics Letters* **1993**, *18*, 1547.
- (174) Banfi, G. P.; Danielius, R.; Piskarskas, A.; Di Trapani, P.; Foggi, P.; Righini, R. Femtosecond traveling-wave parametric generator with lithium triborate. *Optics Letters* **1993**, *18*, 1633.



- (175) Petrov, V.; Seifert, F.; Noack, F. High repetition rate traveling wave optical parametric generator producing nearly bandwidth limited 50 fs infrared light pulses. *Applied Physics Letters* **1994**, *65*, 268.
- (176) Seifert, F.; Petrov, V.; Noack, F. Sub-100-fs optical parametric generator pumped by a high-repetition-rate Ti:sapphire regenerative amplifier system. *Optics Letters* **1994**, *19*, 837.
- (177) Nisoli, M.; De Silvestri, S.; Magni, V.; Svelto, O.; Danielius, R.; Piskarskas, A.; Valiulis, G.; Varanavičius, A. Highly efficient parametric conversion of femtosecond Ti:sapphire laser pulses at 1 kHz. *Optics Letters* **1994**, *19*, 1973.
- (178) Huber, R.; Satzger, H.; Zinth, W.; Wachtveitl, J. Noncollinear optical parametric amplifiers with output parameters improved by the application of a white light continuum generated in CaF<sub>2</sub>. *Optics Communications* **2001**, *194*, 443.
- (179) Karthick Kumar, S. K.; Goswami, T.; Bhattacharyya, I.; Goswami, D. Visible 20-femtosecond pulse generation by double-pass non-collinear optical parametric amplifier. *Current Science* **2009**, *96*, 1496.
- (180) Kobayashi, T.; Shirakawa, A. Sub-10-fs tunable pulses in visible and NIR and visible sub-5-fs pulses generated by noncollinear OPA. *Journal of Luminescence* **2000**, *87-89*, 119.
- (181) Oien, A. L.; McKinnie, I. T.; Jain, P.; Russell, N. A.; Warrington, D. M.; Gloster, L. A. W. Efficient, low-threshold collinear and noncollinear  $\beta$ -barium borate optical parametric oscillators. *Optics Letters* **1997**, *22*, 859.
- (182) Shirakawa, A.; Kobayashi, T. *Applied Physics Letters* **1998**, *72*, 147.
- (183) Shirakawa, A.; Sakane, I.; Takasaka, M.; Kobayashi, T. Sub-5-fs visible pulse generation by pulse-front-matched noncollinear optical parametric amplification. *Applied Physics Letters* **1999**, *74*, 2268.
- (184) Tzankov, P.; Fiebig, T.; Buchvarov, I. Tunable femtosecond pulses in the near-ultraviolet from ultra-broadband parametric amplification. *Applied Physics Letters* **2003**, *82*, 517.
- (185) Kohler, D. D.; Block, S. B.; Kain, S.; Pakoulev, A. V.; Wright, J. C. Ultrafast Dynamics within the 1S Exciton Band of Colloidal PbSe Quantum Dots Using Multiresonant Coherent Multidimensional Spectroscopy. *The Journal of Physical Chemistry C* **2014**, *118*, 5020.
- (186) Pestov, D.; Ariunbold, G. O.; Wang, X.; Murawski, R. K.; Sautenkov, V. A.; Sokolov, A. V.; Scully, M. O. Coherent versus incoherent Raman scattering: molecular coherence excitation and measurement. *Optics Letters* **2007**, *32*, 1725.
- (187) Prior, Y. Three-dimensional phase matching in four-wave mixing. *Applied Optics* **1980**, *19*, 1741.

- (188) Trebino, R.; DeLong, K. W.; Fittinghoff, D. N.; Sweetser, J. N.; Krumbügel, M. A.; Richman, B. A.; Kane, D. J. Measuring ultrashort laser pulses in the time-frequency domain using frequency-resolving optical gating. *Review of Scientific Instruments* **1997**, *68*, 3277.
- (189) Winker, B. K.; Wright, J. C. Nonlinear Atomic Spectroscopy of Flames. *Analytical Chemistry* **1988**, *60*, 2599.
- (190) Kumar, V.; Casella, M.; Molotokaite, E.; Gatti, D.; Kukura, P.; Manzoni, C.; Polli, D.; Marangoni, M.; Cerullo, G. Balanced-detection Raman-induced Kerr-effect spectroscopy. *Physical Review A* **2012**, *86*, 053810.
- (191) An, Y. Q.; Cundiff, S. T. Phase inversion in rotational anisotropy of second harmonic generation at Si(001) interfaces. *Physical Review B* **2003**, *67*, 193302.
- (192) Li, D.; Xiong, W.; Jiang, L.; Xiao, Z.; Golgir, H. R.; Wang, M.; Huang, X.; Zhou, Y.; Lin, Z.; Song, J.; Ducharme, S.; Jiang, L.; Silvain, J.-F.; Lu, Y. Multimodal Nonlinear Optical Imaging of MoS<sub>2</sub> and MoS<sub>2</sub>-Based van der Waals Heterostructures. *ACS Nano* **2016**, *10*, 3766.
- (193) Zhou, X.; Cheng, J.; Zhou, Y.; Cao, T.; Hong, H.; Liao, Z.; Wu, S.; Peng, H.; Liu, K.; Yu, D. Strong Second-Harmonic Generation in Atomic Layered GaSe. *Journal of the American Chemical Society* **2015**, *137*, 7994.
- (194) Veitas, G., Personal Communication.
- (195) Kleinman, D. A. Nonlinear Dielectric Polarization in Optical Media. *Physical Review* **1962**, *126*, 1977.
- (196) Powers, P. E., *Fundamentals of Nonlinear Optics*; CRC Press: Boca Raton, FL, 2011.
- (197) Johnson, L. W.; Riess, R. D.; Arnold, J. T., *Introduction of Linear Algebra*, Fifth; Addison Wesley: Boston, 2002.
- (198) Akhmanov, S. A.; Khokhlov, R. V., *Problems of Nonlinear Optics; Electromagnetic Waves in Nonlinear Dispersive Media*; Gordon and Breach: New York, 1972.
- (199) Bakker, H. J.; Planken, P. C. M.; Muller, H. G. Numerical calculation of optical frequency-conversion processes: a new approach. *The Journal of the Optical Society of America B* **1989**, *6*, 1665.
- (200) Gale, G. M.; Hache, F.; Cavallari, M. Broad-Bandwidth Parametric Amplification in the Visible: Femtosecond Experiments and Simulations. *IEEE Journal of Selected Topics in Quantum Electronics* **1998**, *4*, 224.

- (201) Gale, G. M.; Cavallari, M.; Hache, F. Femtosecond visible optical parametric oscillator. *Journal of the Optical Society of America B* **1998**, *15*, 702.
- (202) Moosmüller, H.; Anderson, S. B.; She, C. Y. Generation of four-wave mixing and stimulated Raman signals in focused Gaussian beams. *Physical Review A* **1989**, *40*, 6977.
- (203) Bjorklund, G. C. Effects of Focusing on Third-Order Nonlinear Processes in Isotropic Media. *IEEE Journal of Quantum Electronics* **1975**, *QE-11*, 287.
- (204) Herring, G. C.; Hillard Jr., M. E. Effect of crossed beams on Stokes gain and interaction length in stimulated Raman gain spectroscopy. *Applied Optics* **1995**, *34*, 6837.
- (205) Teets, R. E. CARS signals: phase matching, transverse modes, and optical damage effects. *Applied Optics* **1986**, *25*, 855.
- (206) Demirdöven, N.; Khalil, M.; Golonzka, O.; Tokmakoff, A. Dispersion compensation with optical materials for compression of intense sub-100-fs mid-infrared pulses. *Optics Letters* **2002**, *27*, 433.
- (207) Fork, R. L.; Brito Cruz, C. H.; Becker, P. C.; Shank, C. V. Compression of optical pulses to six femtoseconds by using cubic phase compensation. *Optics Letters* **1987**, *12*, 483.
- (208) Zhang, D.; Kong, Y.; Zhang, J.-y. Optical parametric properties of 532-nm-pumped beta-barium-borate near the infrared absorption edge. *Optics Communications* **2000**, *184*, 485.
- (209) Kenyon, I. R., *The Light Fantastic: A Modern Introduction to Classical and Quantum Optics*, Second; Oxford University Press: Oxford, 2011.
- (210) Azimov, B. S.; Karamzin, Y. N.; Sukhorukov, A. P.; Sukhorukova, A. K. Interaction of weak pulses with a low-frequency high-intensity wave in a dispersive medium. *Soviet Physics Journal of Experimental and Theoretical Physics* **1980**, *51*, 40.
- (211) Gale, G. M.; Cavallari, M.; Driscoll, T. J.; Hache, F. Generation of highly coherent tunable mid-infrared femtosecond pulses by parametric frequency-mixing at 82 MHz. *Optics Communications* **1995**, *119*, 159.
- (212) Manassah, J. T. Effects of velocity dispersion on a generated second harmonic signal. *Applied Optics* **1988**, *27*, 4365.
- (213) Manassah, J. T. Amplitude and phase of a pulsed second-harmonic signal. *Journal of the Optical Society of America B* **1987**, *4*, 1235.
- (214) Manassah, J. T.; Cockings, O. R. Induced phase modulation of a generated second-harmonic signal. *Optics Letters* **1987**, *12*, 1005.

- (215) Nishikawa, T.; Uesugi, N. Effects of walk-off and group velocity difference on the optical parametric generation in  $\text{KTiOPO}_4$  crystals. *Journal of Applied Physics* **1995**, *77*, 4941.
- (216) Pang, D.; Zhang, R.; Wang, Q. Theoretical Analysis of noncollinear phase-matched optical parametric amplifier seeded by a white-light continuum. *Optics Communications* **2001**, *196*, 293.
- (217) Reisner, S.; Gutmann, M. Numerical treatment of UV-pumped, white-light-seeded single-pass non-collinear parametric amplifiers. *Journal of the Optical Society of America B* **1999**, *16*, 1801.
- (218) Press, W. H.; Teukolsky, S. A.; Vetterling, W. T.; Flannery, B. P., *Numerical Recipes in C: The Art of Scientific Computing*, Second; Cambridge University Press: Cambridge, 1992.
- (219) Moulton, P. F. Spectroscopic and laser characteristics of  $\text{Ti:Al}_2\text{O}_3$ . *Journal of the Optical Society of America B* **1986**, *3*, 125.
- (220) Cundiff, S. F.; Knox, W. H.; Ippen, E. P.; Haus, H. A. Frequency-dependent mode size in broadband Kerr-lens mode locking. *Optics Letters* **1996**, *21*, 662.
- (221) Fluck, R.; Jung, I. D.; Zhang, G.; Kärtner, F. X.; Keller, U. Broadband saturable absorber for 10-fs pulse generation. *Optics Letters* **1996**, *21*, 743.
- (222) Jung, I. D.; Kärtner, F. X.; Matuschek, N.; Sutter, D. H.; Morier-Genoud, F.; Zhang, G.; Keller, U. Self-starting 6.5-fs pulses from a Ti:sapphire laser. *Optics Letters* **1997**, *22*, 1009.
- (223) Kasper, A.; Witte, K. J. 10-fs pulse generation from a unidirectional Kerr-lens mode-locked Ti:sapphire ring laser. *Optics Letters* **1996**, *21*, 360.
- (224) Xu, L.; Spielmann, C.; Krausz, F.; Szipöcs, R. Ultrabroadband ring oscillator for sub-10-fs pulse generation. *Optics Letters* **1996**, *21*, 1259.
- (225) Brabec, T.; Spielmann, C.; Krausz, F. Mode locking in solitary lasers. *Optics Letters* **1991**, *16*, 1961.
- (226) Curley, P. F.; Spielmann, C.; Brabec, T.; Krausz, F.; Wintner, E.; Schmidt, A. J. Operation of a femtosecond Ti:sapphire solitary laser in the vicinity of zero group-delay dispersion. *Optics Letters* **1993**, *18*, 54.
- (227) Knox, W. H. *In situ* measurement of complete intracavity dispersion in an operating Ti:sapphire femtosecond laser. *Optics Letters* **1992**, *17*, 514.
- (228) Zhou, J.; Taft, G.; Huang, C.-P.; Murnane, M. M.; Kapteyn, H. C.; Christov, I. P. Pulse evolution in a broad-bandwidth Ti:sapphire laser. *Optics Letters* **1994**, *19*, 1149.
- (229) Matos, L.; Mücke, O. D.; Jian, C.; Kärtner, F. X. Carrier-envelope phase dynamics and noise analysis in octave-spanning Ti:sapphire lasers. *Optics Express* **2006**, *14*, 2497.

- (230) Fork, R. L.; Martinez, O. E.; Gordon, J. P. Negative dispersion using pairs of prisms. *Optics Letters* **1984**, *9*, 150.
- (231) Pelouch, W. S.; Powers, P. E.; Tang, C. L. Self-starting mode-locked ring-cavity Ti:sapphire laser. *Optics Letters* **1992**, *17*, 1581.
- (232) Spence, D. E.; Kean, P. N.; Sibbett, W. 60-fsec pulse generation from a self-mode-locked Ti:sapphire laser. *Optics Letters* **1991**, *16*, 42.
- (233) Salin, F.; Grangier, P.; Georges, P.; Brun, A. Pulse propagation near zero group-velocity dispersion in a femtosecond dye laser. *Optics Letters* **1990**, *15*, 1374.
- (234) Brée, C.; Demircan, A.; Steinmeyer, G. Saturation of the All-Optical Kerr Effect. *Physical Review Letters* **2011**, *106*, 183902.
- (235) Roy, R.; Schulz, P. A.; Walther, A. Acousto-optic modulator as an electronically selectable unidirectional device in a ring laser. *Optics Letters* **1987**, *12*, 672.
- (236) Huggett, G. Mode-Locking of CW Lasers by Regenerative RF Feedback. *Applied Physics Letters* **1968**, *13*, 186.
- (237) French, P. M. W.; Williams, J. A. R.; Taylor, J. R. Femtosecond pulse generation from a titanium-doped sapphire laser using nonlinear external cavity feedback. *Optics Letters* **1989**, *14*, 686.
- (238) Haus, H. A. Mode-Locking of Lasers. *IEEE Journal on Selected Topics in Quantum Electronics* **2000**, *6*, 1173.
- (239) Hou, D.; Lee, C.-C.; Yang, Z.; Schibli, T. R. Timing jitter characterization of mode-locked lasers with  $<1$  zs/ $\sqrt{\text{Hz}}$  resolution using a simple optical heterodyne technique. *Optics Letters* **2015**, *40*, 2985.
- (240) Haus, H. A.; Shank, C. V.; Ippen, E. P. Shape of Passively Mode-Locked Laser Pulses. *Optics Communications* **1975**, *15*, 29.
- (241) Martinez, O. E.; Fork, R. L.; Gordon, J. P. Theory of passively mode-locked lasers including self-phase modulation and group-velocity dispersion. *Optics Letters* **1984**, *9*, 156.
- (242) Sarukura, N.; Ishida, Y.; Nakano, H.; Yamamoto, Y. cw passive mode locking of a Ti:sapphire laser. *Applied Physics Letters* **1990**, *56*, 814.
- (243) Salin, F.; Squire, J.; Piché, M. Mode locking of Ti:Al<sub>2</sub>O<sub>3</sub> lasers and self-focusing: a Gaussian approximation. *Optics Letters* **1991**, *16*, 1674.
- (244) Piché, M.; Salin, F. S. Self-mode locking of solid-state lasers without apertures. *Optics Letters* **1993**, *18*, 1041.

- (245) Rudd, J. V.; Korn, G.; Kane, S.; Squier, J.; Mourou, G. Chirped-pulse amplification of 55-fs pulses at a 1-kHz repetition rate in a Ti:Al<sub>23</sub> regenerative amplifier. *Optics Letters* **1993**, *18*, 2044.
- (246) Barty, C. P. J.; Korn, G.; Raksi, F.; Rose-Petruck, C.; Squier, J.; Tien, A.-C.; Wilson, K. R.; Yakovlev, V. V.; Yamakawa, K. Regenerative pulse shaping and amplification of ultrabroadband optical pulses. *Optics Letters* **1996**, *21*, 219.
- (247) Roth, U.; Loewenthal, F.; Balmer, J. E.; Weber, H. P. Compensation of Nonlinear Self-Focusing in High-Power Lasers. *IEEE Journal of Quantum Electronics* **2000**, *36*, 687.
- (248) Lenzner, M.; Spielmann, C.; Wintner, E.; Krausz, F.; Schmidt, A. J. Sub-20-fs, kilohertz-repetition-rate Ti:sapphire amplifier. *Optics Letters* **1995**, *20*, 1397.
- (249) Lemoff, B. E.; Barty, C. P. J. Quintic-phase-limited, spatially uniform expansion and recompression of ultrashort optical pulses. *Optics Letters* **1993**, *18*, 1651.
- (250) Pessot, M.; Maine, P.; Mourou, G. 1000 Times Expansion/Compression of Optical Pulses for Chirped Pulse Amplification. *Optics Communications* **1987**, *62*, 419.
- (251) Strickland, D.; Mourou, G. Compression of Amplified Chirped Optical Pulses. *Optics Communications* **1985**, *56*, 219.
- (252) Perry, M. D.; Ditmire, T.; Stuart, B. C. Self-phase modulation in chirped pulse amplification. *Optics Letters* **1994**, *19*, 2149.
- (253) Wynne, K.; Reid, G. D.; Hochstrasser, R. M. Regenerative amplification of 30-fs pulses in Ti:sapphire at 5 kHz. *Optics Letters* **1994**, *19*, 895.
- (254) Konoplev, O. A.; Meyerhofer, D. D. Cancellation of *B*-Integral Accumulation for CPA Lasers. *IEEE Journal of Selected Topics in Quantum Electronics* **1998**, *4*, 459.
- (255) Wong, K. S.; Qui, Z. R.; Wang, H.; Wong, G. K. L. Efficient visible femtosecond optical parametric generator and amplifier using tilted pulse-front pumping. *Optics Letters* **1997**, *22*, 898.
- (256) Fraser, J. M.; Hall, K. C. Interferometric nonlinear mixing in multiple-pass femtosecond optical parametric amplification. *Optics Express* **1999**, *5*, 21.
- (257) Chien, C. Y.; Korn, G.; Coe, J. S.; Squier, J.; Mourou, G.; Craxton, R. S. Highly efficient second-harmonic generation of ultraintense Nd:glass laser pulses. *Optics Letters* **1995**, *20*, 353.
- (258) Fendt, A.; Kranitzky, W.; Laubereau, A.; Kaiser, W. Efficient Generation of Tunable Subpicosecond Pulses in the Infrared. *Optics Communications* **1979**, *28*, 142.

- (259) Wang, Y.; Luther-Davies, B. Frequency-doubling pulse compressor for picosecond high-power neodymium laser pulses. *Optics Letters* **1992**, *17*, 1459.
- (260) Chen, Y.-C.; Fang, X.-J.; Li, J.; Liang, X.-Y.; Zhang, H.-L.; Feng, B.-H.; Zhang, X.-L.; Xu, Z.-Y. Efficient femtosecond optical parametric generator with a birefringent delay compensator. *Applied Optics* **2001**, *40*, 2579.
- (261) Danielius, R.; Piskarskas, A.; Di Trapani, P.; Andreoni, A.; Solcia, C.; Foggi, P. Matching of group velocities by spatial walk-off in collinear three-wave interaction with tilted pulses. *Optics Letters* **1996**, *21*, 973.
- (262) Danielius, R.; Dubietis, A.; Piskarskas, A.; Valiulis, G.; Varanavičius, A. Generation of compressed 600-720-nm tunable femtosecond pulses by transient frequency mixing in a  $\beta$ -barium borate crystal. *Optics Letters* **1996**, *21*, 216.
- (263) Greenfield, S. R.; Wasielewski, M. R. Optical parametric amplification of femtosecond pulses tunable from the blue to the infrared with microjoule energies. *Applied Optics* **1995**, *34*, 2688.
- (264) Nisoli, M.; De Silvestri, S.; Valiulis, G.; Varanavicius, A. Fivefold femtosecond pulse compression by sum frequency generation. *Applied Physics Letters* **1996**, *68*, 3540.
- (265) Yakovlev, V. V.; Kohler, B.; Wilson, K. R. Broadly tunable 30-fs pulses produced by optical parametric amplification. *Optics Letters* **1994**, *19*, 2000.
- (266) Wachman, E. S.; Edelstein, D. C.; Tang, C. L. Continuous-wave mode-locked and dispersion-compensated femtosecond optical parametric oscillator. *Optics Letters* **1990**, *15*, 136.
- (267) Wasylczyk, P.; Walmsley, I. A.; Wasilewski, W.; Radzewicz, C. Broadband noncollinear optical parametric amplifier using a single crystal. *Optics Letters* **2005**, *30*, 1704.
- (268) Wei, P.-F.; Li, C.; Zhang, C.-M.; Wang, J.-L.; Leng, Y.-X.; Li, R.-X. High-Conversion-Efficiency and Broadband Tunable Femtosecond Noncollinear Optical Parametric Amplifier. *Chinese Physical Letters* **2008**, *25*, 2514.
- (269) Wei, P.; Liu, J.; Li, C. Temporal and spectral characterizations of tunable noncollinear optical parametric amplifier. *Optics Communications* **2013**, *286*, 334.
- (270) Gloster, L. A. W.; McKinnie, I. T.; King, T. A. Noncollinear phase matching in a type I barium borate optical parametric oscillator. *Optics Communications* **1994**, *112*, 328.
- (271) Laenan, R.; Graener, H.; Lauberau, A. Broadly tunable femtosecond pulses generated by optical parametric oscillation. *Optics Letters* **1990**, *15*, 971.

- (272) Danielius, R.; Piskarskas, A.; Di Trapani, P.; Andreoni, A.; Solcia, C.; Foggi, P. Visible pulses of 100 fs and 100  $\mu$ J from an upconverted parametric generator. *Applied Optics* **1996**, *35*, 5336.
- (273) Joosen, W.; Agostini, P.; Petite, G.; Chambaret, J. P.; Antonetti, A. Broadband femtosecond infrared parametric amplification in  $\beta$ -BaB<sub>2</sub>O<sub>4</sub>. *Optics Letters* **1992**, *17*, 133.
- (274) Dubietis, A.; Valiulis, G.; Tamošauskas, G.; Danielius, R.; Piskarskas, A. Nonlinear second-harmonic pulse compression with tilted pulses. *Optics Letters* **1997**, *22*, 1071.
- (275) Bromage, J.; Rothhardt, J.; Hädrich, S.; Dorrer, C.; Jocher, C.; Demmler, S.; Limpert, J.; Tünnemann, A.; Zuegel, J. D. Analysis and suppression of parasitic processes in noncollinear optical parametric amplifiers. *Optics Express* **2011**, *19*, 16797.
- (276) Gehr Russell, J.; Kimmel, M. W.; Smith, A. V. Simultaneous spatial and temporal walk-off compensation in frequency-doubling femtosecond pulses in  $\beta$ -BaB<sub>2</sub>O<sub>4</sub>. *Optics Letters* **1998**, *23*, 1298.
- (277) Wilhelm, T.; Piel, J.; Riedle, E. Sub-20-fs pulses tunable across the visible from a blue-pumped single-pass noncollinear parametric converter. *Optics Letters* **1997**, *22*, 1494.
- (278) Osvay, K.; Ross, I. N. Broadband sum-frequency generation by chirp-assisted group-velocity matching. *Journal of the Optical Society of America B* **1996**, *13*, 1431.
- (279) Danielius, R.; Dubietis, A.; Valiulis, G.; Piskarskas, A. Femtosecond high-contrast pulses from a parametric generator pumped by the self-compressed second harmonic a Nd:glass laser. *Optics Letters* **1995**, *20*, 2225.
- (280) Grün, A.; Austin, D. R.; Cousin, S. L.; Biegert, J. Three-wave mixing mediated femtosecond pulse compression in  $\beta$ -barium borate. *Optics Letters* **2015**, *40*, 4679.
- (281) Ziegler, L. D.; Morais, J.; Zhou, Y.; Constantine, S.; Reed, M. K.; Steiner-Shepard, M. K.; Lommel, D. Tunable 50-fs Pulse Generation in the 250-310-nm Ultraviolet Range. *IEEE Journal of Quantum Electronics* **1998**, *34*, 1758.
- (282) Danielius, R.; Di Trapani, P.; Dubietis, A.; Piskarskas, A.; Podenas, D.; Banfi, G. P. Self-diffraction through cascaded second-order frequency-mixing effects in  $\beta$ -barium borate. *Optics Letters* **1993**, *18*, 574.
- (283) Liu, W.; Zhu, L.; Fang, C. Observation of sum-frequency-generation-induced cascaded four-wave mixing using two crossing femtosecond laser pulses in a 0.1 mm beta-barium-borate crystal. *Optics Letters* **2012**, *37*, 3783.



- (284) Liu, W.; Zhu, L.; Wang, L.; Fang, C. Cascaded four-wave mixing for broadband tunable laser sideband generation. *Optics Letters* **2013**, *38*, 1772.
- (285) Petrov, V.; Noack, F. Frequency upconversion of tunable femtosecond pulses by parametric amplification and sum-frequency generation in a single nonlinear crystal. *Optics Letters* **1995**, *20*, 2171.
- (286) Sueptitz, M.; Kaindl, R. A.; Lutgen, S.; Woerner, M.; Riedle, E. 1 kHz solid state laser system for the generation of 50 fs pulses tunable in the visible. *Optics Communications* **1996**, *131*, 195.
- (287) Eimerl, D.; Davis, L.; Velsko, S.; Graham, E. K.; Zalkin, A. Optical, mechanical, and thermal properties of barium borate. *Journal of Applied Physics* **1987**, *62*, 1968.
- (288) Kato, K. Second-Harmonic Generation to 2048 Å in  $\beta$ -BaB<sub>2</sub>O<sub>4</sub>. *IEEE Journal of Quantum Electronics* **1986**, *QE-22*, 1013.
- (289) Lu, M.-H.; Liu, Y.-M. Infrared up-conversion with beta barium borate crystal. *Optics Communications* **1991**, *84*, 193.
- (290) Freund, J. E. *Mathematical Statistics*. **1992**.
- (291) Engel, T.; Reid, P., *Physical Chemistry*; Prentice Hall: Upper Saddle River, NJ, 2006.
- (292) Nautiyal, A.; Bisht, P. B. Broadly tunable parametric line emission from  $\beta$ -barium borate on pumping with picosecond pulses. *Optics Communications* **2008**, *281*, 3351.
- (293) Davis, T. S.; Fackler, J. P.; Weeks, M. J. Spectra of Manganese (III) Complexes. The Origin of the Low-Energy Band. *Inorganic Chemistry* **1968**, *7*, 1994.
- (294) Dingle, R. The Visible and Near Infrared Spectrum of Manganese (III) Complexes. *Acta Chemica Scandinavica* **1966**, *20*, 33.
- (295) Dingle, R. The Jahn-Teller Effect in Manganic Acetylacetonate. *Journal of Molecular Spectroscopy* **1962**, *9*, 426.
- (296) Diaz-Acosta, I.; Baker, J.; Hinton, J. F.; Pulay, P. Calculated and experimental geometries and infrared spectra of metal tris-acetylacetonates: vibrational spectroscopy as a probe of molecular structure for ionic complexes. Part II. *Spectrochimica Acta Part A* **2003**, *59*, 363.
- (297) Stults, B. R.; Marianelli, R. S.; Day, V. W. Distortions of the Coordination Polyhedron in High-Spin Manganese(III) Complexes. I. Synthesis and Characterization of a Series of Five- and Six-Coordinate Bis(acetylacetonato) manganese(III) Complexes. Crystal Structure of Azidobis(acetylacetonato) manganese(III). *Inorganic Chemistry* **1975**, *14*, 722.

- (298) Stults, B. R.; Day, R. O.; Marianelli, R. S.; Day, V. W. Distortions of the Coordination Polyhedron in High-Spin Manganese(III) Complexes. 2. Crystal Structure of Thiocyanatobis(acetylacetonato) manganese(III). *Inorganic Chemistry* **1979**, *18*, 1847.
- (299) Stults, B. R.; Marianelli, R. S.; Day, V. W. Distortions of the Coordination Polyhedron in High-Spin Manganese(III) Complexes. 3. Crystal and Molecular Structure of  $\gamma$ -Tris(acetylacetonato) manganese(III): A Tetragonally Elongated Octahedral Form. *Inorganic Chemistry* **1979**, *18*, 1853.
- (300) Juban, E. A.; McCusker, J. K. Ultrafast Dynamics of  $^2E$  State Formation in  $\text{Cr}(\text{acac})_3$ . *Journal of the American Chemical Society* **2005**, *127*, 6857.
- (301) McCusker, J. K. Femtosecond Absorption Spectroscopy of Transition Metal Charge-Transfer Complexes. *Accounts of Chemical Research* **2003**, *36*, 876.
- (302) Schrauben, J. N.; Dillman, K. L.; Beck, W. F.; McCusker, J. K. Vibrational coherence in the excited state dynamics of  $\text{Cr}(\text{acac})_3$ : probing the reaction coordinate for ultrafast intersystem crossing. *Chemical Science* **2010**, *1*, 405.
- (303) Fielding, P. E.; MacKay, A. G. N.I.R. Absorption Spectra of Phthalocyanines. *Australian Journal of Chemistry* **1975**, *28*, 1445.
- (304) Grobosch, M.; Schmidt, C.; Kraus, R.; Knupfer, M. Electronic properties of transition metal phthalocyanines: The impact of the central metal atom ( $d^5$ - $d^{10}$ ). *Organic Electronics* **2010**, *11*, 1483.
- (305) Kraus, R.; Grobosch, M.; Knupfer, M. Full electronic excitation spectrum of condensed manganese phthalocyanine. *Chemical Physics Letters* **2009**, *469*, 121.
- (306) Liu, K.; Lei, Y.; Wang, G. Correlation between oxygen adsorption energy and electronic structure of transition metal macrocyclic complexes. *The Journal of Chemical Physics* **2013**, *139*, 204306.
- (307) Ghani, F.; Kristen, J.; Riegler, H. Solubility Properties of Unsubstituted Metal Phthalocyanines in Different Types of Solvents. *Journal of Chemical & Engineering Data* **2012**, *57*, 439.
- (308) Boucher, L. J. Manganese Porphyrin Complexes. III. Spectroscopy of Chloroquo Complexes of Several Porphyrins. *Journal of the American Chemical Society* **1970**, *92*, 2725.
- (309) Gaughan, R. R.; Shriver, D. F.; Boucher, L. J. Resonance Raman Spectra of Manganese(III) Tetraphenylporphyrin Halides. *Proceedings of the National Academy of Sciences of the United States of America* **1975**, *72*, 433.
- (310) Gale, R.; Peacock, R. D.; Samori, B. The Linear Dichroism Spectra of Free Base and Manganese(III) Porphyrins. *Chemical Physics Letters* **1976**, *37*, 430.

- (311) Humphrey, J. L.; Kuciauskas, D. Charge Transfer Enhances Two-Photon Absorption in Transition Metal Porphyrins. *Journal of the American Chemical Society* **2006**, *128*, 3902.
- (312) Ha, J.-H.; Chae, W.-S.; Kim, J. Triplet-state dynamics of manganese(III) porphyrin fabricated into PVC film. *Journal of Analytical Science & Technology* **2011**, *2*, 69.
- (313) Gonçalves, P. J.; De Boni, L.; Borissevitch, I. E.; Zilio, S. C. Excited State Dynamics of meso-Tetra(sulphonatophenyl) Metalloporphyrins. *The Journal of Physical Chemistry A* **2008**, *112*, 6522.
- (314) Irvine, M. P.; Harrison, R. J.; Strahand, M. A.; Beddard, G. S. Picosecond Spectroscopy and Kinetics of Metalloporphyrins. *Berichte der Bunsengesellschaft für Physikalische Chemie* **1985**, *86*, 226.
- (315) Yanghee, K.; Choi, J. R.; Yoon, M.; Furube, A.; Asahi, T.; Masuhara, H. Excited-State Dynamics of 5,10,15,20-Tetraphenyl-21H,23H-porphine Manganese(III) Chloride Encapsulated in TiMCM-41 and MCM-41; Probed by fs-Diffuse Reflectance Laser Photolysis. *The Journal of Physical Chemistry B* **2001**, *105*, 8513.
- (316) Yan, X.; Kirmaier, C.; Holten, D. A Picosecond Study of Rapid Multistep Radiationless Decay in Manganese(III) Porphyrins. *Inorganic Chemistry* **1986**, *25*, 4774.
- (317) Jeoung, S. C.; Kim, D.; Cho, D. W. Transient resonance Raman spectroscopic studies of some paramagnetic metalloporphyrins: effects of axial ligand on charge-transfer and photoreduction processes. *Journal of Raman Spectroscopy* **2000**, *31*, 319.
- (318) Brodeur, A.; Chin, S. L. Band-Gap Dependence on the Ultrafast White-Light Continuum. *Physics Review Letters* **1998**, *80*, 4406.
- (319) Nagura, C.; Suda, A.; Kawano, K.; Obara, M.; Midorikawa, K. Generation and characterization of ultrafast white-light continuum in condensed media. *Applied Optics* **2002**, *41*, 3735.
- (320) Brodeur, A.; Chin, S. L. Ultrafast white-light continuum generation and self-focusing in transparent condensed media. *Journal of Optical Society of America B* **1999**, *16*, 637.
- (321) Baltuška, A.; Fuji, T.; Kobayashi, T. Controlling the Carrier-Envelope Phase of Ultrashort Light Pulses with Optical Parametric Amplifiers. *Physical Review Letters* **2002**, *88*, 133901.
- (322) Baum, P.; Lochbrunner, S.; Piel, J.; Riedle, E. Phase-coherent generation of tunable visible femtosecond pulses. *Optics Letters* **2003**, *28*, 185.
- (323) Baum, P.; Riedle, E.; Greve, M.; Telle, H. R. Phase-locked ultrashort pulse trains at separate and independently tunable wavelengths. *Optics Letters* **2005**, *30*, 2028.

- (324) Bellini, M.; Hänsch, T. W. Phase-locked white-light continuum pulses: toward a universal optical frequency-comb synthesizer. *Optics Letters* **2000**, *25*, 1049.
- (325) Corsi, C.; Tortora, A.; Bellini, M. Mutual coherence of supercontinuum pulses collinearly generated in bulk media. *Applied Physics B* **2003**, *77*, 285.
- (326) Gaundalini, A.; Eckle, P.; Anscombe, M.; Schlup, P.; Biegert, J.; Keller, U. 5.1 fs pulses generated by filamentation and carrier envelope phase stability analysis. *Journal of Physics B: Atomic, Molecular and Optical Physics* **2006**, *39*, S257.
- (327) Béjot, P.; Kasparian, J.; Henin, S.; Loriot, V.; Vieillard, T.; Hertz, E.; Faucher, O.; Lavorel, B.; Wolf, J.-P. Higher-Order Kerr Terms Allow Ionization-Free Filamentation in Gases. *Physical Review Letters* **2010**, *104*, 103903.
- (328) Bradler, M.; Baum, P.; Riedle, E. Femtosecond continuum generation in bulk laser host materials with sub- $\mu$ J pump pulses. *Applied Physics B* **2009**, *97*, 561.
- (329) Couairon, A.; Franco, M.; Mysyrowicz, A.; Biegert, J.; Keller, U. Pulse self-compression to the single-cycle limit by filamentation in a gas with a pressure gradient. *Optics Letters* **2005**, *30*, 2657.
- (330) Kasparian, J.; Sauerbrey, R.; Chin, S. L. The critical laser intensity of self-guided light filaments in air. *Applied Physics B* **2000**, *71*, 877.
- (331) Méjean, G.; Kasparian, J.; Yu, J.; Frey, S.; Salmon, E.; Ackermann, R.; Wolf, J. P.; Bergé, L.; Skupin, S. UV-Supercontinuum generated by femtosecond pulse filamentation in air: Meter-range experiments versus numerical simulations. *Applied Physics B* **2006**, *82*, 341.
- (332) Mikalauskas, D.; Dubietis, A.; Danielius, R. Observation of light filaments induced in air by visible picosecond laser pulses. *Applied Physics B* **2002**, *75*, 899.
- (333) Nguyen, N. T.; Salimonia, A.; Liu, W.; Chin, S. L.; Vall'ee, R. Optical Breakdown versus filamentation in fused silica by use of femtosecond infrared laser pulses. *Optics Letters* **2003**, *28*, 1591.
- (334) Petrarca, M.; Petit, Y.; Delagrange, R.; Béjot, P.; Kasparian, J. Higher-order Kerr improve quantitative modeling of laser filamentation. *Optics Letters* **2012**, *37*, 4347.
- (335) Wang, H.; Fan, C.; Shen, H.; Zhang, P. F.; Qiao, C. H. Relative contributions of higher-order Kerr effect and plasma in laser filamentation. *Optics Communications* **2013**, *293*, 113.
- (336) Aközbek, N.; Scalora, M.; Bowden, C. M.; Chin, S. L. White-light continuum generation and filamentation during the propagation of ultra-short laser pulses in air. *Optics Communications* **2001**, *191*, 353.

- (337) Kohl-Landgraf, J.; Nimsch, J.-E.; Wachtveitl, J. LiF, an underestimated supercontinuum source in femtosecond transient absorption spectroscopy. *Optics Express* **2013**, *21*, 17060.
- (338) Hauri, C. P.; Guandalini, A.; Eckle, P.; Kornelis, W.; Biegert, J.; Keller, U. Generation of intense few-cycle laser pulses through filamentation - parameter dependence. *Optics Express* **2005**, *13*, 7541.
- (339) Jang, D. G.; Nam, I. H.; Kim, M. S.; Kang, K.; Suk, H. Generation of broadband supercontinuum light by double-focusing of a femtosecond laser pulse in air. *Applied Physics Letters* **2015**, *107*, 131105.
- (340) Liu, X.-L.; Lu, X.; Liu, X.; Feng, L.-B.; Ma, J.-L.; Li, Y.-T.; Chen, L.-M.; Dong, Q.-L.; Wang, W.-M.; Wang, Z.-H.; Wei, Z.-Y.; Sheng, Z.-M.; Jie, Z. Broadband supercontinuum generation in air using tightly focused femtosecond laser pulses. *Optics Letters* **2011**, *36*, 3900.
- (341) Spokoyny, B.; Koh, C. J.; Harel, E. Stable and high-power few cycle supercontinuum for 2D ultra-broadband electronic spectroscopy. *Optics Letters* **2015**, *40*, 1014.
- (342) Fork, R. L.; Shank, C. V.; Hirlimann, C.; Yen, R.; Tomlinson, W. J. Femtosecond white-light continuum pulses. *Optics Letters* **1983**, *8*, 1.
- (343) Ashcom, J. B.; Gattass, R. R.; Schaffer, C. B.; Mazur, E. Numerical aperture dependence of damage and supercontinuum generation from femtosecond laser pulses in bulk fused silica. *Journal of the Optical Society of America B* **2006**, *23*, 2317.
- (344) Nikolaitchik, A. V.; Korth, O.; Rodgers, M. A. J. Crown Ether Substituted Monomeric and Cofacial Dimeric Metallophthalocyanines. 1. Photophysical Studies of the Free Base, Zinc(II), and Copper(II) Variants. *The Journal of Physical Chemistry A* **1999**, *103*, 7587.
- (345) Hybl, J. D.; Albrecht, A. W.; Gallagher Faeder, S. M.; Jonas, D. M. Two-dimensional electronic spectroscopy. *Chemical Physics Letters* **1998**, *297*, 307.
- (346) Cong, P.; Deuel, H. P.; Simon, J. D. Using optical coherence to measure the ultrafast dephasing of large molecules in room-temperature liquids. *Chemical Physics Letters* **1993**, *212*, 367.
- (347) Maçôas, E. M. S.; Kananavicius, R.; Myllyperkiö, P.; Pettersson, M.; Kunttu, H. Relaxation Dynamics of Cr(acac)<sub>3</sub> Probed by Ultrafast Infrared Spectroscopy. *Journal of the American Chemical Society* **2007**, *129*, 8934.
- (348) Nie, Z.; Long, R.; Sun, L.; Huang, C.-C.; Zhang, J.; Xiong, Q.; Hewak, D. W.; Shen, Z.; Prezhdo, O. V.; Loh, Z.-H. Ultrafast Carrier Thermalization and Cooling Dynamics in Few-Layer MoS<sub>2</sub>. *ACS Nano* **2014**, *8*, 10931.

- (349) Palfrey, S. L.; Heinz, T. F. Coherent interactions in pump-probe absorption measurements: the effect of phase gratings. *Journal of the Optical Society of America B* **1985**, *2*, 674.
- (350) Tomita, M.; Matsuoka, M. Ultrafast pump-probe measurement using intensity correlation of incoherent light. *Journal of the Optical Society of America B* **1986**, *3*, 560.
- (351) Wolfseder, B.; Seidner, L.; Domcke, W.; Stock, G.; Seel, M.; Engleitner, S.; Zinth, W. Vibrational coherence in ultrafast electron-transfer dynamics of oxazine 1 in N,N-dimethylaniline: simulation of a femtosecond pump-probe experiment. *Chemical Physics* **1998**, *1998*, 323.
- (352) Carlson, R. J.; Wright, J. C. Absorption and Coherent Interference Effects in Multiply Resonant Four-Wave Mixing Spectroscopy. *Applied Spectroscopy* **1989**, *43*, 1195.
- (353) Evans, C. L.; Potma, E. O.; Sunney Xie, X. Coherent anti-Stokes Raman scattering spectral interferometry: determination of the real and imaginary components of nonlinear susceptibility  $\chi^{(3)}$  for vibrational microscopy. *Optics Letters* **2004**, *29*, 2923.
- (354) Müller, C.; Backup, T.; von Vacano, B.; Motzkus, M. Heterodyne single-beam CARS microscopy. *Journal of Raman Spectroscopy* **2009**, *40*, 8099.
- (355) Potma, E. O.; Evans, C. L.; Sunney Xie, X. Heterodyne coherent anti-Stokes Raman scattering (CARS) imaging. *Optics Letters* **2006**, *31*, 241.
- (356) Pegoraro, A. F.; Ridsdale, A.; Moffatt, D. J.; Jia, Y.; Pezacki, J. P.; Stolow, A. Optimally chirped multimodal CARS microscopy based on a single Ti:sapphire oscillator. *Optics Express* **2009**, *17*, 2984.
- (357) Brückner, L.; Backup, T.; Motzkus, M. Enhancement of coherent anti-Stokes Raman signal via tailored probing in spectral focusing. *Optics Letters* **2015**, *40*, 5204.
- (358) Kohler, D. D., Personal Communication.
- (359) Krishna, M. B. M.; Rao, D. N. Influence of solvent contribution on nonlinearities of near infra-red absorbing croconate and squaraine dyes with ultrafast laser excitation. *Journal of Applied Physics* **2013**, *114*, 133103.
- (360) Shen, Y.; Voronine, D. V.; Sokolov, A. V.; Scully, M. O. A versatile setup using femtosecond adaptive spectroscopic techniques for coherent anti-Stokes Raman scattering. *Review of Scientific Instruments* **2015**, *86*, 083107.
- (361) Song, J. J.; Eesley, G. L.; Levenson, M. D. *Applied Physics Letters* **1976**, *29*, 567.

- (362) Brixner, T.; Mančal, T.; Stiopkin, I. V.; Fleming, G. R. Phase-stabilized two-dimensional electronic spectroscopy. *The Journal of Chemical Physics* **2004**, *121*, 4221.
- (363) Christensson, N.; F., M.; J., H.; Sperling, J.; Bixner, O.; Nemeth, A.; Kauffmann, H. F. High Frequency Vibrational Modulations in Two-Dimensional Electronic Spectra and Their Resemblance to Electronic Coherence Signatures. *The Journal of Physical Chemistry B* **2011**, *115*, 5383.
- (364) Harel, E.; Long, P. D.; Engel, G. S. Single-shot ultrabroadband two-dimensional electronic spectroscopy of the light-harvesting complex LH2. *Optics Letters* **2011**, *36*, 1665.
- (365) Harel, E.; Rupich, S. M.; Schaller, R. D.; Talapin, D. V.; Engel, G. S. Measurement of electronic splitting in PbS quantum dots by two-dimensional nonlinear spectroscopy. *Physical Review B* **2012**, *86*, 075412.
- (366) Lynch, M. S.; Slenkamp, K. M.; Cheng, M.; Khalil, M. Coherent Fifth-Order Visible-Infrared Spectroscopies: Ultrafast Nonequilibrium Vibrational Dynamics in Solution. *The Journal of Physical Chemistry A* **2012**, *116*, 7023.
- (367) Mančal, T.; Nemeth, A.; Milota, F.; Lukeš, V.; Kauffmann, H. F.; Sperling, J. Vibrational wave packet induced oscillations in two-dimensional electronic spectra. II. Theory. *The Journal of Chemical Physics* **2010**, *132*, 184515.
- (368) Nemeth, A.; Milota, F.; Mančal, T.; Lukeš, V.; Kauffmann, H. F.; Sperling, J. Vibronic modulation of lineshapes in two-dimensional electronic spectra. *Chemical Physics Letters* **2008**, *459*, 94.
- (369) Nemeth, A.; Lukeš, V.; Sperling, J.; Milota, F.; Kauffmann, H. F.; Mančal, T. Two-dimensional electronic spectra of an aggregating dye: simultaneous measurement of monomeric and dimeric lineshapes. *Physical Chemistry Chemical Physics* **2009**, *11*, 5986.
- (370) Tekavec, P. F.; Myers, J. A.; Lewis, K. L. M.; Ogilvie, J. P. Two-dimensional electronic spectroscopy with a continuum probe. *Optics Letters* **2009**, *34*, 1390.
- (371) Zhang, Y.; Meyer, K.; Ott, C.; Pfeifer, T. Passively phase-stable, monolithic, all-reflective two-dimensional electronic spectroscopy based on a four-quadrant mirror. *Optics Letters* **2013**, *38*, 356.
- (372) Block, S. B., Personal Communication.
- (373) Robinson, J. W.; Skelly Frame, E. M.; Frame II, G. M., *Undergraduate Instrumental Analysis*, Sixth; Marcel Dekker: New York, 2005.
- (374) Fox, M., *Quantum Optics: An Introduction*; Oxford University Press: Oxford, 2006.

- (375) Kee, T. W.; Cicerone, M. T. Simple approach to one-laser, broadband coherent anti-Stokes Raman scattering microscopy. *Optics Letters* **2004**, *29*, 2701.
- (376) Knutsen, K. P.; Johnson, J. C.; Miller, A. E.; Petersen, P. B.; Saykally, R. J. High spectral resolution multiplex CARS spectroscopy using chirped pulses. *Chemical Physics Letters* **2004**, *387*, 436.
- (377) Heiman, D.; Hellwarth, R. W.; Levenson, M. D.; Martin, G. Raman-Induced Kerr Effect. *Physical Review Letters* **1976**, *36*, 189.
- (378) McCamant, D. W.; Kukura, P.; Yoon, S.; Mathies, R. A. Femtosecond broadband stimulated Raman spectroscopy: Apparatus and methods. *Review of Scientific Instruments* **2004**, *75*, 4971.
- (379) Klenerman, D. Multiplexed optically heterodyned Raman-induced Kerr-effect spectroscopy in the blue. *Optics Letters* **1991**, *16*, 838.
- (380) Brinkmann, M.; Dobner, S.; Fallnich, C. Light source for narrow and broadband coherent Raman scattering microspectroscopy. *Optics Letters* **2015**, *40*, 5447.
- (381) Duncan, M. D.; Reintjes, J.; Manuccia, T. J. Scanning coherent anti-Stokes Raman microscope. *Optics Letters* **1982**, *7*, 350.
- (382) Duncan, M. D.; Reintjes, J.; Manuccia, T. J. Imaging biological compounds using the coherent anti-Stokes Raman scattering microscope. *Optical Engineering* **1985**, *24*, 352.
- (383) Demirdöven, N.; Khalil, M.; Tokmakoff, A. Correlated Vibrational Dynamics Revealed by Two-Dimensional Infrared Spectroscopy. *Physical Review Letters* **2002**, *89*, 237401.
- (384) Khalil, M.; Demirdöven, N.; Tokmakoff, A. Obtaining Absorptive Line Shapes in Two-Dimensional Infrared Vibrational Correlation Spectra. *Physical Review Letters* **2003**, *90*, 047401.
- (385) Khalil, M.; Demirdöven, N.; Tokmakoff, A. Vibrational coherence transfer characterized with Fourier-transform 2D IR spectroscopy. *The Journal of Chemical Physics* **2004**, *121*, 362.
- (386) Nee, M. J.; Baiz, C. R.; Anna, J. M.; McCanne, R.; Kubarych, K. J. Multilevel vibrational coherence transfer and wavepacket dynamics probed with multidimensional IR spectroscopy. *The Journal of Chemical Physics* **2008**, *129*, 084503.
- (387) Osborne, D. G.; Kubarych, K. J. Rapid and Accurate Measurement of the Frequency-Frequency Correlation Function. *The Journal of Physical Chemistry A* **2013**, *117*, 5891.
- (388) Smeigh, A. L.; Creelman, M.; Mathies, R. A.; McCusker, J. K. Femtosecond Time-Resolved Optical and Raman Spectroscopy of Photoinduced Spin Crossover: Temporal Resolution of Low-to-High Spin Optical Switching. *Journal of the American Chemical Society* **2008**, *130*, 14105.



- (389) Shim, S.; Dasgupta, J.; Mathies, R. A. Femtosecond Time-Resolved Stimulated Raman Reveals the Birth of Bacteriorhodopsin's J and K Intermediates. *Journal of the American Chemical Society* **2009**, *131*, 7592.
- (390) Hoffman, D. P.; Valley, D.; Ellis, S. R.; Crewman, M.; Mathies, R. A. Optically shaped narrowband picosecond pulses for femtosecond stimulated Raman spectroscopy. *Optics Express* **2013**, *21*, 21685.
- (391) Kovalenko, S. A.; Dobryakov, A. L.; Ernsting, N. P. An efficient setup for femtosecond stimulated Raman spectroscopy. *Review of Scientific Instruments* **2011**, *82*, 063102.
- (392) Li, Z.; Li, Z.; Zhou, M.; Wang, Y.; Men, Z.; Sun, C. Stimulated Raman scattering of lattice translational modes in liquid heavy water. *Optics Letters* **2012**, *37*, 1319.
- (393) Li, Z.; Shan, X.; Li, Z.; Cao, J.; Zhou, M.; Wang, Y.; Men, Z.; Sun, C. Estimating the pressure of laser-induced plasma shockwave by stimulated Raman shift of lattice translational modes. *Applied Physics Letters* **2012**, *101*, 029108.
- (394) Rakesh Kumar, V.; Prem Kiran, P. Onset of ice VII phase of liquid water: role of filamentation in stimulated Raman scattering. *Optics Letters* **2015**, *40*, 2802.
- (395) Men, Z.; Li, Z.; Zhou, M.; Lu, G.; Zou, B.; Li, Z.; Sun, C. Stimulated Raman scattering from ice-VIII by shock-induced compression in liquid water. *Physical Review B* **2012**, *85*, 092101.
- (396) Yui, H.; Sawada, T. Interaction of Excess Electrons with Water Molecules at the Early Stage of Laser-Induced Plasma Generation in Water. *Physical Review Letters* **2000**, *85*, 3512.
- (397) Shim, S.; Mathies, R. A. Femtosecond Raman-Induced Kerr effect spectroscopy. *Journal of Raman Spectroscopy* **2008**, *39*, 1526.
- (398) Frontiera, R. R.; Shim, S.; Mathies, R. A. Origin of negative and dispersive features in anti-Stokes and resonance femtosecond stimulated Raman spectroscopy. *The Journal of Chemical Physics* **2008**, *129*, 064507.
- (399) Pontecorvo, E.; Ferrante, C.; Elles, C. G.; Scopigno, T. Spectrally tailored narrowband pulses for femtosecond stimulated Raman spectroscopy in the range 330-750 nm. *Optics Express* **2013**, *21*, 6886.
- (400) Zhu, L.; Liu, W.; Fang, C. A versatile femtosecond stimulated Raman spectroscopy setup with tunable pulses in the visible to near infrared. *Applied Physics Letters* **2014**, *105*, 041106.
- (401) Dunlap, B.; Richter, P.; McCamant, D. W. Stimulated Raman spectroscopy using chirped pulses. *Journal of Raman Spectroscopy* **2014**, *45*, 918.

- (402) Shreve, A. P.; Cherepy, N. J.; Franzen, S.; Boxer, S. G.; Mathies, R. A. Rapid-flow resonance Raman spectroscopy of bacterial photosynthetic reaction centers. *Proceedings of the National Academy of Sciences of the United States of America* **1991**, *88*, 11207.
- (403) Shreve, A. P.; Cherepy, N. J.; Mathies, R. A. Effective Rejection of Fluorescence in Raman Spectroscopy Using a Shifted Excitation Difference Technique. *Applied Spectroscopy* **1992**, *46*, 707.
- (404) McClain, B. L.; Finkelstein, I. J.; Fayer, M. D. Vibrational echo experiments on red blood cells: Comparison of the dynamics of cytoplasmic and aqueous hemoglobin. *Chemical Physics Letters* **2004**, *392*, 324.
- (405) Spector, I. C.; Olson, C. M.; Huber, C. J.; Massari, A. M. Simple fully reflective method of scatter reduction in 2D-IR spectroscopy. *Optics Letters* **2015**, *40*, 1850.
- (406) Borysow, J.; Taylor, R. H.; Keto, J. W. Raman-Induced Kerr Effect Spectroscopy of Solutions. *Journal of Raman Spectroscopy* **1989**, *20*, 203.
- (407) Foggi, P.; Righini, R.; Torre, R.; Kamalov, V. F. Molecular dynamics of  $\beta$ -carotene in solution measured by subpicosecond transient optical Kerr effect. *Chemical Physics Letters* **1992**, *193*, 23.
- (408) Foggi, P.; Kamalov, V. F.; Righini, R.; Torre, R. Resonance-enhanced time-resolved optical Kerr effect of  $\beta$ -carotene in solution. *Optics Letters* **1992**, *17*, 775.
- (409) Orczyk, M. E.; Samoc, M.; Swiatkiewicz, J.; Manickam, N.; Tomoaia-Cotisel, M.; Prasad, P. N. Optical heterodyning of the phase-tuned femtosecond optical Kerr gate signal for the determination of complex third-order susceptibilities. *Applied Physics Letters* **1992**, *60*, 2837.
- (410) Orczyk, M. E.; Samoc, M.; Swiatkiewicz, J.; Prasad, P. N. Dynamics of third-order nonlinearity of canthaxanthin carotenoid by the optically heterodyned phase-tuned femtosecond optical Kerr gate. *The Journal of Chemical Physics* **1993**, *98*, 2524.
- (411) Segal, J.; Huppert, D.; Fainberg, B. Resonance heterodyne optical Kerr effect spectroscopy of population wave packets with intense chirped pulses. *Journal of Luminescence* **2003**, *102-103*, 669.
- (412) Hellerer, T.; Eneider, A. M. K.; Zumbusch, A. *Applied Physics Letters*. **2004**, *85*, 25.
- (413) Oron, D.; Dudovich, N.; Silberberg, Y. Femtosecond Phase-and-Polarization Control for Background-Free Coherent Anti-Stokes Raman Spectroscopy. *Physical Review Letters* **2003**, *90*, 213902.
- (414) Bremard, C.; Dhamelincourt, P.; Laureyns, J.; Turrell, G. The Effect of High Numerical-Aperture Objectives on Polarization Measurements in Micro-Raman Spectrometry. *Applied Spectroscopy* **1985**, *39*, 1036.

- (415) Shim, S.; Mathies, R. A. Generation of narrow-bandwidth picosecond visible pulses from broadband femtosecond pulses for femtosecond stimulated Raman. *Applied Physics Letters* **2006**, *89*, 121124.
- (416) Xing, Q.; Yoo, K. M.; Alfano, R. R. Conical emission by four-photon parametric generation by using femtosecond laser pulses. *Applied Optics* **1993**, *32*, 2087.
- (417) Marangoni, M.; Frida, D.; Quintavalle, M.; Cirimi, G.; Pigozzo, F. M.; Manzoni, C.; Baronio, F.; Capobianco, A. D.; Cerullo, G. Narrow-bandwidth picosecond pulses by spectral compression of femtosecond pulses in a second-order nonlinear crystal. *Optics Express* **2007**, *15*, 8884.
- (418) Conforti, M.; Baronio, F.; De Angelis, C. From femtosecond infrared to picosecond visible pulses: temporal shaping with high-efficiency conversion. *Optics Letters* **2007**, *32*, 1779.
- (419) Marangoni, M.; Brida, D.; Conforti, M.; Capobianco, A. D.; Manzoni, C.; Baronio, F.; Nalesso, G. F.; De Angelis, C.; Ramponi, R.; Cerullo, G. Synthesis of picosecond pulses by spectral compression and shaping of femtosecond pulses in engineered quadratic nonlinear media. *Optics Letters* **2009**, *34*, 241.
- (420) Liebel, M.; Schnedermann, C.; Wende, T.; Kukura, P. Principles and Applications of Broadband Impulse Vibrational Spectroscopy. *The Journal of Physical Chemistry A* **2015**, *119*, 9506.
- (421) Zhu, L.; Liu, W.; Fang, C. Tunable sideband laser from cascaded four-wave mixing in thin glass for ultra-broadband femtosecond stimulated Raman spectroscopy. *Applied Physics Letters* **2013**, *103*, 061110.
- (422) Lagutchev, A.; Hambir Selezion, A.; Dlott, D. D. Nonresonant Background Suppression in Broadband Vibrational Sum-Frequency Generation Spectroscopy. *The Journal of Physical Chemistry C* **2007**, *111*, 13645.
- (423) Lumeau, J.; Glebov, L. B.; Smirnov, V. Tunable narrowband filter based on a combination of Fabry-Perot etalon and volume Bragg grating. *Optics Letters* **2006**, *31*, 2417.
- (424) Raoult, F.; Boscheron, A. C. L.; Husson, D.; Sauteret, C.; Modena, A.; Malka, V.; Dorchies, F.; Migus, A. Efficient generation of narrow-bandwidth picosecond pulses by frequency doubling of femtosecond chirped pulses. *Optics Letters* **1998**, *23*, 1117.
- (425) Donaldson, P. M.; Guo, R.; Fournier, F.; Gardner, E. M.; Barter, L. M. C.; Barnett, C. J.; Gould, I. R.; Klug, D. R.; Palmer, D. J.; Willison, K. R. Direct identification and decongestion of Fermi resonances by control of pulse time ordering in two-dimensional IR spectroscopy. *The Journal of Chemical Physics* **2007**, *127*, 114513.

- (426) Hendra, P. J.; Loader, E. J. Laser Raman Spectra of Adsorbed Species. *Transactions of the Faraday Society* **1971**, *67*, 828.
- (427) Ghavami Sabouri, S.; Khorsandi, A. Multisegment oven scheme for Guoy phase shift compensation in second-harmonic generation. *Applied Optics* **2015**, *54*, 8580.
- (428) Moutzouris, K.; Papamichael, M.; Betsis, S. C.; Stavrakas, I.; Hloupis, G.; Triantis, D. Refractive, dispersive, and thermo-optic properties of twelve organic solvents in the visible and near-infrared. *Applied Physics B* **2014**, *116*, 617.
- (429) Ciddor, P. E. Refractive index of air: new equations for the visible and near infrared. *Applied Optics* **1996**, *35*, 1566.